

POLY(S-ALKYLSULFONYL-L-CYSTEINE)  
IN MODULAR NANOPARTICLE SYNTHESIS

EXPLORING KEY FACTORS FROM DISULFIDE STABILIZATION,  
POLYPEPT(O)IDE ARCHITECTURES TO  
SECONDARY STRUCTURES

Dissertation  
zur Erlangung des Grades  
"Doktor der Naturwissenschaften"  
im Promotionsfach Chemie

am Institut für Organische Chemie  
Fachbereich 09: Chemie, Pharmazie und Geowissenschaften  
Johannes Gutenberg-Universität

OLGA SCHÄFER  
geboren in Karaganda (Kasachstan)

Mainz, Juni 2018









## ABSTRACT

---

RNA interference (RNAi) enables the silencing of gene expression demonstrating enormous clinical potential. Systemic application of RNAi therapeutics, however, requires delivery strategies evading enzymatic degradation in combination with stability in blood for long systemic circulation. This thesis comprises the consecutive development of polypept(o)ide-based core-shell carrier systems to fulfill this task.

Polypept(o)ides show great promise as a synthetic delivery platform in medical application and allow for a controlled synthesis of well-defined materials with conformational and chemical diversity. The presented work closes a relevant synthetic gap in polymerization of these materials with the development of *S*-alkylsulfonyl-L-cysteines. The established novel protective and activating group for thiols, for the first time, mediates direct chemoselective disulfide formation in compatibility with the nucleophilic ring-opening polymerization strategy. (Multi)block copolypept(o)ides with orthogonal thiol reactivity could thus be sequentially polymerized and were implemented in secondary structure-modulated self-assembly of cross-linked nanoparticles with control over size, morphology as well as functionality. *In vivo* application of the resulting cationic systems revealed outstandingly stable blood circulation in combination with passive tumor accumulation and a low systemic burden. Eventually, RNAi mediated knockdown in solid tumors was realized upon systemic delivery by cationic, cross-linked polypept(o)ide-based systems, concluding this journey towards gene delivery vectors in systemic application.

## KURZDARSTELLUNG

---

RNA-Interferenz (RNAi) ermöglicht die Hemmung von Genexpression und zeigt ein enormes klinisches Potential. Für systemische Anwendungen von RNAi-Therapeutika bedarf es jedoch Transportstrategien, welche den enzymatischen Abbau verhindern sollen; dies in Kombination mit Stabilität im Blut für eine lange systemische Zirkulation. Zu diesem Zweck umfasst die vorliegende Dissertation die fortwährende Entwicklung von Kern-Schale-Systemen auf Basis von Polypept(o)iden.

Polypept(o)ide als synthetische Plattform sind hervorragend geeignet für medizinische Anwendungen und erlauben die kontrollierte Synthese wohldefinierter Materialien von struktureller und chemischer Vielfalt. Eine erhebliche synthetische Lücke in der Herstellung dieser Materialien wird durch die Entwicklung von *S*-Alkylsulfonyl-L-Cysteinen geschlossen. Die eingeführte neuartige Aktivierungs- und Schutzgruppe für Thiole eröffnet erstmalig Möglichkeiten für unmittelbare, chemoselektive Bildung von Disulfiden in Kompatibilität mit nucleophiler Ring-öffnenden Polymerisation. (Multi)block Copolypept(o)ide mit orthogonaler Thiol-Reaktivität konnten so sequenziell polymerisiert werden und bieten in der Sekundärstrukturmodulierten Selbssassemblierung von vernetzten Nanopartikeln die Kontrolle über Partikelgröße, Morphologie sowie Funktionalität. Der Einsatz *in vivo* zeigt eine außerordentlich stabile Blutzirkulation von so hergestellten kationischen Systemen, sowie passive Tumoranreicherung und geringe systemische Akkumulation. Schließlich wurde, dank systemischem Transport durch kationische, vernetzte Systeme auf Polypept(o)id-Basis, ein RNAi-vermittelter Knockdown von Genexpression im Tumor demonstriert, womit ein fundamentaler Abschnitt des Weges zu Gentransfersystemen für systemische Anwendungen zurückgelegt wurde.



## PUBLICATIONS

---

List of publications written or contributed to during this PhD thesis. Several chapters have been published as indicated.

- O. Schäfer, T. Miyazaki, L. Capelôa, L. Braun, T. Khan, J. Wan, J. Schultze, K. Koynov, Y. Nie, K. Kataoka, H. Cabral, M. Barz, *to be submitted*  
⇒ Chapter 16
- O. Schäfer, D. Schollmeyer, A. Birke, R. Holm, K. Johann, C. Muhl, C. Seidl, B. Weber, M. Barz, *submitted*.  
⇒ Chapter 8
- I. Negwer, A. Best, M. Schinnerer, O. Schäfer, M. Schmidt, V. Mailänder, M. Helm, M. Barz, H.-J. Butt, K. Koynov, *Nature Communications*, **2018**, *under revision*, NCOMMS-18-12754-T.  
⇒ Chapter 14
- O. Schäfer, M. Barz, *Chemistry – A European Journal* **2018**, *24*, DOI 10.1002/chem.201800681.  
⇒ Chapter 4
- O. Schäfer\*, K. Klinker\*, L. Braun, D. Huesmann, J. Schultze, K. Koynov, M. Barz, *ACS Macro Letters* **2017**, *6*, 1140-1145.  
⇒ Chapter 10
- K. Klinker\*, O. Schäfer\*, D. Huesmann, T. Bauer, L. Capelôa, L. Braun, N. Stergiou, M. Schinnerer, A. Dirisala, K. Miyata, K. Osada, H. Cabral, K. Kataoka, M. Barz, *Angewandte Chemie Intl. Ed.* **2017**, *56*, 9608-9613.  
⇒ Chapter 12
- O. Schäfer\*, D. Huesmann\*, C. Muhl, M. Barz, *Chemistry – A European Journal* **2016**, *22*, 18085-18091.  
⇒ Chapter 7
- O. Schäfer\*, D. Huesmann\*, M. Barz, *Macromolecules* **2016**, *49*, 8146-8153.  
⇒ Chapter 9
- D. Huesmann, O. Schäfer, L. Braun, K. Klinker, T. Reuter, M. Barz, *Tetrahedron Letters* **2016**, *57*, 1138-1142.  
⇒ Chapter 6
- M. Barz, D. Huesmann, O. Schäfer, T. Reuter, A. Birke, P. Heller, *Thiol-Protected Amino Acid Derivatives and Uses Thereof*, **2014**, WO2015169908A1 / EP20140167291.



*Aus diesem hier habe ich einen Hustensaft gemacht, der zwar nicht besonders gut gegen Husten hilft, aber wenn du ihn genommen hast, fangen deine Haare so schön an zu singen, dass du den Husten völlig vergisst.*

— **Walter Moers**

Der Schreckenmeister (2009)





*für David... für alles...*



## CONTENTS

---

<b>I</b>	<b>INTRODUCTION</b>	1
1	<b>Objectives and Overview</b>	3
2	<b>Polypept(o)ides in Nanomedicine</b>	5
2.1	Polymer-Based Nanomedicines . . . . .	5
2.2	On the Synthesis of Polypept(o)ides . . . . .	8
3	<b>Rational Design of Nanocarriers</b>	13
3.1	Delivery of Nucleic Acids . . . . .	13
3.2	Systemic Application of Nanoparticles . . . . .	16
3.3	Requirements for Core-Shell siRNA Delivery Systems . . . . .	24
4	<b>Chemoselective Disulfides in Synthetic Peptides and Polymers</b>	29
4.2	Controlled Radical Polymerization . . . . .	31
4.3	Synthesis of Polypeptides . . . . .	35
4.4	Applications of Thiol-Reactive Polypeptides . . . . .	43
5	<b>Characterization Methods</b>	47
5.2	Physicochemical Characterization . . . . .	48
5.3	Biological Evaluation . . . . .	58
<b>II</b>	<b>THIOL ACTIVATION IN NCAs</b>	63
6	<b>Exploring Reactive Cysteine NCAs</b>	67
6.1	Introduction . . . . .	68
6.2	Results and Discussion . . . . .	69
6.3	Conclusion . . . . .	71
6.5	Experimental Section . . . . .	72
6.6	Supporting Information . . . . .	78
7	<b>Rethinking Cysteine Protective Groups: S-Alkylsulfonyl-L-Cysteines for Chemoselective Disulfide Formation</b>	81
7.1	Introduction . . . . .	82
7.2	Results and Discussion . . . . .	83
7.3	Conclusions . . . . .	91
7.5	Experimental Section . . . . .	92
7.6	Supporting Information . . . . .	94
<b>III</b>	<b>ORTHOGONAL REACTIVE POLYPEPT(O)IDES</b>	117
8	<b>From Absolute Monomer Purity to Controlled NCA Polymerization</b>	121
8.1	Introduction . . . . .	122
8.2	Results and Discussion . . . . .	123
8.3	Conclusion . . . . .	129
8.5	Supporting Information . . . . .	130
9	<b>Poly(S-Ethylsulfonyl-L-Cysteine) for Chemoselective Disulfide Formation</b>	149
9.1	Introduction . . . . .	150
9.2	Results and Discussion . . . . .	151



9.3 Conclusion . . . . .	160
9.5 Supporting Information . . . . .	161
<b>10 Orthogonal Reactive Groups in Block Copolymers for Functional Nanoparticle Synthesis in a Single Step</b>	173
10.1 Introduction . . . . .	174
10.2 Results and Discussion . . . . .	175
10.3 Conclusion . . . . .	181
10.5 Supporting Information . . . . .	182
<b>11 Sequence Alteration of Triblock Copolypept(o)ides with Innate Thiol-Reactivity</b>	195
<b>IV SELF-ASSEMBLY OF BLOCK COPOLYPEPT(O)IDES</b>	199
<b>12 Secondary Structure-Driven Self-Assembly of Reactive Polypept(o)ides</b>	203
12.1 Introduction . . . . .	204
12.2 Results and Discussion . . . . .	205
12.3 Conclusion . . . . .	212
12.5 Supporting Information . . . . .	213
<b>13 Screening Self-Assembly of Diblock Copolypept(o)ides</b>	237
<b>14 Drug Nanocarriers in Human Blood</b>	247
<b>V CORE-SHELL SYSTEMS IN SYSTEMIC APPLICATION</b>	251
<b>15 Polypept(o)ide Nanoparticles in Systemic Circulation</b>	255
15.2 Blood Circulation of Cross-Linked Micelles . . . . .	257
15.3 Biodistribution of Cationic Nanohydrogels . . . . .	261
<b>16 Block-Sequence of Reactive Triblock Copolypept(o)ides Determines Self-Assembly and RNAi Efficacy <i>in vivo</i></b>	273
16.1 Introduction . . . . .	274
16.2 Results and Discussion . . . . .	275
16.3 Conclusion . . . . .	283
16.5 Supporting Information . . . . .	284
<b>VI SUMMARY AND OUTLOOK</b>	301
<b>17 Summary</b>	303
<b>18 Outlook</b>	305
<b>VII APPENDIX</b>	307
LIST OF FIGURES	309
LIST OF SCHEMES	313
LIST OF TABLES	314
LIST OF ACRONYMS	315
BIBLIOGRAPHY	319



Part I  
INTRODUCTION







## OBJECTIVES AND OVERVIEW

---

This thesis evolved around the subject of chemoselective disulfide formation mediated by *S*-alkylsulfonyl-L-cysteines for stabilization of polypept(o)ide-based core-shell carrier systems in systemic application as nanomedicines. To fulfill this goal, protective and activating groups are desired in compatibility with the ring-opening polymerization of  $\alpha$ -amino acid *N*-carboxyanhydrides for synthesis of di- and triblock copolypept(o)ides with orthogonal thiol reactivity. By secondary structure-modulated self-assembly, a versatile nanoparticle platform is then accessible with control over size, morphology and functionality, resulting in long circulating, disulfide stabilized nanocarriers which were eventually employed in systemic gene delivery.

Polypept(o)ides, which feature hybrid blocks of a polypeptide and polypeptoid, are employed in this work as a promising material for nanoparticles in medical application. Synthesis is readily performed on a large scale by ring-opening polymerization (ROP) of  $\alpha$ -amino acid *N*-carboxyanhydride (NCA) monomers, if sequential control is expendable. The resulting polypept(o)ides combine high stability in aqueous media with enzymatic degradability, provide the option to form secondary structures and offer intrinsic multifunctionality of amino acid side chains, marking it a distinguished biomaterial. Since reliable control over materials for medical applications is critical, Chapter 8 elaborates on the impact of monomer purity on ROP as evaluated by X-ray diffraction of numerous NCAs.

With focus on nanomedicines for systemic application, this thesis tackles challenges and provides strategies in nanoparticle design, stressing the importance of controlled carrier synthesis and stabilization. In this context, disulfide mediated cross-linking is introduced and strategies in different polymerization techniques towards directed formation of asymmetric disulfides in synthetic peptides and polymers are discussed in Chapter 4. Thus, the implementation of thiol-reactive moieties for disulfide-mediated stabilization of polypept(o)ide-based nanomedicines was envisioned by use of the thiol side chain of the amino acid cysteine. However, at the origin of investigation, strategies for chemoselective formation of asymmetric disulfides compatible with nucleophilic conditions of the ROP of NCAs were completely lacking.

The desired balance between stability against amine initiators employed in NCA ROP and reactivity towards thiols is not a trivial task to achieve, as portrayed in PART II. The synthetic effort on moieties combining properties of a protective and activating group is presented in Chapter 6, peaking in the development of the novel *S*-alkylsulfonyl group in Chapter 7. Stability towards *N*-nucleophiles, as well as immediate reac-

tivity upon exposure to thiols is evaluated synthetically and by density functional theory DFT calculations of the relevant frontier orbitals, for validation on compatibility of the *S*-alkylsulfonyl group with NCA ROP, paired with chemoselective disulfide formation.

Controlled polypept(o)ide synthesis is evaluated in PART III of this thesis. As stability of the *S*-alkylsulfonyl group during ROP is ensured, polymerization conditions are optimized in Chapter 9, as deduced by kinetic evaluation on poly(*S*-alkylsulfonyl-L-cysteines) (PCysSO<sub>2</sub>R), revealing an innate tendency to exhibit secondary structures. Orthogonal polymer side chain reactivity of the PCysSO<sub>2</sub>R segment is further evaluated in trifunctional PSar-*block*-PCysSO<sub>2</sub>Et diblock copolypept(o)ides in combination with chain end functionality for covalent end group modification (Chapter 10). The versatile synthetic approach of sequential NCA polymerization employing PCysSO<sub>2</sub>Et for thiol reactivity, is also demonstrated in the synthesis of triblock copolypept(o)ides upon sequence permutation (Chapter 11).

With amphiphilic PSar-*block*-PCysSO<sub>2</sub>Et block copolypept(o)ides at hand, self-assembly and nanoparticle stabilization were investigated in PART IV. The polycysteine segment drives nanostructure formation upon its hydrophobic nature, as well as by secondary structure stabilization, and provides thiol-reactive side chains for stabilization of the resulting core-shell structures by core cross-linking. Independent control over particle size, morphology and core functionality is enabled by the unique physico-chemical properties of PSar-*block*-PCysSO<sub>2</sub>Et, as will be introduced for self-assembly structures in Chapter 12 and systematically optimized in Chapter 13. The significance of covalent carrier modification for applications *in vivo*, as achieved for polypept(o)ide-based systems in this thesis by core cross-linking and covalent polymer end group modification, is investigated by near-infrared fluorescence correlation spectroscopy performed in full human blood (Chapter 14).

The final part of this thesis (PART V) combines findings on orthogonal thiol-reactivity, block copolypept(o)ide synthesis and secondary structure stabilization, to accomplish polypept(o)ide-based systems for systemic application as nanomedicines. *In vivo* studies of cross-linked particles varying in size, morphology and core polarity provide substantial information on blood circulation and biodistribution (Chapter 15). Exciting findings on stable circulation of polycationic systems in combination with passive tumor targeting and low systemic accumulation, drive the investigation of polypept(o)ide-based carriers for systemic siRNA delivery (Chapter 16). With this rationale, triblock copolypept(o)ide are employed featuring an outer shielding PSar block in conjunction with a PCysSO<sub>2</sub>R segment, mediating bioreversible carrier stabilization by disulfide cross-linking, and a PLys block for stable siRNA complexation. The influence of block sequence on carrier microstructure and thus performance is examined upon alteration of the triblock sequence. Ultimately, lead candidates are implemented in a mammary carcinoma animal model, for siRNA mediated knockdown of a reporter gene in the tumor.

## 2.1 POLYMER-BASED NANOMEDICINES

Numerous, sometimes life-threatening, diseases arise from deviations in biological processes on the molecular or nanoscale level. Critical defects may originate from mutated genes, infections caused by viruses or bacteria or misfolded proteins to name some sources for malfunction. This complexity of the underlying pathologies gave rise to a multitude of therapeutic approaches rooted in nanotechnology, establishing the field of nanomedicine.<sup>[1-3]</sup> The multidisciplinary nature of nanotechnologies results, however, in a fairly stretched terminology of nano-dimensional carrier systems (especially considering the discrete dimensions of the materials). In general, a *nanomaterial* is defined as a "material having one or more external dimensions in the nanoscale (1 - 100 nm)."<sup>[4]</sup> However, by considering materials approximately up to 300 nm in diameter, many applications with significant contribution in the field of nanomedicine can be included.<sup>[5]</sup> In general, the physiological behavior on this scale is definitely not dictated by size alone, but is also highly dependent on material- and geometry-characteristics. The examination of nanoparticle dimension serves here as a rough estimate to outline the term nanomedicine. An overview of established nanotherapeutic platforms is given in Figure 2.1, illustrating the manifold approaches in nanomedicine used to address clinical relevant targets.

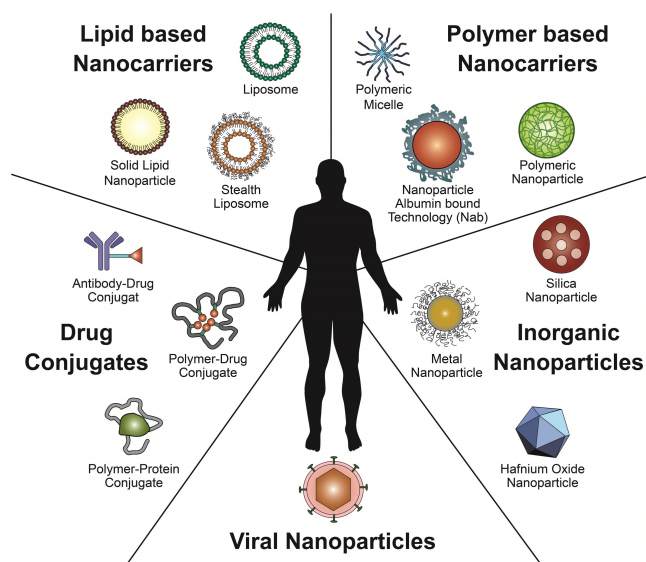


Figure 2.1: Schematic illustration of nanotherapeutic platforms such as drug conjugates, lipid-based nanocarriers, polymer-based nanocarriers, inorganic nanoparticles and viral nanoparticles.<sup>[3]</sup>

The majority of approved nanomedicines or under ongoing clinical investigation are already clinically approved drugs improved by nanoformulation as summarized in Table 2.1. This approach serves to overcome limitations of the therapeutic active agents such as poor solubility, premature degradation in plasma, poor biodistribution and severe side effects. Thus, formulations of highly toxic or poorly soluble drugs such as amphotericin B and paclitaxel, have shown the greatest clinical success.<sup>[6]</sup>

Table 2.1: Approved nanotherapeutics.<sup>[6]</sup>

Trade Name	Formulation	Indication	Initial Approval Date
Exparel	Pegylated Adenosine Deaminase	SCID <sup>†</sup>	1990
Oncospar	Pegylated Asparaginase	ALL	1994
Doxil	Liposomal Doxorubicin	Kaposi's Sarcoma, Ovarian Cancer, MBC <sup>†</sup>	1995
Abelcet, Amphotec, Ambisome	Liposomal Amphotericin B	Fungal Infections	1995, 1996, 1997
Copaxone	Glutaramer Acetate	Multiple Sclerosis	1996
Ferumoxsil	Siloxane-Coated Iron Oxide	Oral Contrast Agent	1997
Pegintron	Pegylated Interferon $\alpha$ -2b	Hepatitis C	2001
Pegasys	Pegylated Interferon $\alpha$ -2a	Hepatitis B, C	2002
Neulasta	Pegylated Filgrastim	Chemotherapy-induced Neutropenia	2002
Abraxane	Albumin Bound Paclitaxel	Advanced lung, pancreatic, breast cancers	2005
Feraheme	Carbohydrate-Coated Iron Oxide	Anemia of Chronic Kidney Disease	2007
Depocyte	Liposomal Cytarabine	Lymphomatous Meningitis	2007
Exparel	Liposomal Bupivacaine	Post-operative Pain	2011
Sienna+	Dextran-Coated Iron Oxide	Sentinel Lymphnode Mapping <sup>†</sup>	2011
Marquibo	Liposomal Vincristine	Adult AML	2012

ALL, Acute Lymphoblastic Leukemia; MBC, Metastatic Breast Cancer; AML, Acute Myelogenous Leukemia.  
<sup>†</sup> Approved by European Regulatory Agency but not FDA.

#### *Delivery strategies based on polymers.*

Along with successful delivery platforms such as liposomal formulations, inorganic nanoparticles, antibody-drug conjugates and viral vectors, approaches employing polymer-based delivery strategies are of great interest. Polymer-based technologies have influenced practically every branch of medicine, including ophthalmology, pulmonary, pain medicine, endocrinology, oncology, cardiology, orthopedics, immunology, neurology and dentistry.<sup>[7,8]</sup> Examples of polymer-based products currently in clinical practice are: **Atridox** (poly(D,L-lactide) (PLA) in *N*-ethyl-2-pyrro-lidone (NMP) and doxycycline / chronic parodontitis),<sup>[9]</sup> **Capronor** (poly( $\epsilon$ -caprolactone and levonoregesrel / contraceptive),<sup>[10]</sup> **Genexol-PM** (PEG-PLA micelles and paclitaxel / cancer (breast, lung, prostate, and pancreatic)),<sup>[11]</sup> **Gliadel** (poly(bis(*p*-carboxyphenoxy)) propane : sebacic acid 20:80 and carmustine / brain cancer along with surgery and irradiation therapy),<sup>[12]</sup> **Nanoxel** (PEGylated micelle of *N*-isopropyl acrylamide (NIPAM) and vinylpyrrolidone (VP) copolymer and paclitaxel / cancer (breast, lung, prostate, and pancreatic)),<sup>[13]</sup> **Sando-statin LAR** (PLGA-glucose copolymer and octreotide / growth hormone suppression),<sup>[14]</sup> **Zoladex** (D,L-lactide glycolide copolymer (PLGA) and goserelin acetate / prostate cancer and endometrioses).<sup>[15]</sup>

As displayed in Figure 2.2, different designs of polymer-based nanomedicines are available such as A) polymer-protein or B) polymer-drug conjugates, C) polymeric micelles obtained by self-assembly of block copolymers, D) core cross-linked nanogels with ability to swell in the core, E) vesicle formation of block copolymers into polymersomes,

F) branched dendrimers or G) polyplexes as non-viral vectors for delivery of negatively charged nucleic acids.<sup>[16]</sup>

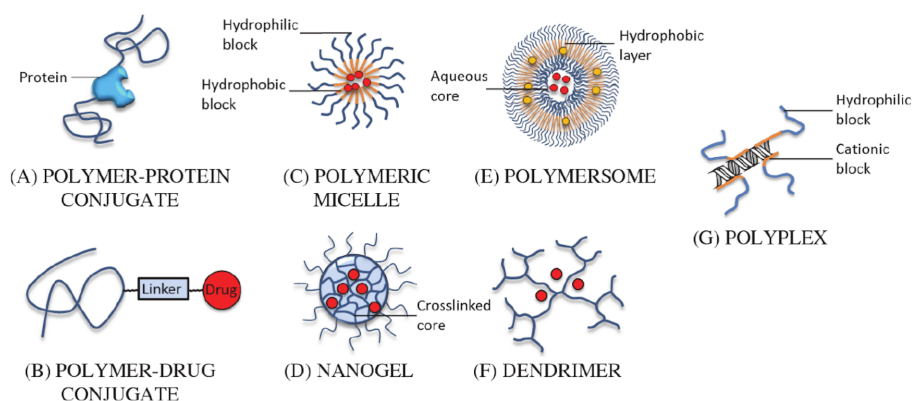


Figure 2.2: Classes of polymer-based nanomedicines for pharmaceutical applications.<sup>[16]</sup>

Polymeric materials offer variability on the structural level (e. g. linear, branched, grafted, star-shaped, homo- or block copolymer architectures and their respective formulations as nanomedicines) as well as in their chemical nature. In this context, additional functionalities in form of stimuli-responsive moieties in the nanocarrier may be desired.<sup>[17]</sup> As summarized in Figure 2.3, spatial- temporal- or dosage-controlled release of a therapeutic active agent from a polymeric nanocarrier can be induced by various internal or external stimuli. Especially for systemic application, delivery systems responding to endogenous stimuli such as change in pH or redox potential are of eminent importance. Deviations in pH, for example, are associated with pathological conditions in cancer or inflammation. Further, redox-sensitive materials are of great interest for delivery to intracellular compartments,<sup>[18]</sup> since materials featuring e. g. disulfide stabilization are stable in mildly oxidizing extracellular milieus such as the blood stream, but are rapidly cleaved once exposed to the reducing environment of intracellular fluids.<sup>[19]</sup>

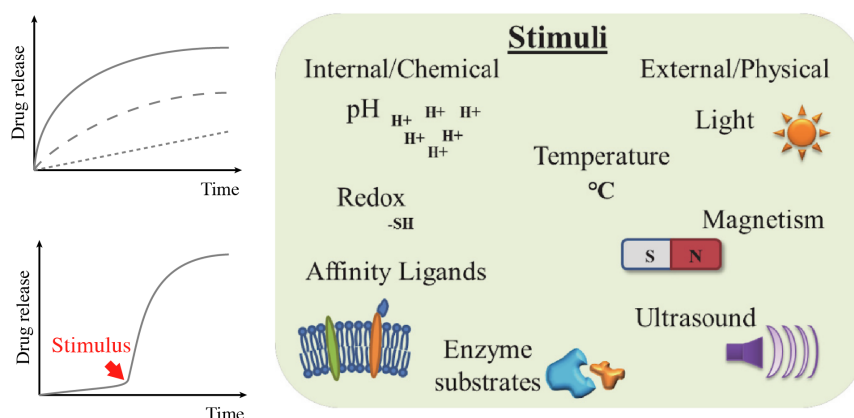


Figure 2.3: External and internal stimuli, which can be used to control the release of active agents from polymer-based nanomedicines (adapted from<sup>[16]</sup>).

This desired "smart" behavior requires highly functional and biomimetic polymeric materials as often accomplished by natural substances. And while much has been realized with traditional synthetic polymers, there is a need for bio-compatible and bio-degradable polymers prepared by robust methods enabling precise control over chemical composition, architecture and incorporation of readily functionalized building blocks. Such complex requirements can pose a challenge for many synthetic polymer-based systems. Due to narrow possibilities for modification, already balanced material properties can be negatively altered by chemical modifications. With applications as nanomedicines in mind, the incorporation of peptide and polypeptide domains allows for introduction of intrinsic functionality of building blocks, moieties for chemical modification, stimuli responsiveness and structural stability. In addition, they combine stability against hydrolysis with enzymatic degradability resulting in non toxic amino acids as metabolites. Hence, the next section will elaborate on synthetic approaches to polypeptides as well as polypept(o)ides as an extension of this material class.

## 2.2 ON THE SYNTHESIS OF POLYPEPT(O)IDES

The chemical structure of polypeptides is based on  $\alpha$ -amino acids as building blocks. Covalent amide bond linkages dominate the chain backbone, while the overall chemical properties are dictated by side chains of the respective amino acid. Thus, highly versatile materials can be obtained with diverse functionalities and the ability to respond to various external stimuli. For example, acidic poly(aspartic acid), poly(L-glutamic acid), neutral poly(histidine) or basic poly(L-lysine) are relevant as pH sensitive entities in nanocarrier systems.<sup>[20]</sup> Further, the redox pair of disulfides and thiols is extensively used to mediate redox-sensitivity. For this purpose, poly(L-cysteine), poly(L-methionine) as well as their derivatives are used.<sup>[21,22]</sup> Additionally, polypeptides introduce the possibility of hydrogen bonding of the backbone and hydrophobic interactions of side chains. This behavior enables hierarchical inter- and intra-molecular organization such as secondary structure formation, which has an impact on solubility properties of the material.<sup>[23,24]</sup> Upon combination of polypeptides based on  $\alpha$ -amino acids and polypeptoids consisting of *N*-substituted amino acids, hybrid materials defined as polypept(o)ides are obtained.<sup>[25]</sup> This introduces the option to exploit the "stealth"-like properties of the polypeptoid polysarcosine (poly(*N*-methylated glycine)),<sup>[26,27]</sup> which has the potential to surrogate the role of poly(ethylene glycol) (PEG) in biomedical applications.<sup>[28–30]</sup>

*N*CAs as monomers.

The amine-initiated ring-opening polymerization (ROP) of  $\alpha$ -amino acid *N*-carboxyanhydrides (NCA) was pioneered by Sigmund and Wessely<sup>[31]</sup> Szwarc,<sup>[32]</sup> as well as Ballard and Bamford.<sup>[33,34]</sup> If sequence control is expendable, it represents now the most commonly applied technique for rapid and large-scale synthesis of both, polypeptides and



polypeptoids.<sup>[35–38]</sup> The first report on NCA synthesis is dated back to 1906, as Leuchs observed methyl- or ethyl-chloride formation upon heating of *N*-ethoxycarbonyl and *N*-methoxycarbonyl amino acid chlorides (Figure 2.4 A).<sup>[39]</sup> An alternative method commonly used today was proposed by Fuchs in 1922<sup>[40]</sup> and improved by Farthing.<sup>[41,42]</sup> It utilizes directly the amino acid which is reacted with phosgene or a phosgene analogon for a more convenient synthesis (Figure 2.4 B).

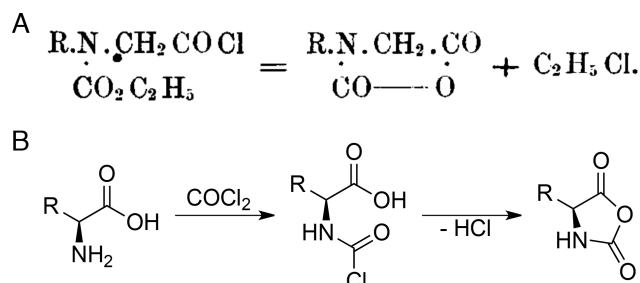


Figure 2.4: A) First report of NCA synthesis<sup>[43]</sup> and B) NCA synthesis by the FUCHS-FARTHING method.<sup>[40–42]</sup>

The ROP of NCAs can potentially follow two pathways as illustrated in Figure 2.5. An attack by nucleophilic initiators on the C-5 will follow the normal amine mechanism (NAM), while deprotonation by initiators with basic character will lead to the activated monomer mechanism (AMM).

*Modes of ring-opening NCA polymerization.*

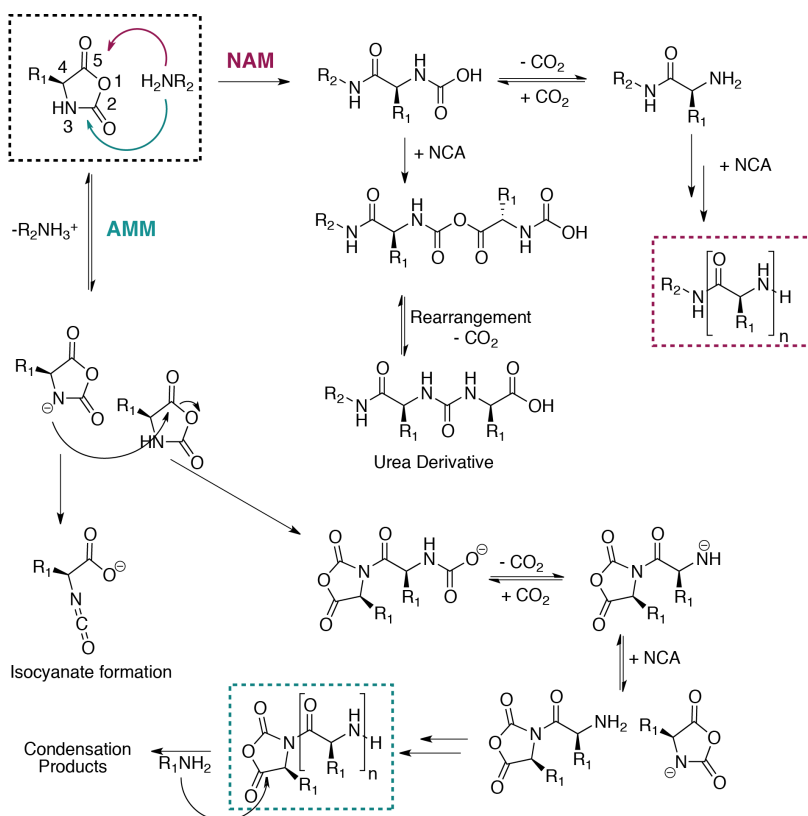


Figure 2.5: Mechanistic pathways for the nucleophilic ring-opening NCA polymerization and frequent side reactions.<sup>[25]</sup>

Ring-opening by primary or secondary amines following the NAM is preceded by subsequent decarboxylation. Thus, another terminal amine is generated and is available for further chain propagation. Polymerizations following the NAM are of living character, as indicated by incorporation of initiator molecules into every polymer chain, linear pseudofirst order reaction kinetics and faster initiation compared to chain propagation.<sup>[44]</sup> This mechanism portrays the desired NCA polymerization pathway, offering control over molecular weights, polymer dispersity and end-group integrity. In contrast, abstraction of the acidic proton by initiators with basic character (e. g. tertiary amines, hydroxides or alkoxides), initiates the undesired AMM.<sup>[45,46]</sup> The generated NCA-anion is highly reactive and can initiate polymerization itself, leading to oligomers with two reactive end groups. Ultimately, an overlap of ROP and condensation processes occurs at the growing polypeptide chain, leading to broad molecular weight distributions. Since NCAs based on *N*-substituted amino acids like sarcosine do not feature a cleavable proton, they follow exclusively the NAM. Thus, following characteristics of living polymerization, high molecular weight polymers upon narrow dispersities are readily available.<sup>[26,44,47]</sup>

*Controlled NCA polymerization.*

Control over polymerization conditions proves a crucial element in NCA polymerization to obtain well-defined materials with narrow dispersities and high molecular weights. The strategies cover variation of initiators such as rare earth catalysts,<sup>[48]</sup> amine hydrochlorides,<sup>[49]</sup> organo-nickel initiators,<sup>[50]</sup> ammonium salts with tetrafluoroborate anions<sup>[51]</sup> as well as hexamethyldisilazane-mediated polymerization approaches.<sup>[52]</sup> Further, high purity reagents employed in high vacuum techniques,<sup>[53]</sup> variation in temperature<sup>[54,55]</sup> and the introduction of N<sub>2</sub> flow<sup>[56]</sup> assure control over NCA polymerization. Purity of employed solvents, initiators and especially NCA monomers is crucial for a controlled ring-opening polymerization mechanism, since impurities may act as chain-transfer agents, terminate growing species or catalyze side reactions. Monomer purification by means of crystallization, or by sublimation (as introduced by Ballard *et al.* for sarcosine NCA<sup>[33,34]</sup>) is a relevant measure to improve the outcome of the polymerization. All purification procedures have to be performed upon exclusion from air (and thus moisture) and employ absolute solvents to ensure the absence of water.<sup>[53,57]</sup>

The benefit of ring-opening polymerizations of NCAs in a controlled fashion is the possibility to construct highly defined, multi functional polypept(o)idic materials as illustrated in Figure 2.6. Random copolymerizations are feasible as well as sequential polymerizations, leading to various architectures such as multiblock copolypept(o)ides, star-like (block co)polypept(o)ides and cylindrical brush polypept(o)ides (Figure 2.6 *left*). Apart from conformational diversity, a remarkably versatile chemical toolbox is readily available for NCA ROP. A multitude of reactive NCAs can be polymerized or accessed by post polymerization modification reactions<sup>[21,58]</sup> and the choice of specialized ini-



tiator molecules allows for end-group functionality<sup>[59,60]</sup> or backbone degradation<sup>[61,62]</sup> (Figure 2.6 *middle*). This level of complexity, however, should not compromise polymer definition, especially in light of applications in the field of nanomedicine. As illustrated exemplarily in Figure 2.6 (*right*), controlled NCA polymerization yields highly multifunctional polypept(o)idic materials with precise control over polymer dispersity, molecular architecture as well as end-group integrity.<sup>[25,63]</sup>

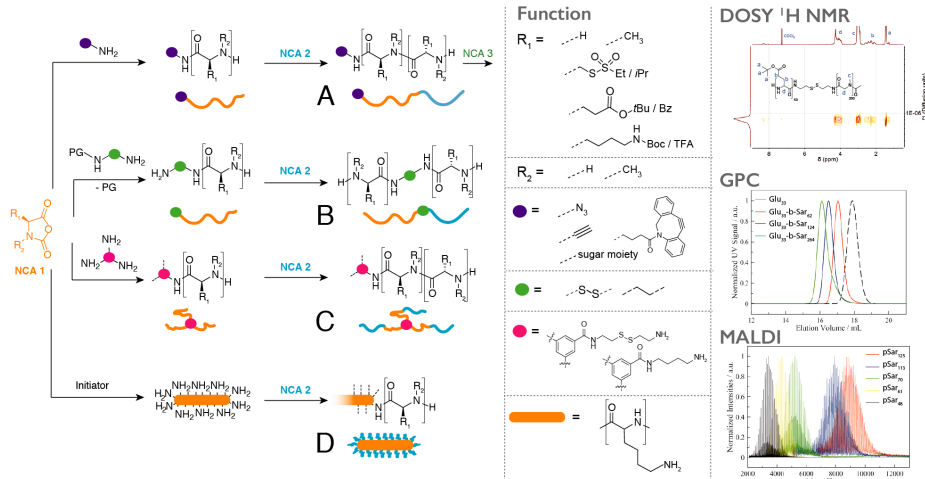


Figure 2.6: Synthetic approaches and architectures of block copolypept(o)ides: A) sequential polymerization of multiblock copolypept(o)ides, B) bifunctional initiator approach, C) star-like block copolypept(o)ides and D) cylindrical core-shell brush pept(o)ides. To the right hand side, available functionalities and exemplary characterization methods of block copolypept(o)ides (DOSY <sup>1</sup>H NMR,<sup>[61]</sup> GPC,<sup>[26]</sup> MALDI<sup>[27]</sup>).

To date, polypept(o)ide-based nanomedicines accomplish promising performances in drug delivery applications as demonstrated for microcapsules based on PSar–PGlu(OMe),<sup>[64,65]</sup> –PLys(Z)<sup>[64,66]</sup> or –PAla<sup>[28,66]</sup> block copolypept(o)ides and micelles based on PSar–b-PLLA<sup>[67,68]</sup> from Kimura and coworkers. Further, PSar–PGlu(OBn) block copolypept(o)ides were employed for drug formulations<sup>[26]</sup> and improved by mannose ligands<sup>[59]</sup> in our group. Polypept(o)ide-based vehicles for gene therapy based on PSar–PLys copolypept(o)ides were also recently explored in our group. Architectures of core-shell cylindrical brush polymers<sup>[69]</sup> were investigated for siRNA delivery as well as (multi)block copolypept(o)ide based peptoplexes for delivery of pDNA<sup>[70,71]</sup> and improved by disulfide cross-linking.<sup>[71]</sup>

Following up on the topic of delivery systems for gene therapies, the next chapter will elaborate on the concept of RNA interference (RNAi) therapeutics as well as the resulting structural and chemical requirements on delivery systems for systemic applications.

*Polypept(o)ides for nanomedical applications.*



## 3.1 DELIVERY OF NUCLEIC ACIDS

Within the last decade, gene therapy has offered promising approaches with a current overwhelming focus on cancer therapies (65.0% of clinical trials, 1688 in total) and inherited monogenetic diseases (11.1% of clinical trials, 287 in total).<sup>[72]</sup> Further, in the last five years an increased focus on alternatives to gene-addition strategies was noted, especially in dominant disease processes, where the mere introduction of a functionally intact gene prove insufficient.<sup>[72-75]</sup> In this context, approximately 20 clinical trials based on the mechanism of RNA interference (RNAi) have been initiated,<sup>[76]</sup> emphasizing the relevance to pursue clinically viable RNAi therapeutics.

The process of RNA interference (RNAi), first described by Mello and Fire in 1998,<sup>[77]</sup> allows for control over gene expression by base-pairing small interfering RNA (siRNA) with messenger RNA (mRNA) of complementary sequence<sup>[78,79]</sup> (see Figure 3.1).

*RNA interference.*

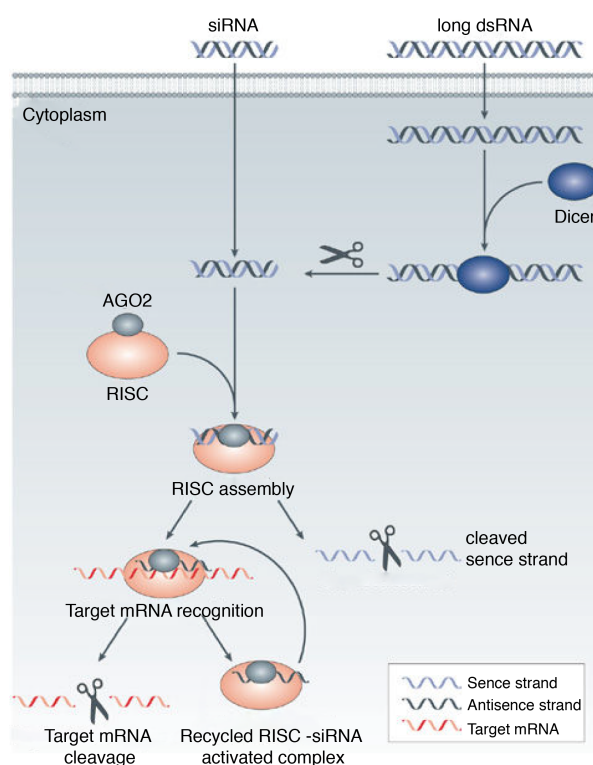


Figure 3.1: Mechanism of RNA interference mediated by small interfering RNA (siRNA) and the RNA-induced silencing complex (RISC). Cleavage of complementary mRNA by the activated RISC-siRNA complex results then in the desired silencing of the target gene.<sup>[80]</sup>

Upon cleavage of double-stranded RNA (dsRNA) by the RNase Dicer or by direct introduction of siRNA into the cytosol, a protein complex called the RNA-induced silencing complex (RISC) is formed. The protein Argonaute 2 (AGO<sub>2</sub>) in the RISC was identified as the responsible factor for mRNA cleavage,<sup>[81]</sup> which results in decreased expression of the corresponding protein. This nobel price winning discovery<sup>[82]</sup> on silencing of endogenous genes has notably developed our understanding of eukaryotic gene regulation and introduced the possibility to exploit the RNAi mechanism therapeutically.<sup>[80,83–85]</sup>

*siRNA delivery strategies.*

Most clinical trials employing siRNA based therapeutics are focused on cancer therapies (e. g. pancreas, lung, liver or solid tumors in general) but also on topical use, e. g. for ocular disorders, the respiratory tract or dermal applications. The therapeutic relevant targets range from various protein kinase types and growth factors, mutations of the p53 protein (which plays a crucial role in the cell cycle and tumor suppression) and many more.<sup>[76,86]</sup> The progress of a selection of ongoing clinical trials is summarized in Table 3.1.

In contrast to small molecule inhibitors (<500 Da), which can passively overcome cellular membranes by diffusion,<sup>[87]</sup> siRNA molecules commonly prove too large (~14 kDa) and too charged (~40 charged phosphates) to enter cells on their own.<sup>[88]</sup> Further, naked siRNA is not stable upon systemic administration due to rapid renal clearance and degradation by ribonucleases.<sup>[89]</sup> Some applications of naked siRNA molecules exist e. g. for inhalative treatment of respiratory viral infections (ALN-RSV01,<sup>[90]</sup> Alnylam Pharmaceuticals). Additionally, increased resistance to enzymatic degradation by chemical modifications of siRNA is feasible, e. g. by *O*-methylation<sup>[91,92]</sup> or charge-neutralizing phosphotriester backbone modifications.<sup>[93]</sup> Most systemic application strategies, however, rely on nanodimensional delivery systems based on lipid nanoparticles, cyclodextrins or polymers.<sup>[85]</sup> Cyclodextrins (e. g. CALAA-1,<sup>[94]</sup> Calando Pharmaceuticals) mediate efficient condensation due to strong basicity of amidine groups, but depend on PEGylation to mediate stabilization.<sup>[95]</sup> And while a wide variety of cationic and ionizable lipids is available (e. g. Atu-027,<sup>[96]</sup> Silence Therapeutics or ApoB SNALPs,<sup>[97]</sup> Tekmira), they suffer from an innate immune response which can be compensated, again, by PEGylation to enhance circulation times.<sup>[98]</sup> Thus, efficient delivery of siRNA molecules remains a crucial technological challenge in the development of RNAi therapeutics.<sup>[78,79,83,93]</sup>

Current strategies in siRNA delivery, e. g. to solid tumors, are gravitating towards polymer based core-shell systems featuring a polycationic core and a shielding corona.<sup>[100,101]</sup> Most prominently, core-shell polyion-complexes (or polyplexes) of negatively charged nucleic acids and positively charged polymers are employed for this purpose.<sup>[70,102,103]</sup> Particle formation is driven by an entropic gain due to release of counterions following multivalent polyanion-polycation interaction. In this case, dimensions are predominantly dictated by the polyanion and additional

Table 3.1: Status of siRNA based therapeutics in the clinic.<sup>[76,99]</sup>

Phase	Drug name	Target	Disease	Administration	Company
II	ALN-RSV01	RSV nucleocapsid	RSV infection	intranasal / inhaled	Anylam
II	PF-04523655	RTP801 gene	AMD, DME	intravitreal	Quark/Pfizer
II	QPI-1002	p53	acute renal failure	intravenous	Quark
II	Excellair	SY kinase	asthma	inhaled	ZaBeCor
I	CALAA-01	RRM2	solid tumors	intravenous (cyclodextrin NP)	Calando
I	ALN-VSP01	VEGF, KSP genes	liver cancer	intravenous (lipid NP)	Anylam
I	Atu-027	PKN3	solid tumors	intravenous (lipoplex)	Silence
I	ApoB SNALP	ApoB	hypercholesterolemia	intravenous (SNALP)	Tekmira
<i>Withdrawn from clinical trials</i>					
in III	Bevasiranib	VEGF A isoforms	AMD	intravitreal (naked siRNA)	OPKO
in II	AGN-211745	VEGF receptor	AMD	intravitreal (naked siRNA)	Sirma

AMD: age-related macular degeneration; ApoB: apolipoprotein B; DME: diabetic macular edema; KSP: kinesin spindle protein; NP: nanoparticle; PKN3: protein kinase N3; RRM2: ribonucleotide reductase M2 subunit; RSV: respiratory syncytial virus; SNALP: stable nucleic acid lipid particles; SYK: spleen tyrosine kinase; VEGF: vascular endothelial growth factor.

structural stabilization proves beneficial for delivery of relatively small siRNAs, in contrast to much larger DNA molecules.<sup>[85]</sup>

As an alternative, cationic nanohydrogels<sup>[104]</sup> can be employed, which are produced by self-assembly of amphiphiles and feature compartmentalization based on phase separation. Subsequent core cross-linking allows for stabilization as well as inversion of the core-polarity upon introduction of polycationic moieties. In this context, Siegwald *et al.* prepared a library of nucleic acid delivery systems based on block copolymers of poly(diethyleneglycol) methacrylate) (PDEGMA) and acrylates with epoxy side chains available for diamine cross-linking.<sup>[105]</sup> Further, Nuhn and colleagues employed nanohydrogels based on poly(triethylene glycol methyl ether methacrylate) and poly(pentafluorophenyl methacrylate) (P(MEO<sub>3</sub>MA)-*b*-P(PFPMA)) combined with oligoamine cross-linkers for siRNA delivery.<sup>[106,107]</sup> Loading of siRNA in the polycationic core is performed after particle formation, ideally without affecting particle size or shape.

Ultimately, the particular physico-chemical properties of gene delivery vectors (or of nanocarriers in general), will determine their pharmacokinetic and pharmacodynamic behavior. Thus, challenges of *in vivo* applications, relevant factors on biodistribution and strategies to promote carrier stability will be discussed in the following section.

### 3.2 SYSTEMIC APPLICATION OF NANOPARTICLES

Since intravascular degradation of naked siRNA by ribonucleases has to be avoided, nanoparticle carriers hold promise for effective intracellular delivery of RNAi therapeutics. However, abundant challenges need to be addressed by polymeric delivery vectors to promote clinical translation of RNAi-based therapeutics as illustrated in Figure 3.2.<sup>[79,108]</sup> When administered intravenously, adsorption of opsonins (plasma proteins responsible for enhanced phagocytosis) is guided by the physico-chemical properties of the particle surface. Opsonization, in turn, facilitates uptake of nano-sized carriers from the blood stream by macrophages of the mononuclear phagocyte system (MPS) in the liver, the lymph nodes and the spleen. If premature degradation and clearance was avoided, penetration of the target tissue, e. g. the tumor, and internalization poses the next challenge. Following cellular uptake, particles are processed in endosomal pathways and the siRNA cargo needs to be released into the cytosol for effective initiation of the RNAi mechanism. Impacts of the outlined barriers on nanoparticle-based siRNA delivery and strategies to overcome those challenges are multifactorial as will be discussed subsequently in detail.

*From intravenous injection to systemic circulation.*

Upon systemic administration (see Figure 3.3), distribution of nanocarriers in the blood stream follows initially the venous network to the heart and passes then entirely to the pulmonary circulation. The lung capillaries constitute some of the smallest blood vessels in the body and are responsible for the first sieving of nanocarriers. Rigid or large mor-

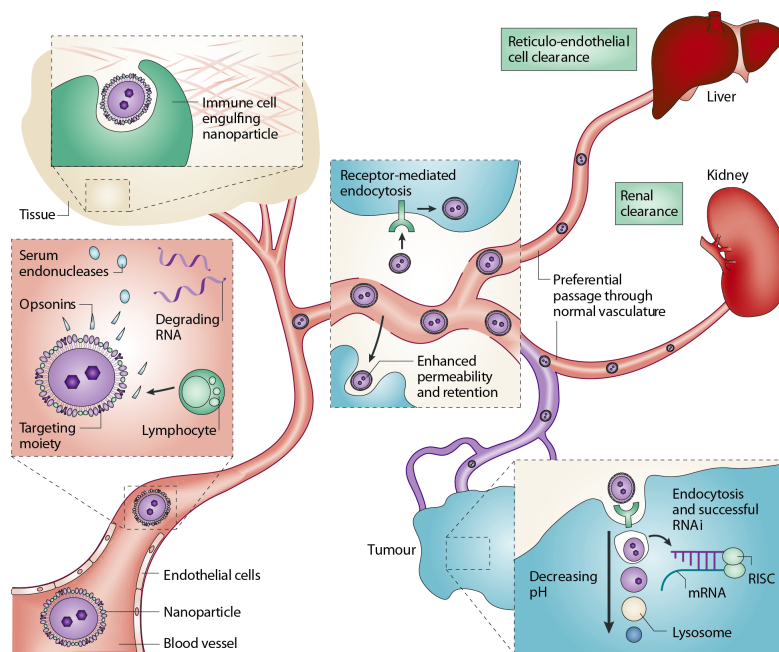


Figure 3.2: Biological barriers in intravenous delivery strategies for RNAi: degradation of naked RNA by serum endonucleases, opsonization and phagocytosis by e. g. macrophages, renal and hepatic clearance as well as trafficking to tumors by the enhanced permeability and retention effect (EPR) and receptor-mediated endocytosis. Once inside the cell, endosomal escape is the premise for interaction with the RISC and effective gene silencing (adapted from<sup>[79]</sup>).

phologies ranging from several hundred nanometers up to tens of microns, especially upon positive surface charge, are sequestered in the lungs.<sup>[109,110]</sup> Carrier instability or interaction with blood components is often responsible for aggregate formation and accumulation in the lung. However, all particles that avoid pulmonary retention, enter the systemic circulation *via* the heart. Now they are subject to the filter organs, most importantly the kidneys, the liver and the spleen (see Figure 3.4 for illustration of the functional structures).

The kidney (Figure 3.4 A) is separated in two areas, the cortex and the medulla. The nephron is the basic functional unit and spans those two parenchyma. It contains the glomerulus, which is responsible for blood filtration. The glomerular capillaries feature a highly-fenestrated endothelium (60-80 nm in size) and are covered in a thick fibrous network consisting of a glycocalyx layer, a hydrated collagen matrix and negatively charged glycoproteins. Additionally, a layer of podocytes forms filtration slits of 4-6 nm, which are ultimately responsible for high permselectivity of the filtration process in the glomerulum.<sup>[110]</sup>

Glomerular filtration, and thus accumulation in the kidneys, is a pathway relevant only for small particle species such as quantum dots or macromolecules resulting from biodegradable nanocarriers.<sup>[112,113]</sup> In approximation, proteins with hydrodynamic diameter smaller than 5-6 nm (corresponding molecular weight for globular proteins

*Renal filtration.*



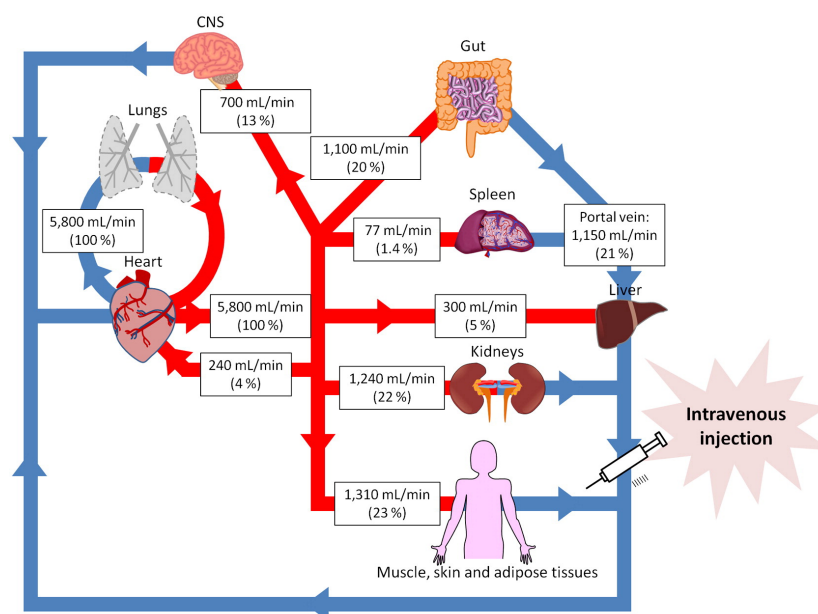


Figure 3.3: Distribution of blood flow in the pulmonary and systemic circulation pathways and percentage of blood flow.<sup>[110,111]</sup>

is 60 kDa) are freely filtered, while particles larger than 6 nm are not typically capable of glomerular filtration.<sup>[114]</sup> The molecular weight limits of renal filtration is especially relevant for bio-compatible hydrophilic polymers, which are not degraded into shorter fragments e. g. linear poly(ethylene glycol) (PEG; 30 kDa), poly(vinyl alcohol) (PVA 30 kDa), poly-(*N*-isopropylacrylamide) (PNIPAM; 32 kDa) or poly(*N*-(2-hydroxypropyl)methacrylamide) (PHPMA; 45 kDa).<sup>[110]</sup> However, macromolecules close to the threshold have to distort and squeeze through the pores. The necessary deformability is heavily affected by parameters such as polymer architecture, general backbone flexibility and hydration state.

#### *Phagocytosis in the liver.*

For particles excluded from renal clearance, the hepatobiliary system in the liver is the main pathway of excretion (Figure 3.4 B). Degradation and excretion *via* the bile is mediated primarily by phagocytosis. The liver is a highly perfused organ (fed by the hepatic artery and the portal vein), while bile drains into the gall bladder. The functional units are hexagonal liver lobules containing hepatocyte plates and the sinusoids. The sinusoids, where the arterial and portal veins merge, do not exhibit any basal membrane and are highly fenestrated (100-150 nm). This structure allows for almost unrestricted transfer to the perisinusoidal space (space of Disse) and access to the hepatocytes. However, inside the sinusoid capillaries in direct contact with the blood flow is the location of the Kupffer cells. These cells of the MPS are key to the phagocytic liver activity and constitute 80-90 % of the total macrophage population in the body.<sup>[110,114]</sup>

Kupffer cells ingest preferably opsonized particles, which are then encapsulated in phagosomes and exposed rapidly to an acidified mi-



lieu during maturation into phagolysosomes. Particle size and curvature poses a considerable effect on cell contact and internalization. Particles smaller than  $1\ \mu\text{m}$  offer less efficient contacts with the ruffled cell surface of the Kupffer cells and are mostly subject to pino- or endocytosis. Diameters of  $1\text{--}3\ \mu\text{m}$  offer optimal conditions for phagocytosis, while larger particles require severe remodeling of the cytoskeleton to achieve internalization (upper size *in vitro*  $20\ \mu\text{m}$  or 3fold exceeding volume of the macrophage).<sup>[110]</sup>

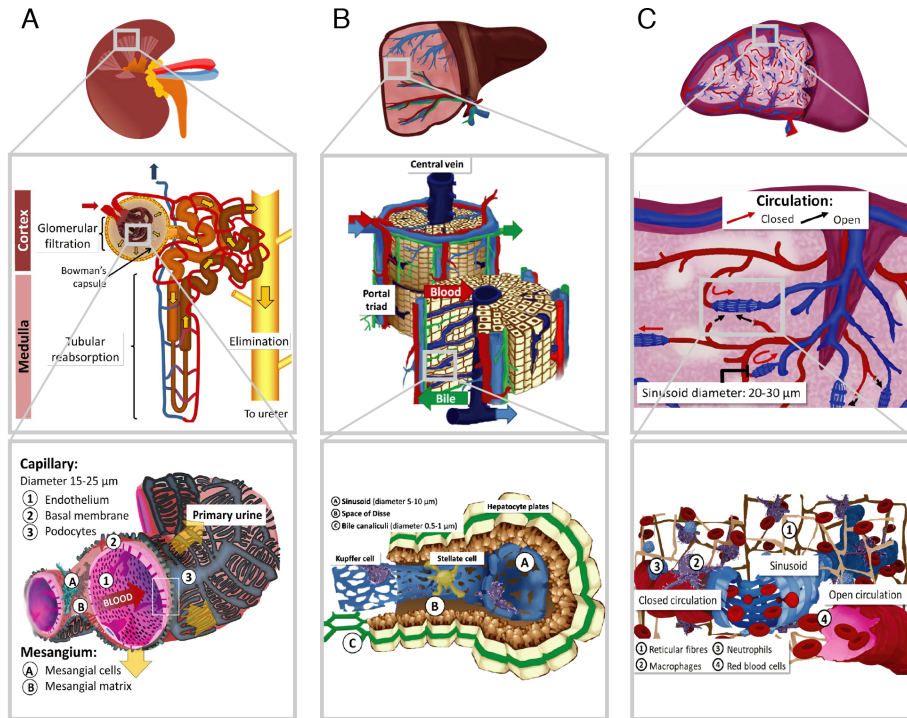


Figure 3.4: Blood filtration A) in the kidney, B) the liver and C) the spleen: (top) illustration of the whole organ, (middle) structural composition and blood flow and (bottom) structure of the functional units (adapted from<sup>[110]</sup>).

The spleen acts as a blood filter system and participates in lymphocyte maturation and recycling. The whole organ is protected by a fibrous capsule and is composed of white and red pulps (Figure 3.4 C). Its perfusing arteries empty into the splenic sinusoids (closed circulation) or directly into the parenchyma (open circulation). While the white pulp is engaged in proliferation of lymphocytes (B and T types), the red pulp is dominated by a tangled architecture of reticular fibers where blood components must pass the  $200\ \text{nm}$  fenestration of the sinusoids. In the fibrous network, aged red blood cells are filtered and pathogens are taken up by macrophages.

In general, sequestration of nanocarriers in the spleen is not desired, since immunogenic reactions can be induced such as the accelerated blood clearance (ABC) phenomenon. It describes faster blood clearance of a second administration compared to the first dose of a therapeutic agent or nanocarrier. The underlying principle is the interaction of the

*Sieving through the spleen.*

nanocarrier with B cells in the spleen, which induces antibody secretion. Upon injection of a second dose during this period of increased antibody levels (usually within 2-4 days), particles in blood are readily opsonized by circulating antibodies and subject to fast hepatic clearance.<sup>[110]</sup>

As outlined above for the most important filter organs, particle size commonly dictates the *in vivo* fate of nanocarriers (Figure 3.5 A). Upon increasing size beyond 150 nm, particles accumulate more and more in the liver and spleen. Especially very large particles of several microns are retained in the lung capillaries upon first passage. In contrast, small-sized nanoparticles (<5 nm) are subject to rapid renal filtration.

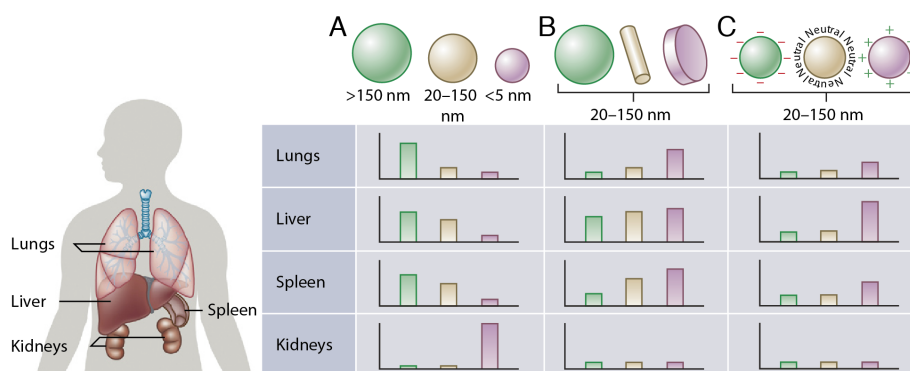


Figure 3.5: Biodistribution in organs relevant for nanoparticle filtration including lungs, liver, spleen and kidneys in relation to A) particle size, B) geometry and C) surface charge.<sup>[115]</sup>

*Influence of particle morphology...*

Different geometries of nanoparticles such as spherical, cylindrical or discoidal morphology can also have an effect on pharmacokinetics and biodistribution (Figure 3.5 B). Upon a difference in flow-characteristics and circulation halftime, both cell membrane interactions and macrophage uptake are affected. In general, rigidity promotes sequestration in the lungs, the liver as well as in the spleen in accordance to the introduced hydrodynamic diameter ranges.<sup>[110]</sup> The factor contributed by nanoparticle shape, however, not a topic commonly agreed on. For example, particles of discoidal morphologies are discussed to exhibit tumbling dynamics that promote vessel wall interaction, while smaller, spherical structures remain in a cell free layer closer to the endothelial epithel. Further, once particles come in contact with endothelial cells, cellular adhesion is also dependent on the available surface area of the nanoparticle.<sup>[115]</sup>

The validation of this perception is based on the hydrodynamic dimensions of nanoparticles in the blood and holds true only for strongly shape anisotropic structures. Particularly rigid or short elongated structures will effectively exhibit a spherical hydrodynamic shape in the blood flow due to rotation. As a consequence, they will not be affected in the same manner by physical forces in flowing blood. On the size scale of micrometers, however, filament-like micelles can align with the blood flow, which extends circulation time in comparison to spherical

counterparts as demonstrated by Discher and co-workers.<sup>[116]</sup> Further, particle curvature affects the speed of phagocytosis by macrophages, since optimal membrane spreading of macrophages is hindered by particles with high aspect ratios. Thus, spherical particles are commonly internalized faster as investigated by Mitragotri and co-workers.<sup>[117]</sup> In agreement to these findings, decreased clearance by the MPS allowed for prolonged circulation of fillomicelles which showed higher accumulation rates in tumors in contrast to spherical micelles.<sup>[118]</sup>

Further, the surface charge of nanoparticles poses a critical parameter on biodistribution (Figure 3.5 C). In general, high surface charges will result in promoted deposition of opsonins on the particle surface and thus result in accelerated blood clearance by the MPS.<sup>[110]</sup> Most cellular membranes bear a negative charge due to composition of the lipid bilayer<sup>[119]</sup>. Thus, toxicity associated with cell wall disruption is mostly associated by cationic particles<sup>[120]</sup> along with poor systemic circulation.<sup>[109]</sup> Neutral or slightly negatively charged nanoparticles, on the other hand, show a reduced adsorption of serum proteins leading to longer circulation times.<sup>[109,112]</sup> As demonstrated by Kataoka and co-workers, neutral (1.3 mV) and anionic (-10.6 mV) surfaces prolonged circulation of PEGylated polymeric micelles with lower accumulation in liver and spleen.<sup>[121]</sup>

*... and surface change.*

Ultimately, nanocarrier systems are supposed to enhance specific delivery to certain cell types or tissues. Apart from excretion or accumulation in the presented filtration organs, options to enhance specificity need to be taken into account (Figure 3.6). One targeting strategy follows a passive accumulation mechanism and exploits pathophysiological characteristics of cancerous or inflamed tissue (see Figure 3.6 A). Accumulation of particles is achieved by promoted extravasation through irregular fenestrated vasculature and retention due to defective lymphatic drainage in those tissues, which coined the term enhanced permeability and retention (EPR) effect<sup>[122]</sup>.

*Targeting strategies.*

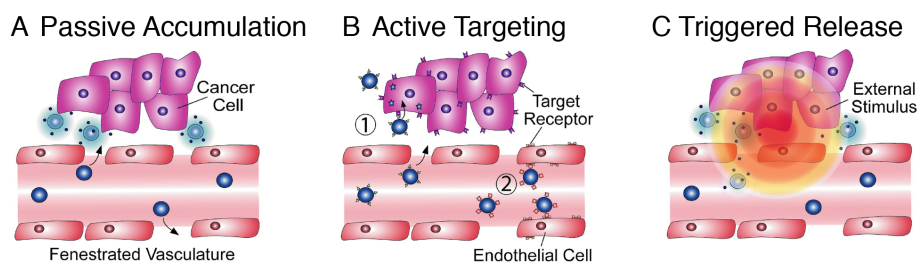


Figure 3.6: Illustration of targeting strategies: A) Passive accumulation of nanomaterials in tumor tissues by extravasation through fenestrated vasculature (EPR effect). B) Active targeting of (1) cancer cells or (2) tumor endothelium by nanocarriers modified with appropriate ligands. C) An external trigger (e. g. acidification due to hypoxia of fast growing, poorly vascularized cancerous tissue) induces payload release from stimuli-responsive nanocarriers.<sup>[3]</sup>

This passive targeting strategy is relevant for nanoparticles sized roughly between several tens to 100 nm and profits heavily from long systemic circulation for sufficient accumulation at the tumor site.<sup>[123]</sup> Further, methods which increase fenestrations in tumor vasculature even further e. g. administration of vascular endothelial growth factor (VEGF) or nitric oxide prove beneficial. Additionally, most solid tumors exhibit a dense extracellular matrix (ECM) which impedes successful penetration by nanomaterials. Thus, administration of collagen-degrading enzymes such as matrix metalloproteinases promote vascular permeability and particle accumulation.<sup>[115]</sup> As demonstrated by Cabral *et al.*, accumulation and tumor penetration depth of nanocarriers profits from a decrease in size (30 nm outperformed sub 100 nm particles).<sup>[124]</sup> Again, an increase in permeability (e. g. by administration of a TGF- $\beta$  inhibitor (transforming growth factor) which decreases pericyte coverage in the endothelium) enhanced tumor accumulation for larger structures (50, 70 and 100 nm hydrodynamic diameter).

Active targeting can be achieved upon interaction of ligands presented on the particle surface with receptors on specific cells e. g. cancer cells or the tumor endothelium as illustrated in Figure 3.6 B. Multiple ligands have been employed for this purpose such as small molecules e. g. folic acid and carbohydrates or complex molecules such as peptides, proteins or antibodies.<sup>[3]</sup> For delivery of RNAi therapeutic platforms to tumors the most prominent example is the cyclic RGD peptide.<sup>[125]</sup> Cyclic RGD binds to integrins, which are highly expressed on endothelial cells of tumors and on a number of tumor cells (about 10–15 %). It has been first exploited as a targeting strategy in antiangiogenic siRNA therapy using poly(ethyleneimine) (PEI) particles targeting the vascular endothelial growth factor (VEGF) by Woodle and co-workers.<sup>[125]</sup> A bottom-up construction of siRNA carriers employing cyclic RGD was recently demonstrated by Kataoka and co-workers. They used unimer polyion complex-assembled gold nanoparticles (poly(ethylene glycol)-block-poly(L-lysine) modified with lipoic acid as the unimer) for delivery to a subcutaneous cervical cancer (HeLa) model.<sup>[126]</sup> In general, active targeting relies on the availability of a specific ligand and a physiologically reasonable target. The choice of the ligand must allow for specific binding to target cells, while avoid or minimize binding to healthy tissue. Further, the density of the targeting ligand need to be tailored carefully to ensure the desired binding characteristics while maintaining low opsonization by plasma proteins.

Another approach to augment specific delivery is the release at the desired site of action upon a stimulus (Figure 3.6 C). As outlined in Chapter 2, stimuli can be categorized into internal (patho-physiological or patho-chemical conditions) or external stimuli (physical stimuli such as light, temperature, magnetic force, ultrasound or electric field). Especially for systemic application, delivery systems responding to endogenous stimuli such as change in pH, redox potential, ionic strength or shear stress in the target tissues can be harnessed.<sup>[3]</sup> For delivery to solid tumors, the extracellular acidic milieu in contrast to systemic pH can be

used or the decreasing pH of intracellular organelles.<sup>[127]</sup> Further, most tumors exhibit hypoxic areas due to poor vascularization. This environment is thus rich in reductive agents, which can be exploited for triggered release from redox-responsive nanocarriers.<sup>[128]</sup>

Once nanocarriers are located at the therapeutic relevant site in the tissue, cellular uptake is the next challenge. As illustrated in Figure 3.7, several endocytic pathways can be accessed, each regulated in a mechanistically distinct manner. Cellular uptake can occur by phagocytosis (especially in macrophages, not illustrated), macropinocytosis, receptor mediated endocytosis (which depends on recruitment of clathrin or caveolin) or other pathways.<sup>[129]</sup> In nonspecialized mammalian cells, clathrin-mediated endocytosis in particular represents the typical uptake mechanism for nanoparticles.<sup>[130]</sup> Upon ligand interaction, clathrins are recruited from the cytosolic side and mediate the engulfment of the cellular membrane. After constriction of the membrane by the enzyme dynamin, internalized particles are confined to intracellular vesicles called endosomes.

*Cellular trafficking.*

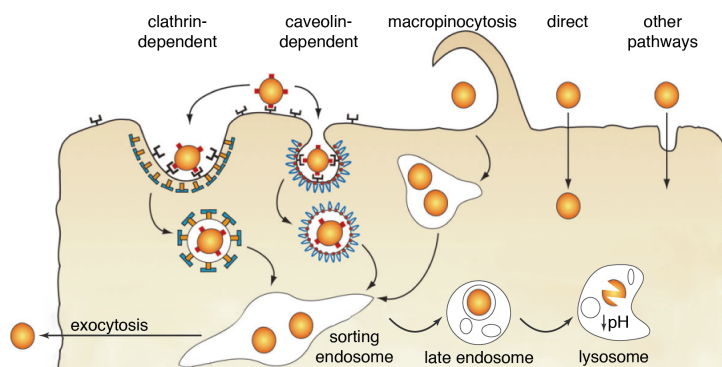


Figure 3.7: Pathways of endocytic internalization of nanocarriers and endosomal trafficking in the cell including the following stages: Vesicular transport of internalized contents into sorting endosomes followed by possible excretion to the cell surface by fusion with the plasma membrane, or alternatively maturation into lysosomes by luminal acidification and recruitment of degradative enzymes (adapted from<sup>[129]</sup>).

Endosomes, however, are subject to manifold trafficking and sorting pathways. Most relevant for intracellular delivery is the maturation to late endosomes and ultimately to lysosomes. This process is characterized by acidification of the endosomal compartment by an ATPase mediated proton influx and recruitment of digestive enzymes.<sup>[129]</sup> The resulting highly degradative environment, however, is preferably avoided in order to preserve the structure of the delivered siRNA. Further, initiation of the RNAi mechanism by formation of the RISC can only be achieved upon presence of siRNA in the cytoplasm. Thus, exit strategies from endosomes are essential for successful siRNA delivery.



## 3.3 REQUIREMENTS FOR CORE-SHELL siRNA DELIVERY SYSTEMS

In light of the discussed challenges for systemic application of RNAi therapeutics, concepts for polymer-based gene delivery systems addressing those issues will be discussed in this section. A selection of synthetic strategies resulting in favorable carrier functionalities is summarized in Figure 3.8.

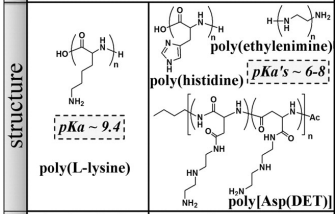
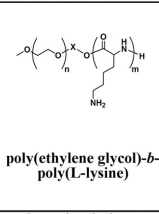
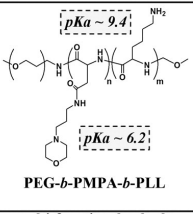
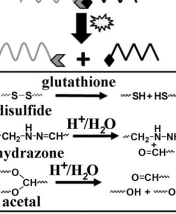

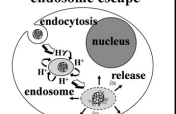
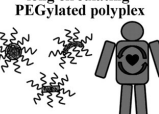
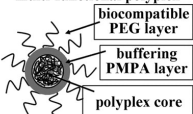
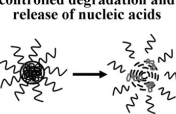
design	homopolymer	diblock polymer	triblock polymer	reversible linkages	
structure	 <p>poly(L-lysine) <math>pK_a \sim 9.4</math></p> <p>poly(ethylenimine)</p> <p>poly(histidine) <math>pK_a</math>'s <math>\sim 6-8</math></p> <p>poly[Asp(DET)]</p>	 <p>poly(ethylene glycol)-<i>b</i>-poly(L-lysine)</p>	 <p>PEG-<i>b</i>-PMPA-<i>b</i>-PLL</p> <p><math>pK_a \sim 9.4</math></p> <p><math>pK_a \sim 6.2</math></p>	 <p>glutathione</p> <p>disulfide</p> <p>hydrazone</p> <p>acetal</p>	
function	 <p>simple polyplex</p> <p><math>\sim 50 - 500</math> nm</p>	 <p>endosome escape</p> <p>nucleus</p> <p>release</p>	 <p>long circulating PEGylated polyplex</p>	 <p>multi-functional polyplex</p> <p>biocompatible PEG layer</p> <p>buffering PMPA layer</p> <p>polyplex core</p>	 <p>controlled degradation and release of nucleic acids</p>

Figure 3.8: Strategies towards polymer-based vectors for delivery of therapeutic nucleic acids.<sup>[84]</sup>

siRNA  
complexation.

All approaches provide a polyelectrolyte mediating complexation of negatively charged siRNA. Commonly, polycations are employed for siRNA complexation, e. g. poly(ethyleneimine) (PEI), which performs excellent in regard to transfection efficiency.<sup>[131]</sup> However, due to its high charge-mediated toxicity the need for alternatives for systemic applications is apparent. Various approaches address this issue such as improved shielding,<sup>[132]</sup> degradability of PEI as demonstrated in the group of Park<sup>[133]</sup> or the use of polyethyleneimine motifs in polymeric side chains as shown in the group of Kataoka.<sup>[102]</sup> Further, Wagner and co-workers employ polycationic polymers prepared by solid phase synthesis.<sup>[103]</sup> This approach enables control over the exact sequence, length as well as order of functional elements such as charge mediating cationic building blocks (e. g. lysine or oligoamine sequences),<sup>[134]</sup> endosomolytically active motifs (e. g. polyhistidines) or moieties for bio-degradation (e. g. disulfides).<sup>[135]</sup> However, due to the poor systemic performance of positively charged delivery vectors, polycationic moieties are preferably restricted to the nanocarrier core.

Prolonged  
blood circulation.

For passive accumulation mediated by the EPR effect, long circulating particles in the range of several tens to 100 nm, are required, with focus on smaller particles for better tumor penetration.<sup>[136]</sup> Additionally, in order to extend blood circulation of the nanocarrier, stealth properties of the particle surface are required to decrease opsonization through steric repulsion.<sup>[137]</sup> Also efficient charge shielding of negatively charged siRNA and the polycationic components is desired, since it reduces adsorption of plasma proteins

and ultimately avoids rapid clearance by the MPS. For this purpose, various materials can be employed as a hydrophilic, non-charged carrier-shell such as poly(ethylene glycol) (PEG),<sup>[138–140]</sup> poly(*N*-(2-hydroxypropyl) methacryl-amide) (PHPMA),<sup>[107,141,142]</sup> poly(sarcosine) (PSar),<sup>[70,143,144]</sup> polyoxazoline (POx),<sup>[145]</sup> poly(oligo(ethylene glycol) methyl ether methacrylate) (POEGMA),<sup>[146]</sup> or poly(phosphoester) (PPE).<sup>[147]</sup>

Strategies to exit the endosomal network prior to full maturation into lysosomes need to be employed in order to deliver the siRNA into the cytosol. This endosomal escape can be mediated by membrane destabilizing peptides e. g. INF7, H5WYG or GALA.<sup>[148]</sup> Further, cationic polymers can destabilize the endosome by interaction with the outer negatively charged membrane leading to membrane flipping.<sup>[149]</sup> Polymers such as PEI and poly(L-lysine) can be employed for this purpose or neutrally charged but ionizable lipids, which turn cationic upon acidification. Additionally, protonation of secondary or tertiary amine groups leads to an influx of water following the adsorbed protons, which can eventually lead to rupture of the membrane. This proton sponge effect can be mediated by e. g. PEI or histidine moieties.<sup>[129]</sup> Again, in order to minimize negative effects associated with high surface charge, these functionalities need to be located in the particle core. If ligands for specific receptor interactions are required, they need to be presented on the outer surface of the nanocarrier without impeding the overall stealth properties of the shell. Stimuli-responsive moieties, such as reversible disulfide linkages, can be implemented in the particle core or as a linker between polymer blocks constituting the core and shell.<sup>[61,103,150]</sup>

*Functionalization.*

In addition to effective shielding, stabilization of carrier systems by cross-linking proves beneficial on blood circulation compared to non cross-linked systems<sup>[151–153]</sup> and can increase stability of siRNA complexes.<sup>[135,154]</sup> As illustrated in Figure 3.9 for the self-assembly of amphiphiles into polymeric micelles, formulations remain in an equilibrium with individual polymer chains (unimers). Thus, the critical micelle concentration (CMC) of the respective amphiphile also determines the maximal concentration of free unimer.

*Stabilization of core-shell self-assembly systems.*

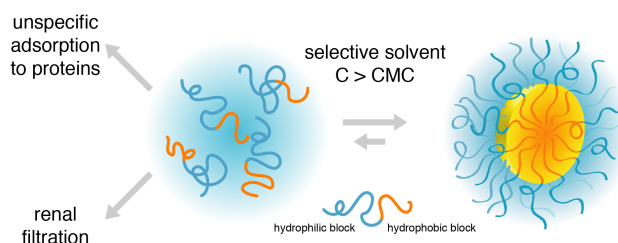


Figure 3.9: Micelle formation by self-assembly of amphiphilic block copolymers above their critical micelle concentration (CMC) (adapted from<sup>[153]</sup>).

As a result, non stabilized core-shell systems obtained by self-assembly of amphiphiles e. g. polymeric micelles or core-shell poly-

plexes generated by electrostatic interactions are prone to destabilization upon introduction into biological environments. Injection stress due to dilution as well as adsorption of unimers to protein surfaces<sup>[152]</sup> shifts the equilibrium towards free unimers. Ultimately, deviating physico-chemical properties of nanocarriers are observed when aqueous solution behavior is compared to biological relevant environments. Loss of the cargo, aggregation with plasma proteins and accelerated blood clearance are possible consequences which need to be avoided.

To bypass those issues, polymeric micelles as well as core-shell polymer complexes can be stabilized by covalent cross-linking.<sup>[153,155]</sup> Core cross-linking is so far the most successful method, since e. g. shell cross-linking might alter surface properties and increases probability of interparticle cross-linking and aggregation. Further, covalent core stabilization offers means for covalent attachment of the therapeutic relevant cargo.<sup>[151]</sup> Chemical approaches to increase stability of core-shell carriers are illustrated in Figure 3.10.

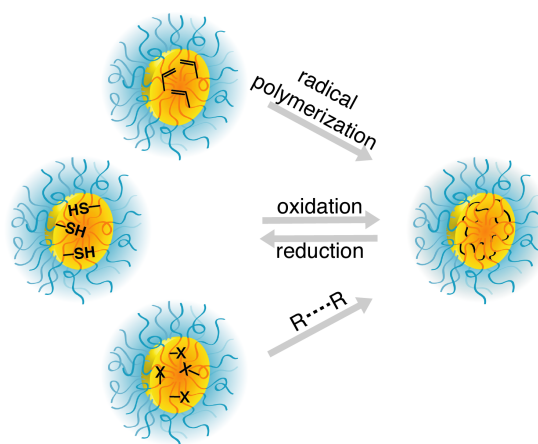


Figure 3.10: Strategies for stabilization of polymeric micelles by core cross-linking (adapted from<sup>[153]</sup>).

Core cross-linking  
by free radical  
polymerization ...

Free radical polymerization can be used with polymerizable groups present in the hydrophobic core-forming block (Figure 3.10 *top*). After micelle formation, cross-linking can be performed e. g. by photo-initiated polymerization or by the addition of free radical initiators.<sup>[156,157]</sup> However, the resulting C–C bonds are not reversible, which might impede release of the therapeutic cargo and does not promote bio-degradability of the carrier system.

... by disulfide  
stabilization ...

In this context, cross-linking by disulfide formation is an especially attractive option to achieve stabilization in a bio-reversible fashion (Figure 3.10 *middle*). Nanocarriers *in vivo* are typically exposed to different redox potentials when in systemic circulation in contrast to intracellular compartments.<sup>[158]</sup> A protein disulfide isomerase is available for catalysis of formation, reduction or isomerization of disulfide bonds inside cells.<sup>[159]</sup> The main impact, however, has the tripeptide glutathione ( $\gamma$ -L-glutamyl-L-cysteinyl-glycine or GSH), since it is the most abundant low-molecular-weight biological thiol. Disulfide bonds are physiologi-



cally stable in the blood stream due to a weak reduction potential mediated by low GSH concentrations of 2-20  $\mu\text{M}$ . In contrast, intracellular levels of glutathione are much higher and range dependent on the cell-cycle between 0.5 and 10 mM.<sup>[160,161]</sup> Thus, carrier systems featuring disulfides are stable in the blood, but are rapidly cleaved once inside cells.<sup>[19]</sup> With view on the development of vaccines, drug or gene delivery systems, the bio-reversibility of disulfides provides enormous benefits for the design of drug delivery systems.<sup>[103,138,162,163]</sup> Stabilization of nucleic acid carriers by disulfide bridging can be achieved by  $\text{O}_2$  oxidation of thiol residues as employed in the Kataoka group with regard to polyion complex micelles<sup>[164,165]</sup> and in the Wagner group for stabilization of lipopolyplexes<sup>[166]</sup> or polyplexes based on oligoethyleneimine building blocks.<sup>[135]</sup> Functionalization of the polymer material itself can be achieved by polymerization of disulfide bearing monomers<sup>[167,168]</sup> or by introduction of thiol-reactive moieties in a post-polymerization modification reaction. As demonstrated in the group of Kataoka, amine side chains of a PLys segment were modified upon reaction with *N*-succinimidyl 3-(2-pyridyldithio)propionate (SPDP) to yield free thiols after reduction with dithiothreitol (DTT).<sup>[169]</sup>

An alternative pose bi-functional cross-linkers, which can be used with reactive groups in the hydrophobic block (Figure 3.10 *bottom*). For successful implementation of this approach, the reactive groups have to remain stable upon polymerization and must not interfere with the self-assembly or complexation process. In contrast to the radical polymerization approach, side or end groups already present in the polymer can be used without previous modification.<sup>[153]</sup> Additionally, cross-linkers can introduce stimuli-responsive functionalities e.g. pH sensitive moieties such as Schiff's base, hydrazone esters, *cis*-aconityl or acetal groups.<sup>[16,18,107]</sup> Also redox-sensitive disulfides can be incorporated into nucleic acid carriers by amine reactive reagents such as dimethyl-3,3'-dithio-bis-propionimidate (DTBP)<sup>[170,171]</sup> or dithio-bis(succinimidyl propionate) (DSP).<sup>[172]</sup> Recent developments in our group on disulfide stabilization in  $\alpha$ -amino acid *N*-carboxyanhydride ring-opening polymerization follow a post polymerization approach and the use of thiol-reactive building blocks. The former strategy uses a post polymerization reaction with SPDP yielding a *S*-pyridyl group as thiol reactive moiety. Cross-linking with various bifunctional thiol cross-linkers results in libraries of functional multiblock polyplexes.<sup>[154]</sup> The other strategy relies on the thiol-reactive *S*-alkylsulfonyl group incorporated in poly(L-cysteines).<sup>[173]</sup> This approach enables the formation of cationic hydrogels by core cross-linking of polymeric micelles, entirely bypassing additional post polymerization modification and activation steps.<sup>[22]</sup>

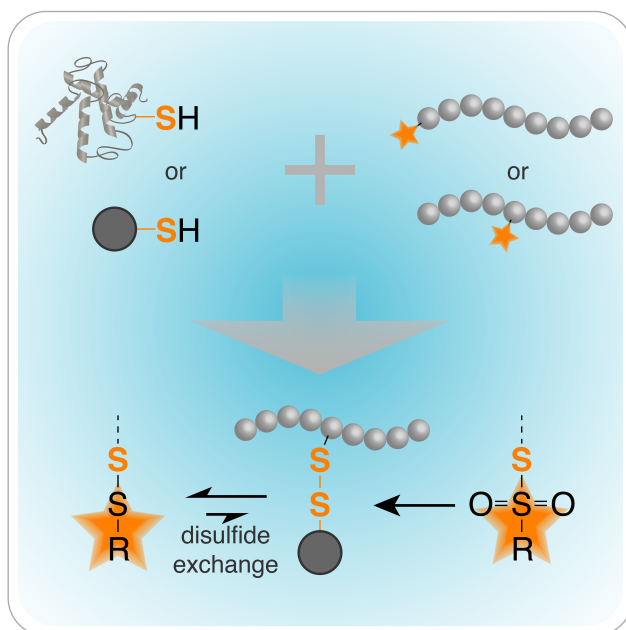
... or incorporation  
of bifunctional  
cross-linkers.

In light of the advantages of disulfide stabilization of nanocarriers, desire for chemical control over the employed material is eminent. Thus, the following chapter will elaborate on strategies for chemoselective formation of asymmetric disulfides in synthetic peptides and polymers.



OF THIOLS AND DISULFIDES: METHODS FOR  
CHEMOSELECTIVE FORMATION OF  
ASYMMETRIC DISULFIDES IN SYNTHETIC  
PEPTIDES AND POLYMERS

Olga Schäfer, Matthias Barz, *Chemistry – A European Journal* 2018, 24, DOI 10.1002/chem.201800681.



**ABSTRACT:** With regard to protein- or peptide chemistry, thiols are frequently chosen as a chemical entity for chemoselective modification reactions. And while it is a well established methodology to address cysteines and homocysteines in aqueous media to form S–C bonds, possibilities for the chemoselective formation of asymmetric disulfide bonds are much less approached. Focusing on bioreversibility in conjugation chemistry, the formation of disulfide bonds is highly desirable for the attachment of thiol-bearing bioactive agents to proteins or in cross-linking reactions, since disulfide bonds can combine stability in blood with degradability inside cells. In this concept article recent approaches in the field of activating groups for thiol moieties incorporated in polymeric and polypeptide materials are highlighted. Advantageous combinations of stability during synthesis of the material with high reactivity towards thiols are explored focusing on simplification and prevention of side reactions as well as additional deprotection and activation steps prior to disulfide formation. Moreover, applications of this chemistry are highlighted and future perspectives are envisioned.

## 4.1 INTRODUCTION

A thiol moiety in natural peptides as well as in chemically or recombinant engineered peptide materials offers a wide range of options for site specific chemical modification.<sup>[174]</sup> The reactivity profile of thiols is mainly directed by their relatively low  $pK_a$ , which distinguishes them as excellent nucleophiles under physiological conditions,<sup>[175,176]</sup> as well as their ability to participate in redox processes to form disulfide bonds upon oxidation.<sup>[177]</sup> This high chemical reactivity of thiols, their abundance in biological systems and the ease of modification gives reason for the significance of reactions addressing thiols in organic chemistry as well as in the life sciences.<sup>[178–180]</sup>

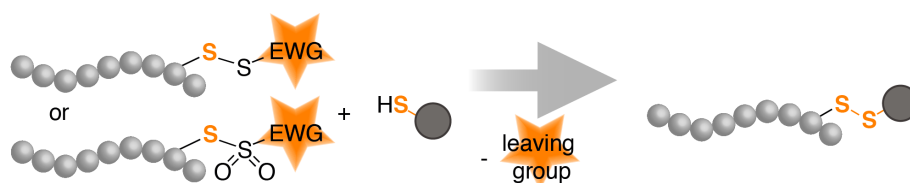
*Conjugating to  
thiol-moieties e. g. in  
cysteine ...*

In this context, the only thiol bearing proteinogenic amino acid cysteine is of great importance. The cysteine moiety offers a gateway to a broad range of bioconjugation techniques<sup>[181]</sup> as well as the possibility to introduce disulfide bonds, both in natural peptides<sup>[182]</sup> and in peptide-based materials.<sup>[183,184]</sup> Bioconjugation, defined as the covalent attachment of biological and synthetic macromolecules, is a growing area of interest in biological as well as material sciences.<sup>[185–187]</sup> Central to this field is the site selective conjunction of macromolecules based on two moieties with distinct directed reactivity. This growing toolbox includes chemoselective reactions at cysteine residues such as disulfide exchanges, alkylation, native chemical ligation (NCL) with thioester reagents, Michael addition with maleimides or thiol-ene components following a free radical or Michael addition mechanism.<sup>[181,188]</sup> NCL<sup>[189,190]</sup> and thiol-ene<sup>[191]</sup> coupling strategies operate efficiently, however, they result in irreversible bonds, and maleimide-thiol conjugates<sup>[192–194]</sup> are widely implemented in bioconjugation settings<sup>[192,193]</sup> yielding succinimide thioethers, which may undergo hydrolysis and thiol scrambling. In contrast to the outlined bioconjugation strategies, disulfides are classified as a dynamic covalent bond, a term covering a multitude of bond-types combining the advantages of non-covalent and covalent bonds.<sup>[165,195,196]</sup> Upon a redox environment present in an extracellular setting, disulfide bonds are stable, unless subject to disulfide exchange, and are cleaved intracellularly due to the more potent redox environment.<sup>[158,159]</sup> Especially in the development of vaccines, drug or gene delivery systems this bioreversibility of disulfides provides enormous benefits for the design of nanomedicines.<sup>[103,138,162,163]</sup>

*... for chemoselective  
disulfide formation?*

While there are numerous pathways which are encountered upon introduction of a disulfide containing component in a biological environment,<sup>[197]</sup> creating materials for biomedical applications with the option of chemoselective disulfide formation is a demanding task on its own. One challenge is the mandatory use of protective groups in the synthesis of reactive polythiol containing polymers, since free thiols interfere with most polymerization techniques according to their nucleophilic and redox-active nature (radical transfer).<sup>[198]</sup> Further, disulfide formation can be directly achieved by a nucleophilic attack of thiol or thiolate

bearing target molecules at nucleophilic sulfur atoms in the synthesized polymer. To ensure a chemoselective formation of disulfides, this process requires soft, often sulfur based leaving groups structurally based on thiosulfonates or disulfides (Scheme 4.1 and Table 4.1).



Scheme 4.1: Synthesis strategy for the chemoselective formation of asymmetric disulfides (EWG = electron withdrawing group).

Paired with these activating group techniques, this article will focus on the synthetic strategies for the incorporation of reactive thiols for chemoselective disulfide formation by post-polymerization modification reactions. In the next chapters we describe the synthesis of such polymers obtained by either controlled radical polymerization (CRP), solid phase peptide synthesis (SPPS) and ring-opening polymerization of  $\alpha$ -amino acid *N*-carboxyanhydride (NCA). Since other polymerization techniques are seldom exploited in the context of chemoselective disulfide formation, these approaches are briefly outlined before introducing the main areas of chemoselective disulfide formation in polymer synthesis.

Aside from the illustrated approaches in Scheme 4.1 for chemoselective disulfide formation, incorporation of disulfides in the main chain is also possible and it is an attractive motif for polymer networks with self-healing properties such as polysulfides obtained by disulfide metathesis under alkaline catalysis,<sup>[199]</sup> as well as polyurethane<sup>[200]</sup> or poly(urea-urethane)<sup>[201]</sup> networks obtained by polyaddition reaction. Further, polycondensation reactions yield polyesters as well as cysteine based poly(disulfide-amides)<sup>[202]</sup> for applications in the field of self-healing materials<sup>[203]</sup> or drug delivery systems.<sup>[204]</sup> Thiol reactivity in the side chain of polyesters can be introduced for example by ring-opening co-polymerization of lactides, followed a post-polymerization conversion of a trityl-thiol protective group into a thiol reactive pyridyl disulfide (PDS) groups.<sup>[205]</sup>

## 4.2 CONTROLLED RADICAL POLYMERIZATION (CRP)

Controlled radical polymerization techniques such as atom transfer radical polymerization (ATRP),<sup>[226]</sup> nitroxide-mediated polymerization (NMP),<sup>[227]</sup> and reversible addition-fragmentation chain transfer (RAFT) polymerization<sup>[228]</sup> provide versatile tools for the preparation of well-defined polymers and offer the great possibility to introduce a multitude of different functionalities into polymers.<sup>[229]</sup> Directed disulfide formation is known for ATRP and RAFT polymerizations and is achieved by thiol transformation processes following two main strategies: the thiol-alkanethiosulfonate reaction and the thiol-disulfide reaction medi-

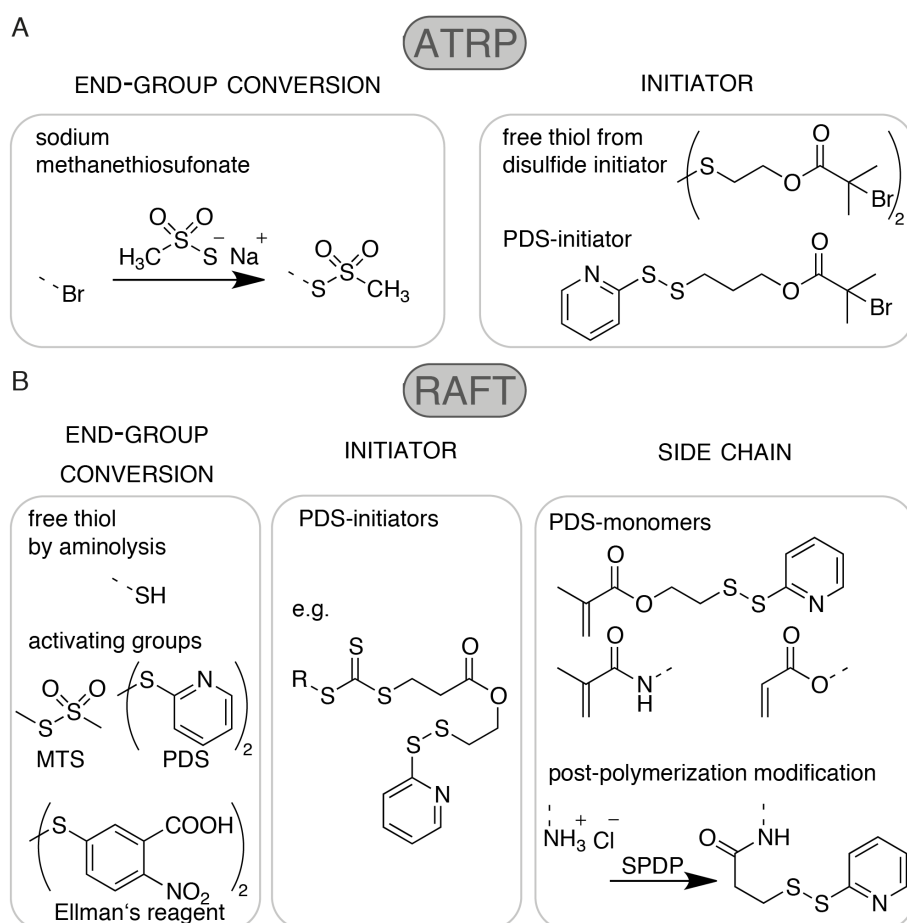
Table 4.1: Activating groups for chemoselective disulfide formation.

structure	group	synthesis strategy
	alkane thiosulfonate- R = Me ( <b>MTS</b> ) = Et, <sup>i</sup> Pr = ONa thiosulfate- ( <b>Bunte salts</b> ) <sup>[206]</sup>	ATRP <sup>[207]</sup> RAFT <sup>[208]</sup> SPPS <sup>[173]</sup> NCA <sup>[173,209]</sup>
	2- or 4-pyridyl- ( <b>S-Pyr</b> or <b>PDS</b> )	ATRP <sup>[210]</sup> RAFT <sup>[211]</sup> SPPS <sup>[212-214]</sup> NCA <sup>[154]</sup>
	2- or 4-nitrophenyl- ( <b>S-Nps</b> )	SPPS <sup>[215-217]</sup>
	alkoxycarbonyl sulfenyl- (R= Me <b>Scm</b> ) ( <i>N'</i> -methyl- <i>N'</i> - phenylcarbamoyl) sulfenyl- ( <b>Snm</b> )	SPPS <sup>[218-220]</sup>
	5-thio-2-nitrobenzoic acid- ( <b>Ellmans reagent</b> )	RAFT <sup>[221]</sup> SPPS <sup>[222]</sup>
	3-nitro-2-pyridyl- ( <b>S-Npys</b> )	SPPS <sup>[223]</sup>
	tert-butylthio- ( <b>S-<sup>t</sup>Bu</b> )	SPPS <sup>[224]</sup>
	trimethoxyphenylthio- ( <b>S-Tmp</b> )	SPPS <sup>[225]</sup>

ated by activated disulfides with electron withdrawing groups (compare Scheme 4.1).<sup>[230]</sup>

An initial protection step, however, is mandatory for the use of redox sensitive functional groups such as thiols, since they interfere severely with the controlled radical polymerization process. Thus, the chemical strategies surrounding the thiol moiety are numerous and in the following section disulfide reactivity in ATRP and RAFT techniques will be examined with focus on chemoselective disulfide formation. Thiol end-functionalized polymers synthesized by ATRP are realized either by a post-polymerization conversion of the bromo end-group or by protected initiator pathways (Scheme 4.2 A). An end-group conversion can yield the free thiol upon reaction with thiourea and NaOH,<sup>[231]</sup> or a thiol reactive methane thiosulfonate (MTS) group upon reaction with sodium methanethiosulfonate for directed disulfide formation.<sup>[207]</sup> Polymerization routes by functional initiators employs either disulfide initiators which yield bioreducible disulfides in the main chain,<sup>[232,233]</sup> or a 2,4-dinitrophenyl group in the initiator, which gives the free thiol upon base mediated thiolysis.<sup>[234]</sup> Directed disulfide formation is achieved by incorporating a pyridyl disulfide group (PDS) in the initiator, which gives asymmetric disulfides upon reaction with thiols.<sup>[210,235]</sup>

*In controlled radical polymerization, e. g. ATRP ...*



Scheme 4.2: Entries for directed disulfide formation in ATRP and RAFT polymerization techniques.

... and RAFT ...

RAFT polymerization is another versatile technique yielding well-defined polymers and offers several routes for introduction of disulfide bonds and thiol reactive moieties.<sup>[230,236,237]</sup> Disulfide bonds can be incorporated by self-condensing vinyl polymerization of RAFT disulfide monomers, yielding hyperbranched architectures with bioreducible moieties.<sup>[238–240]</sup> Further, cross-linking monomers containing disulfide bonds can be implemented in numerous RAFT crosslinking polymerization strategies<sup>[241]</sup> e.g. in arm-first nanogel formation<sup>[242–244]</sup> or core-first approaches.<sup>[245]</sup> Synthetic strategies for a bioreducible, detachable corona of nanoparticles for biomedical applications<sup>[246,247]</sup> also rely on the incorporation of disulfide bonds between two blocks during RAFT polymerization. In terms of end-group functionality, materials synthesized by RAFT polymerization have the advantage of the thiocarbonylthio end-group, which can already be considered a protected thiol group. Thus, many end-group transformation methods involve the free thiol, which is obtained by reduction or through reaction with nucleophiles e.g. aminolysis.<sup>[230,248]</sup> Functionality is then introduced by thiol-ene, thiol-yne, Michael and maleimide reactions either as a separate reaction step or in a one-pot process.<sup>[249–252]</sup>

... MTS  
(-SSO<sub>2</sub>-R) and  
PDS (-SS-R) are  
employed for  
chemoselective  
disulfide formation.

In analogy to ATRP, strategies for directed thiol transformations in RAFT polymerization are mediated by the MTS<sup>[208]</sup> and PDS group (Scheme 4.2 B).<sup>[211]</sup> Both moieties can be introduced by aminolysis of the thiocarbonylthio end-group as a post-polymerization modification and, after directed disulfide formation, were utilized in encapsulation of gold nanoparticles,<sup>[253]</sup> protein-polymer conjugates<sup>[254]</sup> and drug attachment by disulfides.<sup>[255]</sup> Reaction with *Ellman's reagent* (5,5'-dithiobis-2-nitrobenzoic acid)<sup>[221,256]</sup> also yields activated thiols after removal of the thiocarbonylthio moiety.<sup>[257]</sup> Further, thiol reactivity by a PDS group can be introduced during the RAFT polymerization as an end-group by mono- or bifunctional chain transfer agents<sup>[258–260]</sup> or in the side chain. In the latter strategy, polymerization of PDS modified monomers allowed for particle formation and stabilization by disulfide cross-linking.<sup>[261–263]</sup> In addition, side chains can also be functionalized in a post-polymerization reaction with *N*-succinimidyl 3-(2-pyridyldithio)-propionate (SPDP).<sup>[264]</sup>

Concluding, ATRP and RAFT as controlled radical polymerization techniques allow for directed disulfide formation by conversion of thiol moieties into thiol reactive methane thiosulfonates or into activated disulfides. However, since the thiol-reactive compounds are often amine incompatible, a separate step may be required during end-group conversion. Further, upon generating free thiol end-groups, undesired disulfide formation and thiol exchange can pose a synthetic challenge.<sup>[265]</sup> Alternatively, the PDS moiety, which proves to be stable during the controlled radical polymerization process<sup>[266]</sup>, can be introduced upon polymerization via the initiator in ATRP and RAFT or as a functionalized RAFT-monomer.



### 4.3 SYNTHESIS OF POLYPEPTIDES

While the incorporation of activated thiols into polymers was established over the last decade for controlled radical polymerization techniques, their use in polypeptide synthesis was mainly limited to postpolymerization modification techniques in synthetic or natural polypeptides. Researchers encountered complex requirements for protective groups and needed to choose between options in multistep procedures of protection, deprotection, activation and conjugation reactions. A suitable protective group avoiding this complexity, should allow direct conversion into a disulfide and needs to provide the delicate balance of stability towards amines and other hard nucleophiles with reactivity towards thiols as soft nucleophiles.

#### 4.3.1 Solid Phase Peptide Synthesis (SPPS)

Chemical design of peptide materials is a substantial goal in SPPS and enables the formation of sequence defined peptides containing one or several disulfide bridges, as well as peptide materials with disulfides for stabilization of drug<sup>[267,268]</sup> and gene delivery systems<sup>[269,270]</sup> or peptide based molecular transporters.<sup>[271]</sup> Disulfides are commonly introduced via the amino acid cysteine. However, side-chain protection is essential, since the nucleophilic thiol interferes with the peptide coupling reaction and free thiols are generally incompatible with hydrolytic protective groups, as it poisons the catalyst.<sup>[272]</sup> And while a broad spectrum of protective groups for cysteine in SPPS is available, strategies for disulfide formation rely either on (I) orthogonal reactive protective groups, symmetrical removal and formation of disulfide by oxidation, (II) direct oxidative symmetrical removal of protective groups mostly by I<sub>2</sub> or (III) asymmetric activation and disulfide formation in a displacement reaction.<sup>[183,273]</sup>

Oxidation of free thiols after peptide synthesis and removal of protective group will yield symmetrical disulfides when (homo)cysteines react with each other. Various oxidants are known from aerial oxygen,<sup>[164]</sup> dimethylsulfoxide (DMSO)<sup>[274]</sup> and supported methionine sulfoxide in analogy to DMSO oxidation with the advantage of simple removal of the oxidizing agent,<sup>[275]</sup> chlorotrimethylsilane-nitrate salts<sup>[276]</sup> and oxidation of free SH groups by immobilized metal complexes.<sup>[277]</sup> Further selective oxidants are *trans*-3,4-dihydroxyselenolaneoxide (DHS)<sup>[278,279]</sup> and *N*-Chlorosuccinimide (NCS), enabling on resin oxidation with good compatibility to other protective groups.<sup>[280]</sup> Direct oxidation from the protected cysteine is also a popular pathway, employed with the *S*-acetamidomethyl group (*S*-Acm) which is removed by I<sub>2</sub> forming disulfide bonds,<sup>[281,282]</sup> or (microwave-assisted) disulfide formation from *S*-triphenylmethyl protected cysteine (*S*-Trt) by I<sub>2</sub> oxidation.<sup>[283]</sup> Other strategies include reduction the of *p*-nitrobenzyl protective group

*Abundant protective groups ...*

(*S*-pNB) to a *p*-aminobenzyl group (*S*-pAB) prior to oxidation by  $I_2$ ,<sup>[284]</sup> oxidation of the *S*-<sup>t</sup>Bu group by  $O_2$  in a large excess of cysteine and a chaotropic salt<sup>[285]</sup> and enzymatic cleavage of phenylacetamidomethyl groups (*S*-Phacm) followed oxidation in the presence of DMSO in aqueous conditions.<sup>[286]</sup> However, disulfide formation by oxidation allows only the formation of symmetrical disulfides and suffers from drawbacks such as removal of the oxidizing agent, low yield, long reaction time, and the formation of side products.<sup>[287,288]</sup>

*... but for directed disulfide formation, in compatibility with SPPS conditions?*

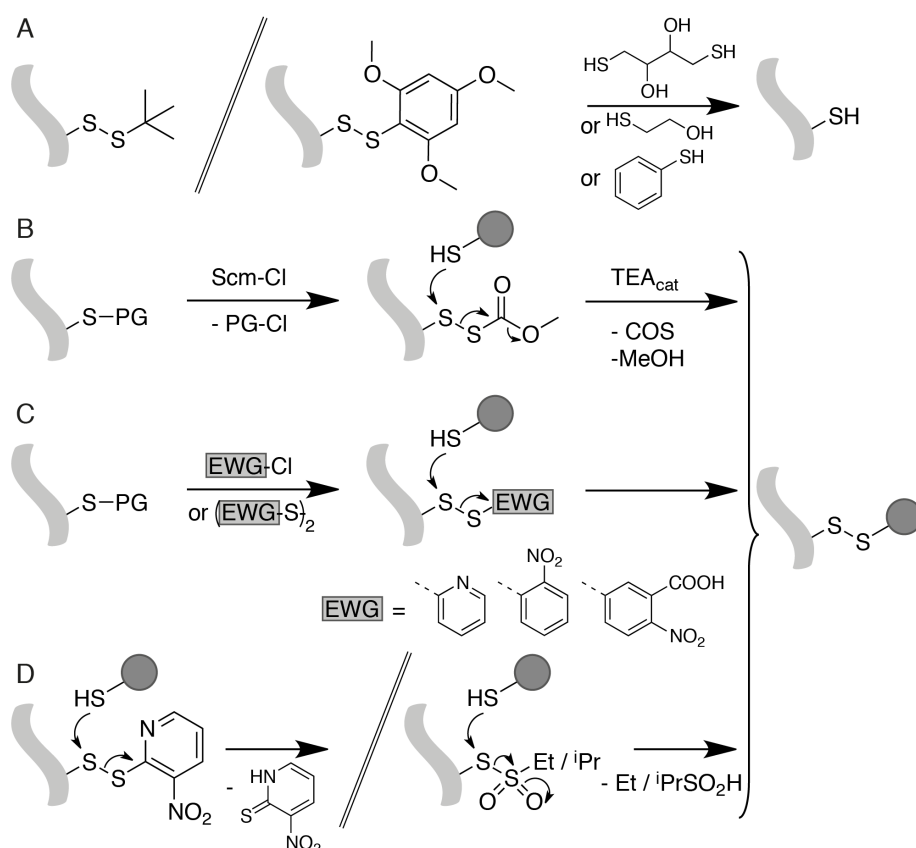
Directed asymmetrical disulfide formation, as required for bioconjugation, remains chemically challenging terrain since a displacement reaction of a free, nucleophilic thiol with a second, activated thiol to form a disulfide needs to be coordinated. Especially in intermolecular disulfide bridging, as in bioconjugation techniques employing native cysteine residues,<sup>[289,290]</sup> formation of homodimers has to be avoided in favor of the desired heterodimer. An approach employing *N*-terminal cysteine enables coupling forming a cleavable thiazolidine heterocycle upon reaction with an aldehyde moiety.<sup>[291]</sup> Additionally, free thiols can be activated by an electron withdrawing group e. g. by chlorination<sup>[292]</sup> or as nitroso-thiols,<sup>[293,294]</sup> yielding, highly electrophilic species prone to side reactions.

*Protected disulfides will give a thiol upon SH mediated cleavage (A).*

A strategy involving mixed aliphatic disulfides relies on the *S*-<sup>t</sup>Bu protective group,<sup>[224]</sup> which is cleaved by thiol containing compounds such as benzenethiol,  $\beta$ -mercaptoethanol or dithiothreitol (DTT) yielding the free thiol.<sup>[295]</sup> The trimethoxyphenylthio group (*S*-Tmp)<sup>[225]</sup> is another thiol labile alternative, since *S*-<sup>t</sup>Bu removal proves to be occasionally difficult<sup>[296]</sup> (Scheme 4.3 A). A similar approach relies on thiol free reducing agents such as tris(2-carboxyethyl)phosphine (TCEP) which liberates the free cysteine thiol for further coupling reactions from an *S*-<sup>i</sup>Pr protective group.<sup>[297]</sup> The advantage of the pathways outlined above is the orthogonal reactivity to most cysteine protective groups, the compatibility with the *N*-(9-Fluorenylmethoxycarbonyl) (Fmoc) strategy and relatively mild deprotection procedures. However, the thiol reactivity of these groups is limited to the thiol moieties employed in the deprotection and they do not mediate a directed disulfide formation.

*Acyl and aryl disulfides yield asymmetric disulfides with thiols, but require multi-step introduction (B).*

Mixed acyl and aryl disulfides are suitable for regiospecific displacement by free thiol groups and yield ultimately unsymmetrical disulfides. Activation by electron-withdrawing *S*-alkoxycarbonyl sulfenyl groups e. g. the *S*-methoxycarbonylsulfenyl group (Scm),<sup>[218,298,299]</sup> ethyl- (Sce), benzyl- (Sz), *tert*-butyl- (Scb) derivatives<sup>[219]</sup> or *S*-([*N'*-methyl-*N'*-phenylcarbamoyl]sulfenyl) (Snm),<sup>[220]</sup> is accomplished by reaction of the free or protected thiol with alkoxycarbonyl sulfenyl chloride (Scheme 4.3 B). Upon reaction with DTT the free thiol is obtained and mixed disulfides with a thiol component upon a mild base catalysis.<sup>[300]</sup> The driving force for disulfide formation is the irreversible decomposition of the Scm group in carbonyl sulfide and the respective alcohol.



Scheme 4.3: Approaches for directed disulfide formation in SPPS: A) the free thiol is obtained upon cleavage with thiol containing compounds, B-C) protective group interconversion and disulfide formation and D) direct disulfide formation from a protective and activating group.

Limiting factors are, however, a possible reaction with the *N*-terminus and the base sensitivity of this class of activating groups.<sup>[220]</sup> Further electron-withdrawing activating group such as 2- and 4-nitrophenyl (*S*-Nps)<sup>[215–217]</sup> and 2- and 4-pyridyl groups (*S*-Pyr)<sup>[212–214]</sup> have been used, since the disulfide formation is promoted by the low  $pK_a$  of the aromatic thiol leaving group (Scheme 4.3 C). The introduction of thiol reactive moieties by 2-pyridinesulfenyl chloride is however susceptible to hydrolysis.<sup>[273,301]</sup> An alternative strategy includes *N*-terminal thiol deprotection followed by activation with excess 2,2'-dipyridyldisulfide and coupling with a free thiol in the presence of DTT at pH 7.<sup>[302]</sup> In analogy, reaction with 5,5'-dithiobis-2-nitrobenzoic acid (*Ellman's reagent*) gives also a suitable activated disulfide.

Although the performance of the above specified activating reagents is efficient in terms of disulfide formation, the additional deprotection and activation step complicates the overall synthetic strategy. An alternative approach operates with the 3-nitro-2-pyridyl group (*S*-Npys) combining characteristics of both, an activation and protective group (Scheme 4.3 D left).<sup>[223]</sup> Introduction of the Npys group is performed by

*Electron-deficient disulfides are possible in terminal position (C).*

*S-Npys avoids deprotection and activation, but shows low compatibility in Fmoc-strategies (D).*

reaction of either the protected cysteine<sup>[303]</sup> or conversion of the free thiol with Npys halides.<sup>[304]</sup> An alternative pathway includes conversion with 2,2'-dithiobis(5-nitropyridine) (DTNP) into Npys and quantitative disulfide formation upon addition of DTT (with and without addition of thioanisole).<sup>[305]</sup> Limiting factors are the high stability which complicates removal and requires enhanced temperatures and an access of DTNP. Further studies include Npys disulfide coupling assisted by microwave irradiation<sup>[306]</sup> and immobilized Npys on resin enabling disulfide formation and facilitated work-up.<sup>[307]</sup> The chemical stability of the Npys group allows for Boc/benzyl synthesis conditions, but cannot be applied to "low-high" cleavage protocols or to bases employed in the Fmoc-strategy.<sup>[308]</sup> Thus, in the Fmoc-strategy, the Npys group can either be incorporated at *N*-terminal position, introduced after solid phase peptide synthesis or by conversion of other protective groups.<sup>[309]</sup>

*The S-alkylsulfonyl group combines thiol reactivity with amine stability for use in Fmoc-strategies (D).*

The *S*-alkylsulfonyl group is an alternative protective and activating group for directed disulfide formation and is based on the thiosulfonate motif (Scheme 4.3 D *right*).<sup>[173]</sup> Ethyl and isopropyl derivatives have shown outstanding chemoselective thiol reactivity, while remaining thermodynamic inert towards various amines, allowing standard Fmoc solid phase peptide synthesis protocols. Thus the site of the cysteine with a thiol-reactive protective group is not limited to a terminal position. The thiosulfonyl groups remained intact during conversion into the corresponding Fmoc derivatives, coupling by *N,N*-diisopropylcarbodiimide (DIC) with *O*<sup>t</sup>Bu-alanine to give the dipeptide and cleavage protocols of the *C*- and *N*-terminal protective group. However, coupling protocols employing 1-hydroxybenzotriazole (HOBt) or related *O*-nucleophiles pose a challenge, since partial cleavage of the activating group resulted in free thiols.

In summary, SPPS offers a well-supplied toolbox for disulfide formation. However, deprotection steps or interconversion to suitable activating groups can increase the synthetic effort. The Npys and *S*-alkylsulfonyl group fall in the advantageous category of protective and activating groups, which enables asymmetric disulfide formation without further modifications, thus simplifying the overall peptide synthesis procedure. In this context, *O*- and *N*-nucleophiles can pose a challenge when present besides thiol activating groups, since the reactivity towards the activated electrophilic sulfur is often high enough to cause side reactions. Strategies in SPPS rely on amine mediated Fmoc-deprotection, which is compatible with the *S*-alkylsulfonyl group but not the Npys group. However, most activating routes also employ *O*-nucleophiles derived from triazoles, rather than sole carbodiimides due to the risk of racemization,<sup>[310]</sup> which results in partial cleavage of the *S*-alkylsulfonyl group due to the oxophilic character of sulfur.

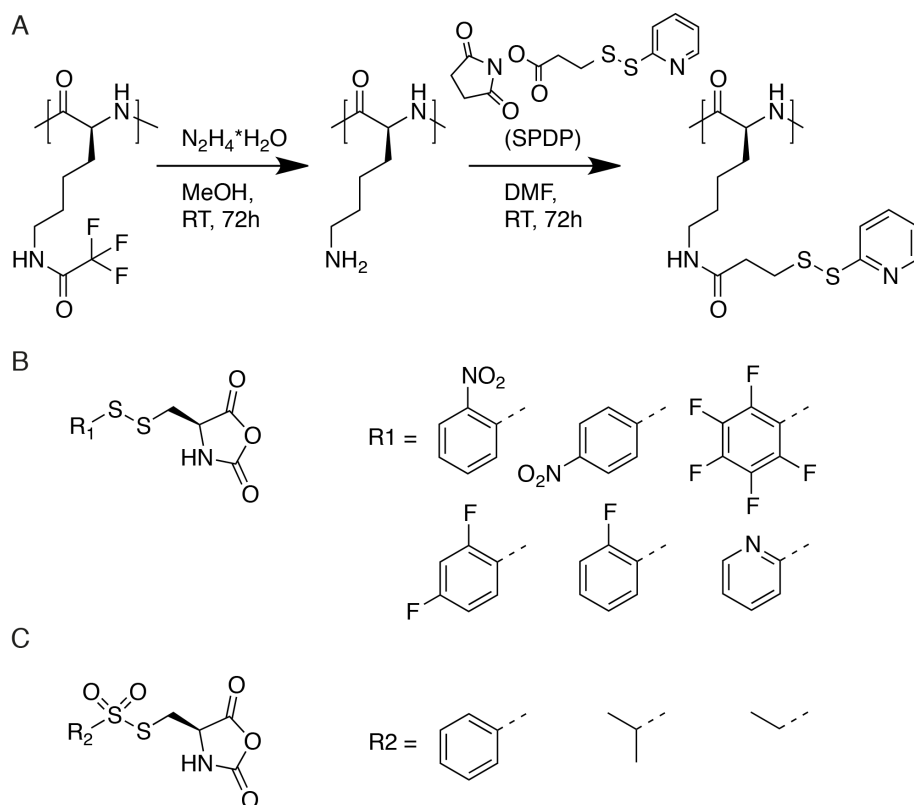
### 4.3.2 NCA Polymerization

The ring-opening polymerization of  $\alpha$ -amino acid *N*-carboxyanhydrides (NCAs) is a well-established methodology for rapid and large scale preparation of synthetic polypeptides.<sup>[35,49–53,55,56,58,311–317]</sup> In contrast to SPPS, NCA polymerization techniques lack the possibility for sequence-defined polypeptides, provides, however, the possibility of (multi) block copolymer synthesis, graft copolymers and high molecular weight polypeptides. In addition, *O*-nucleophiles are absent during polypeptide synthesis. Polypeptides synthesized by this method have already entered clinical trails or, as in the case of copaxone, became multi-billion dollar drugs.<sup>[315,316]</sup>

The high demand for reactive thiols enabling bioreversible conjugation to polypeptides by disulfide bonds is eminent, as illustrated by the well established incorporation of disulfide bonds in initiators, in the main or side chain of polypeptides<sup>[61,62,318,319]</sup> In addition, reactive polypeptides enable a variety of post-polymerization modification techniques.<sup>[21,58]</sup> A multitude of chemoselective modifications, e. g. alkylation,<sup>[312]</sup> azide–alkyne,<sup>[314]</sup> thiol–ene and –yne reactions<sup>[311,313,317]</sup> is available. However, in analogy to controlled radical polymerization and solid phase peptide synthesis, most post-polymerization modifications in NCA polymerization result in irreversible bonds.<sup>[320]</sup> Implementations of reactive thiols in nucleophilic ring-opening polymerization are scarce, since most activated disulfide moieties are prone to nucleophilic initiators as a consequence of their pronounced reactivity required for disulfide formation. A sequential NCA polymerization followed by sequential deprotection procedures allows for a post-polymerization modification approach and enables chemoselective cross-linking by dithiols (Scheme 4.4 A).<sup>[154]</sup> Here, activated pyridyl disulfide moieties were introduced into a poly-*L*-lysine segment in a tri-block polypeptide-block-polypeptoid copolymer (polypept(o)id)<sup>[25,26]</sup> employing *N*-succinimidyl 3-(2-pyridyldithio)-propionate (SPDP).<sup>[154]</sup>

However, to bypass the required deprotection and activation steps after polymerization, a protective group for thiols, which combines stability during NCA peptide synthesis with the ability to form disulfide bonds in a chemoselective reaction, appears highly desirable. Thus, activated cysteines were employed in NCA synthesis and polymerization, first equipped with protective groups of varying potency as electron withdrawing groups (Scheme 4.4 B).<sup>[321]</sup> The findings were, however, humbling, since the protective groups in question are highly reactive like most activated thiols and disulfides and were prone to hydrolysis and aminolysis during NCA synthesis as well as during polymerization. At this point, a related class of sulfur–sulfur containing bonds known for its potency in thiol activation was explored: the thiosulfonyl group.<sup>[206,322,323]</sup> Starting with *S*-pheylsulfonyl-*L*-cysteine<sup>[321]</sup> and followed by *S*-alkylsulfonyl-*L*-cysteines<sup>[173]</sup> (Scheme 4.4 C), thiosulfonyl protective groups were first explored in NCA polymerization to successfully bridge the gap between stability and reactivity.

*Versatile functional NCAs are available, but yield irreversible bonds or require post polymerization modification.*



Scheme 4.4: A) Post-polymerization strategy for incorporation of pyridyl disulfide moieties in polypeptide side chains. B) L-Cysteine NCA with disulfide-based side chains of decreasing electron deficiency. C) S-phenylsulfonyl-, S-ethylsulfonyl- and S-isopropylsulfonyl-L-cysteine NCA. Reproduced with permission from refs.<sup>[154,321]</sup> copyright 2016 and 2017 Elsevier.

*The S-alkylsulfonyl group provides activation for chemoselective disulfide formation ...*

The synthesis of S-alkylsulfonyl-L-cysteines is straightforward and involves the in situ formation of the S-nitrosocysteine followed by conversion with either ethanesulfinic or isopropanesulfinic acid sodium salt forming the corresponding thiosulfonate with retained stereochemistry.<sup>[173]</sup> The desired asymmetric disulfides are obtained upon reaction with soft nucleophiles, like thiols, exhibiting exceedingly fast reaction rates, while hard nucleophiles like amines result in low reaction rates so that a conversion is virtually inhibited<sup>[324]</sup> (Figure 4.1 A). Thus, both protective groups are stable against aminolysis by primary and secondary amines in a low temperature regime, which enables their use in amine-initiated NCA polymerization (Figure 4.1 B). In aqueous conditions, base-mediated hydrolysis needs to be taken into account due to the oxophilic character of sulfur, as reflected in increasing rate constants upon higher pH levels. As a result, mildly acidic conditions are preferred when in aqueous media.



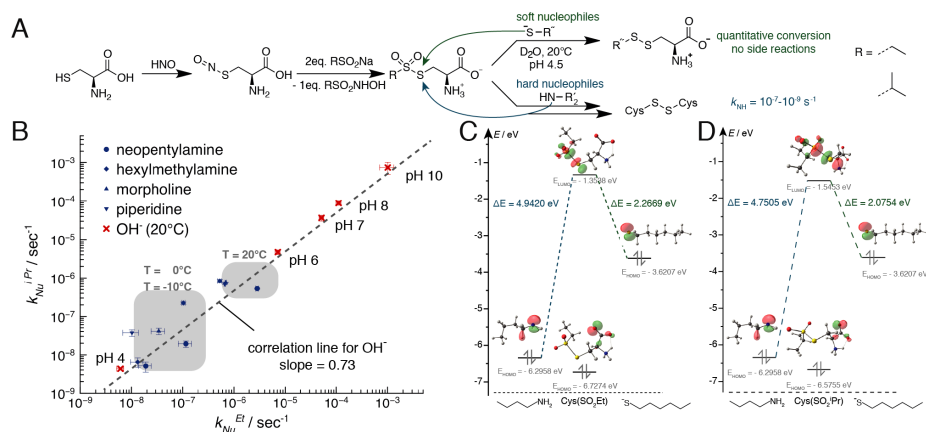


Figure 4.1: A) Synthesis of *S*-alkylsulfonyl-L-cysteines (Cys(SO<sub>2</sub>R)) and reactivity profile towards hard *N*- and soft *S*-nucleophiles. B) Plot of  $\log(k_{Nu})$  for Cys(SO<sub>2</sub>R) under alkaline hydrolysis (red) and aminolysis conditions (blue) at different temperatures. C) DFT calculations of HOMO and LUMO of Cys(SO<sub>2</sub>Et) and D) Cys(SO<sub>2</sub><sup>i</sup>Pr) each in relation to HOMOs of butylamine and hexanethiolate in a nucleophilic attack. Reproduced with permission from ref.<sup>[173]</sup> copyright 2016 Wiley-VCH.

In the case of a nucleophilic attack, the reactivity profile of the *S*-alkylsulfonyl group is directed by the difference between the energy level of the lowest unoccupied molecular orbital (LUMO) of the electrophile and the highest occupied molecular orbital (HOMO) of the nucleophile. Figure 4.1 C and D show density functional theory (DFT) calculations of the frontier orbitals of *S*-ethylsulfonyl- as well as *S*-isopropylsulfonyl-L-cysteine in relation to hexanethiolate as a soft nucleophile and butylamine as a hard nucleophile.<sup>[325,326]</sup> For both protective groups the energy gap between the LUMO and the HOMO of the amine (left) significantly exceeds the gap to the HOMO of the thiol (right). A smaller energy gap, however, facilitates an orbital controlled nucleophilic reaction and the DFT calculations are well in line with the observed reactivity of the *S*-alkylsulfonyl group towards thiols and the hindered aminolysis.

After ensuring the stability of the *S*-alkylsulfonyl group under amine-initiated controlled ring-opening polymerization conditions, both protected L-cysteine derivatives were converted into the corresponding NCAs and polymerized with neopentylamine as initiator (Figure 4.2 A). The resulting poly(*S*-alkylsulfonyl-L-cysteine) (PCys(SO<sub>2</sub>R)) display a narrow, symmetrical molecular weight distribution with low polymer dispersity ( $\bar{D} < 1.2$ ) (Figure 4.2 B). Further, matrix assisted laser desorption/ionization-time of flight (MALDI-TOF) mass spectrometry studies of homopolymers verified the integrity of the protective group during the NCA polymerization and absence of side reaction.<sup>[209]</sup> Full agreement between simulated and measured molecular weights clearly confirms the absence of chemical chain termination or other side reactions due to protective group cleavage and emphasize the highly controlled polymerization of Cys(SO<sub>2</sub>R) NCAs.

... paired with stability in the nucleophilic ring-opening polymerization, yielding well-defined PCys(SO<sub>2</sub>R) with thiol reactivity.

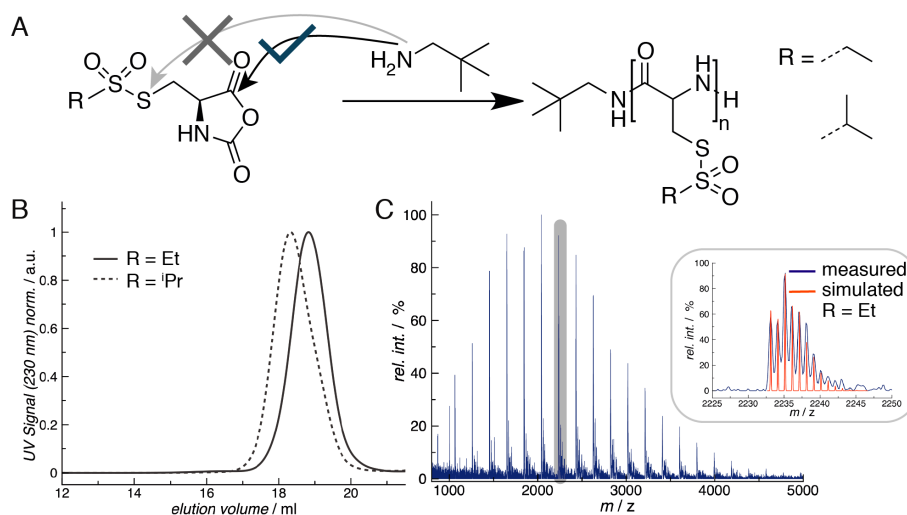


Figure 4.2: A) Polymerization of  $Cys(SO_2R)$  NCA with neopentylamine as initiator, B) HPLC traces of  $PCys(SO_2R)$  and C) MALDI-TOF spectrum of  $PCys(SO_2Et)$ . Reproduced with permission from refs.<sup>[173,209]</sup> copyright 2016 Wiley-VCH and American Chemical Society.

The chemoselective formation of asymmetric disulfides as mediated by the *S*-alkylsulfonyl group in the polymer was carefully verified by conversion with a thiol moiety (Figure 4.3 A). As evaluated by  $^1H$  NMR full chemoselective conversion into the disulfide is achieved with high reaction rates and without detectable side products (Figure 4.3 B).<sup>[209]</sup> Subsequently, block copolypept(o)ides incorporating  $PCys(SO_2R)$  as a cross-linkable segment were realized by sequential polymerization. The orthogonality of the thiol-reactive moiety of the *S*-alkylsulfonyl group towards strain-promoted azide-alkyne cycloaddition (SPAAC) and activated ester-mediated amidation was investigated in amphiphilic poly-sarcosine-*block*-poly(*S*-alkylsulfonyl-L-cysteine) block copolypept(o)ides (Figure 4.3 C). All three functionalities can be addressed independently, thus allowing for functional group interconversion of chain ends, as well as directed disulfide formation in the side chain of the  $PCys(SO_2R)$  block in one step.<sup>[327]</sup>

A combination of this orthogonal direct disulfide formation with further functional polypeptidic segments, such as a cationic poly-L-lysine block as mentioned above in the strategy for post-polymerization modification for disulfide stabilized-polyplexes,<sup>[154]</sup> adumbrates a gateway to numerous multifunctional polypept(o)idic systems and envisions their use as material platform for biomedical applications.



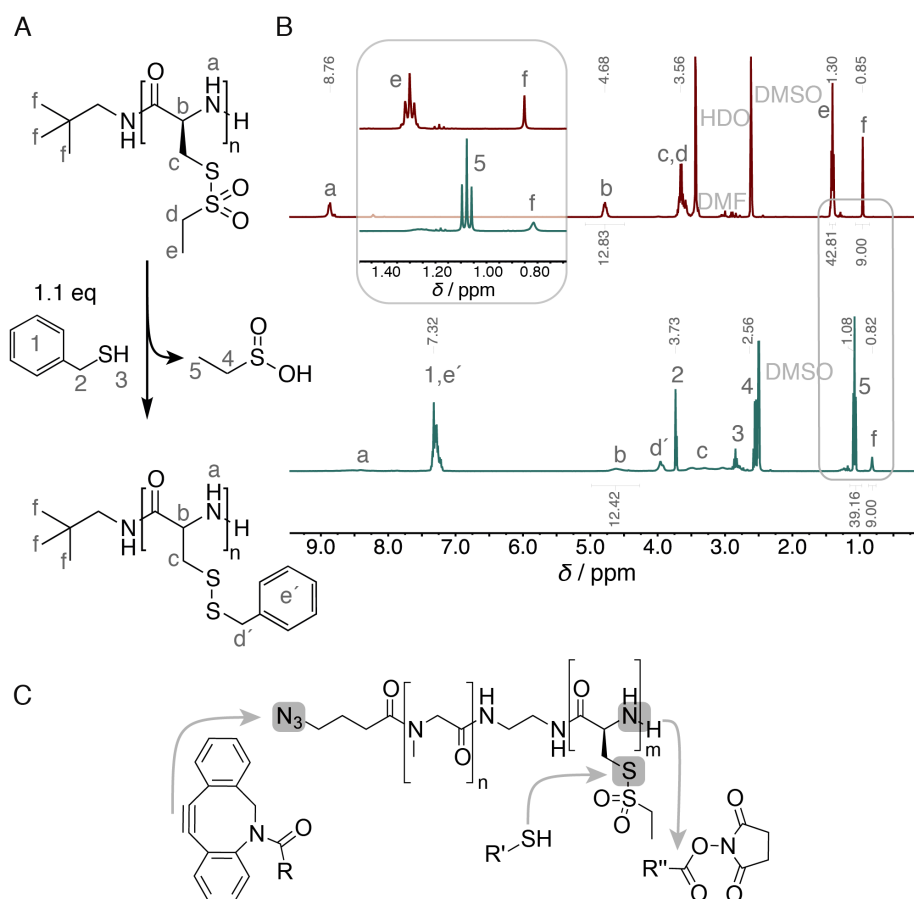


Figure 4.3: A) Reaction of PCys(SO<sub>2</sub>Et) with benzylmercaptan. B) <sup>1</sup>H NMR spectrum of PCys(SO<sub>2</sub>Et) prior to conversion (*red*) and after conversion with benzylmercaptan (*blue*). Enlarged comparison of both <sup>1</sup>H NMR spectra emphasizing the quantitative conversion (disappearance of polymer associated protective group signal at 1.30 ppm (*e*) and emerging signal at 1.08 ppm (*5*) of the fully converted protective group). C) Scheme of PSar-*b*-PCys(SO<sub>2</sub>Et) end-group conversion with NHS-ester and DBCO moieties, respectively, and thiol reactivity of the S-ethylsulfonyl group in the side chain. Reproduced with permission from ref.<sup>[209,327]</sup> copyright 2016 and 2017 American Chemical Society.

#### 4.4 APPLICATIONS OF THIOL-REACTIVE POLYPEPTIDES

The incorporation of activated thiols into polypeptides provides access to reactive copolymers, which can be applied to postpolymerization modification reactions<sup>[21,320,328,329]</sup> leading to the formation of disulfides. Since these bonds are intrinsically reversible and possess a certain dynamic nature, the formation of disulfide bonds is used for bioreversible cross-linking of micelles, polyplexes or protein polymer conjugates or for the attachment of bioactive agents, e. g. antibody or protein drug conjugates<sup>[103,153,330–332]</sup> In another recent example multiple functionalities were introduced into polypept(o)ides bearing PCys(SO<sub>2</sub>R) segments for the formation of asymmetric disulfides.

*Hydrophobic  
PCys(SO<sub>2</sub>R) drives  
self-assembly in  
block copolymers ...*

... and directs morphology by secondary structures.

In addition, self-assembly of polypeptides in solution and of PCys(SO<sub>2</sub>R) containing block copolymers in particular, provides access to compelling micellar morphologies (see Figure 4.4). The Cys(SO<sub>2</sub>R) block adapts a  $\beta$ -sheet conformation (Figure 4.4 A), adding cooperative effects to the self-assembly process. Thus, control over self-assembly in solution is not longer solely directed by block length ratios of the hydrophilic to the hydrophobic block, but can be modulated by hydrogen bond formation between polypeptides of a certain secondary structure.

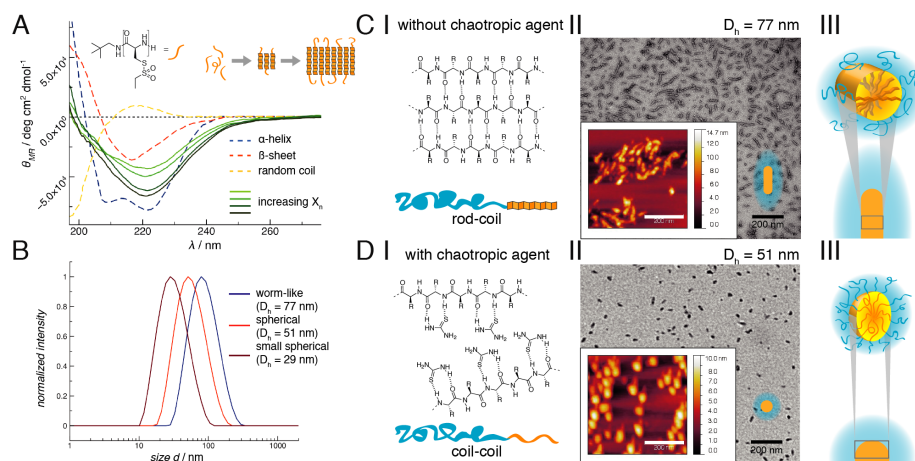


Figure 4.4: A) CD spectrum of PCys(SO<sub>2</sub>Et) of varying degrees of polymerization in HFIP confirming  $\beta$ -sheets in solution. B) Size range of core-cross-linked nanohydrogels as shown in dynamic light scattering experiments. C) Properties of core-cross-linked nanohydrogels in the absence of a chaotropic agent: I) intermolecular hydrogen bond formation resulting in  $\beta$ -sheets and thus rod-coil polymers, II) elongated shapes due to secondary structure stabilization (visualized by AFM/TEM), III) illustration of the core framework of worm-like particles with twisted  $\beta$ -sheets. D) Properties of core-cross-linked nanohydrogels in the presence of a chaotropic agent such as thiourea: I) intermolecular hydrogen bond formation is repressed resulting in coil-coil polymers, II) spherical structures as modulated by the absence of secondary structure stabilization (visualized by AFM/TEM), III) illustration of the core framework of spherical particles with intertwined polymer chains in random coil conformation. Reproduced with permission from refs.<sup>[22,209]</sup> copyright 2016 American Chemical Society and 2017 Wiley-VCH.

Keeping in mind that the secondary structure of proteins can be denatured by different external stimuli,<sup>[333]</sup> the self-assembly of such polypeptides can coherently be controlled by modulation of hydrogen bond formation. In the most prominent case, a rod-coil block copolymer (intact  $\beta$ -sheet conformation, Figure 4.4 C I) can be converted to a coil-coil polymer with help of a chaotropic agent (disturbed  $\beta$ -sheet conformation, Figure 4.4 D). While rod-coil block copolymers (PSar<sub>407</sub>-b-PCys(SO<sub>2</sub>Et)<sub>28</sub>) form worm-like micelles in aqueous solution (without thiourea, Figure 4.4 C II) the same polymer can lead to the formation of spherical micelles in the presence of a chaotropic agent (with thiourea,

Figure 4.4 D II). Disturbing the formation of inter chain hydrogen bonds, the chaotropic agent converts the rod-coil conformation of the block copolymer to an rod-coil block copolymer and subsequently alters the resulting nanoparticle morphology.

Moreover, the reactive poly(*S*-alkylsulfonyl-L-cysteine) block ensures stabilization of the formed morphologies and the introduction of functionality in the micellar core. The formation of disulfide linkages proceeds at the core-forming block in a chemoselective fashion, whenever the cross-linking is realized by the reaction of di- or oligothiols in aqueous solution (Figure 4.5 A). Interestingly, the size and morphology of the previously assembled micellar structures are not affected by this cross-linking reaction even if the core polarity is inverted by hydrophilic dithiols. Therefore, a complex goal, the complete decoupling of aggregate formation and core functionalization as well as stabilization, is realized. As a consequence, core functionality as well as polarity can be easily adjusted according to the implemented dithiol in one single step (Figure 4.5 B). Here, the liponic acid derivatives are implemented after equimolar reduction with TCEP.

*The S-alkylsulfonyl group allows for disulfide stabilization and introduces functionality by cross-linking with functional dithiols.*

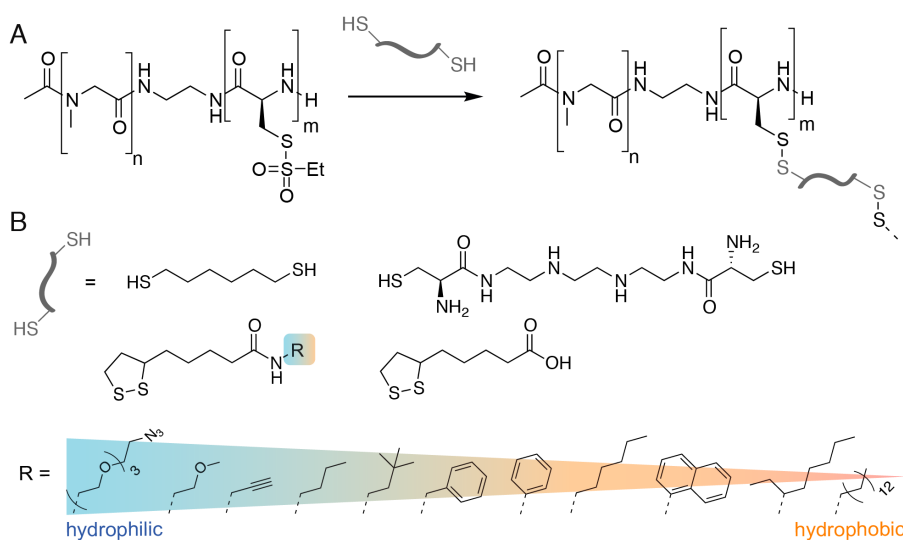


Figure 4.5: A) Illustration of the cross-linking reaction mediated by the thiol reactivity of the *S*-ethylsulfonyl group with various dithiols B) such as hexanedithiol, triethylenetetramine  $\alpha,\omega$ -di(cysteine)diamide (TETA), lipoic acid and lipoic acid derived cross-linkers prior to reduction with side chains of varying polarity. Reproduced with permission from ref.<sup>[22]</sup> copyright 2017 Wiley-VCH

In summary, the implementation of the *S*-alkylsulfonyl group in the core-forming block block leads to adjustable size- and morphology regimes in nanoparticle formation by self-assembly. Further, independent core functionalization in respect to the desired biomedical application is achieved as well as bioreversible core stabilization and thus creating a highly versatile nanoparticle platform.

#### 4.5 CONCLUDING COMMENTS

Activated thiols moieties have already drawn the attention of researchers in the fields of organic chemistry and polymer science as a possibility to introduce functionalities into macromolecules by bioreversible disulfide formation. However, a lack of chemoselectivity in complex proteins for side specific disulfide formation in the presence of amines or other nucleophiles is limiting the use of activated disulfides. In contrast, *S*-alkylsulfonyl protected thiols can overcome these limitations since they enable the desired chemoselective formation of disulfide linkages between macromolecules and peptides or other low molecular weight compounds. We believe that in poly(*S*-alkylsulfonyl-L-cysteines) in particular, an exciting combination of properties is merged to enable asymmetric disulfide formation in a chemoselective manner, while promoting directed self-assembly in solution by  $\beta$ -sheet formation. These properties allow the straightforward synthesis of core-shell nanoparticles with decoupled control over morphology and functionality. Therefore, we anticipate that the *S*-alkylsulfonyl group for thiol-activation will develop into a useful tool in the synthesis of functional nanoparticles and in bioconjugation chemistry.

#### 4.6 ACKNOWLEDGMENTS

M. B. acknowledges financial support by the CRC 1066-2 and O. S. acknowledges support by the "Evangelisches Studienwerk e.V. Villigst".

## 5.1 INTRODUCTORY REMARKS

Single molecules, e. g. building blocks based on functional protected amino acids or corresponding  $\alpha$ -amino acid *N*-carboxyanhydrides (NCAs), can be characterized by nuclear magnetic resonance (NMR) and infrared (IR) spectroscopy as well as electrospray ionization (ESI-MS) or field desorption mass spectrometry (FD-MS). Further, molecular orbitals can be calculated by density functional theory (DFT). Here, a computed quantum mechanical modeling provides information of the electronic structure of a many-electron system for a better understanding of reactivity profiles. X-ray diffraction can be used to evaluate the absolute conformation of a crystalline compound, which proved to be an essential characterization tool, since the polymeric materials used in this work are derived from NCAs of L-amino acids.

*Characterization of single molecules...*

As most polymeric materials, polypept(o)ides (polypeptides-*block*-polypeptoids) are commonly characterized by NMR spectroscopy to evaluate the composition of the (block co-) polypept(o)ide. Further, the presence of secondary structures in polypeptides can be evaluated by means of NMR, IR or circular dichroism (CD) spectroscopy. By gel permeation chromatography (GPC), relative average molecular weights are determined (based on a calibration by polymer standards) as well as polymer dispersity, which is a value for the molecular weight distribution. Further, matrix assisted laser desorption/ionization-time of flight (MALDI-TOF) mass spectrometry can be applied to macromolecules since it is a relatively gentle method avoiding fragmentation. No external calibration is necessary, thus absolute average molecular weights and dispersities are obtained. Additionally, end-group analysis of initiating or terminating species is possible by comparing experimental values with theoretically calculated molecular weights.

*... of macromolecules...*

For polymers and nanoparticles in solution, light scattering techniques such as dynamic light scattering (DLS) and static light scattering (SLS) exploit the interaction of the solute with light of a defined wavelength (monochromatic laser), which induces oscillation of electromagnetic dipoles. The constructive or destructive interference between the emitted light waves results in characteristic interference patterns, which contains information on size and shape of the scattering species. Upon introduction of a fluorescent label, polymers and particles can be analyzed by fluorescence correlation spectroscopy (FCS) or UV-Vis spectroscopy. Visualization of nanoparticles can be achieved by means of atomic force microscopy (AFM). Upon the measurement of forces be-

*... and of nanodimensional carrier-systems.*

tween a cantilever tip and the specimen, height micrographs are generated which depict the overall particle surface. In contrast, transmission electron microscopy (TEM) visualization is based on interactions of an electron beam with a thin sample, yielding a contrast image. Specimen with an overall low electron density, as most carbon-based synthetic polymers and peptides, can be stained by uranylacetate or osmiumtetroxide to increase electron density and thus contrast. A valuable extension is cryogenic transmission electron microscopy (cryoTEM), since visualization is based on transmitted electrons from a vitrified sample, allowing the imaging of specimen in aqueous solution.

The biological evaluation of nanoparticles for nucleic acid delivery includes agarose gel electrophoresis to estimate complexation efficiency of cationic carrier systems with negatively charged nucleic acids. Further, cell viability assays evaluate the exposure of cells to empty or loaded carrier systems. The functional knockdown mediated by transfection with nucleic acids can be evaluated *in vitro* as well as *in vivo* by monitoring bioluminescence in luciferase-expressing cell lines. Ultimately, bioluminescence as well as fluorescence signals can be evaluated in the living organism by an *in vivo* imaging system (IVIS), allowing to track fluorescent-labeled particles and their systemic distribution as well as *ex vivo* imaging of organ and tissue samples.

A broad methodological approach is unmistakably necessary to perpetually monitor the development from single molecule building blocks such as protected amino-acids and  $\alpha$ -amino acid *N*-carboxyanhydrides (NCAs), to (multi)block copolypept(o)ides, towards self-assembly of nanocarriers and their biological application. Thus, only several characterization techniques and underlying theoretical background are described in detail in the following sections. The selection is based on the attempt to elaborate on characterization methods not widely used in the field of organic chemistry as well as the impact of the respective characterization technique on the scope of this thesis.

## 5.2 PHYSICOCHEMICAL CHARACTERIZATION

### 5.2.1 X-ray Diffraction

Based on the discoveries of Max von Laue *et al.*<sup>[334]</sup> showing that crystalline substances act as three-dimensional diffraction gratings for X-ray wavelengths similar to the spacing of planes in a crystal lattice ( $\approx 10^{-10}$  m), X-ray diffraction (XRD) evolved into a popular technique for analysis of crystalline materials. A typical setup is shown in Figure 5.1 based on the elements of the X-ray tube, a rotating sample holder and an X-ray detector.

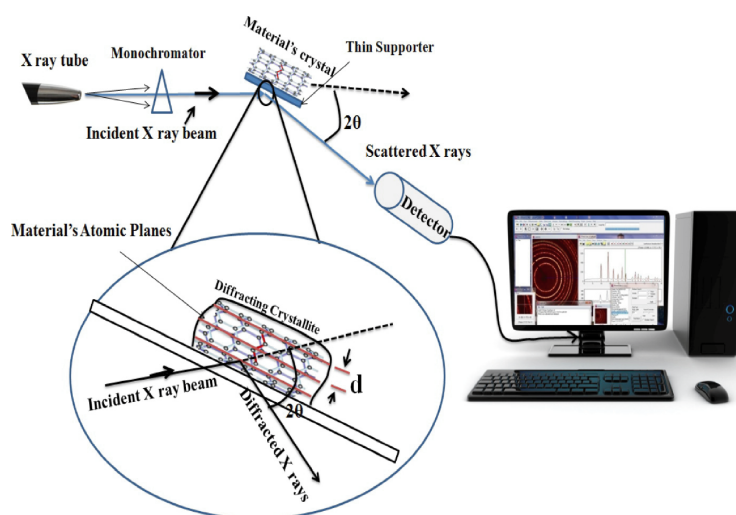


Figure 5.1: Schematic representation of basic principles of X-ray diffraction.<sup>[335]</sup>

The incident beam is a monochromatic X-ray beam which is focused on the sample. Polychromatic X-rays are generated in a cathode-ray tube, where a filament is heated to produce electrons, which are accelerated by applying a voltage. The impact of accelerated electrons on the target material (most commonly molybdenum) results in dislocation of inner shell electrons of the target material which generate a characteristic X-ray spectrum (e. g.  $K_{\alpha}$  and  $K_{\beta}$  named for the K-shell). Filtering by foils or crystal monochrometers results in the required monochromatic X-ray beam.

*Generation of X-rays.*

Interaction of the incident beam with the sample atomic planes create a multitude of events such as diffracted, transmitted, refracted, scattered and absorbed beams. The geometry of incident rays, the orientation of the crystal and the detector can be changed to attain all possible diffraction directions of the lattice. When the geometry of the incident X-rays diffracted off the sample results in constructive interference of the scattered X-rays, a peak in intensity is detected and converted to a count rate by the detector. The necessary constructive interference occurs when conditions satisfy BRAGG's law:

*Premise of constructive interference.*

$$n\lambda = 2d\sin\theta \quad (1)$$

with  $n$  as an integer,  $\lambda$  the wavelength of the X-rays,  $d$  the interplanar spacing of the atomic planes of the material and  $\theta$  the diffraction angle. Thus a relation of wavelength to the diffraction angle and lattice properties is established. Two methods can be applied to X-ray diffraction in terms of the specimen under investigation: single-crystal X-ray diffraction or powder X-ray diffraction as portrayed in the following sections.



*Single-Crystal X-ray Diffraction*<sup>[336]</sup>

Single-crystal X-ray diffraction is a non-destructive method and provides information on the internal lattice of crystalline materials. A prerequisite for this method is a stable crystal of relatively large size (50–250  $\mu\text{m}$ ) and purity, which can not always be accessed. A relatively extensive data collection period of 24–72 h and the acquisition of an adequate crystal are the drawbacks of this analytical technique. Its strengths are the non-destructive manner of analysis as well as details available on the internal crystal structure such as unit cell dimensions, bond-lengths, bond-angles and details of site-ordering.

For single-crystal diffraction, molybdenum is the most common target material with Mo  $K_{\alpha}$  radiation ( $\lambda = 0.71069 \text{ \AA}$ ). The crystalline sample is mounted on thin glass fibers fixed to goniometer heads (three- or four-circle) enabling precise movement of the sample and positioning in the center within the X-ray beam. A preliminary rotational image is often obtained for sample screening and parameter selection. Detection and identification of intensity peaks is commonly performed by a charge-coupled device (CCD), which transforms the X-ray photons into an electrical signal ready for computational processing. After data collection several corrections for instrumental factors, polarization effects, X-ray absorption and (potentially) crystal decomposition are applied. Based on the obtained data with help of complementary chemical information, a model of the arrangement on the atomic level in the lattice is computationally produced and refined.

*Powder X-ray Diffraction*<sup>[335]</sup>

Powder X-ray diffraction utilizes a sample in form of very small crystallites and can give insights on phase identification of a crystalline material as well as unit cell dimensions. Analysis is performed by scanning through a range of  $2\theta$  angles, which enables the detection of all possible diffraction directions of the lattice in the random orientation of a powdered state. The resulting powder diffraction profile exhibits characteristic sharp peaks. Thus, powder diffraction is commonly implemented for material identification of pure and mixed samples. Comparison of peak patterns and intensities with databases of characteristic diffraction profiles allows for identifications. Further, different phases and their percentage in the solid state of a material can be classified.

Limitations of powder X-ray diffraction are mostly associated with the sample itself such as the necessity a single phase material of sufficient homogeneity as well as a relatively large sample size of tenths of a gram. Further, for mixed materials the detection limit is  $\approx 2\%$  and a standard reference of the compound with known d-spacing is mandatory. Cell determination for non-isometric crystal systems is challenging and interpretation may be further complicated by peak overlay. However, powder X-ray diffraction is a powerful and rapid material identification technique with minimal sample preparation.



### 5.2.2 Light Scattering

The foundation of light scattering techniques evaluating properties of polymers and nanoparticles in solution is based on the interaction of the solute with light of a defined wavelength (monochromatic laser). Light of a wavelength  $\lambda$  propagating in space ( $x$ ) and time ( $t$ ) can be described as an electromagnetic wave by the following equation:

$$E(x, t) = E_0 \left( \sin \left( \frac{2\pi x}{\lambda} \right) + \sin \left( \frac{2\pi \frac{c}{\lambda}}{t} \right) \right) \quad (2)$$

The interaction of light as an electromagnetic wave with the observed species in solution induces a modulation of charge distribution. This results in an oscillating electromagnetic dipole, which emits light of the same wavelength as the incoming wave all directions perpendicular to the axis of oscillation (elastic scattering, see Figure 5.2).

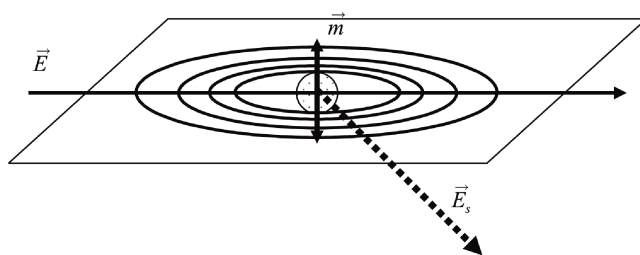


Figure 5.2: Elastic light scattering as the underlying principle of light scattering techniques.<sup>[337]</sup>

In particles or molecules larger than  $\lambda/20$ , several oscillating dipoles are induced simultaneously, which results in a phase difference and a non-isotropic angular dependence of the scattered light intensity. The scattering angle (or scattering vector  $q$ ) is given as the angle of observation towards the incident light beam. Since several dipoles are induced in one particle, the constructive or destructive interference between the emitted light waves results in characteristic interference patterns giving information on the shape of the scattering species. Light scattering experiments of particles  $< \lambda/20$  however, result in scattering intensity independent from the scattering angle.

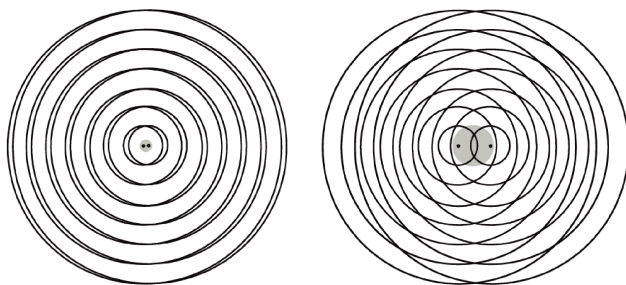


Figure 5.3: Influence of particle size on interference pattern: small  $< \lambda/20$  (left) and large  $> \lambda/20$  (right) particles.<sup>[337]</sup>

### Dynamic Light Scattering (DLS)<sup>[337,338]</sup>

Since particles in solution are in perpetual motion (BROWNIAN motion), scattering intensity is subject to temporal fluctuation (Figure 5.4), which is exploited in dynamic light scattering.

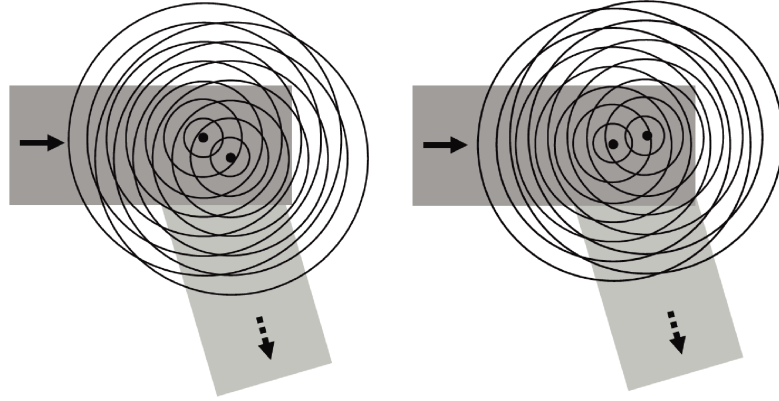


Figure 5.4: Influence of Brownian motion on interference pattern and scattering intensity.<sup>[337]</sup>

A typical DLS setup is shown in Figure 5.5: the sample is illuminated by a laser beam of a known wavelength  $\lambda$  and time-dependent fluctuations of the light scattered from a spatially limited volume within the sample are detected at a known scattering angle  $\theta$  by a photon detector.

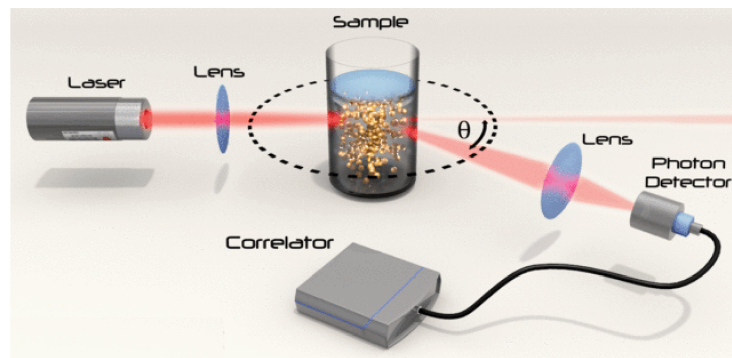


Figure 5.5: Schematic representation of a typical DLS setup.<sup>[339]</sup>

*Principle of auto-correlation.*

A quantitative analysis of the scattering intensity ( $I_s(q, t)$ ) fluctuation is possible by correlating the signal with itself over time in an auto-correlation function ( $I_s(q, t)I_s(q, t + \tau)$ ). Normalization results in the following equation with  $\tau$  as the lag time and  $q$  as the scattering vector:

$$g_2(q, \tau) = \frac{\langle I_s(q, t)I_s(q, t + \tau) \rangle}{\langle |I_s(q, t)|^2 \rangle} \quad (3)$$

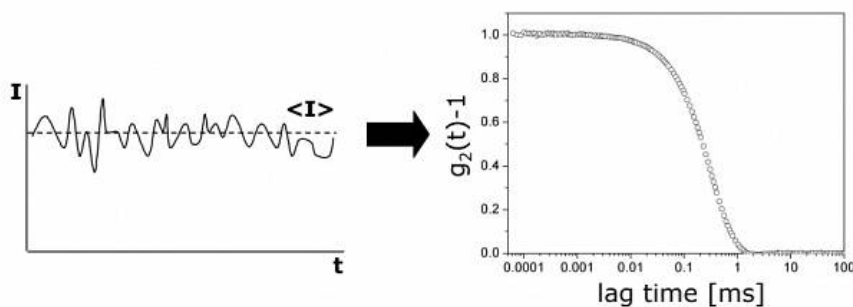


Figure 5.6: Detector signal of fluctuating scattering intensity at a fixed angle and the computed intensity correlation function.<sup>[339]</sup>

Since polydisperse samples result in  $q$ -dependency of the amplitude of the auto-correlation function, the observed decaying function (see Figure 5.6 *left*) is a superposition of several single exponential functions. This intensity correlation function can be analyzed by the cumulant method: by fitting a polynomial of third degree to the logarithm of the intensity correlation function, the decay rate  $\Gamma$  (1<sup>st</sup> cumulant) is obtained and related to the self-diffusion coefficient. Higher orders of the fitting result (2<sup>nd</sup> cumulant) give quantitative information on the polydispersity of the self-diffusion coefficient.

By means of the SIEGERT relation based on the principles of GAUSSIAN random processes (which applies to scattered light), a relation of the auto-correlation function to the electric field correlation function is established:

$$g_2(q, \tau) = 1 + \beta |g_1(q, \tau)|^2$$

$$g_1(q, \tau) = \frac{\langle E_s(q, t) E_s(q, t + \tau) \rangle}{\langle |E_s(q, t)|^2 \rangle} \quad (4)$$

Fitting to an exponential function gives the decay rate  $\Gamma$

$$g_1(q, \tau) = \exp(-\Gamma \tau) \quad (5)$$

which is defined as

$$\Gamma = D_s q^2 \quad (6)$$

establishing ultimately a relation to the self-diffusion coefficient.

Ultimately, by means of the STOKES-EINSTEIN equation a relation to the hydrodynamic radius  $R_h$  is achieved, however, with the approximation of an equally sized, solid spheres ( $k_B$  is the BOLTZMANN-constant,  $T$  the temperature and  $\eta$  the viscosity of the suspending medium).

$$D = \frac{k_B T}{6\pi\eta R_h} \quad (7)$$

*Relation of decay rate to self-diffusion coefficient and to hydrodynamic radius.*

### Zeta-Potential Measurement<sup>[120,340]</sup>

The zeta-potential (commonly abbreviated as  $\zeta$ -potential) is a measure for the electro kinetic potential at the electrical double layer encircling a nanoparticle in solution. Since most cellular membranes bear a negative charge due to composition of the lipid bilayer,<sup>[119]</sup> the  $\zeta$ -potential is a critical parameter when biological applications are considered. Toxicity associated with cell wall disruption is mostly displayed by cationic particles, thus, the tendency to permeate membranes can be anticipated by measurement of the  $\zeta$ -potential.<sup>[120]</sup>

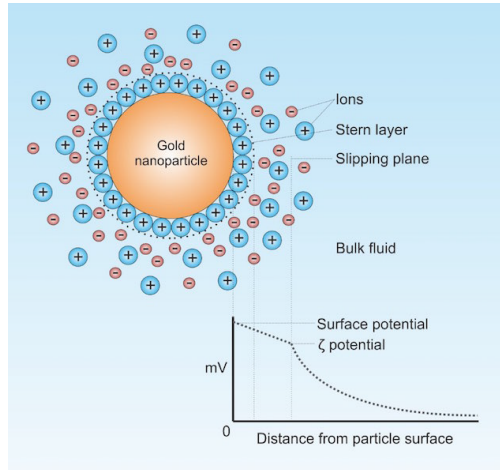


Figure 5.7: Illustration of ionic concentration surrounding a negatively charged particle in solution and the resulting differences in potential relative to distance from the particle surface.<sup>[341]</sup>

For measurement of the  $\zeta$ -potential, DOPPLER electrophoresis measures the net velocity of the nanoparticle in solution upon application of an electric field.<sup>[342]</sup> Most commonly,  $\zeta$ -potential is measured in a DLS setup using a capillary cell equipped with electrodes. Hence, upon an applied electric field, displacement of the particles can be monitored by DLS principles outlined above. The measured parameter is the net electrophoretic mobility ( $\mu$ ), which is converted to the  $\zeta$ -potential upon HENRYs approximation:<sup>[343]</sup>

$$\mu = \frac{2\zeta\epsilon}{3\eta_0} f(\kappa r) \quad (8)$$

with  $\epsilon$  as the dielectric constant,  $\kappa r$  the ratio of particle radius to the DEBYE double layer thickness and  $\eta_0$  the solute viscosity. Generally, a nanoparticle is considered approximately neutral with a  $\zeta$ -potential between  $-10$  and  $+10$  mV, whereas  $\zeta$ -potential of greater than  $+30$  mV or less than  $-30$  mV are recognized as strongly cationic and strongly anionic, respectively.<sup>[120]</sup> However, particle concentration, pH as well as ionic strength of the solute play a role during the measurement and need to be maintained constant for reproducibility of  $\zeta$ -potential measurements.

### Static Light Scattering (SLS)<sup>[337]</sup>

In contrast to dynamic light scattering, which is based on the temporal motion of scattering particles, static light scattering measures the intensity of scattered light itself. The obtained data can be analyzed by means of the ZIMM-equation:

$$\frac{K \cdot c}{R_{\theta}} = \frac{1}{M_w} \left( 1 + \frac{1}{3} R_g^2 q^2 \right) + 2A_2 c \quad (9)$$

with  $K$  as the optical constant of the experimental setup,  $c$  the polymer concentration,  $R_{\theta}$  the reduced scattering intensity,  $M_w$  the mass weighted molecular weight,  $q = 4\pi n \sin(\frac{\theta}{2})/\lambda$  ( $n$  the refractive index,  $\theta$  the scattering angle and  $\lambda$  the wavelength of the beam) and  $A_2$  the second VIRIAL coefficient, which gives information on solvent-solute-interactions.

In a SLS setup scattering intensity is measured at various angles and different concentrations (Figure 5.8).

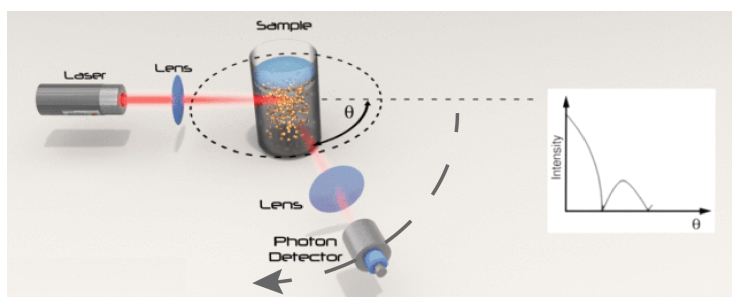


Figure 5.8: Schematic representation of a typical SLS setup.<sup>[339]</sup>

Then,  $\frac{K \cdot c}{R_{\theta}}$  is plotted against  $q^2 + kc$ , with  $k$  as a scaling factor in a ZIMM-plot, followed by extrapolation of all concentrations  $c$  to an angle of  $0^\circ$  and all scattering angles  $\theta$  to a concentration of zero (see Figure 5.9).

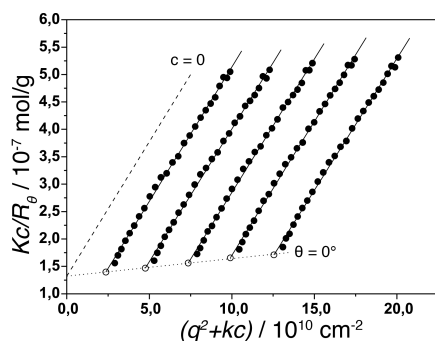


Figure 5.9: Zimm plot analysis resulting in  $M_w$ ,  $R_g$  and  $A_2$ .<sup>[339]</sup>

The radius of gyration ( $R_g$ ) is ultimately calculated from the slope of  $c = 0$ , the second VIRIAL coefficient  $A_2$  from the slope of  $\theta = 0$  and the absolute average molecular weight ( $M_w$ ) from the intercept of both.

*Parameters available  
by means of SLS.*

### 5.2.3 Fluorescence Correlation Spectroscopy (FCS)<sup>[344]</sup>

Principles of FCS...

Fluorescence correlation spectroscopy relies on a setup related to that of a confocal microscope. In the observed confocal volume, fluorescent probes in solution such as small molecules, macromolecules or nanoparticles are subject to random diffusion patterns and temporal fluctuations in the detected fluorescence intensity are detected (compare Figure 5.2.2) As illustrated in Figure 5.10, the laser beam is focused to a diffraction limited spot in the sample by an objective, which also collects the emitted fluorescence light. Fluorescent light originated from other regions than the focal region is blocked by a confocal pinhole after passing through a dichroic mirror and emission filters. Thus a narrow observation volume of less than  $1 \mu\text{m}^3$  is obtained.

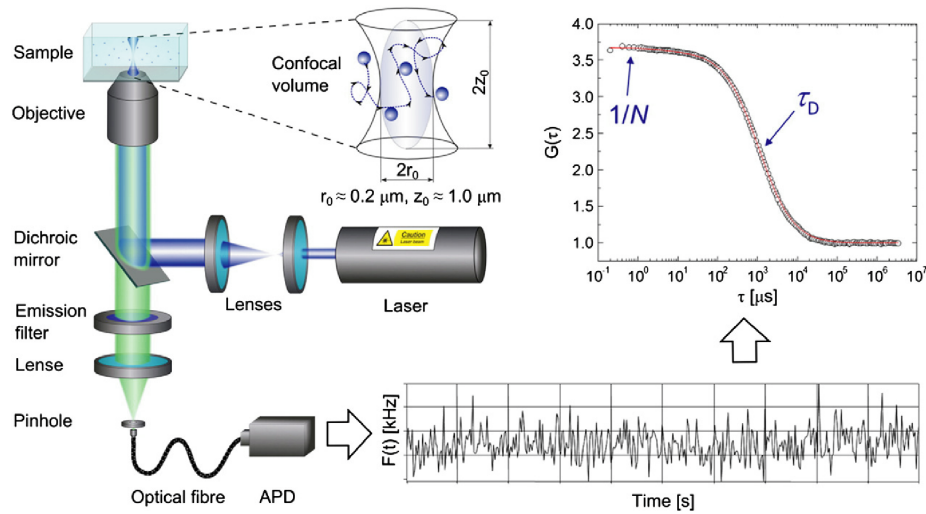


Figure 5.10: Schematic illustration of setup and principles of confocal fluorescence correlation spectroscopy.<sup>[345]</sup>

The fluctuating fluorescence intensity signal can be auto-correlated (self-similarity of a time signal). Thus a fluorescence signal at a certain time ( $F(t)$ ) is measured against its time-average over time ( $\langle F(t) \rangle$ ) and gives the time-dependent fluctuation as:

$$\delta F(t) = F(t) - \langle F(t) \rangle \quad (10)$$

In a confocal setup, this fluctuation from the temporal average can be related in an autocorrelation curve  $G(\tau)$  (see Figure 5.10) with  $\tau$  as lag time and  $F(t)$  the detected fluorescence intensity:

$$G(\tau) = 1 + \frac{\langle \delta F(t) \delta F(t + \tau) \rangle}{\langle \delta F(t) \rangle^2} \quad (11)$$

Parameters such as diffusion time ( $\tau_D$ ), number of molecules in the observed volume ( $\langle N \rangle$ ), diffusion coefficient ( $D$ ) and molecular brightness ( $\eta$ ) can be determined by fitting the autocorrelation curve with suitable

mathematical models. The information on the diffusion coefficient further gives the hydrodynamic radius ( $R_h$ ) of the solute by means of the STOKES-EINSTEIN equation (see Equation 7 in Figure 5.2.2).

An extension of the FCS technique is the fluorescence cross-correlation spectroscopy (FCCS) or dual-color FCCS, which analyses two detection regions simultaneously and thus monitors the interaction of bimolecular processes (Figure 5.11). If the prerequisite of two fluorophores of separated and thus independent emission wavelengths is met, their conjoined or separate movement can be detected by fluorescence cross-correlation spectroscopy (FCCS). The cross-correlation function includes two coordinates (each for one of the two observed volumes) and fluctuations from one volume ( $F_1(t)$ ) and the other ( $F_2(t)$ ) are related. In the event that one molecule moves from one volume to the other, the correlation curve will reach its maximum, otherwise it remains at zero. The amplitude of the cross-correlation function is thus proportional to diffusing species containing both fluorophores.

... and FCCS.

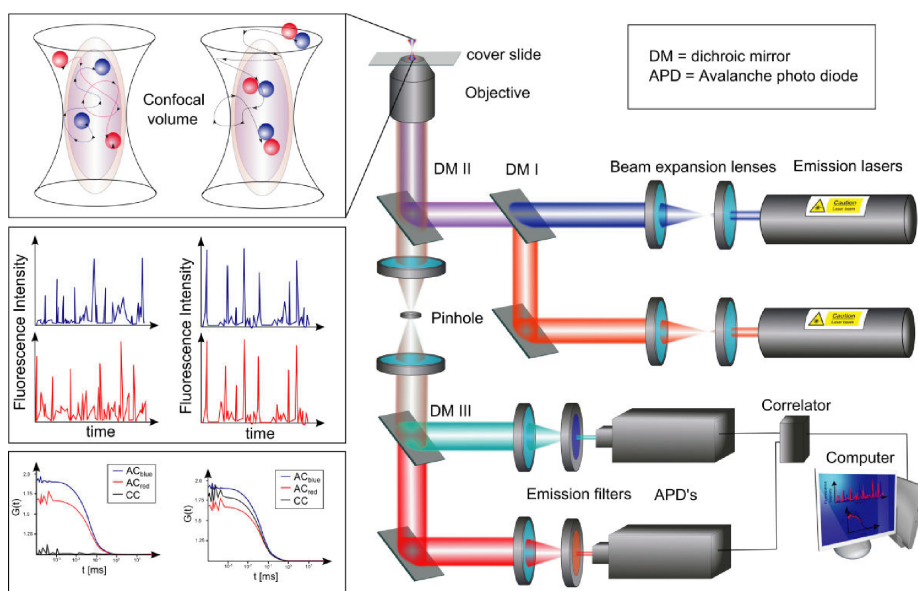


Figure 5.11: Schematic illustration of setup and principles of dual-color fluorescence cross-correlation spectroscopy.<sup>[346]</sup>



## 5.3 BIOLOGICAL EVALUATION

5.3.1 Cell Viability Assay<sup>[347]</sup>

The effect of exposure of cells to polymers, loaded and empty poly-pept(o)idic carrier systems can be evaluated by colorimetric viability assays e. g. cell counting kit-8 (CCK-8). Information on cell viability and cell proliferation is obtained by evaluating the activity of NADH/NADPH dehydrogenases. If active, they will produce the reduction equivalents NADH and NADPH, which are essential in a normal functioning, viable cell. The assay includes a water-soluble, slightly yellow tetrazolium salt (WST-8: 5-(2,4-disulfophenyl)-3-(2-methoxy-4-nitrophenyl)-2-(4-nitrophenyl)-2H-tetrazolium monosodium salt) and an electron mediator (here 1-methoxy-PMS). Upon reduction by NADH and NADPH, a bright orange formazan dye (WST-8 Formazan) is formed (see Figure 5.12). The absorbance of the formazan dye at 450 nm (measured e. g. in a plate reader) is then directly proportional to the number of viable cells.

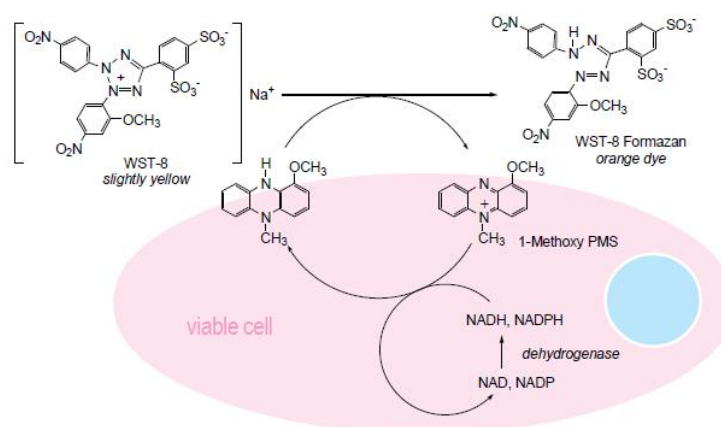


Figure 5.12: Cell viability detection mechanism with CCK-8.<sup>[347]</sup>

*Advantages of CCK-8 over MTT or related assays.*

In contrast, in the MTT assay, MTT ((3-(4,5-dimethylthiazol-2-yl)-2,5-diphenyltetrazolium bromide)) is reduced to a purple formazan dye, which is water insoluble and form (cytotoxic) crystalline needles. Thus for measurement it is required to solubilize the formazan needles and remove floating cells along with cell culture media. Further, this assay involves only the mitochondrial dehydrogenase (thus relies only on mitochondrial activity, not the cell itself). The water-soluble tetrazolium salts as well as the formazan derivatives used in the CCK-8 are not cytotoxic, which allows for continuous cell culture and the reduction mechanism involves most of the dehydrogenases in a cell.

5.3.2 Luciferase Assay<sup>[348]</sup>

A luciferase assay is based on activity of genes encoding the luciferase enzymes from *Renilla reniformis* (sea pansy) or *Photinus pyralis* (firefly). It can be performed with regular cells evaluating transfection with re-



porter genes encoding luciferase enzymes, or with transgenic cells with the corresponding luciferase gene in their genome, evaluating its knock-down e.g. by transfection with corresponding anti-siRNA. When D-luciferin is added to the cell culture or the respective organism (e.g. i.v.), oxidative decarboxylation of D-luciferin is catalyzed by the firefly luciferase and results in oxyluciferin and light emission (see Figure 5.13). Conveniently, D-luciferin is not a substrate for any mammalian enzymes, thus the readout is extremely specific and highly sensitive.

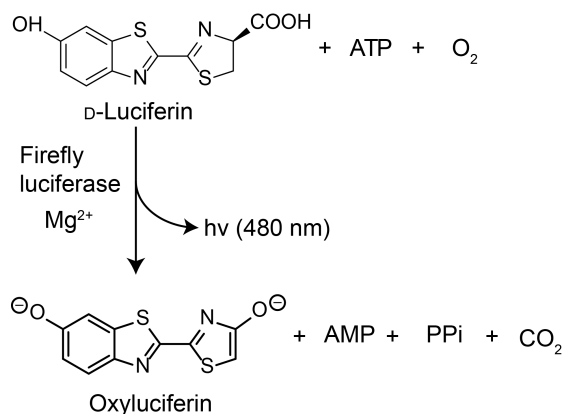


Figure 5.13: Oxidative decarboxylation of D-luciferin and resulting light-emission.

The emitted light at 480 nm is called bioluminescence and can be quantified *in vitro* by a luminometer or an *in vivo* imaging system (IVIS). The light intensity is directly correlated to activity of luciferase and is evaluated depending to the setup (evaluation of transfection or knock-down): increase in bioluminescence indicating successful transfection or decrease in bioluminescence demonstrating successful knock-down.

### 5.3.3 *In Vivo* Imaging System (IVIS)<sup>[349,350]</sup>

To determine the time dependent fate of an agent or its therapeutic potential over time in an specific pathophysiological context *in vivo*, traditional approaches would require large cohorts of laboratory animals. The readout would include sacrifice of the animals at different time points, dissection and tissue histology. Apart from being costly and ethically questionable, this approach decreases its statistical integrity, since each animal is only measured once, and cannot be its own control over time. Traditional clinical techniques such as magnetic resonance imaging (MRI) and X-ray computed tomography (X-ray CT) are an option, but are often expensive, difficult to accommodate and extensive studies with large animal throughput prove to be demanding.

Noninvasive *in vivo* imaging with light photons enables to measure the state of an animal at multiple time points and is an attractive option to gain biological information fast and non-destructively in the living organism.<sup>[349]</sup> However, tissue penetration of photons is highly dependent on the absorption and scattering properties of tissue components.

Why IVIS?

Advantage of the NIR region for *in vivo* studies.

Certain advantages can be exploited in the near-infrared region of the spectrum, since the absorption coefficients of hemoglobin and water (the major absorbers of visible and infrared light) are lowest in the near-infrared (NIR) region between 650–900 nm<sup>[350]</sup> (see Figure 5.14).

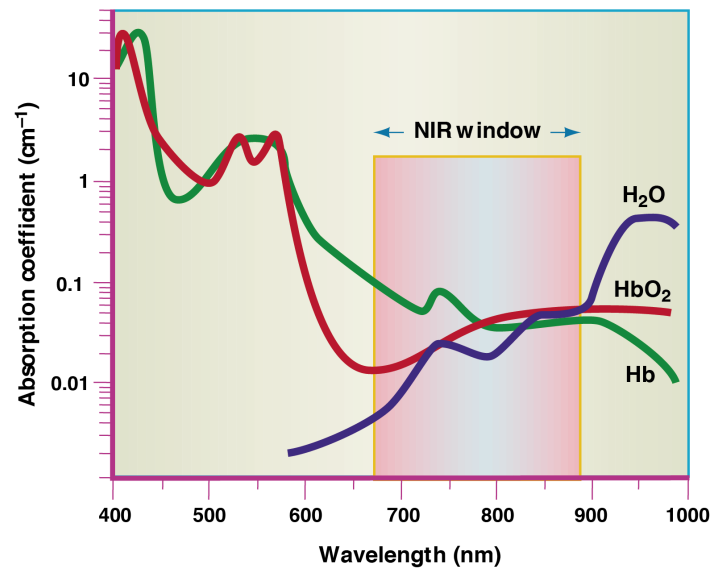


Figure 5.14: The NIR window is ideally suited for *in vivo* imaging due of minimal light absorption by hemoglobin (<650 nm) and water (>900 nm).<sup>[350]</sup>

In addition to absorption and scattering of fluorescence intensity, the autofluorescence of tissue has an influence on signal to background ratio as demonstrated in Figure 5.15.

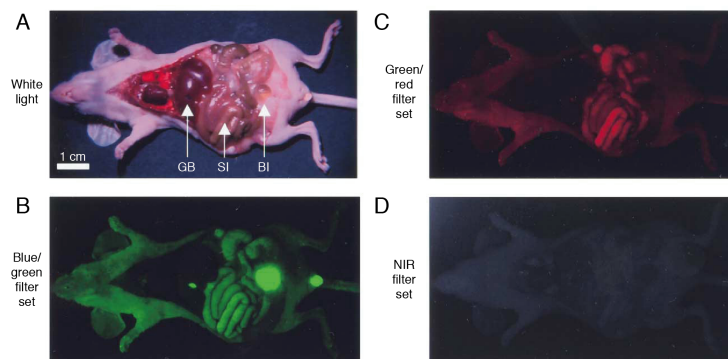


Figure 5.15: Wavelength-dependent autofluorescence of vital organs and bodily fluids. For orientation, the white light color image of the animal is shown in A). Arrows mark the location of the gallbladder (GB), small intestine (SI) and bladder (BI). Tissue autofluorescence was imaged using three different excitation/emission filter sets: B) blue/green (460–500 nm/505–560 nm); C) green/red (525–555 nm/590–650 nm); and D) NIR (725–775 nm/790–830 nm). Fluorescence images have identical normalization.<sup>[351]</sup>

The relation of excitation and emission wavelengths to tissue autofluorescence is least favorable in Figure 5.15 B, due to green autofluorescence of skin, viscera and especially the gallbladder, bladder and urine. This autofluorescence is substantially reduced by a red filter set under green light excitation (Figure 5.15 C), however, with still high intestinal autofluorescence. The use of a NIR filter set in Figure 5.15 D basically eradicates autofluorescence. Thus, NIR dyes are an ideal choice in terms of tissue penetration as well as signal to background ratio in *in vivo* imaging applications.<sup>[351]</sup>

*Principles of IVIS.*

With an *in vivo* imaging system (IVIS), imaging of bioluminescence and fluorescence is enabled in the living organism. Luciferase-based bioluminescence imaging (see Section 5.3.2) depends solely on the energy stored chemically in the substrate D-luciferin. During oxidation only by the enzyme luciferase expressed in distinct cells this energy is released as light of a certain wavelength. Thus emission is detected without an external light source. In contrast, fluorescence imaging depends on external light of a specific wavelength as the energy source for fluorophore activation (Figure 5.16). The fate of exogenous NIR imaging agents can thus be followed *in vivo*.

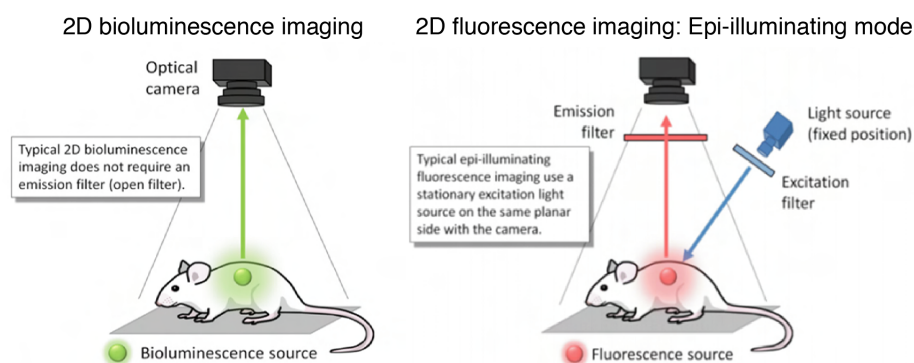


Figure 5.16: Difference between bioluminescence or fluorescence mode.<sup>[352]</sup>

In IVIS the animal is anesthetized (usually 2–3% isoflurane) to reduce movement and thus ensuring focus. Then, a photographic image is recorded for orientation along with the analytical image in the respective mode (bioluminescence or fluorescence). Filters can be applied to adjust excitation to the particular fluorophore as well as its emission. Ultimately, both images are superimposed to create the typical visual outcome of an IVIS experiment as illustrated in Figure 5.17. The actual quantitative information is independent from the visualization (which can be adjusted accordingly by definition of the scale bar limits). An appropriate software enables the selection of regions of interest (ROIs) or the whole image for quantification and the readout gives the light intensity as total radiant efficiency in  $[p/s]/[\mu W/cm]$ .<sup>[352]</sup>

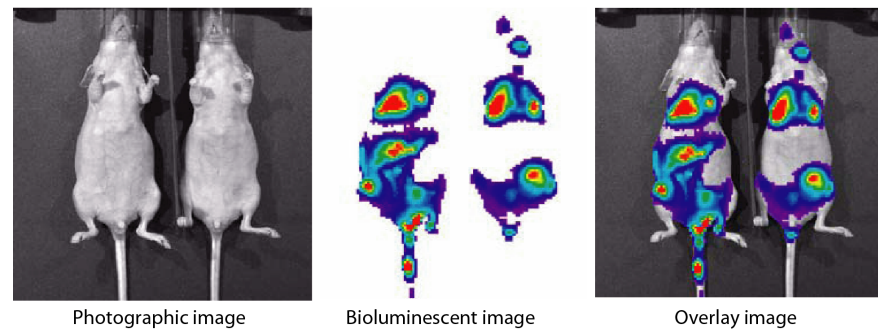


Figure 5.17: Construction of a typical IVIS image by superimposing a photographic image with the bioluminescent (or fluorescent) image.<sup>[353]</sup>

*Factors for consideration.*

In superficial tissues, absorbing and fluorescent contrast is measured by illuminating the tissue and recording emerging diffusely reflected light. Cellular resolution is not possible, since the average path length of the detected light is increased due to tissue absorption. Thus obtained images are strongly weighted by the most superficial layer of the tissue, although they still contain some information on absorption contrast in deeper layers. Evaluation needs to consider different aspects related to depth-sensitivity: If a fluorophore is present only in one organ, few mm below the surface of the skin, it is likely to be detectable due to lack of a larger signal from superficial layers. Detection is possible if fluorescence quantum yield is high enough for the detector and if both excitation and emission light are not excessively attenuated. Tissue autofluorescence with similar spectral properties or fluorophore in overlying tissue may overpower the detector or be indistinguishable from the fluorescence signal of the desired probe. As a result, isolated fluorescent regions can commonly be detected, interpretation and quantification, however, are often far more challenging.

Also factors of the biological model need to be taken into account. If a fluorescent tagged tumor is growing in an axial position, the contributions to the fluorescence signal from superficial and deeper parts vary strongly. Thus, a growth rate to the double tumor volume might not relate to the detected signal over time. Xenograft models of tumors grown subcutaneously reduce the impact of depth on quantification, however, for some tumors this results in loss of their anatomical location (e.g. in the colon, lung or liver) and thus altering the model severely from the native disease. Ultimately, *ex vivo* imaging of the organs and tissues of interest after conclusion of the biological study is necessary to confirm, or critically discuss results gained during the *in vivo* setup.<sup>[349]</sup>

In summary, IVIS is a powerful tool for optical imaging related to *in vivo* applications. For optimal results, different types of optical contrast need to be taken into consideration, starting with the adequacy of the biological animal model for the particular question as well as the choice of operating mode (bioluminescence or fluorescence) and choice of the fluorophore (preferably in the NIR region).



Part II

THIOL ACTIVATION IN  
 $\alpha$ -AMINO ACID *N*-CARBOXYANHYDRIDES



*This PhD thesis was initiated by the need for moieties mediating chemoselective formation of asymmetric disulfide bonds, e. g. for bioreversible stabilization in systemic application of nanomedicines, such as gene delivery vectors. Thus, thiol modifications were investigated, which combine characteristics of an activating group to mediate reactivity towards thiols for directed formation of S-S bonds, with properties of a protective group to ensure chemical stability in presence of amine nucleophiles. The S-alkylsulfonyl group was introduced for immediate thiol-reactivity, yielding asymmetric disulfides in unique compatibility with nucleophilic ring-opening polymerization of respective L-cysteine N-carboxyanhydride derivatives.*

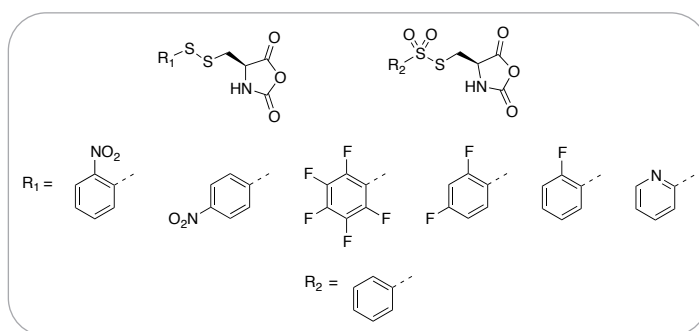






EXPLORING NEW ACTIVATING GROUPS FOR  
REACTIVE CYSTEINE NCAs

David Huesmann, Olga Schäfer, Lydia Braun, Kristina Klinker, Thomas Reuter, Matthias Barz *Tetrahedron Letters* **2016**, 57, 1138-1142. ,



**ABSTRACT:** Due to its ability to reversibly crosslink proteins, cysteine has a unique role as an amino acid in nature. For controlled, asymmetric formation of disulfides from two thiols, one thiol needs to be activated. While few activating groups for cysteine have been proposed, they are usually not stable against amines making them unsuitable for solid phase peptide synthesis or amine initiated polymerization of  $\alpha$ -amino acid *N*-carboxyanhydrides (NCAs). In this Letter we describe a series of new thiol activated cysteines, as well as their NCAs and explore the link between electron deficiency of the leaving group and control over NCA polymerization.

## 6.1 INTRODUCTION

Since their discovery in 1906 Leuchs' anhydrides,<sup>[39]</sup> also known as  $\alpha$ -amino acid *N*-carboxyanhydrides (NCAs), have attracted considerable attention.<sup>[37,38]</sup> NCAs are mostly used as monomers for the preparation of poly(amino acid)s through ring-opening polymerization (ROP), but they were also applied as synthons for the stepwise synthesis of peptides.<sup>[36,354]</sup> In recent years, poly(amino acids) proved to be very successful as carriers or polymeric drugs in the field of nanomedicine. While copaxone is an approved drug with 4.7 billion\$ sales in 2013 clinical studies on multiple polypeptide based polymer drug conjugates or drug formulations (OPAXIO, NC-6004, NK 105) are underway.<sup>[355]</sup> Additionally, polypeptide based polymers for drug delivery applications are emerging.<sup>[25,26,59,355]</sup>

*Cysteine-based strategies for disulfide formation.*

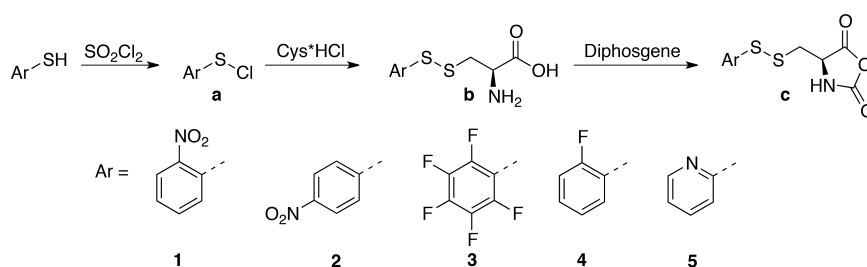
However, while disulfides are already widely used in nanomedicine to reversibly attach drugs to carriers or to stabilize nanoparticles, to our knowledge, poly(cysteine) has not been used for this purpose. Neither protected or activated cysteine derivatives have been explored. The reasons for this fact are on the one hand the tendency of poly(cysteine) to adopt a  $\beta$ -sheet conformation which leads to solubility issues and on the other hand the lack of reactive cysteine protective groups itself. While derivatives of 3-nitro-2-pyridinesulfonyl cysteine<sup>[223]</sup> and 3-(2-pyridyldithio)propionate<sup>[212]</sup> are frequently employed as thiol-reactive moieties, both protective groups can only be utilized for end-group modification in Fmoc solid phase peptide coupling<sup>[356]</sup> or as bifunctional linkers. Further, a series of cysteine NCAs (*S*-allyl-cysteine, *S*-benzyl-cysteine, *S*-benzyloxycarbonyl-cysteine, *S*-benzyloxycarbonylmethylene-cysteine, *S*-butyl-cysteine, *S*-tert-butylmethylcapto-cysteine, a range of *S*-alkyl-cysteines (dodecyl, hexyl, methyl, ethyl, propyl, isopropyl), *S*-(2-trimethylsilylbenzyl)-cysteine, *S*-(4-trimethylsilyl benzyl)-cysteine, cystine (bis-NCA), *S*-thiophenyl-cysteine) from the early years of NCA polymerization have been collected.<sup>[45]</sup> However none of them bear thiol-reactive protective groups, which can be directly addressed after polymerization. Newer cysteine NCAs have either not focused on post-polymerization modification of polymers at all<sup>[312,357,358]</sup> or have worked with deprotection and modification using thiol-ene chemistry, which leads to the formation of biological non-reversible thioethers.<sup>[311,359,360]</sup> Approaches of crosslinking peptidic nanoparticles with disulfides have so far been focused on oxidative disulfide formation<sup>[153,164,169,361,362]</sup> or polymerization of cystine bisNCA,<sup>[363]</sup> while the first method is time-consuming and incomplete the latter hinders control over polymerization and particle formation.

A protective group stable during ROP or standard Fmoc solid phase synthesis of peptides but selectively addressable in post-polymerization modification reactions leading to the formation of a bio-reversible disulfide bond in one step is simply absent. In our search for a reactive cysteine-protective group that is stable under NCA polymerization conditions<sup>[364]</sup> we have come across a range of novel reactive cysteine

NCA, more or less suitable for NCA polymerization. In this Letter we report the synthesis and analysis of these NCAs.

## 6.2 RESULTS AND DISCUSSION

As starting point for the synthesis of cysteine NCAs with a thiol-reactive protective group we synthesized thiol-reactive groups known in the literature starting with *ortho*-nitrothiophenol.<sup>[365]</sup> The strong electron withdrawing effect from the nitro group favors a thiol exchange with a more electron rich thiol. According to Phocas *et al.* *o*-nitrothiophenol sulfenic acid chloride (**1 a**), was reacted with cysteine hydrochloride.<sup>[365]</sup> The product (**1 b**) was transformed into the NCA by reaction with diphosgene in the absence of water (**1 c**, Scheme 6.1).



Scheme 6.1: Synthesis of disulfide-based NCAs.

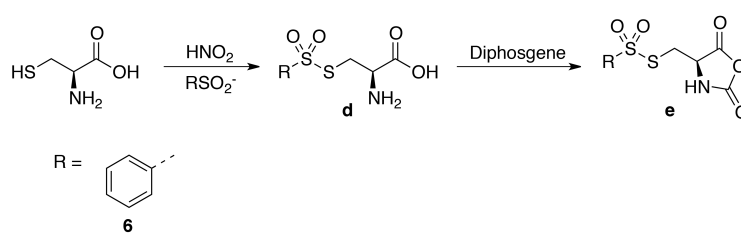
This reaction scheme was used for all disulfide based NCAs. When the sulfonyl chloride was not commercially available, it was synthesized from the thiophenol by chlorination with sulfuryl chloride according to Shang *et al.*<sup>[366]</sup> The modified cysteines **1–5 b** were synthesized with yields ranging from 13 % to 98 %, while the NCAs **1 c**, **3–4 c** were synthesized with 22–65 % yields after 3 recrystallization steps. The NCA of ((*p*-nitrophenyl)disulfanyl)cysteine (**2 c**) as well as *S*-(*o*-thiopyridinyl) cysteine (**5 c**) could not be purified. While in the case of **2 c** cystine impurities could not be removed, **5 c** is not even stable, since the pyridine can act as an initiator in the NCA polymerization<sup>[37]</sup> which was additionally confirmed by polymerizing Lys(Z)NCA with pyridine under the polymerization conditions applied in this study. The suitability of the NCA **1 c** for amine initiated NCA polymerization was investigated by polymerization with neopentylamine in absolute *N,N*-dimethyl formamide (see Supplementary data).<sup>[24,367]</sup> The gel permeation chromatography plots corresponding to the molecular weight distribution of polymers were multimodal or broad indicating the existence of multiple side reactions. These side reactions can be attributed to protective group cleavage by the amine chain end and reinitiation by the free thiol (see Figure 6.1). After **1 c** failed to yield defined polymers we lowered the strength of the electron-withdrawing group (EWG) to decrease the reactivity of the disulfide and prevent a reaction of the disulfide with the primary amine initiator (neopentylamine) or the polymer chain end. The reactivity was reduced to pentafluoro thiophenol and *ortho*-Fluoro thiophenol. With

*Polymerization of NCAs with activated disulfide groups...*

decreasing electron deficiency of the thiol, the quality of the polymers increased ( $\bar{M}_w = 2.1, 1.8$  and  $1.6$  for **1 c**, **3 c**, and **4 c** respectively, see Figures 6.2, 6.3 and 6.4) but not to a point which we considered satisfying.

... and with  
thiosulfonate side  
chain.

Realizing, that weakening of the EWG would not be enough to facilitate successful NCA polymerization and keep reactivity high enough for postpolymerization modification reactions, we turned our attention to different thiol activating groups. A group that has been used to form asymmetrical disulfides are thiosulfonates.<sup>[368,369]</sup> Of this class *S*-phenylsulfonates are known to react readily with free thiols achieving complete conversions upon minutes,<sup>[290,370]</sup> thus a cysteine NCA based on phenylthiosulfonate was synthesized. To achieve this, cysteine was activated by transforming it into *S*-nitroso cysteine, which was reacted with the corresponding sulfinate without purification. The synthesis of thiosulfonates was based on work of Hart *et al.*,<sup>[371,372]</sup> which was chosen over the more complex route of Weidner *et al.*<sup>[373]</sup> After purification the *S*-phenylsulfonyl-L-cysteine was transformed into the corresponding NCA using diphosgene (Scheme 6.2). The *S*-phenylsulfonyl-L-cysteine **6 b** was successfully synthesized with 48 % yield, while its NCA (**6 c**) was synthesized with 77 % yield after 3 recrystallization steps to achieve very high purity.



Scheme 6.2: Synthesis of a thiosulfonyl-based NCAs.

This NCA performed better than the disulfide based NCAs in the amine-initiated polymerization yielding polymers with narrower molecular weight distribution ( $\bar{M}_w = 1.16$  for **6 e**, see Figure 6.5). The gel permeation chromatography (GPC) plots however display the presence of low molecular weight oligomers, which indicates partial protective group cleavage. Although we have developed new reactive cysteine NCA derivatives, further investigation of the influence of the electron deficiency of the substituent with even less electron-deficient *S*-alkylsulfonyl-L-cysteine NCAs seems necessary to achieve protective groups with high stability against amines and combine it with high reactivity toward thiols. Since the thiosulfonate group does only partially engage in side reactions toward amines this class of protective groups needs to be further investigated in future. The next generation of derivatives, however, can be synthesized using the herein reported synthetic pathway.

### 6.3 CONCLUSION

We have reported the syntheses of a range of new, activated cysteine amino acids and NCAs based on electron deficient disulfides and thio-sulfonates. While especially the more reactive disulfides cannot be polymerized in a controlled manner using primary amines as initiators, they might be polymerized more controlled using organometallic catalyst<sup>[48,50,374]</sup> or trimethylsilyl initiators.<sup>[52,375]</sup> In contrast, the thiosulfonate based monomer can be polymerized in a controlled fashion using primary amines, leading to a new class of reactive polypeptides, showing that higher electron density leads to higher stability against primary amines and thus decreases side reactions during NCA polymerization.

### 6.4 ACKNOWLEDGMENTS

We would like to thank Prof. K. W. Klinkhammer and Prof. H. Kunz for stimulating discussions. M.B. acknowledges financial support by the SFB 1066-1 and the NMFZ Mainz. D.H. would like to acknowledge the support by the "Verband der Chemischen Industrie" (VCI) and the "Max Planck Graduate Center with the Johannes Gutenberg-Universität Mainz" (MPGC).

## 6.5 EXPERIMENTAL SECTION

6.5.1 *Materials and Instrumentation*

All chemicals were purchased from Sigma Aldrich and used as received unless otherwise noted. Tetrahydrofuran THF and hexane were distilled from Na/K and ethyl acetate from  $C_{\alpha}H_2$ . Cysteine was purchased from OPREGEN and diphosgene from Alfa Aesar. Deuterated solvents were purchased from Deutero.  $^1H$ ,  $^{19}F$  and  $^{13}C$  nuclear magnetic resonance (NMR) spectra were recorded on a Bruker AC 400 at a frequency of 400, 376 and 101 MHz, respectively.  $^1H$  and  $^{19}F$  NMR spectra were also recorded on a Bruker Avance III HD 300 at 300 and 282 MHz, respectively. The spectra were recorded at room temperature (25 °C) and calibrated using the solvent signals.<sup>[376]</sup> Field desorption mass spectrometry FD-MS was performed on a FD Finnigan MAT90 spectrometer. Melting points were measured using a Mettler FP62 melting point apparatus at a heating rate of 0.5 °C min<sup>-1</sup>. Preparative reverse phase-HPLC was performed with a Knauer HPLC-System (Berlin, Germany), consisting of two HPLC pumps (Smartline 1000), an UV/viSdetector (Smartline 2500), a RI-detector (Smartline 2400) and a Phenomenex (Torrance, U.S. A.) Luna-column (10  $\mu$ m, C18(2), 100A, 250  $\times$  30 mm) run at a flow of 10.0 mL/min and loaded with a 2 mL injection loop. The system was operated and samples analyzed with D-7000 HPLC-System-Manager software (version 4.1). The detector was run at a wavelength of 214 nm.

6.5.2 *Synthetic Procedures**(o-Nitrophenyl)disulfanyl-L-cysteine (Cys(oNTP)) 1b*

To a suspension of 5.86 g (37.18 mmol) cysteine hydrochloride in 150 mL acetic acid 10 g (52.74 mmol) (commercial) 2-nitrobenzenesulfenyl chloride was added. The suspension was stirred until it got solid, then 100 mL acetic acid was added and the mixture was heated to 70 °C for 3.5 h. The solvent was removed *in vacuo*, the residue was dissolved in 20 mL DMSO and precipitated with 250 mL  $CHCl_3$ . After filtration the precipitate was suspended in 200 mL  $CHCl_3$ , stirred for 30 min, and collected by filtration twice. The product was dried *in vacuo* yielding 8.63 g (31.45 mmol, 85 %) of a yellow solid.

$^1H$ NMR (400 MHz,  $DMSO-d_6$ )  $\delta$  [ppm] = 8.85 (s, 3H,  $NH_3^+$ ), 8.28 (dd,  $J_{H,H}$  = 9.6, 8.2 Hz, 2H,  $H_{Ar}$ ), 7.89 (dd,  $J_{H,H}$  = 8.3, 7.2 Hz, 1H,  $H_{Ar}$ ), 7.55 (dd,  $J_{H,H}$  = 8.3, 7.2 Hz, 1H,  $H_{Ar}$ ), 4.20 (t,  $J_{H,H}$  = 5.8 Hz, 1H,  $CHNH_3$ ), 3.43–3.26 (m, 2H,  $CHCH_2S$ ).

$^{13}C$ NMR (101 MHz,  $DMSO-d_6$ )  $\delta$  [ppm] = 169.09 (COO), 145.26 ( $C_{Ar}NO_2$ ), 135.31 ( $C_{Ar}S$ ,  $C_{Ar}$ ), 127.42 ( $C_{Ar}$ ), 127.36 ( $C_{Ar}$ ), 126.44 ( $C_{Ar}$ ), 51.22 ( $C_{\alpha}$ ), 37.14 ( $C_{\beta}$ ).

FD-MS: 274.3  $[M+H]^+$ .

*(o*-Nitrophenyl)*disulfanyl-L-cysteine* NCA (*Cys(oNTP)* NCA) **1c**

A suspension of 2.015 g (7.35 mmol) of ((2-nitrophenyl)disulfanyl)-cysteine and 1.55 mL (9.56 mmol) limonene in 40 mL dry THF was heated to 70 °C. 0.8 mL (4.59 mmol) diphosgene was added in 3 steps every 20 min. The yellow solution was heated for 4 h. Nitrogen was bubbled through the solution for 2 h to remove excess HCl and diphosgene and most of the solvent was removed. The residue was redissolved in 11 mL THF and precipitated by adding 100 mL of cyclohexane very slowly. The precipitate was redissolved in 14 mL THF and insoluble solids were removed by filtration. The product was recrystallized two more times from THF/cyclohexane avoiding contact to air yielding 1.437g (4.78 mmol; 65 %) of a pale yellow powder.

<sup>1</sup>H NMR (300 MHz, DMSO-*d*<sub>6</sub>) δ [ppm] = 9.33 (s, 1H, NH), 8.31 (dd, *J*<sub>H,H</sub> = 8.2, 1.4 Hz, 1H, H<sub>Ar</sub>), 8.23 (dd, *J*<sub>H,H</sub> = 8.2, 1.2 Hz, 1H, H<sub>Ar</sub>), 7.90 (ddd, *J*<sub>H,H</sub> = 8.4, 7.2, 1.4 Hz, 1H, H<sub>Ar</sub>), 7.56 (ddd, *J*<sub>H,H</sub> = 8.4, 7.3, 1.3 Hz, 1H, H<sub>Ar</sub>), 4.77 (ddd, *J*<sub>H,H</sub> = 6.0, 4.8, 1.3 Hz, 1H, C<sub>α</sub>H), 3.38–3.16 (m, 2H, CH<sub>2</sub>).

<sup>1</sup>H NMR (400 MHz, THF-*d*<sub>8</sub>) δ [ppm] = 8.47 (s, 1H, NH), 8.30 (td, *J*<sub>H,H</sub> = 8.0, 1.2 Hz, 2H, H<sub>Ar</sub>), 7.81 (ddd, *J*<sub>H,H</sub> = 8.4, 7.2, 1.4 Hz, 1H, H<sub>Ar</sub>), 7.47 (ddd, *J*<sub>H,H</sub> = 8.1, 7.1, 1.1 Hz, 1H, H<sub>Ar</sub>), 4.68 (dd, *J*<sub>H,H</sub> = 7.8, 3.7 Hz, 1H, C<sub>α</sub>H), 3.26 (dd, *J*<sub>H,H</sub> = 14.0, 3.9 Hz, 2H, CH<sub>2</sub>), 3.17 (dd, *J*<sub>H,H</sub> = 14.0, 7.8 Hz, 1H, CH<sub>2</sub>).

<sup>13</sup>C NMR (101 MHz, THF-*d*<sub>8</sub>) δ [ppm] = 170.27 (C<sub>α</sub>(CO)O), 152.57 (NH(CO)O), 146.98 (C<sub>Ar</sub>NO<sub>2</sub>), 136.85 (C<sub>Ar</sub>S), 135.53 (C<sub>Ar</sub>), 128.21 (C<sub>Ar</sub>), 127.88 (C<sub>Ar</sub>), 127.14 (C<sub>Ar</sub>), 57.77 (C<sub>α</sub>), 40.34 (CH<sub>2</sub>).

*(p*-Nitrophenyl)*disulfanyl-L-cysteine* (*Cys(pNTP)*) **2b**

To a suspension of 277 mg (1.76 mmol) cysteine hydrochloride in 2 mL DMF was added 6 mL acetic acid followed by 500 mg (2.64 mmol) commercial 4-nitrobenzenesulfonyl chloride. The suspension was stirred at room temperature for 2 days during which it lost most of its yellow color. The AcOH was removed *in vacuo*. Then 30 mL CHCl<sub>3</sub> was added slowly to precipitate the product. After filtration the precipitate was suspended in 30 mL CHCl<sub>3</sub>, stirred for 30 min, and collected by filtration three times. The product was dried *in vacuo* yielding 394 mg (1.44 mmol, 82 %) of a pale yellow solid.

<sup>1</sup>H NMR (300 MHz, DMSO-*d*<sub>6</sub>) δ [ppm] = 10.02–8.36 (br, 3H, NH<sub>3</sub><sup>+</sup>), 8.24 (d, *J*<sub>H,H</sub> = 8.9 Hz, 2H, H<sub>Ar</sub>), 7.84 (d, *J*<sub>H,H</sub> = 9.0 Hz, 2H, H<sub>Ar</sub>), 4.15 (t, *J*<sub>H,H</sub> = 5.9 Hz, 1H, C<sub>α</sub>H), 3.36 (dd, *J*<sub>H,H</sub> = 6.0, 2.4 Hz, 2H, CH<sub>2</sub>).

*Pentafluorophenylsulfenyl chloride* (PFTPCI) **3a**

A solution of 5 mL pentafluorothiophenol (7.505 g, 37.5 mmol) in 75 mL DCM was cooled to 0 °C. 4.56 mL sulfuryl chloride (7.59 g, 56.3 mmol) was added and the solution was stirred overnight. DCM and excess sulfuryl chloride were removed *in vacuo* at 40 °C yielding 8.35 g (4.97 mL, 35 mmol, 93 %) of an orange liquid.



$^{19}\text{F}$ NMR (400 MHz,  $\text{CDCl}_3$ )  $\delta$  [ppm] = 128.57 (m, 2F, *o*-F), 145.49 (tt, 1F, *p*-F), 160.17 (m, 2F, *m*-F).

*S*-(Pentafluorophenyl)-L-cysteine (*Cys*(PFTP)) **3b**

To a suspension of 1.35 g (8.59 mmol) cysteine hydrochloride in 35 mL acetic acid, 3.02 g (13 mmol) pentafluorophenylsulfenyl chloride was added. The suspension solidified after 5 min and another 23 mL of acetic acid was added, yielding a yellow solution, which was stirred at 70 °C for 3.5 h. During the reaction the yellow color of the solution got weaker. The solvent was removed *in vacuo* and the slightly yellow residue was extracted twice with 58 mL  $\text{CHCl}_3$ , yielding 2.7 g (8.46 mmol, 98 %) of a colorless solid.

$^1\text{H}$  NMR (400 MHz,  $\text{CD}_3\text{CN}/\text{TFA}-d$ )  $\delta$  [ppm] = 4.43 (dd,  $J_{\text{H,H}}$  = 8.5, 4.3 Hz, 1H,  $\text{C}_\alpha\text{H}$ ), 3.51 (dd,  $J_{\text{H,H}}$  = 15.3, 4.3 Hz, 1H,  $\text{CH}_2$ ), 3.35 (dd,  $J_{\text{H,H}}$  = 15.3, 8.6 Hz, 1H,  $\text{CH}_2$ ).

$^{19}\text{F}$ NMR (400 MHz,  $\text{CD}_3\text{CN}/\text{TFA}-d$ )  $\delta$  [ppm] = 134.66 (m, 2F, *o*-F), 153.01 (tt,  $J_{\text{H,H}}$  = 20.0, 3.9 Hz, 1F, *p*-F), 163.35 (m, 2F, *m*-F).

$^{13}\text{C}$ NMR (101 MHz,  $\text{CD}_3\text{CN}/\text{TFA}-d$ )  $\delta$  [ppm] = 168.95 (COO), 147.61 (ddd,  $J_{\text{H,H}}$  = 246.4, 11.6, 4.4 Hz, *o*- $\text{C}_{\text{Ar}}$ ), 144.73–140.78 (m, *p*- $\text{C}_{\text{Ar}}$ ), 139.72–135.61 (m, *m*- $\text{C}_{\text{Ar}}$ ), 110.06 (t,  $J_{\text{H,H}}$  = 20.6 Hz,  $\text{C}_{\text{ArS}}$ ), 53.23 ( $\text{CH}_2$ ), 39.31 ( $\text{C}_\alpha$ ).

FD-MS: 319.1 [M+H] $^+$ .

*S*-(Pentafluorophenyl)-L-cysteine NCA (*Cys*(PFTP) NCA) **3c**

2.35 g (7.35 mmol) *S*-(pentafluorophenyl)cysteine was suspended in 40 mL abs. THF and the suspension was heated to 70 °C. Then 0.8 mL (6.63 mmol) of diphosgene was added over 1 h in which the solid dissolved. The solution was stirred for 1.5 more hours. Nitrogen was bubbled through the solution overnight to remove HCl and diphosgene. The slightly yellow solid was then dissolved in 11 mL abs. THF and precipitated by slowly adding 130 mL abs. hexane. The precipitate was collected by filtration without contact to air and recrystallized 3 times from THF/hexane yielding 568 mg (1.64 mmol, 22 %) of the *S*(pentafluorophenyl)cysteine NCA.

$^1\text{H}$  NMR (400 MHz,  $\text{THF}-d_8$ )  $\delta$  [ppm] = 4.77 (dd,  $J_{\text{H,H}}$  = 7.8, 3.6 Hz, 1H,  $\text{C}_\alpha\text{H}$ ), 3.41 (dd,  $J_{\text{H,H}}$  = 14.4, 3.6 Hz, 1H,  $\text{CH}_2$ ), 3.22 (dd,  $J_{\text{H,H}}$  = 14.3, 7.6 Hz, 1H,  $\text{CH}_2$ ).

$^{19}\text{F}$ NMR (400 MHz,  $\text{THF}-d_8$ )  $\delta$  [ppm] = 134.64 (m, 2F, *o*-F), 152.94 (tt,  $J_{\text{H,H}}$  = 20.7, 3.5 Hz, 1F, *p*-F), 163.28 (m, 2F, *m*-F).

$^{13}\text{C}$ NMR (101 MHz,  $\text{THF}-d_8$ )  $\delta$  [ppm] = 168.99 ( $\text{C}_\alpha(\text{CO})\text{O}$ ), 151.50 ( $\text{NH}(\text{CO})\text{O}$ ), 147.47 (ddq,  $J_{\text{H,H}}$  = 247.0, 11.8, 4.2 Hz, *o*- $\text{C}_{\text{Ar}}$ ), 142.75 (dt,  $J_{\text{H,H}}$  = 256.2, 13.8, 5.3 Hz, *p*- $\text{C}_{\text{Ar}}$ ), 139.08–136.55 (*m*- $\text{C}_{\text{Ar}}$ ), 111.68–110.23 (m,  $\text{C}_{\text{ArS}}$ ), 56.59 ( $\text{CH}_2$ ), 40.94 ( $\text{C}_\alpha$ ).

*o*-Fluorophenylsulfenyl chloride (*o*FTPCl) **4a**

5 mL (46 mmol) *o*-fluorothiophenol was dissolved in 92 mL DCM and cooled to 0 °C. 5.65 mL (70 mmol) sulfurylchloride was added and the



solution was stirred for 16 h at room temperature. DCM and excess sulfonyl chloride were removed *in vacuo*, yielding 7.39 g (45 mmol, 98 %) of an orange-red liquid. That was used without further purification.

$^1\text{H}$  NMR (400 MHz,  $\text{CDCl}_3$ )  $\delta$  [ppm] = 7.74 (td, 1H,  $J_{\text{H,H}} = 1.7, 5.8$  Hz, 1H,  $\text{H}_{\text{Ar}}$ ), 7.51–7.46 (m, 1H,  $\text{H}_{\text{Ar}}$ ), 7.26–7.17 (m, 2H,  $\text{H}_{\text{Ar}}$ ).

$^{19}\text{F}$  NMR (400 MHz,  $\text{CDCl}_3$ )  $\delta$  [ppm] = 105.82 (m, 1F,  $\text{F}_{\text{Ar}}$ ).

#### *S*-(*o*-Fluorophenyl)-L-cysteine (*Cys(oFTP)*) **4b**

7.94 g (49 mmol) *o*-fluorophenylsulfenyl chloride was mixed with 3 mL TFA and cooled in an ice-bath. 3.68 g (23 mmol) cysteine hydrochloride was dissolved in 40 mL TFA and added to the solution at a rate of 15 mL/h under constant stirring. The TFA was removed *in vacuo* at 45 °C and 100 mL  $\text{CHCl}_3/\text{MeOH}$  (1:1) was added to the resulting solid to extract the product (residue: cystine, side product). The residue was filtered off and the filtrate was concentrated *in vacuo*. 150 mL  $\text{Et}_2\text{O}$  was added and the product was collected by filtration. This was repeated one more time yielding 0.99 g (2.88 mmol, 13 %) a slightly yellow/brownish solid (TFA salt).

$^1\text{H}$  NMR (400 MHz,  $\text{MeOD}$ )  $\delta$  [ppm] = 7.73 (td,  $J_{\text{H,H}} = 7.6, 1.7$  Hz, 1H,  $\text{H}_{\text{Ar}}$ ), 7.50–7.38 (m, 1H,  $\text{H}_{\text{Ar}}$ ), 7.3–7.13 (m, 2H,  $\text{H}_{\text{Ar}}$ ), 4.40 (dd,  $J_{\text{H,H}} = 8.3, 4.2$  Hz, 1H,  $\text{C}_\alpha\text{H}$ ), 3.39 (dd,  $J_{\text{H,H}} = 14.9, 4.2$  Hz, 1H,  $\text{CH}_2$ ), 3.21 (dd,  $J_{\text{H,H}} = 14.8, 8.3$  Hz, 1H,  $\text{CH}_2$ ).

$^{19}\text{F}$  NMR (400 MHz,  $\text{MeOD}$ )  $\delta$  [ppm] = 112.16 (ddd,  $J_{\text{H,H}} = 9.4, 7.5, 5.1$  Hz, 1F,  $\text{F}_{\text{Ar}}$ ).

#### *S*-(*o*-Fluorophenyl)-L-cysteine NCA (*Cys(oFTP)* NCA) **4c**

0.99 g (2.88 mmol) *S*-(*o*-fluorophenyl)cysteine was suspended in 30 mL abs. THF and the suspension was heated to 70 °C. Then 0.35 mL (2.88 mmol) of diphosgene was added over 1 h in which the solid dissolved. The solution was stirred for 1.5 more hours. Nitrogen was bubbled through the solution overnight to remove HCl and diphosgene. The slightly yellow solid was then dissolved in 11 mL abs.  $\text{AcOEt}$  and precipitated by slowly adding 60 mL abs. hexane. The precipitate was collected by filtration without contact to air and recrystallized 3 times from  $\text{AcOEt}$ /hexane yielding 332 mg (1.21 mmol, 42 %) of the *S*-(*o*-fluorophenyl)-cysteine NCA.

$^1\text{H}$  NMR (400 MHz,  $\text{DMSO}-d_6$ )  $\delta$  [ppm] = 9.31 (s, 1H, NH), 7.73 (td,  $J_{\text{H,H}} = 7.8, 1.8$  Hz, 1H,  $\text{H}_{\text{Ar}}$ ), 7.45 (dddd,  $J_{\text{H,H}} = 8.7, 7.2, 5.3, 1.7$  Hz, 1H,  $\text{H}_{\text{Ar}}$ ), 7.37–7.21 (m, 2H,  $\text{H}_{\text{Ar}}$ ), 4.82 (ddd,  $J_{\text{H,H}} = 6.0, 4.6, 1.3$  Hz, 1H,  $\text{C}_\alpha\text{H}$ ), 3.32–3.15 (m, 2H,  $\text{CH}_2$ ).

$^{19}\text{F}$  NMR (376 MHz,  $\text{DMSO}-d_6$ )  $\delta$  [ppm] = 111.70 (ddd,  $J_{\text{H,H}} = 10.2, 7.8, 5.2$  Hz, 1F,  $\text{F}_{\text{Ar}}$ ).

$^{13}\text{C}$  NMR (101 MHz,  $\text{DMSO}-d_6$ )  $\delta$  [ppm] = 170.48 ( $\text{C}_\alpha(\text{CO})\text{O}$ ), 160.53 (d,  $J_{\text{H,H}} = 244.3$  Hz,  $\text{C}_{\text{Ar}}\text{F}$ ), 152.21 ( $\text{NH}(\text{CO})\text{O}$ ), 131.93 ( $\text{C}_{\text{Ar}}$ ), 131.16 (d,  $J_{\text{H,H}} = 7.9$  Hz,  $\text{C}_{\text{Ar}}$ ), 125.95 (d,  $J_{\text{H,H}} = 3.5$  Hz,  $\text{C}_{\text{Ar}}$ ), 122.96 (d,  $J_{\text{H,H}} = 17.0$  Hz,  $\text{C}_{\text{Ar}}$ ), 116.62 (d,  $J_{\text{H,H}} = 21.5$  Hz,  $\text{C}_{\text{Ar}}$ ), 57.14 ( $\text{C}_\alpha$ ), 39.51 ( $\text{CH}_2$ ).

*o*-Pyridinylsulfenyl chloride hydrochloride (*o*TPCl) **5 a**

See *o*-fluorophenylsulfenyl chloride. Yield: 97%.

<sup>1</sup>H NMR (300 MHz, DMSO-*d*<sub>6</sub>) δ [ppm] = 14.50 (s, 1H, C<sub>Ar</sub>H<sup>+</sup>), 8.49 (ddd, J=4.9, 1.9, 0.9 Hz, 1H, H<sub>Ar</sub>), 7.84 (ddd, J=8.1, 7.5, 1.8 Hz, 1H, H<sub>Ar</sub>), 7.65 (dt, J<sub>H,H</sub> = 8.1, 1.0 Hz, 1H, H<sub>Ar</sub>), 7.31 (ddd, J<sub>H,H</sub> = 7.5, 4.9, 1.0 Hz, 1H, H<sub>Ar</sub>).

*S*-(*o*-Pyridinylsulfenyl)-L-cysteine (Cys(*o*TP)) **5 b**

7.90 g (54.25 mmol) *o*-pyridinylsulfenyl chloride and 5.70 g (36.17 mmol) cysteine hydrochloride were heated in 50 mL acetic acid for 30 min. The solution turned bright yellow. The reaction mixture was kept in the fridge overnight. The solid was collected by filtration and washed with acetic acid. The solid was further washed by suspending it in chloroform, stirring for 1 h and filtering of the chloroform 3 times, yielding a bright yellow powder. The powder was further purified by HPLC yielding 4.01 g (17.41 mmol, 48 %) of a yellow powder.

<sup>1</sup>H NMR (300 MHz, DMSO-*d*<sub>6</sub>) δ [ppm] = 8.52 (ddd, J<sub>H,H</sub> = 4.8, 1.8, 0.9 Hz, 1H, H<sub>Ar</sub>), 7.84 (ddd, J<sub>H,H</sub> = 8.1, 7.4, 1.9 Hz, 1H, H<sub>Ar</sub>), 7.73 (dt, J<sub>H,H</sub> = 8.1, 1.0 Hz, 1H, H<sub>Ar</sub>), 7.32 (ddd, J<sub>H,H</sub> = 7.4, 4.9, 1.1 Hz, 1H, H<sub>Ar</sub>), 4.21 (dd, J<sub>H,H</sub> = 7.5, 5.0 Hz, 1H, C<sub>α</sub>H), 3.48–3.22 (m, 2H, CH<sub>2</sub>).

ESI-MS: 231.0 [M+H]<sup>+</sup>.

The *S*-(*o*-thiopyridinyl)cysteine NCA (**5 c**) could not be completely purified. It is not stable, as the pyridine can act as an initiator in the NCA polymerization, which was confirmed by polymerizing Lys(Z)NCA with pyridine.

*S*-Phenylsulfonyl-L-cysteine (Cys(SO<sub>2</sub>Ph)) **6 b**

3 g (17.08 mmol) cysteine hydrochloride monohydrate was dissolved in 17 mL 2 M hydrochloric acid and cooled to 5 °C in an ice bath. 1.18 g (17.08 mmol) Sodium nitrite was dissolved in 10 mL milli-Q water, cooled and added to the cysteine solution via a dropping funnel. The solution turned red. After stirring for 80 min at 5 °C, 5.61 g (34.16 mmol) sodium benzylsulfinate was added. After 2 h discoloration of the solution was observed and a precipitate formed. Another 1.40 g (8.54 mmol) sodium benzylsulfinate was added and the mixture was stirred for 2 more hours and stored at 4 °C overnight. The solid was collected by filtration and washed two times with ice-cold milli-Q water. The brown solid was recrystallized from water, washed with ethanol and diethyl ether and dried *in vacuo* to yield 2.14 g (8.20 mmol, 48 %) of a slightly yellowish solid.

<sup>1</sup>H NMR (400 MHz, D<sub>2</sub>O/TFA-*d*) δ [ppm] = 7.90 - 7.81 (m, 2H, H<sub>Ar</sub>), 7.69 - 7.61 (m, 1H), 7.58 - 7.48 (m, 2H, H<sub>Ar</sub>), 4.27 (dd, J<sub>H,H</sub> = 7.3, 4.6 Hz, 1H, C<sub>α</sub>H), 3.48 (dd, J<sub>H,H</sub> = 15.8, 4.6 Hz, 1H, CH<sub>2</sub>), 3.39 (dd, J<sub>H,H</sub> = 15.8, 7.3 Hz, 1H, CH<sub>2</sub>).

<sup>13</sup>C NMR (101 MHz, D<sub>2</sub>O) δ [ppm] = 171.52 (COOH), 144.52 (C<sub>Ar</sub>S), 137.88 (C<sub>Ar</sub>), 132.51 (C<sub>Ar</sub>), 129.69 (C<sub>Ar</sub>), 54.71 (CH<sub>2</sub>), 36.97 (C<sub>α</sub>).

*S*-Phenylsulfonyl-L-cysteine NCA (Cys(SO<sub>2</sub>Ph)NCA) **6c**

In an inert gas atmosphere 5 g (19.13 mmol) phenyl cysteine thiosulfonate was suspended in 50 mL abs. THF and heated to 70 °C. Diphosgene (2.08 mL, 17.22 mmol) was added in three steps every 20 min and the suspension was stirred for another 2 h, in which all solid dissolved. The solution was allowed to cool down and THF was removed, by passing dry nitrogen through the solution overnight. The crude product was dried *in vacuo* and recrystallized 3 times by dissolving in THF and precipitating with hexane, yielding 4.20 g (14.73 mmol, 77 %) of a slightly yellow powder.

<sup>1</sup>H NMR (400 MHz, DMSO-*d*<sub>6</sub>) δ [ppm] = 9.23 (s, 1H, NH), 7.95 (d, *J*<sub>H,H</sub> = 7.6 Hz, 2H, H<sub>Ar</sub>), 7.81 (t, *J*<sub>H,H</sub> = 7.4 Hz, 1H, H<sub>Ar</sub>), 7.71 (t, *J* = 7.7 Hz, 2H, H<sub>Ar</sub>), 4.73 (t, *J* = 5.6 Hz, 1H, C<sub>α</sub>H), 3.49 (d, *J* = 5.6 Hz, 2H, CH<sub>2</sub>).

<sup>13</sup>C NMR (101 MHz, DMSO-*d*<sub>6</sub>) δ [ppm] = 169.29 (C<sub>α</sub>(CO)O), 151.47 (NH(CO)O), 143.59 (C<sub>Ar</sub>S), 134.69 (C<sub>Ar</sub>), 130.02 (C<sub>Ar</sub>), 126.69 (C<sub>Ar</sub>), 56.52 (CH<sub>2</sub>), 36.04 (C<sub>α</sub>).

FD-MS: 287.0 [M]<sup>+</sup>.

## 6.6 SUPPORTING INFORMATION

6.6.1 *Polymerization of Activated Cysteine NCAs*

DMF was purchased dry over molecular sieve. It was further purified by stirring over molecular sieve (3 Å) and BaO. It was then distilled and stored at  $-80\text{ }^{\circ}\text{C}$ . Neopentylamine was dried over  $\text{C}_{\alpha}\text{H}_2$  and fractionally distilled. GPC in hexafluoro 2-propanol (HFIP) was performed with  $3\text{ g l}^{-1}$  potassium trifluoroacetate (KTFA) at  $40\text{ }^{\circ}\text{C}$ . The columns were packed with modified silica (PFG columns, particle size:  $7\text{ }\mu\text{m}$ , porosity:  $100\text{ }\text{\AA}$  and  $1000\text{ }\text{\AA}$ ). A refractive index detector (G 1362A RID, Jasco) was used to detect the polymer. Molecular weights were calculated using a calibration performed with Polymethyl methacrylate PMMA standards (Polymer Standards Services GmbH).

6.6.2 *Typical Polymerization Procedure*

500 mg (1.74 mmol)  $\text{Cys}(\text{SO}_2\text{Ph})\text{NCA}$  were transferred in a Schlenk tube under nitrogen counterflow. 4 ml dry DMF were added. A stock solution of the initiator was prepared immediately prior to use: 1 ml dry DMF and  $8.20\text{ }\mu\text{L}$  (6.07 mg, 0.07 mmol) neopentylamine were added in a glass vial. 0.5 ml of this solution was added via syringe to initiate the polymerization. A steady flow of dry nitrogen was sustained during the polymerization, preventing any impurities from entering the Schlenk tube, while ensuring the escape of produced  $\text{CO}_2$ . The progress of the polymerization was monitored via infrared (IR) spectroscopy by the disappearing NCA carbonyl peaks at  $1858\text{ cm}^{-1}$  and  $1788\text{ cm}^{-1}$ . Samples were taken using a nitrogen flushed syringe through a septum. The polymer was precipitated after 3 days in a mixture of cold diethylether. The suspension was centrifuged (4500 rpm, 15 min,  $0\text{-}10\text{ }^{\circ}\text{C}$ ) and decanted. This procedure was repeated twice yielding 134 mg of a colorless to slightly yellow solid.

Table 6.1: Analytical data of cysteine homopolymers.

polymer	$M_n/\text{g mol}^{-1}$	$D$
PCys(oNTP)	8000	2.10
PCys(PFTP)	1800	1.84
PCys(oFTP)	6700	1.59
PCys( $\text{SO}_2\text{Ph}$ )	6600	1.16

The broad distribution of the disulfide-based polymers can be explained by chain termination due to attack of the amine chain end with the activated disulfide. The resulting thiol can initiate further polymerization. This leads to broad molecular weight distributions. Less activated disulfides (i.e. more electron rich aromates) lead to a decrease of the termination reaction and more defined polymers.



Figure 6.1: Side reaction resulting in chain termination.

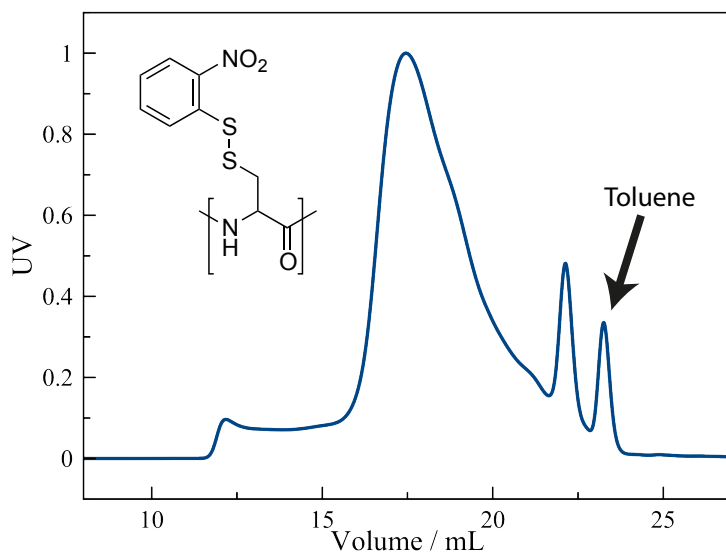


Figure 6.2: GPC plot of PCys(oNTP).

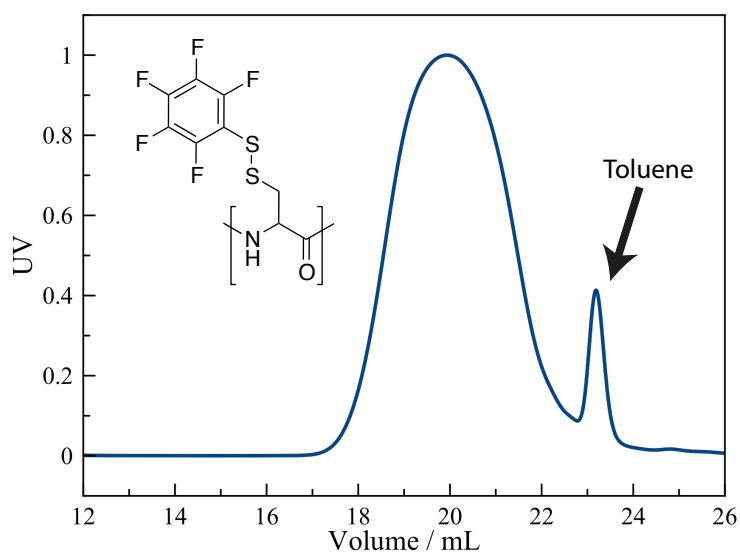


Figure 6.3: GPC plot of PCys(PFTP).

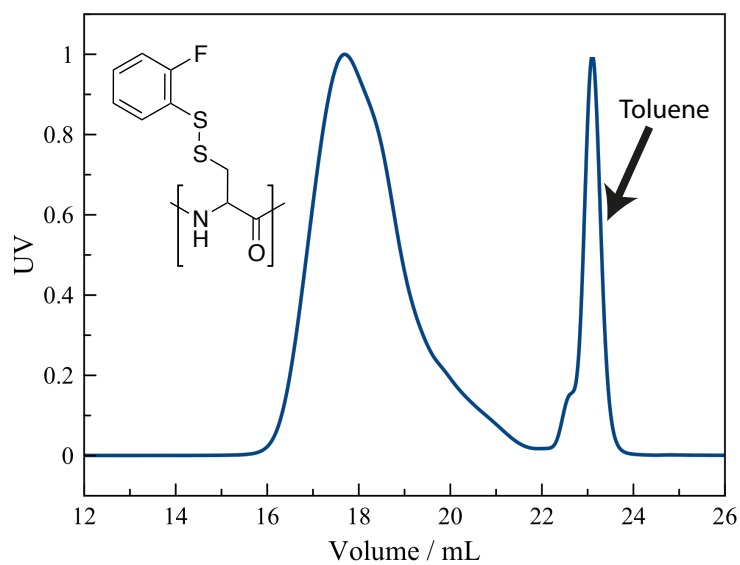
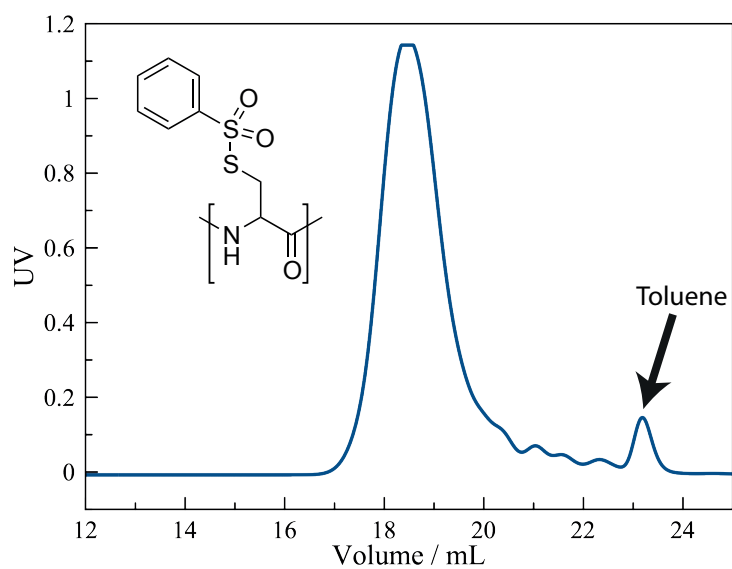
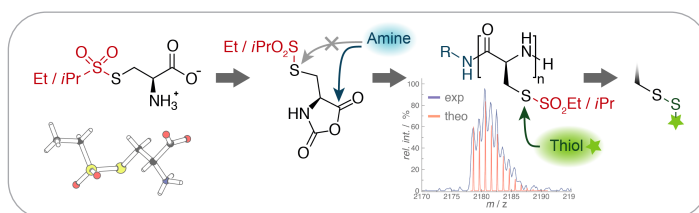


Figure 6.4: GPC plot of PCys(oFTP).

Figure 6.5: GPC plot of PCys(SO<sub>2</sub>Ph).

RETHINKING CYSTEINE PROTECTIVE GROUPS:  
S-ALKYLSULFONYL-L-CYSTEINES FOR  
CHEMOSELECTIVE DISULFIDE FORMATION

Olga Schäfer\*, David Huesmann\*, Christian Muhl, Matthias Barz,  
*Chemistry – A European Journal* **2016**, 22, 18085-18091. (\*authors contributed  
equally)



**ABSTRACT:** The ability to reversibly cross-link proteins and peptides grants the amino acid cysteine its unique role in nature as well as in peptide chemistry. We report a novel class of S-alkylsulfonyl-L-cysteines and corresponding  $\alpha$ -amino acid N-carboxyanhydrides (NCAs) thereof for peptide synthesis. The S-alkylsulfonyl group is stable against amines and thus enables its use under Fmoc chemistry conditions and the controlled polymerization of the corresponding NCAs yielding well-defined homo- as well as block co-polymers. Yet, thiols react immediately with the S-alkylsulfonyl group forming asymmetric disulfides. Therefore, we introduce the first reactive cysteine derivative for efficient and chemoselective disulfide formation in synthetic polypeptides, thus bypassing additional protective group cleavage steps.

## 7.1 INTRODUCTION

The incorporation of cysteines into peptides by solid phase peptide synthesis (SPPS) or during polymerization of  $\alpha$ -amino acid *N*-carboxyanhydrides (NCAs) commonly relies on the protection of the thiol group in order to avoid side reactions. Numerous protective groups enable peptide synthesis or NCA polymerization (e.g., benzyl, trityl or acetamidomethyl thioethers along with *tert*-butyl disulfides),<sup>[179]</sup> but in order to retain the free thiol group for further peptide modification, a cleavage step is mandatory.

For rapid and large-scale synthesis of synthetic polypeptides in the field of NCA polymerization,<sup>[35,49–53,55]</sup> a variety of reactive amino acid derivatives as well as the corresponding NCAs have been established and implemented in functional polypeptides, providing a remarkable chemical diversity using post polymerization modification reactions.<sup>[21,58]</sup> This chemical toolbox covers multiple functional groups for chemoselective modification, for example, alkylation,<sup>[312]</sup> azide–alkyne,<sup>[314]</sup> thiol–ene and –yne reactions.<sup>[311,313,317]</sup> However, none of them can be applied to direct chemoselective disulfide bond formation. Regarding the conjugation of synthetic peptides to proteins or synthetic polymers,<sup>[188,377]</sup> a protective group for thiols combining stability during peptide synthesis with the ability to form disulfide bonds by a chemoselective reaction<sup>[181,378]</sup> appears favorable. Disulfide bond formation is particularly attractive for a variety of biological and medical applications since disulfides are stable extracellularly but cleavable inside cells.<sup>[159]</sup> Although this characteristic may not be required in all cases, the bioreversibility of disulfide bonds appears to be highly desirable in the development of vaccines, drug or gene delivery systems.<sup>[103,138,163]</sup>

Until now, disulfide formation is accomplished either by oxidation of thiols,<sup>[164,274,276]</sup> which is time consuming, incomplete and does not allow the formation of asymmetric disulfides, or by the formation of reactive thiols (chlorinated thiol and nitrosothiols),<sup>[292,294]</sup> disulfides like 2- or 4-nitrophenyl (Nps),<sup>[215,379]</sup> 2- or 4-pyridyl (<sup>[212,214]</sup> and 3-nitro-2-pyridyl (Npys)<sup>[223,308]</sup>) or *S*-phenylsulfonates in the final polypeptide.<sup>[290,322]</sup> Activated thiols or disulfides, however, share a drawback, consisting of their limited stability against hydrolysis and aminolysis which prohibits their use in peptide synthesis and NCA polymerization. Therefore, a protective group for thiols, which combines stability during peptide synthesis with the ability to form disulfide bonds by a chemoselective reaction, appears highly desirable.<sup>[181,378]</sup> We have recently reported that *S*-phenylsulfonyl cysteines show better, but insufficient, stability towards amines compared to activated disulfides in NCA polymerization.<sup>[321]</sup> The critical challenge is to achieve the delicate balance between stability against amine and hydroxyl nucleophiles and reactivity towards thiols.



## 7.2 RESULTS AND DISCUSSION

In this work we introduce the use of a novel class of *S*-alkylsulfonyl-L-cysteines ( $\text{Cys}(\text{SO}_2\text{R})$ ) (Figure 7.1) to address this issue. The *S*-alkylsulfonyl groups provide steric hindrance in conjunction with a +I effect, which enhances electron density at the *S*-alkylsulfonyl group ensuring stability in contrast to other activated disulfides, while remaining highly reactive towards thiols as demonstrated in this work.

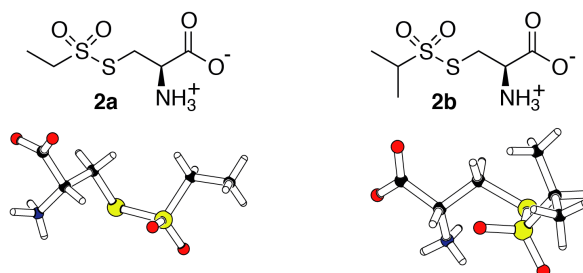
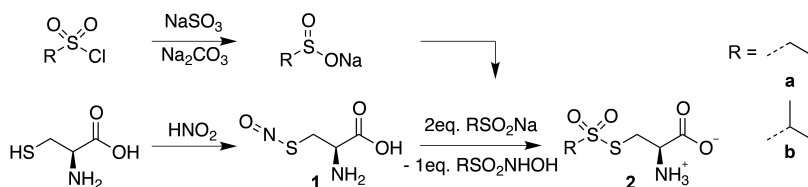


Figure 7.1: *S*-ethylsulfonyl-L-cysteine ( $\text{Cys}(\text{SO}_2\text{Et})$ ) **2a** and *S*-isopropylsulfonyl-L-cysteine ( $\text{Cys}(\text{SO}_2^i\text{Pr})$ ) **2b**.

The synthesis of the thiosulfonates **2a** and **2b** was adapted from the work of Hart *et al.*<sup>[371,372]</sup> (Scheme 7.1) where the *S*-nitrosocysteine **1** is generated *in situ* and reacts with either ethanesulfinic or isopropanesulfinic acid sodium salt forming the corresponding thiosulfonate **2** and *N*-hydroxyalkylsulfonamide in a 1:1 ratio.<sup>[290,323]</sup> The stereochemistry is fully preserved during the process as confirmed by X-ray crystallography.



Scheme 7.1: Synthesis of  $\text{Cys}(\text{SO}_2\text{R})$  **2**.

7.2.1 Evaluation of the *S*-Alkylsulfonyl Group towards Nucleophiles

The reactions of the *S*-alkylsulfonyl-L-cysteines in the presence of various nucleophiles were evaluated in detail. From a mechanistic point of view, the sulfonyl sulfur is the relevant moiety in a nucleophilic attack<sup>[380,381]</sup> (Figure 7.2 A) while the protective group is removed as a sulfinate. Deviating reactivity is only relevant in electron-deficient halogenated derivatives, in an attack on the sulfinyl sulfur atom.<sup>[380]</sup> Both amino acids were subjected to buffers of varying pH and amine containing organic solutions (see Supporting Information for details). The apparent rate constants<sup>[370]</sup> for hydrolysis were found to be in the range of  $10^{-3} \text{ s}^{-1}$  under alkaline conditions and in the range of  $10^{-9} \text{ s}^{-1}$  in mildly acidic media (Table 7.2).

Stability against  
*N*-nucleophiles...

The stability towards aminolysis was investigated by using nucleophiles such as neopentylamine ( $pK_a$  10.2)<sup>[382,383]</sup> and hexylmethylamine ( $pK_a$  10.5)<sup>[384]</sup> as potential initiators in NCA ring-opening polymerization (ROP), along with morpholine ( $pK_a$  8.5)<sup>[383]</sup> and piperidine ( $pK_a$  11.1)<sup>[383]</sup> as possible deprotection reagents in peptide synthesis. The apparent rate constants were found to be temperature dependent ranging between  $10^{-6} \text{ s}^{-1}$  to  $10^{-7} \text{ s}^{-1}$  ( $20^\circ\text{C}$ ) and  $10^{-8} \text{ s}^{-1}$  to  $10^{-9} \text{ s}^{-1}$  at ( $-10^\circ\text{C}$ , Table 7.3). As displayed in Figure 7.2 B, the plot of the rate constants for all examined nucleophiles ( $k_{\text{Nu}}^{\text{Et}}$  vs.  $k_{\text{Nu}}^{\text{iPr}}$ ) shows good correlation of the kinetic data, the slope of the correlation line being slightly below one (0.73). This result confirms that both protective groups behave alike when exposed to *O*- and *N*-nucleophiles, with the *S*-isopropylsulfonyl group providing enhanced stability. Ultimately, both protective groups are stable against primary and secondary amines; this enables their use in NCA polymerization.

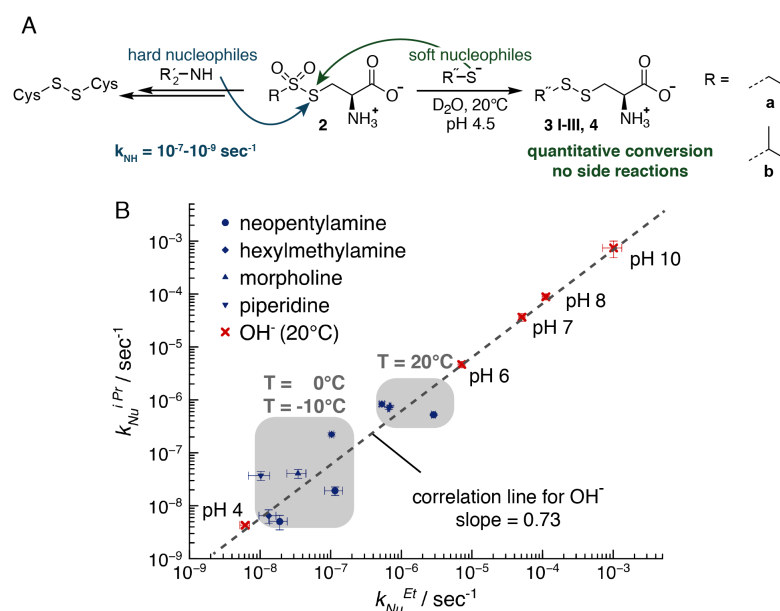
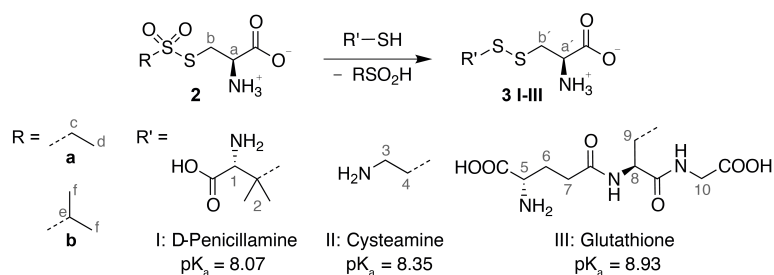


Figure 7.2: Reactivity of  $\text{Cys}(\text{SO}_2\text{R})$  **2** towards nucleophiles: A) Attack of hard and soft nucleophiles on **2** with  $\text{R}' =$  neopentylamine, hexylmethylamine, morpholine, piperidine, 1-butanamine;  $\text{R}'' =$  d-penicillamine, cysteamine, glutathione, 1-hexanethiol. B) Plot of  $\log(k_{\text{Nu}})$  for **2** under alkaline hydrolysis (red) and aminolysis (blue) conditions at different temperatures.

... in combination  
with reactivity  
towards  
*S*-nucleophiles

In contrast, reaction rates for thiol nucleophiles are known to surpass the rates for  $\text{OH}^-$  ions and nitrogen bases by several orders of magnitude.<sup>[324]</sup> To confirm the superior thiol-reactivity of **2**, reactions in water with a series of thiol-containing biomolecules (resulting in compounds **3 I–III**, see Scheme 7.2) were monitored by  $^1\text{H}$  nuclear magnetic resonance (NMR) spectroscopy as illustrated in Figure 7.3.



Scheme 7.2: Reactions of  $\text{Cys}(\text{SO}_2\text{R}) \mathbf{2}$  with thiols of varying  $pK_a$ <sup>[385–387]</sup> yielding asymmetric disulfides  $\mathbf{3 \text{ I-III}}$ , annotations of  $^1\text{H}$  NMR spectra in Figures 7.3, 7.4 and 7.9 in the Supporting Information (*grey*).

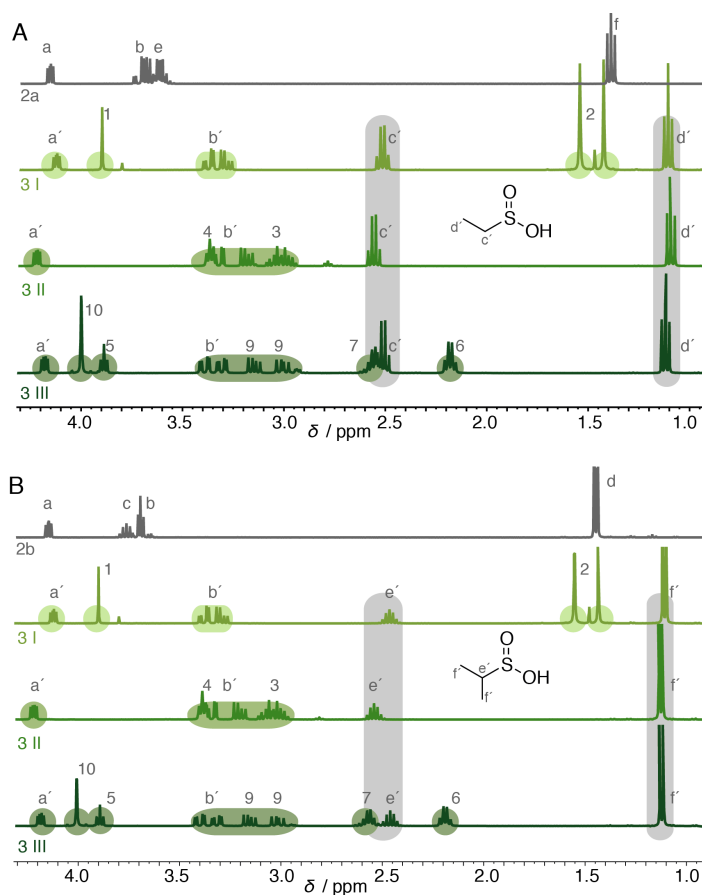


Figure 7.3:  $^1\text{H}$  NMR spectra after reaction of: A)  $\text{Cys}(\text{SO}_2\text{Et}) \mathbf{2a}$ , and B)  $\text{Cys}(\text{SO}_2^i\text{Pr}) \mathbf{2b}$  with various thiols (**I** d-penicillamine, **II**: cysteamine, **III**: glutathione) forming the corresponding asymmetric disulfide  $\mathbf{3}$ . The fully reacted protective group is highlighted and annotations are given in Scheme 7.2.

The conversions of  $\mathbf{2a}$  (Figure 7.3 A) and  $\mathbf{2b}$  (Figure 7.3 B) yield the same mixed disulfide for each thiol compound **I-III**. The signals of the S-alkylsulfonyl group of the intact, protected cysteine ( $c-f$ ) fully vanished after 60 s (minimum time to perform the  $^1\text{H}$  NMR spectroscopy experiment), while signals corresponding to the converted protective group ( $c'-f'$ ) are present, along with the signals corresponding to the

asymmetric disulfides **3I–III**. Differences in reactivity of the individual thiols can be expected, but could not be resolved at this time frame. Ultimately, mass spectrometry confirmed the sole presence of the mixed disulfides in the absence of traceable side products. The observed rapid and quantitative conversion of **2** with thiols is in line with reported rate constants of thiosulfonates (e.g., phenylthiosulfonate)<sup>[370]</sup> in the range of  $10^5 \text{ mol}^{-1} \text{ s}^{-1}$  to  $10^7 \text{ mol}^{-1} \text{ s}^{-1}$ . The selective reactivity of the *S*-alkylsulfonyl group towards thiols (1-hexanethiol,  $\text{p}K_{\text{a}}$  10.7)<sup>[388]</sup> was evaluated in the presence of a competing *N*-nucleophile (1-butanamine,  $\text{p}K_{\text{a}}$  10.6)<sup>[389]</sup> see Figure 7.4 A and Figure 7.9 A in the Supporting Information). The sole presence of an amine does not result in a conversion as discussed above, though the cysteine sulfur atom is readily attacked by the thiol to yield *S*-hexane-*L*-cysteine (**4**). This effect is consistently observed, even if the amino acid **2** is exposed to both nucleophiles simultaneously with excess amine.

### 7.2.2 DFT Calculations

*Small energy gap  
in case of  
S-nucleophiles  
mediates reactivity.*

For a deeper understanding of the experimental data, density functional theory (DFT) calculations were carried out to estimate the relevant frontier orbitals in a nucleophilic attack (Table 7.4 in the Supporting Information). According to the principles outlined by Pearson and Songstad<sup>[325,326,390]</sup> soft nucleophiles exhibit highest occupied molecular orbitals (HOMOs) of higher energy levels compared to hard nucleophiles, with the reciprocal trend for lowest unoccupied molecular orbitals (LUMOs) of electrophiles. This classifies hexanethiolate as a soft nucleophile and butaneamine as a hard nucleophile.

The LUMO of the *S*-alkylsulfonyl-*L*-cysteines is located at the *S*-alkylsulfonyl group ( $E_{\text{LUMO}} = 1.3538 \text{ eV}$  for **2a** and  $E_{\text{LUMO}} = 1.5453 \text{ eV}$  for **2b**). However, the accessibility of the sulfonyl sulfur is highly hindered by the steric demand of the oxygen atoms and the alkyl chain, therefore the soft cysteine sulfur engages in a nucleophilic attack.<sup>[380,381,391]</sup> The HOMOs of both nucleophiles are located on the heteroatoms of the nucleophiles. The active *S*-nucleophile in question is the dissociated thiol, although considering the  $\text{p}K_{\text{a}}$  and the aprotic conditions only a small fraction is present as the anion. However, thiolates are discussed as the relevant nucleophiles compared to thiols<sup>[390,392]</sup> and fast reaction rates are sufficient to drive the reaction.<sup>[370]</sup> Further the non-protonated amine is taken into consideration, since protonated amines react as weak acids rather than as nucleophiles. As illustrated in Figure 7.4 B and Figure 7.9 B in the Supporting Information, the energy gap between the LUMO and the HOMO of the amine significantly exceeds the gap to the HOMO of the thiol. A smaller energy gap, however, facilitates an orbital controlled nucleophilic reaction, thus the DFT calculations are in line with the stated conversion rates. In conclusion, under the reported conditions, the *S*-alkylsulfonyl group rapidly engages in reactions with thiol nucleophiles,<sup>[370]</sup> while competing hydrolysis and aminolysis are suppressed.

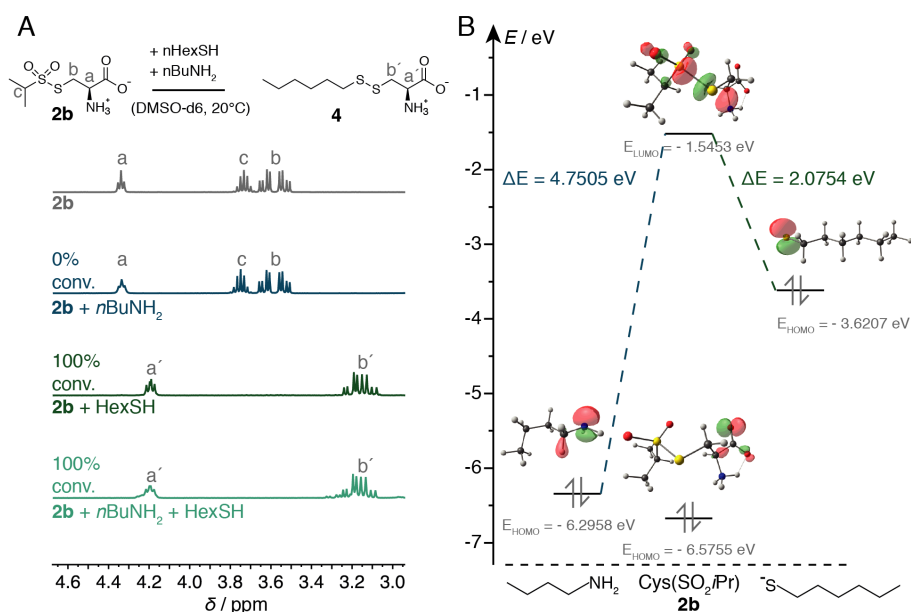
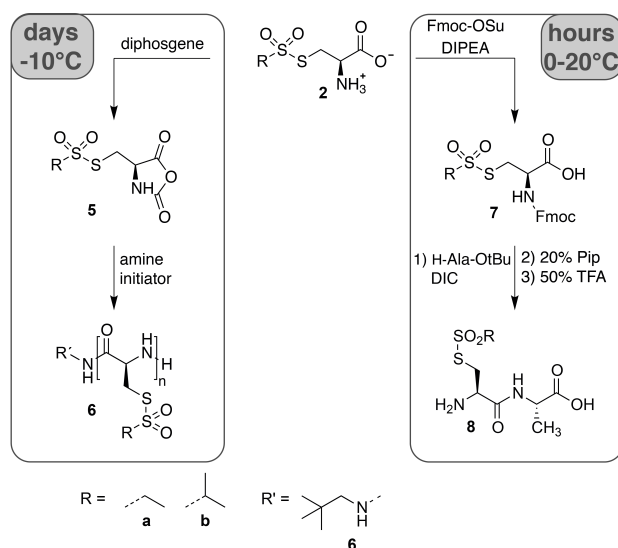


Figure 7.4: A) Detail on the <sup>1</sup>H NMR spectra of the reaction of Cys(SO<sub>2</sub><sup>i</sup>Pr) **2b** with 1-butylamine and 1-hexanethiol forming exclusively *S*-hexane-L-cysteine **4**. B) DFT calculations of HOMO and LUMO of Cys(SO<sub>2</sub><sup>i</sup>Pr) **2b** and HOMOs of butylamine (*left*) and hexanethiol (*right*).

### 7.2.3 Polypeptide Synthesis

The main need for protected amino acids is in peptide synthesis as well as ring-opening polymerization of NCAs. Employing Cys(SO<sub>2</sub>R)s in peptide synthesis according to the *N*-(9-Fluorenylmethoxycarbonyl) (Fmoc) strategy requires only short deprotection times with *N*-nucleophiles,



Scheme 7.3: Synthesis of Cys(SO<sub>2</sub>R) NCA **5** and polymerization with neopentylamine as initiator **6** (*left*) and synthesis of Fmoc-Cys(SO<sub>2</sub>R) **7** and the resulting dipeptide **8** (*right*).

on the range of hours. Thus, the *S*-alkylsulfonyl group can be handled at room temperature. In contrast, controlled polymerization of NCAs requires several days to reach high yields for well-defined polypeptides, which are obtained at low temperatures. Those two major pathways employed with the novel protected cysteines are shown in Scheme 7.3

*Compatibility with the nucleophilic ring-opening polymerization...*

The amine-initiated-controlled ROP of NCAs<sup>[37–39]</sup> derived from *S*-alkylsulfonyl-L-cysteines is depicted in the left part of Scheme 7.3. First, the protected amino acids **2** were transferred into the corresponding NCAs **5** by the Fuchs–Farthing method using diphosgene.<sup>[40–42]</sup> Both NCAs were successfully polymerized with neopentylamine as initiator,<sup>[24]</sup> yielding Cys(SO<sub>2</sub>R) homopolymers **6**. The 9 equivalent methyl-protons of the neopentylamine allow a reliable end group analysis and thus determination of repeating units by <sup>1</sup>H NMR spectroscopy. All polymers display a narrow, symmetrical molecular weight distribution with low dispersity indices (Figure 7.5 and Table 7.1). To verify the integrity of the protective group during the NCA polymerization, matrix assisted laser desorption/ionization-time of flight (MALDI-TOF) mass spectrometry of homopolymers was performed as demonstrated in Figure 7.6.

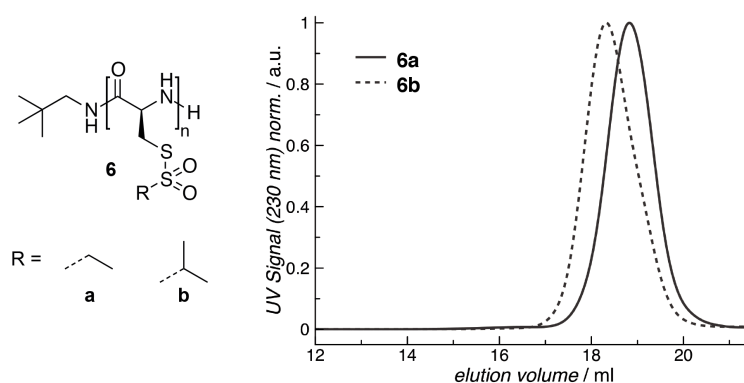


Figure 7.5: HFIP GPC traces of PCys(SO<sub>2</sub>Et) **6a** and PCys(SO<sub>2</sub><sup>i</sup>Pr) **6b**.

The polymer distribution in MALDI-TOF mass spectrometry is narrow, displaying dispersities of  $\bar{D} = 1.11$  for poly(*S*-ethylsulfonyl-L-cysteine) (PCys(SO<sub>2</sub>Et)) and  $\bar{D} = 1.14$  for poly(*S*-isopropylsulfonyl-L-cysteine) (PCys(SO<sub>2</sub><sup>i</sup>Pr)). The degrees of polymerization are in good agreement with the values from the <sup>1</sup>H NMR and gel permeation chromatography (GPC) experiments. As can be noted from the magnification (Figure 7.6 B), initiation by impurities or termination reactions does not occur. In addition, each chain is equipped with a terminal primary amine. Figure 7.6 C compares the simulated peaks of PCys(SO<sub>2</sub><sup>i</sup>Pr) with the measured spectrum revealing an identical isotope distribution due to the natural occurrence of <sup>32</sup>S and <sup>34</sup>S. MALDI-TOF experiments, therefore, clearly confirm the absence of chemical chain termination or other side reactions due to protective group cleavage and emphasize the highly controlled polymerization of *S*-alkylsulfonyl-L-cysteine NCAs.

Table 7.1: Polymer characteristics of PCys(SO<sub>2</sub>Et) **6a** and PCys(SO<sub>2</sub><sup>i</sup>Pr) **6b**.

No.	$X_n$		$\mathcal{D}$		$M_n/\text{kg mol}^{-1}$	
	NMR	MALDI	GPC	MALDI	GPC	MALDI
<b>6a</b>	13	11	1.13	1.11	6.03	2.19
	28	- <sup>a</sup>	1.15	- <sup>a</sup>	11.64	- <sup>a</sup>
<b>6b</b>	15	13	1.15	1.14	8.07	2.61
	23	- <sup>a</sup>	1.17	- <sup>a</sup>	9.50	- <sup>a</sup>

<sup>a</sup> Longer homopolymers could not be ionized.

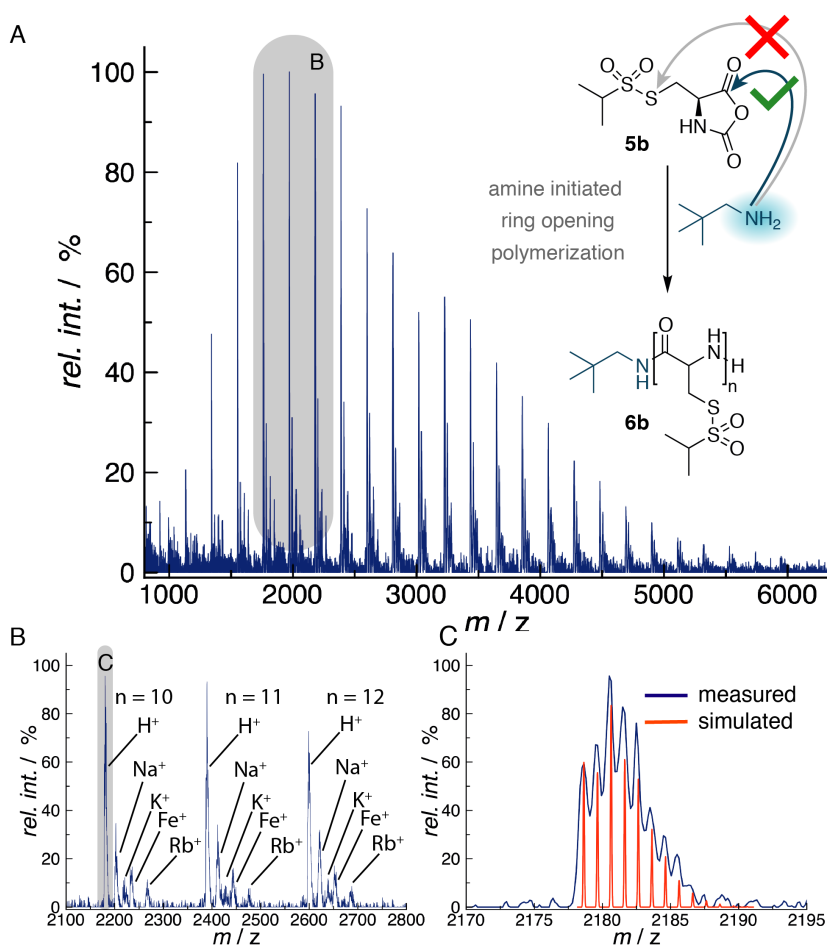


Figure 7.6: MALDI-TOF spectrum of PCys(SO<sub>2</sub><sup>i</sup>Pr) **6b** with a  $X_{n, \text{NMR}} = 15$ .

The sequential peptide synthesis with Cys(SO<sub>2</sub>R) using peptide-coupling techniques as Fmoc chemistry and carbodiimide coupling<sup>[393]</sup> is illustrated on the right-hand side of Scheme 7.3. Both protected amino acids (**2a** and **b**) were converted into the corresponding Fmoc-derivatives **7** and coupled to a C-terminally protected amino acid (in this study *O*<sup>t</sup>Bu-alanine) to form a dipeptide **8**, illustrating the use of Cys(SO<sub>2</sub>R) in peptide synthesis. The synthesis in solution was chosen over a solid phase approach to monitor the peptide coupling itself as well as the individual

... and solid phase peptide synthesis.

deprotection steps by  $^1\text{H}$  NMR spectroscopy. The *S*-alkylsulfonyl group remained intact during the coupling procedure with *N,N*-diisopropylcarbodiimide (DIC), the protective group removal and the workup of the Cys(SO<sub>2</sub>R)-Ala dipeptide **8** (see Supporting Information). These findings suggest that Cys(SO<sub>2</sub>R) is a candidate for solid phase peptide synthesis (SPPS), although a suitable protocol needs to be established.

#### 7.2.4 Polypeptide Conversion

*Fast conversion of polymer side-chains yields asymmetric disulfides.*

Concluding, the thiol-reactivity of the *S*-alkylsulfonyl group in the polymeric state was investigated in analogy to the conversions of Cys(SO<sub>2</sub>R) with thiols (Scheme 7.2, Figure 7.3, 7.4 and 7.9).

The homopolymer **6b** readily engages in post polymerization modification reactions with a thiol (in this study benzylmercaptan), ultimately resulting in an asymmetric disulfide and the corresponding sulfinate (Figure 7.7 A). In agreement with the reactivity of the amino acids, quantitative conversion was observed already after 60 s. As can be noted in Figure 7.7 B and C, signals corresponding to the polycysteine backbone and the end-group signal remain present. Further, signals in Figure 7.7 C originating from the benzyl group as well as the sulfinate appear.

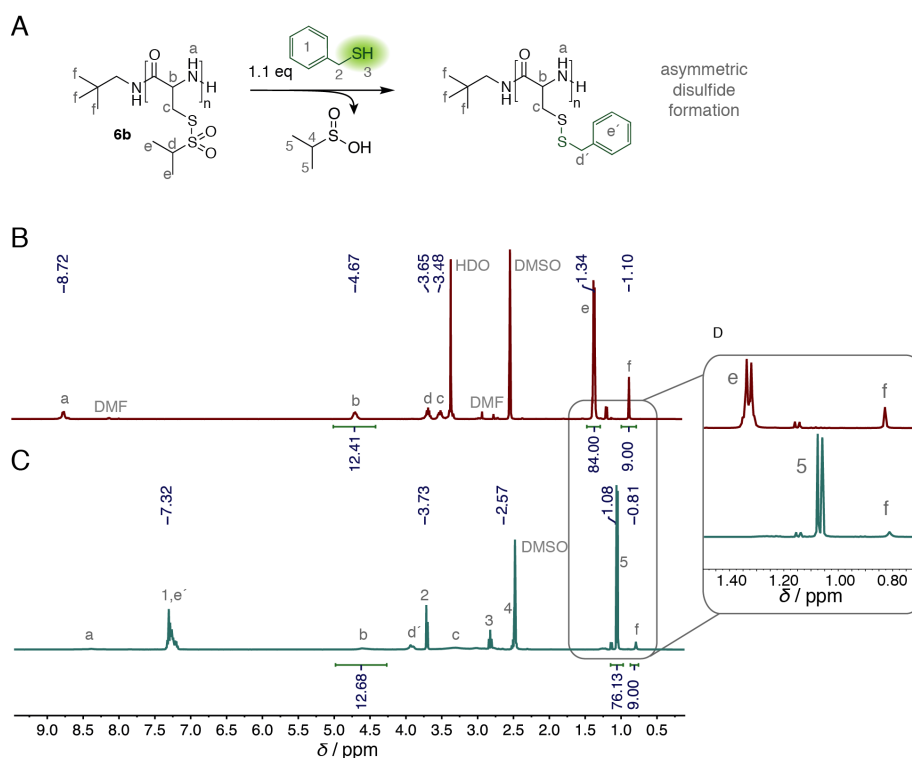


Figure 7.7: A) Scheme of the reaction of PCys(SO<sub>2</sub><sup>i</sup>Pr) **6b** with benzylmercaptan. B)  $^1\text{H}$  NMR spectrum of **6b** with polymer-associated protective group signal at 1.34 ppm. C)  $^1\text{H}$  NMR spectrum after conversion with benzylmercaptan showing a signal at 1.08 ppm corresponding to the fully converted protective group. D) Enlarged comparison of both  $^1\text{H}$  NMR spectra emphasizing the quantitative conversion.



The magnification in Figure 7.7 D reveals the complete disappearance of the polymer associated signal of the *S*-isopropylsulfonyl group at 1.34 ppm (*e*), which is replaced by the signal at 1.08 ppm (*5*) corresponding to the reacted protective group. Therefore,  $\text{Cys}(\text{SO}_2\text{R})$  prove to be the first reactive amino acids for direct disulfide formation applicable to NCA polymerization, enabling the synthesis and implementation of a new class of reactive polypeptides.<sup>[21]</sup>

### 7.3 CONCLUSIONS

We report a novel class of *S*-alkylsulfonyl-L-cysteine derivatives  $\text{Cys}(\text{SO}_2\text{Et})$  and  $\text{Cys}(\text{SO}_2^i\text{Pr})$ <sup>[364]</sup> for chemoselective disulfide formation. The *S*-alkylsulfonyl group provides stability towards amine nucleophiles, as was confirmed experimentally as well as theoretically by DFT calculations. The  $\text{Cys}(\text{SO}_2\text{R})$  were successfully transferred into the corresponding NCAs and Fmoc-derivatives and were implemented in peptide synthesis by ring-opening polymerization and peptide coupling, respectively. Moreover, instant disulfide formation of the *S*-alkylsulfonyl group with thiol nucleophiles was demonstrated with both the protected amino acid and the well-defined poly(*S*-alkylsulfonyl-L-cysteines).

Thus, the *S*-alkylsulfonyl group combines properties of a protective and activating moiety. It is the first thiol modification that provides stability during nucleophilic ring-opening polymerization of NCAs and is compatible with peptide coupling chemistry, while being directly addressable by thiols yielding asymmetric disulfides without additional modification steps. Combined with the intrinsically bioreversible character of disulfides, this straightforward concept offers attractive options for the conjugation of polypeptides to thiol-containing molecules.

### 7.4 ACKNOWLEDGMENTS

We would like to thank Prof. H. Kunz for stimulating discussions during the preparation of the manuscript, Dr. D. Schollmeyer for X-ray crystal structure analysis and S. Türk for MALDI-TOF measurements. M.B. acknowledges financial support by the SFB 1066. D.H. would like to acknowledge the support by the Verband der Chemischen Industrie (VCI) and the Max Planck Graduate Center with the Johannes Gutenberg-Universität Mainz (MPGC). O.S. is grateful for the support by the "Evangelisches Studienwerk e.V. Villigst".

## 7.5 EXPERIMENTAL SECTION

Protocols for the preparation of all compounds as well as materials, instrumentation details and spectra are provided in the Supporting Information. Syntheses of compounds **5–8** were performed under an inert nitrogen atmosphere.

### 7.5.1 *pH Stability*

To investigate the stability of the *S*-thiosulfonyl group, the protected amino acids **2a** and **2b** were subjected to different pH in D<sub>2</sub>O at room temperature and the reactions were monitored by <sup>1</sup>H NMR spectroscopy. Therefore, Cys(SO<sub>2</sub>Et) (6.40 mg, 30 μmol) or Cys(SO<sub>2</sub><sup>i</sup>Pr) (6.82 mg, 30 μmol) were dissolved in D<sub>2</sub>O (0.7 mL) with varying pH immediately prior to the measurement. The pH was adjusted with a Na<sub>2</sub>HPO<sub>4</sub>/KH<sub>2</sub>PO<sub>4</sub> buffer to pH 4, 6, 7, and 8 and with [D<sub>1</sub>]TFA or NaOD (40 wt % in D<sub>2</sub>O) to a pH of 2, 10 and 13, respectively. <sup>1</sup>H NMR spectra were recorded after 2, 30 min and 1, 3 and 6 h. The protective group was removed as ethane- and isopropanesulfinic acid, respectively, as the corresponding anions. The mechanism of the alkaline hydrolysis of thiosulfonates in general is rather complex, but subsequently an intermediately formed thiolate readily reacts with the starting thiosulfonate, resulting in a symmetrical disulfide,<sup>[290,391]</sup> which was cysteine in this study. Overall hydrolysis was evaluated relating the integral of protected amino acid signals to the integral of removed protective group signals and thus giving the conversion. Since the concentration of the OH<sup>-</sup> ions is approximately constant due to the large excess of the buffer, pseudo-first order kinetic behavior can be assumed. A plot of the logarithmic residual concentration of Cys(SO<sub>2</sub>R) ( $\log[M_0 - \text{conv.} \times M_0]$ )<sup>[370]</sup> over time gives a straight line as shown in Figure 7.8 A in the Supporting Information. The apparent pseudo-first order rate constant  $-k/s$  is given as the slope. The rate constants of **2a** and **2b** at different pH are listed in Table 7.2 in the Supporting Information and the relation to the pH is illustrated in Figure 7.8 B.

### 7.5.2 *Amine Stability*

Stability of **2a** and **2b** was tested towards neopentylamine, hexylmethylamine, morpholine and piperidine at different temperatures. The nucleophiles were present in large excess to ensure that the reaction followed pseudo-first order kinetics. All reactions were carried out in absolute [D<sub>6</sub>]DMSO under inert atmosphere, analyzed by <sup>1</sup>H NMR spectroscopy and evaluated in the same fashion as the pH stability studies. Deuterated solvents and amines were dried prior to use. [D<sub>6</sub>]DMSO and [D<sub>4</sub>]MeOD were dried over molecular sieve (3 Å) and filtered directly before use. Oven-dried Schlenk tubes and NMR tubes with PTFE valves were used to prevent moisture from entering the reaction vessel.

Samples were prepared as followed: Cys(SO<sub>2</sub>Et) (6.93 mg, 32.5 mmol) or Cys(SO<sub>2</sub><sup>i</sup>Pr) (7.39 mg, 32.5 mmol) were dried *in vacuo*, overnight, and dissolved in dry [D<sub>6</sub>]DMSO (0.7 mL for 20 °C measurements) or a mixture of dry [D<sub>6</sub>]DMSO and dry [D<sub>4</sub>]MeOD (0.6 mL and 0.1 mL for 0 °C and 10 °C measurements). The NMR tubes were filled in a glove box under an argon atmosphere. Two equivalents (65.0 mmol) of the particular amine were added, kept at the given temperature and <sup>1</sup>H NMR spectra were measured at 1, 6, 24 h, followed by every 24 h for one week. The long time period was chosen for evaluating the stability of the protective group in regard to NCA polymerizations, which are typically conducted at low temperatures for several days. The pseudo-first order rate constants were determined as described above and are given in Table 7.3 in the Supporting Information.

### 7.5.3 Reactions with Thiols

Aside from the stability of the *S*-alkylsulfonyl group reactivity against thiols was also investigated. Cys(SO<sub>2</sub>R) (1.0 equiv) and 1.1 equiv of a thiol component (see Scheme 7.2, Figures 7.3, 7.4 and 7.9) were separately dissolved in D<sub>2</sub>O (0.35 mL each). Immediately prior to the measurement both solutions were mixed and the reaction progress was monitored by <sup>1</sup>H NMR spectroscopy. Cys(SO<sub>2</sub>R) (1.0 equiv) was dissolved in [D<sub>6</sub>]DMSO (0.70 mL) and butylamine (1.0 equiv) or hexanethiol (1.0 equiv) were added. In the sample containing hexanethiol a colorless precipitate formed immediately. Adding [D<sub>1</sub>]TFA dissolved the precipitate and the <sup>1</sup>H NMR spectrum was measured. Complete conversion and presence of *S*-(hexylsulfanyl)-L-cysteine (**4**) could be observed after 1 min (minimal time for measurement). The sample containing butylamine remained a colorless solution and the reaction was quenched after 15 min by adding [D<sub>1</sub>]TFA. <sup>1</sup>H NMR spectroscopy revealed fully preserved signals of **2**, thus no reaction with butylamine occurred. Addition of 1.0 equiv of both butylamine and hexanethiol also immediately resulted in a colorless precipitate. The precipitate was identified as *S*-(hexylsulfanyl)-L-cysteine (**4**) by <sup>1</sup>H NMR spectroscopy and electrospray ionization mass spectrometry (ESI-MS). No adduct of the amine was observed.

## 7.6 SUPPORTING INFORMATION

### 7.6.1 Materials and Instrumentation

All chemicals were purchased from Sigma Aldrich and used as received unless otherwise noted. Tetrahydrofuran THF and hexane were distilled from Na/K and ethyl acetate and dichloromethane (DCM) from CaH<sub>2</sub>. *N,N*-dimethyl formamide (DMF) was purchased dry over molecular sieve. It was further purified by stirring over molecular sieve (3 Å) and BaO. It was then distilled and stored at -80 °C under exclusion of light. Prior to use DMF was degassed *in vacuo* to remove traces of dimethylamine. Neopentylamine (purchased from TCI Europe) and hexylmethylamine were dried over NaOH followed by distillation, morpholine was distilled from Na. Cysteine was purchased from OPREGEN, diphosgene from Alfa Aesar, hexafluoro 2-propanol (HFIP) was purchased from Fluorochem and deuterated solvents from Deutero GmbH.

<sup>1</sup>H and <sup>13</sup>C NMR spectra were recorded on a Bruker Avance II HD 400 at a frequency of 400 and 101 MHz respectively. <sup>1</sup>H NMR spectra were also recorded on a Bruker Avance III HD 300 at 300 MHz. Two-dimensional NMR spectra as <sup>1</sup>H diffusion ordered spectroscopy (DOSY), correlation spectroscopy (COSY) and heteronuclear single-quantum correlation spectroscopy (HSQC) were recorded on a Bruker Avance III HD 400 at 400 MHz. All spectra were recorded at room temperature (25 °C) and calibrated on solvent signals.<sup>[394]</sup> Crystallographic data were collected on a STOE IPDS 2T diffractometer using graphite monochromated Mo K<sub>α</sub> radiation (λ = 0.710 69 Å). Lorentz and polarisation correction was implemented and the structure was solved by direct methods (SIR-2004)<sup>[395]</sup> and refined (SHELXL-2014).<sup>[396]</sup> Hydrogen atoms were refined isotropically assuming riding motion, other atoms were refined anisotropically. Crystallographic data reported in this publication has been deposited with the Cambridge Crystallographic Data Centre (CCDC) and are provided free of charge. Supplementary publication numbers and further details are given with the characterization data.

Electrospray ionization mass spectrometry (ESI-MS) was performed on a Micromass Q-TOF-Ultima spectrometer. Melting points were measured using a Mettler FP62 melting point apparatus at a heating rate of 1 °C min<sup>-1</sup>. Preparative reverse phase-HPLC was performed with a Jasco LC-4000 series system equipped with a VariTide RPC column (PL1E12-5A05, 250 x 21.2 mm) run at a flow of 10.0 ml min<sup>-1</sup> and loaded with a 2 ml injection loop. The system was operated and samples analyzed with ChromNAV FC software (version 2.0). The UV-detector was run at a wavelength of 214 nm. Gel permeation chromatography (GPC) was performed with HFIP containing 3 g l<sup>-1</sup> potassium trifluoroacetate (KTFA) as eluent at 40 °C and a flow rate of 0.8 ml min<sup>-1</sup>. The columns were packed with modified silica (PFG columns particle size: 7 μm, porosity: 100 Å and 1000 Å). Polymethyl methacrylate PMMA standards (Polymer Standards Services GmbH) were used for calibration and toluene was used as internal standard. A refractive index detector (G1362A RID) and an

UV/Vis detector (at 230 nm unless otherwise stated; Jasco UV-2075 Plus) were used for polymer detection.

Matrix assisted laser desorption ionization time of flight (MALDI-TOF) mass spectra<sup>[397]</sup> were recorded using a Bruker Reflex II MALDI-TOF mass spectrometer equipped with a 337 nm N<sub>2</sub> laser. Acceleration of the ions was performed with pulsed ion extraction (PIE, Bruker) at a voltage of 20 kV. The analyzer was operated in reflection mode and a microchannel plate detector was used. Mass spectra were processed by the X-TOF 5.1.0 software (Bruker). A solvent free sample preparation was performed using trans-2-[3-(4-*tert*butylphenyl)-2-methyl-2-propenylidene]malononitrile (DCTB) as the matrix and sodium trifluoroacetate NaTFA as the cationizing salt. Calibration was carried out using a C<sub>60</sub>/C<sub>70</sub> fullerene mixture. Spectra were analyzed and simulated using mMass. Density functional calculations were performed with the ORCA<sup>[398]</sup> series of programs. The B3LYP<sup>[399]</sup> formulation of density functional theory was used employing the Def2-SVP<sup>[400]</sup> basis set. Solvent modeling were simulated by COSMO<sup>[401]</sup> and the relative correction was performed by ZORA.<sup>[402,403]</sup> For accelerated calculations the RIJCOSX-approximation<sup>[404,405]</sup> with the supplementary basis set Def2-SVP/J<sup>[406]</sup> was used. Illustration of the frontier orbitals was performed by the ChemCraft software, isosurface parameters were kept constant at 0.1 a. u.

### 7.6.2 Synthetic Procedures

#### *Ethanesulfinic acid sodium salt*

A solution of sodium sulfite (391.98 g, 3.11 mol) in water (800 mL) was heated to 80 °C. Ethanesulfonyl chloride (147.40 mL, 199.30 g, 1.55 mol) and sodium carbonate (329.63 g, 3.11 mol) were added simultaneously while significant quantities of CO<sub>2</sub> evolved. The reaction mixture was stirred for one hour at 80 °C, afterwards water was removed *in vacuo* at 60 °C. The resulting solid was suspended in methanol and filtered. Evaporation of methanol gave ethanesulfinic acid sodium salt (153.54 g, 1.32 mol, 85 %) as a colorless solid.

<sup>1</sup>H NMR (400 MHz, DMSO-*d*<sub>6</sub>) δ [ppm] = 1.79 (q, <sup>3</sup>J<sub>H,H</sub> = 7.6 Hz, 2H, -CH<sub>2</sub>-), 0.90 (t, <sup>3</sup>J<sub>H,H</sub> = 7.6 Hz, 3H, -CH<sub>3</sub>).

#### *Propane-2-sulfinic acid sodium salt*

The synthesis was carried out analogous to the ethanesulfinic acid sodium salt using sodium sulfite (88.23 g, 700 mmol), propane-2-sulfonyl chloride (39.29 mL, 49.91 g, 350 mmol) and sodium carbonate (74.19 g, 700 mmol). Purification yielded propane-2-sulfinic acid sodium salt (40.56 g, 312 mmol, 89 %) as a colorless solid.

<sup>1</sup>H NMR (400 MHz, DMSO-*d*<sub>6</sub>) δ [ppm] = 1.59 (hept., <sup>3</sup>J<sub>H,H</sub> = 6.9 Hz, 1H, =CH-), 0.87 (d, <sup>3</sup>J<sub>H,H</sub> = 6.9 Hz, 6H, -(CH<sub>3</sub>)<sub>2</sub>).

*S*-ethylsulfonyl-L-cysteine (Cys(SO<sub>2</sub>Et)) **2 a**

An ice-cold solution of sodium nitrite (5.94 g, 86 mmol) in degassed water (45 mL) was slowly added to a stirred solution of L-cysteine hydrochloride (13.57 g, 86 mmol) in previously degassed 2N HCl (90 mL) at 0 °C. After 1 h, ethanesulfinic acid sodium salt (20.00 g, 172 mmol) was added to the deep red solution and was stirred for 2 h. Additional sodium ethanesulfinate (5.00 g, 43 mmol) was added and eventually a colorless solid precipitated. The reaction mixture was stirred at 0 °C overnight. The precipitate was filtered off and the pH of the colorless filtrate was adjusted with 2N NaOH to pH 4-5, resulting in additional colorless solid precipitating. The filtrate was allowed to stand at 4 °C until precipitation was complete. The combined precipitates were washed with MeOH to remove residual sulfinate and dried *in vacuo* yielding Cys(SO<sub>2</sub>Et) (5.03 g, 24 mmol, 27 %) as a colorless, crystalline solid. Crystal Structure (CCDC-1440861): colorless platelet from H<sub>2</sub>O (0.026 × 0.280 × 0.550 mm), monoclinic space group P 2<sub>1</sub>, refinement: wR2 = 0.1223 (R1 = 0.0467 for observed reflections, 0.0509 for all reflections), flack parameter  $x = -01(1)$ , crystal structure contains two independent molecules with slightly different conformations.

<sup>1</sup>H NMR (400 MHz, DMSO-*d*<sub>6</sub>/ TFA-*d*)  $\delta$  [ppm] = 4.34 (t, <sup>3</sup>J<sub>H,H</sub> = 6.4 Hz, <sup>3</sup>J<sub>H,H</sub> = 6.0 Hz, 1H,  $\alpha$ -H), 3.66 (dd, <sup>2</sup>J<sub>H,H</sub> = 14.4 Hz, <sup>3</sup>J<sub>H,H</sub> = 6.0 Hz, 1H, -CHH-S), 3.62 (q, J<sub>H,H</sub> = 7.2 Hz, 2H, -CH<sub>2</sub>-SO<sub>2</sub>), 3.53 (dd, <sup>3</sup>J<sub>H,H</sub> = 14.4 Hz, <sup>3</sup>J<sub>H,H</sub> = 6.4 Hz, 1H, -CHH-S), 1.30 (t, <sup>3</sup>J<sub>H,H</sub> = 7.2 Hz, 3H, -CH<sub>3</sub>).

<sup>13</sup>C NMR (101 MHz, DMSO-*d*<sub>6</sub>/ TFA-*d*)  $\delta$  [ppm] = 168.88 (-COO), 56.27 (-CH<sub>2</sub>SO<sub>2</sub>), 51.84 (-CHN), 34.79 (-CH<sub>2</sub>S), 8.30 (-CH<sub>3</sub>).

ESI-MS:  $m/z = 214.03$  [M+H]<sup>+</sup>, (calc. 213.28 g mol<sup>-1</sup>); 236.01 [M+Na]<sup>+</sup>, (calc. 236.15 g mol<sup>-1</sup>).

*S*-isopropylsulfonyl-L-cysteine (Cys(SO<sub>2</sub><sup>*i*</sup>Pr)) **2 b**

The synthesis was carried out analogous to **2 a** using sodium nitrite (11.60 g, 168 mmol), L-cysteine hydrochloride (26.50 g, 168 mmol) and propane-2-sulfinic acid sodium salt (43.30 g, 465 mmol). The purification yielded Cys(SO<sub>2</sub><sup>*i*</sup>Pr) (8.78 g, 39 mmol, 23 %) as a colorless, crystalline solid. Crystal Structure (CCDC-1440862): colorless needle from H<sub>2</sub>O (0.060 × 0.200 × 0.630 mm), monoclinic space group C 2, refinement: wR2=0.1794 (R1=0.0639 for observed reflections, 0.0805 for all reflections), flack parameter  $x = -014(17)$ , crystal structure contains two independent molecules with slightly different conformations.

<sup>1</sup>H NMR (400 MHz, DMSO-*d*<sub>6</sub>)  $\delta$  [ppm] = 4.34 (t, <sup>3</sup>J<sub>H,H</sub> = 6.0 Hz, 1H,  $\alpha$ -H), 3.76 (hept, J<sub>H,H</sub> = 6.7 Hz, 1H, =CH-SO<sub>2</sub>), 3.65 (dd, <sup>2</sup>J<sub>H,H</sub> = 14.4 Hz, <sup>3</sup>J<sub>H,H</sub> = 6.0 Hz, 1H, -CHH-S), 3.54 (dd, <sup>2</sup>J<sub>H,H</sub> = 14.4 Hz, <sup>3</sup>J<sub>H,H</sub> = 6.2 Hz, 1H, -CHH-S), 1.35 (d, <sup>3</sup>J<sub>H,H</sub> = 6.7 Hz, 6H, -(CH<sub>3</sub>)<sub>2</sub>).

<sup>13</sup>C NMR (101 MHz, DMSO-*d*<sub>6</sub>)  $\delta$  [ppm] = 169.08 (-COO), 63.04 (-CHSO<sub>2</sub>), 52.18 (-CHN), 35.29 (-CH<sub>2</sub>S), 16.39-16.12 ((-CH<sub>3</sub>)<sub>2</sub>).

ESI-MS:  $m/z = 228.04$  [M+H]<sup>+</sup>, (calc. 227.30 g mol<sup>-1</sup>); 250.01 [M+Na]<sup>+</sup>, (calc. 249.86 g mol<sup>-1</sup>).



*S*-ethylsulfonyl-L-cysteine *N*-carboxyanhydride (Cys(SO<sub>2</sub>Et) NCA) **5 a**

Dried Cys(SO<sub>2</sub>Et) (7.00 g, 32.82 mmol) was suspended in absolute THF (100 mL) and heated to 70 °C. Diphosgene (3.60 mL, 5.84 g, 29.52 mmol) was slowly added and the suspension was heated for an additional 4 h. Dry nitrogen was bubbled through the reaction mixture overnight into a gas washing bottle with an aqueous KOH solution to remove excess diphosgene, HCl and most of the solvent. The remaining solvent was removed *in vacuo* and the residue was dissolved in 100 mL absolute ethyl acetate. Any insoluble compounds were removed by filtration avoiding contact with air and the NCA was precipitated by adding 800 mL absolute hexane. The recrystallization of the product was repeated two more times yielding Cys(SO<sub>2</sub>Et) NCA (6.43 g, 26.87 mmol, 82%) as a colorless, crystalline powder (m.p. 113–115 °C).

<sup>1</sup>H NMR (400 MHz, DMSO-*d*<sub>6</sub>) δ [ppm] = 9.32 (s, 1H, -NHCO), 4.86 (td, <sup>3</sup>J<sub>H,H</sub> = 6.0 Hz, <sup>3</sup>J<sub>H,H</sub> = 4.8 Hz, <sup>3</sup>J<sub>H,H</sub> = 1.6 Hz, 1H, α-H), 3.64 (dd, <sup>2</sup>J<sub>H,H</sub> = 14.4 Hz, <sup>3</sup>J<sub>H,H</sub> = 4.8 Hz, 1H, -CHH-S), 3.62 (q, <sup>3</sup>J<sub>H,H</sub> = 7.2 Hz, 2H, -CH<sub>2</sub>-SO<sub>2</sub>), 3.57 (dd, <sup>2</sup>J<sub>H,H</sub> = 14.4 Hz, <sup>3</sup>J<sub>H,H</sub> = 6.4 Hz, 1H, -CHH-S), 1.29 (t, <sup>3</sup>J<sub>H,H</sub> = 7.2 Hz, 3H, -CH<sub>3</sub>).

<sup>13</sup>C NMR (101 MHz, DMSO-*d*<sub>6</sub>) δ [ppm] = 169.58 (CNOO), 151.68 (-COO), 56.99 (-CHSO<sub>2</sub>), 56.16 (-CHN), 36.00 (-CH<sub>2</sub>S), 8.24 (-CH<sub>3</sub>).

*S*-isopropylsulfonyl-L-cysteine *N*-carboxyanhydride (Cys(SO<sub>2</sub><sup>*i*</sup>Pr) NCA) **5 b**

The synthesis of Cys(SO<sub>2</sub><sup>*i*</sup>Pr) NCA was carried out under identical conditions as **5 a** employing Cys(SO<sub>2</sub>Et) (6.04 g, 26.57 mmol) and diphosgene (4.00 mL, 6.56 g, 33.14 mmol). Recrystallization yielded Cys(SO<sub>2</sub><sup>*i*</sup>Pr) NCA (4.64 g, 18.3 mmol, 69 %) as a colorless, crystalline powder (m.p. 98–100 °C).

<sup>1</sup>H NMR (400 MHz, DMSO-*d*<sub>6</sub>) δ [ppm] = 9.33 (s, 1H, -NHCO), 4.84 (td, <sup>3</sup>J<sub>H,H</sub> = 5.4 Hz, 3J = 1.4 Hz, 1H, α-H), 3.75 (hept, J<sub>H,H</sub> = 6.6 Hz, 1H, =CH-SO<sub>2</sub>), 3.59 (ddd, <sup>2</sup>J<sub>H,H</sub> = 14.4 Hz, <sup>3</sup>J<sub>H,H</sub> = 5.6 Hz, <sup>3</sup>J<sub>H,H</sub> = 5.1 Hz, 2H, -CH<sub>2</sub>-S), 1.33 (dd, <sup>3</sup>J<sub>H,H</sub> = 6.6 Hz, <sup>3</sup>J<sub>H,H</sub> = 0.9 Hz, 6H, -(CH<sub>3</sub>)<sub>2</sub>).

<sup>13</sup>C NMR (101 MHz, DMSO-*d*<sub>6</sub>) δ [ppm] = 169.52 (CNOO), 151.65 (-COO), 62.69 (-CHSO<sub>2</sub>), 52.12 (-CHN), 36.18 (-CH<sub>2</sub>S), 15.90-15.87 ((-CH<sub>3</sub>)<sub>2</sub>).

*poly*(*S*-ethylsulfonyl-L-cysteine) (PCys(SO<sub>2</sub>Et)) **6 a**

Cys(SO<sub>2</sub>Et) NCA (107 mg, 447 μmol) was transferred into a Schlenk tube under dry nitrogen counter flow. Absolute DMF (3 mL) and absolute neopentylamine (1.74 μL, 1.30 mg, 15 μmol) were added and the vessel was cooled to -10 °C. A steady flow of dry nitrogen was sustained during the polymerization, preventing any impurities from entering the Schlenk tube, while ensuring the escape of produced CO<sub>2</sub>. The progress of the polymerization was monitored via IR spectroscopy by the disappearing NCA carbonyl peaks intensities at 1858 cm<sup>-1</sup> and 1788 cm<sup>-1</sup>. Samples were taken using a nitrogen flushed syringe through a septum. The polymer was precipitated after 70 % conversion in a mixture of cold diethyl ether and tetrahydrofuran (THF) (5:1 v/v) to solubilize

and remove remaining NCA. The suspension was centrifuged (4500 rpm, 15 min, 0–10 °C) and decanted. This procedure was repeated twice concluding with pure diethyl ether yielding poly(*S*-ethylsulfonyl-L-cysteine) (65 mg, 73 %) as a colorless to slightly yellow solid.

$^1\text{H}$  NMR (400 MHz, DMSO- $d_6$ )  $\delta$  [ppm] = 8.76 (m, 1nH,  $-\text{NHCO}$ ), 4.68 (m, 1nH,  $\alpha\text{-H}$ ), 3.63–3.42 (m, 4nH,  $-\text{CH}_2\text{-SSO}_2\text{-CH}_2\text{-}$ ), 1.30 (t, 3nH,  $-\text{CH}_3$ ), 0.85 (s, 9H,  $-(\text{CH}_3)_3$ ).

*poly(S-isopropylsulfonyl-L-cysteine) (PCys(SO<sub>2</sub><sup>i</sup>Pr)) 6b*

Polymerization of PCys(SO<sub>2</sub><sup>i</sup>Pr) was conducted under identical conditions as synthesis of **6a**. Cys(SO<sub>2</sub><sup>i</sup>Pr) NCA (146 mg, 576  $\mu\text{mol}$ ) was polymerized using dry neopentylamine (4.50  $\mu\text{L}$ , 3.35 mg, 38  $\mu\text{mol}$ ) in absolute DMF (3 mL) at -10 °C yielding poly(*S*-isopropylsulfonyl-L-cysteine) (80 mg, 80 %) after purification.

$^1\text{H}$  NMR (400 MHz, DMSO- $d_6$ )  $\delta$  [ppm] = 8.72 (m, 1nH,  $-\text{NHCO}$ ), 4.65 (m, 1nH,  $\alpha\text{-H}$ ), 3.64 (m, 1nH,  $=\text{CH-SO}_2$ ), 3.47–3.33 (m, 2nH,  $-\text{CH}_2\text{-S}$ ), 1.33 (d, 6nH,  $-(\text{CH}_3)_2$ ), 0.84 (s, 9H,  $-(\text{CH}_3)_3$ ).

*N-(9-Fluorenylmethoxycarbonyl)-S-ethylsulfonyl-L-cysteine*

*(Fmoc-Cys(SO<sub>2</sub>Et)) 7a*

Dried Cys(SO<sub>2</sub>Et) (621 mg, 2.91 mmol) were suspended in absolute DCM (2 mL) and cooled to 0 °C. Absolute DIPEA (545  $\mu\text{L}$ , 414 mg, 3.20 mmol) and Fmoc-OSu (983 mg, 2.91 mmol) were added under dry nitrogen counter flow. The reaction mixture was stirred at room temperature for 4 h followed by removal of the solvent under reduced pressure. The crude product was purified by flash chromatography (DCM + 10 % MeOH), dissolved in benzene and lyophilized yielding Fmoc-Cys(SO<sub>2</sub>Et) (552 mg, 1.27 mmol, 44 %).

$^1\text{H}$  NMR (400 MHz, DMSO- $d_6$ )  $\delta$  [ppm] = 7.94 (d,  $^3J_{\text{H,H}} = 8.5$  Hz, 1H,  $-\text{NH}$ ), 7.90 (d,  $^3J_{\text{H,H}} = 7.5$  Hz, 2H,  $=\text{CH-}$ ), 7.71 (d,  $^3J_{\text{H,H}} = 7.4$  Hz, 2H,  $=\text{CH-}$ ), 7.42 (t,  $^3J_{\text{H,H}} = 7.4$  Hz, 2H,  $=\text{CH-}$ ), 7.33 (t,  $^3J_{\text{H,H}} = 6.9$  Hz, 2H,  $=\text{CH-}$ ), 4.36–4.21 (m, 4H,  $\alpha\text{-H}$ ,  $=\text{CH-}$ ,  $-\text{OCH}_2\text{-}$ ), 3.61–3.48 (m, 2H,  $-\text{CH}_2\text{-SO}_2$ ), 3.41–3.28 (m, 2H,  $-\text{CH}_2\text{-S}$ ), 1.25 (t,  $^3J_{\text{H,H}} = 7.2$  Hz, 3H,  $-\text{CH}_3$ ).

$^{13}\text{C}$  NMR (101 MHz, DMSO- $d_6$ )  $\delta$  [ppm] = 171.33 ( $-\text{COO}$ ), 155.99 (NCOO), 143.77 ( $=\text{CH-}$ ), 140.76 ( $=\text{CH-}$ ), 127.70 ( $=\text{CH-}$ ), 127.12 ( $=\text{CH-}$ ), 125.24 ( $=\text{CH-}$ ), 120.19 ( $=\text{CH-}$ ), 65.84 ( $\text{OCH}_2\text{-}$ ), 55.58 ( $-\text{CH}_2\text{SO}_2\text{-}$ ), 53.58 ( $-\text{CHN}$ ), 46.59 ( $=\text{CH-}$ ), 36.57 ( $-\text{CH}_2\text{S-}$ ), 8.29 ( $-\text{CH}_3$ ).

ESI-MS:  $m/z = 458.09$  [ $\text{M}+\text{Na}$ ]<sup>+</sup>, (calc. 458.33 g mol<sup>-1</sup>); 474.06 [ $\text{M}+\text{K}$ ]<sup>+</sup>, (calc. 474.18 g mol<sup>-1</sup>).

*N-(9-Fluorenylmethoxycarbonyl)-S-isopropylsulfonyl-L-cysteine*

*(Fmoc-Cys(SO<sub>2</sub><sup>i</sup>Pr)) 7b*

The synthesis was carried out analogous to **5a** using Cys(SO<sub>2</sub><sup>i</sup>Pr) (3.99 g, 17.55 mmol), Fmoc-OSu (5.92 g, 17.55 mmol) and DIPEA (3.28 mL, 2.50 g, 19.31 mmol). Purification yielded Fmoc-Cys(SO<sub>2</sub><sup>i</sup>Pr) (2.70 g, 6.01 mmol, 34 %).



$^1\text{H}$  NMR (400 MHz, DMSO- $d_6$ )  $\delta$  [ppm] = 7.92 (d,  $^3J_{\text{H,H}} = 7.0$  Hz, 1H, -NH), 7.89 (d,  $^3J_{\text{H,H}} = 7.6$  Hz, 2H, =CH-), 7.72 (d,  $^3J_{\text{H,H}} = 7.4$  Hz, 2H, =CH-), 7.42 (t,  $^3J_{\text{H,H}} = 7.4$  Hz, 2H, =CH-), 7.33 (t,  $^3J_{\text{H,H}} = 6.9$  Hz, 2H, =CH-), 4.36–4.21 (m, 4H,  $\alpha$ -H, =CH-, -OCH<sub>2</sub>-), 3.69 (hept,  $J_{\text{H,H}} = 6.7$  Hz, 1H, =CH-SO<sub>2</sub>), 3.55 (dd,  $^2J_{\text{H,H}} = 14.0$  Hz,  $^3J_{\text{H,H}} = 4.7$  Hz, 1H, -CHH-S), 3.36 (dd,  $^2J_{\text{H,H}} = 13.8$  Hz,  $^3J_{\text{H,H}} = 9.7$  Hz, 1H, -CHH-S), 1.31 (d,  $^3J_{\text{H,H}} = 6.7$  Hz, 6H, -(CH<sub>3</sub>)<sub>2</sub>).  
 $^{13}\text{C}$  NMR (101 MHz, DMSO- $d_6$ )  $\delta$  [ppm] = 171.27 (-COO), 155.95 (NCOO), 143.75 (=CH-), 140.74 (=CH-), 127.68 (=CH-), 127.10 (=CH-), 125.22 (=CH-), 120.16 (=CH-), 65.84 (OCH<sub>2</sub>-), 62.22 (-CHSO<sub>2</sub>-), 53.80 (-CHN), 46.59 (=CH-), 36.82 (-CH<sub>2</sub>S-), 15.98-15.82 ((-CH<sub>3</sub>)<sub>2</sub>).  
 ESI-MS:  $m/z = 472.10$  [M+Na]<sup>+</sup>, (calc. 472.54 g mol<sup>-1</sup>); 488.06 [M+K]<sup>+</sup>, (calc. 488.01 g mol<sup>-1</sup>).

### *S*-isopropylsulfonyl-L-cysteine-L-alanine (Cys(SO<sub>2</sub><sup>*i*</sup>Pr)-Ala) **8**

Dried Fmoc-Cys(SO<sub>2</sub><sup>*i*</sup>Pr) (131.5 mg, 293  $\mu\text{mol}$ ) and dried Ala-O<sup>*t*</sup>Bu (44.3 mg, 244  $\mu\text{mol}$ ) were solved in absolute DCM (2.5 mL) in a Schlenk tube. *N,N*-diisopropylcarbodiimide (DIC) (45.0  $\mu\text{L}$ , 36.29 mg, 292  $\mu\text{mol}$ ) were added under dry nitrogen counter flow. The opaque reaction mixture was stirred for 2 h at 20 °C and the solvent was removed *in vacuo*.  $^1\text{H}$  NMR revealed a coupling efficiency of 84 %. The Fmoc protective group removal was conducted at 0 °C with 2 mL of a 20 % solution of absolute piperidine in absolute DCM for 10 min. The solvent was evaporated *in vacuo*, 2 mL absolute DCM were added and removed *in vacuo* three times to remove residual piperidine. The tert-butyl protective group was removed at 0 °C with 2 mL of a 50 % solution of TFA in DCM for 1 h. The solvent was evaporated *in vacuo*. The crude product was purified by preparative reverse phase-HPLC (H<sub>2</sub>O + 1 % acetonitrile + 0.1 % TFA). An overall yield however was not determined due so numerous samples taken for  $^1\text{H}$  NMR analytics to evaluate the coupling efficiency and protective group removal.

$^1\text{H}$  NMR (400 MHz, DMSO- $d_6$ )  $\delta$  [ppm] = 4.22 (t,  $^3J_{\text{H,H}} = 7.2$  Hz, 1H,  $\alpha$ -H)<sub>Cys</sub>, 4.12 (m, 1H,  $\alpha$ -H)<sub>Ala</sub>, 3.77 (hept,  $J_{\text{H,H}} = 6.7$  Hz, 1H, =CH-SO<sub>2</sub>)<sub>Cys</sub>, 3.52 (ddd,  $^2J_{\text{H,H}} = 13.7$  Hz,  $^3J_{\text{H,H}} = 7.7$  Hz, 3J = 6.8 Hz, 2H, -CH<sub>2</sub>-S)<sub>Cys</sub>, 1.36 (dd,  $^3J_{\text{H,H}} = 6.7$  Hz,  $^3J_{\text{H,H}} = 1.1$  Hz, 6H, -(CH<sub>3</sub>)<sub>2</sub>)<sub>Cys</sub>, 1.30 (d,  $^3J_{\text{H,H}} = 7.2$  Hz, 3H, -CH<sub>3</sub>)<sub>Ala</sub>.  
 ESI-MS:  $m/z = 299.05$  [M+H]<sup>+</sup>, (calc. 298.07 g mol<sup>-1</sup>).

#### 7.6.3 pH Stability

The protective group remained fully intact at pH 2 and 4. Hydrolysis sets slowly in at pH 6 proceeding with increasing pH. Hydrolysis at pH 13 was complete before the first time point measurement at 1 min. The *S*-isopropylsulfonyl group proved to be slightly more stable towards hydrolysis in comparison to the *S*-ethylsulfonyl group. Summarized it can be stated that long term exposure of the *S*-alkylsulfonyl group to neutral to alkaline conditions bears the issue of hydrolysis. However,

stability of both Cys(SO<sub>2</sub>Et) and Cys(SO<sub>2</sub><sup>i</sup>Pr) under acidic to neutral conditions was confirmed for extended periods of time.

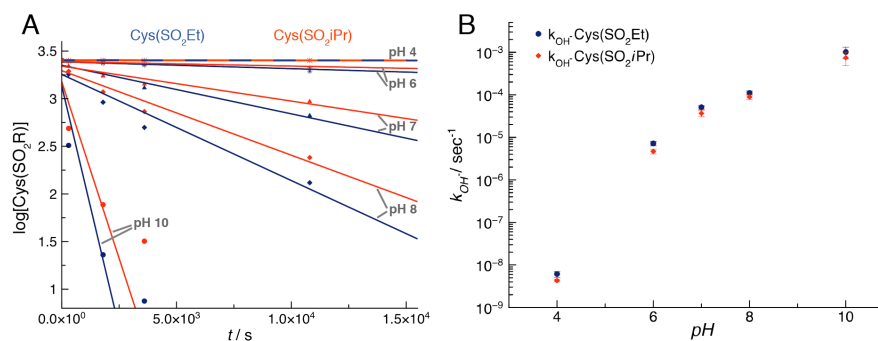


Figure 7.8: pH influence on Cys(SO<sub>2</sub>R) **2a** and **2b**: A) Plots of the logarithmic residual concentration of the protected amino acids as monitored by <sup>1</sup>H NMR over time. B) Rate constants of the alkaline hydrolysis in relation to the pH.

Table 7.2: Apparent rate constants for hydrolysis of Cys(SO<sub>2</sub>R) at 20 °C.

pH	$k_{OH}^{Et}/s^{-1}$	$k_{OH}^{iPr}/s^{-1}$
4	$6.1 \times 10^{-9}$	$4.2 \times 10^{-9}$
6	$7.2 \times 10^{-6}$	$4.7 \times 10^{-6}$
7	$5.1 \times 10^{-5}$	$3.7 \times 10^{-5}$
8	$1.1 \times 10^{-4}$	$8.9 \times 10^{-5}$
10	$1.0 \times 10^{-3}$	$7.4 \times 10^{-4}$

#### 7.6.4 Amine Stability

Lowering the temperature results in slower reaction rates for all amines. Gradual protective group removal was observed for Cys(SO<sub>2</sub>Et) and Cys(SO<sub>2</sub><sup>i</sup>Pr) when exposed amines at 20 °C. At 0 °C and -10 °C on the other hand degradation does not occur over time and the protective groups are stable for more than 7 days.

Table 7.3: Rate constants for reactions of Cys(SO<sub>2</sub>R) with amines at different temperatures.

amines	$k^{Et}/s^{-1}$			$k^{iPr}/s^{-1}$		
	20 °C	0 °C	-10 °C	20 °C	0 °C	-10 °C
Neo	$2.9 \times 10^{-6}$	$1.2 \times 10^{-7}$	$1.9 \times 10^{-8}$	$5.3 \times 10^{-7}$	$1.9 \times 10^{-8}$	$5.0 \times 10^{-9}$
Hex	$5.3 \times 10^{-7}$	$1.0 \times 10^{-7}$	$1.3 \times 10^{-8}$	$8.3 \times 10^{-7}$	$2.2 \times 10^{-7}$	$6.5 \times 10^{-9}$
Morph	$6.9 \times 10^{-7}$	$3.4 \times 10^{-8}$	- <sup>a</sup>	$7.6 \times 10^{-7}$	$4.1 \times 10^{-8}$	- <sup>a</sup>
Pip	$6.7 \times 10^{-7}$	$1.0 \times 10^{-8}$	- <sup>a</sup>	$6.9 \times 10^{-7}$	$3.7 \times 10^{-8}$	- <sup>a</sup>

<sup>a</sup> Not determined

7.6.5 Reactions of Cys(SO<sub>2</sub>R) with ThiolsCompound **3I-III**

Reactivity against thiols was investigated by reaction of Cys(SO<sub>2</sub>R) (1.0 eq.) and 1.1 eq. of a thiol component (see Scheme 7.2), which were separately solved in D<sub>2</sub>O (0.35 mL each) and combined immediately before the measurement. The specific reaction components for the formation of **3I-III** were as followed:

11.80 mg (55.32 μmol) Cys(SO<sub>2</sub>Et) and 6.91 mg (60.86 μmol) cysteamine; 11.05 mg (48.61 μmol) Cys(SO<sub>2</sub><sup>i</sup>Pr) and 6.08 mg (53.48 μmol) cysteamine; 8.88 mg (41.64 μmol) Cys(SO<sub>2</sub>Et) and 14.07 mg (45.80 μmol) glutathione; 8.50 mg (37.40 μmol) Cys(SO<sub>2</sub><sup>i</sup>Pr) and 12.64 mg (41.14 μmol) glutathione; 8.82 mg (41.35 μmol) Cys(SO<sub>2</sub>Et) and 6.79 mg (45.49 μmol) D-penicillinamine; 9.77 mg (42.98 μmol) Cys(SO<sub>2</sub><sup>i</sup>Pr) and 7.05 mg (47.28 μmol) D-penicillinamine.

ESI-MS: S-(D-penicillinamine)-L-cysteine [**3I**] (calc. 268.06): 269.06 (3I+H<sup>+</sup>), 537.11 (2x3I+H<sup>+</sup>); S-(cysteamine)-L-cysteine [**3II**] (calc. 196.03): 197.04 (3II+H<sup>+</sup>), 393.07 (2x3II+H<sup>+</sup>); S-(glutathione)-L-cysteine [**3III**] (calc. 426.09): 427.06 (3III+H<sup>+</sup>), 613.14 (glutathione ox.).

*S*-(hexylsulfanyl)-L-cysteine (**4**) in competing reaction with 1-butylamine

Cys(SO<sub>2</sub>R) (1.0 eq.) was dissolved in DMSO-*d*<sub>6</sub> (0.70 mL) and butylamine (1.0 eq.), hexanethiol (1.0 eq.) or both were added. Individual reaction components were: 4.93 mg (23.12 μmol) Cys(SO<sub>2</sub>Et) and 2.28 μL (1.69 mg, 23.12 μmol) butylamine; 5.35 mg (25.08 μmol) Cys(SO<sub>2</sub>Et) and 3.53 μL (2.97 mg, 25.08 μmol) hexanethiol; 6.80 mg (31.88 μmol) Cys(SO<sub>2</sub>Et) and 4.49 μL (3.77 mg, 31.88 μmol) hexanethiol and 3.15 μL (2.33 mg, 31.88 μmol) butylamine; 5.45 mg (23.98 μmol) Cys(SO<sub>2</sub><sup>i</sup>Pr) and 3.38 μL (2.84 mg, 23.98 μmol) hexanethiol; 5.41 mg (23.80 μmol) Cys(SO<sub>2</sub><sup>i</sup>Pr) and 3.14 μL (2.41 mg, 23.80 μmol) butylamine; 5.54 mg (25.56 μmol) Cys(SO<sub>2</sub><sup>i</sup>Pr) and 3.60 μL (3.02 mg, 25.56 μmol) hexanethiol and 2.53 μL (1.87 mg, 25.56 μmol) butylamine.

<sup>1</sup>H NMR (400 MHz, DMSO-*d*<sub>6</sub>) δ [ppm] = 4.20 (m, 1H, α-H), 3.20 (dd, <sup>2</sup>J<sub>H,H</sub> = 14.4, 3J = 4.9 Hz, 2H, -CH<sub>2</sub>-), 3.13 (dd, <sup>2</sup>J<sub>H,H</sub> = 14.4, <sup>3</sup>J<sub>H,H</sub> = 7.1 Hz, 2H, -CH<sub>2</sub>-), 2.74 (t, <sup>3</sup>J<sub>H,H</sub> = 7.1 Hz, 2H, -CH<sub>2</sub>-S), 1.66-1.56 (m, 2H, -CH<sub>2</sub>-), 1.38-1.19 (m, 6H, (-CH<sub>2</sub>-)<sub>3</sub>), 0.87-0.80 (m, 3H, -CH<sub>3</sub>).

ESI-MS: S-(hexylsulfanyl)-L-cysteine **4** (calc. 237.09): 238.11 (4+H<sup>+</sup>), 241.05 (cystine+H<sup>+</sup>), 259.89 (4+Na<sup>+</sup>), 263.14 (cystine+Na<sup>+</sup>), 475.20 (2x4+H<sup>+</sup>).

## 7.6.6 DFT Calculations

The DFT calculated energy levels of the frontier orbitals are given in Table 7.4, their visualization and  $^1\text{H}$  NMR spectra of the conversions are given in Figure 7.3 and 7.10.

Table 7.4: HOMO/LUMO energy levels of 1-butanamine, 1-hexanethiol and  $\text{Cys}(\text{SO}_2\text{R})$ .

	HOMO/eV	LUMO/eV
$\text{Cys}(\text{SO}_2\text{Et})$	-6.6845	-1.3190
$\text{Cys}(\text{SO}_2^i\text{Pr})$	-6.6748	-1.3231
1-butanamine	-6.2958	
1-hexanamine	-3.6207	

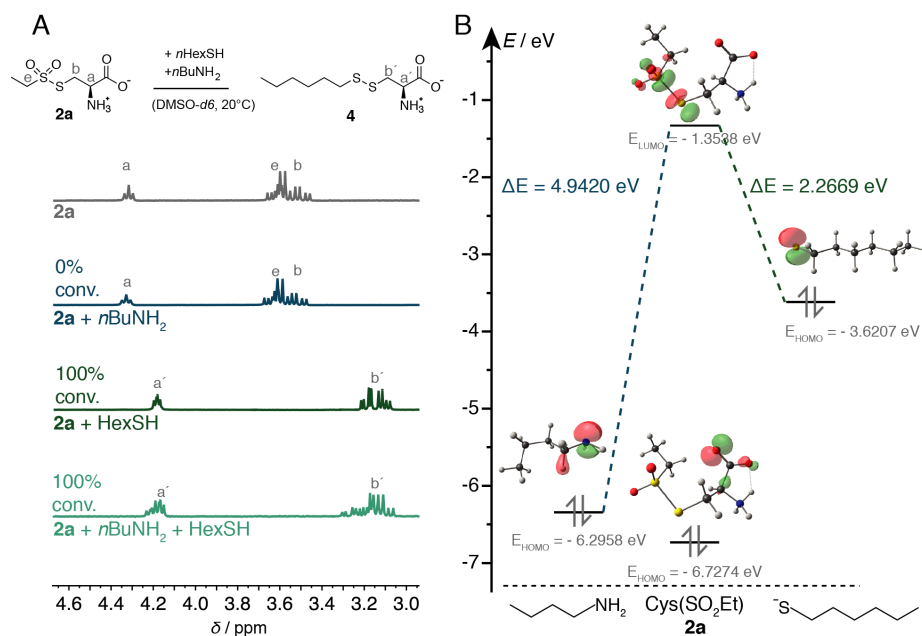


Figure 7.9: A) Detail on  $^1\text{H}$  NMR spectra of the reaction of  $\text{Cys}(\text{SO}_2\text{Et})$  **2a** with 1-butylamine and 1-hexanethiol forming exclusively  $S$ -hexane-L-cysteine **4**. B) DFT calculations of HOMO and LUMO of  $\text{Cys}(\text{SO}_2\text{Et})$  **2a** and HOMOs of butylamine (*left*) and hexanethiol (*right*).

## 7.6.7 Crystallographic Data

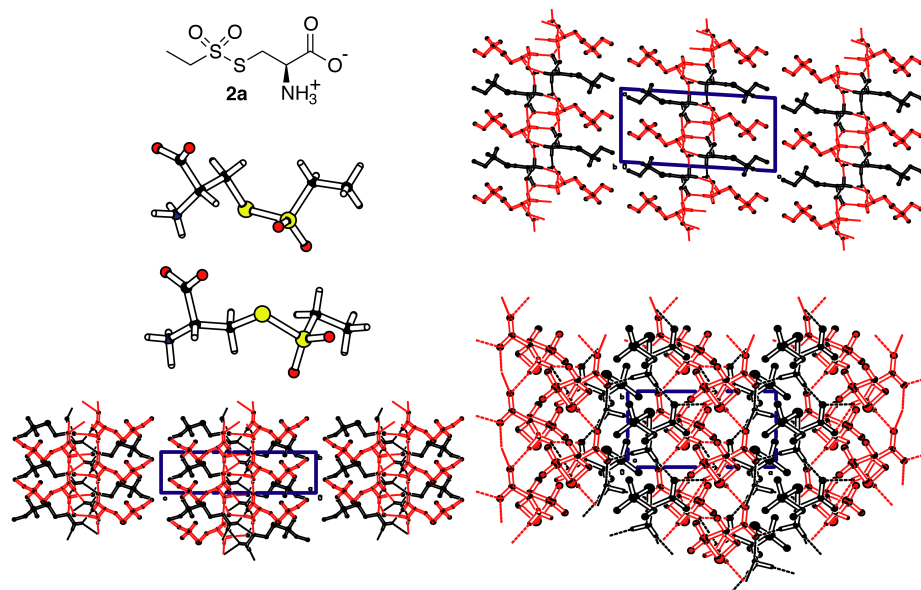


Figure 7.10: Crystallographic data of L-Cys(SO<sub>2</sub>Et) **2a** showing two possible conformations.

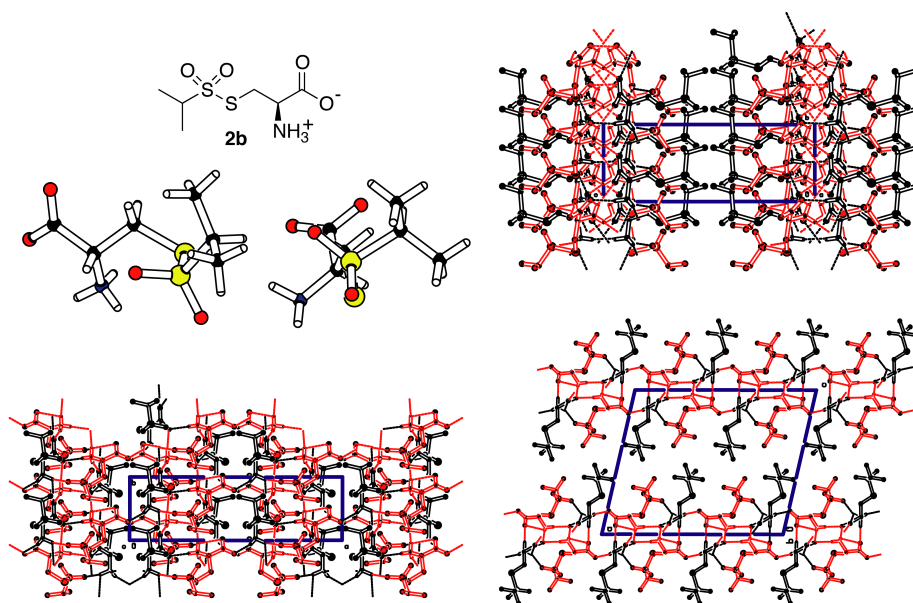
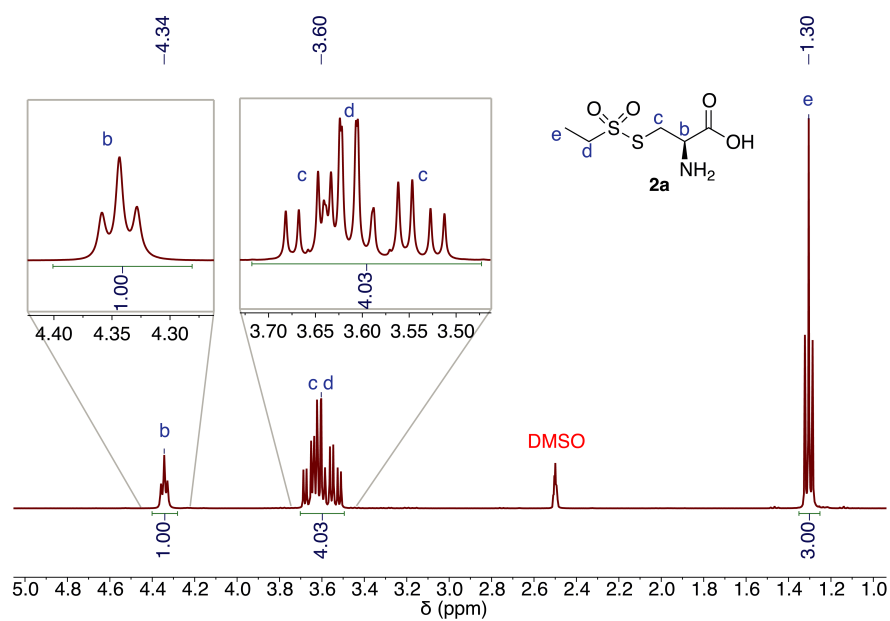
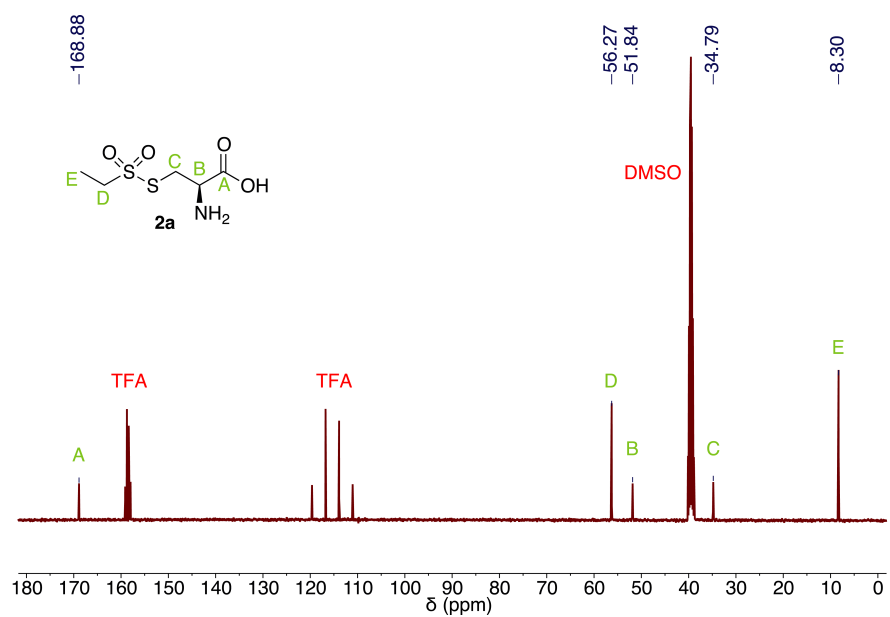
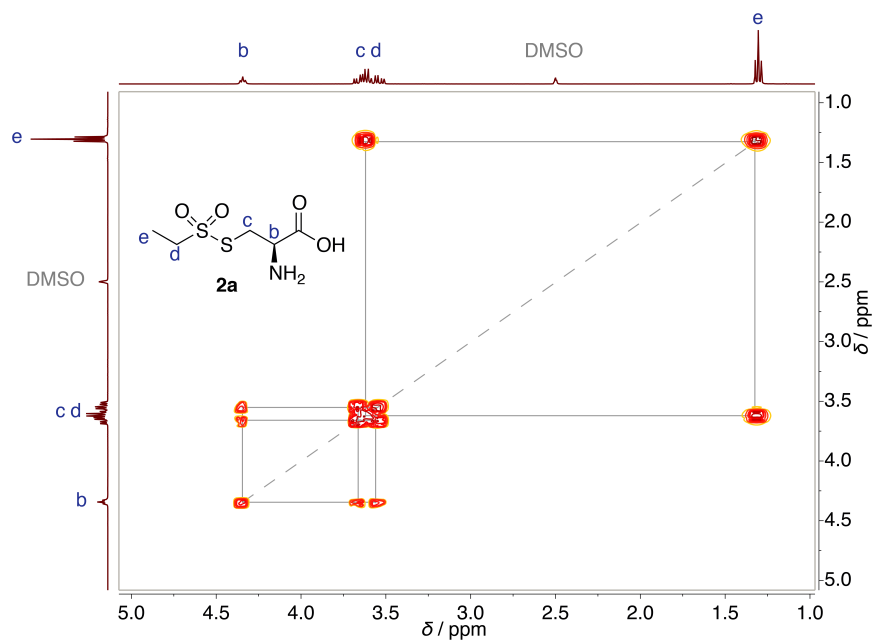
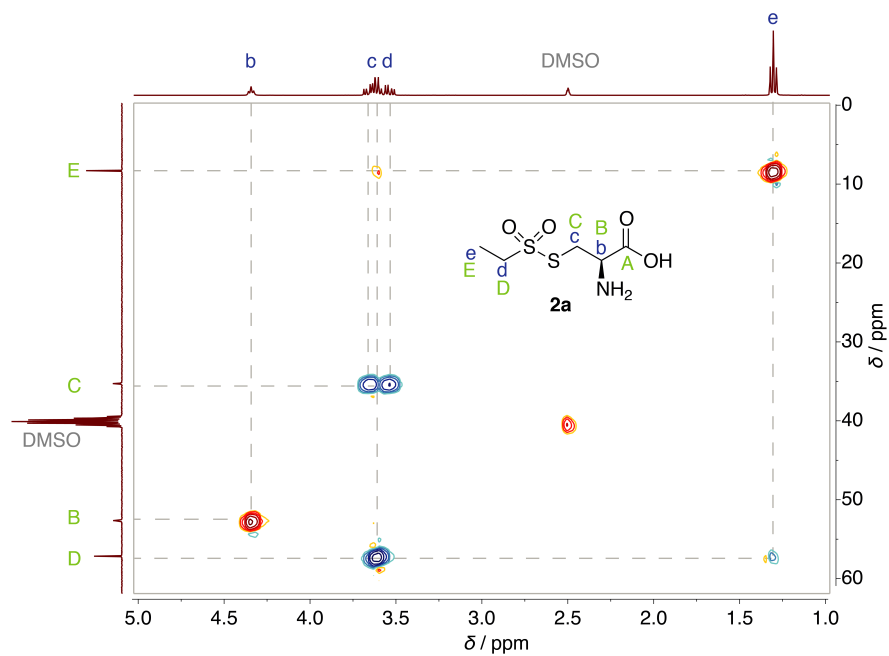
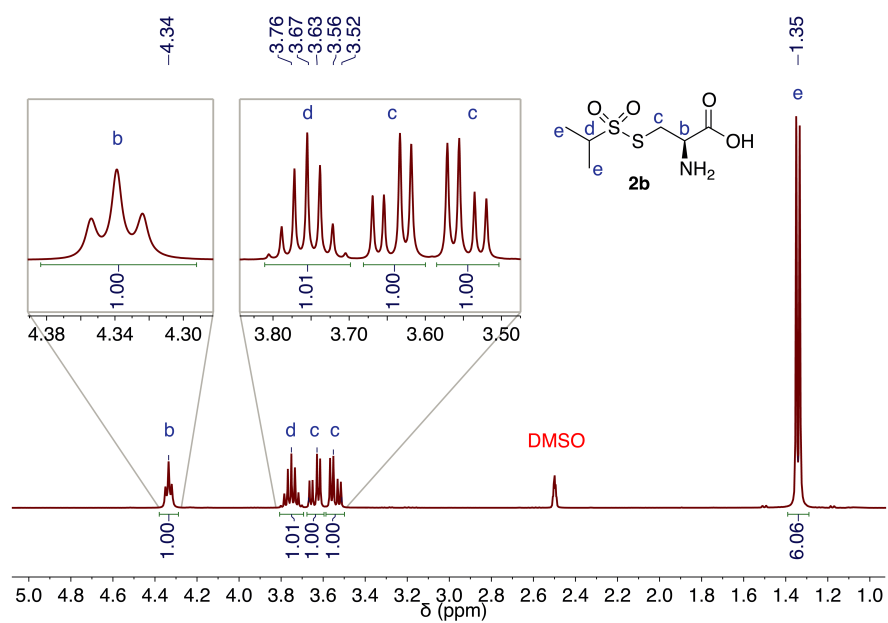
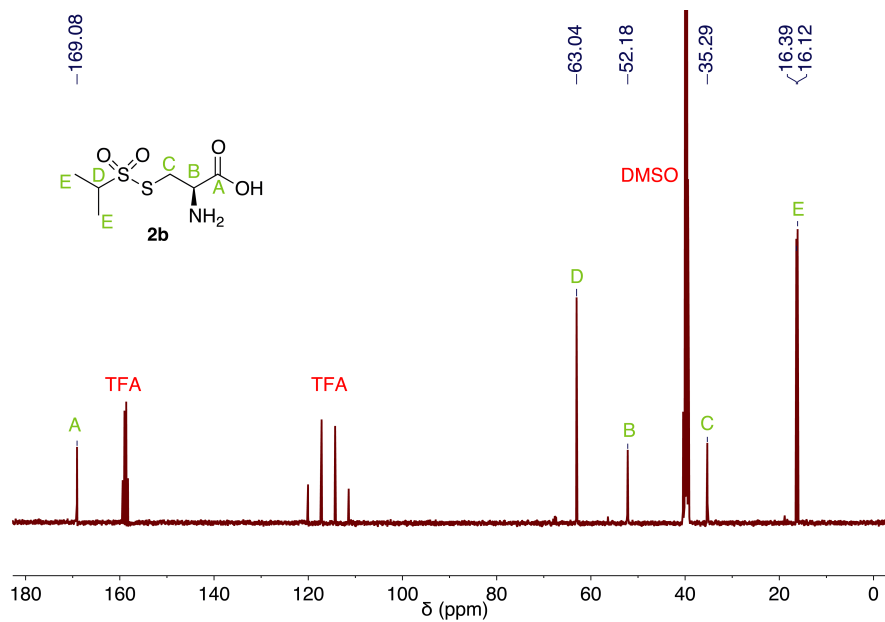


Figure 7.11: Crystallographic data of L-Cys(SO<sub>2</sub><sup>i</sup>Pr) **2b** showing two possible conformations.

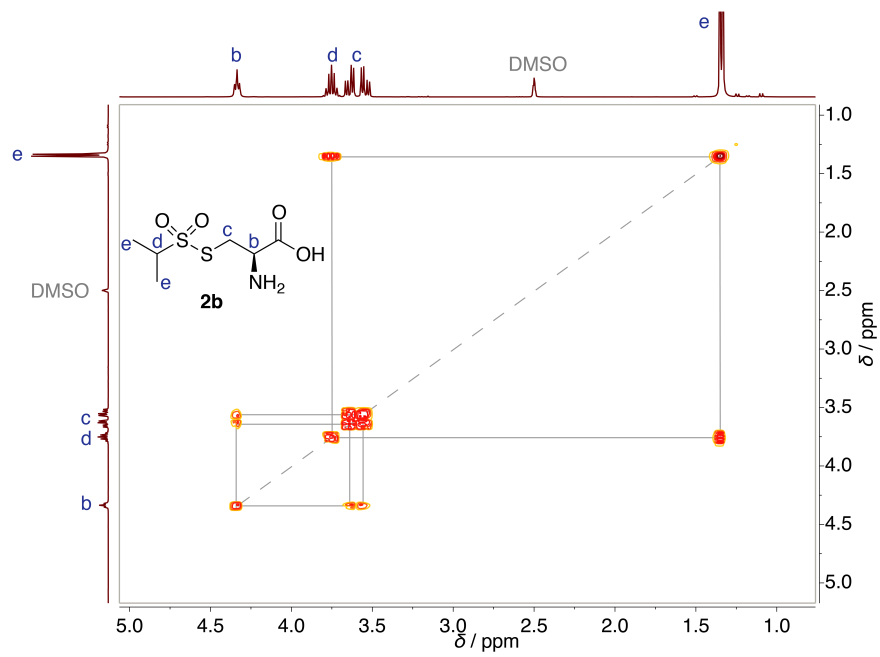
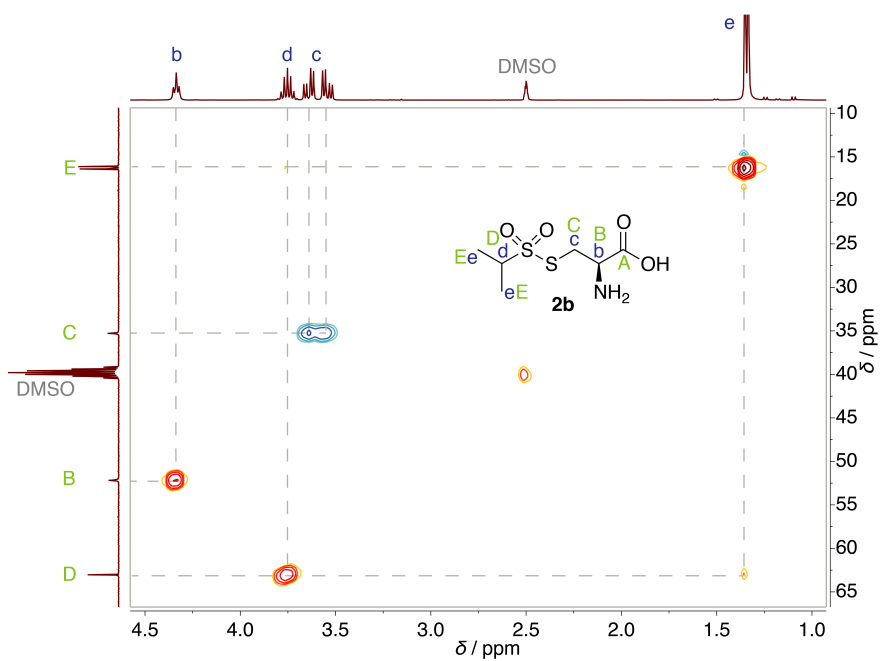
## 7.6.8 NMR Spectra

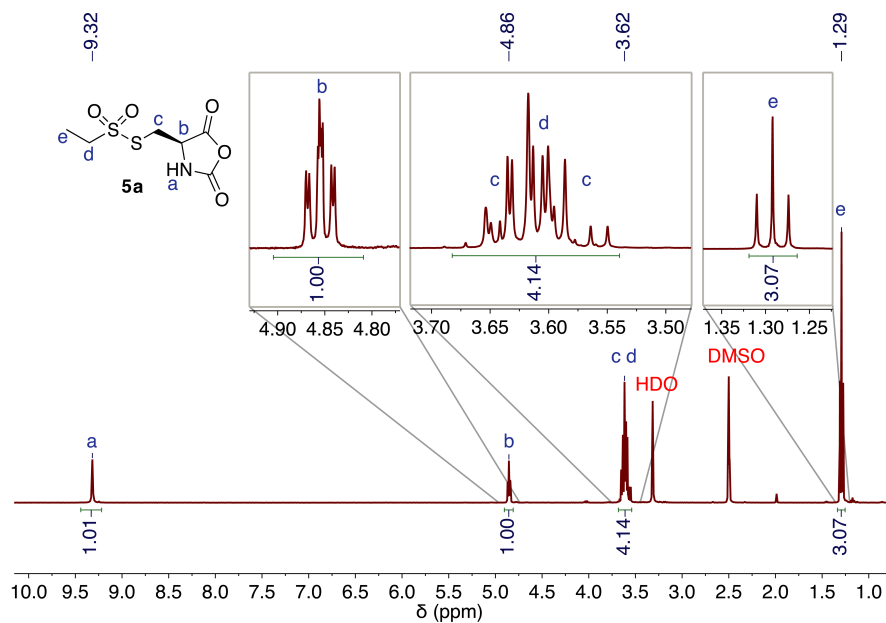
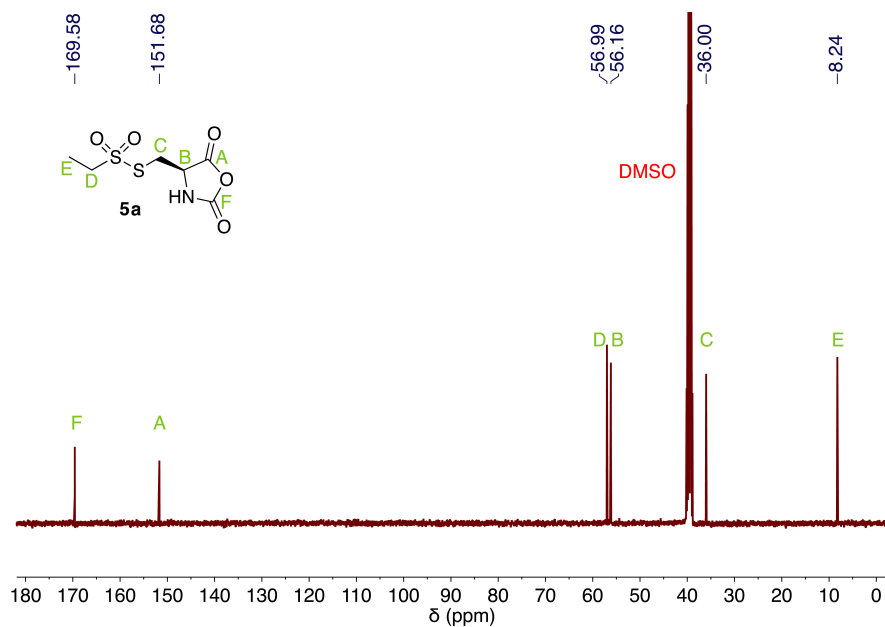
Figure 7.12:  $^1\text{H}$  NMR spectrum of **2a**.Figure 7.13:  $^{13}\text{C}$  NMR spectrum of **2a**.

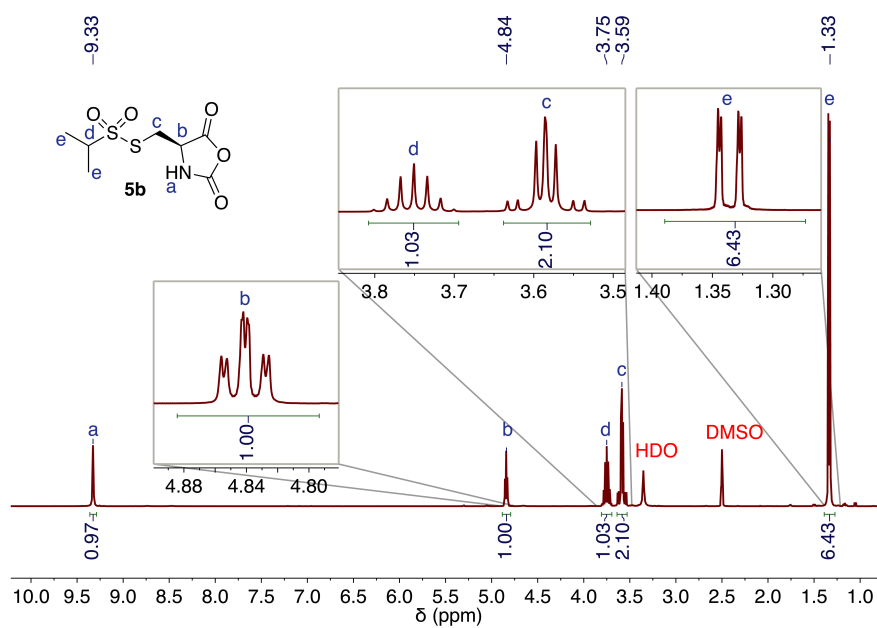
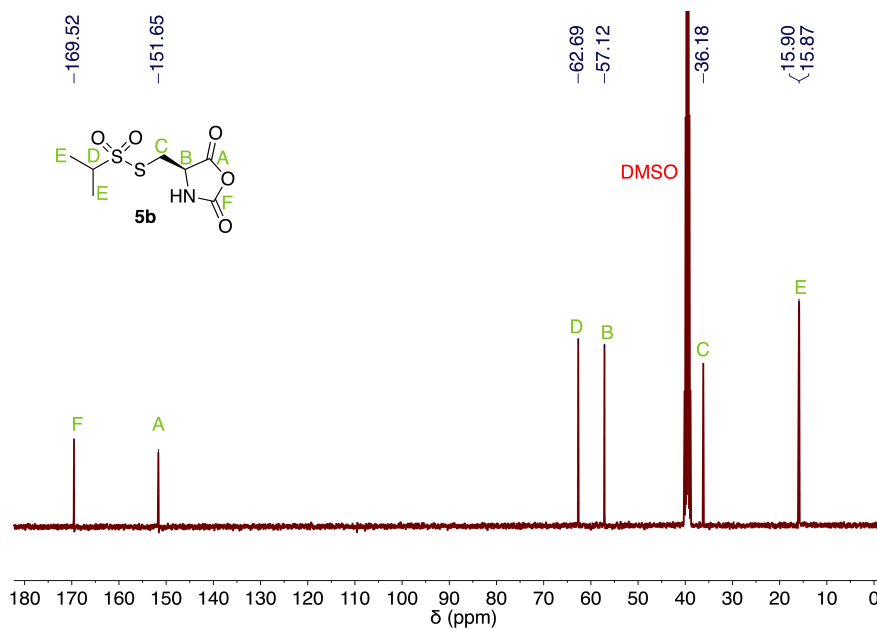
Figure 7.14: COSY NMR spectrum of **2a**.Figure 7.15: HSQC NMR spectrum of **2a**.

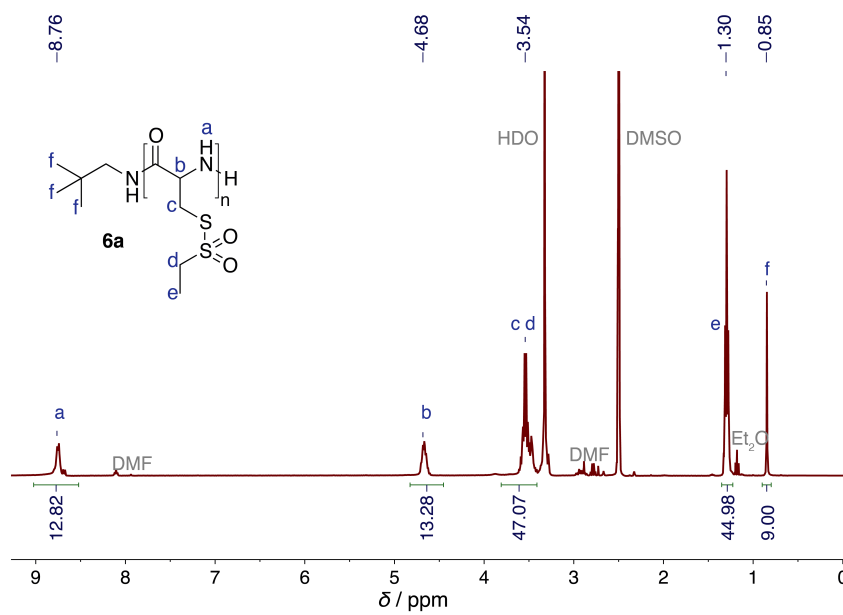
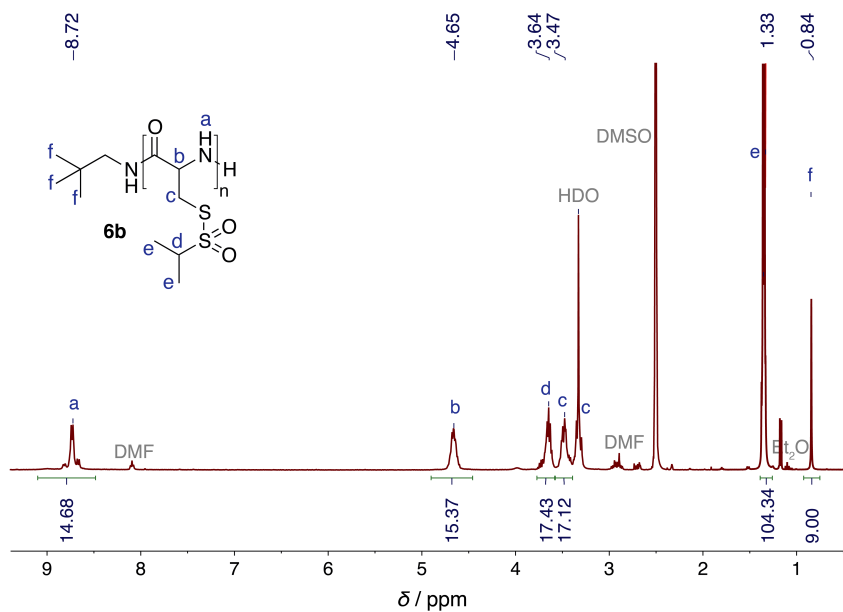
Figure 7.16:  $^1\text{H}$  NMR spectrum of **2b**.Figure 7.17:  $^{13}\text{C}$  NMR spectrum of **2b**.

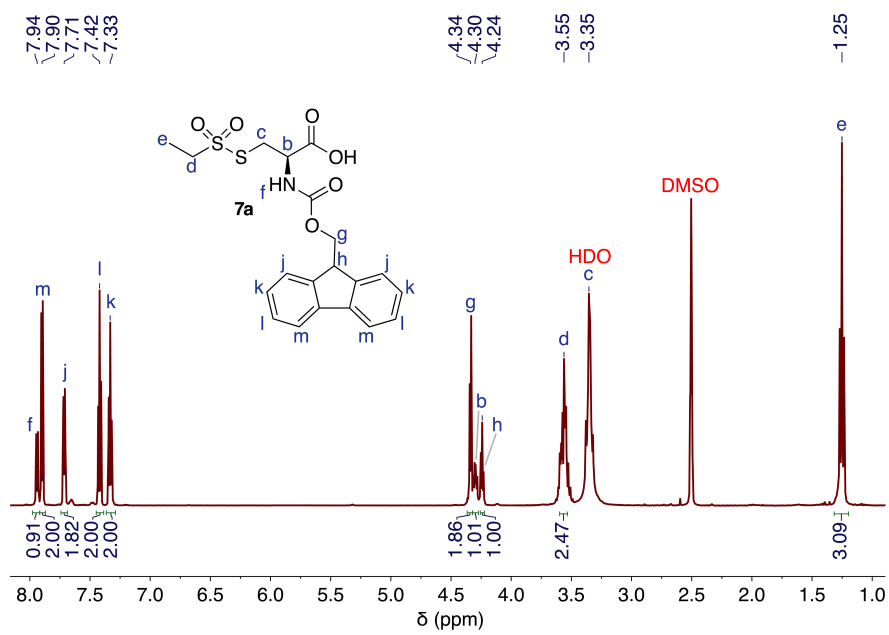
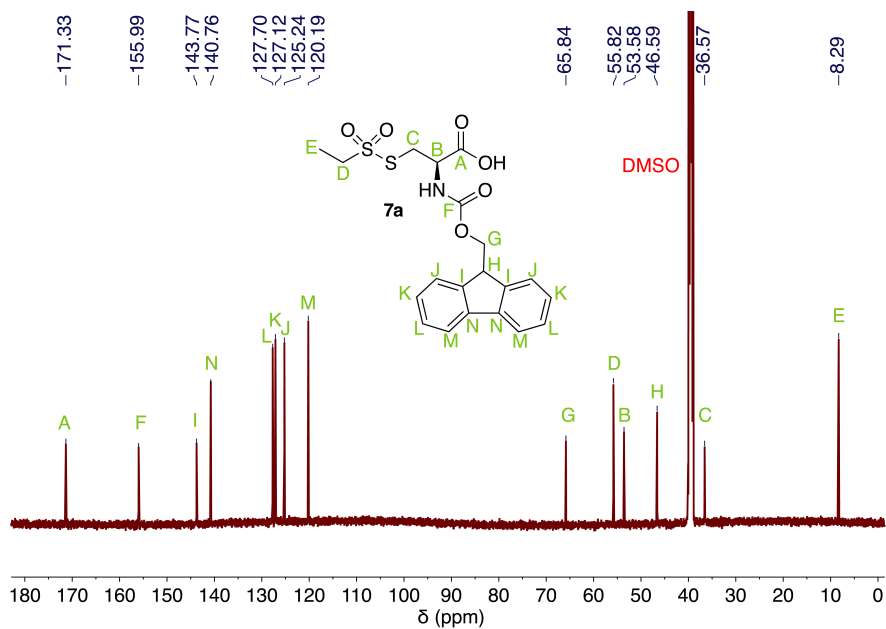


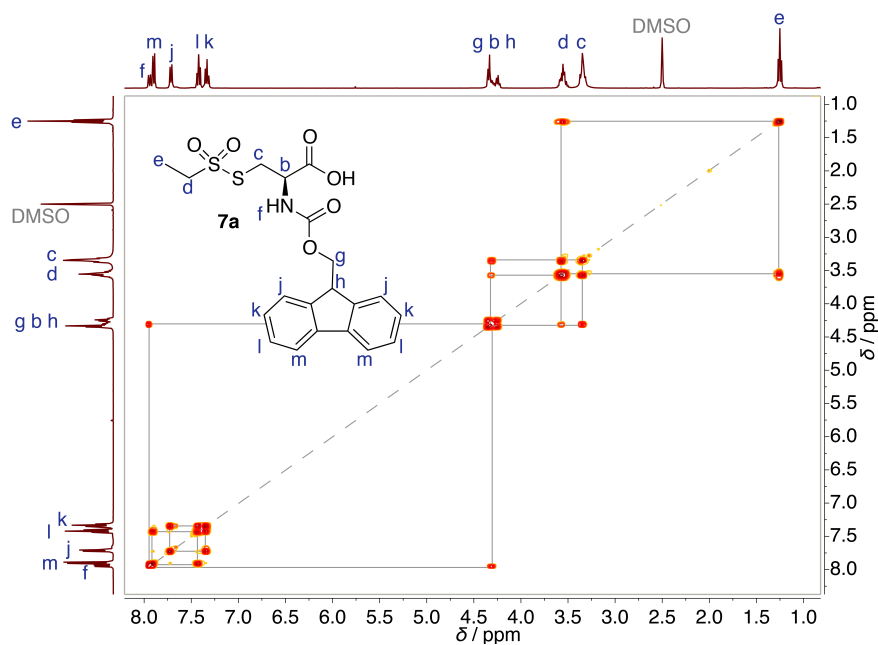
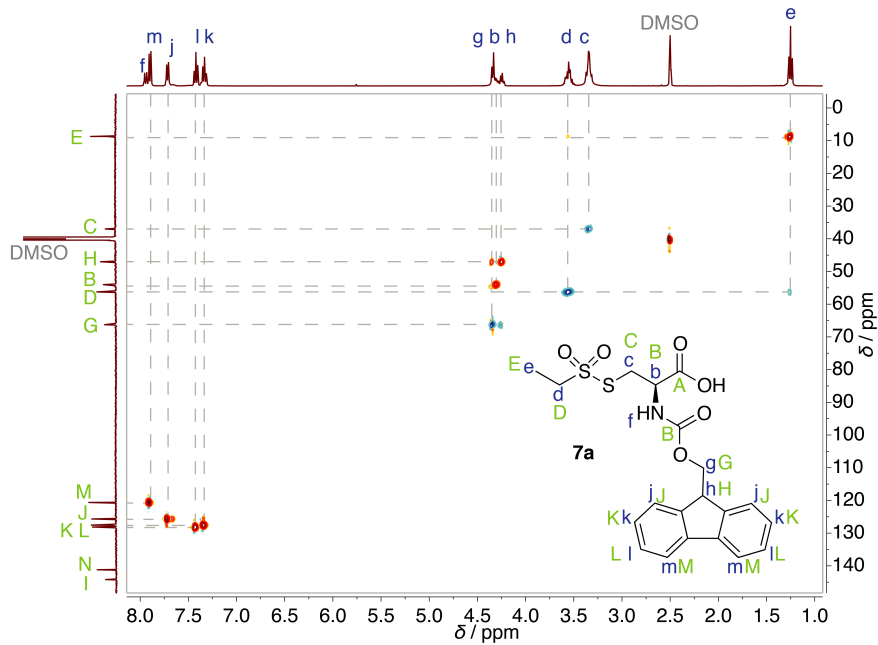
Figure 7.18: COSY NMR spectrum of **2b**.Figure 7.19: HSQC NMR spectrum of **2b**.

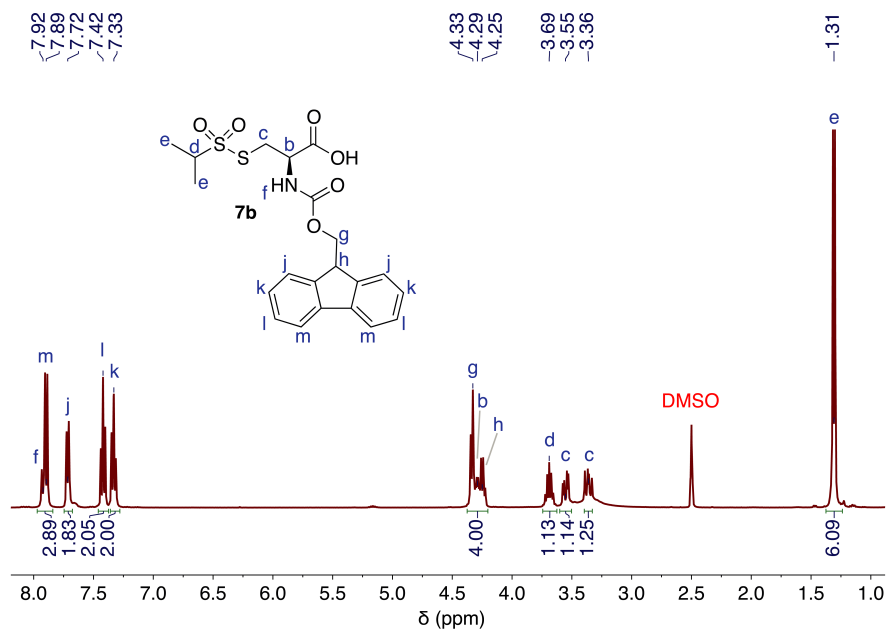
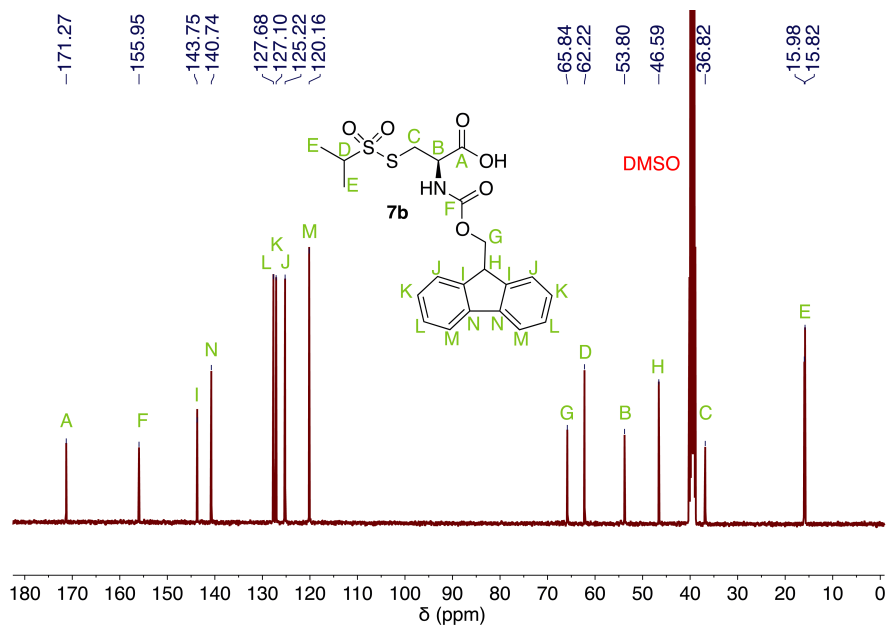
Figure 7.20:  $^1\text{H}$  NMR spectrum of **5a**.Figure 7.21:  $^{13}\text{C}$  NMR spectrum of **5a**.

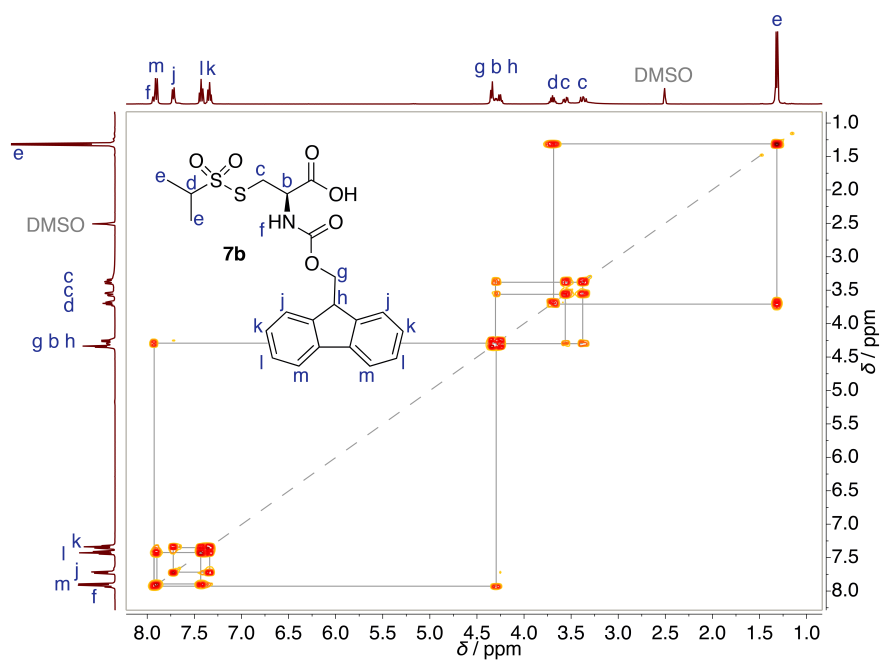
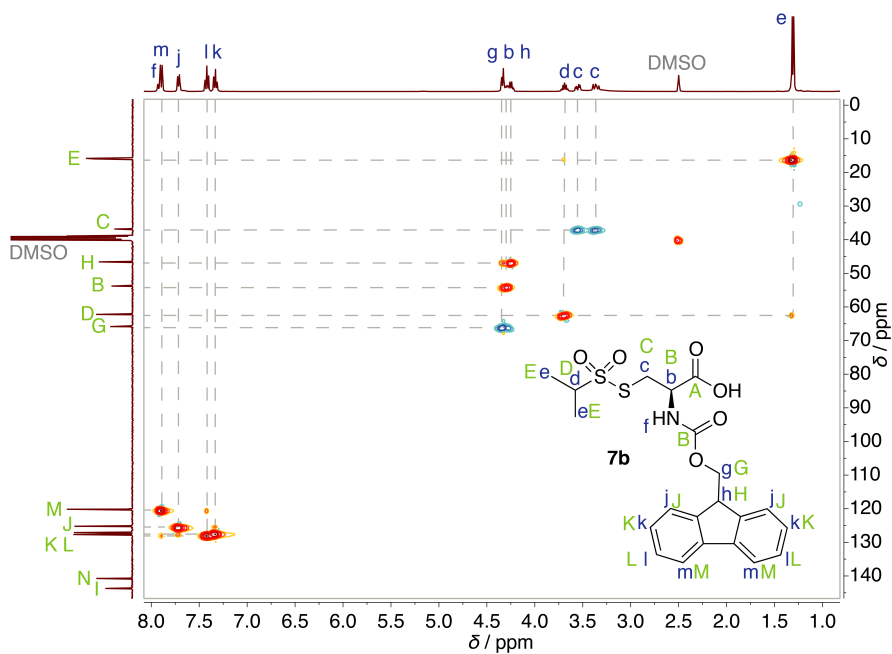
Figure 7.22: <sup>1</sup>H NMR spectrum of **5b**.Figure 7.23: <sup>13</sup>C NMR spectrum of **5b**.

Figure 7.24:  $^1\text{H}$  NMR spectrum of **6a**.Figure 7.25:  $^1\text{H}$  NMR spectrum of **6b**.

Figure 7.26: <sup>1</sup>H NMR spectrum of **7a**.Figure 7.27: <sup>13</sup>C NMR spectrum of **7a**.

Figure 7.28: COSY NMR spectrum of **7a**.Figure 7.29: HSQC NMR spectrum of **7a**.

Figure 7.30: <sup>1</sup>H NMR spectrum of **7b**.Figure 7.31: <sup>13</sup>C NMR spectrum of **7b**.

Figure 7.32: COSY NMR spectrum of **7b**.Figure 7.33: HSQC NMR spectrum of **7b**.



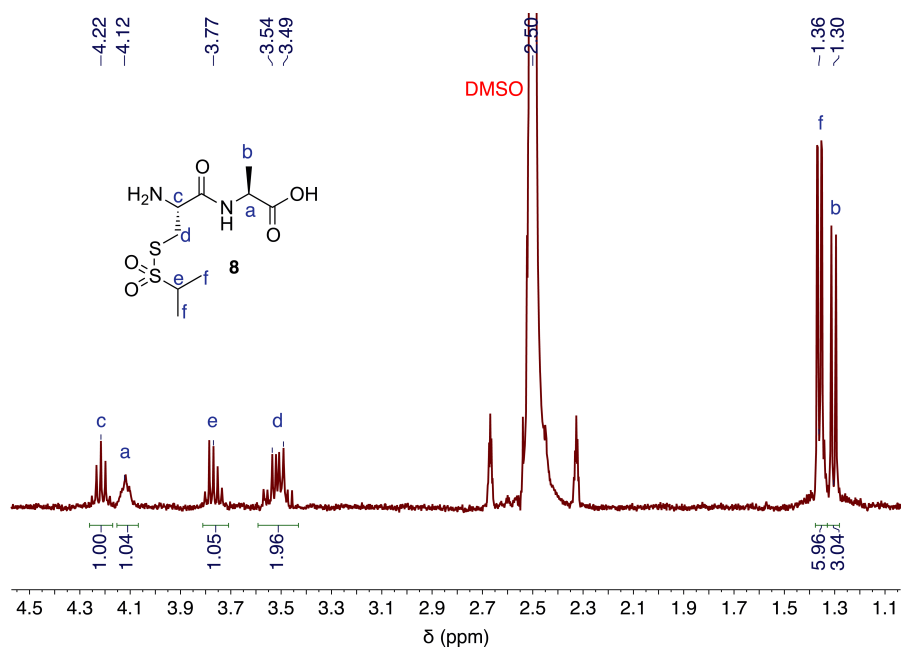


Figure 7.34:  $^1\text{H}$  NMR spectrum of **8**.



Part III

ORTHOGONAL REACTIVE  
POLYPEPT(O)IDES



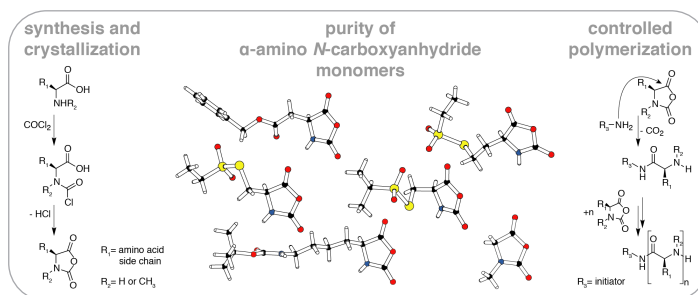


The next part covers controlled polypept(o)ide (polypeptoid-block-polypeptide) synthesis by means of ring-opening polymerization of  $\alpha$ -amino acid *N*-carboxyanhydrides. Correlation between absolute monomer purity and control over the polymerization was disclosed by X-ray crystallography. Further, analysis of polymerization kinetics investigated optimized conditions of poly(*S*-alkylsulfonyl-L-cysteine) (PCys(SO<sub>2</sub>R)) synthesis. Thus, sequential polymerization including the thiol-reactive *S*-alkylsulfonyl moiety could be performed, to give PSar-block-PCys(SO<sub>2</sub>R) diblock copolypept(o)ides, in order to demonstrate three orthogonal functionalities in one polymer. In addition, triblock terpolymers with PSar, PCys(SO<sub>2</sub>R) and PLys segments were prepared, to illustrate sequence inversion, while maintaining constant block length.



FROM ABSOLUTE MONOMER PURITY TO  
CONTROLLED NCA POLYMERIZATION

Olga Schäfer, Dieter Schollmeyer, Alexander Birke, Regina Holm, Kerstin Johann, Christian Muhl, Christine Seidl, Benjamin Weber, Matthias Barz, *submitted*.



**ABSTRACT:** The need for synthetic strategies of not sequence defined polypeptides on a large scale as biomaterials is met by the ring-opening polymerization of  $\alpha$ -amino acid *N*-carboxyanhydrides (NCAs). Even though this polymerization technique appears straight forward, it holds pitfalls in terms of reproducibility and overall control over the polymerization conditions, which depends, beside choice of solvent or initiator, significantly on reagent purity. Thus, in this work, we describe the benefits of highly pure monomers in order to control nucleophilic ring-opening polymerization NCAs. For the first time, monomer purity is investigated by relating melting points of NCAs with single-crystal and powder X-ray diffraction crystallography data, which further proves retained stereo-information of NCAs.

## 8.1 INTRODUCTION

The discovery of Leuchs' anhydrides, also known as  $\alpha$ -amino acid *N*-carboxyanhydrides (NCAs), in 1906<sup>[39]</sup> initiated the field of polypeptide synthesis by nucleophilic ring-opening polymerization (ROP) techniques.<sup>[35–37,407]</sup> Amine-initiated ROP of NCAs was pioneered by Sigmund and Wessely<sup>[31]</sup> Szwarc,<sup>[32]</sup> as well as Ballard and Bamford.<sup>[33,34]</sup> If sequence control is expendable, it represents now the most commonly applied technique for rapid and large-scale synthesis of polypeptides.<sup>[25,38,58,63,313,317]</sup> With arising applications of the resulting poly(amino acid)s as defined therapeutic products in nanomedicine, the need for precise control over polymer dispersity, molecular architecture as well as end-group integrity is apparent.<sup>[30,59,316,355,408,409]</sup> Thus, manipulation of polymerization conditions evolved into a substantial element in research topics employing materials obtained by means of NCA polymerization. The strategies cover various initiators from rare earth catalysts,<sup>[48]</sup> to amine hydrochlorides,<sup>[49]</sup> to organo-nickel initiators<sup>[50]</sup> and ammonium salts with tetrafluoroborate anions<sup>[51]</sup> as well as hexamethyldisilazane-mediated polymerization approaches.<sup>[52]</sup> Further, variation in temperature,<sup>[54,55]</sup> the introduction of N<sub>2</sub> flow<sup>[56]</sup> and high purity reagents employed in high vacuum techniques<sup>[53]</sup> were evaluated as means to control NCA polymerization.

*Importance of  
NCA purity.*

One of the parameters with tremendous influence on the polymerization outcome is the purity of employed solvents, initiators and in particular NCA monomers. Exclusion of impurities such as solvent traces, water, residues of amino acid or acid chlorides has been commonly accepted as mandatory to realize living polymerization. Nucleophilic impurities bear the potential to terminate growing electrophilic chain ends, catalyze side reactions or act as chain-transfer agents, ultimately generating shorter chains resulting in broad molecular weight distribution of the material.<sup>[410]</sup> Hence, considerable emphasis on monomer purification is required. NCA crystallization by a slow decrease in solubility, is a valuable method to achieve pure monomer materials to for high molecular weight polypeptides by NCA ROP polymerization.

In this context, X-ray diffraction (XRD) proves a powerful analytical technique, granting insights into structural parameters by analysis of internal lattice properties of crystalline materials. Although external adsorbed impurities, such as solvent traces, may not be detected, XRD offers the means to evaluate NCA crystal purity in terms of co-crystallizing molecules and elucidate the absolute conformation. The ability of isotactic polypeptides to form secondary structures such as  $\alpha$ -helices or  $\beta$ -sheets will be compromised in an atactic arrangement and result in a random coil conformation. Thus, loss or conservation of stereo-information during (multi-step) synthesis of the particular monomer need to be assured in order to achieve material properties based on secondary structure formation. In addition, most peptides synthesized by NCA polymerization originate from L-amino acids. Since D-amino acids

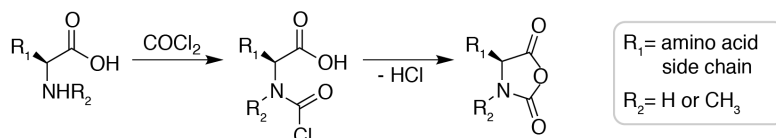


are uncommon in most organisms, their employment in materials designated for systemic or local application bears a certain risk regarding the potential to induce an undesired immune response.<sup>[411–413]</sup> Ultimately, validation of NCA purity and structural integrity as an overall quality control seems highly desirable. Structural characterization multiple NCAs has been contributed over the past 40 years e. g. by Kanazawa *et al.* including NCAs of glycine,<sup>[414]</sup> L-alanine,<sup>[415]</sup> L and DL-leucine,<sup>[416,417]</sup>  $\gamma$ -benzyl-L-glutamate,<sup>[418]</sup> L-valine,<sup>[419]</sup> L and DL-phenylalanine,<sup>[420,421]</sup>  $\beta$ -benzyl-L-aspartate,<sup>[422]</sup> and L-glutamic  $\gamma$ -ethyl ester.<sup>[423]</sup> Polymerization outcome, however, was only evaluated in order to compare polymerization rates by IR spectroscopy.

Much so our surprise, a systematic correlation of crystal structure to the living character of ROP and definition of the resulting polymers is lacking, although identifying parameters of monomer purity would help to control the polymerization of NCAs. In this work, we thus correlate the high purity of NCA monomers achieved by crystallization and confirmed by XRD with the readily accessible parameter of melting point to the control over amine initiated NCA ROP. Definition of polymers is judged towards completeness of monomer conversion, match of target chain length as well as narrow molecular weight distribution.

## 8.2 RESULTS AND DISCUSSION

Most commonly, NCAs are synthesized by the method proposed by Fuchs in 1922<sup>[40]</sup> and improved by Farthing.<sup>[41,42]</sup> It utilizes the respective amino acid and phosgene (or a phosgene equivalent such as diphosgene<sup>[424,425]</sup> or triphosgene<sup>[426,427]</sup>) as the cyclizing agent for a convenient and fast synthesis upon high atom efficiency as illustrated in Scheme 8.1.



Scheme 8.1: Scheme of  $\alpha$ -amino acid *N*-carboxyanhydride (NCA) synthesis by the Fuchs-Farthing method.<sup>[40,42]</sup>

As outlined in the introduction, monomer purity is crucial for a controlled ring-opening polymerization mechanism, since impurities may act as chain-transfer agents or terminate growing species and catalyze side reactions. Purification by means of crystallization is a convenient step which can be included subsequently to the synthesis procedure and repeated several times to increase purity of the NCA. Exclusion from air (and thus moisture), as well as use of thoroughly dried, absolute solvents is necessary to ensure the absence of water.<sup>[53,57]</sup> Additionally, sublimation proves a straightforward and effective purification method *N*-substituted NCAs as described in detail for sarcosine NCA by Ballard *et al.*<sup>[33,34]</sup> and employed by many groups.<sup>[26,44,428]</sup>

NCA  
characterization by  
X-ray diffraction.

If the NCA is obtained as a single crystal of pure composition and regular structure (no cracks, twinning or other internal imperfections), single-crystal X-ray diffraction (XRD) can be performed. This non-destructive method is based on discoveries of Max von Laue and co-workers<sup>[334]</sup> who observed how crystalline substances act as three-dimensional diffraction gratings for X-rays, which are similar in wavelength to the spacing of planes in a crystal lattice.<sup>[336]</sup> Exposure of the crystalline material results, amongst other events, in diffraction of the X-rays due to interaction with atomic planes. Ultimately, processing of scattering information by computational modeling offers insights on multiple parameters of the crystalline state such as unit cell dimensions, bond-lengths and -angles as well as details on site-ordering. Single crystal XRD was thus performed for NCAs illustrated in Figure 8.1, revealing exclusivity L-conformation and absence of co-crystallizing molecules e. g. solvents.

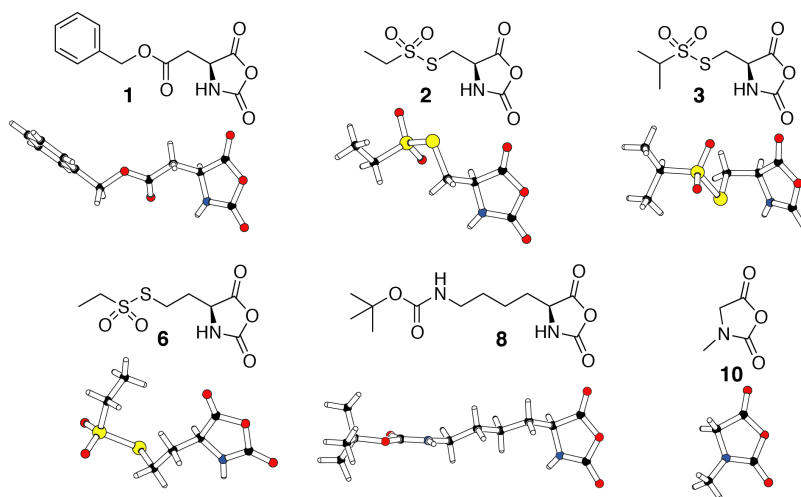


Figure 8.1: Crystal structure of NCAs evaluated by single-crystal X-ray diffraction: **1** Asp(OBn) NCA, **2** Cys(SO<sub>2</sub>Et) NCA, **3** Cys(SO<sub>2</sub><sup>i</sup>Pr) NCA, **6** Hcy(SO<sub>2</sub>Et) NCA, **8** Lys(Boc) NCA and **10** Sar NCA. Sarcosine NCA single crystals were obtained by sublimation, all other NCAs by crystallization.

The arrangement of NCAs molecules in the elemental cells was found to be dominated by hydrogen-bond formation as illustrated in Section 8.5.4 in the supporting information. In case of Hcy(SO<sub>2</sub>Et) (**6**), even supra molecular stacking in a helical fashion was observed. These insights on the inter-molecular arrangement of NCAs derived from protected amino acids translate to formation of secondary structures in the respective polypeptides.<sup>[24,37,209]</sup> An exception for hydrogen-bond driven arrangement poses sarcosine NCA (**10**), *N*-methylation renders it as an exclusive hydrogen bond acceptor. As no sites acting as hydrogen-bond donor are present in the polymer chain, stabilization into secondary structures is not possible and results in random coil conformation of polysarcosine.<sup>[25,27]</sup>

Other NCAs than in Figure 8.1, yielded too small or fragile crystals for successful single-crystal XRD, and were thus analyzed by powder XRD. Although this method does not provide structural information, sharp peaks characteristic for a crystalline phase confirm the crystalline state of the NCAs as illustrated in powder diffraction profiles in Section 8.5.5 in the supporting information.

Although XRD is the analytical method of choice to characterize the internal structure of crystalline substances, adequate instrumentation and data analysis is far from trivial. A readily accessible parameter for characterization of solid, crystalline substances is the melting point and measurements can be conveniently included in the work-flow e. g. to monitor purification success or to evaluate monomer quality prior to polymerization. NCA characterization is commonly performed by  $^1\text{H}$  NMR and assignment of the respective proton signals (compare Section 8.5.7 in the supporting information) or by mass spectroscopy. However, sensitivity of those characterization methods towards trace impurities such as residual solvents or unreacted amino acid is low compared to measurement of the melting point. The presence of any impurities will result in immediate depression of the melting point compared to of the pure substance. In addition, single crystals feature a distinct and sharp melting point, thus crystalline samples will give a narrow melting point range. Thus, melting point ranges for single crystals of NCAs were measured by an optical device and are summarized in Table 8.1 in comparison with melting points according to literature.

*Melting points as easily accessible characterization parameter.*

Table 8.1: Melting points of NCAs (alphabetically on the basis of the amino acid). Crystal melting points were determined at a heating rate of  $1^\circ\text{C}$  per minute, beginning and end of the melting process were recorded ( $n = 3$ ). Single crystals were obtained crystallization unless stated otherwise.

No	NCA	<i>mp.</i> / $^\circ\text{C}$ crystal	<i>mp.</i> / $^\circ\text{C}$ literature	<i>mp.</i> / $^\circ\text{C}$ previously reported
1	Asp(OBn)	124.7 – 124.9	135 <sup>[45,429,430]</sup>	-
2	Cys(SO <sub>2</sub> Et)	100.8 – 101.1	113 – 115 <sup>[173]</sup>	113 – 115 <sup>[173]</sup>
3	Cys(SO <sub>2</sub> <sup>i</sup> Pr)	92.9 – 93.2	98 – 100 <sup>[173]</sup>	98 – 100 <sup>[173]</sup>
4	Glu(OBn)	91.3 – 91.7	93– 94 <sup>[45,431,432]</sup>	93 – 94 <sup>[26]</sup>
5	Glu( <sup>t</sup> Bu)	99.4 – 100.0	95 – 96 <sup>[45,433]</sup>	100.9 <sup>[61]</sup>
6	Hcy(SO <sub>2</sub> Et)	94.9 – 95.2	-	-
7	Lys(Z)	98.1 – 98.5	101 <sup>[45,434,435]</sup>	100.9 <sup>[26]</sup>
8	Lys(Boc)	136.9 – 137.6	134 – 137 <sup>[436,437]</sup>	138.3 <sup>[59]</sup>
9	Lys(TFA)	94.5 – 95.0	94 <sup>[45,438]</sup>	101 <sup>[24]</sup>
10	Sar	103.0 – 103.7	102 – 105 <sup>[31,44,45,439]</sup>	102 – 104 <sup>[26]</sup>

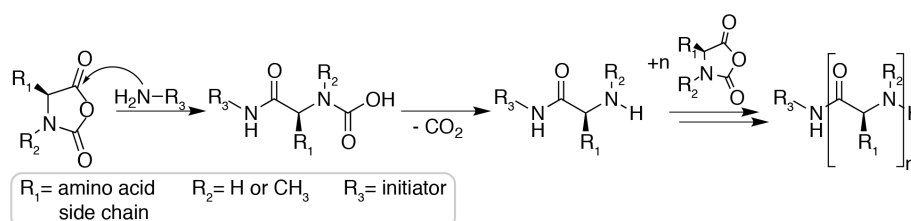
<sup>a</sup> Sarcosine NCA single crystals were obtained by sublimation.

Compared to literature, lower melting points were observed for **2**, **3**, **4** and **9**. In this context, automated melting point measurement based on light transmission from a refracting solid to a clear liquid upon melting might hold pitfalls. Thermal decomposition and thus evolution of gaseous fragments, can cause bubbles in the otherwise clear liquid (e. g. sulfoxides in the case of cysteine and homocysteine based compounds). Thus, an automated melting point apparatus may not determine the end of a melting process reliably and indicate too high values due to refracting bubbles as in case of e. g. **2** (113–115 °C) and **3** (98–100 °C). An optical device, however, allows to follow the exact beginning and completion of the decomposition process and thus measurements of the correct melting point gave 100.8–101.1 °C for **2** and 92.9–93.2 °C for **3**. For **5**, **7**, **8** and **10**, melting point ranges were in good agreement with literature or even surpassing, as in case of **5** with 99.4–100.0 °C compared to 95–96, °C.<sup>[45,433]</sup> In summary, measurements of melting points by a device allowing for optical control is a sensitive and reproducible method to evaluate NCA purity. Use of crystals devoid of co-crystallizing molecules, which required confirmation by XRD since melting point measurement is sensitive to trace impurities, gave high and narrow melting point ranges as reference for characterization of NCAs.

*Controlled  
ring-opening  
polymerization.*

To bridge the gap between findings on NCA monomer purity and success of ring-opening polymerization thereof, all presented NCAs were employed in amine-initiated ROP as illustrated in Scheme 8.2.

Polymerizations following the normal amine mechanism (NAM) are of living character, as indicated by incorporation of initiator molecules into every polymer chain and a faster initiation step compared to chain propagation.<sup>[44]</sup> In contrast, abstraction of the acidic proton by initiators with basic character, would lead to the undesired activated monomer mechanism (AMM) resulting in an overlap of ROP and condensation processes and thus broad molecular weight distributions.<sup>[45,46]</sup> The NAM is the desired pathway of NCA polymerization, since it provides control over molecular weights, polymer dispersity and end-group integrity. Thus, in order to ensure chain propagation by the NAM, exclusion of nucleophilic impurities has to be ensured since chain termination, side reactions or chain-transfer will impair the living chain propagation and thus polymer definition.



Scheme 8.2: Polymerization of NCA by an amine initiator following the normal amine mechanism.

Polymers were characterized in terms of conversion rate, agreement of target block length with experimental findings and molecular weight distribution as summarized in Table 8.2. The polymerization rate was determined by infrared (IR) spectroscopy and NCA conversion was followed by the decrease of the carbonyl peaks at  $1858\text{ cm}^{-1}$  and  $1788\text{ cm}^{-1}$ . For relation of theoretical and experimental block lengths by  $^1\text{H NMR}$ , the signal of the 9 equivalent protons of the neopentylamine initiator at 0.83 ppm was related to signals of the  $\alpha$ -proton of the respective amino acid. Ultimately, molecular weight distribution and dispersities were determined by gel permeation chromatography (GPC) in hexafluoro 2-propanol (HFIP).

Table 8.2: Characterization of polypeptides and polypeptoids obtained by amine initiated ring-opening polymerization of NCAs with neopentylamine as initiator unless stated otherwise.

polymer	NCA	M / I	% conversion <sup>a</sup>	$X_{n,NMR}$	$M_{n,GPC}^b$ /g mol <sup>-1</sup>	$D_{GPC}^b$
PAsp(OBn) <sup>c</sup>	<b>1</b>	40	100	38	28100	1.19
PCys(SO <sub>2</sub> Et)	<b>2</b>	15	88	17	8360	1.16
PCys(SO <sub>2</sub> <sup>i</sup> Pr)	<b>3</b>	30	80	23	13000	1.19
PGlu(OBn)	<b>4</b>	30	100	31	10300	1.08
PGlu( <sup>t</sup> Bu)	<b>5</b>	25	100	27	13300	1.11
PHcy(SO <sub>2</sub> Et)	<b>6</b>	50	100	37	8320	1.16
PLys(Z)	<b>7</b>	50	100	48	15200	1.08
PLys(Boc)	<b>8</b>	50	100	50	14800	1.18
PLys(TFA)	<b>9</b>	30	100	32	12200	1.12
PSar	<b>10</b>	100	100	104	25000	1.06

<sup>a</sup> Determined by IR spectroscopy.

<sup>b</sup> Relative to PMMA standards.

<sup>c</sup> Diblock copolypept(o)ide initiated by PSar<sub>390</sub> as determined by  $^1\text{H NMR}$  end-group analysis.

Monomer conversion of 100 % is reached in all cases with good agreement of target and experimental block length, with the exception of **2** and **3** due to physical chain growth termination by secondary structure formation of  $\beta$ -sheets.<sup>[209]</sup> High molecular weights and narrow dispersities well below 1.2 confirm well-defined polymers. Initiation by water or intermediates in the AMM, chain termination or other side reactions, however, would yield poorly defined polypeptides. Thus, the predominant controlled ring-opening chain propagation follows the normal amine mechanism as shown in Scheme 8.2.

As illustrated in Figure 8.2, all polymers exhibit monomodal molecular weight distributions as determined by HFIP GPC. To facilitate distinction of individual elugrams, polymers were grouped in molecular weights < 10000, 10000–15000 and > 25000 g mol<sup>-1</sup>.

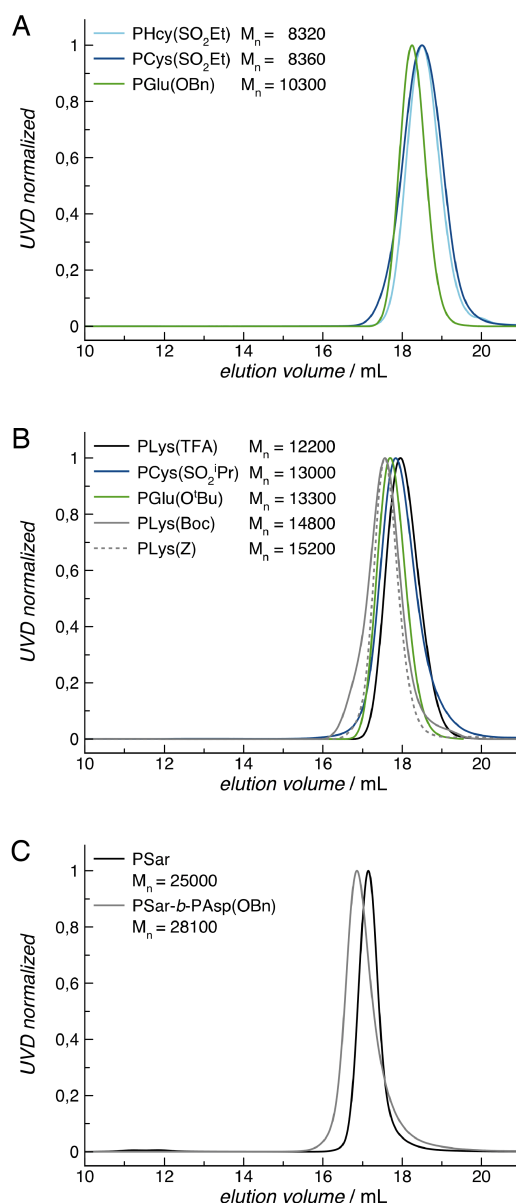


Figure 8.2: HFIP GPC traces of polypeptides and polypeptoids obtained by amine initiated ring-opening polymerization of NCAs: A)  $M_{n,GPC} < 10000$ , B)  $M_{n,GPC} = 10000-15000$  and C)  $M_{n,GPC} > 25000$ .

All investigated polymers with the exception of polysarcosine are capable of hydrogen bond formation.<sup>[23,202,440-442]</sup> Thus formation of secondary structures is possible, resulting in different persistence lengths of the polypeptides and thus variation in elution behavior.<sup>[24]</sup> Further, polypeptides evaluated in this work feature different side chain chemistry and protective groups. As a result, differences in column and solvent interactions are expected based on the chemical variability and again variation in GPC elution. Thus, elugrams of different polypeptides obtained by GPC are of qualitative nature and polymer chain length from <sup>1</sup>H NMR should not be related to molecular weight obtained relative to PMMA standards. The symmetrical GPC elugrams and narrow

dispersities confirm, however, the synthesis well-defined polymers. In summary, ring-opening polymerizations of all NCAs proceeded in a controlled fashion, stressing the importance of pure monomers with high melting points as obtained by crystallization and evaluated by means of XRD.

### 8.3 CONCLUSION

We have reported on the benefits of highly pure monomers in regard to control of nucleophilic ring-opening polymerization  $\alpha$ -amino acid *N*-carboxyanhydrides (NCAs). Monomer purity was investigated by relating melting points of NCAs with single-crystal and powder X-ray diffraction crystallography data. NCA monomers were purified by crystallization and preserved stereo-information as well as the absence of any co-crystallizing impurities was confirmed by XRD. In addition, single crystal melting points were determined as an easily accessible parameter to monitor monomer purity. Ultimately, well-defined polymers were synthesized by controlled amine-initiated ring-opening polymerization of the investigated NCAs. Thus, NCA monomer purity, which can conveniently be monitored by evaluation of melting points, was demonstrated to be essential in order to achieve control over NCA polymerization.

### 8.4 ACKNOWLEDGMENTS

We would like to thank Dr. D. Schollmeyer for X-ray crystal structure measurements and analysis. O.S. acknowledges support by the "Evangelisches Studienwerk e.V. Villigst" and M.B. acknowledges financial support by the SFB 1066-2.



## 8.5 SUPPORTING INFORMATION

### 8.5.1 Materials and Instrumentation

All chemicals were purchased from Sigma Aldrich and used as received unless otherwise noted. Tetrahydrofuran (THF) and hexane were distilled from Na/K and ethyl acetate and dichloromethane (DCM) from CaH<sub>2</sub>. *N,N*-dimethyl formamide (DMF) was purchased dry over molecular sieve. It was further purified by stirring over molecular sieve (3 Å) and BaO. It was then distilled and stored at -80 °C under exclusion of light. Prior to use DMF was degassed *in vacuo* to remove traces of dimethylamine. Neopentylamine (purchased from TCI Europe) and hexylmethylamine were dried over NaOH followed by distillation, morpholine was distilled from Na.  $\alpha$ -amino acids were purchased from OPREGEN, sarcosine and diphosgene from Alfa Aesar, HFIP was purchased from Fluorochem and deuterated solvents from Deutero GmbH.

<sup>1</sup>H NMR spectra were recorded on a Bruker Avance II HD 400 at a frequency of 400 MHz or a Bruker Avance III HD 300 at 300 MHz. All spectra were recorded at room temperature (25 °C) and calibrated using the solvent signals.<sup>[394]</sup>

Crystallographic data for powder diffraction profiles was collected on a BRUKER D8 Discover diffractometer using monochromated Cu monochromated K $\alpha$  radiation ( $\lambda = 1.5418 \text{ \AA}$ ) and a High-Star detector. Crystallographic data for single crystal analysis were collected on a STOE IPDS 2T diffractometer using graphite monochromated Mo K $\alpha$  radiation ( $\lambda = 0.7107 \text{ \AA}$ ). Lorentz and polarisation correction was implemented and the structure was solved by direct methods (SIR-2004)<sup>[395]</sup> and refined (SHELXL-2014).<sup>[396]</sup> Hydrogen atoms were refined isotropically assuming riding motion, other atoms were refined anisotropically. Crystallographic data for the structures in this paper have been deposited with the Cambridge Crystallographic Data Centre as supplementary publication nos. . Copies of the data can be obtained, free of charge, on application to Cambridge Crystallographic Data Centre, 12 Union Road, Cambridge CB2 1EZ, UK, (fax: +44-(0)1223-336033 or e-mail: deposit@ccdc.cam.ac.uk). Publication numbers and further details are given with individual characterization data. Melting points were measured using a Mettler FP62 and a Krüss KSP1D melting point apparatus at a heating rate of 1 °C min<sup>-1</sup>.

Gel permeation chromatography (GPC) was performed with HFIP containing 3 g l<sup>-1</sup> potassium trifluoroacetate (KTFA) as eluent at 40 °C and a flow rate of 0.8 ml min<sup>-1</sup>. The columns were packed with modified silica (PFG columns particle size: 7  $\mu\text{m}$ , porosity: 100 Å and 1000 Å). Polymethyl methacrylate PMMA standards (Polymer Standards Services GmbH) were used for calibration and toluene was used as internal standard. A refractive index detector (G1362A RID) and an UV/Vis detector (at 230 nm unless otherwise stated; Jasco UV-2075 Plus) were used for polymer detection.



## 8.5.2 Synthetic Procedures

*β*-benzyl-L-aspartate N-carboxyanhydride (*Asp(OBn)* NCA) **1**

The synthesis was adapted from literature and modified.<sup>[424]</sup> Into pre-dried glassware, 8.9 g (40.0 mmol) of benzylester protected asparagine and 200 mL of absolute THF were added under a steady flow of nitrogen. The condenser outlet was connected to two gas washing bottles filled with aqueous NaOH, removing excess HCl and phosgene. Then, 4.1 mL (33.7 mmol) of diphosgene were added slowly *via* syringe and the nitrogen stream was reduced. The colorless suspension was mildly refluxed for 1.5 h, yielding a slightly yellow solution. After the last particles were dissolved, a steady flow of dry nitrogen was lead throw the solution for 3 h. The solvent was evaporated under reduced pressure and absolute THF was added to completely dissolve the reaction product. Excess of absolute hexane was added to the solution and kept at 4 °C overnight to crystallize. The solid was filtered under dry nitrogen atmosphere and the crude product was recrystallized from THF/hexane twice, washed with absolute hexane, dried in a dry nitrogen flow, and finally in high vacuum. A total of 8.7 g of purified product (35.0 mmol, 88 % yield, colorless needles, melting point: 124.7–124.9 °C) was obtained and stored in a Schlenk tube at -80 °C. CCDC-1261403.<sup>[422]</sup>

<sup>1</sup>H NMR (300 MHz, CDCl<sub>3</sub>) δ [ppm] = 9.00 (s, 1H, -NHCO), 7.37 (m, 5H, -C<sub>6</sub>H<sub>5</sub>), 5.13 (s, 2H, -CH<sub>2</sub>-C<sub>6</sub>H<sub>5</sub>), 4.70 (dd, <sup>3</sup>J<sub>H,H</sub> = 7.9 Hz, <sup>3</sup>J<sub>H,H</sub> = 5.4 Hz, 1H, α-H) 3.12–2.87 (dd, <sup>3</sup>J<sub>H,H</sub> = 4.6 Hz, 2H, -CH<sub>2</sub>-CH=).

*S*-ethylsulfonyl-L-cysteine N-carboxyanhydride (*Cys(SO<sub>2</sub>Et)* NCA)<sup>[173]</sup> **2**

Dried *S*-ethylsulfonyl-L-cysteine (*Cys(SO<sub>2</sub>Et)*) (7.0 g, 32.8 mmol) was suspended in absolute THF (100 mL ) and heated to 70 °C. Diphosgene (3.6 mL, 5.8 g, 29.5 mmol) was slowly added and the suspension was heated for an additional 4 h. Dry nitrogen was bubbled through the reaction mixture overnight into a gas washing bottle with an aqueous KOH solution to remove excess diphosgene, HCl and most of the solvent. The remaining solvent was removed *in vacuo* and the residue was dissolved in 100 mL absolute ethyl acetate. Any insoluble compounds were removed by filtration avoiding contact with air and the NCA was precipitated by adding 800 mL absolute hexane. The recrystallization of the product was repeated two more times. After recrystallization a total of 6.4 g of purified product (26.9 mmol, 82 % yield, colorless and crystalline powder, melting point: 100.8–101.1 °C) was obtained and stored in a Schlenk tube at -80 °C.

<sup>1</sup>H NMR (400 MHz, DMSO-*d*<sub>6</sub>) δ [ppm] = 9.32 (s, 1H, -NHCO), 4.86 (td, <sup>3</sup>J<sub>H,H</sub> = 6.0 Hz, <sup>3</sup>J<sub>H,H</sub> = 4.8 Hz, <sup>3</sup>J<sub>H,H</sub> = 1.6 Hz, 1H, α-H), 3.64 (dd, <sup>2</sup>J<sub>H,H</sub> = 14.4 Hz, <sup>3</sup>J<sub>H,H</sub> = 4.8 Hz, 1H, -CHH-S), 3.62 (q, <sup>3</sup>J<sub>H,H</sub> = 7.2 Hz, 2H, -CH<sub>2</sub>-SO<sub>2</sub>), 3.57 (dd, <sup>2</sup>J<sub>H,H</sub> = 14.4 Hz, <sup>3</sup>J<sub>H,H</sub> = 6.4 Hz, 1H, -CHH-S), 1.29 (t, <sup>3</sup>J<sub>H,H</sub> = 7.2 Hz, 3H, -CH<sub>3</sub>).

*S*-isopropylsulfonyl-L-cysteine *N*-carboxyanhydride (Cys(SO<sub>2</sub><sup>*i*</sup>Pr) NCA)<sup>[173]</sup> **3**

The synthesis of *S*-isopropylsulfonyl-L-cysteine (Cys(SO<sub>2</sub><sup>*i*</sup>Pr) NCA) was carried out under identical conditions as Cys(SO<sub>2</sub>Et) NCA employing Cys(SO<sub>2</sub>Et) (6.0 g, 26.6 mmol) and diphosgene (4.0 mL, 6.6 g, 33.1 mmol). Recrystallization yielded a total of 4.6 g of purified product (18.3 mmol, 69% yield, colorless and crystalline powder, melting point: 92.9–93.2 °C) was obtained and stored in a Schlenk tube at -80 °C.

<sup>1</sup>H NMR (400 MHz, DMSO-*d*<sub>6</sub>) δ [ppm] = 9.33 (s, 1H, -NHCO), 4.84 (td, <sup>3</sup>J<sub>H,H</sub> = 5.4 Hz, 3J = 1.4 Hz, 1H, α-H), 3.75 (hept, J<sub>H,H</sub> = 6.6 Hz, 1H, =CH-SO<sub>2</sub>), 3.59 (ddd, <sup>2</sup>J<sub>H,H</sub> = 14.4 Hz, <sup>3</sup>J<sub>H,H</sub> = 5.6 Hz, <sup>3</sup>J<sub>H,H</sub> = 5.1 Hz, 2H, -CH<sub>2</sub>-S), 1.33 (dd, <sup>3</sup>J<sub>H,H</sub> = 6.6 Hz, <sup>3</sup>J<sub>H,H</sub> = 0.9 Hz, 6H, -(CH<sub>3</sub>)<sub>2</sub>).

*γ*-benzyl-L-glutamate *N*-carboxyanhydride (Glu(OBn) NCA)<sup>[26]</sup> **4**

The synthesis was adapted from literature and modified.<sup>[424]</sup> Into pre-dried glassware, 10.0 g (42.1 mmol) of benzylester protected glutamine and 200 mL of absolute THF were added under a steady flow of nitrogen. The condenser outlet was connected to two gas washing bottles filled with aqueous NaOH, removing excess HCl and phosgene. Then, 4.1 mL (33.7 mmol) of diphosgene were added slowly *via* syringe and the nitrogen stream was reduced. The colorless suspension was mildly refluxed for 1.5 h, yielding a slightly yellow solution. After the last particles were dissolved, a steady flow of dry nitrogen was lead throw the solution for 3 h. The solvent was evaporated under reduced pressure and absolute THF was added to completely dissolve the reaction product. Excess of absolute hexane was added to the solution and kept at 4 °C overnight to crystallize. The solid was filtered under dry nitrogen atmosphere and the crude product was recrystallized from THF/hexane twice, washed with absolute hexane, dried in a dry nitrogen flow, and finally in high vacuum. A total of 10.5 g of purified product (40.0 mmol, 95% yield, colorless needles, melting point: 91.3–91.7 °C) was obtained and stored in a Schlenk tube at -80 °C. CCDC-1102908.<sup>[418]</sup>

<sup>1</sup>H NMR (300 MHz, CDCl<sub>3</sub>) δ [ppm] = 9.11 (s, 1H, -NHCO), 7.42–7.20 (m, 5H, -C<sub>6</sub>H<sub>5</sub>), 5.10 (s, 2H, -CH<sub>2</sub>-C<sub>6</sub>H<sub>5</sub>), 4.52–4.42 (dd, <sup>3</sup>J<sub>H,H</sub> = 7.9 Hz, <sup>3</sup>J<sub>H,H</sub> = 5.5 Hz, 1H, α-H), 2.52–2.48 (t, <sup>3</sup>J<sub>H,H</sub> = 7.9 Hz, 2H, BnO-CO-CH<sub>2</sub>-), 2.15–1.85 (m, 2H, -CH<sub>2</sub>-CH=).

*γ*-tert-butylloxycarbonyl-L-glutamate *N*-carboxyanhydride (Glu(<sup>*t*</sup>Bu) NCA)<sup>[61]</sup> **5**

7.6 g (37.0 mmol) of H-Glu(O<sup>*t*</sup>Bu)-OH were pestled thoroughly and weighed into a three-necked round-bottomed flask equipped with a magnetic stir bar, a condenser, a rubber septum, and a glass stopper and dried under vacuum. After 30 min, 200 mL absolute THF were used to suspend the solid under a steady flow of nitrogen. 9.5 mL (8.1 g, 75.0 mmol) of absolute trimethyl-silylchloride were added, dissolving the amino acid and yielding a clear solution. Immediately afterwards, 10.4 mL (7.6 g, 75.0 mmol) absolute triethylamine TEA were added. 3.6 mL (5.9 g, 30.0 mmol) diphosgene were added slowly *via* syringe in

two portions to the reaction mixture at room temperature and heated to 70 °C. After the reaction mixture had cooled down, a stream of nitrogen was led through the mixture for 3 h to remove HCl. Then, the  $\text{NEt}_3\text{H}^+\text{Cl}^-$  salt was removed by filtration under nitrogen and washed with 30 mL absolute THF twice. The solution was concentrated *in vacuo* to a volume of approx. 40 mL and the product was precipitated by addition of 400 mL absolute hexane with instant sonication. The procedure was repeated twice and yielded a colorless precipitate by filtration under nitrogen. A total of 5.2 g of purified product (22.7 mmol, 61 % yield, colorless crystals, melting point: 99.4–100.0 °C) was obtained and stored in a Schlenk tube at -80 °C.

$^1\text{H}$  NMR (300 MHz,  $\text{CDCl}_3$ )  $\delta$  [ppm] = 9.06 (s, 1H,  $-\text{NH}-\text{CO}-\text{O}-\text{CO}$ ), 4.45 (ddd,  $^3J_{\text{H,H}} = 6.9$  Hz, 5.0 Hz, 0.9 Hz, 1H,  $\alpha\text{-H}$ ), 2.34 (m, 2H,  $-\text{CH}_2-\text{CH}_2-\text{CO}$ ), 1.76–2.02 (m, 2H,  $-\text{CH}_2-\text{CH}_2-\text{CO}$ ), 1.40 (s, 9H,  $-\text{O}-\text{C}(\text{CH}_3)_3$ ).

#### *S*-ethylsulfonyl-L-homocysteine *N*-carboxyanhydride (*Hcy*( $\text{SO}_2\text{Et}$ ) NCA) **6**

2.4 g dried *S*-ethylsulfonyl-L-homocysteine (10.7 mmol) were suspended in absolute THF (200 mL) at room temperature (25 °C) under nitrogen atmosphere. 1.0 mL diphosgene (1.7 g, 8.6 mmol) were added at once and the suspension became clear after 1 minute. The colorless solution was stirred for additional 5 minutes before THF, excess diphosgene and HCl were removed *in vacuo*. The residue was dissolved in 30 mL absolute ethyl acetate and any insoluble compounds were removed by filtration while avoiding contact with air. The NCA was precipitated by adding a mixture of 150 mL absolute *n*-hexane and 150 mL absolute diethylether. After filtration under nitrogen atmosphere, 1.2 g *S*-ethylsulfonyl-L-homocysteine NCA (4.7 mmol, 44 % yield, colorless powder, melting point: 94.9–95.2 °C) was obtained and stored in a Schlenk tube at -80 °C.

$^1\text{H}$  NMR (300 MHz,  $\text{DMSO}-d_6$ )  $\delta$  [ppm] = 9.14 (s, 1H,  $-\text{NH}-\text{CO}-\text{O}-\text{CO}$ ), 4.53 (ddd,  $^3J_{\text{H,H}} = 7.77$ , 5.52, 1.08 Hz, 1H,  $\alpha\text{-H}$ ), 3.57 (q,  $^3J_{\text{H,H}} = 7.26$  Hz, 2H,  $\text{CH}_3-\text{CH}_2-\text{SO}_2$ ), 3.29–3.18 (m, 2H,  $-\text{S}-\text{CH}_2-$ ), 2.24–2.07 (m, 2H,  $-\text{S}-\text{CH}_2-\text{CH}_2-$ ), 1.30 (t,  $^3J_{\text{H,H}} = 7.26$  Hz, 3H,  $\text{CH}_3-\text{CH}_2-\text{SO}_2$ ).

#### *N*- $\epsilon$ -benzyloxycarbonyl-L-lysine *N*-carboxyanhydride (*Lys*(Z) NCA)<sup>[26]</sup> **7**

The synthesis was adapted from literature and modified.<sup>[424,443]</sup> In a three-necked flask equipped with a reflux condenser and a septum, 15.0 g (53.5 mmol) Z-protected lysine was suspended in 300 mL of absolute THF. Afterward, 5.2 mL (42.8 mmol) of diphosgene were added slowly *via* syringe and the nitrogen stream was reduced. The solution was heated to 70 °C, yielding a slightly yellow clear solution after 2 h of stirring. Afterward, a steady flow of dry nitrogen was led through the solution into two gas washing bottles filled with aqueous NaOH. The solution was concentrated *in vacuo*, precipitated with absolute hexane and stored in the fridge for 1 h. The precipitate was collected by filtration in dry nitrogen atmosphere and washed with absolute hexane.

The crude reaction product was recrystallized twice from absolute THF/hexane. A total of 14.3 g of purified product (46.7 mmol, 87 % yield, colorless needles, melting point: 98.1–98.5 °C) was obtained and stored in a Schlenk tube at -80 °C.

$^1\text{H}$  NMR (300 MHz,  $\text{DMSO-}d_6$ )  $\delta$  [ppm] = 9.09 (s, 1H, -NH-CO-O-CO), 7.40–7.25 (m, 6H, -C<sub>6</sub>H<sub>5</sub>, -NH-CH<sub>2</sub>), 5.01 (s, 2H, -O-CH<sub>2</sub>-C<sub>6</sub>H<sub>5</sub>), 4.43 (t, 1H,  $^3J_{\text{H,H}}$  = 6.0 Hz,  $\alpha$ -H), 2.99 (q, 2H,  $^3J_{\text{H,H}}$  = 6.3 Hz, -CH<sub>2</sub>-NH-), 1.74–1.31 (m, 6H, -CH<sub>2</sub>-CH<sub>2</sub>-CH<sub>2</sub>-NH-).

*N*- $\epsilon$ -tert-butylloxycarbonyl-L-lysine *N*-carboxyanhydride (*Lys*(Boc) NCA)<sup>[367]</sup> **8**

9.8 g (39.8 mmol) of *N*- $\epsilon$ -Boc-protected lysine was weighed into a three-necked flask and dried *in vacuo* for 1 h. The solid was suspended in 300 mL of absolute THF under a steady flow of dry nitrogen. Afterwards, 9.9 mL (79.6 mmol) of absolute trimethyl-silylchloride and 11.0 mL (79.6 mmol) of absolute triethylamine TEA were added slowly *via* syringe. The suspension was stirred for 2 h followed by addition of 4.8 mL (39.8 mmol) of diphosgene, *via* syringe. The suspension was mildly refluxed for another 2 h. Overnight, a steady flow of dry nitrogen was lead through the solution into two gas washing bottles filled with aqueous NaOH solution removing excess phosgene and HCl. The suspension was filtered under dry nitrogen atmosphere to remove the salts of TEA and unconverted amino acid. The solid was washed with absolute THF and the filtrate was evaporated under reduced pressure. Subsequently, absolute THF was added to completely dissolve the crude reaction product. The solution was precipitated with absolute hexane and stored at 4 °C for 1 h. The solid was collected by filtration under dry nitrogen atmosphere and washed with absolute hexane. The crude reaction product was then recrystallized twice with absolute THF/hexane. A total of 6.5 g of purified product (23.9 mmol, 68 % yield, colorless needles, melting point: 136.9–137.6 °C) was obtained and stored in a Schlenk tube at -80 °C.

$^1\text{H}$  NMR (400 MHz,  $\text{DMSO-}d_6$ )  $\delta$  [ppm] = 9.07 (s, 1H, -NH-CO-O-CO), 6.95–6.34 (br, 1H, -NH-CO-O-C(CH<sub>3</sub>)<sub>3</sub>), 4.42 (t, 1H,  $^3J_{\text{H,H}}$  = 6.35 Hz, -CO-CH-CH<sub>2</sub>-), 2.90 (q, 2H,  $^3J_{\text{H,H}}$  = 6.03 Hz, -CH<sub>2</sub>-NH-CO-O-C(CH<sub>3</sub>)<sub>3</sub>), 1.79–1.56 (m, 2H, -CH-CH<sub>2</sub>-CH<sub>2</sub>-CH<sub>2</sub>-CH<sub>2</sub>-NH-), 1.45–1.12 (m, 13H, -CH-CH<sub>2</sub>-CH<sub>2</sub>-CH<sub>2</sub>-CH<sub>2</sub>-NH-, -NH-CO-O-C(CH<sub>3</sub>)<sub>3</sub>).

*N*- $\epsilon$ -trifluoroacetyl-L-lysine *N*-carboxyanhydride (*Lys*(TFA) NCA)<sup>[24]</sup> **9**

10.2 g (41.9 mmol) of *Lys*(TFA) was dissolved in 150 mL of absolute ethyl acetate, and the suspension was heated to 70 °C. 6.0 mL (50.3 mmol) of diphosgene was added via a syringe over 3 h. After an additional 1 h, in which the solution remained slightly cloudy, a nitrogen stream was passed through the solution for 1 h, and solution was concentrated *in vacuo*. 35 mL of absolute AcOEt was added, and the cloudy solution was filtered. The product was crystallized by slowly adding 80 mL of absolute hexane to the filtrate over 2.5 h. The product was collected by filtration, recrystallized two times and dried *in vacuo* for 1 h. A total of 7.1 g

of purified product (26.6 mmol, 63 % yield, colorless crystals, melting point: 84.5–85.0 °C) was obtained and stored in a Schlenk tube at -80 °C.  $^1\text{H}$  NMR (400 MHz, DMSO- $d_6$ )  $\delta$  [ppm] = 9.40 (t, 1H, -CONH-CF<sub>3</sub>), 9.09 (s, 1H, -CONH-CH), 4.43 (t,  $^3J_{\text{H,H}}$  = 6.3 Hz, 1H,  $\alpha$ -H), 3.17 (q,  $^3J_{\text{H,H}}$  = 6.3 Hz, 2H, CH<sub>2</sub>-NH), 1.86–1.58 (m, 2H, CH-CH<sub>2</sub>), 1.50 (p, 2H, CH<sub>2</sub>-CH<sub>2</sub>-CH<sub>2</sub>-CH<sub>2</sub>-NH), 1.44–1.21 (m, 2H, CH<sub>2</sub>-CH<sub>2</sub>-CH<sub>2</sub>-CH<sub>2</sub>-NH).

#### Sarcosine N-carboxyanhydride (Sar NCA)<sup>[26]</sup> **10**

The synthesis of sarcosine NCA was adapted from literature and modified.<sup>[44]</sup> A total of 14.9 g (167.4 mmol) sarcosine, dried *in vacuo* for 1 h, was weighed into a pre-dried, three-neck, round-bottom flask. A total of 300 mL of absolute THF was added under a steady flow of nitrogen and 16.2 mL (134.0 mmol) of diphosgene were added slowly *via* syringe, and the nitrogen stream was reduced. The colorless suspension was mildly refluxed for 3 h, yielding a clear solution. Afterward, a steady flow of dry nitrogen was led through the solution for another 3 h into two gas washing bottles filled with aqueous NaOH solution. The solvent was evaporated under reduced pressure, yielding a brown oil as crude reaction product. The oil was heated to 50 °C and dried under reduced pressure (20 mbar, then < 10<sup>-2</sup> mbar for 2 h) to obtain an amorphous solid, free of phosgene and HCl, confirmed by testing against silver nitrate solution. The crude product was dissolved in 40 mL absolute THF and precipitated with 300 mL absolute hexane. The solution was cooled to -18 °C overnight for complete precipitation. The solid was filtered under dry nitrogen atmosphere, dried in a stream of dry nitrogen for 60–90 min and afterwards under high vacuum for 2 h in a sublimation apparatus. The crude product was sublimated at 80–85 °C and < 10<sup>-2</sup> mbar. The product was collected from the sublimation apparatus in a glovebox on the same day. This procedure yielded 12.6 g of purified product (110.0 mmol, 65 % yield, colorless crystals, melting point: 103.0–103.7 °C) which was stored in a Schlenk tube at -80 °C and only handled under nitrogen atmosphere.

$^1\text{H}$  NMR (400 MHz, CDCl<sub>3</sub>)  $\delta$  [ppm] = 4.22 (s, 2H, -CH<sub>2</sub>-), 2.86 (s, 3H, -CH<sub>3</sub>).

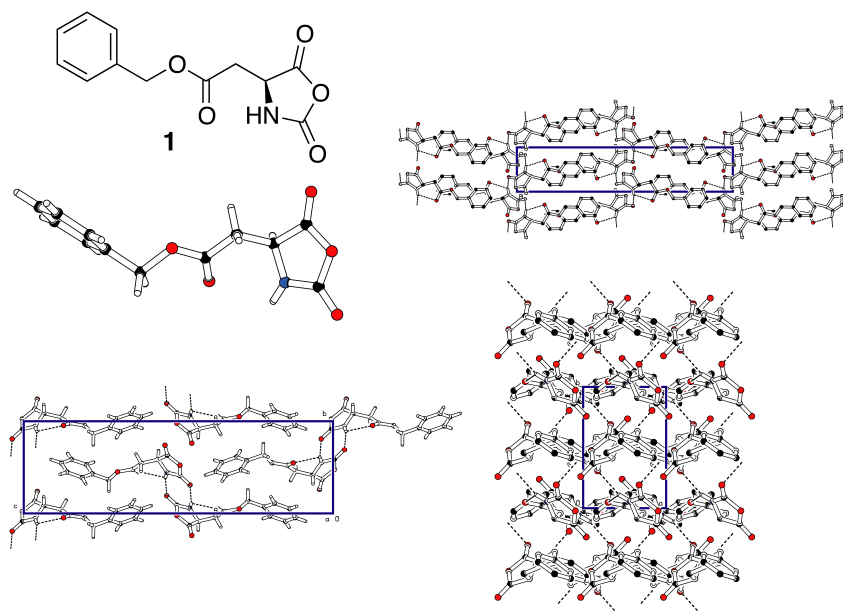
#### 8.5.3 Typical polymerization procedure<sup>[26]</sup>

A 400 mg aliquot of Glu(OBn) NCA (1.5 mmol) was transferred under nitrogen counter flow into a pre-dried Schlenk tube equipped with a stir bar and dried in high vacuum for 1 h. Then the 400 mg of NCA was dissolved in 2.8 mL of dry DMF. A total of 5.6  $\mu\text{L}$  of neopentylamine was added to 2 mL of dry DMF in a glass vial flooded with nitrogen and mixed. For initiation, 1 mL of the prepared stock solution was directly added to the Schlenk tube *via* syringe (yielding a total of 4 mL with 100 mg/mL in respect to monomer). The solution was stirred at room temperature and kept at a constant pressure of 1.25 bar of dry nitrogen via the Schlenk line to prevent impurities from entering the

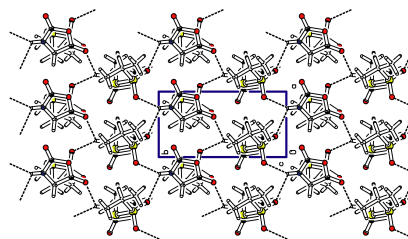
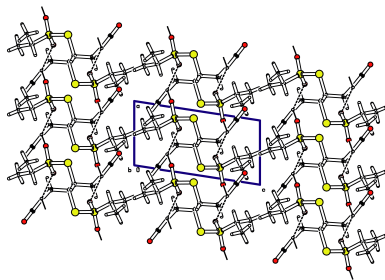
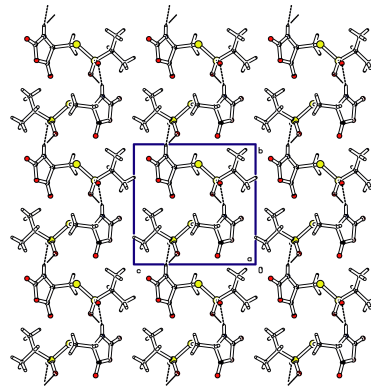
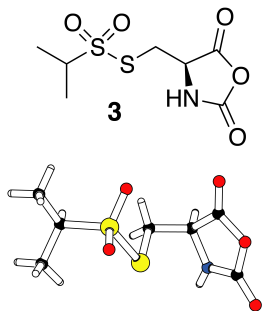
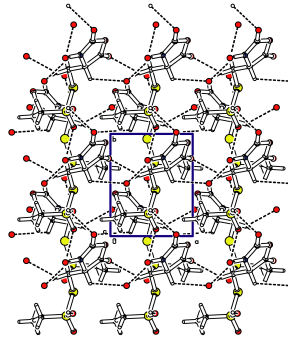
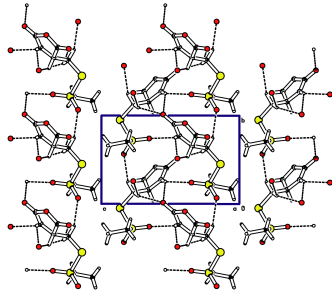
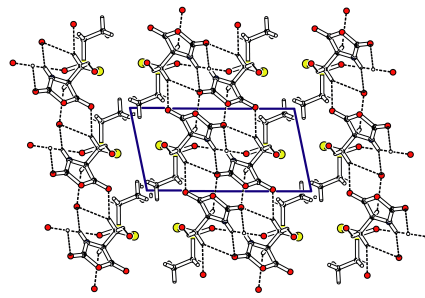
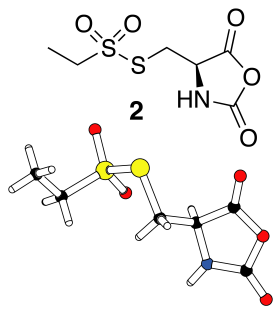
reaction vessel while allowing CO<sub>2</sub> to escape. Completion of the reaction was confirmed by IR spectroscopy (disappearance of the NCA peaks (1858 cm<sup>-1</sup> and 1788 cm<sup>-1</sup>). Directly after completion of the reaction, the polymer was precipitated to cold ether and centrifuged (4500 rpm at 4 °C for 15 min). After discarding the liquid fraction, new ether was added and the polymer was resuspended in a sonic bath. The suspension was centrifuged again and the procedure was repeated. After DMF removal by the resuspension steps, the polymer was dissolved in dioxane and lyophilized, obtaining a stiff, porous mass of polymer (65.3 mg from the 1 mL precipitated; yield 70 %).

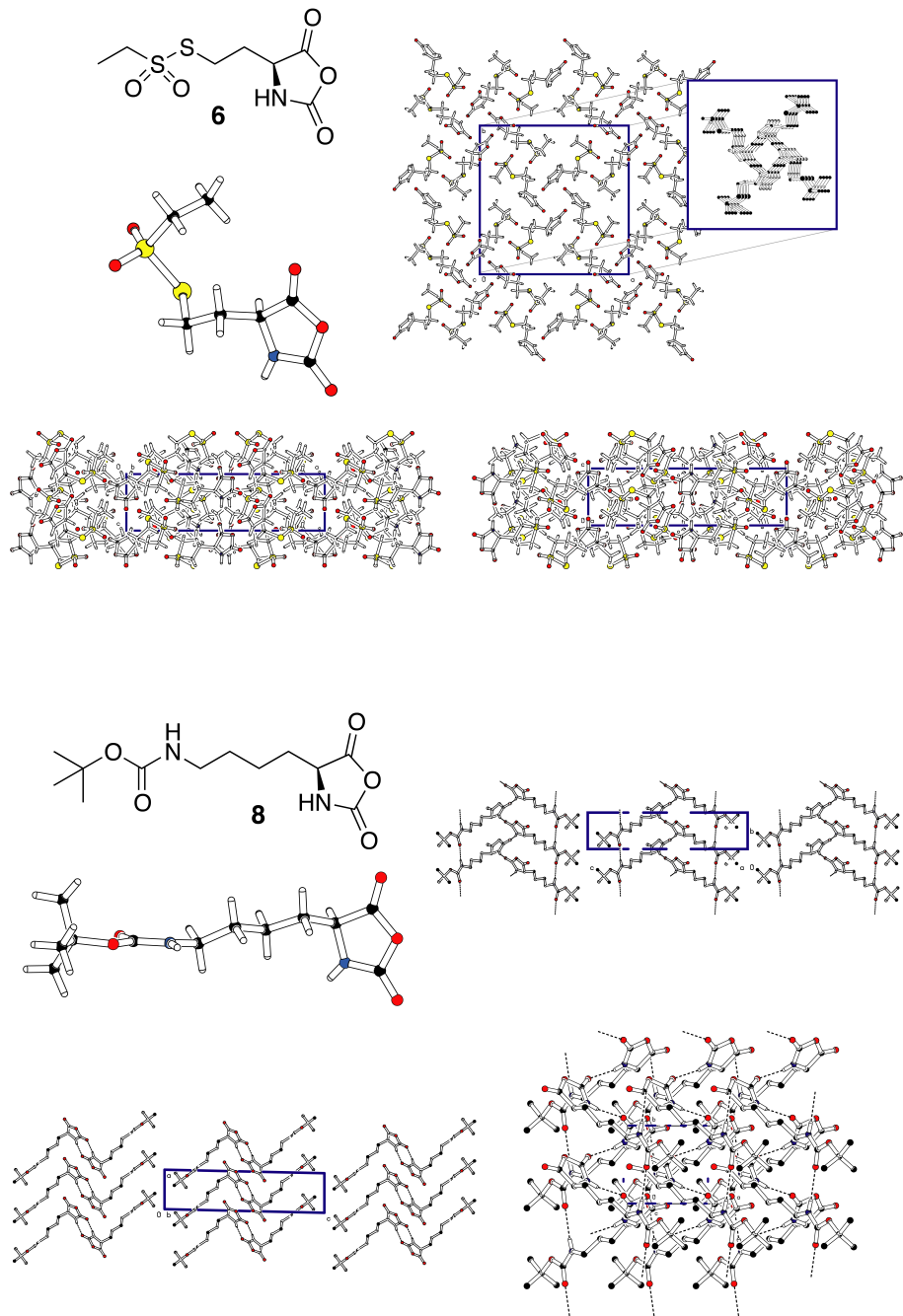
For different NCA polymerizations the reaction temperature ranges between -10°C and room temperature (25°C) and work-up conditions vary as reported in literature.<sup>[24,26,61,173,367]</sup>

#### 8.5.4 Single-crystal X-ray diffraction of NCAs

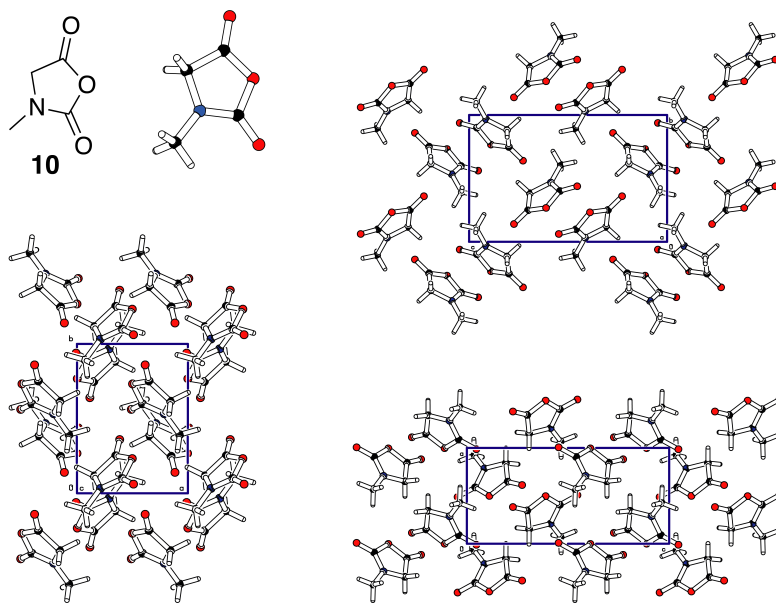












### 8.5.5 X-ray powder diffraction of NCAs

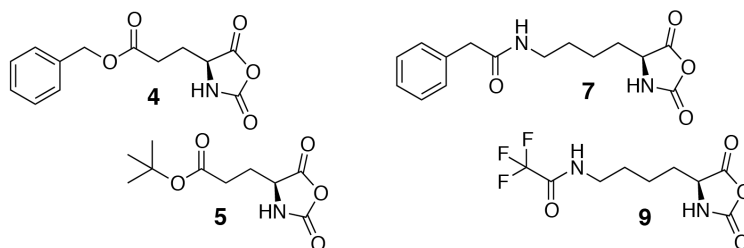
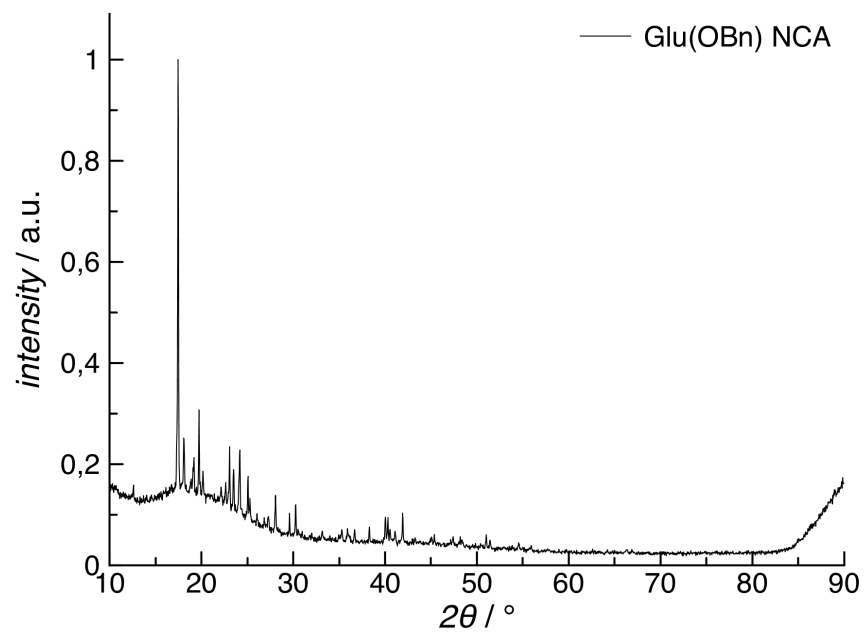
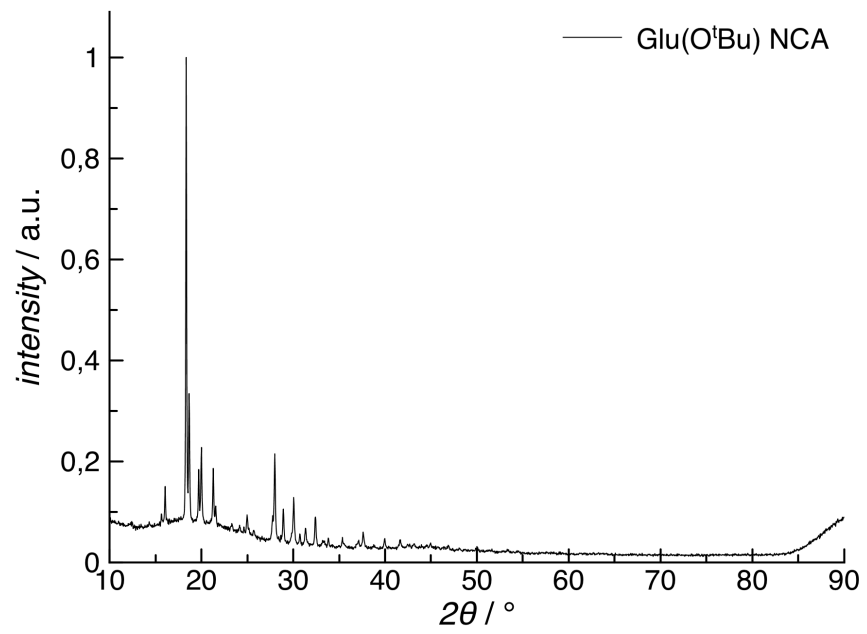
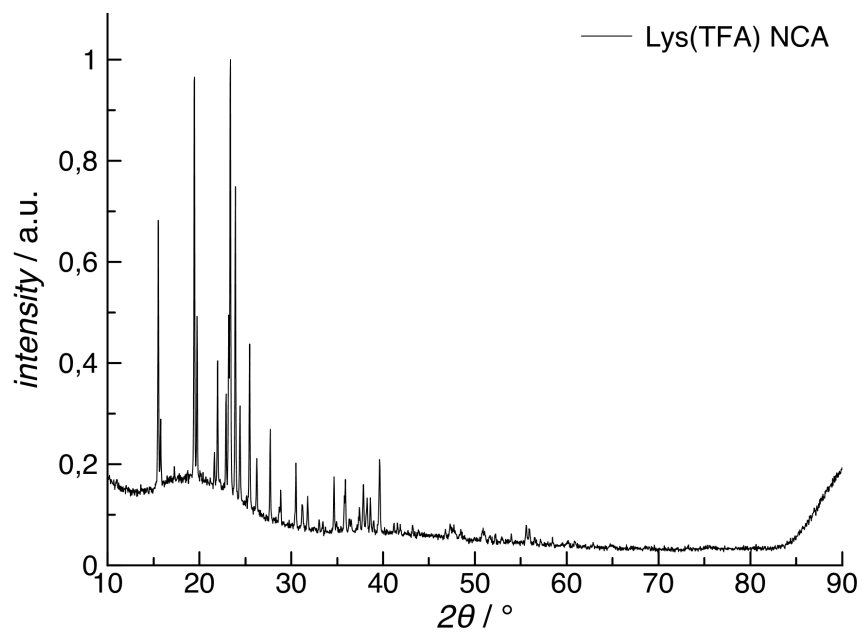
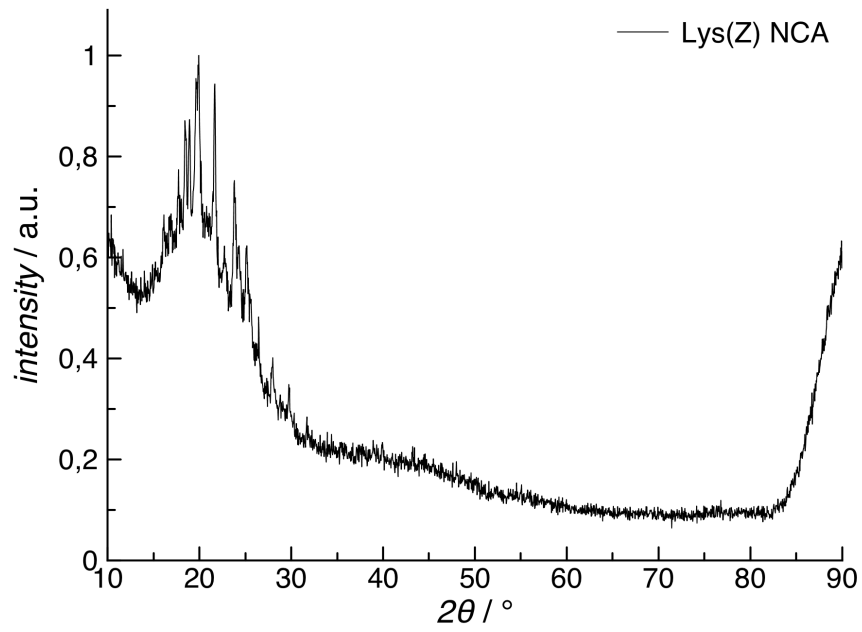
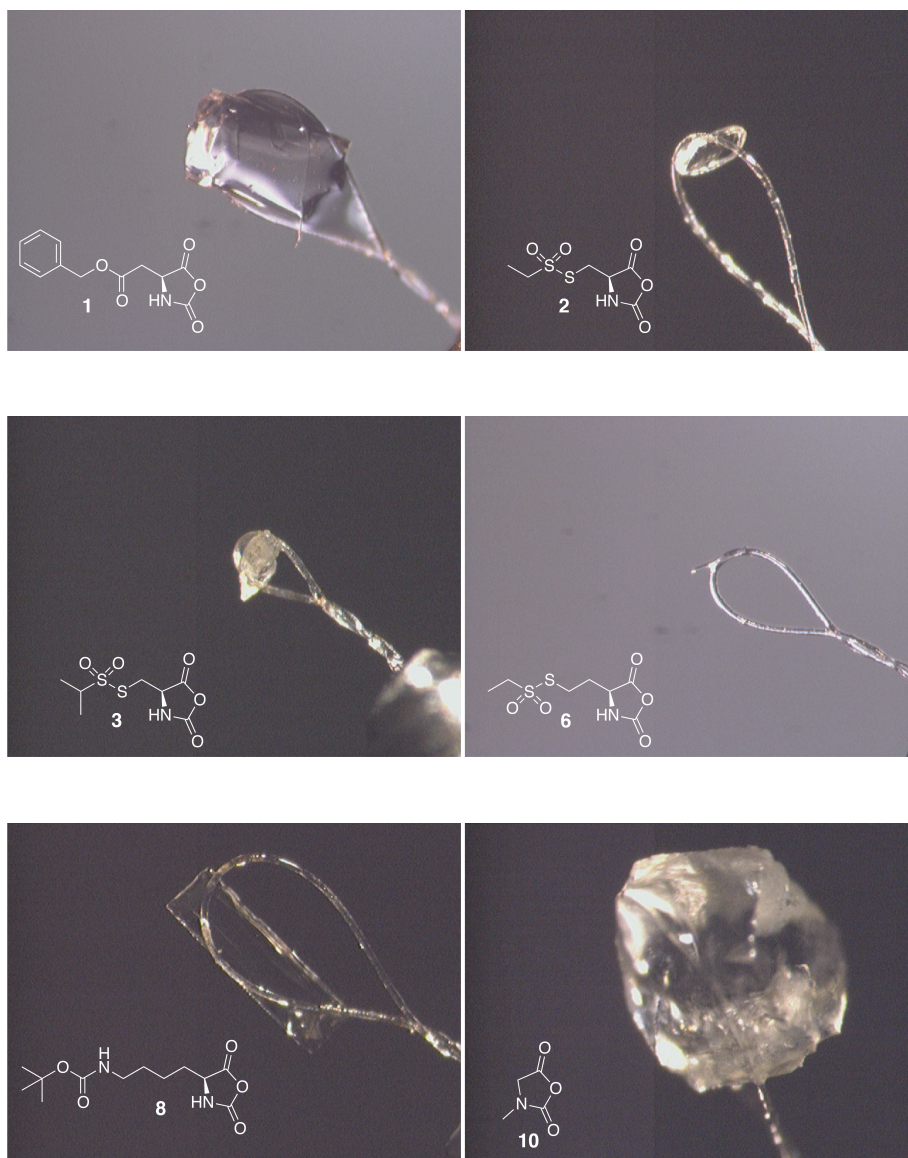


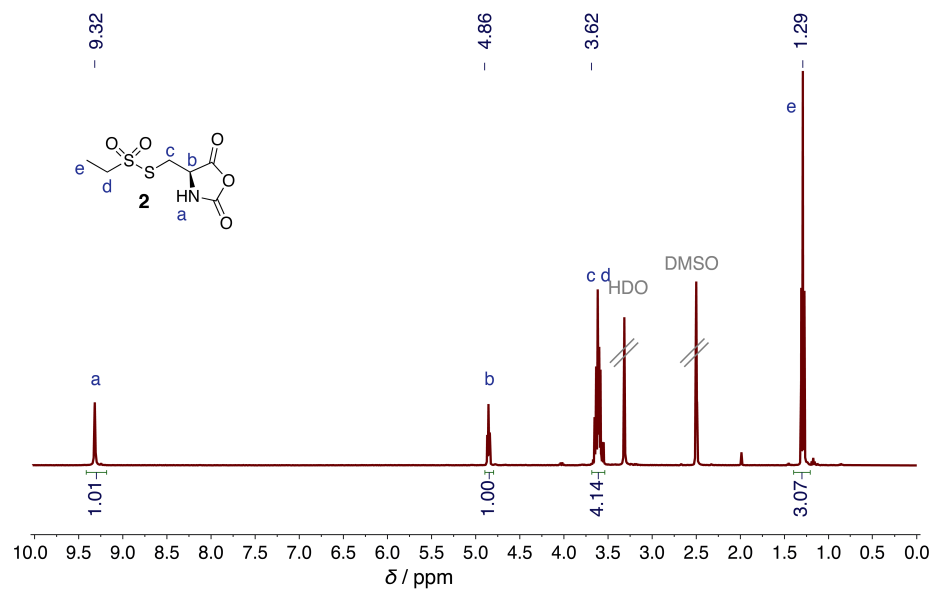
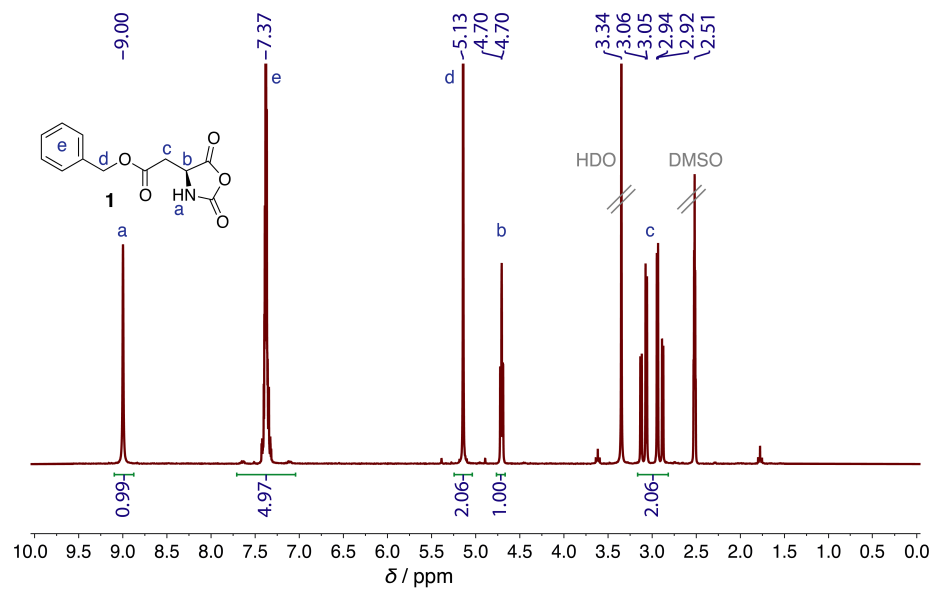
Figure 8.3: Structure of NCAs evaluated by X-ray powder diffraction: **4** Glu(OBn) NCA, **5** Glu(<sup>t</sup>Bu) NCA, **7** Lys(Z) NCA and **9** Lys(TFA) NCA.

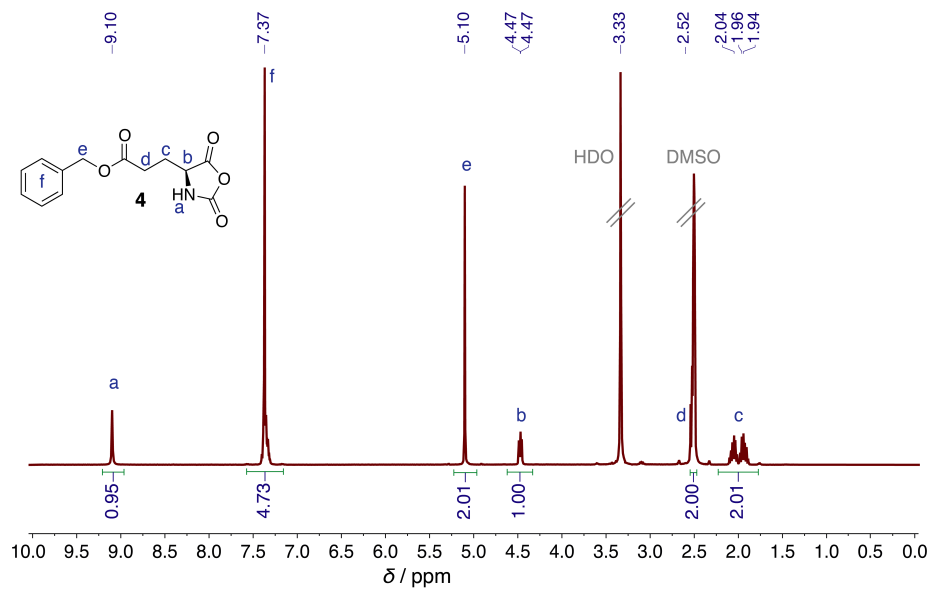
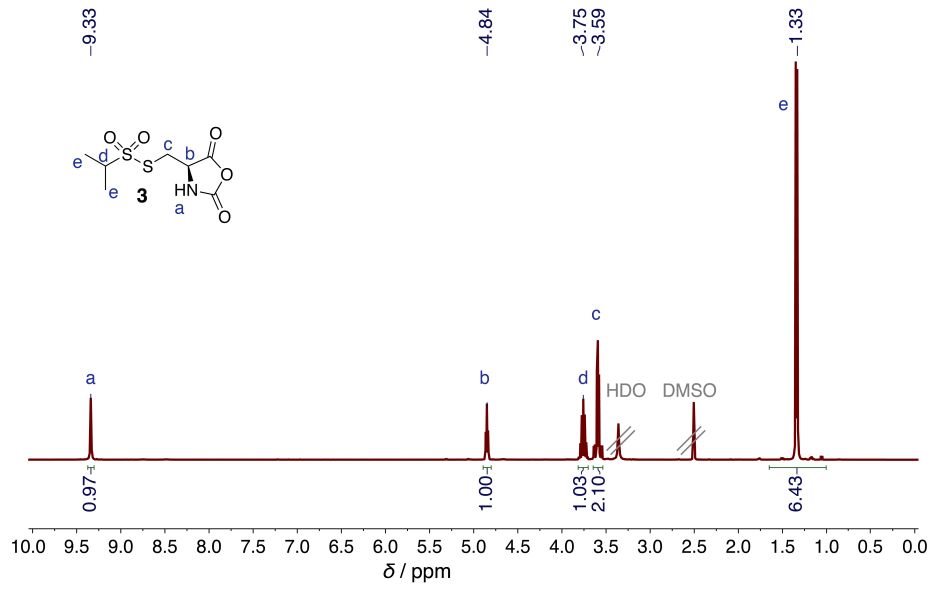


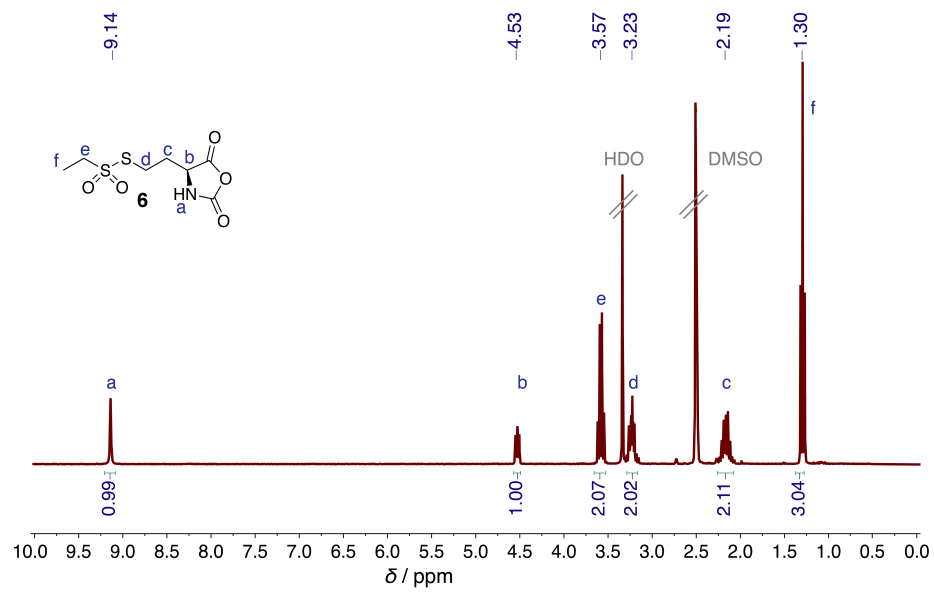
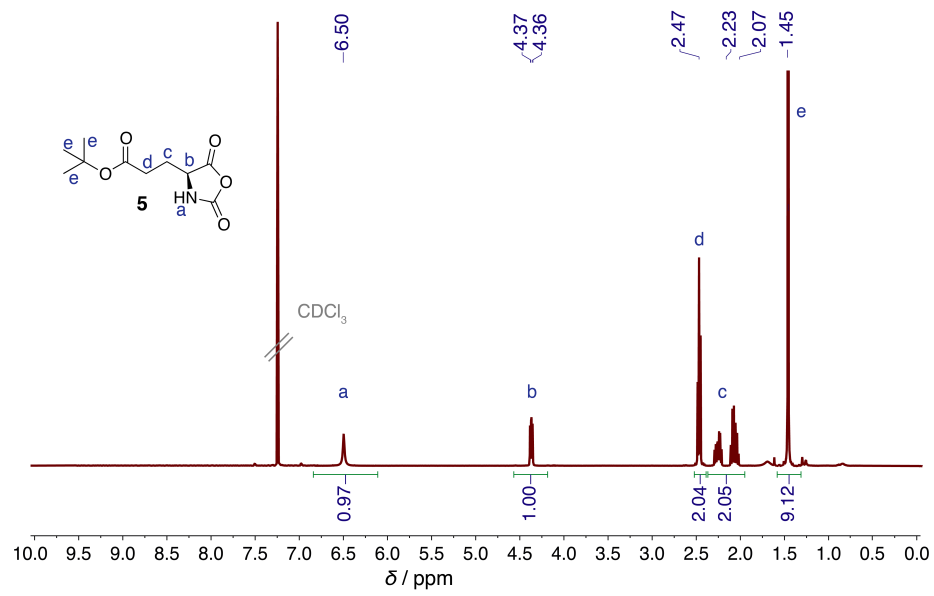


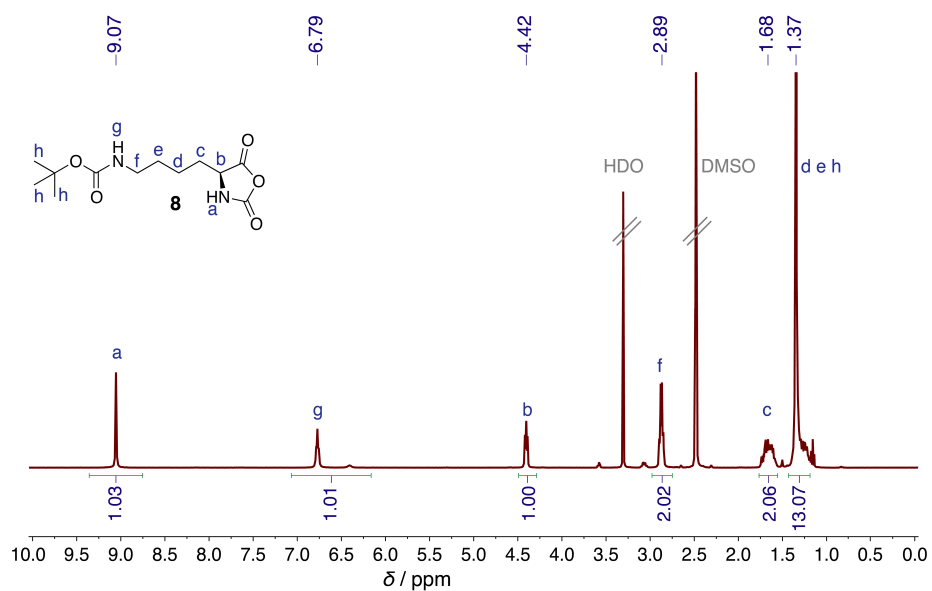
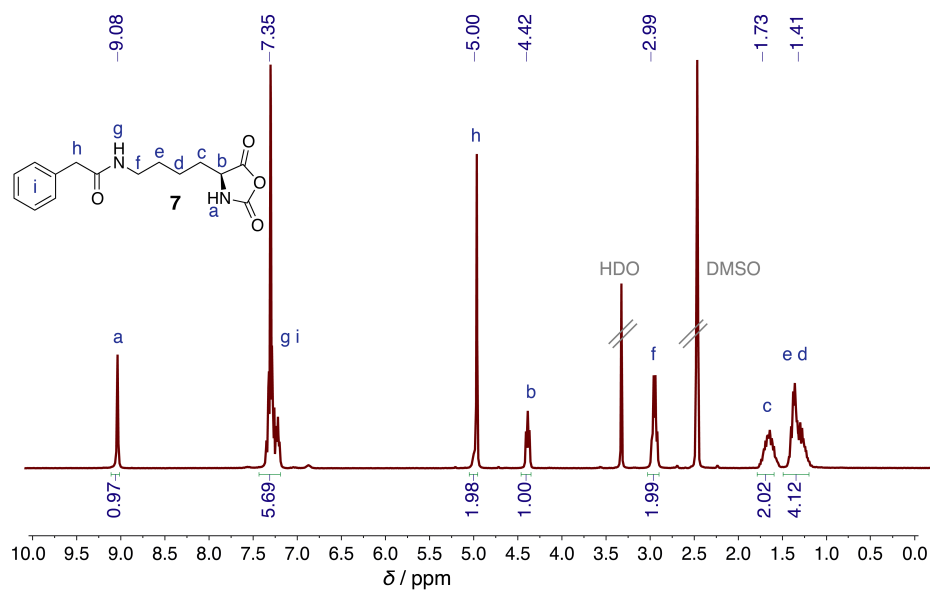
## 8.5.6 Images of NCA single-crystals used for X-ray diffraction



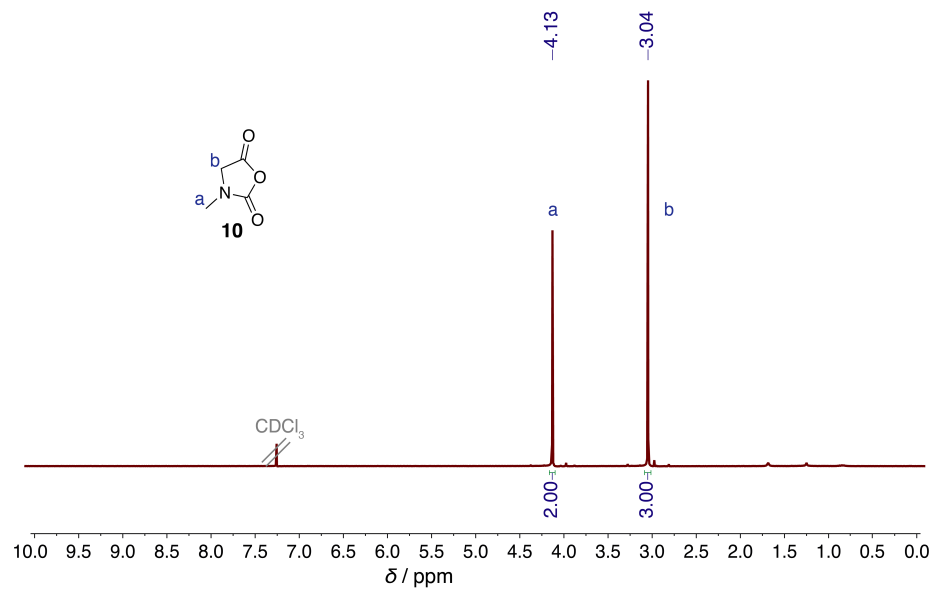
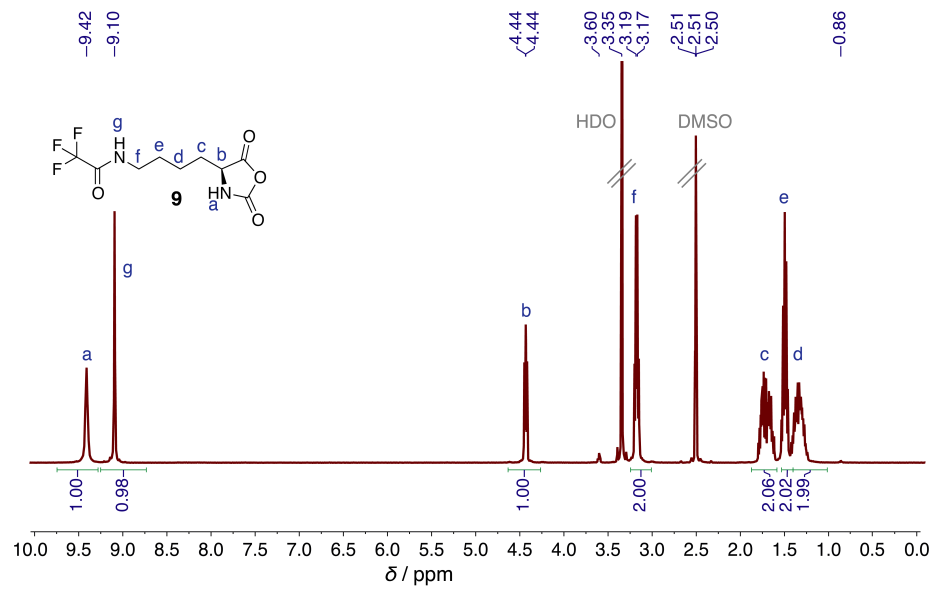
8.5.7  $^1\text{H}$  NMR Spectra of NCAs







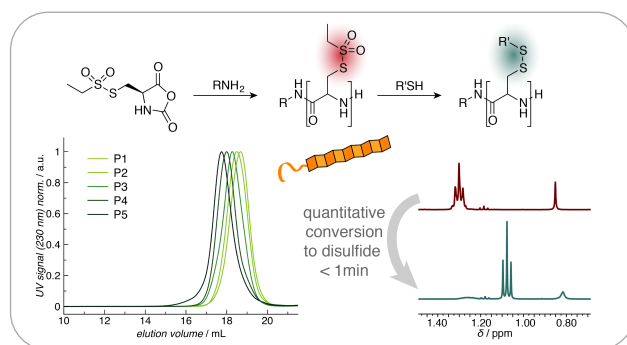






POLY(*S*-ETHYLSULFONYL-L-CYSTEINE) FOR  
CHEMOSELECTIVE DISULFIDE FORMATION

Olga Schäfer\*, David Huesmann\*, Matthias Barz, *Macromolecules* **2016**, *49*, 8146-8153. (\*authors contributed equally)



**ABSTRACT:** The amino acid cysteine possesses a unique role in nature due to its ability to reversibly cross-link proteins. To transfer this feature to polypeptides and control the process of disulfide formation, a protective group needs to provide stability against amines during synthesis, combined with chemoselective reactivity toward thiols. A protective group providing this unique balance of stability and reactivity toward different nucleophiles is the *S*-alkylsulfonyl group. In this work we report the polymerization of *S*-ethylsulfonyl-L-cysteine  $\alpha$ -amino acid *N*-carboxyanhydride (NCA) and kinetic evaluations with respect to temperature ( $-10\text{ }^{\circ}\text{C}$ ,  $0\text{ }^{\circ}\text{C}$  and  $10\text{ }^{\circ}\text{C}$ ) and monomer concentration. The polymerization degree of poly(*S*-ethylsulfonyl-L-cysteine) (PCys(SO<sub>2</sub>Et)) can be controlled within a range of 10 to 30, yielding well-defined polymers with molecular weights of  $6900\text{ g mol}^{-1}$  to  $12\,300\text{ g mol}^{-1}$  with dispersity indices of 1.12 – 1.19 as determined by gel permeation chromatography (GPC) and matrix assisted laser desorption/ionization-time of flight (MALDI-TOF) analysis. The limitation of chain length is, however, not related to side reactions during ring-opening polymerization, but to physical termination during  $\beta$ -sheet assembly. In the case of poly(*S*-ethylsulfonyl-L-cysteine), circular dichroism (CD) as well as fourier transform infrared (FT-IR) spectroscopy confirm an antiparallel  $\beta$ -sheet conformation. The reaction of PCys(SO<sub>2</sub>Et) with thiols is completed in less than a minute, leading quantitatively to asymmetric disulfide bond formation in the absence of side reactions. Therefore, poly(*S*-ethylsulfonyl-L-cysteines) are currently the only reactive cysteine derivative applicable to NCA synthesis and polymerization, which allows efficient and chemoselective disulfide formation in synthetic polypeptides, bypassing additional protective group cleavage steps.

## 9.1 INTRODUCTION

The synthesis of polypeptides by ring-opening polymerization of  $\alpha$ -amino acid *N*-carboxyanhydrides (NCAs) has been the subject of intensive studies since the early 20th century, when Leuchs discovered this class of monomers.<sup>[37,39,45]</sup> From the end of the 20th century, various techniques to control the polymerization have been explored, including metal catalysts, different initiators, extremely pure chemicals, and low temperatures.<sup>[48–54,56]</sup> Achieving control over molecular architecture and end-group integrity as well as polymer dispersity seems to be of particular importance for an application of polypeptides in nanomedicine.<sup>[30,355,408,409]</sup> A fairly young field of research is NCAs with side chain functionalities that are stable under polymerization conditions but directly addressable by post polymerization modification reactions.<sup>[58,444–446]</sup> Bio-orthogonal reactive groups like azides (copper(I)-catalyzed azide–alkyne cycloaddition (CuAAC)<sup>[314]</sup>), alkynes (CuAAC,<sup>[447]</sup> thiol–yne<sup>[313]</sup>), double bonds (thiol–ene,<sup>[313]</sup> oxidations,<sup>[448]</sup> Michael addition,<sup>[360]</sup> olefin metathesis,<sup>[449]</sup> Suzuki coupling<sup>[449]</sup>), thioethers (alkylation<sup>[450]</sup>), and chlorides (nucleophilic substitution,<sup>[451]</sup> ATRP<sup>[452]</sup>) have been successfully established. However, while all of these polymers can be modified in one post polymerization step, the covalent bonds formed (triazines, thioethers, carbon–carbon bonds) are not reversible, leading to a permanent modification of the polymer. For biomedical applications a stimuli responsive linkage is often preferred for the release of cargo or the degradation of carriers.<sup>[153]</sup> These linkages can be redox (disulfides) or acid labile (acetals and hydrazones), enabling cleavage of the bond in different intracellular compartments. In contrast to radical polymerizations, acetals and hydrazones are neither compatible to NCA synthesis and polymerization nor applicable to chemoselective cross-linking reactions.

Since cysteine is also involved in reversible disulfide bond formation in natural proteins,<sup>[159]</sup> it seems to be an ideal candidate for the synthesis of reactive polypeptides for disulfide formation via post polymerization reactions. To realize this concept, two requirements have to be fulfilled: (I) The thiol at the cysteine side chain needs to be activated to react with other thiols after polymerization under disulfide formation, and (II) the modified thiol needs to be stable during NCA synthesis and polymerization (presence of amine nucleophiles).

Achieving these requirements is not a trivial task because on one hand a rapid reaction with thiols (soft nucleophiles) is desired, while on the other hand with amines (hard nucleophiles) need to be strictly avoided with respect to a controlled polymerization. While a wide range of cysteine NCAs (*S*-allylcysteine, *S*-benzylcysteine, *S*-benzyloxycarbonylcysteine, *S*-benzyloxycarbonylmethylenecysteine, *S*-butylcysteine, *S*-tert-butylmethylcysteine, a range of *S*-alkylcysteines (dodecyl, hexyl, methyl, ethyl, propyl, isopropyl), *S*-(2-trimethylsilylbenzyl)cysteine, *S*-(4-trimethylsilylbenzyl)-cysteine, cystine (bisNCA), *S*-

thiophenylcysteine) from the early years of NCA polymerization has been collected,<sup>[45]</sup> none of them is suitable for activation of the cysteine thiol for direct disulfide formation. Recent developments of cysteine NCAs were either not focused on post polymerization modification at all,<sup>[312,357,358,453]</sup> have implemented disulfide moieties prior to NCA formation<sup>[454]</sup> or have worked with deprotection and subsequent modification using irreversible thiol–ene chemistry leading to stable thioethers.<sup>[311,359,360]</sup> In previous studies, we investigated activated cysteine NCAs and their polymerization for post polymerization modification. However, all compounds proved to be prone to side reactions during the polymerization due to high electron deficiency of the side groups,<sup>[321]</sup> once again emphasizing the need for a protective group with a balanced reactivity profile.

In this work we describe the polymerization of the recently developed *S*-ethylsulfonyl-L-cysteine (Cys(SO<sub>2</sub>Et)) NCA<sup>[173,364]</sup> (Cys(SO<sub>2</sub>Et) NCA) and the post polymerization modification of these polymers. The *S*-ethylsulfonyl protective group fulfills all the requirements mentioned above since it is stable under NCA synthesis and polymerization conditions, while being highly reactive toward thiols. Detailed analyses of polymerization kinetics and polymer properties are presented. In the end, we report on the stability at different pH values and the reactivity in post polymerization modification reactions with thiols, underlining the enormous potential of this new class of reactive NCAs.

## 9.2 RESULTS AND DISCUSSION

To obtain the Cys(SO<sub>2</sub>Et) NCA, first the corresponding protected amino acid was received by nitrosation of L-cysteine followed by reaction with sodium ethanesulfinate (Figure 9.1 A). The NCA was then synthesized by the Fuchs–Farthing method using diphosgene as the phosgene source<sup>[40–42]</sup> and was obtained in high purity (melting point range: 113–115 °C) after repeated recrystallization. The <sup>1</sup>H NMR of the Cys(SO<sub>2</sub>Et) NCA is given in Figure 9.1 B and its rather complex spin–spin coupling pattern is discussed in the Supporting Information (Figure 9.8). When solid state as well as liquid film infrared (IR) spectroscopy (Figure 9.1 C and 9.4 A) is performed, two carbonyl stretching bands can be observed at frequencies characteristic for mixed anhydrides.<sup>[45]</sup> -bond formation in the crystalline, solid state of the Cys(SO<sub>2</sub>Et) NCA.

The polymerization of the Cys(SO<sub>2</sub>Et) NCA was initiated by neopentylamine (Figure 9.2 A), since the 9 equiv methyl-protons allow reliable determination of repeating units by NMR (Figure 9.9). In regard to a ring-opening polymerization in a controlled fashion, it has to be considered, that any deprotection reaction at the *S*-ethylsulfonyl group during polymerization bears the risk of side reactions. A possible side reaction would be an attack of the living chain end at the *S*-ethylsulfonyl site. If this side reaction was present even at minimal amounts, it would hinder the polymerization dramatically due to capping of the propagating end

*Synthesis of  
PCys(SO<sub>2</sub>Et).*

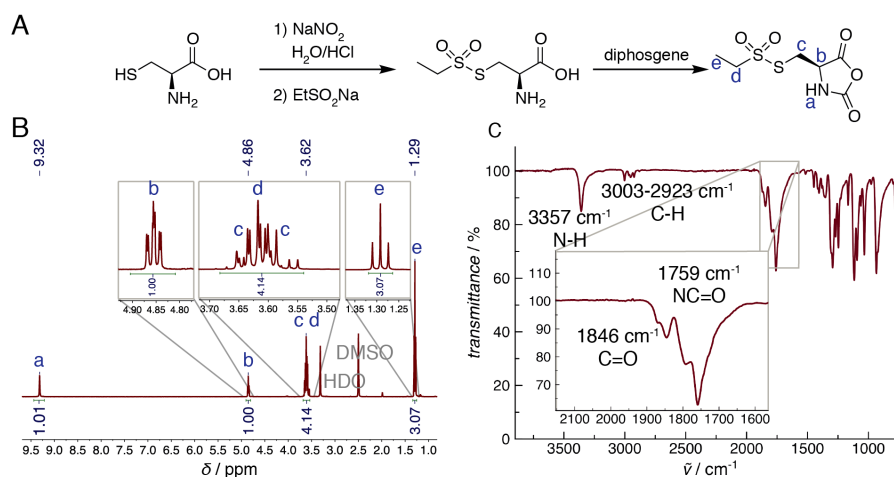


Figure 9.1: A) Synthesis of Cys(SO<sub>2</sub>Et) NCA. B) <sup>1</sup>H NMR and C) solid state IR of Cys(SO<sub>2</sub>Et) NCA.

group. Furthermore, deprotection reactions may then originate from the free nucleophilic thiol group, and control over the polymerization process would be lost. However, <sup>1</sup>H diffusion-ordered NMR experiments (<sup>1</sup>H DOSY NMR) of poly(*s*-ethylsulfonyl-L-cysteine) (PCys(SO<sub>2</sub>Et)), as well as further characterization methods such as gel permeation chromatography (GPC), matrix assisted laser desorption/ionization-time of flight (MALDI-TOF), and end-group functionalization, fully eliminates this concern. <sup>1</sup>H DOSY NMR reveals only two diffusing species, of which one is the solvent (DMSO-*d*<sub>6</sub>) while all other signals originate from PCys(SO<sub>2</sub>Et) (Figure 9.3). Since no other polymeric or small molecular species can be observed, signals in <sup>1</sup>H NMR correspond exclusively to the polymer, and thus, end group analysis is a valid method to determine the degree of polymerization.

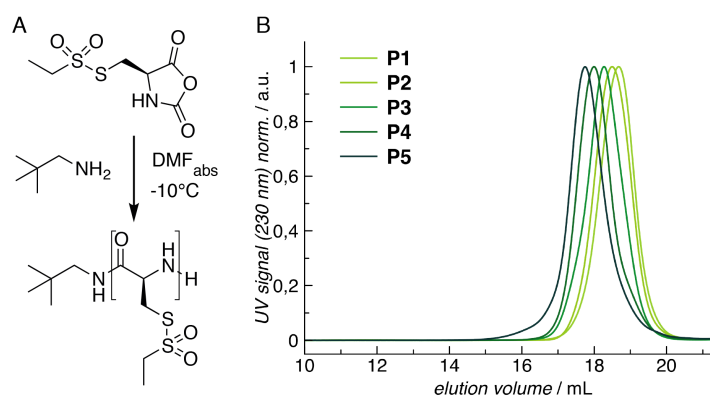


Figure 9.2: A) Polymerization of Cys(SO<sub>2</sub>Et) NCA with neopentylamine as initiator. B) HPLC traces of PCys(SO<sub>2</sub>Et) at various degrees of polymerization (see also Table 9.1).

As can be seen in Table 9.1 and Figure 9.2 B, the polymerization proceeds in a controlled fashion and yields PCys(SO<sub>2</sub>Et) well-defined homopolymers with narrow, symmetric distributions ( $\bar{M}_w/\bar{M}_n < 1.2$ ). Due to the ag-

gregation of  $\beta$ -sheets (as exhibited by most polycysteine derivatives, discussion below) at degrees of polymerization above 30, no reliable GPC characterization can be carried out for longer polymers (see Figure 9.11). Propagating  $\beta$ -sheet formation is also responsible for a change in polymerization kinetics, which leads to slower polymerization rates reaching high conversions (see also below). Therefore,  $\text{PCys}(\text{SO}_2\text{Et})$  polymerizations are usually terminated by precipitation before full conversion is reached.

Table 9.1: Characterization of  $\text{PCys}(\text{SO}_2\text{R})$ .

No.	M/I	% conversion	$X_{n,NMR}$	$M_{n,GPC}^a/\text{g mol}^{-1}$	$D_{GPC}^a$
P1	15	80	13	6900	1.12
P2	15	92	15	7000	1.14
P3	20	88	17	8400	1.16
P4	50	39	20	9000	1.15
P5	50	63	27	12300	1.19

<sup>a</sup> Relative to PMMA standards.

Additionally, the following general aspects regarding *S*-alkylsulfonyl-L-cysteine are noteworthy: molecular weights obtained by GPC should not be interpreted as the real molecular weight. First, as circular dichroism (CD) spectra confirm (Figure 9.3 B), the polymer adapts  $\beta$ -sheet conformation in solution, thus hydrodynamic volumes will differ significantly from a polymer in random coil conformation. Second, the calibration of the GPC is performed with PMMA standards, whose C-C backbone does not fully correlate to a polypeptide backbone. Therefore, the  $M_{n,GPC}$  can only serve for comparison between the polymers, but should not be considered as the real molecular weight. Further, in order to evaluate handling of the  $\text{PCys}(\text{SO}_2\text{Et})$  homopolymers, their stability in different pH buffers was examined (see Figure 9.12). The *S*-ethylsulfonyl group proved to be sensitive to a nucleophilic  $\text{OH}^-$  attack followed by removal of the protective group. As a result, precautions have to be taken considering dry solvents and reagents, whenever bases are present. Acidic to neutral conditions, however, do not affect the protective group of  $\text{PCys}(\text{SO}_2\text{Et})$  at all.

Poly-L-cysteine is known to form  $\beta$ -sheets<sup>[37,455]</sup> as illustrated in Figure 9.3 A. This also applies to most of its derivatives<sup>[358,453]</sup> (although, equipped with hydrophilic sugar residues<sup>[312]</sup> or oligo(ethylene glycol) chains<sup>[456]</sup> other conformations of varying amounts are possible). Thus, the  $\beta$ -sheet conformation of  $\text{PCys}(\text{SO}_2\text{Et})$  was evaluated by CD and IR spectroscopy. All CD spectra (Figure 9.3 B) show traces shaped typically for  $\beta$ - sheets and the IR spectrum (Figure 9.3 C) exhibits a strong amide I band at  $1637\text{ cm}^{-1}$  as well as the amide II band at  $1514\text{ cm}^{-1}$ , which are both characteristic for polypeptides in a  $\beta$ -sheet conformation.<sup>[457]</sup> The shoulder at  $1690\text{ cm}^{-1}$  to  $1702\text{ cm}^{-1}$  implies that the polypeptides are ar-

*Secondary structure  
formation of  
 $\text{PCys}(\text{SO}_2\text{Et})$ .*

ranged in an antiparallel direction.<sup>[458]</sup>

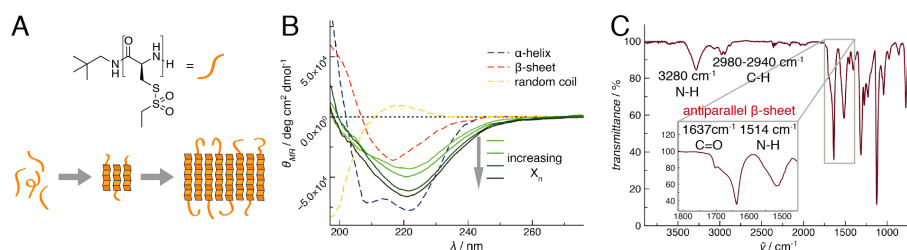


Figure 9.3: A) Schematic illustration of  $\beta$ -sheet formation during growth of the peptide chain. B) CD spectrum of PCys(SO<sub>2</sub>Et) in HFIP showing  $\beta$ -sheets in solution. C) IR spectrum of PCys(SO<sub>2</sub>Et) in solid state displaying typical absorption bands of antiparallel  $\beta$ -sheets.

Above an  $X_n$  of 30, PCys(SO<sub>2</sub>Et) has the tendency to form  $\beta$ -sheet aggregates, leading to a high molecular weight shoulder in HFIP GPC (Figure 9.11). Further, increasing turbidity of the polymerization solution due to aggregation can be observed for higher degrees of polymerization (see Figure 9.11 where  $X_n = 43$  shows a significant amount of aggregated polymer chains). However, a length of more than 30 repeating units is not required for applications like cross-linking; usually, 10–20 repeating units are sufficient as an effective cross-linkable block.

*Theoretical and experimental evaluation of polymerization kinetics.*

To gain a deeper insight into the kinetic behavior of PCys(SO<sub>2</sub>Et) polymerization, IR spectroscopy was performed during ongoing synthesis (Figure 9.4 A). The decrease of the carbonyl peaks of the NCA at 1858 cm<sup>-1</sup> and 1788 cm<sup>-1</sup> is directly related to conversion of the monomer and thus can be used in kinetic studies to precisely determine monomer conversion. The signals were integrated to calculate the conversion for each time point. To enhance accuracy and underline reproducibility, the kinetic studies were performed for three individual polymerization entries. Standard deviations are included in Figure 9.3 B. It can be observed that the individual error is negligible for short time points and still minor for higher conversions.

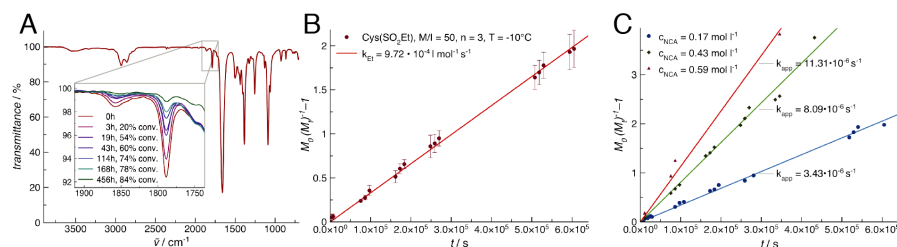


Figure 9.4: A) IR spectra of a PCys(SO<sub>2</sub>Et) polymerization at different reaction times (in DMF, liquid film). B) Kinetic plot of the PCys(SO<sub>2</sub>Et) polymerization with  $n = 3$ . C) Kinetic plot of PCys(SO<sub>2</sub>Et) polymerizations at varying monomer concentrations ( $M/I = 50$ ).



While most NCA polymerizations show pseudo first-order kinetics, the formation of  $\beta$ -sheets dramatically alters this behavior. Iguchi adapted the Avrami equation for the kinetics of crystal growth to describe heterogeneous polymerizations,<sup>[459]</sup> while Kōmoto *et al.* used it in analyzing NCA polymerizations of aggregating peptide chains.<sup>[460,461]</sup> Several assumptions are made to suit the heterogeneous polymerization system: At the beginning of the polymerization the system is homogeneous, consisting of the solvent, the monomer and the initiator. It is assumed, that the initiation starts immediately after addition of the initiator. Termination or transfer do not occur chemically. However, oligomers associate at very early stages of the polymerization. The chains then propagate at the surface of those soluble nanocrystallites (see Figure 9.3 A). Eventually a physical termination of the “living” chain end can occur, due to steric restrictions of secondary structures (especially when high degrees of polymerization are reached). The linear chain growth after aggregation is considered a one-dimensional transformation of the growing units. This situation attributes to the growth of needle-like crystals. In fact, most derivatives of poly-L-cysteine exhibit such fibrous structures at the initial phase of the polymerization.<sup>[460,461]</sup> The Avrami equation, adapted for NCA polymerization is given by<sup>[459]</sup>

$$\frac{\delta(x)}{\delta(t)} = k[I][M_0] \left(1 - \frac{x}{[M_0]}\right)^2 \quad (12)$$

with  $[M_0]$  = initial monomer concentration,  $[I]$  = initiator concentration,  $x = [M_0] - [M_t]$  = monomer consumed at time  $t$ , and  $k$  = rate constant. It follows that the polymerization rate is proportional to the square of the residual monomer concentration  $[M_t]$ :

$$\frac{\delta(x)}{\delta(t)} = k[I] \frac{[M_t]^2}{[M_0]} \quad (13)$$

This signifies, that polymerization rates drop dramatically at high conversions. This was also observed experimentally and PCys(SO<sub>2</sub>Et) polymerizations were terminated latest at conversions of 90 % due to stagnation of the NCA consumption. From Equation 12 can be derived using Equation 13:

$$\frac{[M_0]}{[M_0] - x} = k[I]t + 1 \quad (14)$$

By plotting  $\frac{[M_0]}{[M_t]} - 1$  versus the reaction time  $t$ , the apparent rate constant  $k_{app} = k[I]$ , and thereby the rate of polymerization  $k$  can be calculated. Experimental values obtained from IR spectroscopy following this kinetic approach are shown in 9.4 B, C and Figure 9.13 A.

According to the kinetic interpretation presented above, the polymerization rates depend on the initial monomer concentration. This behavior can indeed be observed by comparison of the apparent rate constants at varying initial monomer concentrations, while maintaining the

same monomer to initiator ratio (Figure 9.4 C). Additionally, the probability for side reactions can be decreased by lowering the reaction temperature,<sup>[55,462]</sup> ensuring faster polymerization rates and narrow molecular weight distributions (see Figure 9.13).

Characterization by  
MALDI-TOF mass  
spectroscopy.

In terms of polymer characterization, MALDI-TOF mass spectroscopy provides an absolute method of determining molecular weights.<sup>[461]</sup> However, the transfer of larger cysteine polymers into the gas phase presents a challenge. Since the solubility of PCys(SO<sub>2</sub>Et) is limited to fringhigh boiling solvents like DMSO and DMF, a solvent free sample preparation was chosen. P1 ( $X_{n,NMR} = 13$ ) was investigated and the results are illustrated in Figure 9.5 A. The polymer distribution is narrow, yielding calculated molecular weights of  $M_n = 2194 \text{ g mol}^{-1}$  and  $M_w = 2446 \text{ g mol}^{-1}$  ( $\mathcal{D} = 1.11$ ). The degree of polymerization derived from  $M_{n,MALDI}$  is  $X_{n,MALDI} = 11$  and in good agreement with the value from NMR  $X_{n,NMR} = 13$ .

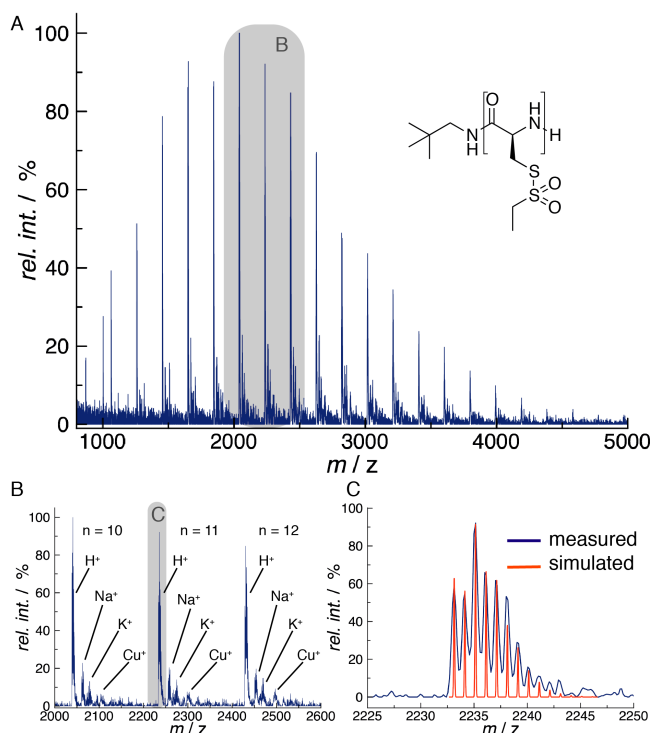


Figure 9.5: MALDI-TOF spectrum of PCys(SO<sub>2</sub>Et) P1 with  $X_{n,NMR} = 13$ .

A magnification of the spectrum (Figure 9.5 B) reveals the individual signals of PCys(SO<sub>2</sub>Et) initiated by neopentylamine and each equipped with a primary amine chain end. Signals indicating initiation by impurities or terminations are absent. The most prominent signals correspond to an additional proton (+1). Signals correlating to an additional sodium cation (+23), a potassium cation (+39) and a copper cation (+64) were also identified. When comparing the calculated masses of PCys(SO<sub>2</sub>Et) with the experimental results, the accumulation of heavier

sulfur atoms has to be taken into account.  $^{32}\text{S}$  is the most frequent isotope (95.02 %) followed by  $^{34}\text{S}$  (4.21 %).<sup>[463]</sup> Because of this natural variety of isotopes and the two sulfur atoms per repeating unit, a rather broad signal is observed. Figure 9.5 C compares the simulated peaks for  $\text{PCys}(\text{SO}_2\text{Et}) + \text{H}^+$  with  $X_n = 11$  to the measured spectrum, showing the peaks for individual isotopes, revealing the same isotope distribution for simulated and experimental data.

In summary, MALDI-TOF experiments clearly reveal the absence of chemical chain termination when polymerizations are carried out at  $-10^\circ\text{C}$  in absolute solvents. For different polymerization conditions chain termination can rapidly occur, which explains the slow polymerization kinetics and broad molecular weight distributions observed under sub-optimal conditions (see Supporting Information). To further investigate the presence of living chain ends and absence of free thiols, labeling of  $\text{NH}_2$  groups and potential SH groups was performed.

$\text{PCys}(\text{SO}_2\text{Et})$  was analyzed by means of fluorescent side chain and end group labeling, evaluating two possible reaction sites. The amine end group is an important feature of the polypeptides synthesized via NCA polymerization, since it is a prerequisite for initiation of a second block leading to diblock copolymers. A second reactive group is a free thiol, which might be present due to the removal of the protective group by amine nucleophiles. This presents an undesirable case, since interference with the polymerization process can be expected, as well as uncontrolled cross-linking by disulfide bond formation.

First, the absence of free thiol groups was verified, since they might interfere with labeling of the amine end group. A maleimide dye (fluorescein diacetate 5 maleimide) is a suitable reagent to label thiols (Figure 9.6 A), but not amines.<sup>[464]</sup> As can be observed with the bare eye (Figure 9.6 C), the sample treated with the maleimide dye yielded a colorless polymer. Figure 9.6 E displays the ultra violet (UV) signal of the HFIP GPC traces at the excitation maximum (492 nm) before and after reaction with the maleimide dye. Only absorption of the free dye, but no absorption of polymer conjugated dye can be observed. Therefore, it is apparent that free thiol groups are absent in the polymer and that the S-ethylsulfonyl group is stable during NCA polymerization. To verify end group integrity of  $\text{PCys}(\text{SO}_2\text{Et})$ , labeling of the amine end group was performed with a *N*-hydroxysuccinimide (NHS) ester dye (Oregon Green 488-X, succinimidyl ester; Figure 9.6 B).<sup>[465]</sup> This treatment yielded a bright yellow polymer (Figure 9.6 D). The results are depicted in Figure 9.6 F comparing the UV signal of the HFIP GPC traces (excitation maximum 496 nm) before and after reaction with the succinimidyl ester dye. In contrast to the labeling with the maleimide dye, the GPC trace shows a strong absorbance of a polymer-dye conjugate with a narrow molecular weight distribution in analogy to the parent polymer.

In addition to the findings from MALDI-TOF experiments, this labeling reaction also confirms the presence of a functional amine chain end.

*Fluorescent labeling of  $\text{PCys}(\text{SO}_2\text{Et})$  end groups without affecting thiol-reactive side chains.*

Thus, we clearly state, that the polymerization of PCys(SO<sub>2</sub>Et) proceeds in a controlled fashion and in the absence of chemical termination reactions.

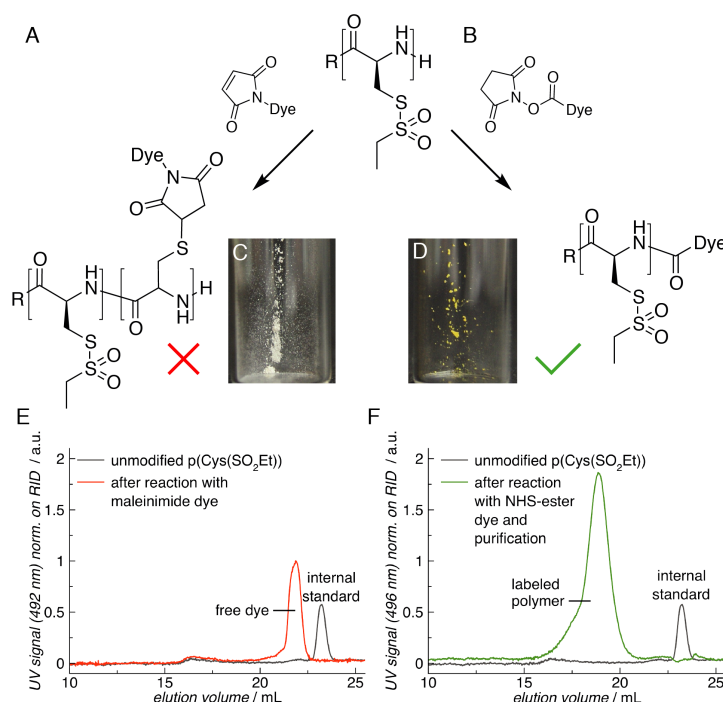


Figure 9.6: Labeling reactions of PCys(SO<sub>2</sub>Et) with a maleimide dye A) and a NHS ester dye B) respectively. Illustrating photograph of the sample treated with maleimide dye, which is colorless C), while the one treated with NHS ester dye D) shows a bright yellow color. HPLC traces (UV detector signal at excitation maximum of dye) of PCys(SO<sub>2</sub>Et) before and after reaction with the maleimide dye E) and the succinimidyl ester dye respectively F).

*Chemoselective  
disulfide formation  
in PCys(SO<sub>2</sub>Et).*

Finally, the ability of PCys(SO<sub>2</sub>Et) to react with thiols in a post polymerization modification reaction was investigated. Therefore, benzylmercaptan was added immediately prior to the measurement to a solution of P1 and the reaction progress was monitored by <sup>1</sup>H NMR. The thiol was implemented in sufficient stoichiometric excess relative to the protected cysteine residues (see Supporting Information), to ensure a complete conversion of each cysteine side chain into the corresponding disulfide. The protective group readily engages in a nucleophilic reaction with the thiol, ultimately resulting in an asymmetric disulfide and the corresponding sulfinate (Figure 9.7 A) with quantitative conversion after 60 s. As can be noted in Figure 9.7 B and C, all peaks corresponding to the poly cysteine backbone and to the end group (*a-c, f*) remain present. Furthermore, signals in Figure 9.7 B originating from the benzyl group (*d'+e'*) as well as the free sulfinate (*4+5*) appear after conversion. Ultimately, a magnification in Figure 9.7 D reveals the complete disappearance of the polymer associated triplet of the *S*-ethylsulfonyl group (*e*, 1.30 ppm, being replaced by a triplet (5, 1.08 ppm) corresponding to the converted protective group.

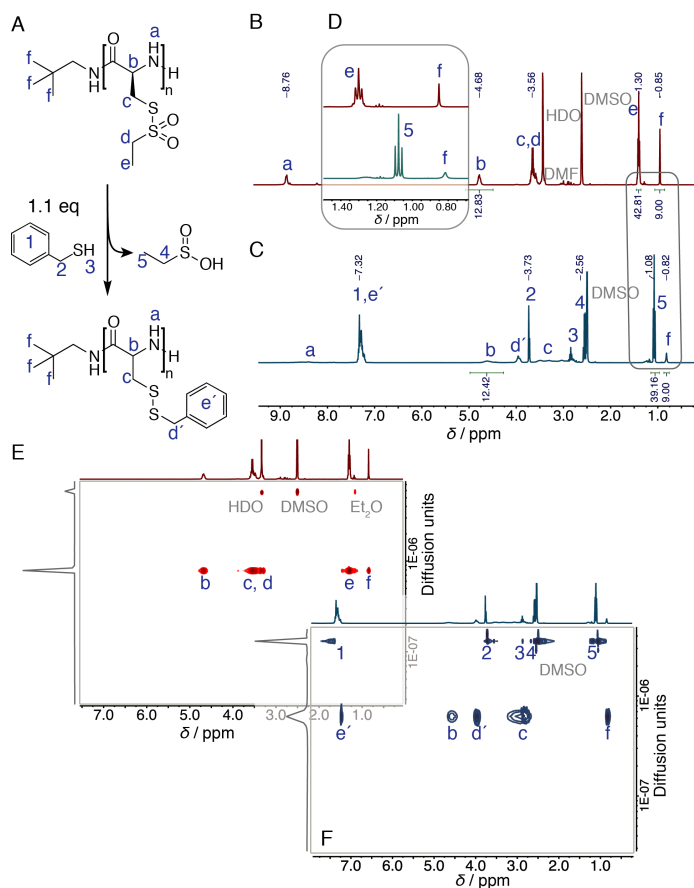


Figure 9.7: A) Scheme of the reaction of PCys(SO<sub>2</sub>Et) with benzylmercaptan. B) <sup>1</sup>H NMR spectrum of PCys(SO<sub>2</sub>Et) prior to conversion. C) <sup>1</sup>H NMR spectrum after conversion with benzylmercaptan. D) Enlarged comparison of both <sup>1</sup>H NMR spectra emphasizing the quantitative conversion (disappearance of polymer associated protective group signal at 1.30 ppm and emerging signal at 1.08 of the fully converted protective group). E) <sup>1</sup>H DOSY NMR spectrum of PCys(SO<sub>2</sub>Et) prior to conversion. F) <sup>1</sup>H DOSY NMR spectrum after conversion with benzylmercaptan showing one single diffusing polymeric species without signals corresponding to the protective group, but including signals of a benzyl group.

Additionally, the conjunction of the relevant signals to a polymeric species was confirmed by <sup>1</sup>H DOSY NMR experiments. Figure 9.7 E shows PCys(SO<sub>2</sub>Et) prior to the reaction. All signals annotated to PCys(SO<sub>2</sub>Et) exhibit identical diffusion traces (b–f). Signals corresponding to low molecular weight compounds (such as solvents) diffuse cumulated above. Once the reaction with the thiol is conducted (Figure 9.7 F), signals annotated the protective group at the polymer are absent, being replaced by a low molecular weight species corresponding to the reacted protective group (4, 5). Signals corresponding to a benzyl group (d', e') are present in line with those from the backbone (b, c) and the end group (f), confirming a single diffusing, polymeric species. Therefore, poly(S-ethylsulfanyl-L-cysteine) proved to be capable of direct disulfide formation providing access to a novel class of reactive polypeptides

### 9.3 CONCLUSION

We have presented the ring-opening polymerization of the novel *S*-ethylsulfonyl-L-cysteine NCA which is, under optimized polymerization conditions, a well-controlled process without side reactions. At  $-10\text{ }^{\circ}\text{C}$  the polymerization proceeds faster in comparison to higher temperatures, with rate constants at  $k = 10\text{--}11 \times 10^{-4}\text{ L mol}^{-1}\text{ s}^{-1}$ . The *S*-ethylsulfonyl-L-cysteine homo- polymers exhibit a  $\beta$ -sheet conformation in solid phase as well as in solution, thus they tend to form aggregates at degrees of polymerization above 30. The polymers are fully stable at neutral and acidic pH and react directly with thiols in one simple post polymerization modification reaction, leading to disulfide-modified poly-L-cysteines. This new class of activated cysteine polymers possesses high potential for biomedical applications, since the generated disulfides are cleavable in the reductive intracellular environment. Exploiting this process will allow the reversible conjugation of drugs as well as reversible cross-linking of nanostructures. Combined with a hydrophilic block, for example polypept(o)ides,<sup>[26,59,70]</sup> poly(*S*-ethylsulfonyl-L-cysteine) is expected to lead to a new, promising class of polypeptidic nanomaterials.

### 9.4 ACKNOWLEDGMENTS

The SFB 1066 is acknowledged for financial support. D. Huesmann would like to acknowledge support by the "Verband der Chemischen Industrie" (VCI) and the "Max Planck Graduate Center with the Johannes Gutenberg-Universität Mainz" (MPGC). O.S. acknowledges support by the "Evangelisches Studienwerk e.V. Villigst". We would like to thank Dr. D. Schollmeyer for X-ray crystal structure analysis and S. Türk for MALDI-TOF measurements.

## 9.5 SUPPORTING INFORMATION

9.5.1 *Materials and Instrumentation*

n-Hexane was distilled from Na/K and ethyl acetate from CaH<sub>2</sub>. DMF was purchased from Acros and dried over BaO and molecular sieve (3 Å), fractionally distilled in vacuo at 20 °C and stored at -80 °C under exclusion of light. Prior to use, *N,N*-dimethyl formamide (DMF) was degassed in vacuo to remove traces of dimethylamine. Millipore water was prepared by a MILLI-Q® Reference A+ System. Neopentylamine was purchased from TCI Europe and was dried over NaOH and fractionally distilled before use. Cysteine was purchased from OPREGEN and used as received and diphosgene was purchased from Alfa Aesar. Deuterated solvents were purchased from Deutero GmbH and hexafluoro 2-propanol (HFIP) from Fluorochem. Other chemicals were purchased from Sigma-Aldrich and used as received unless otherwise stated.

<sup>1</sup>H, <sup>19</sup>F and <sup>13</sup>C nuclear magnetic resonance (NMR) spectra were recorded on a Bruker AC 400 at a frequency of 400, 376 and 101 MHz, respectively. <sup>1</sup>H and <sup>19</sup>F NMR spectra were also recorded on a Bruker Avance III HD 300 at 300 and 282 MHz, respectively. Two-dimensional NMR spectra as <sup>1</sup>H diffusion ordered spectroscopy (DOSY), correlation spectroscopy (COSY) and heteronuclear single-quantum correlation spectroscopy (HSQC) were recorded on a Bruker Avance III HD 400 at 400 MHz. All spectra were recorded at room temperature (25 °C) and calibrated using the solvent signals.<sup>[376]</sup> Melting points were measured using a Mettler FP62 melting point apparatus at a heating rate of 5 °C min<sup>-1</sup>. Electrospray ionization mass spectrometry (ESI-MS) was performed on a Micromass Q-TOF-Ultima spectrometer and gel permeation chromatography (GPC) was performed with HFIP containing 3 g l<sup>-1</sup> potassium trifluoroacetate (KTFA) as eluent at 40 °C and a flow rate of 0.8 ml min<sup>-1</sup>. The columns were packed with modified silica (PFG columns particle size: 7 μm, porosity: 100 Å and 1000 Å). Polymethyl methacrylate PMMA standards (Polymer Standards Services GmbH) were used for calibration and toluene was used as internal standard. A refractive index detector (G1362A RID) and an UV/Vis detector (at 230 nm unless otherwise stated; Jasco UV-2075 Plus) were used for polymer detection.

Matrix assisted laser desorption ionization time of flight (MALDI-TOF) mass spectra<sup>[397]</sup> were recorded using a Bruker Reflex II MALDI-TOF mass spectrometer equipped with a 337 nm N<sub>2</sub> laser. Acceleration of the ions was performed with pulsed ion extraction (PIE, Bruker) at a voltage of 20 kV. The analyzer was operated in reflection mode and a microchannel plate detector was used. Mass spectra were processed by the X-TOF 5.1.0 software (Bruker). A solvent free sample preparation was performed using *trans*-2-[3-(4-*tert*butylphenyl)-2-methyl-2-propenylidene]malononitrile DCTB as the matrix and sodium trifluoroacetate NaTFA as the cationizing salt. Calibration was carried out using a C<sub>60</sub>/C<sub>70</sub> fullerene mixture. Spectra were analyzed and simulated using



mMass. IR spectroscopy was performed on a Jasco FT/IR- 4100 with an ATR sampling accessory (MIRacle, Pike Technologies) and Spectra Manager 2.0 (Jasco) was used for integration.

Circular dichroism (CD) spectroscopy was performed on a Jasco J-815 spectrometer at room temperature and Spectra Manager 2.0 (Jasco) was used to analyze the spectra. A cell with a path length of 1 mm was used. Spectra were recorded at a concentration of 0.5 mg ml<sup>-1</sup> polymer in HFIP containing 3 g l<sup>-1</sup> KTEA.  $\theta$  was calculated using Equation 15 with  $M_{\text{Repeating Unit}} = 195.00 \text{ g mol}^{-1}$ ,  $c_M = 0.1 \text{ g l}^{-1}$  and  $l = 0.1 \text{ cm}$  for Cys(SO<sub>2</sub>Et).

$$\theta_{\text{MR}} = \frac{\theta \cdot M_{\text{Repeating Unit}}}{10 \cdot c_M \cdot l} \text{ deg cm}^2 \text{ dmol}^{-1} \quad (15)$$

### 9.5.2 Synthetic Procedures

#### *Synthesis of ethanesulfinic acid sodium salt*

A solution of sodium sulfite (391.98 g, 3.11 mol) in water (800 mL) was heated to 80 °C. Ethanesulfonyl chloride (147.40 mL, 199.30 g, 1.55 mol) and sodium carbonate (329.63 g, 3.11 mol) were added simultaneously while significant quantities of CO<sub>2</sub> evolved. The reaction mixture was stirred for one hour at 80 °C, afterwards water was removed *in vacuo* at 60 °C. The resulting solid was suspended in methanol and filtered. Evaporation of methanol gave ethanesulfinic acid sodium salt (153.54 g, 1.32 mol, 85 %) as a colorless solid.

<sup>1</sup>H NMR (400 MHz, DMSO-*d*<sub>6</sub>)  $\delta$  [ppm] = 1.79 (q, <sup>3</sup>J<sub>H,H</sub> = 7.6 Hz, 2H, -CH<sub>2</sub>-), 0.90 (t, <sup>3</sup>J<sub>H,H</sub> = 7.6 Hz, 3H, -CH<sub>3</sub>).

#### *Synthesis of S-ethylsulfonyl-L-cysteine (Cys(SO<sub>2</sub>Et))<sup>[173]</sup>*

An ice-cold solution of sodium nitrite (5.94 g, 86 mmol) in degassed water (45 mL) was slowly added to a stirred solution of L-cysteine hydrochloride (13.57 g, 86 mmol) in previously degassed 2N HCl (90 mL) at 0 °C. After 1 h, ethanesulfinic acid sodium salt (20.00 g, 172 mmol) was added to the deep red solution and was stirred for 2 h. Additional sodium ethanesulfinate (5.00 g, 43 mmol) was added and eventually a colorless solid precipitated. The reaction mixture was stirred at 0 °C overnight. The precipitate was filtered off and the pH of the colorless filtrate was adjusted with 2N NaOH to pH 4-5, resulting in additional colorless solid precipitating. The filtrate was allowed to stand at 4 °C until precipitation was complete. The combined precipitates were washed with MeOH to remove residual sulfinate and dried *in vacuo* yielding Cys(SO<sub>2</sub>Et) (5.03 g, 24 mmol, 27 %) as a colorless, crystalline solid.

Crystal Structure (CCDC-1440861): colorless platelet from H<sub>2</sub>O (0.026 × 0.280 × 0.550 mm), monoclinic space group P 2<sub>1</sub>, refinement: wR2 = 0.1223 (R1 = 0.0467 for observed reflections, 0.0509 for all reflections), flack parameter  $x = -01(1)$ , crystal structure contains two independent molecules with slightly different conformations.



$^1\text{H}$  NMR (400 MHz, DMSO- $d_6$ / TFA- $d$ )  $\delta$  [ppm] = 4.34 (t,  $^3J_{\text{H,H}} = 6.4$  Hz,  $^3J_{\text{H,H}} = 6.0$  Hz, 1H,  $\alpha$ -H), 3.66 (dd,  $^2J_{\text{H,H}} = 14.4$  Hz,  $^3J_{\text{H,H}} = 6.0$  Hz, 1H, -CHH-S), 3.62 (q,  $J_{\text{H,H}} = 7.2$  Hz, 2H, -CH<sub>2</sub>-SO<sub>2</sub>), 3.53 (dd,  $^3J_{\text{H,H}} = 14.4$  Hz,  $^3J_{\text{H,H}} = 6.4$  Hz, 1H, -CHH-S), 1.30 (t,  $^3J_{\text{H,H}} = 7.2$  Hz, 3H, -CH<sub>3</sub>).

$^{13}\text{C}$  NMR (101 MHz, DMSO- $d_6$ / TFA- $d$ )  $\delta$  [ppm] = 168.88 (-COO), 56.27 (-CH<sub>2</sub>SO<sub>2</sub>), 51.84 (-CHN), 34.79 (-CH<sub>2</sub>S), 8.30 (-CH<sub>3</sub>).

ESI-MS:  $m/z = 214.03$  [M+H]<sup>+</sup>, (calc. 213.28 g mol<sup>-1</sup>); 236.01 [M+Na]<sup>+</sup>, (calc. 236.15 g mol<sup>-1</sup>).

*Synthesis of S-ethylsulfonyl-L-cysteine N-carboxyanhydride*  
(Cys(SO<sub>2</sub>Et) NCA)<sup>[173]</sup>

Dried Cys(SO<sub>2</sub>Et) (7.00 g, 32.82 mmol) was suspended in absolute THF (100 mL) and heated to 70 °C. Diphosgene (3.60 mL, 5.84 g, 29.52 mmol) was slowly added and the suspension was heated for an additional 4 h. Dry nitrogen was bubbled through the reaction mixture overnight into a gas washing bottle with an aqueous KOH solution to remove excess diphosgene, HCl and most of the solvent. The remaining solvent was removed *in vacuo* and the residue was dissolved in 100 mL absolute ethyl acetate. Any insoluble compounds were removed by filtration avoiding contact with air and the NCA was precipitated by adding 800 mL absolute hexane. The recrystallization of the product was repeated two more times yielding Cys(SO<sub>2</sub>Et) NCA (6.43 g, 26.87 mmol, 82%) as a colorless, crystalline powder (m.p. 113-115 °C).

$^1\text{H}$  NMR (400 MHz, DMSO- $d_6$ )  $\delta$  [ppm] = 9.32 (s, 1H, -NHCO), 4.86 (td,  $^3J_{\text{H,H}} = 6.0$  Hz,  $^3J_{\text{H,H}} = 4.8$  Hz,  $^3J_{\text{H,H}} = 1.6$  Hz, 1H,  $\alpha$ -H), 3.64 (dd,  $^2J_{\text{H,H}} = 14.4$  Hz,  $^3J_{\text{H,H}} = 4.8$  Hz, 1H, -CHH-S), 3.62 (q,  $^3J_{\text{H,H}} = 7.2$  Hz, 2H, -CH<sub>2</sub>-SO<sub>2</sub>), 3.57 (dd,  $^2J_{\text{H,H}} = 14.4$  Hz,  $^3J_{\text{H,H}} = 6.4$  Hz, 1H, -CHH-S), 1.29 (t,  $^3J_{\text{H,H}} = 7.2$  Hz, 3H, -CH<sub>3</sub>).

$^{13}\text{C}$  NMR (101 MHz, DMSO- $d_6$ )  $\delta$  [ppm] = 169.58 (CNOO), 151.68 (-COO), 56.99 (-CHSO<sub>2</sub>), 56.16 (-CHN), 36.00 (-CH<sub>2</sub>S), 8.24 (-CH<sub>3</sub>).

*Ring-Opening Polymerization of poly(S-ethylsulfonyl-L-cysteine) (PCys(SO<sub>2</sub>Et))*

Cys(SO<sub>2</sub>Et) NCA (107 mg, 447  $\mu\text{mol}$ ) was transferred into a Schlenk tube under dry nitrogen counter flow. Absolute DMF (3 mL) and absolute neopentylamine (1.74  $\mu\text{L}$ , 1.30 mg, 15  $\mu\text{mol}$ ) were added and the vessel was cooled to -10 °C. A steady flow of dry nitrogen was sustained during the polymerization, preventing any impurities from entering the Schlenk tube, while ensuring the escape of produced CO<sub>2</sub>. The progress of the polymerization was monitored via IR spectroscopy by the disappearing NCA carbonyl peaks intensities at 1858 cm<sup>-1</sup> and 1788 cm<sup>-1</sup>. Samples were taken using a nitrogen flushed syringe through a septum. The polymer was precipitated after 70 % conversion in a mixture of cold diethyl ether and tetrahydrofuran (THF) (5:1 v/v) to solubilize and remove remaining NCA. The suspension was centrifuged (4500 rpm, 15 min, 0-10 °C) and decanted. This procedure was repeated twice concluding with pure diethyl ether yielding poly(S-ethylsulfonyl-L-cysteine) (65 mg, 73 %) as a colorless to slightly yellow solid.

$^1\text{H}$  NMR (400 MHz,  $\text{DMSO-}d_6$ )  $\delta$  [ppm] = 8.76 (m, 1nH,  $-\text{NHCO}$ ), 4.68 (m, 1nH,  $\alpha\text{-H}$ ), 3.63-3.42 (m, 4nH,  $-\text{CH}_2\text{-SSO}_2\text{-CH}_2\text{-}$ ), 1.30 (t, 3nH,  $-\text{CH}_3$ ), 0.85 (s, 9H,  $-(\text{CH}_3)_3$ ).

#### *Labeling with Fluorescein Diacetate 5-Maleimide*

$\text{PCys}(\text{SO}_2\text{Et})$  was dissolved in HFIP (1 mL) containing potassium trifluoroacetate ( $3\text{ g l}^{-1}$  KTFA). One equivalent (for each cysteine side chain) of fluorescein diacetate-5-maleimide was added and the mixture was stirred at room temperature for 1 day under exclusion of light. Characterization was carried out by HFIP GPC at with the UV detector set at  $\lambda = 492\text{ nm}$ . The UV signals were normalized using the RI signal, to exclude signal strength variation due to differences in concentration.

#### *Labeling with Oregon Green 488-X, Succinimidyl Ester*

$\text{PCys}(\text{SO}_2\text{Et})_{13}$  (1.10 mg) was dissolved in dry DMF 450 ( $\mu\text{L}$ ). Oregon Green 488-X succinimidylester (2.09 mg, 7.7 eq. per  $\text{NH}_2$  end group) in dry DMF (50  $\mu\text{L}$ ) was added. The dye solution was added under nitrogen and the reaction was stirred for 3 days at room temperature under exclusion of light. The polymer was then precipitated in cold diethyl ether followed by the usual work-up yielding a yellow solid. Free dye was removed by collecting fractions at the GPC outlet. The polymer was characterized by HFIP GPC at with the UV detector set at  $\lambda = 496\text{ nm}$ . The UV signals were normalized using the RI signal, to exclude signal strength variation due to differences in concentration.

#### *Thiol-Reactivity*

To investigate the ability of  $\text{PCys}(\text{SO}_2\text{Et})$  to react with thiols in a post polymerization modification reaction, a mixture of  $\text{PCys}(\text{SO}_2\text{Et})$  and benzylmercaptan in  $\text{DMSO-}d_6$  were observed by  $^1\text{H}$  NMR. Therefore  $\text{PCys}(\text{SO}_2\text{Et})_{13}$  (**P1**, 7.30 mg, 1.0 eq.) was dissolved in  $\text{DMSO-}d_6$  (0.7 mL) and benzylmercaptan (4.94 mg, 1.1 eq. in respect to  $X_n$  Cys) was added immediately prior to the measurement. The disappearance of the  $\text{CH}_3$  signal from the  $\text{SO}_2\text{Et}$  group was used to monitor the conversion. Additionally, the conjunction of the relevant signals to a polymeric species was confirmed by  $^1\text{H}$  DOSY NMR experiments.

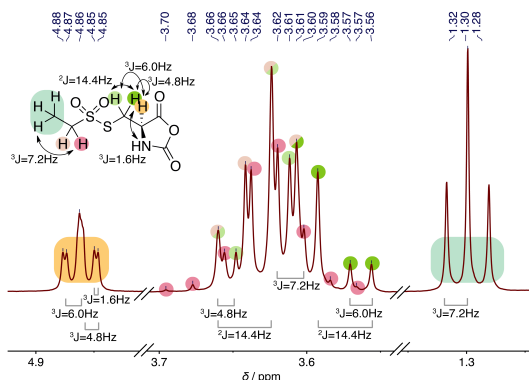
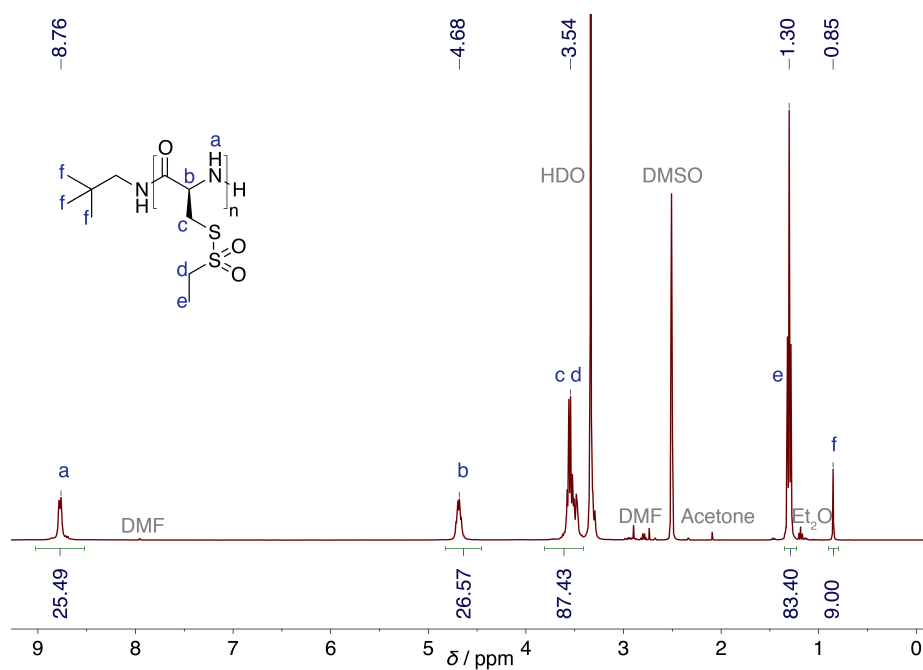
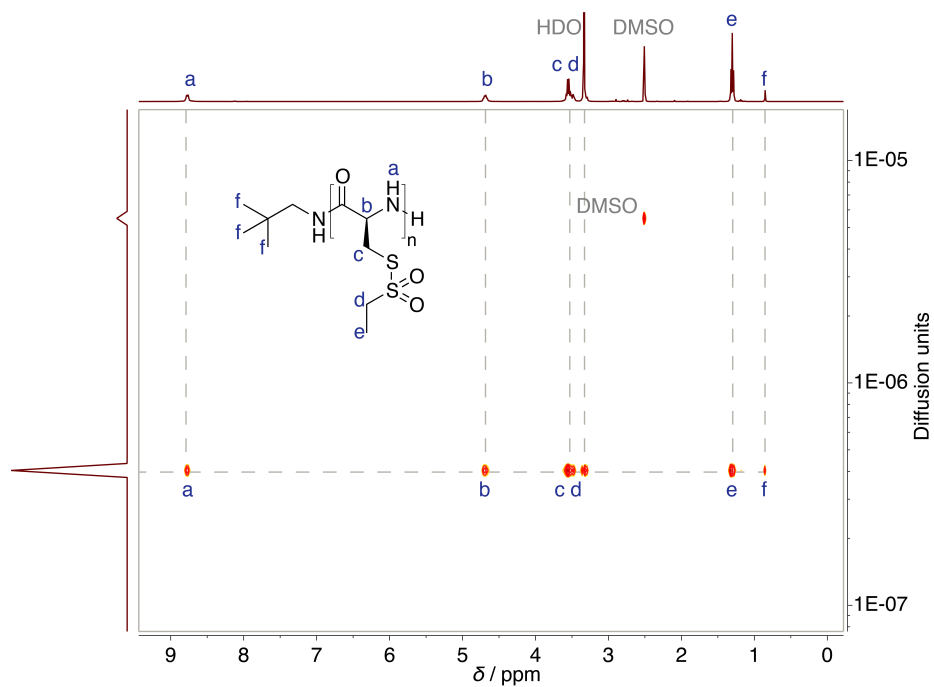
9.5.3 NMR Analysis of Cys(SO<sub>2</sub>Et) NCA

Figure 9.8: <sup>1</sup>H NMR of Cys(SO<sub>2</sub>Et) NCA with assignments and coupling constants.

Due to the rather complex <sup>1</sup>H NMR spin-spin coupling pattern of the Cys(SO<sub>2</sub>Et) NCA the signals overlap strongly. The assignment of the protons is given in Figure 9.8. The two methylene protons of the cysteine side chain (*green*) exhibit a large geminal proton-proton coupling constant of  $^2J_{\text{H,H}} = 14.4$  Hz and two different coupling constants to the  $\alpha$ -proton ( $^3J_{\text{H,H}} = 4.8$  Hz and  $^3J_{\text{H,H}} = 6.0$  Hz). For the  $\alpha$ -proton a long distance interaction between and the two protons of the methylene of the protective group can be observed. Thus, the signal of the  $\alpha$ -proton (*orange*) results in a doublet of doublets of doublets with the two coupling constants ( $^3J_{\text{H,H}} = 4.8$  Hz and  $^3J_{\text{H,H}} = 6.0$  Hz) to the methylene protons of the cysteine side chain (*green*) and a coupling constant of  $^6J_{\text{H,H}} = 1.6$  Hz to the methylene protons of the protective group (*pink*). The signal of the methyl group (*blue*) shows a triplet with a coupling constant of  $^3J_{\text{H,H}} = 7.2$  Hz which can again be found in the coupling pattern of the methylene protons of the protective group (*pink*).

9.5.4 NMR Analysis of PCys(SO<sub>2</sub>Et)Figure 9.9: <sup>1</sup>H NMR of PCys(SO<sub>2</sub>Et) with assignments (in DMSO-*d*<sub>6</sub>).Figure 9.10: hoch1H DOSY NMR of PCys(SO<sub>2</sub>Et) with assignments (in DMSO-*d*<sub>6</sub>) showing a single diffusing polymeric species.

### 9.5.5 GPC Analysis of PCys(SO<sub>2</sub>Et)

Upon higher molecular weight a complication in the analysis by HFIP-GPC related to  $\beta$ -sheet formation can be observed, as illustrated in ???. Above a  $X_n$  of 30 aggregation processes occur, as detected in HFIP-GPC, thus no reliable GPC characterization can be carried out for these polymers. However, a length of 30 repeating units of PCys(SO<sub>2</sub>Et) is sufficient for the desired applications as discussed.

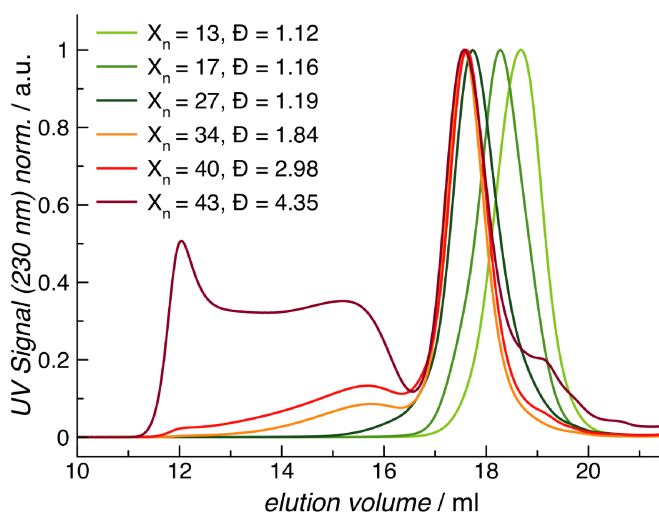


Figure 9.11: HFIP GPC of PCys(SO<sub>2</sub>Et) with different chain lengths below and above  $X_n$  of 30.

### 9.5.6 pH Stability

The stability of PCys(SO<sub>2</sub>Et) in acidic and alkaline media was evaluated with <sup>1</sup>H NMR. Therefore PCys(SO<sub>2</sub>Et) (7 mg) were dissolved in DMSO-*d*<sub>6</sub> (0.7 mL) and *ce*TFA-*d* or NaOD (40 wt% in D<sub>2</sub>O) were added to reach a pH of 4 or 10 respectively. Spectra were recorded after 10 min and 24 h and compared to a spectrum in pure in DMSO-*d*<sub>6</sub>.

As illustrated in Figure 9.12, the *S*-ethylsulfonyl group is removed when exposed to alkaline conditions. After 10 min PCys(SO<sub>2</sub>Et) associated signals (*a-f*) decreased significantly. Signals corresponding to the removed protective group in form of EtSO<sub>2</sub><sup>-</sup> (*I* and *II*) emerge. After 24 h no polymer signals can be detected. The free thiol group results in cross-linking, which caused precipitation and is responsible for the vanished polymer signals. Acidic to neutral conditions however do not affect the protective group of PCys(SO<sub>2</sub>Et). All polymer-associated signals remain intact and no free protective group can be seen. The only notable difference is the disappearance of the amide proton (*a*) after 24 h due to hydrogen-deuterium exchange.

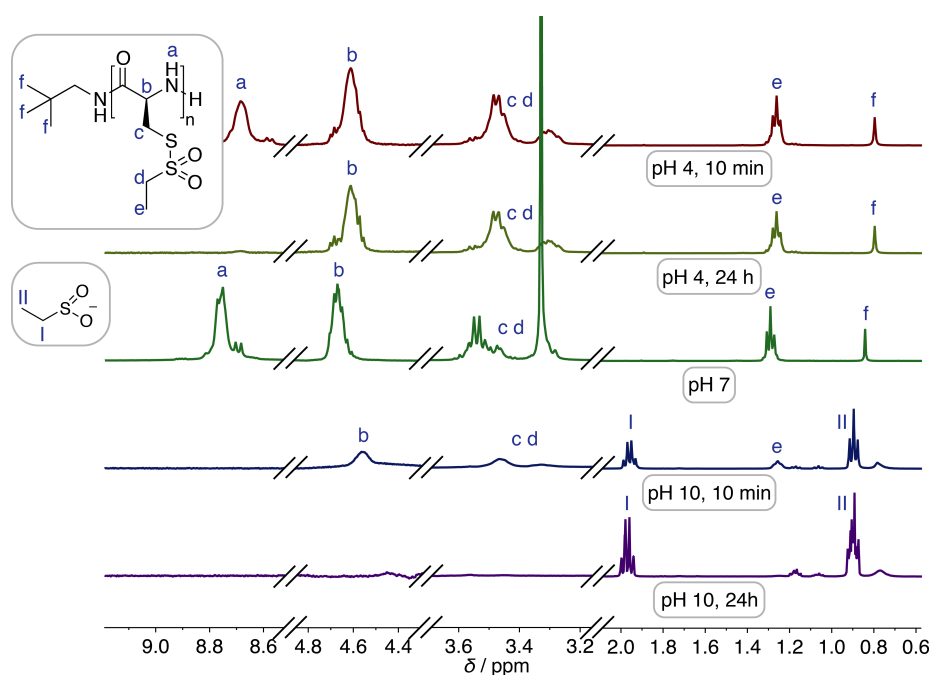


Figure 9.12: pH-Influence on PCys(SO<sub>2</sub>Et) as monitored by <sup>1</sup>H NMR in DMSO-*d*<sub>6</sub> (pH4: +TFA-*d*, pH10: +NaOD).

### 9.5.7 Kinetic Measurements

Polymerizations were analyzed over a period of 7 days while samples were taken using a nitrogen flushed syringe through a septum. The decreasing NCA carbonyl peaks at 1858 cm<sup>-1</sup> and 1788 cm<sup>-1</sup> were monitored and the integrals were correlated with the NCA concentration for kinetic evaluations. Polymerizations carried out at higher initial monomer concentrations exhibit the fastest rate constant (see Figure 9.4 C). However, aggregation of the growing chains is observed upon monomer concentrations above 0.80 mol/L resulting in gelation and thus termination. Derived from those findings, polymerizations of PCys(SO<sub>2</sub>Et) are conveniently conducted at concentrations around 0.40–0.60 mol/L without the issue of premature gelation. Further investigation of the kinetic behavior of the PCys(SO<sub>2</sub>Et) polymerization revealed, that lowering the reaction temperature resulted in faster polymerization. The rate constants increase from  $2.62 \times 10^{-4} \text{ L mol}^{-1} \text{ s}^{-1}$  (10 °C) to  $4.53 \times 10^{-4} \text{ L mol}^{-1} \text{ s}^{-1}$  (0 °C) and ultimately to  $10.95 \times 10^{-4} \text{ L mol}^{-1} \text{ s}^{-1}$  (-10 °C) (Figure 9.13 A). Thus, higher conversions were realized at low temperatures, indicating chain termination reactions at higher temperatures.

NCA polymerizations are known to be sensitive to side reactions and lowering the temperature results in a decrease of end group termination.<sup>[54,55]</sup> In the case of PCys(SO<sub>2</sub>Et), the controlled fashion of polymerizations at -10 °C is lost at 0 °C or above. To underline this finding, the polymerizations of PCys(SO<sub>2</sub>Et) carried out at different temperatures were compared using HFIP GPC (?? B). Having the same monomer

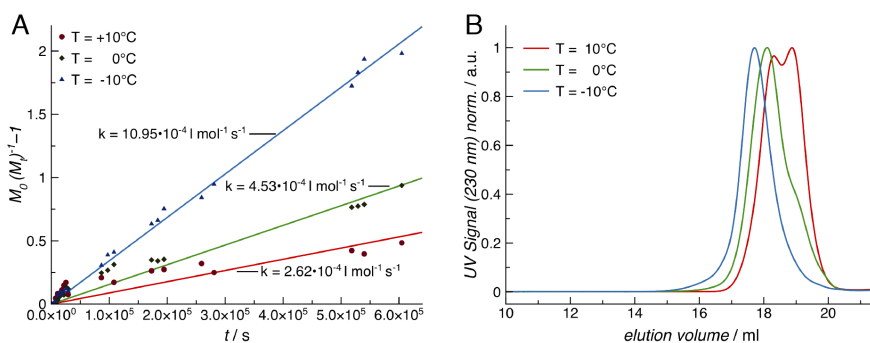


Figure 9.13: A Kinetic plots and B HFIP GPC traces of PCys(SO<sub>2</sub>Et) polymerizations at different temperatures (M/I = 50).

to initiator ratio, the polymer synthesized at  $-10^\circ\text{C}$  reached the highest degree of polymerization ( $P_5$ ,  $X_n$  of 27), while exhibiting a narrow, symmetrical distribution ( $\bar{D} = 1.19$ ). The distribution broadens upon higher polymerization temperature. At  $0^\circ\text{C}$  a low molecular weight shoulder can be observed, at  $10^\circ\text{C}$  even a bimodal distribution. Thus, in order to maintain chain propagation in a controlled fashion and yielding well-defined polymers, polymerization at  $-10^\circ\text{C}$  is essential.

#### 9.5.8 Supplementary NMR Spectra of Cys(SO<sub>2</sub>Et) NCA

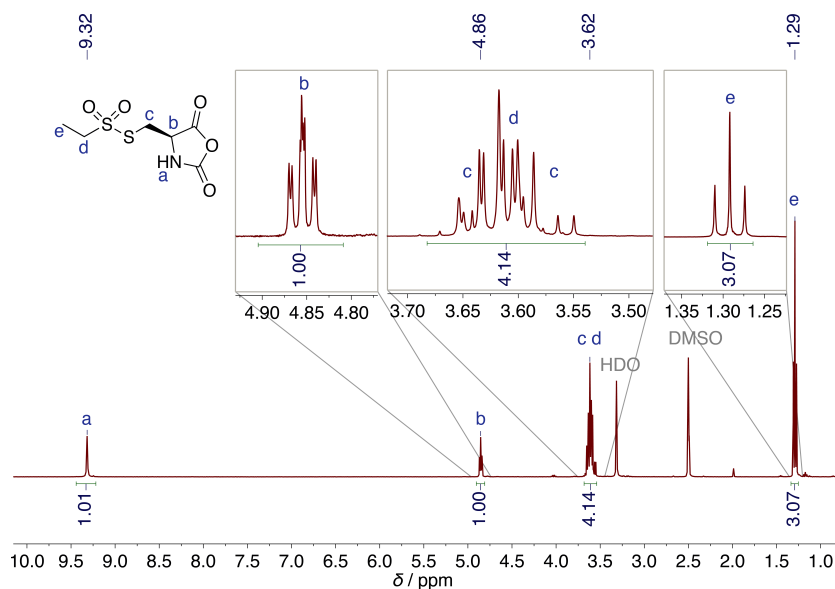
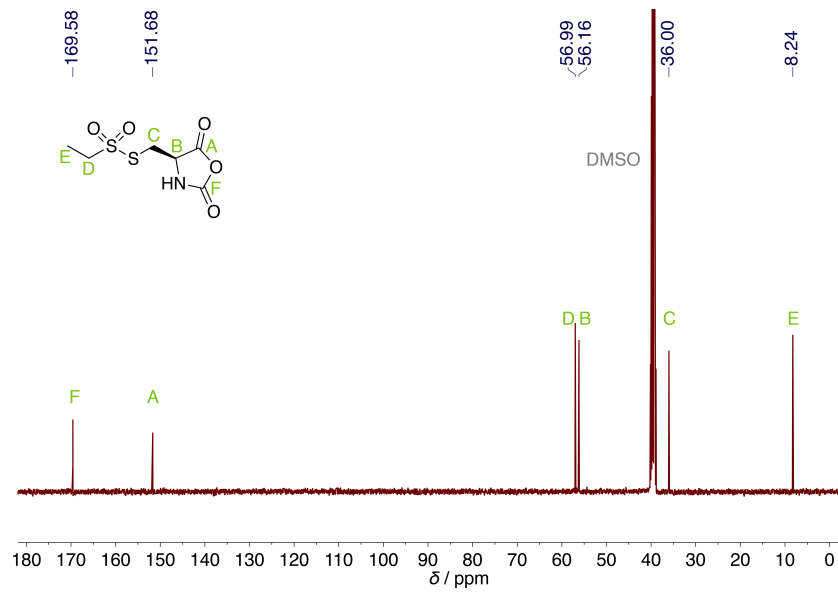
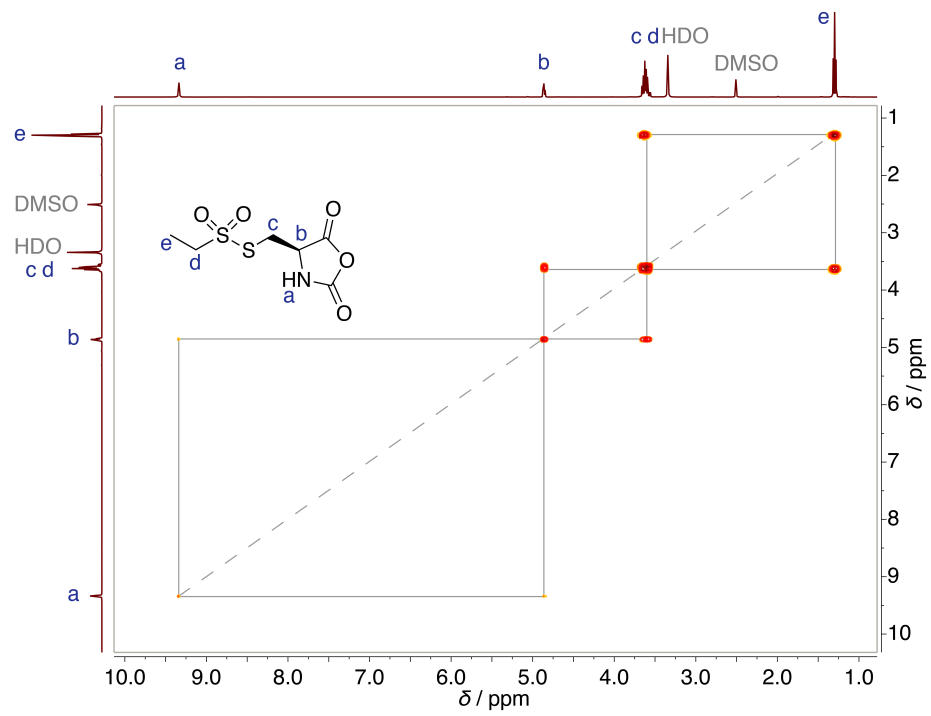
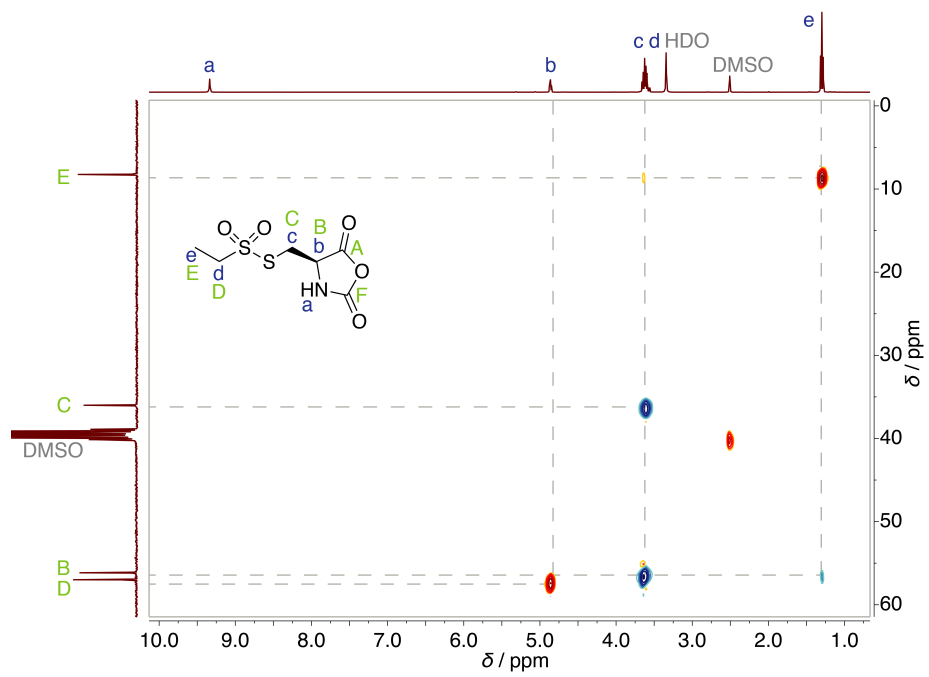


Figure 9.14: <sup>1</sup>H NMR spectrum of Cys(SO<sub>2</sub>Et) NCA

Figure 9.15:  $^{13}\text{C}$  NMR spectrum of  $\text{Cys}(\text{SO}_2\text{Et})$  NCAFigure 9.16: COSY NMR spectrum of  $\text{Cys}(\text{SO}_2\text{Et})$  NCA

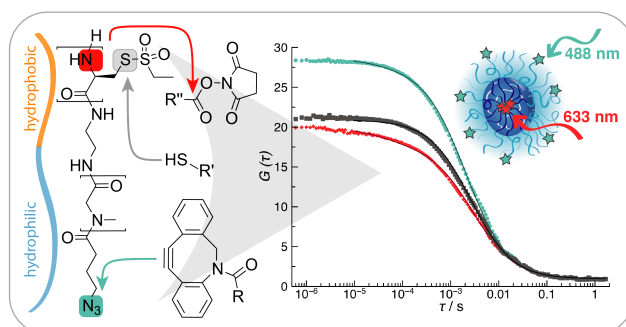


Figure 9.17: HSQC NMR spectrum of Cys(SO<sub>2</sub>Et) NCA



COMBINING ORTHOGONAL REACTIVE GROUPS  
IN BLOCK COPOLYMERS FOR FUNCTIONAL  
NANOPARTICLE SYNTHESIS IN A SINGLE STEP

Olga Schäfer\*, Kristina Klinker\*, Lydia Braun, David Huesmann, Jennifer Schultze, Kaloian Koynov, Matthias Barz, *ACS Macro Letters* 2017, 6, 1140-1145. (\*authors contributed equally)



**ABSTRACT:** We report on the synthesis of polysarcosine-*block*-poly-(*S*-alkylsulfonyl-L-cysteine) block copolymers, which combine three orthogonal addressable groups enabling site specific conversion of all reactive entities in a single step. The polymers are readily obtained by ring-opening polymerization (ROP) of corresponding  $\alpha$ -amino acid *N*-carboxyanhydrides (NCAs) combining azide and amine chain ends, with thiol-reactive *S*-alkylsulfonyl-L-cysteine side chains. Functional group interconversion of chain ends using strain-promoted azide-alkyne cycloaddition (SPAAC) and activated ester chemistry with NHS and DBCO-containing fluorescent dyes could be readily performed without affecting the cross-linking reaction between thiols and *S*-alkylsulfonyl protective groups. Eventually, all three functionalities can be combined in the formation of multifunctional disulfide core cross-linked nanoparticles bearing spatially separated functionalities. The simultaneous attachment of dyes in core and corona during the formation of core-cross-linked nanostructures with controlled morphology is confirmed by fluorescence cross-correlation spectroscopy (FCCS).

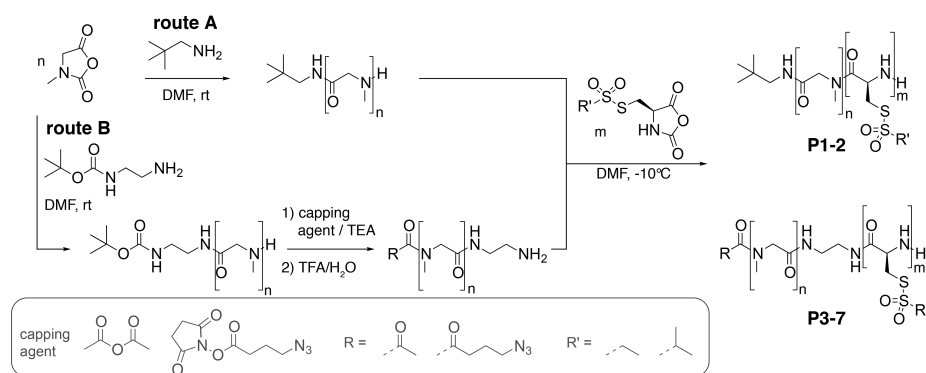
## 10.1 INTRODUCTION

Polymers bearing one or several different reactive functional groups are of great interest to create multifunctional polymeric architectures.<sup>[466–468]</sup> Telechelic polymers, i. e. , polymer chains with either the same (homotelechelic),<sup>[469–472]</sup> one (semitelechelic),<sup>[60,473–475]</sup> or two different functional end groups (heterotelechelic)<sup>[253,476–478]</sup> provide access to (multi)-block copolymers,<sup>[479]</sup> graft polymers,<sup>[480,481]</sup> miktoarm star polymers,<sup>[482]</sup> polymer–peptide<sup>[210,483–485]</sup> and polymer drug conjugates,<sup>[486]</sup> and functional building blocks for supramolecular chemistry.<sup>[487]</sup> They are accessible by a variety of different controlled polymerization methods like controlled radical polymerization (RAFT, ATRP) or ring-opening polymerization (ROMP, anionic and NCA ROP).<sup>[229]</sup> Additional reactive functional groups can be introduced through the copolymerization of functionalized monomers, but the incompatibility of many of these groups with a variety of polymerization conditions remains a considerable synthetic challenge. As building blocks in core-shell micellar aggregates, amphiphilic block copolymers that combine two or several spatially separated and orthogonally addressable reactive functional groups are highly valuable because spatial separation of functional groups in the core and corona is achieved.<sup>[488]</sup> While chain end functionalities can be used to introduce targeting moieties or fluorophores in a site-specific manner, side chain functionalities in the hydrophobic segment are relevant for drug attachment or core cross-linking of polymeric micelles. In this respect, reactive functional groups enabling bioreversible modifications are highly attractive.<sup>[153]</sup> By incorporating three orthogonally reactive functional groups into one block copolymer, multifunctional nanoparticles are accessible in a chemically very elegant manner.<sup>[489,490]</sup>

Polypept(o)ides (polypeptide-*block*-polysarcosine block copolymers) have emerged as promising materials for nanomedicines and are readily synthesized by controlled ring-opening polymerization (ROP) of the corresponding  $\alpha$ -amino acid *N*-carboxyanhydrides (NCAs). While the corona-forming PSar block provides stealth-like properties, the polypeptide segment creates a functional compartment for the drug or biomolecule encapsulation or attachment. Polypeptides represent particularly interesting core-forming blocks because of their high propensity to form secondary structures and their intrinsic side-chain-related stimuli responsiveness (pH, redox).<sup>[22,25]</sup> While side-chain reactivity of the functional polypeptide block is so far mostly limited to irreversible modifications, such as thiol-ene, CuAAC, or alkylation,<sup>[21,320]</sup> the recently developed *S*-alkylsulfonyl group for cysteine enables NCA synthesis and controlled polymerization, enabling thiol-selective asymmetric disulfide formation as a postpolymerization modification method.<sup>[173,209,321]</sup> In addition, the tendency for  $\beta$ -sheet formation of *S*-alkylsulfonylcysteine blocks enables morphology control by secondary structure-directed self-assembly.<sup>[22]</sup>

## 10.2 RESULTS AND DISCUSSION

In the present study, we have investigated the orthogonality of the thiol-reactive *S*-alkylsulfonyl group toward SPAAC and activated ester-mediated amidation to create multifunctional building blocks, which allow for the formation and functionalization for core-shell nanostructures in one step. For this purpose, we have synthesized trifunctional polysarcosine-*block*-poly(*S*-alkylsulfonyl-L-cysteine) (PSar-*b*-PCys(SO<sub>2</sub>R)) block copolymers bearing three orthogonally reactive groups by a macroinitiator approach.<sup>[61]</sup> They are incorporated as reactive chain ends either in the hydrophilic segment or result from the polymerization in the hydrophobic block. Incorporated in the latter, the *S*-alkylsulfonyl side chain provides an additional terminal functionality in the polycysteine segment. The synthesis of PSar<sub>n</sub>-*b*-PCys(SO<sub>2</sub>R)<sub>m</sub> block copolymers can in principle be accomplished by pursuing two different synthetic routes (see Scheme 10.1).



Scheme 10.1: Reaction scheme of PSar<sub>n</sub>-*b*-PCys(SO<sub>2</sub>R)<sub>m</sub> block copolymer synthesis using sequential polymerization (route A) or a bifunctional initiator (route B).

Route A involves standard sequential polymerization of sarcosine NCA (SarNCA) using neopentylamine or propargylamine as initiator. *S*-ethylsulfonyl-L-cysteine or *S*-isopropylsulfonyl-L-cysteine NCAs (Cys(SO<sub>2</sub>Et) or Cys(SO<sub>2</sub><sup>i</sup>Pr) NCAs) are then subsequently polymerized using PSar as macroinitiator. On the other hand, route B exploits *N*-boc-ethylenediamine as a bifunctional initiator. After polymerization of SarNCA, resulting macroinitiators can be functionally capped using, e. g. azide-containing capping agents (see Figure 10.4) before liberating the primary amine for polymerization upon deprotection using TFA/H<sub>2</sub>O (see Figure 10.5). The fundamental difference of the presented synthetic routes constitutes the chemical nature of the initiating species. For route A, a secondary amine initiates polymerization of Cys(SO<sub>2</sub>R) NCAs, whereas for route B, the initiating species is a primary amine. Since the *S*-alkylsulfonyl group exhibits reduced stability toward species with enhanced basic character, the temperature during initiation needs to be meticulously controlled. At -10 °C, this is the case, and well-defined block copolymers result for both synthetic approaches as summarized

*Synthesis of  
PSar-block-PCys(SO<sub>2</sub>R)  
block copolymers.*

for different monomer-to-initiator (M/I) ratios and monomer combinations (Cys(SO<sub>2</sub>Et) or Cys(SO<sub>2</sub><sup>i</sup>Pr) NCA in Table 10.1) (see Figure 10.6-10.9 for <sup>1</sup>H NMR characterization). Block copolymers with comparably low dispersities ( $\bar{D}$  = 1.2–1.3) and monomodal molecular weight distributions are obtained by hexafluoro 2-propanol (HFIP) gel permeation chromatography (GPC), considering the presence of polypeptides in different secondary structures (random coil and  $\beta$ -sheet).<sup>[24]</sup> Figure 10.1 A exemplarily displays the GPC elugram of P3 and its precursor bifunctional PSar macroinitiator. The shift toward lower elution volumes indicates successful chain extension upon block copolymerization. Moreover, the observation of only one diffusing species in <sup>1</sup>HDOSY-NMR further supports the results obtained by GPC (see Figure 10.1 B).

Table 10.1: Characterization of block copolymers.

No.	macro-initiator	2 <sup>nd</sup> NCA	$n : m^a$	$M_n^b / \text{g mol}^{-1}$	$\bar{D}^b$	end groups
P1	PSar	Cys(SO <sub>2</sub> Et)	104/8	27260	1.2	NA <sup>c</sup> /NH <sub>2</sub>
P2	PSar	Cys(SO <sub>2</sub> <sup>i</sup> Pr)	104/8	30480	1.3	NA <sup>c</sup> /NH <sub>2</sub>
P3	bi PSar	Cys(SO <sub>2</sub> Et)	320/21	32170	1.3	Ac/NH <sub>2</sub>
P4	bi PSar	Cys(SO <sub>2</sub> <sup>i</sup> Pr)	425/23	32550	1.3	Ac/NH <sub>2</sub>
P5	bi PSar	Cys(SO <sub>2</sub> Et)	69/8	22480	1.2	N <sub>3</sub> /NH <sub>2</sub>
P6	bi PSar	Cys(SO <sub>2</sub> Et)	382/12	32900	1.3	Ac/NH <sub>2</sub>
P7	bi PSar	Cys(SO <sub>2</sub> Et)	310/12	32230	1.2	N <sub>3</sub> /NH <sub>2</sub>

<sup>a</sup> Determined by <sup>1</sup>H NMR in DMSO-*d*<sub>6</sub>.

<sup>b</sup> Determined by GPC in HFIP relative to PMMA standards.

<sup>c</sup> NA = neopentylamine

While under controlled polymerization conditions, sequential polymerization seems straightforward from a synthesis point of view, the approach is not as modular and, therefore, as versatile as the bifunctional initiator approach. During the capping step, not only azide-containing but also other functionalities (here shown with simple acetylation to reinforce the “stealth” character of PSar) can be introduced into the PSar macroinitiator without the need of synthesizing a new functional macroinitiator each time. Certainly, route A does also offer the possibility to use functional initiators instead of neopentylamine, and initiator functionalities have been shown to be incorporated with high end group integrity.<sup>[25]</sup> Unfortunately, polymer chain lengths cannot always be reliably determined due to a lack of distinct chain end group signals detectable in <sup>1</sup>H NMR. Accordingly, trifunctional block copolymers with an azide and a primary amine end group as well as *S*-alkylsulfonyl side chains were obtained by following synthetic route B (bifunctional initiator) and employing azide-containing capping agents.

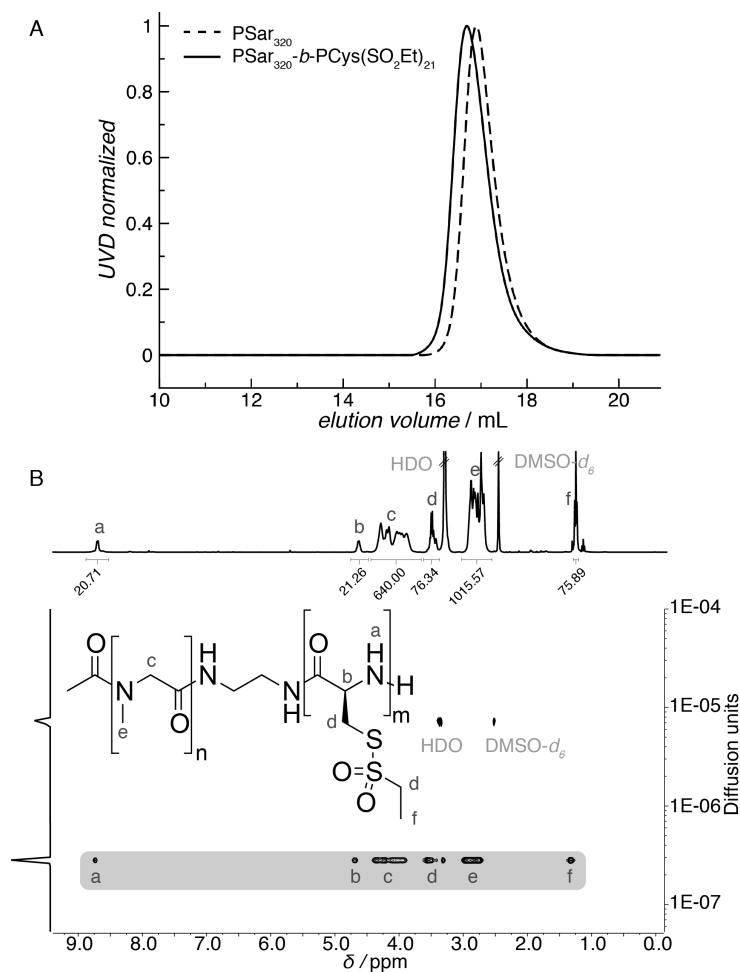


Figure 10.1: Characterization of **P3**: A) GPC elugrams in HFIP of the macroinitiator and the resulting block copolypept(o)ide **P3** after polymerization with Cys(SO<sub>2</sub>Et) NCA and B) <sup>1</sup>H NMR and <sup>1</sup>H DOSY NMR spectrum in DMSO-*d*<sub>6</sub> of **P3**, indicating only one diffusing species with a uniform diffusion coefficient.

To verify if the incorporated functional groups were indeed orthogonal to each other, their reactivity was separately addressed using their respective reactive counterparts (see Figure 10.2 A). While azide functionality readily undergoes cycloaddition reactions with alkynes in the presence of copper(I) (copper-catalyzed alkyne azide cycloaddition (CuAAC)) or cyclooctynes (SPAAC), the primary amine readily forms amide bonds using activated ester derivatives. The *S*-ethylsulfonyl group is reactive toward thiols (see Scheme 10.2). Polymer **P5** was chosen as a model system, and labeling was performed with either DBCO-carboxyrhodamine 110 (DBCO-CR110) or Alexa Fluor 647-NHS ester (AF647-NHS), and the resulting labeled block copolymers were analyzed by GPC in HFIP (see Figure 10.2 B). UV detection at 495 nm (CR110) and 600 nm (AF647), respectively, confirmed qualitatively covalent fluorophore attachment. Detection at 230 nm was performed to ensure that the detected peak was indeed of polymer origin. Furthermore, the *S*-ethylsulfonyl group remained stable under the applied labeling condition. Cross-linking was

*End-group conversion combined with side-chain reactivity.*

not observed, which would result in an additional peak at lower elution volumes, and  $^1\text{H}$  NMR measurements confirmed the presence of the intact protective group (see Figure 10.10 and 10.11). The presence of the respective dyes was further confirmed using UV-Vis spectroscopy (see Figure 10.12).

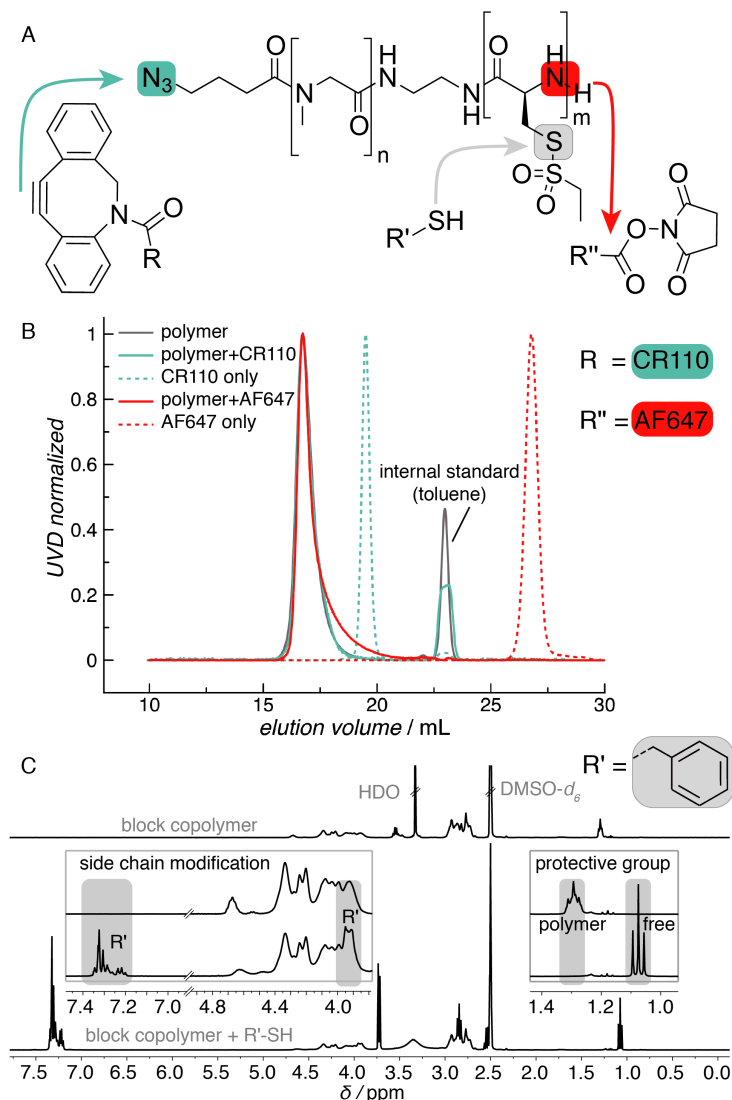


Figure 10.2: A) Synthetic scheme of  $\text{PSAr}_n\text{-}b\text{-PCys(SO}_2\text{R)}_m$  end group conversion with NHS-AF647 and DBCO-CR110 fluorophores, respectively, and thiol-reactivity of the *S*-ethylsulfonyl group in the side chain. B) GPC elugrams in HFIP after conversion and purification, indicating successful fluorophore labeling (UV detection at 230 nm (gray), 495 nm (green), and 600 nm (red), respectively). C) Thiol conversion as monitored by  $^1\text{H}$  NMR showing full conversion of the protective group to the asymmetric disulfide.

To ascertain that the *S*-alkylsulfonyl group is, however, still reactive toward thiols, block copolymers were reacted with benzylmercaptan in  $\text{DMSO-}d_6$ , and the reaction was monitored by  $^1\text{H}$  NMR (see Figure 10.2 C and Figure 10.14 and 10.15). Fast and selective conversion of thi-



ols with the *S*-alkylsulfonyl group was observed, identical to the reports on the protected amino acid and on neopentylamine-initiated homopolymers.<sup>[173,209]</sup> It can be concluded from these results that both chain end functionalities can be selectively addressed using their reactive counterparts without affecting the *S*-alkylsulfonyl group under the experimental conditions applied. This marks these trifunctional block copolymers as ideal building blocks to create functional core-shell nanostructures in one step.

Consequently, we exploited the tendency for microphase separation of amphiphilic PSar-*b*-PCys(SO<sub>2</sub>R) block copolymers to evaluate the three functionalities in a combined approach. We have recently reported on the self-assembly behavior of these reactive block copolymers, which can be deliberately manipulated by exploiting secondary structure formation of the polycysteine segment, thus controlling size and morphology.<sup>[22]</sup> The thiol-reactivity of the *S*-alkylsulfonyl group further enables bioreversible core cross-linking and complete decoupling of aggregate formation from function. With respect to the present approach, the azide functionality is located at the end of the PSar block and thus will be presented on the corona of core-shell nanoparticles. The amine end group of the PCys(SO<sub>2</sub>Et) segment on the other hand will be situated in the nanoparticles core. This spatial separation is highly attractive for the formation of multifunctional core-shell systems. It is of great value to be able to selectively address functionalities on the outside, e. g. for active targeting purposes, as well as on the inside of the particle, e. g. for fluorescent labeling for detection in *in vitro* and *in vivo* experiments.

For simplified analysis reasons, azide and amine block copolymer end groups were labeled with spectroscopically different dyes for detection in fluorescence cross-correlation spectroscopy (FCCS). PSar-*b*-PCys(SO<sub>2</sub>Et) block copolymers were self-assembled under controlled conditions using a solvent switch procedure in the presence of thiourea to suppress  $\beta$ -sheet formation of the polycysteine block as previously reported and core cross-linked using the dithiol triethylenetetramine  $\alpha,\omega$ -di(cysteine)-diamide (TETA), thus addressing side chain functionality (see SI).<sup>[22]</sup> Resulting core cross-linked micelles were labeled with DBCO-carboxy-rhodamine 110 (DBCO-CR110) and Cy5-NHS at respective polymer end groups as schematically illustrated in Figure 10.3 A. Labeling reactions were performed in phosphate buffered saline (PBS) (pH 8) for Cy5-NHS and H<sub>2</sub>O for DBCO-CR110. It should be noted here that we employed Cy5-NHS for functional particle modification instead of AF647-NHS, which is spectroscopically similar but bears the advantage of being less hydrophilic. This facilitates purification and is also more transferable for use in core crosslinked polymeric micelles with hydrophobic cores. The synthesis of functional nanoparticles was followed by repetitive spin filtration with ethanol and H<sub>2</sub>O to remove excess dye and cross-linker from the particles (see SI for particle preparation). Although labeling of polymer end groups can in principle be performed prior to self-assembly and cross-linking, it is preferential to form core cross-linked particles

*Spatial separated  
functionality in  
core-shell structures.*

first and accomplish the modification in one step to avoid any influence of the, e. g. dye polarity or steric demands on the self-assembly process.

After particle labeling with both dyes in a consecutive manner, samples were analyzed by dynamic light scattering (DLS). Figure 10.3 B shows intensity-weighted size distributions of polymeric micelles after cross-linking (unlabeled) and after sequential reaction with both dyes as well as single-labeled particles. As can be deduced from the very similar intensity-weighted size distributions obtained in all cases, hydrodynamic diameters ( $D_h$ ) and size distributions were not significantly affected by the labeling reaction. Moreover, the obtained results indicate that the labeling step is not significantly influenced by the order of dye addition, although a slight broadening of the size distribution is observed for CR110 first.

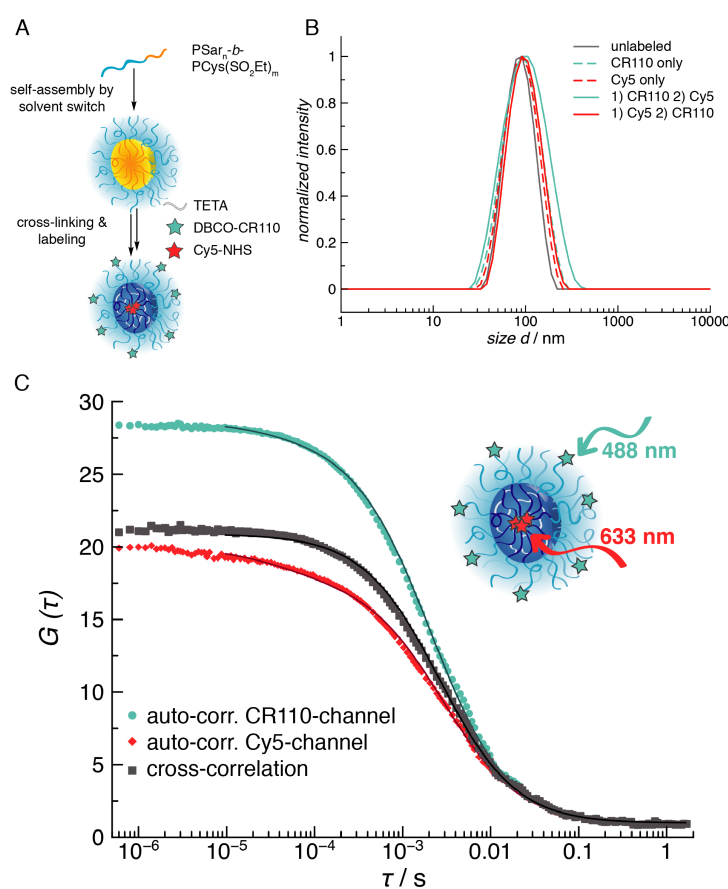


Figure 10.3: A) Amphiphilic trifunctional block copolymers are self-assembled into micelles, and orthogonal end groups as well as side-chain functionalities can be addressed subsequently by cross-linking with dithiol cross-linkers and labeling with DBCO-CR110/NHS-Cy5. B) DLS of cross-linked particles prior to and after labeling with one dye or both dyes, respectively. C) FCCS auto- and cross-correlation curves of dual labeled particles (1) Cy5 and (2) CR110, showing strong cross-correlation that confirms dual labeling.

To verify if the respective functionalization was effective for the two dyes in both the PS<sub>ar</sub> corona (CR110) and the PCys(SO<sub>2</sub>Et) core (Cy5), dual labeled particles were analyzed by FCCS. Typical auto- and cross-correlation curves are shown in Figure 10.3 C. The large amplitude of the cross-correlation curve  $G(0)$  is comparable to that of the autocorrelation curves, which implies that both dyes are attached to the core cross-linked particles (see Figure 10.3 C).<sup>[491]</sup> Interestingly, a slight dependence on the order of labeling was also noticed in FCCS. Cross-correlation was not as strong when particles were labeled with Cy5-NHS first (see Figure 10.13), which is presumably due to the fact that Cy5-NHS reacts with the primary amine functionality localized in the core of the micelle, whereas DBCO-CR110 converts with the azide attached to the corona-forming block. As a consequence, core labeling might be partially impeded, when CR110 is incorporated first.

*Evaluation by  
dual-color  
fluorescence  
cross-correlation  
spectroscopy.*

### 10.3 CONCLUSION

In conclusion, we have presented a versatile synthetic concept toward trifunctional PS<sub>ar</sub>-*b*-PCys(SO<sub>2</sub>R) block copolymers with independently addressable functional groups that are spatially separated from each other. Notably, the *S*-alkylsulfonyl group remains intact during functional group conversion of azide and amine chain end under the applied reaction conditions. These amphiphilic trifunctional block copolymers provide the basis to form functional core-shell nanostructures in a clean, simple, and versatile manner. While the *S*-alkylsulfonyl group provides stability by bioreversible core cross-linking, distinct reactive groups at polymer chain ends empower simultaneous introduction of functional moieties in the core and corona, e. g. pilot molecules for active targeting and fluorophores for detection, in one step.

### 10.4 ACKNOWLEDGMENTS

D.H. acknowledges support by the “Verband der Chemischen Industrie” (VCI) and the “Max Planck Graduate Center with the Johannes Gutenberg-Universität Mainz” (MPGC). K.K. acknowledges financial support from the graduate school MAINZ and a fellowship through the Excellence Initiative (DFG/GSC 266). O.S. acknowledges support by the “Evangelisches Studienwerk e.V. Villigst”. M.B. and K. K. is thankful for support of this project as part of the SFB 1066-2.

## 10.5 SUPPORTING INFORMATION

### 10.5.1 *Materials and Instrumentation*

DMF was purchased from Acros and dried over BaO and molecular sieve (3 Å), fractionally distilled *in vacuo* at 20 °C and stored at -80 °C under exclusion of light. Prior to use, *N,N*-dimethyl formamide (DMF) was degassed *in vacuo* to remove residing traces of dimethylamine. tetrahydrofuran (THF) and hexane were distilled from Na/K and ethyl acetate from CaH<sub>2</sub>. Neopentylamine was purchased from TCI Europe and was dried over NaOH followed by distillation. Cysteine was purchased from OPREGEN, sarcosine and diphosgene from Alfa Aesar. Hexafluoro-2-propanol (HFIP) and *N*-Boc-1,2-diaminoethane were purchased from Fluorochem. Millipore water was prepared by a MILLI-Q<sup>®</sup> Reference A+ System and used at a resistivity of 18.2 MΩ cm<sup>-1</sup> and total organic carbon < 5 ppm. Deuterated solvents were obtained from Deutero GmbH. CR110 DBCO was purchased from Jena Bioscience, AF647-NHS ester from Invitrogen, Cy5-NHS ester from Lumiprobe and Sephadex<sup>®</sup> LH 20 from Sigma Aldrich.

<sup>1</sup>H NMR spectra were recorded on a Bruker Avance II HD 400 at a frequency of 400 MHz or a Bruker Avance III HD 300 at 300 MHz. Two-dimensional nuclear magnetic resonance (NMR) spectra (<sup>1</sup>H diffusion ordered spectroscopy (DOSY)) were recorded on a Bruker Avance III HD 400 at 400 MHz. All spectra were recorded at room temperature (25 °C) and calibrated using the solvent signals.<sup>[394]</sup> Melting points were measured using a Mettler FP62 melting point apparatus at a heating rate of 1 °C min<sup>-1</sup>.

Gel permeation chromatography (GPC) was performed with HFIP containing 3 g l<sup>-1</sup> potassium trifluoroacetate (KTFA) as eluent at 40 °C and a flow rate of 0.8 ml min<sup>-1</sup>. GPC columns were packed with modified silica (PFG columns particle size: 7 μm, porosity: 100 Å and 1000 Å). Polymethyl methacrylate PMMA standards (Polymer Standards Services GmbH) were used for calibration and toluene was used as internal standard. A refractive index detector (G1362A RID) and an UV/Vis detector (at 230 nm or as indicated; Jasco UV-2075 Plus) were used for polymer detection.

Infrared IR spectroscopy was performed on a Jasco FT/IR-4100 with an ATR sampling accessory (MIRacle, Pike Technologies) using Spectra Manager 2.0 (Jasco) for integration and data processing. UV-Vis absorbance spectra were recorded using a Jasco spectrophotometer V-630 and Spectra Manager 2.0 (Jasco) for data processing.

Single-angle dynamic light scattering (DLS) measurements were performed with a ZetaSizer Nano ZS instrument (Malvern Instruments Ltd., Worcestershire, UK) equipped with a He-Ne laser (λ = 633 nm) as the incident beam. All measurements were conducted at 25 °C and a detection angle of 173 °C. Disposable polystyrene or PMMA cuvettes (VWR, Darmstadt, Germany) were used for DLS measurements. Cumulant size, polydispersity index (PDI), and size distribution (intensity-weighted) his-

tograms were calculated based on the autocorrelation function of samples, with automated attenuator adjustment and multiple scans (typically 10–15 scans) for optimal accuracy.

Dual color fluorescence cross-correlation spectroscopy (DCFCCS) experiments were performed on an LSM 880 (Carl Zeiss, Jena, Germany). For simultaneous excitation of the CR110 and Cy5 fluorophores the laser beams of an argon-ion laser (488 nm) and a helium-neon laser (633 nm) were made collinear and focused through a Zeiss C-Apochromat 40x/1.2 W water immersion objective into the sample solutions. Emitted fluorescence light was collected with the same objective, passed through a confocal pinhole and directed to a spectral detection unit (Quasar, Carl Zeiss). In this unit emission is spectrally separated by a grating element on a 32 channel array of GaAsP detectors operating in a single photon counting mode. The emission of CR110 was detected in the spectral range 500–562 nm and that of Cy5 in the range 642–696 nm. The observations volumes were calibrated using AlexaFluor488 and AlexaFluor647 as reference dyes with known diffusion coefficients. An eight-well polystyrene, chambered cover glass (Laboratory-Tek, Nalge Nunc International) was used as a sample cell. For each sample, 30 measurements (5 seconds each) were performed.

### 10.5.2 Synthetic Procedures

#### *Synthesis of ethanesulfinic acid sodium salt*

A solution of sodium sulfite (391.98 g, 3.11 mol) in water (800 mL) was heated to 80 °C. Ethanesulfonyl chloride (147.40 mL, 199.30 g, 1.55 mol) and sodium carbonate (329.63 g, 3.11 mol) were added simultaneously while significant quantities of CO<sub>2</sub> evolved. The reaction mixture was stirred for one hour at 80 °C, afterwards water was removed *in vacuo* at 60 °C. The resulting solid was suspended in methanol and filtered. Evaporation of methanol gave ethanesulfinic acid sodium salt (153.54 g, 1.32 mol, 85 %) as a colorless solid.

<sup>1</sup>H NMR (400 MHz, DMSO-*d*<sub>6</sub>) δ [ppm] = 1.79 (q, <sup>3</sup>J<sub>H,H</sub> = 7.6 Hz, 2H, -CH<sub>2</sub>-), 0.90 (t, <sup>3</sup>J<sub>H,H</sub> = 7.6 Hz, 3H, -CH<sub>3</sub>).

#### *Synthesis of S-ethylsulfonyl-L-cysteine (Cys(SO<sub>2</sub>Et))<sup>[173]</sup>*

An ice-cold solution of sodium nitrite (5.94 g, 86 mmol) in degassed water (45 mL) was slowly added to a stirred solution of L-cysteine hydrochloride (13.57 g, 86 mmol) in previously degassed 2N HCl (90 mL) at 0 °C. After 1 h, ethanesulfinic acid sodium salt (20.00 g, 172 mmol) was added to the deep red solution and was stirred for 2 h. Additional sodium ethanesulfinate (5.00 g, 43 mmol) was added and eventually a colorless solid precipitated. The reaction mixture was stirred at 0 °C overnight. The precipitate was filtered off and the pH of the colorless filtrate was adjusted with 2N NaOH to pH 4–5, resulting in additional colorless solid precipitating. The filtrate was allowed to stand at 4 °C until precipitation was complete. The combined precipitates were washed

with MeOH to remove residual sulfinate and dried *in vacuo* yielding Cys(SO<sub>2</sub>Et) (5.03 g, 24 mmol, 27 %) as a colorless, crystalline solid.

<sup>1</sup>H NMR (400 MHz, DMSO-*d*<sub>6</sub>/ TFA-*d*) δ [ppm] = 4.34 (t, <sup>3</sup>J<sub>H,H</sub> = 6.4 Hz, <sup>3</sup>J<sub>H,H</sub> = 6.0 Hz, 1H, α-*H*), 3.66 (dd, <sup>2</sup>J<sub>H,H</sub> = 14.4 Hz, <sup>3</sup>J<sub>H,H</sub> = 6.0 Hz, 1H, -CHH-S), 3.62 (q, J<sub>H,H</sub> = 7.2 Hz, 2H, -CH<sub>2</sub>-SO<sub>2</sub>), 3.53 (dd, <sup>3</sup>J<sub>H,H</sub> = 14.4 Hz, <sup>3</sup>J<sub>H,H</sub> = 6.4 Hz, 1H, -CHH-S), 1.30 (t, <sup>3</sup>J<sub>H,H</sub> = 7.2 Hz, 3H, -CH<sub>3</sub>).

*Synthesis of S-ethylsulfonyl-L-cysteine N-carboxyanhydride*  
(Cys(SO<sub>2</sub>Et) NCA)<sup>[173]</sup>

Dried Cys(SO<sub>2</sub>Et) (7.00 g, 32.82 mmol) was suspended in absolute THF (100 mL) and heated to 70 °C. Diphosgene (3.60 mL, 5.84 g, 29.52 mmol) was slowly added and the suspension was heated for an additional 4 h. Dry nitrogen was bubbled through the reaction mixture overnight into a gas washing bottle with an aqueous KOH solution to remove excess diphosgene, HCl and most of the solvent. The remaining solvent was removed *in vacuo* and the residue was dissolved in 100 mL absolute ethyl acetate. Any insoluble compounds were removed by filtration avoiding contact with air and the NCA was precipitated by adding 800 mL absolute hexane. The recrystallization of the product was repeated two more times yielding Cys(SO<sub>2</sub>Et) NCA (6.43 g, 26.87 mmol, 82 %) as a colorless, crystalline powder (m.p. 113–115 °C).

<sup>1</sup>H NMR (400 MHz, DMSO-*d*<sub>6</sub>) δ [ppm] = 9.32 (s, 1H, -NHCO), 4.86 (td, <sup>3</sup>J<sub>H,H</sub> = 6.0 Hz, <sup>3</sup>J<sub>H,H</sub> = 4.8 Hz, <sup>3</sup>J<sub>H,H</sub> = 1.6 Hz, 1H, α-*H*), 3.64 (dd, <sup>2</sup>J<sub>H,H</sub> = 14.4 Hz, <sup>3</sup>J<sub>H,H</sub> = 4.8 Hz, 1H, -CHH-S), 3.62 (q, <sup>3</sup>J<sub>H,H</sub> = 7.2 Hz, 2H, -CH<sub>2</sub>-SO<sub>2</sub>), 3.57 (dd, <sup>2</sup>J<sub>H,H</sub> = 14.4 Hz, <sup>3</sup>J<sub>H,H</sub> = 6.4 Hz, 1H, -CHH-S), 1.29 (t, <sup>3</sup>J<sub>H,H</sub> = 7.2 Hz, 3H, -CH<sub>3</sub>).

*Propane-2-sulfinic acid sodium salt*

The synthesis was carried out analogous to the ethanesulfinic acid sodium salt using sodium sulfite (88.23 g, 700 mmol), propane-2-sulfonyl chloride (39.29 mL, 49.91 g, 350 mmol) and sodium carbonate (74.19 g, 700 mmol). Purification yielded propane-2-sulfinic acid sodium salt (40.56 g, 312 mmol, 89 %) as a colorless solid.

<sup>1</sup>H NMR (400 MHz, DMSO-*d*<sub>6</sub>) δ [ppm] = 1.59 (hept., <sup>3</sup>J<sub>H,H</sub> = 6.9 Hz, 1H, =CH-), 0.87 (d, <sup>3</sup>J<sub>H,H</sub> = 6.9 Hz, 6H, -(CH<sub>3</sub>)<sub>2</sub>).

*Synthesis of S-isopropylsulfonyl-L-cysteine* (Cys(SO<sub>2</sub><sup>*i*</sup>Pr))<sup>[173]</sup>

The synthesis was carried out analogous to Cys(SO<sub>2</sub>Et) using sodium nitrite (11.60 g, 168 mmol), L-cysteine hydrochloride (26.50 g, 168 mmol) and propane-2-sulfinic acid sodium salt (43.30 g, 465 mmol). The purification yielded Cys(SO<sub>2</sub><sup>*i*</sup>Pr) (8.78 g, 39 mmol, 23 %) as a colorless, crystalline solid. Crystal Structure (CCDC-1440862): colorless needle from H<sub>2</sub>O (0.060 × 0.200 × 0.630 mm), monoclinic space group C 2, refinement: wR<sub>2</sub>=0.1794 (R<sub>1</sub>=0.0639 for observed reflections, 0.0805 for all reflections), flack parameter *x* = -014(17), crystal structure contains two independent molecules with slightly different conformations.



$^1\text{H}$  NMR (400 MHz,  $\text{DMSO-}d_6$ )  $\delta$  [ppm] = 4.34 (t,  $^3J_{\text{H,H}} = 6.0$  Hz, 1H,  $\alpha\text{-H}$ ), 3.76 (hept,  $J_{\text{H,H}} = 6.7$  Hz, 1H,  $\text{-CH-SO}_2$ ), 3.65 (dd,  $^2J_{\text{H,H}} = 14.4$  Hz,  $^3J_{\text{H,H}} = 6.0$  Hz, 1H,  $\text{-CHH-S}$ ), 3.54 (dd,  $^2J_{\text{H,H}} = 14.4$  Hz,  $^3J_{\text{H,H}} = 6.2$  Hz, 1H,  $\text{-CHH-S}$ ), 1.35 (d,  $^3J_{\text{H,H}} = 6.7$  Hz, 6H,  $\text{-(CH}_3)_2$ ).

*Synthesis of S-isopropylsulfonyl-L-cysteine N-carboxyanhydride*  
( $\text{Cys}(\text{SO}_2^i\text{Pr})$  NCA)<sup>[173]</sup>

The synthesis of  $\text{Cys}(\text{SO}_2^i\text{Pr})$  NCA was carried out under identical conditions as  $\text{Cys}(\text{SO}_2\text{Et})$  NCA employing  $\text{Cys}(\text{SO}_2\text{Et})$  (6.04 g, 26.57 mmol) and diphosgene (4.00 mL, 6.56 g, 33.14 mmol). Recrystallization yielded  $\text{Cys}(\text{SO}_2^i\text{Pr})$  NCA (4.64 g, 18.3 mmol, 69 %) as a colorless, crystalline powder (m.p. 98–100 °C).

$^1\text{H}$  NMR (400 MHz,  $\text{DMSO-}d_6$ )  $\delta$  [ppm] = 9.33 (s, 1H,  $\text{-NHCO}$ ), 4.84 (td,  $^3J_{\text{H,H}} = 5.4$  Hz, 3J = 1.4 Hz, 1H,  $\alpha\text{-H}$ ), 3.75 (hept,  $J_{\text{H,H}} = 6.6$  Hz, 1H,  $\text{-CH-SO}_2$ ), 3.59 (ddd,  $^2J_{\text{H,H}} = 14.4$  Hz,  $^3J_{\text{H,H}} = 5.6$  Hz,  $^3J_{\text{H,H}} = 5.1$  Hz, 2H,  $\text{-CH}_2\text{-S}$ ), 1.33 (dd,  $^3J_{\text{H,H}} = 6.6$  Hz,  $^3J_{\text{H,H}} = 0.9$  Hz, 6H,  $\text{-(CH}_3)_2$ ).

*Synthesis of sarcosine N-carboxyanhydride (Sar NCA)*<sup>[26]</sup>

The synthesis of sarcosine NCA was adapted from literature and modified.<sup>[44]</sup> A total of 14.92 g (167.4 mmol) sarcosine, dried *in vacuo* for 1 h, was weighed into a pre-dried, three-neck, round-bottom flask. A total of 300 mL of absolute THF was added under a steady flow of nitrogen and 16.2 mL (134 mmol) of diphosgene were added slowly *via* syringe, and the nitrogen stream was reduced. The colorless suspension was mildly refluxed for 3 h, yielding a clear solution. Afterward, a steady flow of dry nitrogen was led through the solution for another 3 h into two gas washing bottles filled with aqueous NaOH solution. The solvent was evaporated under reduced pressure, yielding a brown oil as crude reaction product. The oil was heated to 50 °C and dried under reduced pressure (20 mbar, then  $< 10^{-2}$  mbar for 2 h) to obtain an amorphous solid, free of phosgene and HCl, confirmed by testing against silver nitrate solution. The crude product was dissolved in 40 mL absolute THF and precipitated with 300 mL absolute hexane. The solution was cooled to -18 °C overnight for complete precipitation. The solid was filtered under dry nitrogen atmosphere, dried in a stream of dry nitrogen for 60–90 min and afterwards under high vacuum for 2 h in a sublimation apparatus. The crude product was sublimated at 80–85 °C and  $< 10^{-2}$  mbar. The product was collected from the sublimation apparatus in a glovebox on the same day. This procedure yielded 12.64 g of purified product (110 mmol, 65 % yield, colorless crystals, which was stored in a Schlenk tube at -80 °C and only handled under nitrogen atmosphere; mp 102–104 °C).

$^1\text{H}$  NMR (400 MHz,  $\text{CDCl}_3$ )  $\delta$  [ppm] = 4.22 (s, 2H,  $\text{-CH}_2\text{-}$ ), 2.86 (s, 3H,  $\text{-CH}_3$ ).

*Synthesis of polysarcosine using neopentylamine (route A)*

1.02 g (8.9 mmol) sarcosine NCA were dried *in vacuo* and dissolved in 5 mL dry DMF. To the monomer solution 10.4  $\mu$ L absolute neopentylamine (7.7 mg, 89  $\mu$ mol) were added. The clear, colorless solution was stirred at room temperature under a steady flow of dry nitrogen. The reaction was completed after 2 days (monitored by IR-spectroscopy). Precipitation in diethyl ether yielded 559 mg (55 %) of a colorless solid.

$^1\text{H NMR}$  (400 MHz,  $\text{DMSO-}d_6$ )  $\delta$  [ppm] = 4.34–3.92 (m, 2nH,  $-\text{CH}_2-$ ), 2.93–2.73 (m, 3nH,  $-\text{CH}_3$ ), 0.82 (s, 9H,  $-(\text{CH}_3)_3$ ).

*Synthesis of polysarcosine using N-Boc-1,2-diaminoethane (route B)*

1.6 g (13.8 mmol) sarcosine NCA were dried *in vacuo* and dissolved in 7 mL dry DMF and 5.5  $\mu$ L (5.5 mg, 34.5  $\mu$ mol) *N*-Boc-1,2-diaminoethane were added. The clear, colorless solution was stirred at room temperature under a steady flow of dry nitrogen. The reaction was completed after 3 days (monitored by IR-spectroscopy). The sarcosine amino terminus was quenched by addition of 96  $\mu$ L (691  $\mu$ mol) triethylamine and 32.6  $\mu$ L (345  $\mu$ mol) acetic anhydride. The clear solution was allowed to stir for an additional day at room temperature. Precipitation in diethylether yielded 823 mg (52 %) of a colorless solid.

The Boc protective group was removed in a mixture of  $\text{H}_2\text{O}/\text{TFA}$  1:1 for 2 h. The clear yellow solution was stirred under an argon atmosphere at room temperature for 1 hour under the exclusion of light. Precipitation in diethyl ether yielded a colorless solid, which was dialyzed against Millipore water (MWCO 3.5 kDa), saturated with  $\text{NaHCO}_3$  for 2 days. Afterwards, dialysis in pure Millipore water was carried out for additional 2 days. The polymer was lyophilized from water and 689 mg (43 %) of a colorless solid were obtained.

$^1\text{H NMR}$  (400 MHz,  $\text{DMSO-}d_6$ )  $\delta$  [ppm] = 4.35–3.94 (m, 2nH,  $-\text{CH}_2-$ ), 2.97–2.73 (m, 3nH,  $-\text{CH}_3$ ), 2.01–1.99 (m, 3H,  $-\text{OCCH}_3$ ). Additionally 1.37 (m, 9H,  $-\text{OC}(\text{CH}_3)_3$ ) for Boc-terminated.

*Synthesis of polysarcosine-block-poly(S-ethylsulfonyl-L-cysteine) (routes A and B)*

144 mg (19.3  $\mu$ mol) polysarcosine macroinitiator were dried *in vacuo* and dissolved in 3 mL dry DMF. The pale yellow monomer solution of 92 mg (383  $\mu$ mol)  $\text{Cys}(\text{SO}_2\text{Et})$  NCA in 1 mL dry DMF was added. The polymerization was carried out at  $-10^\circ\text{C}$  under a steady flow of dry nitrogen and monitored *via* IR spectroscopy. After 2 days (conversion rate of 47 %), the reaction was stopped by precipitation in THF/diethyl ether 1:5. The work-up by precipitation and centrifugation was repeated two times in THF/diethyl ether 1:5 and then once in pure diethyl ether. After extensive drying *in vacuo*, 114 mg (52 %) of a colorless solid were obtained.

$^1\text{H NMR}$  (400 MHz,  $\text{DMSO-}d_6$ )  $\delta$  [ppm] = 8.76 (m, 1mH,  $-\text{NHCO}$ ) $_{\text{Cys}}$ , 4.69 (m, 1mH,  $\alpha\text{-H}$ ) $_{\text{Cys}}$ , 4.34–3.92 (m, 2nH,  $-\text{CH}_2-$ ) $_{\text{Sar}}$ , 3.57–3.47 (m, 4mH,



$-\text{CH}_2-\text{SSO}_2-\text{CH}_2-$ )<sub>Cys</sub>, 2.93–2.72 (m, 3nH,  $-\text{CH}_3$ )<sub>Sar</sub>, 1.29 (t, 3mH,  $-\text{CH}_3$ )<sub>Cys</sub>; additionally 0.82 (s, 9H,  $-(\text{CH}_3)_3$ ) for route A.

*Synthesis of polysarcosine-block-poly(S-isopropylsulfonyl-L-cysteine)*  
(routes A and B)

143 mg (19.1  $\mu\text{mol}$ ) polysarcosine macroinitiator were dried *in vacuo* and dissolved in 3 mL dry DMF. The pale yellow monomer solution of 97 mg (382  $\mu\text{mol}$ ) Cys(SO<sub>2</sub><sup>i</sup>Pr) NCA in 1 mL dry DMF was added. The polymerization was carried out at -10 °C under a steady flow of dry nitrogen and monitored *via* IR spectroscopy. After 2 days (conversion rate of 42 %), the reaction was stopped by precipitation in THF/diethyl ether 1:5. The work-up by precipitation and centrifugation was repeated two times in THF/diethyl ether 1:5 and then once in pure diethyl ether. After extensive drying *in vacuo*, 135 mg (62 %) of a colorless solid were obtained.

<sup>1</sup>H NMR (400 MHz, DMSO-*d*<sub>6</sub>)  $\delta$  [ppm] = 8.72 (m, 1mH,  $-\text{NHCO}$ )<sub>Cys</sub>, 4.66 (m, 1mH,  $\alpha\text{-H}$ )<sub>Cys</sub>, 4.34–3.93 (m, 2nH,  $-\text{CH}_2-$ )<sub>Sar</sub>, 3.64 (hept, 1mH,  $=\text{CH}-\text{SO}_2$ )<sub>Cys</sub>, 3.48–3.36 (m, 2mH,  $-\text{CH}_2-\text{S}$ )<sub>Cys</sub>, 2.94–2.72 (m, 3nH,  $-\text{CH}_3$ )<sub>Sar</sub>, 1.33 (d, 6n H,  $-(\text{CH}_3)_2$ ); additionally 0.82 (s, 9H,  $-(\text{CH}_3)_3$ ) for route A.

*Labeling of polysarcosine-block-poly(S-ethylsulfonyl-L-cysteine) Block Copolymers with Fluorophores*

1.0 eq. of **P5** (PSar<sub>69</sub>-*b*-PCys(SO<sub>2</sub>Et)<sub>10</sub>) (0.6 mg) were dissolved in acetate buffer (2 g L<sup>-1</sup>) and 1.2 eq. dibenzylcyclooctyne-PEG<sub>4</sub>-5/6-carboxyrhodamine 110 (CR110) (90  $\mu\text{L}$ , 1 g L<sup>-1</sup> in DMF) were added, respectively 1.0 eq. of **P5** (PSar<sub>69</sub>-*b*-PCys(SO<sub>2</sub>Et)<sub>10</sub>) (1.0 mg) were dissolved in PBS buffer (pH 8.18, 2 g L<sup>-1</sup>) and 1.2 eq. Alexa Fluor<sup>®</sup> 647 N-hydroxysuccinimidyl ester (AF647) (213  $\mu\text{L}$ , 1 g L<sup>-1</sup> in DMF) were added. The labeling reactions were carried out at room temperature overnight followed by purification using column chromatography (Sephadex LH 20 and DMSO).

*Conversion of polysarcosine-block-poly(S-ethylsulfonyl-L-cysteine) Block Copolymers with Benzylmercaptan in DMSO-*d*<sub>6</sub>*

1.0 eq. of **P3** (PSar<sub>320</sub>-*b*-PCys(SO<sub>2</sub>Et)<sub>21</sub>) (7.30 mg) were dissolved in 700  $\mu\text{L}$  DMSO-*d*<sub>6</sub> and 1.1 eq. of benzyl mercaptan (4.94 mg) were added immediately prior to the <sup>1</sup>H NMR measurement. The disappearance of the signal originating from  $-\text{CH}_3$  of the S-ethylsulfonyl group was used to monitor the conversion. Additionally, the conjunction of the relevant signals to a polymeric species was confirmed by <sup>1</sup>H diffusion-ordered NMR experiments (<sup>1</sup>H DOSY NMR).

### *Particle Preparation*<sup>[22]</sup>

Amphiphilic block copolymers were self-assembled and core cross-linked using a protocol reported previously.<sup>[22]</sup> Briefly, the polymer was dissolved in *N,N*-dimethyl acetamide (DMAc), containing 1 M thiourea to prevent  $\beta$ -sheet formation of the polycysteine segment, at a concentration of  $7.5 \text{ g L}^{-1}$  for 2 h. 1 mM acetate buffer (pH = 4.7, 10 mM thiourea) was added to adjust the concentration to  $6.4 \text{ g L}^{-1}$ . The solution was left to equilibrate for 3 h and was then dialyzed against 1 mM acetate buffer (pH = 4.7, 10 mM thiourea). The solution was filtered using a 200 nm syringe filter (GHP) and the cross-linker TETA was added with SH-groups equimolar to the number of cysteines as a  $100 \text{ g L}^{-1}$  stock solution in water. The synthesis of TETA has been reported previously.<sup>[22]</sup> The reaction mixture was shaken and allowed to stand for 18 h. Subsequently, the solution was diluted with 1 mM acetate buffer (pH 4.7), filtered via a 200 nm syringe filter (GHP), and purified by repetitive spin filtration (MWCO 100 kDa) and dilution steps followed by lyophilization.

### *Labeling of Nanohydrogels with Fluorophores*

After the preparation steps described above, nanohydrogels were dissolved at a concentration of  $2 \text{ g L}^{-1}$  in the particular solvents and an equimolar amount of fluorophore in DMF ( $1 \text{ g L}^{-1}$ ) was added. The labeling reactions were carried out at room temperature overnight followed by repetitive spin filtration (MWCO 100 kDa) diluting at least 10 times with EtOH/H<sub>2</sub>O followed by 10 times H<sub>2</sub>O. The second labeling step followed in analogy subsequently after the first work-up and GPC and DLS characterization.

The exact procedure was as followed: 0.1 mg of nanohydrogel were dissolved in water and 4.6  $\mu\text{L}$  dibenzylcyclooctyne-PEG<sub>4-5/6</sub>-carboxy-rhodamine 110 (CR110) solution were added. The second labeling step was carried out with 0.05 mg of nanohydrogel and included the addition of 10-fold concentrated PBS to adjust the pH to 8 and 1.6  $\mu\text{L}$  cyanin 5 *N*-hydroxysuccinimidyl ester (Cy5) solution. The inverted procedure was carried out with 6.74 mg of nanohydrogel in PBS buffer (pH 8.18) and 217.8  $\mu\text{L}$  Cy5 solution followed by double labeling of 1 mg of nanohydrogel in water with 40  $\mu\text{L}$  of CR110 solution.

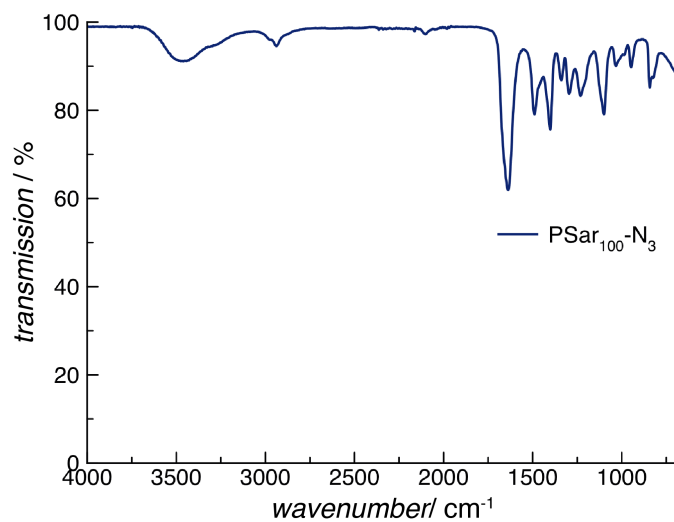


Figure 10.4: FT-IR spectrum of PSar<sub>100</sub>-N<sub>3</sub> confirming the incorporation of the azide moiety into the macroinitiator during capping at 2100 cm<sup>-1</sup>.

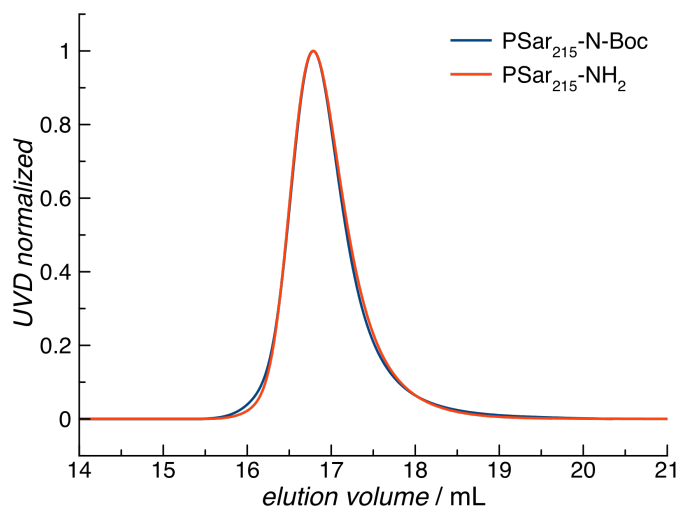


Figure 10.5: PSar<sub>215</sub> macroinitiator before (PSar<sub>215</sub>-N-Boc) and after (PSar<sub>215</sub>-NH<sub>2</sub>) deprotection in TFA/H<sub>2</sub>O.

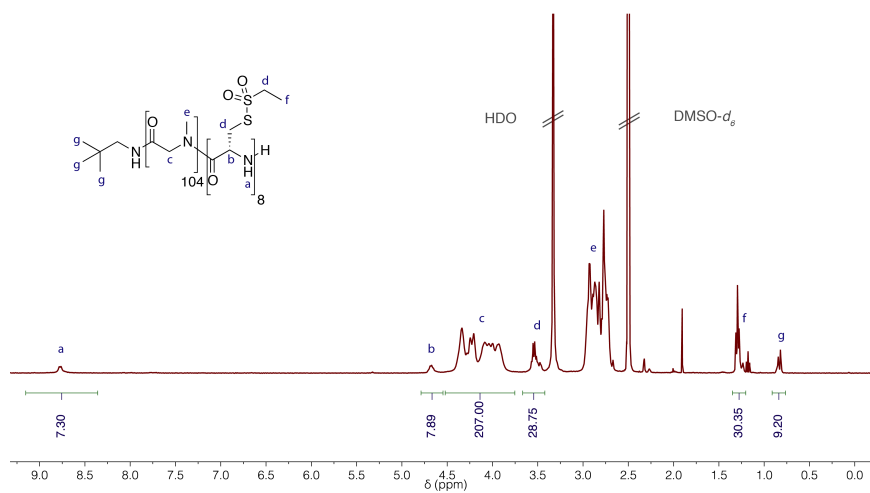


Figure 10.6:  $^1\text{H}$  NMR spectrum (400 MHz) of P1 in  $\text{DMSO-}d_6$ .

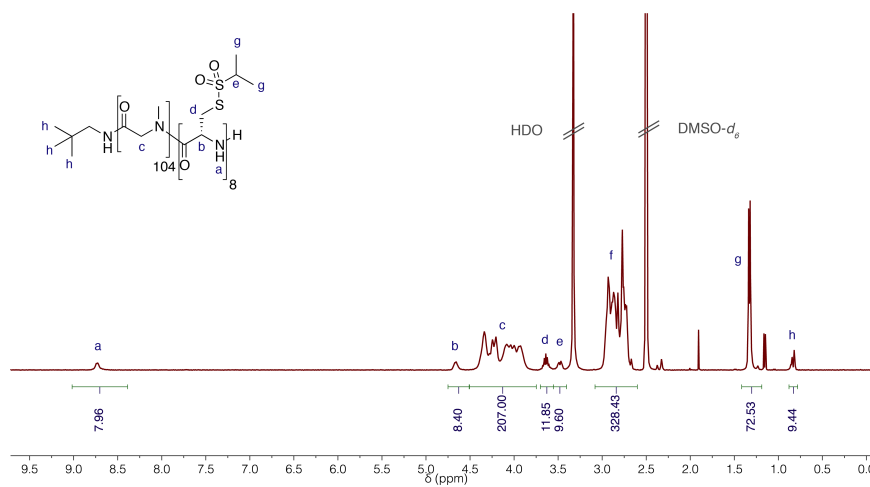
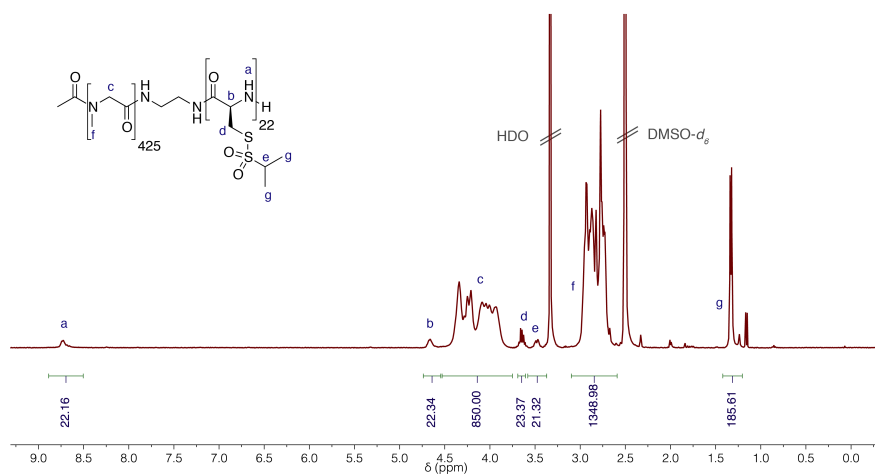
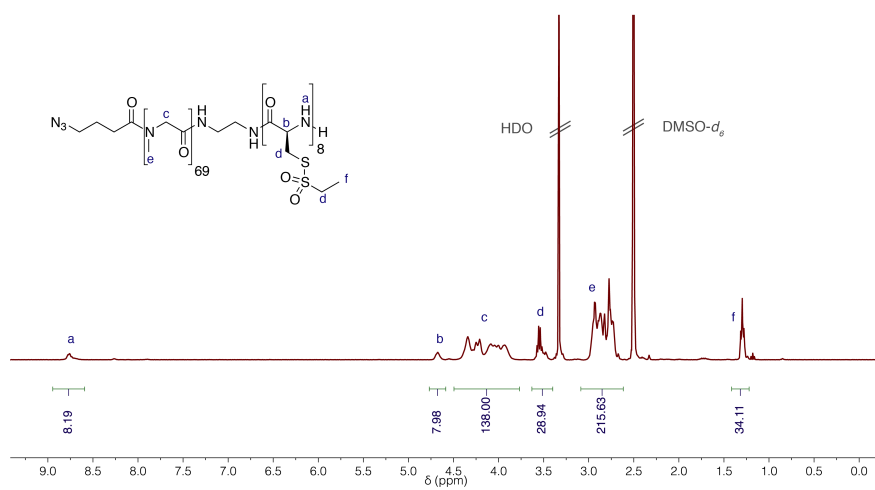


Figure 10.7:  $^1\text{H}$  NMR spectrum (400 MHz) of P2 in  $\text{DMSO-}d_6$ .

Figure 10.8: <sup>1</sup>H NMR spectrum (400 MHz) of P4 in DMSO-d<sub>6</sub>.Figure 10.9: <sup>1</sup>H NMR spectrum (400 MHz) of P5 in DMSO-d<sub>6</sub>.

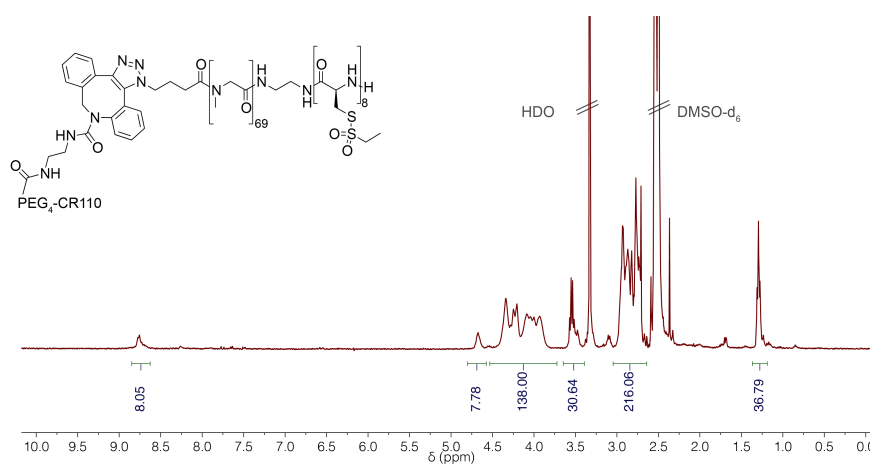


Figure 10.10:  $^1\text{H}$  NMR spectrum (400 MHz) after conversion of **P5** with CR110-DBCO in  $\text{DMSO-}d_6$ .

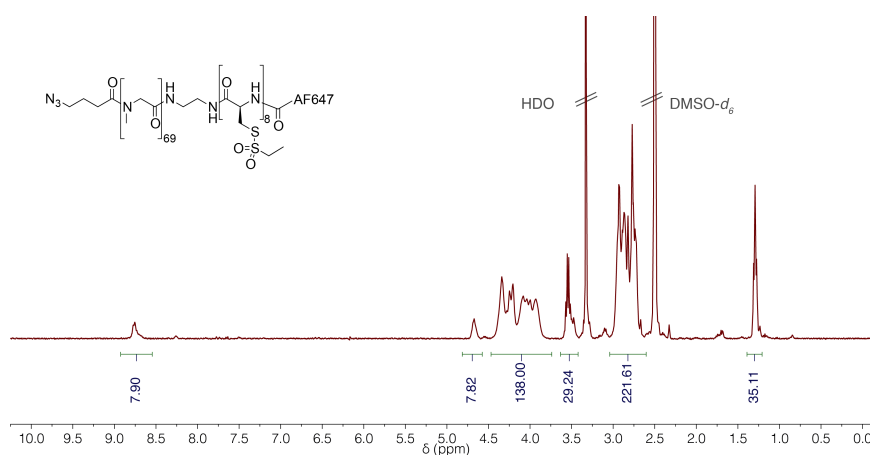
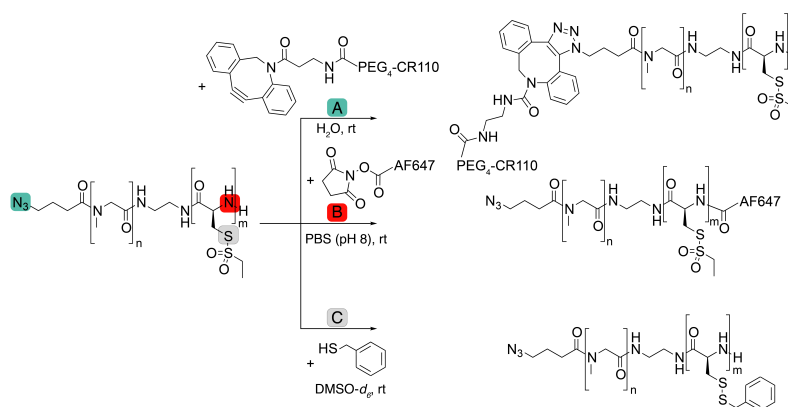


Figure 10.11:  $^1\text{H}$  NMR spectrum (400 MHz) after conversion of **P5** with AF647-NHS in  $\text{DMSO-}d_6$ .



Scheme 10.2: Functional group conversion by subsequently addressing polymer chain end functionalities and thiol-reactive side chain functionality.

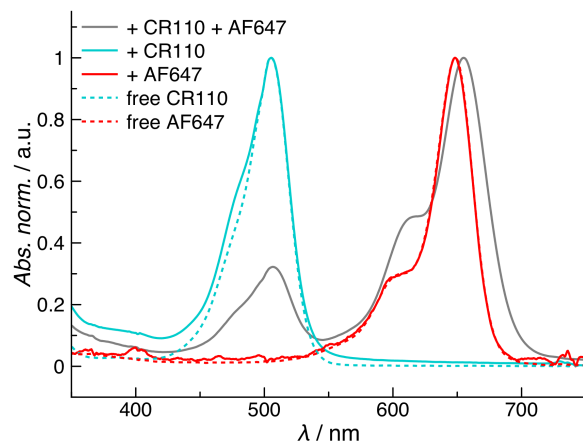


Figure 10.12: UV-Vis absorbance spectra of PSar-*b*-PCys(SO<sub>2</sub>Et) **P5** labeled with CR110, AF647 or both dyes.

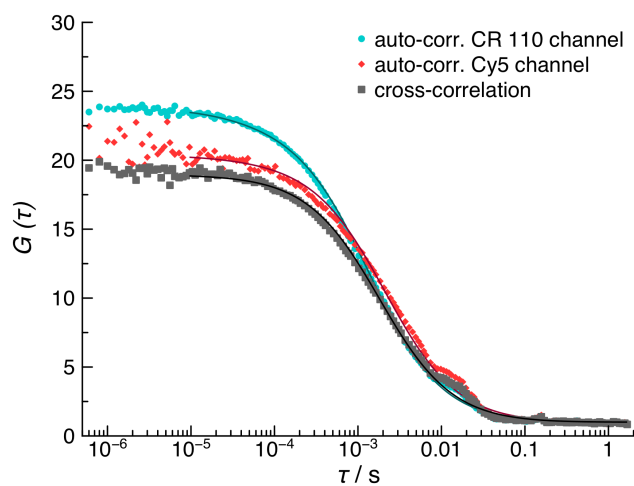


Figure 10.13: Auto- and cross-correlation curves measured for dual labeled particles (1) CR110 and (2) Cy5 showing strong cross-correlation that confirms dual labeling.

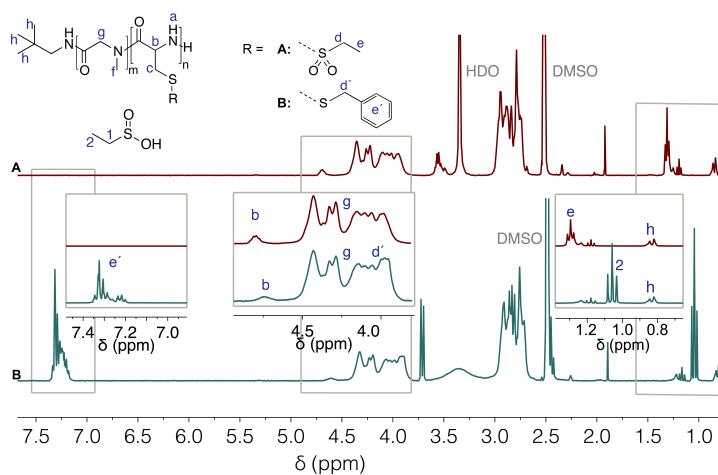


Figure 10.14: Asymmetric disulfide formation upon conversion of benzylmercaptane with **P1** S-(ethylsulfonyl)-L-cysteine in PSar-*b*-PCys(SO<sub>2</sub>Et) block copolymers synthesized by route A using neopentylamine as initiator.

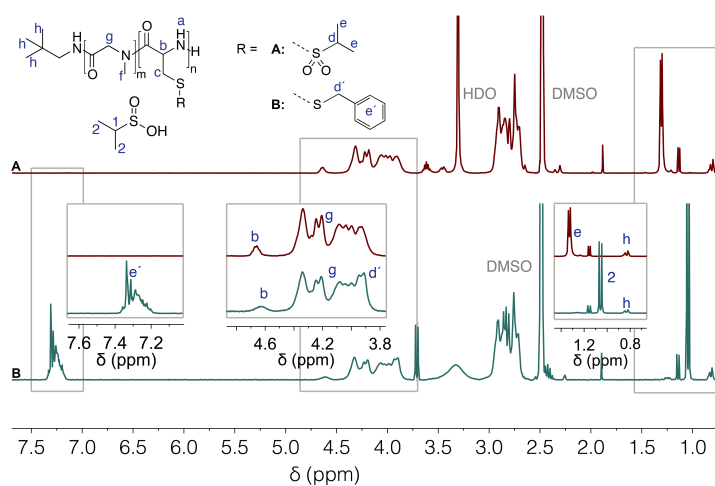


Figure 10.15: Asymmetric disulfide formation upon conversion of benzylmercaptane with **P2** S-(isopropylsulfonyl)-L-cysteine in PSar-*b*-PCys(SO<sub>2</sub><sup>i</sup>Pr) block copolymers synthesized by route A using neopentylamine as initiator.



## SEQUENCE ALTERATION OF TRIBLOCK COPOLYPEPT(O)IDES WITH INNATE THIOL-REACTIVITY

---

RNA interference (RNAi) therapeutics faces several challenges in systemic application e. g. enzymatic degradation by ribonucleases, short circulation times and entrapment in cellular compartments.<sup>[80,83,84]</sup> These delivery barriers can be addressed by nanodimensional delivery strategies, in which ideal polymeric materials should combine a shielding segment with a cross-linkable one as well as a cationic block for efficient siRNA complexation. These demanding structural requirements are met e. g. by ABC-type amphiphilic cationic triblock terpolymers.<sup>[492]</sup> Up to now, the influence of block sequence of triblock copolymers on nanoparticle properties and systemic delivery properties has not been investigated. However, there is a broad consensus that the properties of nanoparticles formed by triblock copolymers are governed by the microstructure of the employed block copolymer.<sup>[493–498]</sup>

To derive first structure-property relationships, we synthesized triblock copolymers, which contain a polysarcosine (PSar), a poly(*S*-ethylsulfonyl-L-cysteine) (PCys(SO<sub>2</sub>Et)) and a polylysine (PLys) block by sequential ring-opening polymerization of the corresponding  $\alpha$ -amino acid *N*-carboxyanhydrides, but upon alteration of block sequence. In polymer **P1** the sequence is PSar-*block*-PCys(SO<sub>2</sub>Et)-*block*-PLys (A-B-C) and in **P2** PSar-*block*-PLys-*block*-PCys(SO<sub>2</sub>Et) (A-C-B) while the overall block length of PCys(SO<sub>2</sub>Et) and PLys are kept constant. The PCys(SO<sub>2</sub>Et) block was introduced for bioreversible cross-linking by chemoselective disulfide formation, which provides stability in circulation and degradability upon cellular uptake.<sup>[158]</sup> Our group recently demonstrated modification of PLys in triblock copolypept(o)ides (polypeptoid-*block*-peptide-*block*-peptide) with *N*-succinimidyl 3-(2-pyridyl-dithio)propionate (SPDP) and by dithiol cross-linking, a library of polypept(o)ide-based pDNA polyplexes was created.<sup>[154]</sup> However, this strategy involved three post polymerization modification steps to achieve thiol-reactivity, while the presented *S*-alkylsulfonyl group introduces directed disulfide formation in polypept(o)ides, bypassing all post polymerization modification and activation steps.<sup>[173,327]</sup>

Thus, we report on the synthesis of triblock copolypept(o)ides differing in block sequence of cross-linkable and complexing segments to investigate the role of block sequence alteration on nanocarrier formation and efficacy as small interfering RNA (siRNA) delivery vectors (compare Chapter 16 for nanoparticle formation and biological investigation). The functional elements are a hydrophilic, non-ionic shielding block based on PSar,<sup>[27,143]</sup> combined with a polycationic PLys block for complexa-

tion of siRNA, as well as a hydrophobic PCys(SO<sub>2</sub>Et) segment mediating chemoselective disulfide stabilization without the need of post polymerization modification steps.<sup>[22,173]</sup>

*Synthesis of A-B-C and A-C-B triblock copolypept(o)ides.*

The synthesis of triblock copolypept(o)ides was performed by sequential ring-opening polymerization (ROP) of  $\alpha$ -amino acid *N*-carboxyanhydrides (NCAs), enabling precise control over block length and block sequence according to Birke *et al.*<sup>[26]</sup> Polysarcosine (PSar) was chosen as the starting block A with a degree of polymerization of 85 units to mediate sufficient shielding of the resulting carrier systems (see supporting information for polymerization procedures).<sup>[70]</sup> For the hydrophobic PCys(SO<sub>2</sub>R) B block, 25-30 repeating units were chosen, in order to provide sufficient carrier stability upon disulfide cross-linking.<sup>[154]</sup> The polycationic PLys block C was set to 12-13 repeating units to be able to form polyplexes by electrostatic interactions with negatively charged nucleic acids as shown by Heller *et al.*<sup>[70,367]</sup> For complexation of small siRNA molecules, a relatively short cationic segment is sufficient, particularly in combination with a cationic cross-linker.<sup>[22,154]</sup> For the synthesis of the A-B-C block copolymer the bifunctional initiator approach was chosen as reported by Schäfer *et al.*<sup>[327]</sup> while for the A-C-B block copolymer sequential polymerization provided best control over block length (see Figure 11.1 A and B).

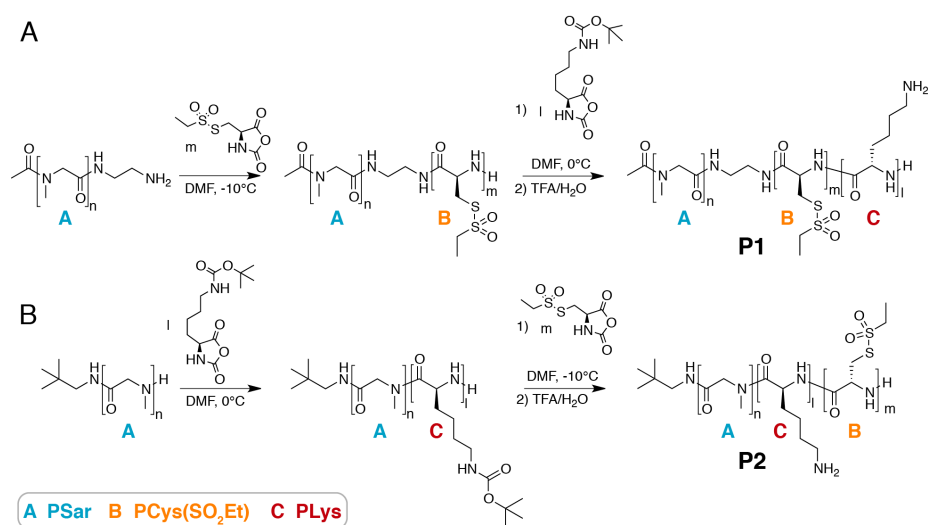


Figure 11.1: Polymerization scheme of triblock copolypept(o)ides by sequential ring-opening polymerization of NCAs: A) A-C-B triblock copolypept(o)ide (**P1**) with A: PSar<sub>n</sub>, B: PCys(SO<sub>2</sub>Et)<sub>m</sub> and C: PLys<sub>l</sub> as well as B) A-C-B triblock copolypept(o)ide (**P2**) upon inverted sequence of the cross-linking and polycationic block.

*Polymer characterization.*

Characterization of triblock copolypept(o)ides was performed by <sup>1</sup>H NMR as well as gel permeation chromatography (GPC) as summarized in Figure 11.2 and 11.3, indicating well-defined block copolymers with narrow size distribution. Successful chain extension into triblock copolymers and the absence of homopolymers or diblock copolymer impuri-

ties was confirmed by GPC and diffusion ordered  $^1\text{H}$  NMR spectroscopy (DOSY) as illustrated in Figure 11.2 A (see additionally 16.6 and 16.9 in Chapter 16). Block lengths of PSar macroinitiators were determined by GPC relative to PSar standards<sup>[47]</sup> and were in good agreement with  $^1\text{H}$  NMR experiments. Repeating units of PCys(SO<sub>2</sub>Et) and PLys(Boc) were determined by  $^1\text{H}$  NMR by evaluation of the  $\alpha$ -proton signal at 4.70 ppm and  $\epsilon$ -amide proton signal at 6.3–6.7 ppm, respectively (compare Figure 16.5 and 16.8 in Chapter 16).

Table 11.1: Characterization data of of triblock polymers.

No	polypept(o)ide architecture <sup>a, b</sup>	$M_{n, GPC}^c$ /g mol <sup>-1</sup>	$M_{n, GPC}^d$ /g mol <sup>-1</sup>	$D_{GPC}^d$
P1	PSar <sub>71</sub> - <i>b</i> -PCys(SO <sub>2</sub> Et) <sub>29</sub> - <i>b</i> -PLys <sub>13</sub>	9050	26200	1.14
P2	PSar <sub>104</sub> - <i>b</i> -PLys <sub>12</sub> - <i>b</i> -PCys(SO <sub>2</sub> Et) <sub>26</sub>	9190	26500	1.27

<sup>a</sup>  $X_n$  PSar relative to PSar standards.<sup>[47]</sup>

<sup>b</sup>  $X_m$  and  $X_l$  from  $^1\text{H}$  NMR relative to  $X_{n, GPC}$  PSar.

<sup>c</sup> Relative to PSar standards.

<sup>d</sup> Relative to PMMA standards.

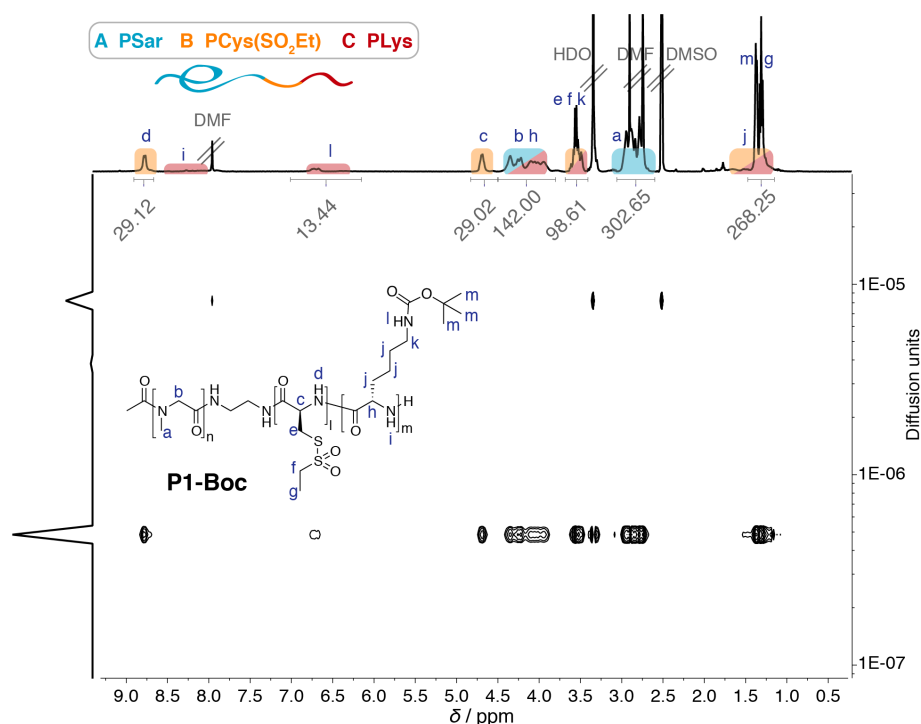


Figure 11.2:  $^1\text{H}$  NMR and  $^1\text{H}$  DOSY NMR characterization in DMSO-*d*<sub>6</sub> of A-B-C triblock P1-Boc, indicating only one diffusing species with a uniform diffusion coefficient.

Quantitative removal of the Boc protective group was accomplished by cleavage with a 1:1 mixture of H<sub>2</sub>O / TFA as reported previously<sup>[367]</sup> and verified by disappearance of the characteristic Boc signal at 1.3–1.5 ppm (compare Figure 16.7 and 16.10 in Chapter 16). As illustrated in Figure 11.3, both triblock copolypept(o)ides **P1** and **P2** exhibit monomodal molecular weight distributions in HFIP GPC. Moreover, virtually identical molecular weights and distributions are obtained for both polymers, independent from A-B-C or A-C-B block sequence alteration. The higher dispersity of 1.27 for A-C-B polymer **P2**, in contrast to a PDI of 1.14 for A-B-C polymer **P1**, may arise from the inverted block sequence, as **P2** features a terminal hydrophobic B segment in contrast to terminal hydrophilic A and C blocks in **P1**. Since <sup>1</sup>H DOSY NMR confirms equivalent diffusion coefficients (see Figure 11.2), the observed dispersity of **P2** may be attributed to secondary effects, e. g. interactions with the column material in GPC.

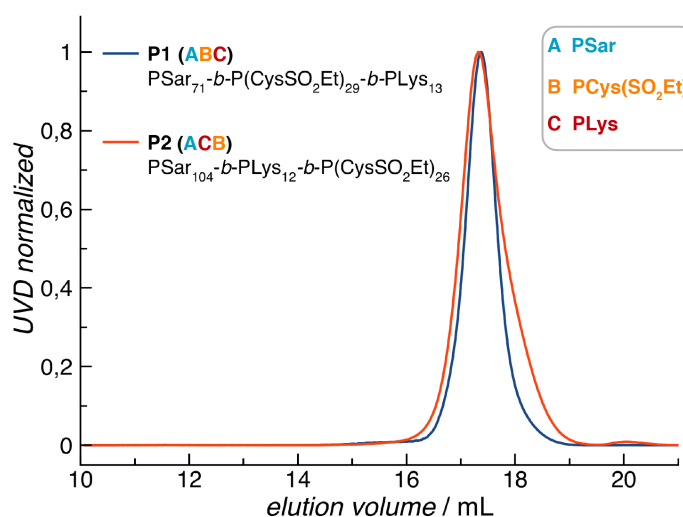


Figure 11.3: GPC characterization in HFIP of triblock polypept(o)ides **P1** and **P2** after deprotection of the PLys segment.

#### Conclusion.


In summary, we prepared A-B-C and A-C-B triblock copolypept(o)ides in order to evaluate the impact of block sequence alterations on formation and *in vivo* performance of siRNA delivery systems. As functional elements, a PSar-based shielding block, a hydrophobic PCys(SO<sub>2</sub>R) segment for bioreversible disulfide stabilization and a polycationic PLys block for complexation of siRNA were combined in triblock copolymers. Synthesis was performed by sequential ring-opening polymerization of  $\alpha$ -amino acid *N*-carboxyanhydride yielding well defined triblock copolypept(o)ides with permuted block sequence but identical individual block lengths and effective hydrodynamic volume. The influence of triblock copolymer microstructure and block sequence on nanoparticle properties and RNAi *in vivo* are investigated in Chapter 16.

Part IV

SELF-ASSEMBLY OF  
BLOCK COPOLYPEPT(O)IDES







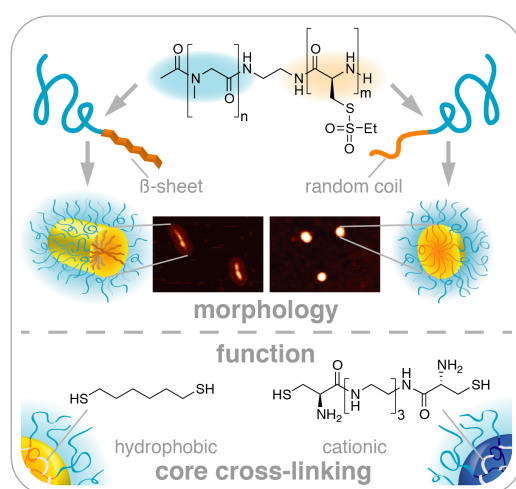
*The secondary structure-driven self-assembly of amphiphilic PSar-block-PCys(SO<sub>2</sub>R) block copolypept(o)ides into disulfide stabilized core-shell nanoparticles was investigated in the following part. Parameters of the self-assembly process were systematically screened and offered precise control over the resulting core-shell structures, especially by manipulation of secondary structure stabilization of the PCys(SO<sub>2</sub>R) segment. In addition to control over size and morphology, complete decoupling of function from particle preparation was achieved by dithiol cross-linkers. Thus, hydrophobic core cross-linked polymeric micelles for, e. g. chemotherapeutic agents and cationic nanohydrogels for complexation of negatively charged nucleic acids, e. g. siRNA could be realized upon variation in size and shape. Concluding, near-infrared fluorescence correlation spectroscopy in flowing human blood demonstrated the significance of covalent modification (cross-linking, covalent attachment of cargo or fluorescent probes) in nanocarriers aiming for systemic administration.*





SECONDARY STRUCTURE-DRIVEN SELF-ASSEMBLY  
OF REACTIVE POLYPEPT(O)IDES: CONTROLLING  
SIZE, SHAPE AND FUNCTION OF CORE  
CROSS-LINKED NANOSTRUCTURES

Kristina Klinker\*, Olga Schäfer\*, David Huesmann, Tobias Bauer, Leon Capelôa, Lydia Braun, Natascha Stergiou, Meike Schinnerer, Anjaneyulu Dirisala, Kanjiro Miyata, Kensuke Osada, Horacio Cabral, Kazunori Kataoka, Matthias Barz, *Angewandte Chemie Intl. Ed.* **2017**, *56*, 9608-9613. (\*authors contributed equally)



**ABSTRACT:** Achieving precise control over the morphology and function of polymeric nanostructures during self-assembly remains a challenge in materials as well as biomedical science, especially when independent control over particle properties is desired. Herein, we report on nanostructures derived from amphiphilic block copolypept(o)ides by secondary structure-directed self-assembly, presenting a strategy to adjust core polarity and function separately from particle preparation in a bioreversible manner. The peptide-inherent process of secondary structure formation allows for the synthesis of spherical and worm-like core-cross-linked architectures from the same block copolymer, introducing a simple yet powerful approach to versatile peptide-based core-shell nanostructures.

## 12.1 INTRODUCTION

Controlling the self-assembly of block copolymers in solution offers a versatile and powerful method to create nanometer-sized particles with defined and controllable geometry, size, and functionality.<sup>[441,499–501]</sup> The size, shape, and internal structure of nanosized objects that are obtained by the aggregation of amphiphilic coil–coil block copolymers in a block-selective solvent in thermodynamic equilibrium are mainly dictated by the volume ratio of the solvophilic and the solvophobic block.<sup>[495]</sup> The self-assembly of rod–coil block copolymers is additionally driven by the aggregation of the rod segment and the formation of orientational order, which may lead to morphologies that are different from those obtained from typical coil–coil polymers.<sup>[502–505]</sup> In crystallization-driven self-assembly, different types of polymers have been described as rod segments throughout the literature, among them polyferrocenylsilane (PFS) block copolymers with polydimethylsiloxane (PDMS), polyisoprene (PI), and poly(lactic acid).<sup>[506–508]</sup> In contrast to this type of organization, anisotropic nanomaterials can also be obtained by the controlled aggregation of peptide amphiphiles (PAs), a concept that is well-established in supramolecular chemistry.<sup>[503,509–511]</sup> In these systems, self-assembly is predominantly driven by the formation of secondary structures in the peptide segment.

It is noteworthy that  $\beta$ -sheet-driven polypeptide self-assembly is thus far mostly limited to sequence-defined peptides.<sup>[512–515]</sup> Approaches based on ring-opening polymerizations of  $\alpha$ -amino acid *N*-carboxyanhydrides (NCAs) to create the peptidic rod-like segment have also been used to stabilize micellar aggregates *in vivo*,<sup>[516]</sup> to induce oligomer aggregation, or to create smart materials that can be switched from rod–coil to coil–coil with external stimuli, such as a change in temperature or pH or the addition of chaotropic agents.<sup>[517,518]</sup> However, approaches utilizing synthetic polypeptides derived from NCA polymerization are mostly restricted to  $\alpha$ -helical motifs as the synthesis of  $\beta$ -sheet-forming polymers is not trivial.<sup>[37]</sup> Therefore, directing the morphology of polymeric micelles by  $\beta$ -sheet formation of the hydrophobic core-forming synthetic polypeptide has not yet been realized.

Cysteine is a particularly interesting amino acid because of its thiol side chain with its potential bioreversible modification and its propensity to form  $\beta$ -sheets in solution.<sup>[453]</sup> Our group has recently introduced *S*-ethylsulfonyl-L-cysteine NCAs,<sup>[364]</sup> which enabled controlled ring-opening polymerization to yield well-defined polymers with average chain lengths of up to 30 repeat units and intrinsic antiparallel  $\beta$ -sheet conformations.<sup>[209]</sup> When this amino acid was used as a building block in polypept(o)ides, a unique material was obtained that combines the functionality, stimuli responsiveness, and secondary structure formation of polypeptides with the stealth-like properties of the coil-forming polypeptoid polysarcosine (PSar).<sup>[25]</sup>

## 12.2 RESULTS AND DISCUSSION

Keeping in mind that the secondary structure of proteins can be denatured by different external stimuli,<sup>[333]</sup> the self-assembly of these block copolypept(o)ides should be controllable by switching from rod-coil block copolymers (intact  $\beta$ -sheet conformation, Figure 12.1 A) to coil-coil polymers with a chaotropic agent (disturbed  $\beta$ -sheet conformation, Figure 12.1 B).

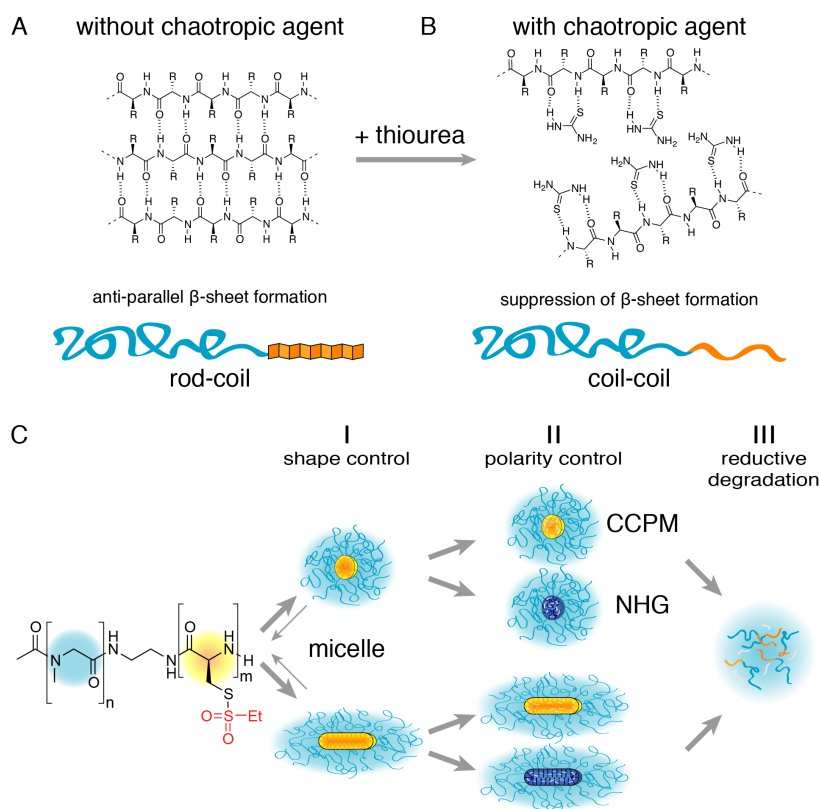


Figure 12.1: A) Formation of antiparallel  $\beta$ -sheets and B) suppressed formation of secondary structures by chaotropic agents (e. g. thiourea). C) Proposed platform featuring the following phases: I) Self-assembly of amphiphilic PSar-*b*-PCys(SO<sub>2</sub>Et) block copolymers into different micellar morphologies directed by secondary structure alignment; II) subsequent core cross-linking by disulfides of choice, yielding core cross-linked polymeric micelles (CCPMs) or nanohydrogels (NHGs); III) disintegration of the system upon a reductive stimulus.

Apart from constituting the driving force for self-assembly (Figure 12.1 C I), the *S*-alkylsulfonyl cysteine block also remains highly reactive towards thiols after polymerization.<sup>[173]</sup> This chemoselective reactivity enables core cross-linking through the formation of asymmetric disulfides (Figure 12.1 C II), which seems to be a suitable approach to preserve the morphologies of the formed nanoparticles. PSar-*b*-PCys(SO<sub>2</sub>Et) block copolymers can be obtained by NCA polymerization with a bifunctional initiator as reported previously (see the supporting Information, Scheme 12.1).<sup>[61]</sup> Block copolymers with

*Role of poly(S-ethylsulfonyl-L-cysteine) in self-assembly.*

differing block length ratios and total block lengths were prepared with dispersity indices ( $\mathcal{D}$ ) between 1.2 and 1.4 (Table 12.3 and Figure 12.5). The self-assembly of PSar-*b*-PCys(SO<sub>2</sub>Et) block copolymers was investigated methodically by varying two major factors contributing to the overall morphology, namely the composition of the amphiphile as well as favoring/suppressing the formation of the secondary structure in the absence/presence of the chaotropic agent thiourea. The amount of the hydrophobic cysteine block was kept at 15wt. % (P1  $X_n/X_m = 407:28$  and P2  $X_n/X_m = 265:17$ , determined by <sup>1</sup>H NMR spectroscopy) or 30 wt. % (P3  $X_n/X_m = 97:15$ , determined by <sup>1</sup>H NMR spectroscopy).

*Self-assembly of  
PSar-*b*-PCys(SO<sub>2</sub>Et)  
block copoly-  
pept(o)ides ...*

To obtain well-defined micelles, the block copolymers were first dissolved in *N,N*-dimethyl acetamide (DMAc), aggregated in the presence of 20 vol. % 1 mM acetate buffer (Figure 12.6), and subsequently dialyzed against 1 mM acetate buffer to allow for the formation of thermodynamically favored structures. For  $\beta$ -sheet suppression (Figure 12.1 C II), thiourea (1M in DMAc and 10 mM in the buffer) was used. Upon solvent exchange, the micelle cores were cross-linked by disulfide formation to stabilize the formed aggregates (triethylenetetramine  $\alpha,\omega$ -di(cysteine)-diamide (TETA) **c2** was used throughout Figure 12.2 yielding nanohydrogels (NHG), see also Table 12.2) for characterization. As the obtained morphologies were fixated by cross-linking while the size distributions were fully preserved (Figure 12.3 B I), thus enabling detailed particle characterization by dynamic light scattering (DLS), circular dichroism (CD), transmission electron microscopy (TEM), and atomic force microscopy (AFM).

*... and  
characterization of  
the resulting  
structures.*

As determined by cumulant analysis of DLS, P1 formed structures with a hydrodynamic diameter of  $D_h = 77$  nm (wNHG1) in the absence of thiourea and considerably smaller structures with  $D_h = 51$  nm (sNHG2) in the presence of thiourea (Figure 12.2 A II and Table 12.1). From a theoretical point of view, block copolymers with a 15 wt. % hydrophobic block are expected to form spherical micelles.<sup>[495]</sup> As briefly outlined above, the self-assembly behavior of rod-coil polymers differs considerably from that of coil-coil polymers. In the case of  $\beta$ -sheet rods, intermolecular interactions between rod chains dominate, and an enhanced packing of the crystallizing chains can lead to the formation of shape-anisotropic/ elongated objects. Moreover,  $\beta$ -sheets tend to arrange in twisted structures,<sup>[519]</sup> which is also typical for natural peptides, such as  $\beta$ -sheet barrels (Figure 12.2 A I).<sup>[520]</sup> Coil-coil polymers, on the other hand, favor rounded interfaces to minimize contact between the less soluble block and the solvent (Figure 12.2 A III). TEM and AFM were subsequently used to elucidate the morphology of core-cross-linked self-assembly structures (Figure 12.2 B and 12.7). TEM images were recorded after staining with uranyl acetate to visualize the polycysteine core,<sup>[521]</sup> whereas AFM showed the dimensions of the whole particle. Both methods demonstrate the formation of worm-like structures wNHG1 in the rod-coil case (without thiourea) and of spherical ones sNHG2 in the coil-

coil case (with thiourea). The larger  $D_h$  of **wNHG1** observed by DLS can thus be explained by the one-dimensional growth of twisted antiparallel  $\beta$ -sheet alignments into worm-like nanohydrogels. The retained internal  $\beta$ -sheet structure was further confirmed by CD analysis before and after core cross-linking and purification (Figure 12.8). Worm-like micelles show a negative Cotton effect at  $\lambda \approx 220$  nm, confirming the presence of  $\beta$ -sheets throughout the particle preparation. Reliable CD data of micelles in the presence of thiourea could not be obtained owing to the high UV absorption of thiourea at relevant concentrations (10 mM–1M).

Table 12.1: Particle characterization of NHGs and CCPMs.

particle	polymer	thiourea	morphology	cross-linker
<b>wNHG1</b>	<b>P1</b>	-	worm-like	cationic ( <b>c2</b> )
<b>sNHG2</b>	<b>P1</b>	+	spherical	cationic ( <b>c2</b> )
<b>swNHG3</b>	<b>P2</b>	-	mixed	cationic ( <b>c2</b> )
<b>sNHG4</b>	<b>P2</b>	+	spherical	cationic ( <b>c2</b> )
<b>wNHG5</b>	<b>P3</b>	-	worm-like	cationic ( <b>c2</b> )
<b>wNHG6</b>	<b>P3</b>	+	worm-like	cationic ( <b>c2</b> )
<b>sCCPM8</b>	<b>P2</b>	+	spherical	hydrophobic ( <b>c1</b> )
<b>sCCPM10</b>	<b>P2</b>	+	spherical	hydrophobic ( <b>c1</b> )
<b>wNHG11</b>	<b>P1</b>	-	worm-like	cationic ( <b>c2</b> )

Polymer **P2**, with the same block-to-block ratio (15 wt. %) but a shorter total chain length, gave rise to a mixture of spherical and worm-like nanohydrogels **swNHG3** in the absence of thiourea and small spherical nanohydrogels **sNHG4** ( $D_h = 29$  nm; (Figure 12.2 A II, 12.2 C and 12.9) in the presence of thiourea. This coexistence of morphologies most likely originates from the fact that synthetic block copolymers bear a certain polydispersity, indicating that not all polymer chain have attained the critical length to successfully participate in the  $\beta$ -sheet alignments necessary to exclusively form elongated structures. Hence multi-angle DLS revealed angle-dependent scattering for **swNHG3**, indicating non-spherical and/or polydisperse samples, with a  $\mu_2$  value of 0.17, whereas **sNHG4** showed no angular dependence, as is typical for spherical and uniform particles, with a  $\mu_2$  value of 0.06 indicating low polydispersity (Figure 12.10). Increasing the percentage of the hydrophobic block to 30 wt. % in polymer **P3** resulted in the formation of worm-like nanohydrogels **wNHG5** and **wNHG6** both in the presence and in the absence of thiourea, which differ only slightly in the hydrodynamic diameter ( $D_h = 62$  and 50 nm, respectively; Figure 12.2 D, 12.9 C and 12.11). This behavior was anticipated for coil-coil polymers with a 30 wt. % hydrophobic block.<sup>[495]</sup>

*$\beta$ -sheet formation as a modulator in self-assembly processes.*



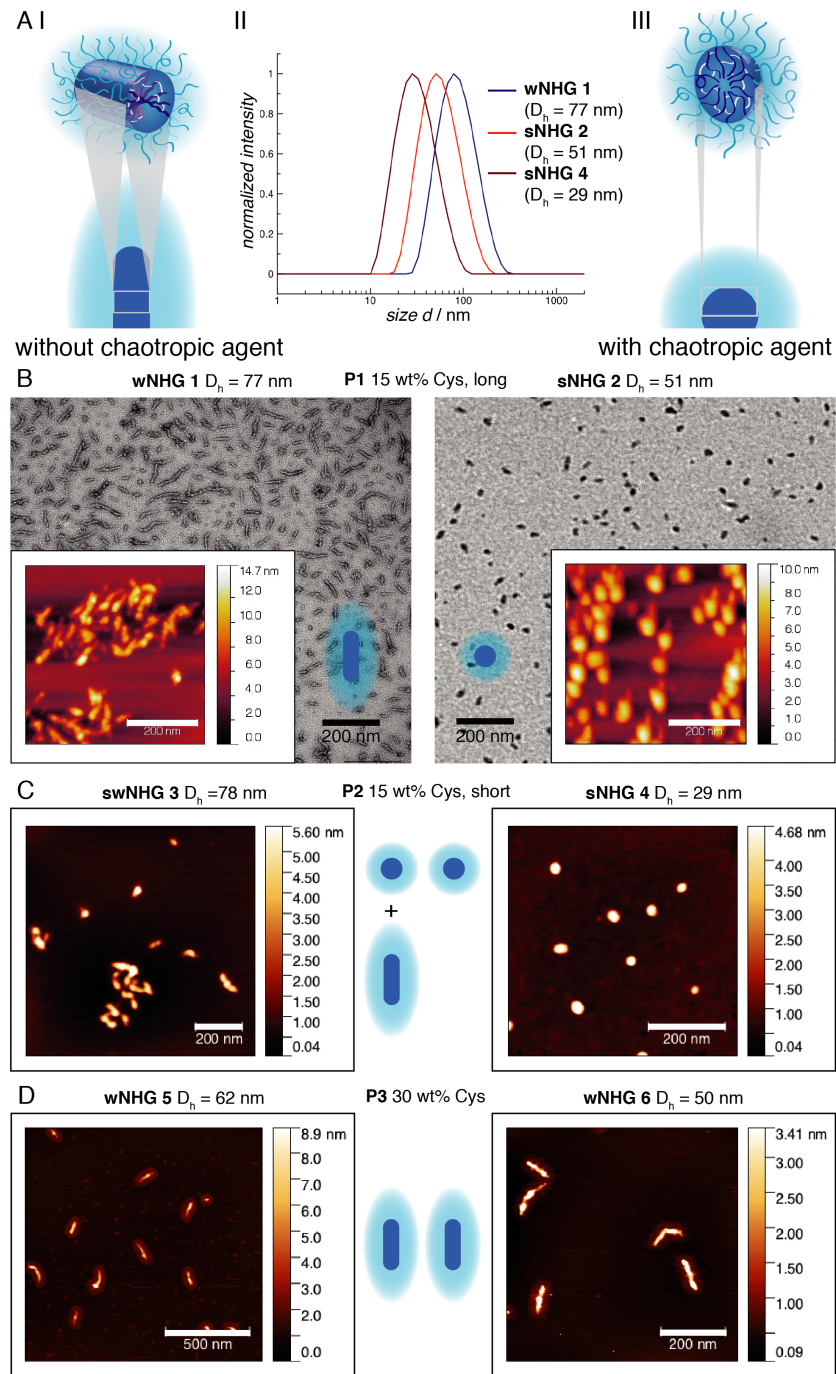


Figure 12.2: A I) Core framework of worm-like particles with twisted  $\beta$ -sheets in the absence of a chaotropic agent. II) Size range of the obtained core-cross-linked nanohydrogels wNHG1, sNHG2, and sNHG4 (DLS). III) Core framework of the spherical particles with intertwined polymer chains in random coil conformation in the presence of a chaotropic agent. B) Shape control of nanohydrogels wNHG1 and sNHG2 (visualized by AFM/TEM), modulated by the presence or absence of secondary structure stabilization (from P1, hydrophobic segment: 15 wt.%). C) Nanohydrogels from a shorter block copolymer (P2, 15 wt.%) exhibit either a mixed morphology in the presence of secondary structures swNHG3 or small-scale spheres sNHG4 (AFM). D) Worm-like nanohydrogels wNHG5 and wNHG6 (AFM) are obtained independently from secondary structure stabilization, due to higher weight percentage of the hydrophobic segment in P3 (30 wt.%).

Our findings underline the fact that  $\beta$ -sheet formation of the polycysteine block in block copolypept(o)ides substantially influences the self-assembly behavior as it leads to a rigid rod segment by intermolecular interactions that can be transformed into a coil conformation by the chaotropic agent thiourea. Consequently, a PSar-*b*-PCys(SO<sub>2</sub>Et) block copolymer with a hydrophobic ratio known to lead to spherical micelles and a certain critical total length will form elongated structures when undisturbed (rod-coil) and spherical structures when transformed into a coil-coil polymer in the presence of thiourea.

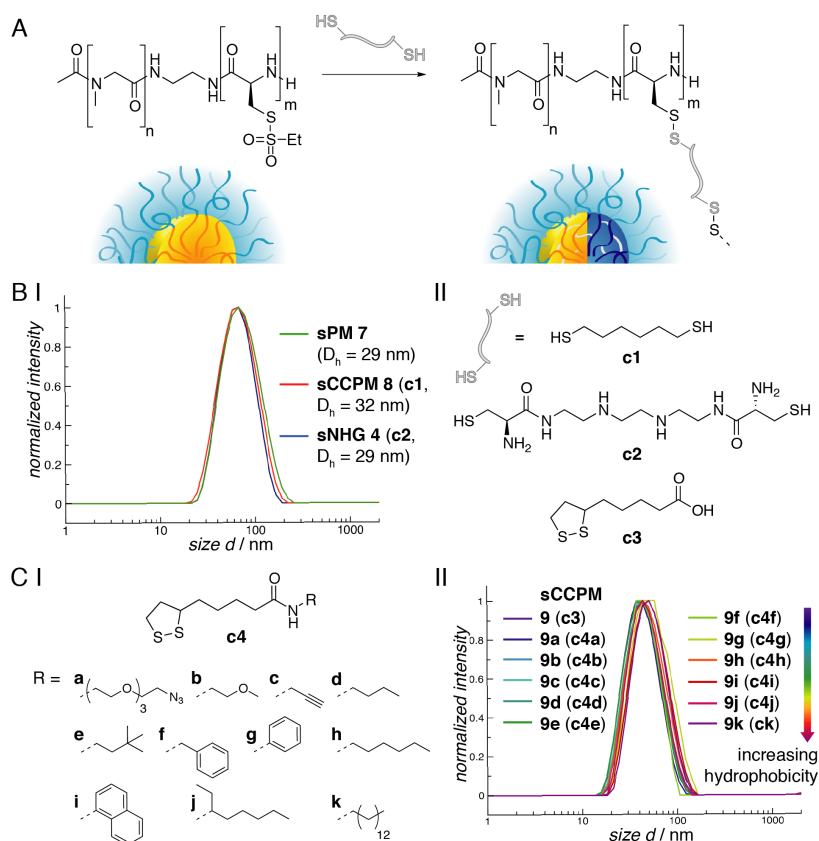


Figure 12.3: A) Cross-linking of self-assembled nanostructures by using the thiol-reactivity of the *S*-ethylsulfonyl group with various dithiols and thus introducing bioreversible disulfide bonds in core cross-linked polymeric micelles (CCPMs, yellow core) and nanohydrogels (NHGs, blue core). B I) The particle size remains constant in the presence of various cross-linkers II) while the core functionality is changed. C I) Adjusting the core polarity of CCPMs with lipoic acid derived cross-linkers with various side chains II) without affecting the particle size.

In addition to morphology control and covalent core cross-linking, the *S*-alkylsulfonyl group in the PSar-*b*-PCys(SO<sub>2</sub>Et) block copolymers is particular attractive for the construction of drug delivery systems. This approach can not only be used to incorporate functionality into the core of micelles, but also leads to bioreversible disulfide bonds (Figure 12.3 A and 12.12). Micelles with disulfide cross-linkages and polyplexes are

*Reductive degradation of disulfide-stabilization.*

known to be stable in the blood (10  $\mu$ M glutathione (GSH)) but are rapidly cleaved inside cells (10 mM GSH).<sup>[19,159]</sup> Therefore, this type of cross-linking appears to be ideal to stabilize nanoparticles while they are in circulation, but makes them responsive to a change in redox potential once they enter cells in order to disintegrate and release their cargo specifically.<sup>[522]</sup> In contrast to the disulfide cross-linking frequently reported in the literature, for example, by oxidation in the presence of oxygen<sup>[164]</sup> or DMSO,<sup>[274]</sup> the cross-linking reaction of Cys(SO<sub>2</sub>Et) is thiol-selective, proceeds rapidly, and yields asymmetric disulfides in aqueous solution.<sup>[173,209]</sup>

*Choice of the cross-linker allows for control over core polarity.*

Having established that core crosslinking does not alter the size distribution under optimized cross-linking conditions (Figure 12.3 B I and Table 12.2), it seemed highly interesting to investigate whether the core polarity could be adjusted or even inverted. In this case, the desired function of the carrier system can be introduced in one single step by the cross-linker itself, enabling the rapid production of nanoparticle libraries from one precursor micelle. Whereas hydrophobic cross-linkers (e.g. hexanedithiol **c1**) form core cross-linked polymeric micelles (CCPMs)<sup>[153]</sup>, cationic cross-linkers (e.g. TETA **c2**) invert the core polarity and thus lead to the formation of cationic nanohydrogels (NHGs)<sup>[104]</sup> (Figure 12.3 B II). Successful core cross-linking was confirmed by gel permeation chromatography in hexafluoro 2-propanol (HFIP), which is a good solvent for both blocks (Figure 12.13). With core-cross-linked polymeric micelles and nanohydrogels as the core polarity extremes, a library of lipoic acid based cross-linkers **c4 a–k** was synthesized to finetune the core polarity (Figure 12.3 C I and Table 12.4). In addition to simply altering polarity, the residues R of the cross-linker **c4** can be readily adjusted to match, for example, a certain cargo to covalently attach drugs or imaging probes.<sup>[523,524]</sup> As shown earlier, the cross-linking reaction (for **c3** and **c4a–k** after equimolar reduction with tris(2-carboxyethyl)phosphine (TCEP); Scheme 12.2) is independent of the chemical nature of the cross-linker and results in particles **sCCPM9a–g** with comparable size distributions (Figure 12.3 C II and Table 12.2). These findings underline that nanostructure formation is completely separated from chemical functionality in this approach, which is a very desirable characteristic in a new material.

*Application of core cross-linked particles ...*

Furthermore, the function of the core-cross-linked polymeric micelles on the one hand and the nanohydrogels on the other hand was investigated. Spherical **sCCPM8** was formulated with the hydrophobic chemotherapeutic agent paclitaxel (PTX), yielding **sCCPM10** with  $D_h = 39$  nm. The hydrodynamic diameter did not change significantly upon loading with paclitaxel (Figure 12.4 A and Table 12.2). Successful loading and release was confirmed indirectly by in vitro cell experiments using human breast cancer cells (TD47 cells). Whereas PTX-loaded CCPMs led to substantially decreased cell viability, comparable to that



achieved with free paclitaxel, empty CCPMs were non-toxic (Figure 12.4 A II).

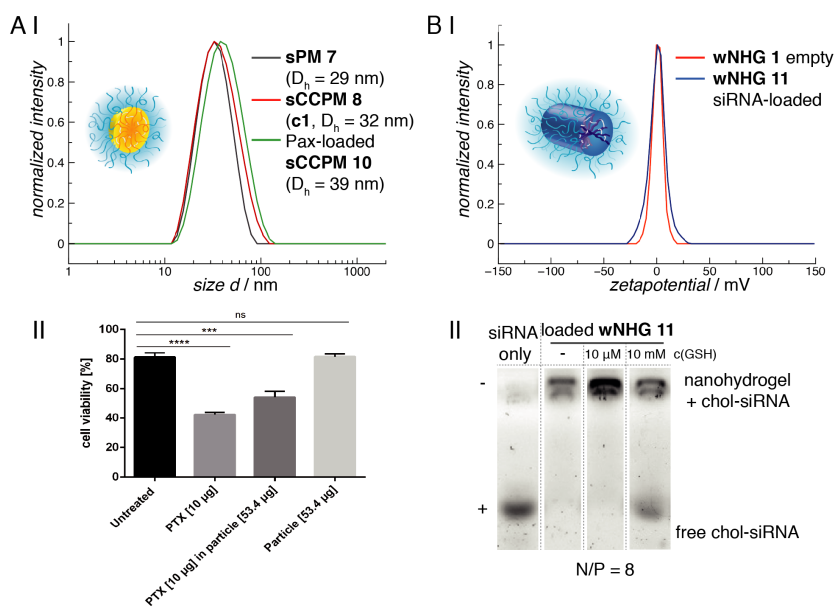


Figure 12.4: A) sCCPM8 with cross-linker c1 was loaded with Paclitaxel (PTX) to give sCCPM10 and shows I) uniform sizes prior to and after loading as well as II) pronounced in vitro efficacy on TD47 cells. B) Cationic nanohydrogels with cross-linker c2 prior to (wNHG1) and after complexation of siRNA (wNHG11) I) exhibit near-neutral  $\zeta$ -potential and II) enable stimuli-responsive release at intracellular glutathione levels (10 mM).

On the other hand, worm-like nanohydrogels wNHG1 enabled the complexation of chol-siRNA at N/P ratios of 8 (Figure 12.14), resulting in wNHG11 with  $D_h = 81 \text{ nm}$ , once again upon unchanged size distributions (Figure 12.15 and Table 12.22). In addition, nanohydrogels exhibited near-neutral  $\zeta$ -potentials before and after loading (surface  $\zeta = 0.4 \text{ mV}$  and  $0.5 \text{ mV}$ , respectively; Figure 12.4 B I), which is due to the effective shielding of the PSar segment. The bioreversible nature of the siRNA complexation was evaluated by agarose gel electrophoresis using extra- and intracellularly relevant GSH concentrations (Figure 12.4 B II). In the absence of GSH and with  $10 \mu\text{M}$  GSH (extracellular), chol-siRNA-loaded nanohydrogels remained stable whereas the siRNA was released at  $10 \text{ mM}$  GSH (intracellular). The successful loading of the respective core-functionalized particles as well as cargo release upon a reductive stimulus portray the last phase of the proposed platform (Figure 12.1 C III).

... and cationic nanohydrogels.

### 12.3 CONCLUSION

In summary, our findings highlight the potential of secondary structure-driven self-assembly to control the size and shape of polymeric nanostructures in combination with adjustable core functionality by bioreversible core cross-linking in a separate, single post-polymerization step. The *S*-alkylsulfonyl group for cysteine enables the controlled NCA ring-opening polymerization, which was exploited here for the synthesis of amphiphilic *PSar-b-PCys(SO<sub>2</sub>Et)* block copolypept(o)ides. Their self-assembly behavior can be directed by switching the conformation of the polycysteine segment from rod to coil, and the polymer association can be tuned by manipulating the secondary structures. In addition to size and shape control, this approach enables the complete decoupling of function from the self-assembly process as the polarity of the micellar core is introduced only after particle formation by using dithiol-containing cross-linkers. This novel polypept(o)ide-based nanoparticle platform can be used to generate nanoparticle libraries for various biomedical applications, ranging from nucleic acid delivery (RNAi) over drug delivery to imaging, and may help to further elucidate the size and shape dependence of circulation, biodistribution, and cellular response.

### 12.4 ACKNOWLEDGMENTS

We thank Prof. Angelika Kühnle and Prof. Manfred Schmidt for providing AFM and DLS facilities, respectively. D.H. acknowledges support by the “Verband der Chemischen Industrie” (VCI) and the “Max Planck Graduate Center with the Johannes Gutenberg-Universität Mainz” (MPGC). K.K. acknowledges financial support from the graduate school MAINZ and a fellowship through the Excellence Initiative (DFG/GSC 266). O.S. acknowledges support by the “Evangelisches Studienwerk e.V. Villigst”. M.B. is thankful for support of this project as part of the SFB 1066-1.

## 12.5 SUPPORTING INFORMATION

12.5.1 *Materials and Instrumentation*

Tetrahydrofuran (THF) and n-hexane were distilled from Na/K, ethyl acetate from CaH<sub>2</sub> prior to use. *N,N*-dimethyl formamide (DMF) was purchased from Acros and dried over BaO and molecular sieve (3 Å), fractionally distilled *in vacuo* at 20 °C and stored at -80 °C under exclusion of light. Prior to use, DMF was degassed *in vacuo* to remove residing traces of dimethylamine. *N*-Boc-1,2-diaminoethane and HFIP were purchased from Fluorochem. Millipore water was prepared by a MILLI-Q® Reference A+ System used at a resistivity of 18.2 Ω cm and total organic carbon < 5 ppm. Cysteine and sarcosine were purchased from OPREGEN and Alfa Aesar, respectively and used as received. Diphosgene was purchased from Alfa Aesar, deuterated solvents were obtained from Deutero GmbH. 1,6-Hexanedithiol was purchased from Sigma Aldrich, DL-lipoic acid was purchased from TCI Europe. Paclitaxel was obtained from Biotrend or used as Taxol formulation (pharmacy) as stated in the experimental section. siRNA sequences were purchased from Hokkaido System Science Co., Ltd. (Hokkaido, Japan) and used as follows: (1) Firefly chol-GL3-luciferase siRNA: sense strand: 5'-CUUACGCUGAGUACUUCGAdTdT-3'-chol; antisense strand: 3'-dTdTGA AUGCGACUCAUGAAGCU-5'. Other chemicals were purchased from Sigma-Aldrich and used as received unless otherwise stated.

<sup>1</sup>H, <sup>19</sup>F and <sup>13</sup>C nuclear magnetic resonance (NMR) spectra were recorded on a Bruker AC 400 or a Bruker AC 300. All spectra were recorded at room temperature (25 °C) and calibrated using the solvent signals.<sup>[394]</sup> Melting points were measured using a Mettler FP62 melting point apparatus at a heating rate of 5 °C min<sup>-1</sup>. Gel permeation chromatography (GPC) was performed with HFIP containing 3 g l<sup>-1</sup> potassium trifluoroacetate (KTFA) as eluent at 40 °C and a flow rate of 0.8 mL min<sup>-1</sup>. GPC columns were packed with modified silica (PFG columns, particle size: 7 μm porosity: 100 Å and 1000 Å, respectively). Polymethyl methacrylate standards (PMMA, Polymer Standards Services GmbH) were used for calibration and toluene was used as the internal standard. A refractive index detector (G1362A RID) and an UV/Vis detector (230 nm; Jasco UV-2075 Plus) were used for polymer detection. Infrared IR spectroscopy was performed on a Jasco FT/IR-4100 with an ATR sampling accessory (MIRacle, Pike Technologies) using Spectra Manager 2.0 (Jasco) for integration. Circular dichroism (CD) spectroscopy was performed on a Jasco J-815 spectrometer at 20 °C and Spectra Manager 2.0 (Jasco) was used to analyze the spectra. A cell with a path length of 2 mm was employed. Spectra were recorded at varying concentrations in HFIP, 3 g L<sup>-1</sup> KTFA or 1 mM acetate buffer as indicated.

Atomic force microscopy AFM was measured on mica using a Cypher®AFM (Asylum Research) using tapping mode at a scan rate of 1 Hz. Samples were prepared by spin-casting a drop of particle solution (0.1 g L<sup>-1</sup> in water) onto freshly cleaned mica. The sample was dried

overnight at room temperature. Images were evaluated and apparent height profiles were extracted using Gwyddion. The core morphology of polymeric micelles was characterized by TEM imaging on a H-7000 electron microscope (Hitachi Ltd., Tokyo, Japan) according to a previous report.<sup>[525]</sup> Briefly, a glow-discharged carbon-coated collodion membrane containing copper TEM grid (Nisshin EM Co., Ltd., Japan) was dipped into the polymeric micelle solution, which was pre-treated with an equivalent volume of uranyl acetate (UA) (2% (w/v)) for 30 s to obtain effective deposition of the samples onto the grid. The sample-deposited grids were blotted onto a filter paper to remove excess sample solution, air-dried for 30 min at room temperature, and then transferred to the TEM machine for imaging. Images were captured at an acceleration voltage of 75 kV. Polymeric micelles size distributions were obtained by measuring the diameter of the core from the TEM images using Image J 1.48v software (National Institutes of Health, USA).

Single-angle dynamic light scattering (DLS) measurements were performed with a ZetaSizer Nano ZS instrument (Malvern Instruments Ltd., Worcestershire, UK) equipped with a He-Ne laser ( $\lambda = 633$  nm) as the incident beam. All measurements were conducted at 25 °C and a detection angle of 173° unless otherwise stated. Disposable polystyrene or PMMA cuvettes (VWR, Darmstadt, Germany) were used for DLS measurements, for zeta potential measurements disposable folded capillary cells (Malvern Instruments Ltd., Worcestershire, UK) were employed. Cumulant size, polydispersity index (PDI), and size distribution (intensity-weighted) histograms were calculated based on the autocorrelation function of samples, with automated attenuator adjustment and multiple scans (typically 10–15 scans) for optimal accuracy. Aggregation and Dissociation experiments were performed at fixed attenuator of 8 and 9, respectively at concentrations as indicated.

For multi-angle DLS, cylindrical quartz cuvettes (Hellma, Mühlheim, Germany) were cleaned by dust-free distilled acetone. Particle solutions were filtered into these cuvettes through Millex GHP filters, 0.2  $\mu\text{m}$  pore-size (Millipore). DLS measurements were performed on a He-Ne Laser (25 mW output power at  $\lambda = 632.8$  nm) and on an ALV-CGS 8F SLS/DLS 5022F goniometer with eight simultaneously working ALV 7004 correlators and eight QEAPD avalanche photodiode detectors. The correlation functions of the particles were fitted using a sum of two exponentials. The z-average diffusion coefficient  $D_z$  was calculated by extrapolating  $D_{\text{app}}$  for  $q = 0$ . By formal application of Stokes law, the inverse z-average hydrodynamic radius is  $R_h = \langle R_h^{-1} \rangle_z^{-1}$ .

## 12.5.2 Experimental Procedures

*Ethanesulfinic acid sodium salt*

A solution of sodium sulfite (391.98 g, 3.11 mol) in water (800 mL) was heated to 80 °C. Ethanesulfonyl chloride (147.40 mL, 199.30 g, 1.55 mol) and sodium carbonate (329.63 g, 3.11 mol) were added simultaneously while significant quantities of CO<sub>2</sub> evolved. The reaction mixture was stirred for one hour at 80 °C, afterwards water was removed *in vacuo* at 60 °C. The resulting solid was suspended in methanol and filtered. Evaporation of methanol gave ethanesulfinic acid sodium salt (153.54 g, 1.32 mol, 85 %) as a colorless solid.

<sup>1</sup>H NMR (400 MHz, DMSO-*d*<sub>6</sub>) δ [ppm] = 1.79 (q, <sup>3</sup>J<sub>H,H</sub> = 7.6 Hz, 2H, -CH<sub>2</sub>-), 0.90 (t, <sup>3</sup>J<sub>H,H</sub> = 7.6 Hz, 3H, -CH<sub>3</sub>).

*Synthesis of S-ethylsulfonyl-L-cysteine (Cys(SO<sub>2</sub>Et))<sup>[173]</sup>*

An ice-cold solution of sodium nitrite (5.94 g, 86 mmol) in degassed water (45 mL) was slowly added to a stirred solution of L-cysteine hydrochloride (13.57 g, 86 mmol) in previously degassed 2N HCl (90 mL) at 0 °C. After 1 h, ethanesulfinic acid sodium salt (20.00 g, 172 mmol) was added to the deep red solution and was stirred for 2 h. Additional sodium ethanesulfinate (5.00 g, 43 mmol) was added and eventually a colorless solid precipitated. The reaction mixture was stirred at 0 °C overnight. The precipitate was filtered off and the pH of the colorless filtrate was adjusted with 2N NaOH to pH 4-5, resulting in additional colorless solid precipitating. The filtrate was allowed to stand at 4 °C until precipitation was complete. The combined precipitates were washed with MeOH to remove residual sulfinate and dried *in vacuo* yielding Cys(SO<sub>2</sub>Et) (5.03 g, 24 mmol, 27 %) as a colorless, crystalline solid.

<sup>1</sup>H NMR (400 MHz, DMSO-*d*<sub>6</sub>/ TFA-*d*) δ [ppm] = 4.34 (t, <sup>3</sup>J<sub>H,H</sub> = 6.4 Hz, <sup>3</sup>J<sub>H,H</sub> = 6.0 Hz, 1H, α-H), 3.66 (dd, <sup>2</sup>J<sub>H,H</sub> = 14.4 Hz, <sup>3</sup>J<sub>H,H</sub> = 6.0 Hz, 1H, -CHH-S), 3.62 (q, J<sub>H,H</sub> = 7.2 Hz, 2H, -CH<sub>2</sub>-SO<sub>2</sub>), 3.53 (dd, <sup>3</sup>J<sub>H,H</sub> = 14.4 Hz, <sup>3</sup>J<sub>H,H</sub> = 6.4 Hz, 1H, -CHH-S), 1.30 (t, <sup>3</sup>J<sub>H,H</sub> = 7.2 Hz, 3H, -CH<sub>3</sub>).

*Synthesis of S-ethylsulfonyl-L-cysteine N-carboxyanhydride (Cys(SO<sub>2</sub>Et) NCA)<sup>[173]</sup>*

Dried Cys(SO<sub>2</sub>Et) (7.00 g, 32.82 mmol) was suspended in absolute THF (100 mL) and heated to 70 °C. Diphosgene (3.60 mL, 5.84 g, 29.52 mmol) was slowly added and the suspension was heated for an additional 4 h. Dry nitrogen was bubbled through the reaction mixture overnight into a gas washing bottle with an aqueous KOH solution to remove excess diphosgene, HCl and most of the solvent. The remaining solvent was removed *in vacuo* and the residue was dissolved in 100 mL absolute ethyl acetate. Any insoluble compounds were removed by filtration avoiding contact with air and the NCA was precipitated by adding 800 mL absolute hexane. The recrystallization of the product was repeated two more

times yielding Cys(SO<sub>2</sub>Et) NCA (6.43 g, 26.87 mmol, 82 %) as a colorless, crystalline powder (m.p. 113–115 °C).

<sup>1</sup>H NMR (400 MHz, DMSO-*d*<sub>6</sub>) δ [ppm] = 9.32 (s, 1H, -NHCO), 4.86 (td, <sup>3</sup>J<sub>H,H</sub> = 6.0 Hz, <sup>3</sup>J<sub>H,H</sub> = 4.8 Hz, <sup>3</sup>J<sub>H,H</sub> = 1.6 Hz, 1H, α-H), 3.64 (dd, <sup>2</sup>J<sub>H,H</sub> = 14.4 Hz, <sup>3</sup>J<sub>H,H</sub> = 4.8 Hz, 1H, -CHH-S), 3.62 (q, <sup>3</sup>J<sub>H,H</sub> = 7.2 Hz, 2H, -CH<sub>2</sub>-SO<sub>2</sub>), 3.57 (dd, <sup>2</sup>J<sub>H,H</sub> = 14.4 Hz, <sup>3</sup>J<sub>H,H</sub> = 6.4 Hz, 1H, -CHH-S), 1.29 (t, <sup>3</sup>J<sub>H,H</sub> = 7.2 Hz, 3H, -CH<sub>3</sub>).

#### *Synthesis of sarcosine N-carboxyanhydride (Sar NCA)*<sup>[26]</sup>

The synthesis of sarcosine NCA was adapted from literature and modified.<sup>[44]</sup> A total of 14.92 g (167.4 mmol) sarcosine, dried *in vacuo* for 1 h, was weighed into a pre-dried, three-neck, round-bottom flask. A total of 300 mL of absolute THF was added under a steady flow of nitrogen and 16.2 mL (134 mmol) of diphosgene were added slowly *via* syringe, and the nitrogen stream was reduced. The colorless suspension was mildly refluxed for 3 h, yielding a clear solution. Afterward, a steady flow of dry nitrogen was led through the solution for another 3 h into two gas washing bottles filled with aqueous NaOH solution. The solvent was evaporated under reduced pressure, yielding a brown oil as crude reaction product. The oil was heated to 50 °C and dried under reduced pressure (20 mbar, then < 10<sup>-2</sup> mbar for 2 h) to obtain an amorphous solid, free of phosgene and HCl, confirmed by testing against silver nitrate solution. The crude product was dissolved in 40 mL absolute THF and precipitated with 300 mL absolute hexane. The solution was cooled to -18 °C overnight for complete precipitation. The solid was filtered under dry nitrogen atmosphere, dried in a stream of dry nitrogen for 60–90 min and afterwards under high vacuum for 2 h in a sublimation apparatus. The crude product was sublimated at 80–85 °C and < 10<sup>-2</sup> mbar. The product was collected from the sublimation apparatus in a glovebox on the same day. This procedure yielded 12.64 g of purified product (110 mmol, 65 % yield, colorless crystals, which was stored in a Schlenk tube at -80 °C and only handled under nitrogen atmosphere; mp 102–104 °C).

<sup>1</sup>H NMR (400 MHz, CDCl<sub>3</sub>) δ [ppm] = 4.22 (s, 2H, -CH<sub>2</sub>-), 2.86 (s, 3H, -CH<sub>3</sub>).

#### *Synthesis of polysarcosine (PSar)*<sup>[327]</sup>

2.21 g (192 mmol) sarcosine NCA, was dissolved in 10 mL dry DMF and 7.6 μL (4.19 μg, 48.1 μmol) *N*-*boc*-1,2-diaminoethane were added. The clear, colorless solution was stirred at room temperature and the reaction was completed after three days (monitored by IR spectroscopy). The sarcosine amino terminus was quenched by addition of 133.4 μL (0.96 mmol) triethylamine and 45.5 μL (0.48 mmol) acetic anhydride. The clear solution was allowed to stir for an additional day at room temperature. Precipitation in diethyl ether yielded 1.44 g (64%) of a colorless solid.



The Boc protective group was removed in a mixture of H<sub>2</sub>O/TFA 1:1 for 2 h. The clear yellow solution was stirred under an argon atmosphere at room temperature for 1 hour under the exclusion of light. Precipitation in diethyl ether yielded a colorless solid, which was dialyzed against Millipore water (MWCO = 3.5 kDa), saturated with NaHCO<sub>3</sub> for 2 days. Afterwards, dialysis in pure Millipore water was carried out for additional 2 days. The polymer was lyophilized from water and 479 mg (22 %) of a colorless solid were obtained.

<sup>1</sup>H NMR (400 MHz, DMSO-*d*<sub>6</sub>) δ [ppm] = 4.35–3.94 (m, 2nH, –CH<sub>2</sub>–), 2.97–2.73 (m, 3nH, –CH<sub>3</sub>), 2.01–1.99 (m, 3H, –OCCH<sub>3</sub>). Additionally 1.37 (m, 9H, –OC(CH<sub>3</sub>)<sub>3</sub>) for Boc-terminated.

*Synthesis of polysarcosine<sub>n</sub>-block-poly(S-ethylsulfonyl-L-cysteine)<sub>m</sub> block copolymers (PSar<sub>n</sub>-b-PCys(SO<sub>2</sub>Et)<sub>m</sub>)<sup>[327]</sup>*

200 mg (6.9 μmol) polysarcosine macroinitiator were dried *in vacuo* and dissolved in 3 mL dry DMF. The pale yellow monomer solution of 83 mg (345 μmol) Cys(SO<sub>2</sub>Et) NCA in 1 mL dry DMF was added. The polymerization was carried out at -10 °C and monitored *via* IR spectroscopy. After 3 days (conversion rate of 47%), the reaction was stopped by precipitation in THF/diethyl ether 1:5. The work-up by precipitation and centrifugation was repeated two times in THF/diethyl ether 1:5 and then once in pure diethyl ether. After extensive drying *in vacuo*, 183 mg (69%) of a colorless solid were obtained.

<sup>1</sup>H NMR (400 MHz, DMSO-*d*<sub>6</sub>) δ [ppm] = 8.76 (m, 1mH, –NHCO)<sub>Cys</sub>, 4.69 (m, 1mH, α-H)<sub>Cys</sub>, 4.34–3.92 (m, 2nH, –CH<sub>2</sub>–)<sub>Sar</sub>, 3.57–3.47 (m, 4mH, –CH<sub>2</sub>–SSO<sub>2</sub>–CH<sub>2</sub>–)<sub>Cys</sub>, 2.93–2.72 (m, 3nH, –CH<sub>3</sub>)<sub>Sar</sub>, 1.29 (t, 3mH, –CH<sub>3</sub>)<sub>Cys</sub>.

*Triethylenetetramine α,ω-di((S-Trt-N-Boc)cysteine)diamide*

1.20 g (2.60 mmol) Cys(S-Trt)N-Boc and 472 mg (3.50 mmol) HOBt (12 % water) were dissolved in 10 mL DMF and 589 mg (3.12 mmol) EDC·HCl were added. The solution was stirred for 1 h at rt. 193 μL triethylenetetramine were added and the solution was stirred for 30 more minutes. The solvent was removed *in vacuo* and the product purified by flash chromatography (AcOEt:MeOH (3:5) +2 % NEt<sub>3</sub>).

<sup>1</sup>H NMR (300 MHz, CDCl<sub>3</sub>) δ [ppm] = 7.45–7.33 (m, 12H, *m*-H<sub>Ar</sub>), 7.29–7.21 (m, 12H, *o*-H<sub>Ar</sub>), 7.22–7.13 (m, 6H, *p*-H<sub>Ar</sub>), 6.62 (s, 2H, –CO–NH–), 5.05 (s, br, 2H, α-H), 3.92 (s, 2H, –NH), 3.39–3.09 (m, 4H, –CH<sub>2</sub>–S–), 2.68–2.60 (m, 8H, –CO–NH–CH<sub>2</sub>–CH<sub>2</sub>–), 2.58 (s, 4H, –NH–CH<sub>2</sub>–CH<sub>2</sub>–NH–), 1.39 (s, 18H, –O–C(CH<sub>3</sub>)<sub>3</sub>).

ESI-MS: m/z = 1038.7 [M+H]<sup>+</sup>, (calc. 1037.5 g mol<sup>-1</sup>); 1059.6 [M+Na]<sup>+</sup>, (calc. 1059.5 g mol<sup>-1</sup>).

*Triethylenetetramine α,ω-di(cysteine)diamide*

442 mg (0.426 mmol) triethylenetetramine α,ω-di((S-Trt-N-Boc)cysteine)diamide and 263 mg (1.7 mmol) dithiothreitol (DTT) were dissolved in 18 mL DCM. 0.7 mL (3.4 mmol) triisopropylsilane followed by 2 mL

TFA. The solution was stirred under argon for 3 h and and precipitated in diethyl ether. The crude product was dissolved in 4 mL water/acetonitrile (97:3 + 0.1% TFA), 130 mg DTT were added and the mixture was purified by HPLC. Lyophilization yielded 287 mg triethylenetetramine  $\alpha,\omega$ -di(cysteine) diamide tetratrifluoroacetate.

$^1\text{H NMR}$  (400 MHz,  $\text{D}_2\text{O}$ )  $\delta$  [ppm] = 4.24 (dd,  $^3J_{\text{H,H}} = 6.3, 5.2$  Hz, 2H,  $\alpha\text{-H}$ ), 3.79–3.66 (m, 2H,  $-\text{CH}_2\text{-S-}$ ), 3.65–3.54 (m, 2H,  $-\text{CH}_2\text{-S-}$ ), 3.52 (s, 4H,  $-\text{NH-CH}_2\text{-CH}_2\text{-NH-}$ ), 3.33 (q,  $^3J_{\text{H,H}} = 5.8$  Hz, 4H,  $-\text{CO-NH-CH}_2$ ), 3.17–3.02 (dq,  $^3J_{\text{H,H}} = 5.8, 14.1$  Hz, 4H,  $-\text{CH}_2\text{-NH-}$ ).

ESI-MS:  $m/z = 353.2$  [ $\text{M}+\text{H}$ ] $^+$ , (calc.  $353.2$  g  $\text{mol}^{-1}$ ).

#### *Synthesis of perfluorophenyl 5-(1,2-dithiolan-3-yl)pentanoate*

2.00 g (9.69 mmol) of DL-lipoic acid were weighed into a pre-dried Schlenk-flask and dissolved in 5.0 mL of absolute THF. Next, DIPEA (1.98 mL, 11.6 mmol, 1.2 eq.) and pentafluorophenyl trifluoroacetate (2.0 mL, 11.6 mmol, 1.2 eq.) were added. The solution was stirred in the absence of light in a dry nitrogen atmosphere for 24 h at room temperature. Subsequently, the solvent was removed in high vacuum, yielding a yellow oil. Upon purification by column chromatography (cyclohexane/ethyl acetate, 9/1–6/1), 3.21 g of perfluorophenyl 5-(1,2-dithiolan-3-yl)pentanoate (8.62 mmol, 89 % yield) were obtained as a yellow solid. The product was stored at  $-20$  °C in the absence of light.

$^1\text{H NMR}$  (300 MHz,  $\text{CDCl}_3$ )  $\delta$  [ppm] = 3.57 (1H, dq,  $^3J_{\text{H,H}} = 8.3$  Hz, 6.4 Hz,  $-\text{CHS}$ ), 3.15 (2H, m,  $-\text{CH}_2\text{S}$ ), 2.69 (2H, t,  $^3J_{\text{H,H}} = 7.4$  Hz,  $-\text{CH}_2\text{CO}$ ), 2.48 (1H, dtd,  $^2J_{\text{H,H}} = 13.1$  Hz,  $^3J_{\text{H,H}} = 6.6$  Hz, 5.4 Hz,  $-\text{CH}^{\text{H}}\text{CH}_2\text{S}$ ), 1.93 (1H, dq,  $^2J_{\text{H,H}} = 12.7$  Hz,  $^3J_{\text{H,H}} = 6.9$  Hz,  $-\text{CH}^{\text{H}}\text{CH}_2\text{S}$ ), 1.78 (4H, m,  $-\text{CH}_2\text{CHS}$ ,  $-\text{CH}_2\text{CH}_2\text{CO}$ ), 1.57 (2H, m,  $-\text{CH}_2\text{CH}_2\text{CH}_2\text{CO}$ ).

$^{13}\text{C NMR}$  (101 MHz,  $\text{CDCl}_3$ )  $\delta$  [ppm] = 169.40, 142.41, 140.81, 139.91, 139.25, 138.29, 136.72, 110.12, 56.28, 40.33, 38.66, 34.64, 33.25, 28.60, 24.62.

$^{19}\text{F NMR}$  (282 MHz,  $\text{CDCl}_3$ )  $\delta$ /ppm = -154.0, -159.2, -163.5.

FD-MS:  $m/z = 372.4$ , [ $\text{M}$ ] $^+$ , (calc.  $372.4$  g  $\text{mol}^{-1}$ ).

#### *Synthesis of liponamides (c4a-4k)*

250 mg (0.671 mmol, 1 eq.) of perfluorophenyl 5-(1,2-dithiolan-3-yl)pentanoate were weighed into a pre-dried Schlenk-flask and dissolved in 5.0 mL of absolute DMF. Next, DIPEA (685  $\mu\text{L}$ , 4.03 mmol, 6.0 eq.) and the respective amine (0.739 mmol, 1.1 eq.) were added and the solution was stirred for 18 h in a dry nitrogen atmosphere at room temperature. Upon full conversion as monitored by thin layer chromatography (TLC), the solvent was removed under reduced pressure and the crude reaction product was purified by column chromatography (cyclohexane/ethyl acetate or dichloromethane/methanol).

#### *N-(2-(2-(2-(2-Azidoethoxy)ethoxy)ethoxy)ethyl)-5-(1,2-dithiolan-3-yl)pentanamide (c4a)*

Yield: 53 %,  $\log P = 1.41$ .



$^1\text{H}$  NMR (300 MHz,  $\text{CDCl}_3$ )  $\delta$  [ppm] = 6.18 (1H, s, -CONH), 3.68 (10H, m,  $-\text{O}(\text{CH}_2\text{CH}_2\text{O})_2\text{CH}_2$ ), 3.55 (3H, m, -CHS, -CONHCH<sub>2</sub>CH<sub>2</sub>), 3.46 (2H, m, -CONHCH<sub>2</sub>), 3.40 (2H, m, -CH<sub>2</sub>N<sub>3</sub>), 3.14 (2H, m, -CH<sub>2</sub>S), 2.46 (1H, dtd,  $^2J_{\text{H,H}} = 13.1$  Hz,  $^3J_{\text{H,H}} = 6.6$  Hz, 5.4 Hz, -CH'HCH<sub>2</sub>S), 2.20 (2H, t,  $^3J_{\text{H,H}} = 7.4$  Hz, -CH<sub>2</sub>CO), 1.91 (1H, dq,  $^2J_{\text{H,H}} = 12.7$  Hz,  $^3J_{\text{H,H}} = 6.9$  Hz, -CH''HCH<sub>2</sub>S), 1.68 (4H, m, -CH<sub>2</sub>CHS, -CH<sub>2</sub>CH<sub>2</sub>CO), 1.46 (2H, m, -CH<sub>2</sub>CH<sub>2</sub>CH<sub>2</sub>CO).

$^{13}\text{C}$  nmR (101 MHz,  $\text{CDCl}_3$ )  $\delta$  [ppm] = 174.05, 70.80, 70.74, 70.65, 70.35, 70.17, 69.81, 56.53, 50.82, 40.37, 39.58, 38.61, 36.43, 34.71, 28.97, 25.54.

FD-MS:  $m/z = 429.2$ ,  $[\text{M}+\text{Na}]^+$ , (calc. 406.2 g mol<sup>-1</sup>).

*5-(1,2-Dithiolan-3-yl)-N-(2-methoxyethyl)pentanamide (c4b)*

Yield: 85 %,  $\log P = 1.48$ .

$^1\text{H}$  NMR (300 MHz,  $\text{CDCl}_3$ )  $\delta$  [ppm] = 5.91 (1H, s, -CONH), 3.56 (1H, dq,  $^3J_{\text{H,H}} = 8.5$ , 6.4 Hz, -CHS), 3.46 (4H, m, -NHCH<sub>2</sub>CH<sub>2</sub>O), 3.37 (3H, s, -OCH<sub>3</sub>), 3.13 (2H, m, -CH<sub>2</sub>S), 2.46 (1H, dtd,  $^2J_{\text{H,H}} = 13.1$  Hz,  $^3J_{\text{H,H}} = 6.6$  Hz, 5.4 Hz, -CH'HCH<sub>2</sub>S), 2.22 (2H, t,  $^3J_{\text{H,H}} = 7.2$  Hz, -CH<sub>2</sub>CO), 1.91 (1H, dq,  $^2J_{\text{H,H}} = 12.7$  Hz,  $^2J_{\text{H,H}} = 6.9$  Hz, -CH''HCH<sub>2</sub>S), 1.68 (4H, m, -CH<sub>2</sub>CHS, -CH<sub>2</sub>CH<sub>2</sub>CO), 1.46 (2H, m, -CH<sub>2</sub>CH<sub>2</sub>CH<sub>2</sub>CO).

$^{13}\text{C}$  nmR (101 MHz,  $\text{CDCl}_3$ )  $\delta$  [ppm] = 173.39, 71.24, 58.95, 56.54, 40.38, 39.38, 38.62, 36.57, 34.75, 28.99, 25.52.

FD-MS  $m/z = 263.3$ ,  $[\text{M}]^+$ , (calc. 263.4 g mol<sup>-1</sup>).

*5-(1,2-Dithiolan-3-yl)-N-(prop-2-yn-1-yl)pentanamide (c4c)*

Yield: 95 %,  $\log P = 1.76$ .

$^1\text{H}$  NMR (300 MHz,  $\text{CDCl}_3$ )  $\delta$  [ppm] = 5.71 (1H, s, -CONH), 4.05 (2H, dd,  $^3J_{\text{H,H}} = 5.3$  Hz,  $^4J_{\text{H,H}} = 2.6$  Hz, -CONHCH), 3.57 (1H, dq,  $^3J_{\text{H,H}} = 8.6$  Hz, 6.4 Hz, -CHS), 3.14 (2H, m, -CH<sub>2</sub>S), 2.46 (1H, dtd,  $^2J_{\text{H,H}} = 13.1$  Hz,  $^3J_{\text{H,H}} = 6.6$  Hz, 5.4 Hz, -CH'HCH<sub>2</sub>S), 2.22 (3H, m, -CCH, -CH<sub>2</sub>CO), 1.91 (1H, dq,  $^2J_{\text{H,H}} = 12.6$  Hz,  $^3J_{\text{H,H}} = 6.9$  Hz, -CH''HCH<sub>2</sub>S), 1.68 (4H, m, -CH<sub>2</sub>CHS, -CH<sub>2</sub>CH<sub>2</sub>CO), 1.47 (2H, m, -CH<sub>2</sub>CH<sub>2</sub>CH<sub>2</sub>CO).

$^{13}\text{C}$  nmR (101 MHz,  $\text{CDCl}_3$ )  $\delta$  [ppm] = 172.69, 79.55, 71.86, 56.50, 40.38, 38.62, 36.26, 34.71, 29.38, 28.95, 25.32.

FD-MS  $m/z = 243.3$ ,  $[\text{M}]^+$ , (calc. 243.4 g mol<sup>-1</sup>).

*N-Butyl-5-(1,2-dithiolan-3-yl)pentanamide (c4d)*

Yield: 51 %,  $\log P = 2.85$ .

$^1\text{H}$  NMR (300 MHz,  $\text{CDCl}_3$ )  $\delta$  [ppm] = 5.44 (1H, s, -CONH), 3.57 (1H, dq,  $^3J_{\text{H,H}} = 8.5$  Hz, 6.4 Hz, -CHS), 3.24 (2H, td,  $^3J_{\text{H,H}} = 7.1$  Hz, 5.7 Hz, -CONHCH<sub>2</sub>), 3.13 (2H, m, -CH<sub>2</sub>S), 2.45 (1H, dtd,  $^2J_{\text{H,H}} = 13.0$  Hz,  $^3J_{\text{H,H}} = 6.6$  Hz, 5.4 Hz, -CH'HCH<sub>2</sub>S), 2.16 (2H, t,  $^3J_{\text{H,H}} = 7.3$  Hz, -CH<sub>2</sub>CO), 1.90 (1H, dq,  $^3J_{\text{H,H}} = 12.7$  Hz,  $^3J_{\text{H,H}} = 6.9$  Hz, -CH''HCH<sub>2</sub>S), 1.68 (4H, m, -CH<sub>2</sub>CHS, -CH<sub>2</sub>CH<sub>2</sub>CO), 1.46 (4H, m, -CH<sub>2</sub>CH<sub>2</sub>CO, -CONHCH<sub>2</sub>CH<sub>2</sub>), 1.34 (2H, m, -CH<sub>2</sub>CH<sub>3</sub>), 0.93 (3H, m, -CH<sub>3</sub>).

$^{13}\text{C}$  nmR (101 MHz,  $\text{CDCl}_3$ )  $\delta$  [ppm] = 172.74, 56.57, 40.38, 39.38, 38.61, 36.71, 34.77, 31.88, 29.04, 25.59, 20.21, 13.90.

FD-MS:  $m/z = 261.4$ ,  $[M]^+$ , (calc.  $261.5 \text{ g mol}^{-1}$ ).

*5-(1,2-Dithiolan-3-yl)-N-neopentylpentanamide (c4e)*

Yield: 35 %,  $\log P = 3.15$ .

$^1\text{H NMR}$  (300 MHz,  $\text{CDCl}_3$ )  $\delta$  [ppm] = 5.48 (1H, s, -CONH), 3.57 (1H, dq,  $^3J_{\text{H,H}} = 8.5 \text{ Hz}$ , 6.4 Hz, -CHS), 3.12 (4H, m, -CH<sub>2</sub>S, -CONHCH<sub>2</sub>), 2.45 (1H, dtd,  $^2J_{\text{H,H}} = 13.0 \text{ Hz}$ ,  $^3J_{\text{H,H}} = 6.6 \text{ Hz}$ , 5.4 Hz, -CH'HCH<sub>2</sub>S), 2.20 (2H, t,  $^3J_{\text{H,H}} = 7.4 \text{ Hz}$ , -CH<sub>2</sub>CO), 1.90 (1H, dq,  $^2J_{\text{H,H}} = 12.7 \text{ Hz}$ ,  $^3J_{\text{H,H}} = 7.0 \text{ Hz}$ , -CH''HCH<sub>2</sub>S), 1.68 (4H, m, -CH<sub>2</sub>CHS, -CH<sub>2</sub>CH<sub>2</sub>CO), 1.48 (2H, m, -CH<sub>2</sub>CH<sub>2</sub>CH<sub>2</sub>CO), 1.34 (9H, s, -CH<sub>3</sub>).

$^{13}\text{C NMR}$  (101 MHz,  $\text{CDCl}_3$ )  $\delta$  [ppm] = 172.84, 77.16, 56.55, 50.62, 40.37, 38.61, 36.87, 34.78, 31.95, 29.07, 27.35, 25.70.

FD-MS:  $m/z = 275.4$ ,  $[M]^+$ , (calc.  $275.5 \text{ g mol}^{-1}$ ).

*N-Benzyl-5-(1,2-dithiolan-3-yl)pentanamide (c4f)*

Yield: 56 %,  $\log P = 3.25$ .

$^1\text{H NMR}$  (300 MHz,  $\text{CDCl}_3$ )  $\delta$  [ppm] = 7.40–7.15 (5H, m, H<sub>Ar</sub>), 5.72 (1H, s, -CONH), 4.44 (1H, d,  $3J_{\text{H,H}} = 5.7 \text{ Hz}$ , -CONHCH<sub>2</sub>), 3.57 (1H, dq,  $3J_{\text{H,H}} = 8.4 \text{ Hz}$ , 6.4 Hz, -CHS), 3.14 (2H, m, -CH<sub>2</sub>S), 2.46 (1H, dtd,  $2J_{\text{H,H}} = 13.0 \text{ Hz}$ ,  $^3J_{\text{H,H}} = 6.6 \text{ Hz}$ , 5.4 Hz, -CH'HCH<sub>2</sub>S), 2.23 (2H, t,  $^3J_{\text{H,H}} = 7.7 \text{ Hz}$ , -CH<sub>2</sub>CO), 1.91 (1H, dq,  $^2J_{\text{H,H}} = 12.7 \text{ Hz}$ ,  $^3J_{\text{H,H}} = 6.9 \text{ Hz}$ , -CH''HCH<sub>2</sub>S), 1.68 (4H, m, -CH<sub>2</sub>CHS, -CH<sub>2</sub>CH<sub>2</sub>CO), 1.48 (2H, m, -CH<sub>2</sub>CH<sub>2</sub>CH<sub>2</sub>CO).

FD-MS:  $m/z = 295.3$ ,  $[M]^+$ , (calc.  $295.3 \text{ g mol}^{-1}$ ).

*5-(1,2-Dithiolan-3-yl)-N-phenylpentanamide (c4g)*

Yield: 53 %,  $\log P = 3.55$ .

$^1\text{H NMR}$  (300 MHz,  $\text{CDCl}_3$ )  $\delta$  [ppm] = 7.51 (2H, d,  $^3J_{\text{H,H}} = 8.3 \text{ Hz}$ , *o*-H<sub>Ar</sub>), 7.31 (2H, t,  $^3J_{\text{H,H}} = 8.0 \text{ Hz}$ , *m*-H<sub>Ar</sub>), 7.10 (1H, t,  $^3J_{\text{H,H}} = 7.4 \text{ Hz}$ , *p*-H<sub>Ar</sub>), 3.57 (1H, dq,  $^3J_{\text{H,H}} = 8.4 \text{ Hz}$ , 6.4 Hz, -CHS), 3.14 (2H, m, -CH<sub>2</sub>S), 2.46 (1H, dtd,  $^2J_{\text{H,H}} = 13.1 \text{ Hz}$ ,  $^3J_{\text{H,H}} = 6.6 \text{ Hz}$ , 5.4 Hz, -CH'HCH<sub>2</sub>S), 2.37 (2H, t,  $^3J_{\text{H,H}} = 7.4 \text{ Hz}$ , -CH<sub>2</sub>CO), 1.91 (1H, dq,  $^2J_{\text{H,H}} = 12.8 \text{ Hz}$ ,  $^3J_{\text{H,H}} = 6.9 \text{ Hz}$ , -CH''HCH<sub>2</sub>S), 1.74 (4H, m, -CH<sub>2</sub>CHS, -CH<sub>2</sub>CH<sub>2</sub>CO), 1.52 (2H, m, -CH<sub>2</sub>CH<sub>2</sub>CH<sub>2</sub>CO).

FD-MS:  $m/z = 281.3$ ,  $[M]^+$ , (calc.  $281.4 \text{ g mol}^{-1}$ ).

*5-(1,2-Dithiolan-3-yl)-N-hexylpentanamide (c4h)*

Yield: 59 %,  $\log P = 3.74$ .

$^1\text{H NMR}$  (300 MHz,  $\text{CDCl}_3$ )  $\delta$  [ppm] = 5.49 (1H, s, -CONH), 3.57 (1H, dq,  $^3J_{\text{H,H}} = 8.4$ , 6.4 Hz, -CHS), 3.24 (2H, td,  $^3J_{\text{H,H}} = 7.2 \text{ Hz}$ , 5.6 Hz, -CONHCH<sub>2</sub>), 3.13 (2H, m, d), 2.46 (1H, dtd,  $^2J_{\text{H,H}} = 13.0 \text{ Hz}$ ,  $^3J_{\text{H,H}} = 6.6$ , 5.3 Hz, -CH'HCH<sub>2</sub>S), 2.17 (2H, t,  $^3J_{\text{H,H}} = 7.5 \text{ Hz}$ , -CH<sub>2</sub>CO), 1.91 (1H, dq,  $^2J_{\text{H,H}} = 12.7 \text{ Hz}$ ,  $^3J_{\text{H,H}} = 6.9 \text{ Hz}$ , -CH''HCH<sub>2</sub>S), 1.68 (4H, m, -CH<sub>2</sub>CHS, -CH<sub>2</sub>CH<sub>2</sub>CO), 1.47 (4H, m, -CH<sub>2</sub>CH<sub>2</sub>CO, -CONHCH<sub>2</sub>CH<sub>2</sub>), 1.29 (6H, m, -CONHCH<sub>2</sub>CH<sub>2</sub>CH<sub>2</sub>CH<sub>2</sub>), 0.84 (6H, m, -CH<sub>3</sub>).

FD-MS:  $m/z = 289.2$ ,  $[M]^+$ , (calc.  $289.3 \text{ g mol}^{-1}$ ).

*5-(1,2-Dithiolan-3-yl)-N-(naphthalen-1-yl)pentanamide (c4i)*Yield: 65 %, log*P* = 4.54.<sup>1</sup>H NMR (300 MHz, CDCl<sub>3</sub>) δ [ppm] = 7.89–7.45 (7H, m, H<sub>Ar</sub>, -CONH), 3.61 (1H, m, -CHS), 3.16 (2H, m, -CH<sub>2</sub>S), 2.51 (3H, m, -CH<sub>2</sub>CO-, CH'HCH<sub>2</sub>S), 1.86 (5H, m, -CH''HCH<sub>2</sub>S, -CH<sub>2</sub>CHS, -CH<sub>2</sub>CH<sub>2</sub>CO), 1.60 (2H, m, -CH<sub>2</sub>CH<sub>2</sub>CH<sub>2</sub>CO).<sup>13</sup>C nmR (101 MHz, CDCl<sub>3</sub>) δ [ppm] = 171.76, 134.21, 132.30, 128.88, 127.42, 126.43, 126.12, 126.06, 125.83, 121.40, 120.82, 56.53, 40.39, 38.63, 37.39, 34.80, 29.08, 25.60.ESI-MS: m/z = 332.1, [M]<sup>+</sup>, (calc. 331.5 g mol<sup>-1</sup>).*5-(1,2-Dithiolan-3-yl)-N-(2-ethylhexyl)pentanamide (c4j)*Yield: 90 %, log*P* = 4.55.<sup>1</sup>H NMR (300 MHz, DMSO-*d*<sub>6</sub>) δ [ppm] = 7.67 (1H, t, <sup>3</sup>J<sub>H,H</sub> = 5.8 Hz, -CONH), 3.59 (1H, dq, <sup>3</sup>J<sub>H,H</sub> = 8.6 Hz, 6.2 Hz, -CHS), 3.13 (2H, m, -CH<sub>2</sub>S), 2.96 (2H, t, <sup>3</sup>J<sub>H,H</sub> = 6.0 Hz, -CONHCH<sub>2</sub>), 2.41 (1H, m, -CH'HCH<sub>2</sub>S), 2.06 (2H, t, <sup>3</sup>J<sub>H,H</sub> = 7.2 Hz, -CH<sub>2</sub>CO), 1.90 (1H, dq, <sup>2</sup>J<sub>H,H</sub> = 12.8 Hz, <sup>3</sup>J<sub>H,H</sub> = 6.8 Hz, -CH''HCH<sub>2</sub>S), 1.56 (4H, m, -CH<sub>2</sub>CHS, -CH<sub>2</sub>CH<sub>2</sub>CO), 1.25 (11H, m, CH<sub>2</sub>CH<sub>2</sub>CH<sub>2</sub>CO, -CH<sub>2</sub>CH<sub>2</sub>CH<sub>2</sub>CH<sub>3</sub>, -CHCH<sub>2</sub>ce-CH<sub>3</sub>), 0.84 (6H, m, -CH<sub>3</sub>, -CH<sub>3</sub>).<sup>13</sup>C nmR (101 MHz, DMSO-*d*<sub>6</sub>) δ [ppm] = 173.00, 56.56, 42.47, 40.38, 39.51, 38.61, 36.79, 34.78, 31.15, 29.04, 29.01, 25.64, 24.38, 23.16, 14.22, 11.02.FD-MS: m/z = 317.4, [M]<sup>+</sup>, (calc. 317.6 g mol<sup>-1</sup>).*5-(1,2-Dithiolan-3-yl)-N-tetradecylpentanamide (c4k)*Yield: 70 %, log*P* = 7.30.<sup>1</sup>H NMR (300 MHz, DMSO-*d*<sub>6</sub>) δ [ppm] = 5.41 (1H, s, -CONH), 3.57 (1H, m, -CHS), 3.17 (4H, m, -CH<sub>2</sub>S, -CONHCH<sub>2</sub>), 2.45 (1H, m, -CH'HCH<sub>2</sub>S), 2.17 (2H, t, <sup>3</sup>J<sub>H,H</sub> = 7.2 Hz, -CH<sub>2</sub>CO), 1.90 (1H, dq, <sup>2</sup>J<sub>H,H</sub> = 12.6 Hz, <sup>3</sup>J<sub>H,H</sub> = 6.9 Hz, -CH''HCH<sub>2</sub>S), 1.67 (4H, m, -CH<sub>2</sub>CHS, -CH<sub>2</sub>CH<sub>2</sub>CO), 1.48 (4H, m, -CH<sub>2</sub>CH<sub>2</sub>CH<sub>2</sub>CO, -CONHCH<sub>2</sub>CH<sub>2</sub>), 1.25 (22H, -(CH<sub>2</sub>)<sub>11</sub>-), 0.93 (3H, m, -CH<sub>3</sub>).<sup>13</sup>C nmR (101 MHz, DMSO-*d*<sub>6</sub>) δ [ppm] = 172.78, 110.13, 56.59, 40.40, 39.74, 38.62, 36.72, 34.78, 32.07, 29.84, 29.82, 29.81, 29.75, 29.71, 29.51, 29.46, 29.06, 27.09, 25.62, 22.85, 14.28.FD-MS: m/z = 401.6, [M]<sup>+</sup>, (calc. 401.7 g mol<sup>-1</sup>).*Particle Preparation*

The polymer was dissolved in DMAc at a concentration of 7.5 g L<sup>-1</sup> for 1.5 h. 1 mM acetate buffer (pH=4.7) was added to adjust the concentration to 6 g L<sup>-1</sup>. The solution was left to equilibrate for 3 h and then dialyzed against 1 mM acetate buffer. The solution was filtered using a 200 nm filter (GHP) and concentrated to 6 g L<sup>-1</sup> using a spin filter (Amicon MWCO: 3 kDa). The cross-linker was added with SH-groups equimolar to the number of cysteines (**c1** in EtOH/DMAc and **c2** as a 50 g/L stock solution in 1 mM acetate buffer). Liponamide-based cross-linkers

(**c3** and **c4a-k**) were dissolved in DMAc, EtOH or *i*PrOH at a concentration of  $c = 25 \text{ mmol L}^{-1}$  and one equivalent of concentrated aqueous TCEP solution ( $c = 50 \text{ g L}^{-1}$ ) was added per disulfide. After 18 h, the cross-linker solution was added to the micelle solution. The reaction mixture was shaken and allowed to stand for 18 h. Subsequently, the solution was diluted with 1 mM acetate buffer (pH = 4.7), filtered *via* GHP 200 nm syringe filter, and purified by repetitive spin filtration (MWCO = 100 kDa) and dilution steps. In cases, where  $\beta$ -sheet suppression was desired, thiourea was added. The concentrations were 1 M and 10 mM thiourea in DMAc and acetate buffer, respectively.

Table 12.2: Characterization of CCPMs (cross-linker **c1**, **c3** or **c4a-k**) and NHGs (cross-linker **c2**).

particle	thiourea	cross-linker	$D_{h,DLS}$	$PDI_{DLS}$	polymer
wNHG1	-	<b>c2</b>	77	0.162	P1
sNHG2	+	<b>c2</b>	51	0.156	P1
swNHG3	-	<b>c2</b>	78	0.199	P2
sNHG4	+	<b>c2</b>	29	0.127	P2
wNHG5	-	<b>c2</b>	62	0.132	P3
wNHG6	+	<b>c2</b>	50	0.144	P3
sPM7	+	- <sup>a</sup>	29	0.140	P2
sCCPM8	+	<b>c1</b>	32	0.185	P2
sCCPM9	+	<b>c3</b>	44	0.181	P4
sCCPM9a	+	<b>c4a</b>	40	0.168	P4
sCCPM9b	+	<b>c4b</b>	41	0.152	P4
sCCPM9c	+	<b>c4c</b>	44	0.193	P4
sCCPM9d	+	<b>c4d</b>	43	0.161	P4
sCCPM9e	+	<b>c4e</b>	41	0.184	P4
sCCPM9f	+	<b>c4f</b>	43	0.162	P4
sCCPM9g	+	<b>c4g</b>	51	0.219	P4
sCCPM9h	+	<b>c4h</b>	45	0.194	P4
sCCPM9i	+	<b>c4i</b>	50	0.201	P4
sCCPM9j	+	<b>c4j</b>	45	0.194	P4
sCCPM9k	+	<b>c4k</b>	48	0.145	P4
sCCPM10	+	<b>c1</b>	39	0.242	P4
wNHG11	-	<b>c2</b>	81	0.153	P1

<sup>a</sup> Micelle prior to cross-linking.

### Agarose Gel Electrophoresis

Agarose gels were prepared by adding agarose (1.5 g) to a Tris-acetate-EDTA buffer (TAE) buffer (150 mL, pH = 7.4). The mixture was heated to dissolve the agarose powder and then allowed to cool down before

preparing the gels. Samples were loaded into the gel and electrophoresed (100 V, 20 min) in TAE running buffer. After electrophoresis, siRNA was stained by CYBRGreen and gel images were captured by a Typhoon 9410 instrument equipped with a 532 nm laser.

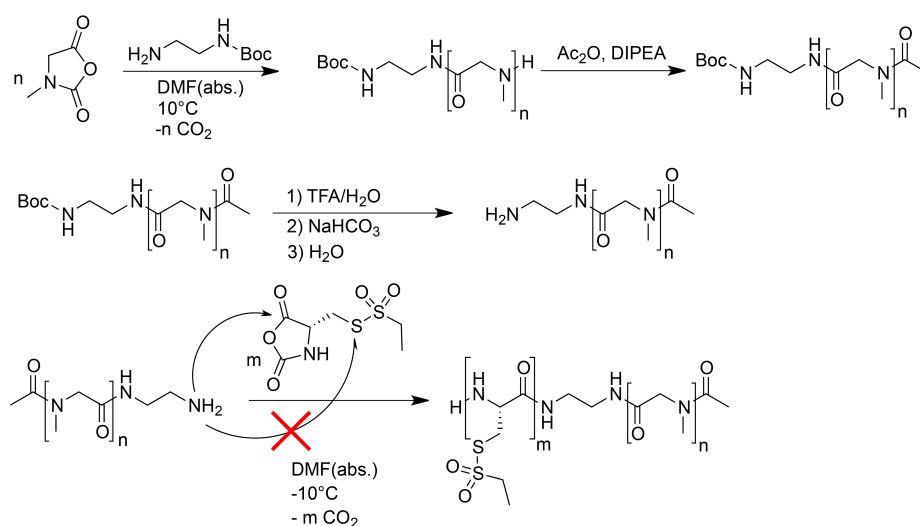
#### PTX Loading

750  $\mu\text{L}$  of CCPMs ( $1 \text{ g L}^{-1}$  in MilliQ-water) were mixed with 2.8 mL of DMSO and 150  $\mu\text{L}$  Paclitaxel ( $1 \text{ g L}^{-1}$ ) (attempted loading 17 wt.%) was added. The solution was incubated for 1.5 h and subsequently dialyzed against MilliQ-water (MWCO = 6–8 kDa). Paclitaxel-loaded CCPMs were filtered using a GHP 200 nm filter and lyophilized.

#### *In vitro* Effect of Paclitaxel-loaded Core Cross-linked Polymeric Micelles

$5 \times 10^5$  human breast cancer cells (T47D) were cultured in 24 well plates for 48 h. The cells were treated with either 10  $\mu\text{g}$  paclitaxel or 10  $\mu\text{g}$  paclitaxel stabilized in the particles (53.4  $\mu\text{g}$ ). Untreated cells and cells treated with the empty particles (53.4  $\mu\text{g}$ ) served as controls. T47D cells were stained with a fixable viability dye (eFluor 780) and cell viability was determined by Flow Cytometry. The mean of three independent experiments ( $\pm\text{SD}$ ) is shown (two-tailed unpaired t-test). \*\*\* $\leq P$  0.001, \*\*\*\* $\leq P$  0.0001, ns = not significant. Paclitaxel: concentrate for solution for infusion (Taxol®), diluted in phosphate buffered saline (PBS) ( $2 \text{ g L}^{-1}$ ), paclitaxel stabilized in the particle: dissolved in PBS ( $1 \text{ g L}^{-1}$ ), particle: dissolved in PBS ( $0.1 \text{ g L}^{-1}$ ).

#### 12.5.3 Supporting Results



Scheme 12.1: Polymerization scheme of PSar<sub>n</sub>-b-PCys(SO<sub>2</sub>Et)<sub>m</sub> highlighting chemoselective reactivity of the S-ethylsulfonyl group.

Table 12.3: Characterization of PSar<sub>n</sub>-*b*-PCys(SO<sub>2</sub>Et)<sub>m</sub>.

polymer	$X_n^a$	$X_m^a$	wt. %	$M_n^b / \text{g mol}^{-1} / \text{g mol}^{-1}$	$D^b$
P1	407	28	15	32100	1.38
P2	265	17	15	30600	1.29
P3	94	15	30	31200	1.25
P4	373	13	9	31200	1.26

<sup>a</sup> Determined by <sup>1</sup>H NMR in DMSO-*d*<sub>6</sub>.

<sup>b</sup> Determined by GPC in HFIP relative to PMMA standards.

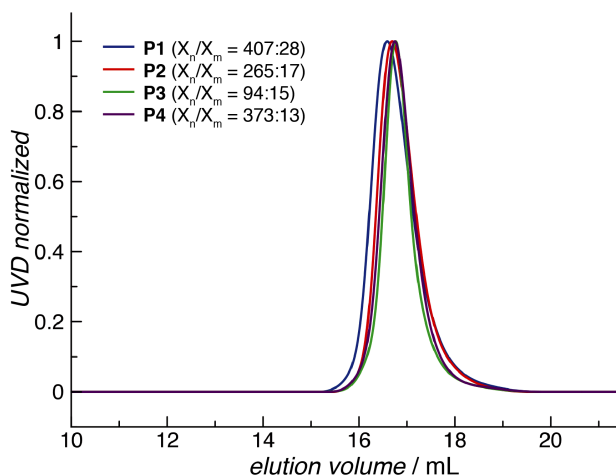


Figure 12.5: HFIP GPC traces of P1-4 (see also Table 12.3). Note that secondary structures are present in the eluent (HFIP containing 3 g L<sup>-1</sup> KTFE, Figure 12.8 A), thus elution volumes may be influenced not only by the total polymer length, but also by the length and degree of secondary structure formation of the PCys(SO<sub>2</sub>Et) block.

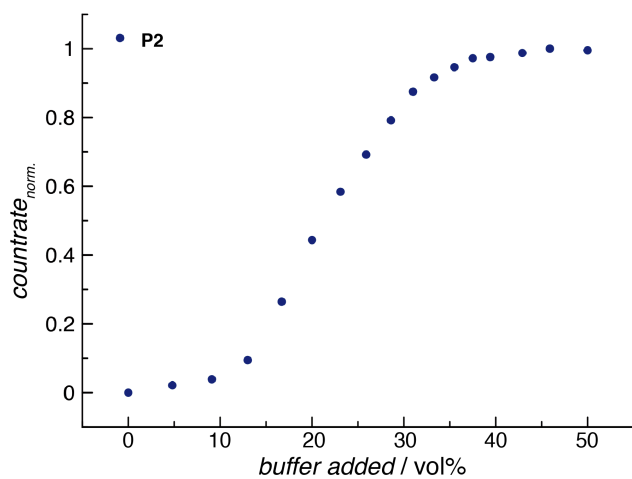


Figure 12.6: Aggregation behavior of **P2** in DMAc observed with respect to added vol.% buffer *via* DLS. The attenuator was fixed and the normalized count rate is plotted as a function of vol.% buffer added.

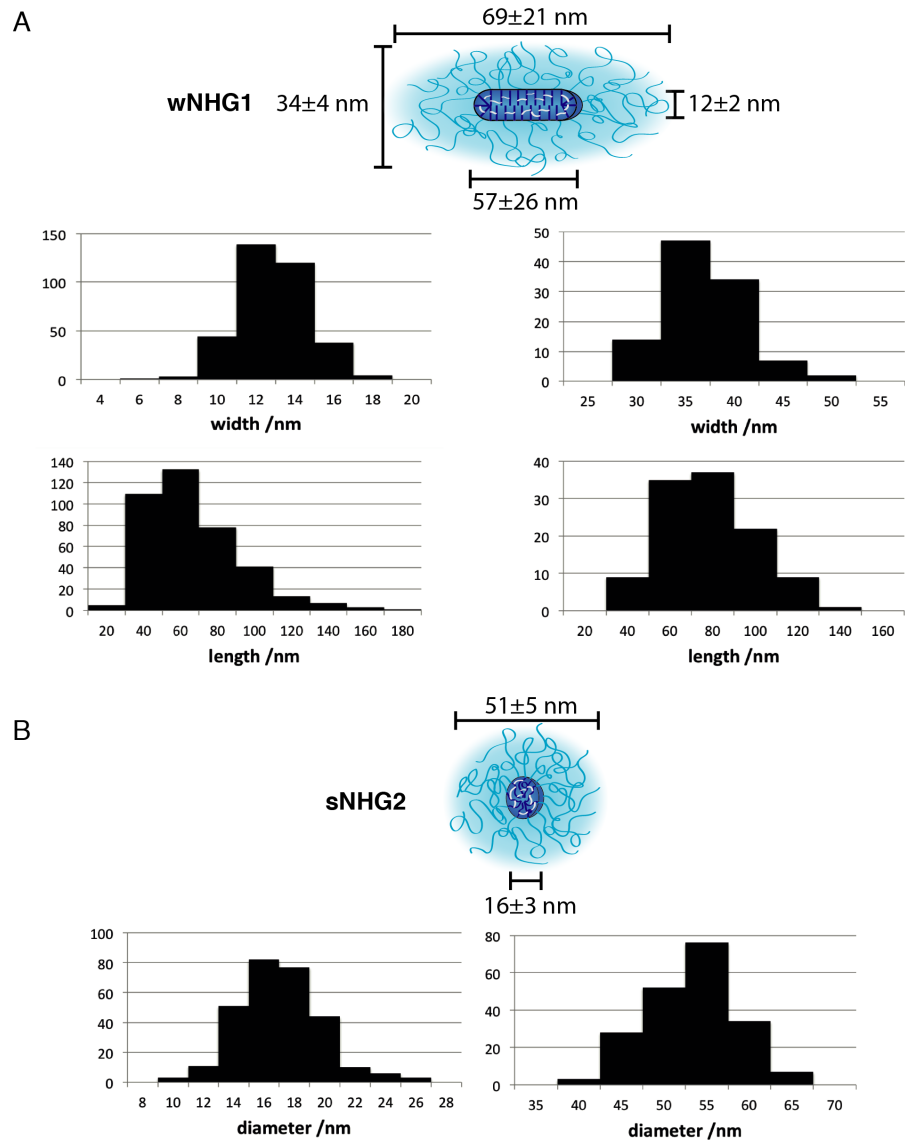


Figure 12.7: Size range of A) worm-like nanohydrogels (wNHG1) and B) spherical nanohydrogels (sNHG2) as derived from statistical analysis of AFM and TEM data presented in Figure 12.2 B). Characterization of the core was derived from TEM (due to the selective uranyl acetate staining of the peptidic core-building block) and overall apparent particle dimensions from AFM.



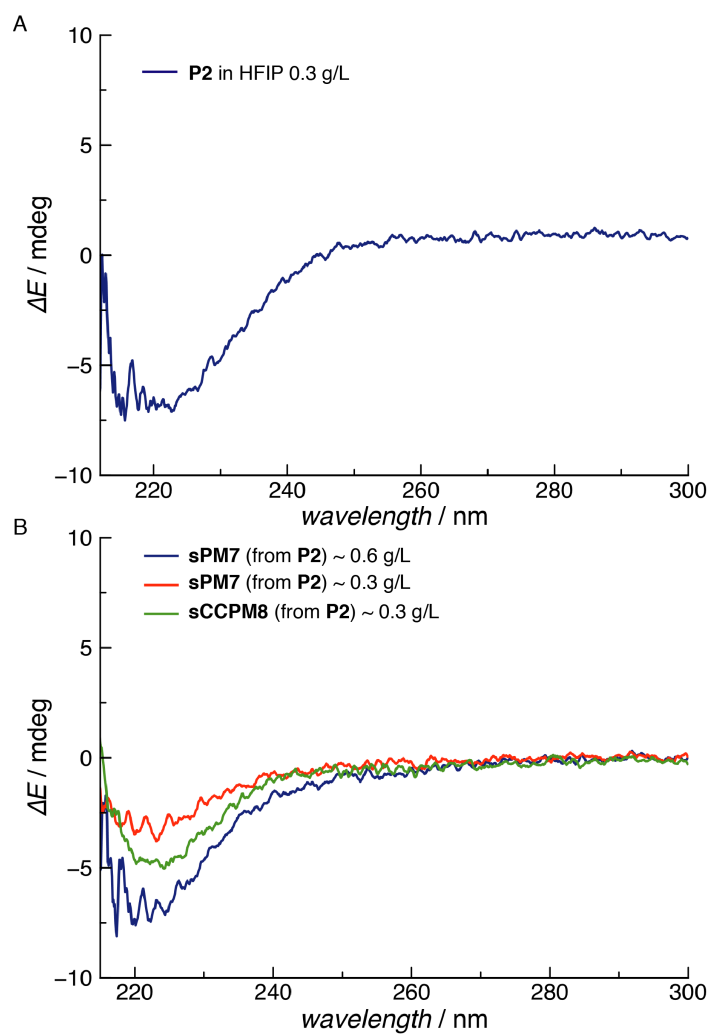


Figure 12.8: CD spectra of A) P2 in HFIP ( $+3 \text{ g L}^{-1}$  KTFA) and B) of micelles (PM) and core cross-linked micelles (CCPM) from P2 in 1 mM acetate buffer.

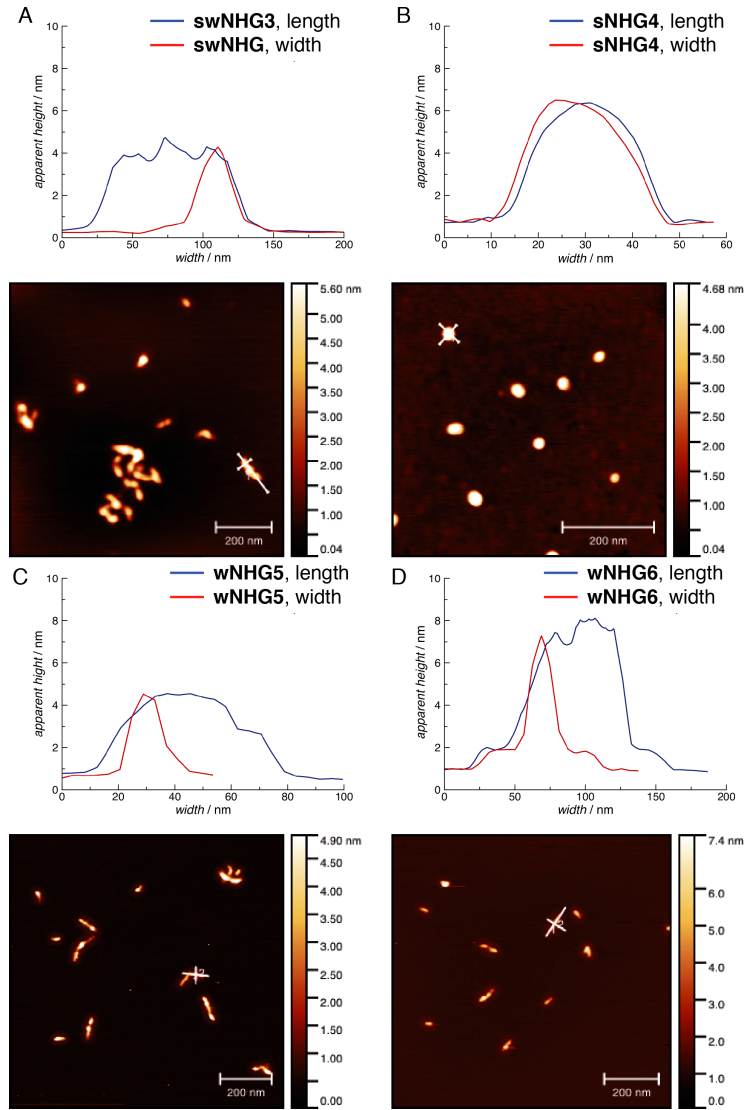


Figure 12.9: Extracted apparent height profiles of nanohydrogels **swNHG3**, **sNHG4**, **wNHG5** and **wNHG6** corresponding to AFM micrographs shown in Figure 12.2 C) and D).

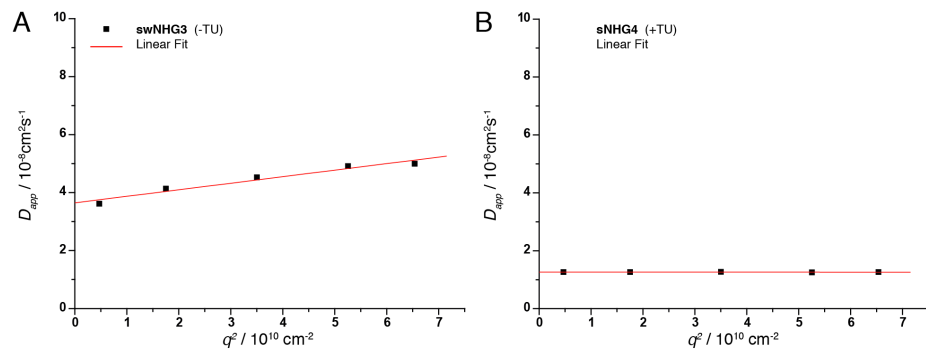


Figure 12.10: Multi-angle dynamic light scattering (DLS) of nanohydrogels from **P2**: A) **swNHG3** with  $R_h = 59.4$  nm and  $\mu_2 = 0.17$  in the absence and B) **sNHG4** with  $R_h = 17.2$  nm and  $\mu_2 = 0.06$  in the presence of thio-urea.

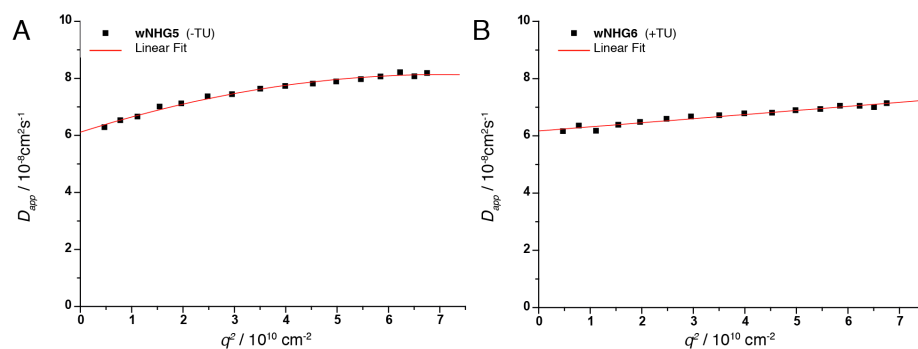


Figure 12.11: Multi-angle DLS of nanohydrogels from P3: A) wNHG5 with  $R_h = 35.6$  nm and  $\mu_2 = 0.19$  in the absence and B) wNHG6 with  $R_h = 35.2$  nm and  $\mu_2 = 0.15$  in the presence of thiourea.

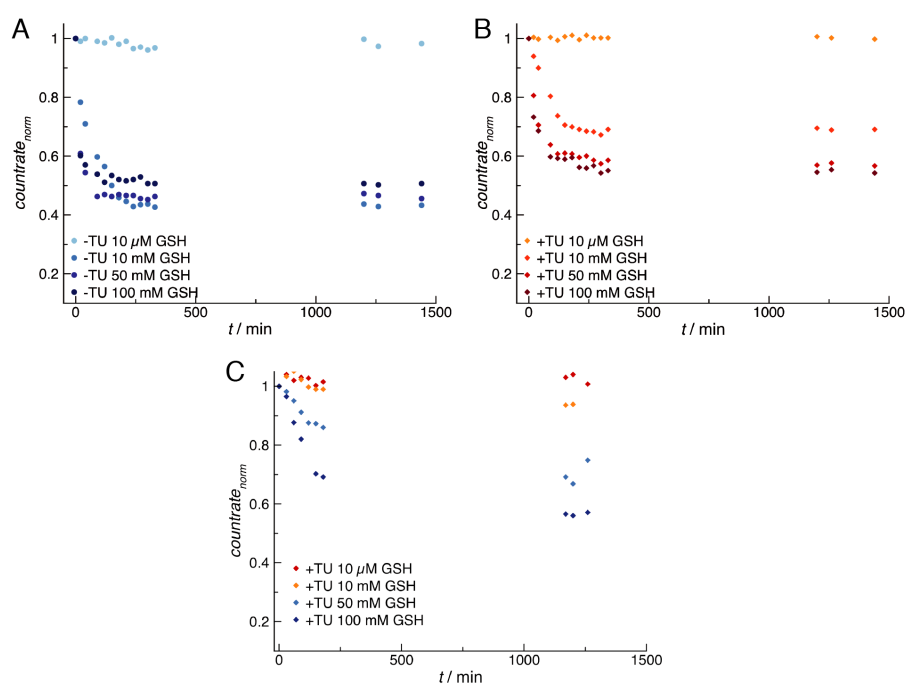


Figure 12.12: Degradation of NHGs and CCPMs depending on glutathione concentration observed at different time points via DLS. All reactions were carried out under physiological relevant conditions (PBS buffer at pH7.1 and 37 °C). The attenuator remained fixed and the normalized count rate is plotted as a function of time. Degradation of nanohydrogels A) in absence or B) presence of thiourea and C) degradation of cross-linked polymeric micelles in presence of thiourea.

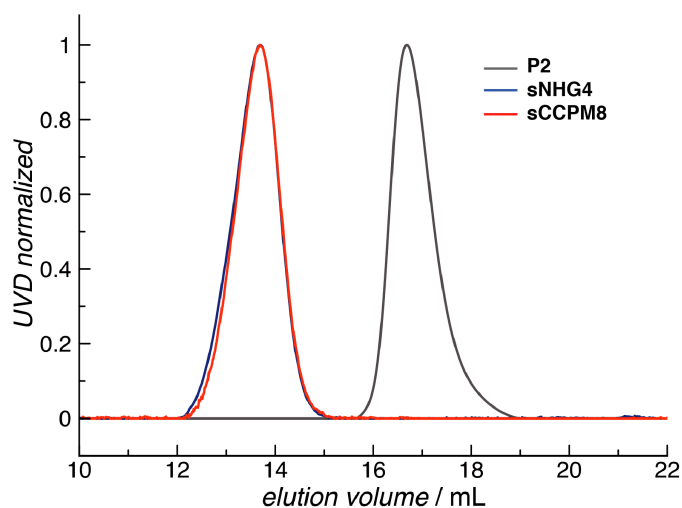
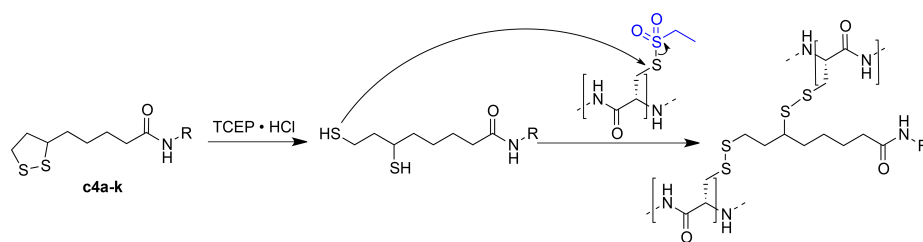


Figure 12.13: HFIP GPC traces of **P2** and **sNHG4** after cross-linking with **c2** and **sCCPM8** after cross-linking with **c1** both after purification using spin filters (MWCO = 100 kDa).

Table 12.4:  $\log P$  values for cross-linkers **c1**, **c3** and **c4a-k** as calculated from MarvinSketch V16.718.0.

cross-linker	$\log P$	cross-linker	$\log P$
<b>c1</b>	2.76	<b>c4f</b>	3.25
<b>c3</b>	2.11 <sup>a</sup>	<b>c4g</b>	3.55
<b>c4a</b>	1.41	<b>c4h</b>	3.74
<b>c4b</b>	1.48	<b>c4i</b>	4.54
<b>c4c</b>	1.76	<b>c4j</b>	4.55
<b>c4d</b>	2.85	<b>c4k</b>	7.30

<sup>a</sup> for the sodium salt  $\log P = -1.4$ .



Scheme 12.2: Mechanism of cross-linking using pre-reduced lipoic acid-based cross-linkers **c4a-k**.

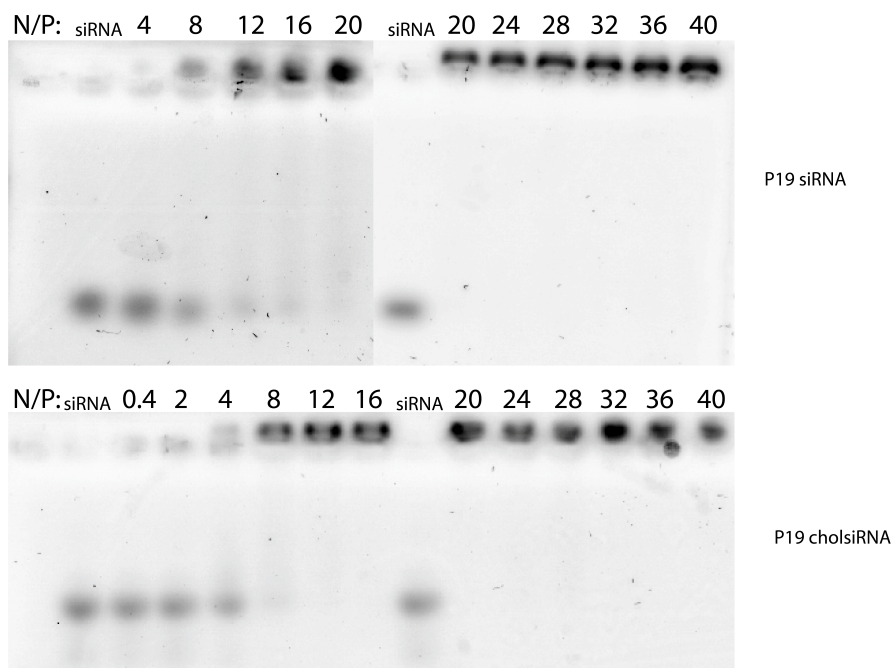


Figure 12.14: Agarose gel electrophoresis of chol-siRNA loaded wNHG1 at different N/P ratios. Complete complexation can be obtained at  $N/p=8$ .

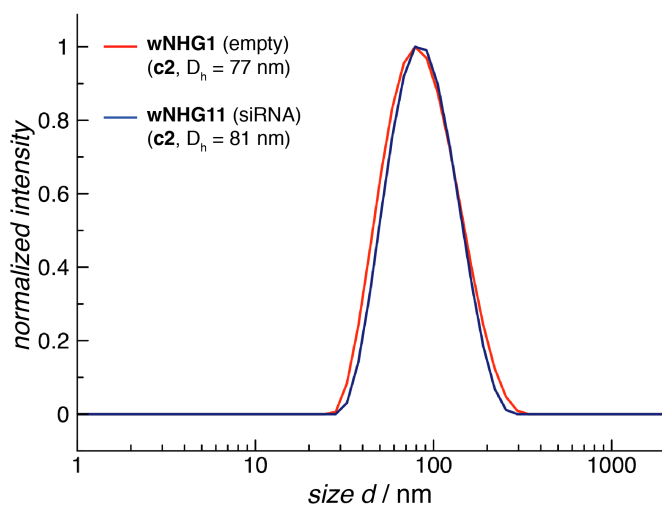
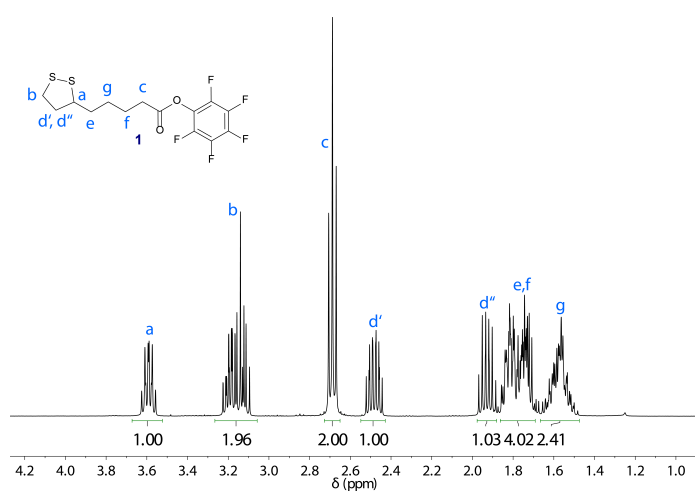
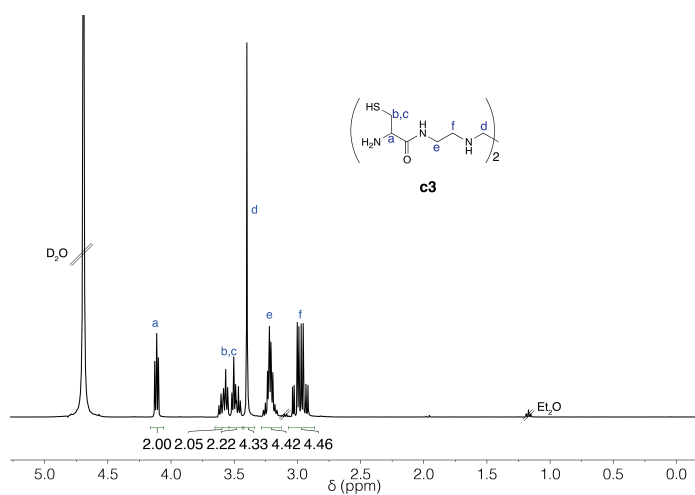
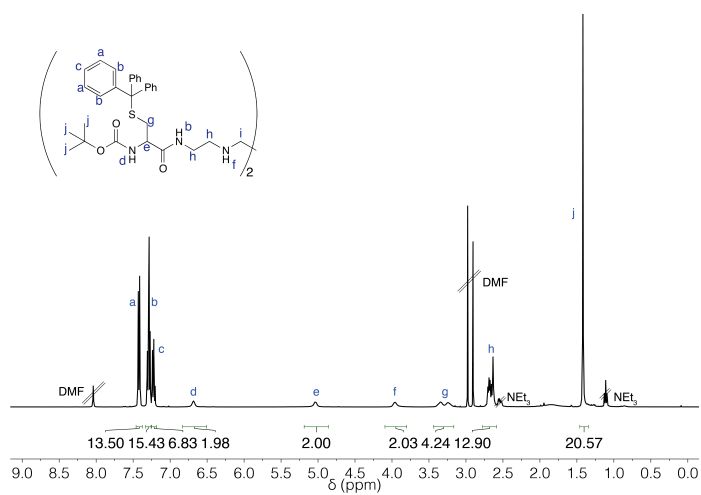
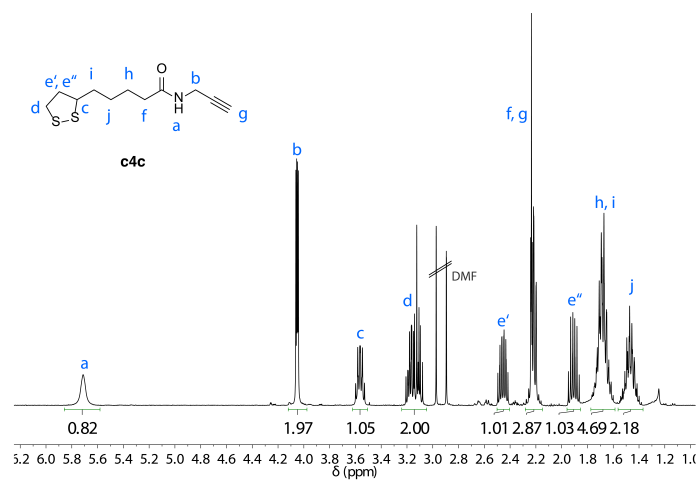
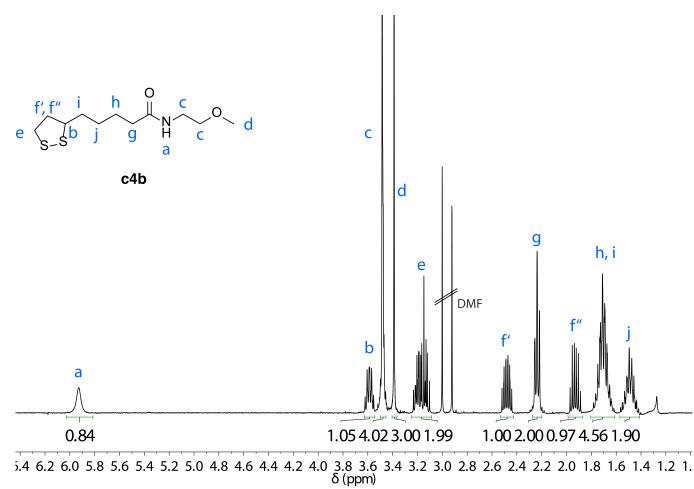
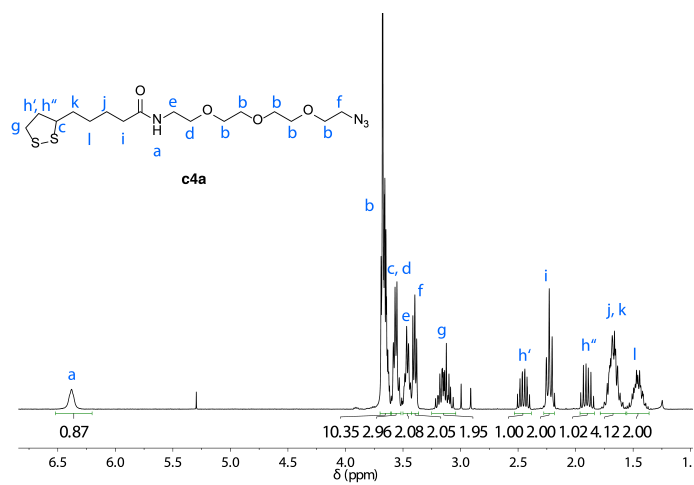
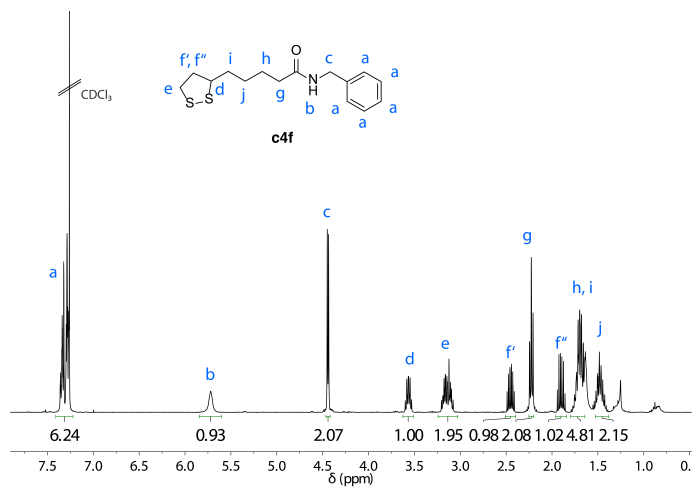
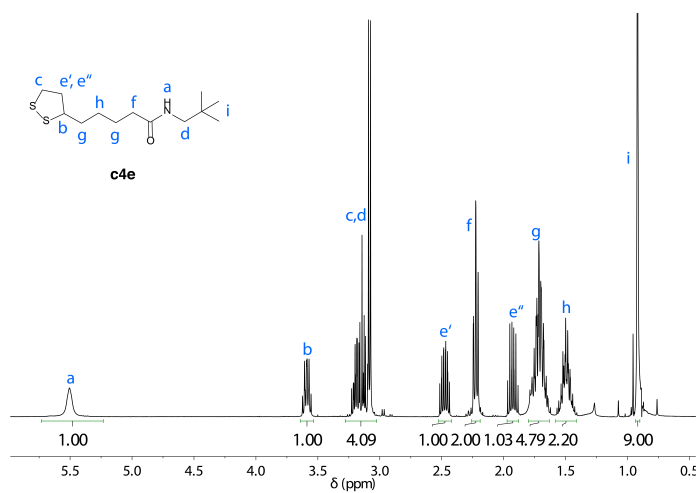
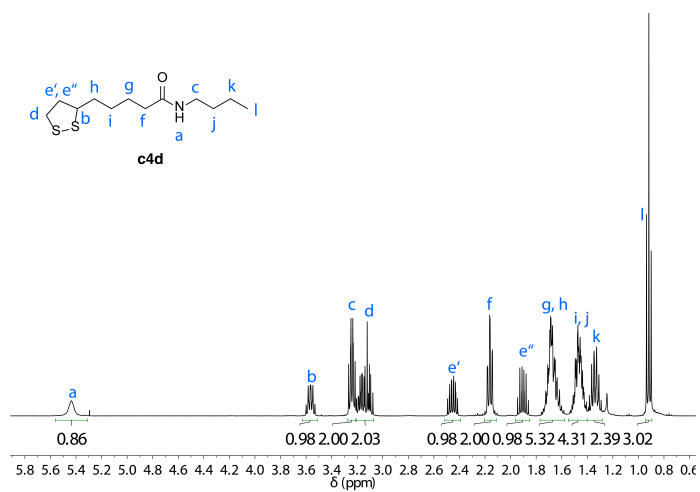


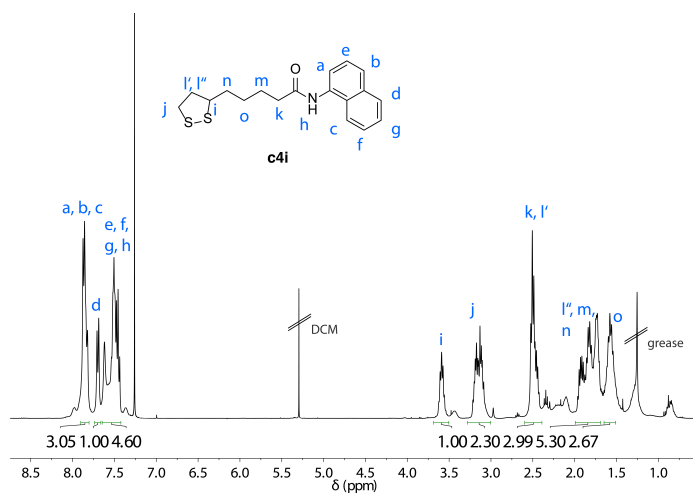
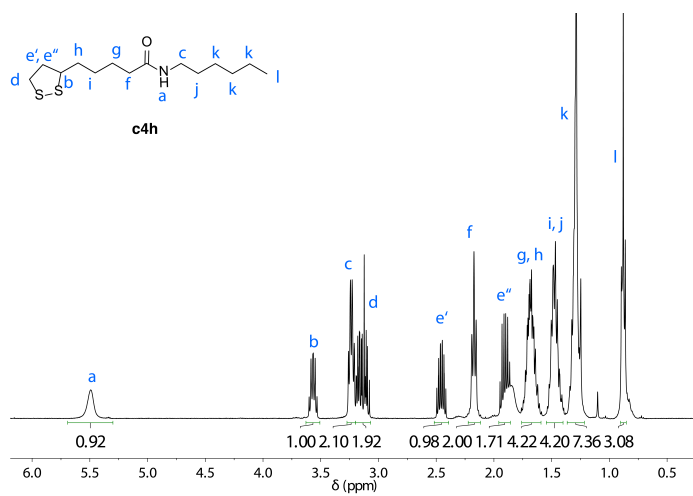
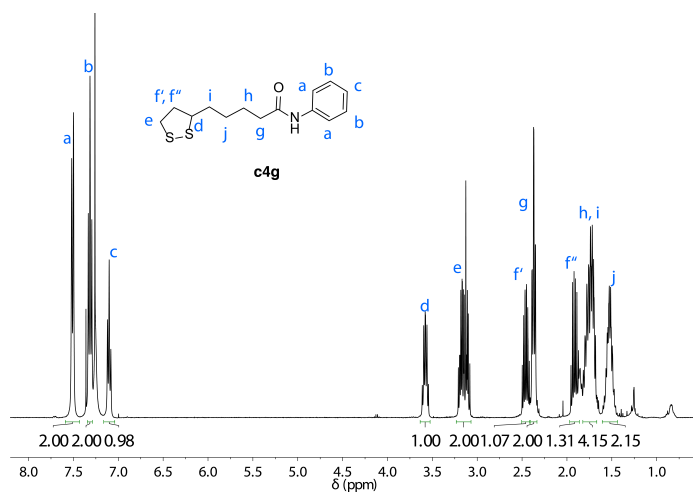
Figure 12.15: DLS of nanohydrogel from polymer P1 before (wNHG1) and after loading with siRNA (wNHG11).

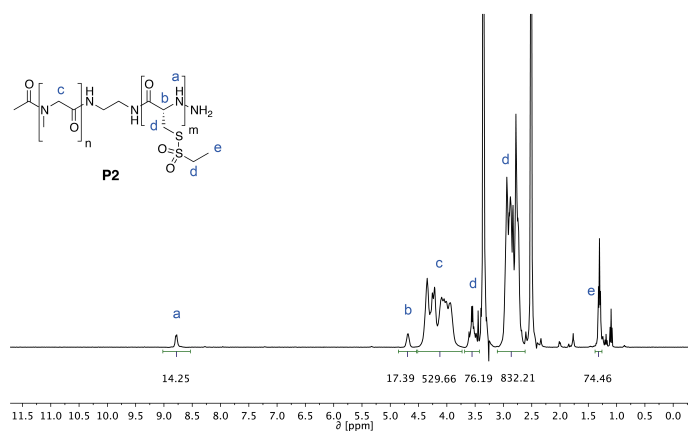
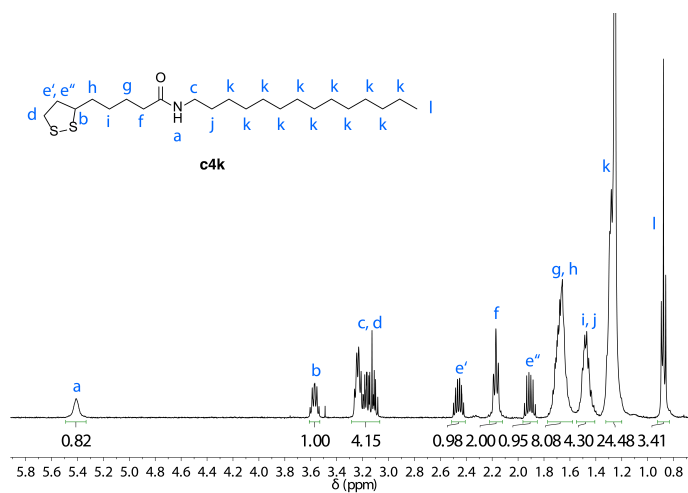
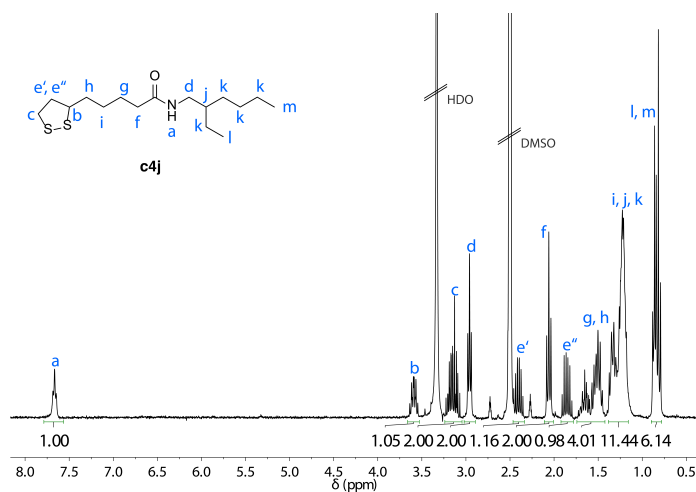
12.5.4  $^1\text{H}$  NMR Spectra











SCREENING PARAMETERS OF DIBLOCK  
 COPOLYPEPT(O)IDE SELF-ASSEMBLY

Self-assembly of amphiphiles is typically influenced by parameters such as block length ratio and solvent composition.<sup>[495]</sup> In addition, as demonstrated in Chapter 12, the choice whether chaotropic agents are employed or not, will have a distinct influence on self-assembly on polypept(o)ides exhibiting secondary structures, as micellar structures were found to vary in size and shape. Thus, to provide a better understanding of underlying principles, conditions of self-assembly of poly-sarcosine-*block*-poly(*S*-alkylsulfonyl-L-cysteine) (PSar-*b*-PCys(SO<sub>2</sub>R)) block copolypept(o)ides were screened methodically in this chapter. The possible modes of the self-assembly of PSar-*b*-PCys(SO<sub>2</sub>R) in respect to secondary structure formation are illustrated in Figure 13.1.

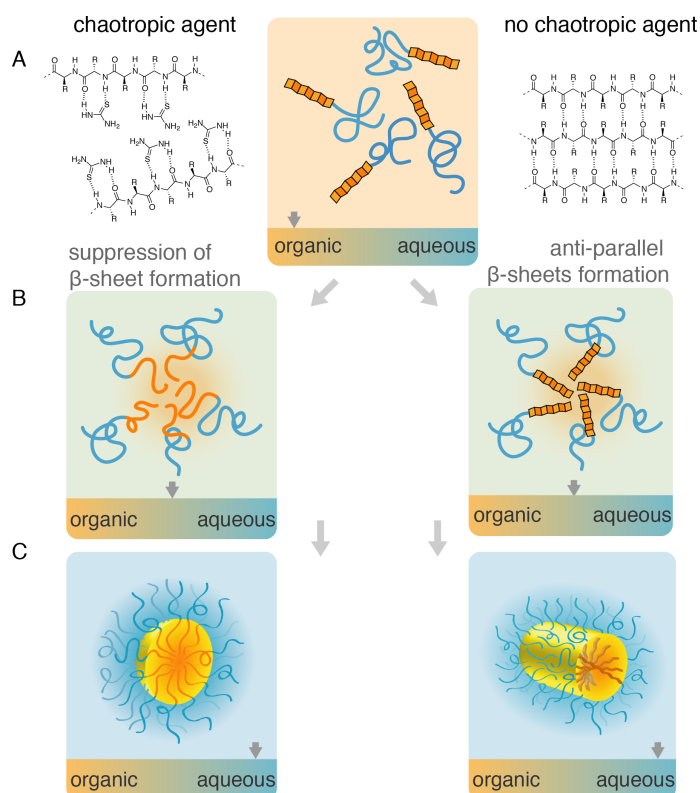


Figure 13.1: Self-assembly of amphiphilic PSar-*b*-PCys(SO<sub>2</sub>R) block copolymers by the solvent switch method. A) PCys(SO<sub>2</sub>R) (*orange*) exhibits anti parallel  $\beta$ -sheets in an organic solvent (*right*) which are suppressed by addition of a chaotropic agent (*left*). B) Self-assembly of coil-coil polymers in the case of suppressed secondary structures (*left*) or self-assembly of rod-coil polymers (*right*) into C) predominantly spherical structures in presence of chaotropic agents (*left*) or elongated structures stabilized by  $\beta$ -sheets in the particle core (*right*).

The PCys(SO<sub>2</sub>R) segment exhibits  $\beta$ -sheets in aqueous solution as well as in organic solvents.<sup>[209]</sup> In contrast, addition of chaotropic agents such as thiourea will disrupt intra molecular hydrogen-bond formation (Figure 13.1 A). During the solvent-switch, amphiphilic macromolecules arrange in accordance to the volume ratio of the hydrophobic and hydrophilic segment.<sup>[495]</sup> In the absence of  $\beta$ -sheets, the resulting polymer is in a coil-coil conformation and follows solely those parameters.

However, if  $\beta$ -sheet formation is enabled, the self-assembly of resulting rod-coil polymers does not necessarily follow the anticipated principles directed by blocklength ratios (depicted in Figure 13.1 B).<sup>[503,504]</sup> A one-dimensional growth by the controlled aggregation of peptide amphiphiles in e. g. filamentous aggregates is a well established concept in supramolecular chemistry.<sup>[502,509–511]</sup> Further,  $\beta$ -sheets are known to form  $\beta$ -sheet barrels in natural peptides.<sup>[520]</sup> Thus, a one-dimensional arrangement of PSar-*b*-PCys(SO<sub>2</sub>R) into elongated structures as illustrated in Figure 13.1 C is proposed. In extreme cases, the same polymer can then yield elongated structures if  $\beta$ -sheet formation is enabled, and spherical structures when prepared in presence of chaotropic agents.<sup>[22]</sup>

### 13.1 RESULTS AND DISCUSSION

The parameters, by which self assembly of polysarcosine-*block*-poly-(S-ethylsulfonyl-L-cysteine) (PSar-*b*-PCys(SO<sub>2</sub>Et)) block copolypept(o)ides can be controlled are the ratio of hydrophobic-hydrophilic segment and the use of chaotropic agents. First, block copolypept(o)ides of varying hydrophobic-hydrophilic ratio were prepared, which is expressed by weight percentage (wt. %) of the PCys(SO<sub>2</sub>Et) segment on the total molecular weight. Figure 13.2 gives an overview on the investigated polymer compositions and shows the possible relations which can be compared.

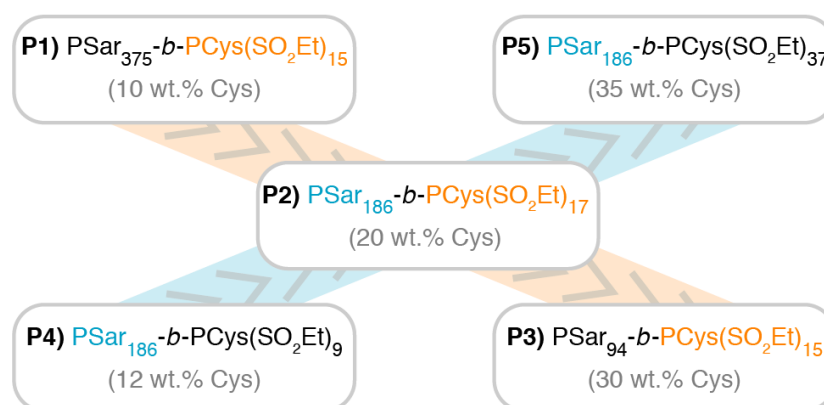


Figure 13.2: PSar-*b*-PCys(SO<sub>2</sub>Et) diblock copolypept(o)ides of varying compositions for evaluation of self-assembly conditions: *from top left to bottom right* increasing hydrophobic block ratio upon constant S-ethylsulfonyl-cysteine block length (constant PCys(SO<sub>2</sub>Et) in orange) and *from bottom left to top right* increasing hydrophobic block ratio upon constant polysarcosine block length (constant PSar in blue).

Polymers P1-3 maintain a comparable total length of the hydrophobic PCys(SO<sub>2</sub>Et) block (in *orange*), while the relative hydrophobic fraction increases due to the shorter polysarcosine chain length (*from top left to bottom right*). In contrast, P4, P2 and P5 maintain the same length of the hydrophilic polysarcosine (in *blue*), again while the relative hydrophobic fraction increases due to the longer PCys(SO<sub>2</sub>Et) chain length (*from bottom left to top right*).

The mechanism of self-assembly is based on microphase separation of two immiscible blocks, which is driven by a decrease in free energy due to hydrophobic interactions.<sup>[441,526]</sup> Upon variation of the solvent composition, polymer-polymer interactions slowly override polymer-solvent interactions of the hydrophobic block. Ultimately, an amphiphilic system arranges a local thermodynamic equilibrium structure characteristic for this particular block copolymer under the specific conditions. Thus, at a certain solvent composition, a block copolymer will arrange in a thermodynamic stable fashion. Since all micellar aggregation processes are of dynamic nature, micelles exist in equilibrium with block copolymer unimers above their critical aggregation concentration CMC.<sup>[527]</sup> In terms of micelle stability, this thermodynamic regime favored to a kinetically obtained structure, which are always prone to disassembly without further stabilization.<sup>[153]</sup>

The structures discussed in Chapter 12 in Figure 12.6) were prepared in a local thermodynamic equilibrium for the particular system. In the present study, the self-assembly process was tightly screened to cover all possible self-assembly structures. Thus, solvent compositions ranged from 10 vol. % of block-selective solvent to 30 vol. % in increments of 2.5 vol. %. Micelles were prepared under identical conditions, changing only the solvent composition, and the particle size was analyzed by dynamic light scattering (DLS) after workup. Figure 13.3 summarizes the results divided in four cohorts for comparison: (*top*) self-assembly of P1-3 with same length of the hydrophobic block in absence (A) or presence (B) of  $\beta$ -sheets and (*bottom*) self-assembly of P4, P2 and P5 with same length of the hydrophilic block, also in absence (C) or presence (D) of  $\beta$ -sheets.

A first inspection shows, how polymers with similar wt. % hydrophobic block behave alike, as can be seen from comparing general trends of data sets from the top to the bottom row. Detailed information on self-assembly of individual polymers with respect to size and distribution is given in Figure 13.4-13.8. Polymers with highest wt. % hydrophobic block ratios (P3 and P5) yield small, well defined particles above 20 vol. % of block-selective solvent. Upon hydrodynamic diameters of 30-40 nm, micelle distributions range around  $PDI \lesssim 0.1$  independently of chaotropic agent (compare Figure 13.6 and 13.8). This finding is consistent with the general concept of solvent-solute interaction: a larger hydrophobic block collapses at lower vol. % of block-selective solvent, favoring chain-chain instead chain-solvent interactions. Thus, self-assembly at high vol. % of block-selective solvent will yield kinetically

*Hydrophobic volume ratio dictates the overall aggregation behavior.*

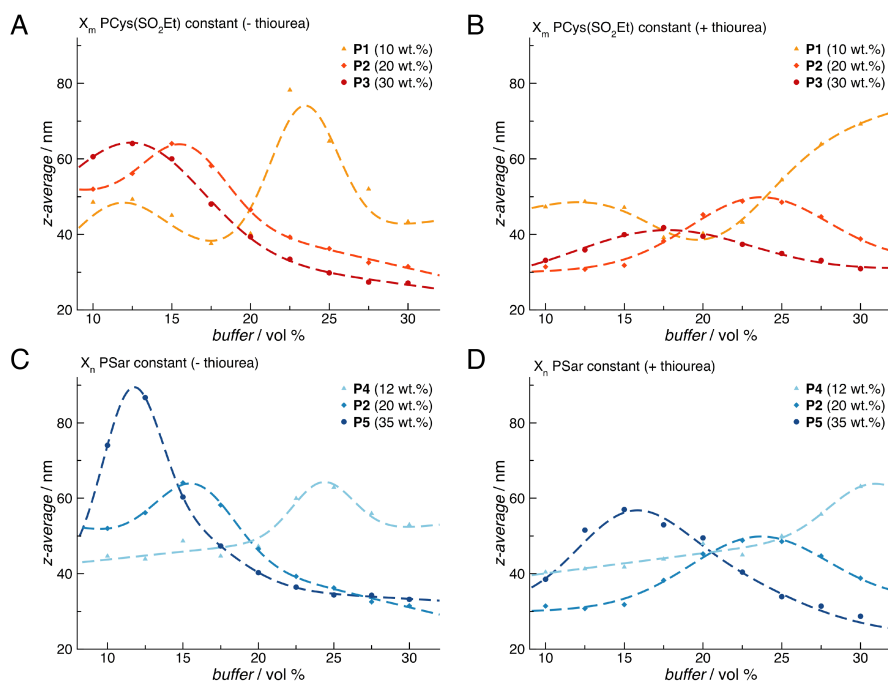


Figure 13.3: Evaluation of self-assembly behavior of diblock copolypept(o)ides: (top) constant *S*-ethylsulfonyl-cysteine block length and self-assembly A) without and B) in the presence of thiourea as chaotropic agent, (bottom) constant polysarcosine block length and self-assembly C) without and D) in the presence of thiourea as chaotropic agent.

driven structures instead of a slow, thermodynamically driven aggregation of polymer chains.

In contrast, P1 and P4 with lowest wt. % hydrophobic block ratios yield large structures upon higher vol. % of block-selective solvent. Especially for self-assembly with chaotropic agent above 25 vol. %, particles are poorly defined. In this case, micelles exhibit poor distributions with PDIs  $\gtrsim 0.2$  for micellar aggregates of hydrodynamic diameters well above 50 nm (compare Figure 13.4 and 13.7). With loss of the ability to form intra molecular hydrogen bonds, stabilization depends solely on hydrophobic chain-chain interactions. As a consequence, definition of structures derived from polymers with short PCys(SO<sub>2</sub>Et) blocks suffers considerably from self-assembly in a kinetically driven regime and will profit from the possibility of  $\beta$ -sheet stabilization. Thus, self-assembly in presence of chaotropic agents upon polymers with short PCys(SO<sub>2</sub>Et) block should be avoided.

As can be derived from comparing self-assembly in absence of chaotropic agents (left) to their presence (right), larger micellar structures were obtained without a chaotropic agent. The cooperative effect of  $\beta$ -sheet stabilization will presumably allow for aggregation of more polymer chains in one structure.  $\beta$ -sheets are known to form  $\beta$ -sheet barrels in natural peptides,<sup>[520]</sup> thus a one-dimensional growth into elongated structures is plausible. During a slow self-assembly in the regime below 20 vol. % of block-selective solvent, the driving force for this one dimen-

sional aggregation is higher than in the large vol. % regime. Again, this effect is more pronounced for P3 and P5 with highest ratio of the  $\beta$ -sheet forming PCys(SO<sub>2</sub>Et) block. From the findings stated above, it can be concluded that the hydrophobic block ratio dictates the overall aggregation behavior in block selective solvent mixtures, mostly independently from overall polymer length. Further, no notable change in particle size of the non cross-linked micelles was observed upon extended storage (over 1 year) in respective buffer at 4 °C (Figure 13.4 to 13.8 in the supporting information). In addition, stable and well defined micelles exhibiting distributions approximately below a PDI  $\lesssim$  0.15 maintained this good distribution over 1 year. As a consequence, the pronounced stability of the obtained PSar-*b*-PCys(SO<sub>2</sub>Et) based micelles stresses the importance of self-assembly in a thermodynamic equilibrium.

Additionally, valuable implications are accessible from the display of self-assembly of the same polymer in presence or absence of a chaotropic agent. Conditions which give comparable results independently from chaotropic agents, are most likely driven by the hydrophobic-hydrophilic volume ratio. This can be either due to self-assembly in a kinetic regime (compare P3 in Figure 13.6 or P5 in Figure 13.8 above 20 vol. %) or due to low influence of secondary structure stabilization of short chains in a thermodynamic regime (compare P1 in Figure 13.4 or P4 in Figure 13.7 below 20 vol. %). The most intriguing conditions were found for P2 in Figure 13.5: The opposing trends in size for presence or absence of a chaotropic agent indicate considerable influence of secondary structure stabilization on the resulting self-assembled structures. Thus, deviating morphology as proposed in Figure 13.1 and demonstrated in Chapter 12 may be achieved when self-assembly is performed under those conditions.

*Influence of secondary structures on self-assembly outcome.*

## 13.2 CONCLUSION

The presented study enables orientation on self-assembly conditions for amphiphilic PSar-*b*-PCys(SO<sub>2</sub>Et) diblock copolypept(o)ides. A broad range of nanodimensional core-shell carrier systems were evaluated based on secondary structure modulated self-assembly of amphiphilic PSar-*b*-PCys(SO<sub>2</sub>Et) diblock copolypept(o)ides. Upon variation of parameters such as hydrophobic to hydrophilic block length ratio and/or block selective solvent composition, size and shape of the resulting micelles can be modulated as follows:

- Self-assembly of polymers with low wt. % hydrophobic block in presence of chaotropic agents should be avoided, due to insufficient control without secondary structure stabilization.
- Polymers with high wt. % hydrophobic block have a tendency to aggregate faster compared to polymers with low wt. %. As a result, small, well defined structures are obtained above 20 vol. % of block-selective solvent independent of secondary structures.

- Elongated structures are expected for polymers with high wt. % hydrophobic block in a slow, thermodynamically controlled aggregation. This can be achieved below 20 vol. % of block-selective solvent independent of secondary structures.
- However, overall larger structures can be obtained in absence of chaotropic agents, indicating a one dimensional growth mediated by  $\beta$ -sheet stabilization.
- Polymers with intermediate wt. % hydrophobic block (15-20 wt. %) follow opposing trends for self-assembly with and without chaotropic agents in a thermodynamic regime below 20 vol. % of block-selective solvent.
  - In presence of chaotropic agents, small micelles of presumably spherical morphology are obtained.
  - In absence of chaotropic agents, large micelles of presumably elongated morphology are obtained due to one dimensional growth by  $\beta$ -sheet stabilization.
- Well-defined PSar-*b*-PCys(SO<sub>2</sub>Et) based micelles will maintain overall dimensions as well as particle distribution upon extended storage in solution.

In conclusion, a prediction on micellar dimensions and shape prior to self-assembly of new batches of block copolypept(o)ides can be made based on principles outlined above. The parameters of interest are the block-length ratio, deviation of self-assembly behavior from presence to absence of chaotropic agents and the amount of block selective solvent during self-assembly.

### 13.3 SUPPORTING INFORMATION

#### 13.3.1 Self-Assembly of Amphiphilic Micelles

For preparation of polysarcosine-*block*-poly(*S*-ethylsulfonyl-L-cysteine) (PSar-*b*-PCys(SO<sub>2</sub>Et)) block copolymers see Chapter 12 or 10.<sup>[22,327]</sup> The resulting amphiphilic block copolymers were self-assembled using a protocol reported previously.<sup>[22]</sup> Briefly, the polymer was dissolved in *N,N*-dimethyl acetamide (DMAc) at a concentration of 7.5 g L<sup>-1</sup> for 2 h. Various volume percentages of 1 mM acetate buffer (pH = 4.7) were added as the block-selective solvent. Self-assembly was carried out in the presence or absence of thiourea as chaotropic agent with 10-30 volume % of block selective solvent. For self-assembly processes with suppression of the  $\beta$ -sheet formation of the polycysteine segment the DMAc contained 1 M and the 1 mM acetate buffer contained 10 mM thiourea as chaotropic agent. The solutions were left to equilibrate for 3 h, dialyzed against the respective buffer (3.5 kDa) and filtered using a 200 nm filter (GHP). Micelles were stored in the respective buffer at 4°C. The size range of



micelles prepared from **P1-5** was evaluated by DLS at 25°C. DLS experiments were performed immediately after self-assembly and work-up as well as after 1 year storage in the respective aqueous buffer at 4°C.

Table 13.1: Characterization of  $\text{PSar}_n\text{-}b\text{-PCys}(\text{SO}_2\text{Et})_m$  diblock copoly-pept(o)ides.

No	$X_{n, \text{GPC}}^a$	$X_{m, \text{NMR}}^b$	$M_{n, \text{GPC}}^c / \text{g mol}^{-1}$	$D_{\text{GPC}}^c$
<b>P1</b>	375	15	32000	1.24
<b>P2</b>	186	17	27900	1.21
<b>P3</b>	94	15	22500	1.17
<b>P4</b>	186	9	25300	1.23
<b>P5</b>	186	37	31200	1.25

<sup>a</sup>  $X_n$  PSar relative to PSar standards.<sup>[47]</sup>

<sup>b</sup>  $X_m$  from  $^1\text{H NMR}$  relative to  $X_{n, \text{GPC}}$  PSar.

<sup>c</sup> Relative to PMMA standards.

### 13.3.2 Size Range and Distribution of Micelles (immediately after preparation / 1 year storage)

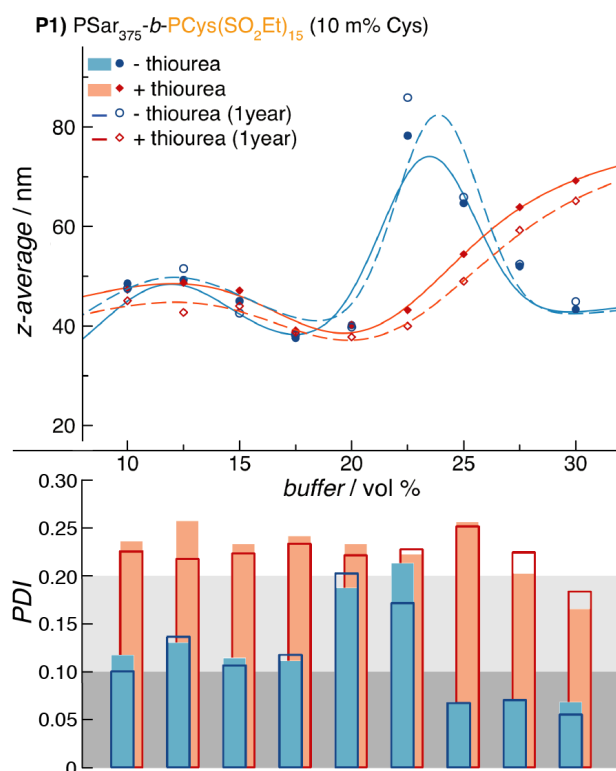


Figure 13.4: Size range and PDI of micelles prepared from **P1**(determined by DLS).

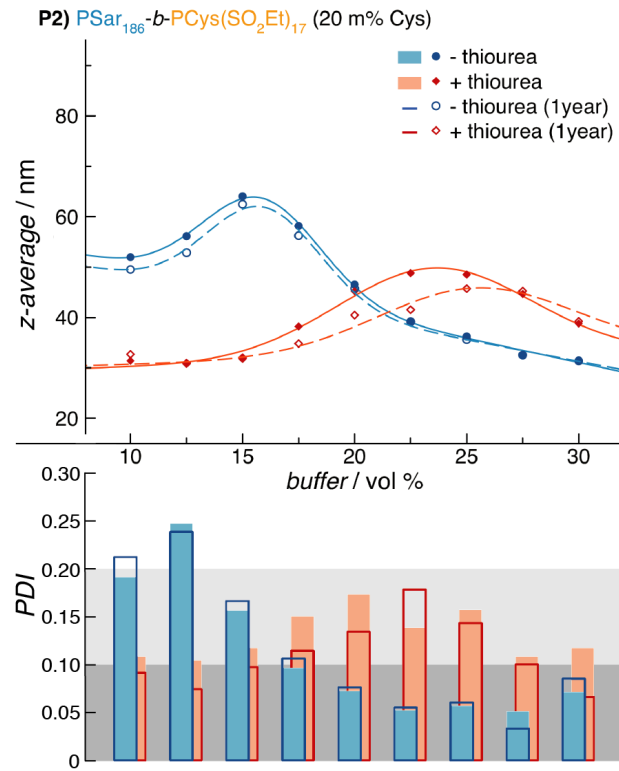


Figure 13.5: Size range and PDI of micelles prepared from P2 (determined by DLS).

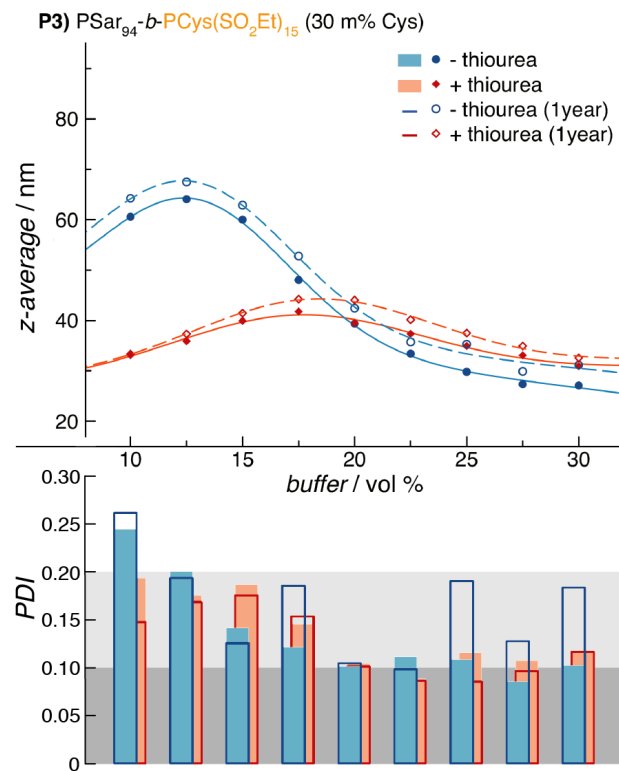


Figure 13.6: Size range and PDI of micelles prepared from P3 (determined by DLS).

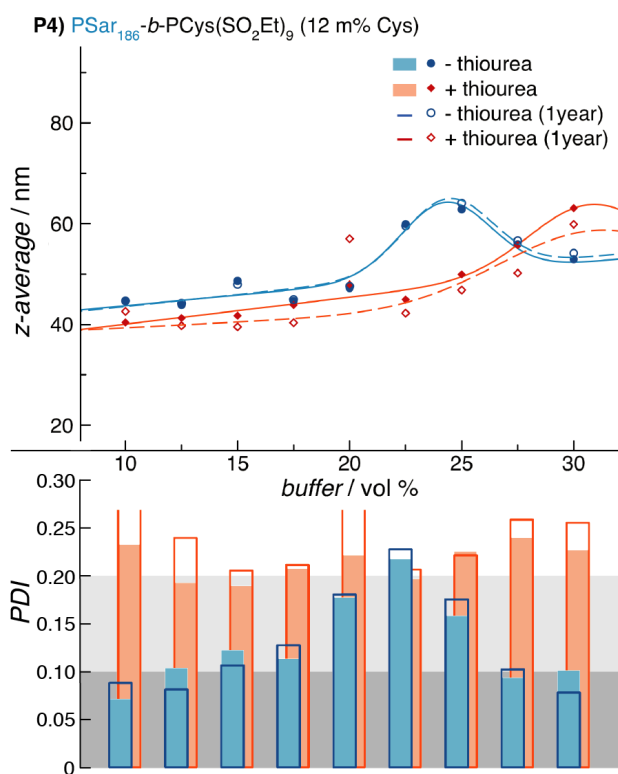


Figure 13.7: Size range and PDI of micelles prepared from P4 (determined by DLS).

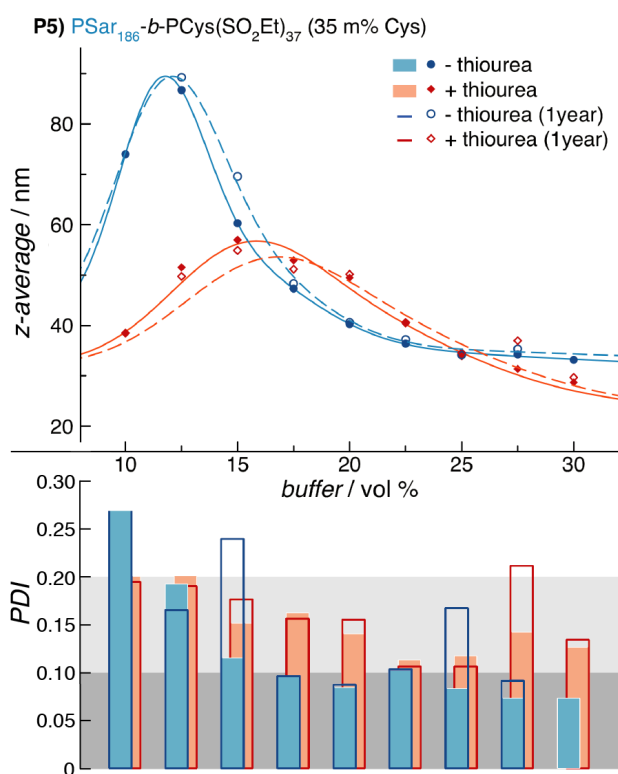


Figure 13.8: Size range and PDI of micelles prepared from P5 (determined by DLS).



MONITORING DRUG NANOCARRIERS IN HUMAN BLOOD BY NEAR-INFRARED FLUORESCENCE CORRELATION SPECTROSCOPY

The polymeric micelles presented in Chapter 13 proved remarkable stability in terms of size and definition when stored in aqueous media. Without covalent stabilization e. g. by disulfide bridges (Figure 14.1 A), however, the introduction of micellar nanocarriers in biological relevant environments such as the blood stream, will considerably destabilize the self-assembled system. Dilution, shear forces in flowing blood as well as presence of surfaces for adsorption such as proteins, will result in leakage of the amphiphilic unimers from a non-stabilized micelle (Figure 14.1 B) and demonstrate poor systemic circulation.

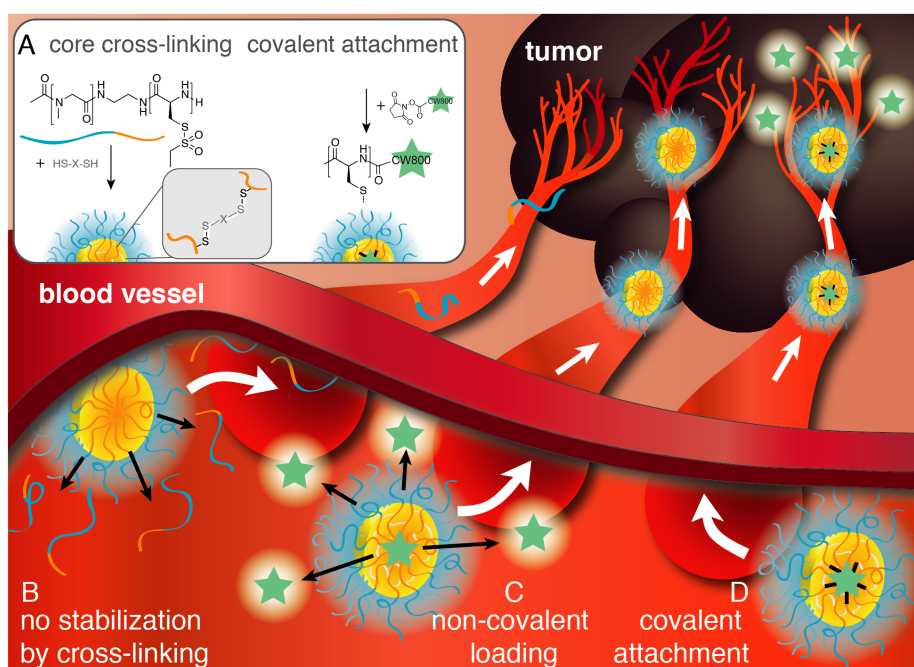


Figure 14.1: Illustration of the fate of covalently or non-covalently modified nanocarriers in the blood stream: A) Covalent modifications in the compartment such as disulfide core cross-linking and covalent labeling with amine-reactive IRDye<sup>®</sup> 800CW NHS-ester. B) Without covalent stabilization of micellar nanocarriers, amphiphilic unimers may diffuse from the micelle. C) Nanocarriers loaded non-covalently with IRDye<sup>®</sup> 800CW are prone to loss of cargo (adsorption to biological surfaces). Thus, observed fluorescence signal is no longer associated with the carrier system. D) Covalent attachment ensures co-localization of observed fluorescence with the carrier system, as far as cellular internalization occurs followed by a stimuli-responsive breakdown of the disulfide core-stabilization and release of cargo/fluorescence.

Further, non-covalently loaded or labeled nanocarriers are prone to loss of cargo due to a surfaces available for adsorption upon introduction into biological environments.<sup>[151]</sup> As a consequence, co-localization of the monitored label with the carrier system is no longer guaranteed (Figure 14.1 C). Thus, the rational design of well defined and reliable carrier systems has to ensure stabilization of the nanocarrier itself as well as consider covalent attachment of the encapsulated cargo.

NIR-FCS  
evaluation of drug  
nanocarriers in  
full blood.

Loading stability of core cross-linked micelles, can be demonstrated by near-infrared fluorescence correlation spectroscopy (NIR-FCS) allowing for evaluation of drug nanocarriers in blood. Furthermore, fluorescence correlation spectroscopy (FCS) measurements offer complementary to light scattering access to nanocarrier dimensions in solution (compare Section 5.2.3 for theoretical background). Especially the resemblance of hydrodynamic radii in aqueous media (as present during particle preparation and characterization) to biological relevant media such as serum, plasma or full blood is a desirable feature validating stability of the particles as well as low protein adsorption. To demonstrate how the NIR-FCS method can be used to monitor the behavior of drug nanocarriers in blood spherical core cross-linked polymeric micelles (CCPMs) were employed. Polymeric micelles were prepared by means of self assembly in the presence of thiourea from PSar<sub>203</sub>-*b*-PCys(SO<sub>2</sub>Et)<sub>11</sub> (13 wt% of the hydrophobic block) at 23 vol. % block selective solvent (see micelle preparation and labeling). Subsequent core cross-linking by hexanedithiol and fluorescent labeling of the *N*-terminus of the PCys(SO<sub>2</sub>Et) segment in the core-compartment (as introduced in Chapter 10) yielded a covalently modified particle, as illustrated in Figure 14.1 D.

*The following passages and results are reproduced with permission from: Inka Negwer, Andreas Best, Meike Schinnerer, Olga Schäfer, Manfred Schmidt, Volker Mailänder, Mark Helm, Matthias Barz, Hans-Jürgen Butt, Kaloian Koynov, "Monitoring Drug Nanocarriers in Human Blood by Near-Infrared Fluorescence Correlation Spectroscopy" Nature Communications 2018, under revision, NCOMMS-18-12754-T.*

CCPMs were loaded with IRDye<sup>®</sup> 800CW, which was used as a model for a small drug molecule. IRDye<sup>®</sup> 800CW was either covalently (**PM1**) or non-covalently (**PM2**) attached to the nanocarriers (see supporting information). A first NIR-FCS characterization in water revealed hydrodynamic radii for **PM1** and **PM2** of 51 nm and 44 nm, respectively (Figure 14.2 A). These values were in accordance with the multi-angle dynamic light scattering data obtained for the unloaded micelles ( $R_{h,PM} = 45$  nm) and indicated that the IRDye<sup>®</sup> 800CW molecules were indeed loaded to the micelles. Nevertheless, the FCS fits also indicated the presence of a second type of fluorescent species with  $R_h$  1 nm, which was identified as free dye with apparent fractions of 6 % for **PM1** and 23 % for **PM2**. After 30 h of incubation in blood, the micelles were sub-

jected to NIR-FCS measurements in flowing blood. The processed autocorrelation curves devoid of cell contributions are shown together with the corresponding fits in Figure 14.2 B.

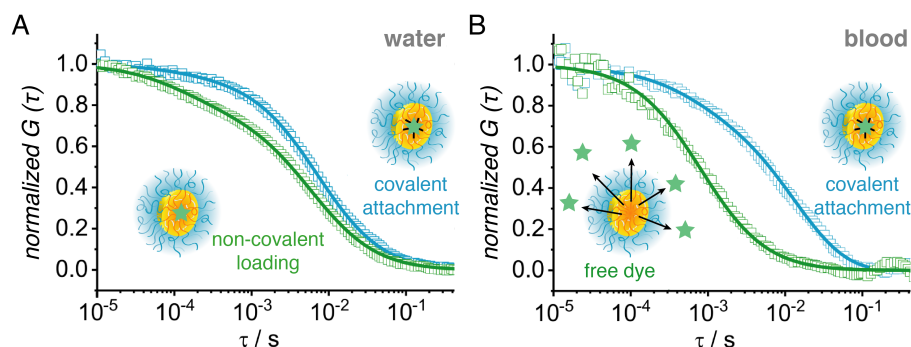


Figure 14.2: NIR-FCS studies of the loading stability of core cross-linked nanocarriers in blood. Normalized autocorrelation curves (symbols) and the corresponding fits (lines) are shown for micelles that were either covalently (**PM 1**, blue) or non-covalently (**PM 2**, green) loaded with IRDye<sup>®</sup> 800CW. A) Measurements in water. The dye is mainly loaded to the micelles and only a small fraction of free dye was detected for both systems. B) Measurements in the blood flow (velocity of  $50 \mu\text{L h}^{-1}$ ) upon incubation with blood for 30 h (at  $4^\circ\text{C}$ ). The dye is fully released from **PM 2**, but still loaded to **PM 1**.

As in water, two fluorescent species with different hydrodynamic radii of 55 nm and 2.9 nm were observed for **PM 1**. The larger species corresponded to dye loaded micelles and the smaller one to free dye molecules that have formed one-to-one complexes with plasma proteins.<sup>[528]</sup> Furthermore, the apparent fraction of free dye had increased to 18%. This increase could be a result of a partial degradation of the peptide-dye bond and/or the presence of a small fraction of dyes that were non-covalently attached and thus dissociated from the micelles in blood. The dominant fraction of the dye cargo, however, was still loaded on the micelles which were intact and did not change their size e. g. due to decomposition or aggregation even after 30 h in blood. The fit to the autocorrelation curve measured for **PM 2** in blood (Figure 14.2 B) revealed the presence of only one type of fluorescent species with  $R_h$  of 3.4 nm. This indicates a complete loss of the non-covalently attached dye cargo from the nanocarrier, which is in line with observations on the loss of encapsulated dexamethasone from CCPMs *in vivo*.<sup>[151]</sup>

Near-infrared fluorescence correlation spectroscopy (NIR-FCS) studies in flowing blood, provided quantitative understanding of the *in vivo* behavior of nanocarrier-based therapeutics. Upon covalent stabilization by disulfides, properties of a core-cross-linked polymeric micelle were not altered when transferred from aqueous solution and exposed to full blood for 30 h. Hence, decomposition, aggregation or extensive protein adsorption can be plausibly ruled out. Further, covalent attachment of fluorescent probes clearly performed superior to non-covalent loading with regard to loss of cargo. Thus, by means of the NIR-FCS technique

Covalent attachment  
of dye in  
nanocarriers...

... compared to  
non-covalent  
loading.

Conclusion.

implemented in full blood, the significance of covalent modification of nanocarriers evaluated *in vivo* is stressed.

*Experimental:  
preparation and  
labeling of  
core-cross-linked  
polymeric micelles  
evaluated by  
NIR-FCS.*

A P<sub>Sar203</sub>-*b*-PCys(SO<sub>2</sub>Et)<sub>11</sub> block copolymer<sup>[22]</sup> was dissolved in *N,N*-dimethyl acetamide (DMAc) with 1 M thiourea at a concentration of 7.5 g L<sup>-1</sup> for 1.5 h to prevent β-sheet formation of the polycysteine segment. For self-assembly, 1 mM acetate buffer with 10 mM thiourea (pH = 4.7) was added to adjust the concentration to 6 g L<sup>-1</sup>. The solution was left to equilibrate for 3 h and then dialyzed against 1 mM acetate buffer. The cross-linker hexanedithiol was added as a DMAc solution to the micelle solution in 1 mM acetate buffer with 10 mM thiourea with SH-groups equimolar to the number of cysteines. The reaction mixture was shaken and allowed to stand for 18 h. Subsequently, the solution was dialyzed against water, filtered via GHP200 syringe filter, and purified by repetitive spin filtration (MWCO 100 kDa) and dilution steps. After the preparation steps described above, the particle solution was divided for covalent and non-covalent labeling with an equimolar amount of fluorophore in *N,N*-dimethyl formamide (DMF) (5 mM).<sup>[327]</sup> The labeling reactions were carried out at room temperature overnight followed by purification. For covalent labeling, 10-fold concentrated PBS was added to adjust the pH to 8 and followed by 14.1 μL IRDye<sup>®</sup> 800CW succinimidyl ester (LI-COR Biotechnology) solution. Purification was performed by repetitive spin filtration (MWCO 100 kDa) diluting at least 10 times with EtOH/H<sub>2</sub>O followed by 10 times H<sub>2</sub>O. For non-covalent labeling, 14.1 μL IRDye<sup>®</sup> 800CW dibenzocyclooctyne (DBCO) solution were added to the aqueous particle solution followed by purification using column chromatography (Sephadex LH 20 in H<sub>2</sub>O).




Part V

CORE-SHELL SYSTEMS IN  
SYSTEMIC APPLICATION



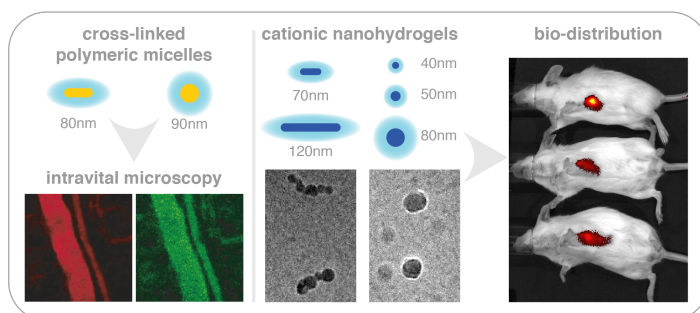




*This last part combined the gathered knowledge on chemoselective disulfide formation of the *S*-alkylsulfonyl group, controlled sequential ring-opening polymerization of (multi)block copolypept(o)ides and self assembly thereof into cross-linked core-shell systems. *In vivo* studies were composed, evaluating blood circulation, biodistribution and tumor accumulation of fluorescently labeled cross-linked polymeric micelles and cationic nanohydrogels, varying in size and morphology. Promising findings from this investigation led to the latest stage of polypept(o)ide-based core-shell carrier systems for systemic application. Cross-linked core-shell system for systemic siRNA delivery were prepared from triblock copolypept(o)ides, which combined cationic PLys for efficient siRNA complexation, a PCys(SO<sub>2</sub>R) segment for chemoselective disulfide stabilization and a stealth-like PSar block in a single polymer. In a comparative study, the connection was drawn between block sequence alteration and physicochemical properties of cross-linked core-shell nanoparticles, which were successfully applied in intratumoral RNAi mediated gene silencing *in vivo*.*



## BLOOD CIRCULATION AND BIODISTRIBUTION OF POLYPEPT(O)IDE-BASED NANOPARTICLES



**ABSTRACT:** Self-assembly of polysarcosine-*block*-poly(*S*-ethylsulfonylethyl-L-cysteine) (PSar-*b*-PCys(SO<sub>2</sub>Et)) diblock copolypept(o)ides offers access to a broad range of core-shell structures with control over particle size and morphology. Disulfide core cross-linking of the PCys(SO<sub>2</sub>R) segment ensures bioreversible stabilization of the resulting structures, combined with the possibility to adjust core polarity and functionality by choice of the cross-linker. Thus, available carrier functionalities range from hydrophobic core cross-linked polymeric micelles for e. g. hydrophobic chemotherapeutic agents, to cationic nanohydrogels for complexation of negatively charged nucleic acids e. g. small interfering RNA (siRNA). In order to evaluate PSar-*b*-PCys(SO<sub>2</sub>Et)-based carrier systems in systemic applications, core cross-linked structures with spherical or worm-like morphology, varying hydrodynamic dimensions and core polarities were prepared, covalently labeled and evaluated *in vivo*. By means of intravital real-time confocal microscopy and *in vivo* as well as *ex vivo* imaging by an *in vivo* imaging system, blood circulation as well as biodistribution was evaluated by observation up to 24 h in systemic circulation.

## 15.1 INTRODUCTION

*PSar-b-PCys(SO<sub>2</sub>Et)-based core-shell nanoparticles.*

Self-assembly of polysarcosine-*block*-poly(*S*-ethylsulfonyl-L-cysteine) (PSar-*b*-PCys(SO<sub>2</sub>Et)) diblock copolypept(o)ides offers the means to prepare a broad range of core-shell structures with control over particle size and morphology as demonstrated in Chapter 13. The self-assembly process is regulated by varying parameters such as hydrophobic to hydrophilic block length ratio,<sup>[495]</sup> composition of the block selective solvent and whether self assembly is directed by secondary structure formation of the  $\beta$ -sheets forming PCys(SO<sub>2</sub>R) segment.<sup>[22]</sup> For systemic applications, covalent cross-linking significantly improves carrier stability<sup>[153,529]</sup>, thus stabilization was ensured by disulfide formation in the core compartment.<sup>[22,209]</sup> Bioreversible stabilization by disulfides proves an attractive option, since carriers are typically exposed to different redox potentials when in systemic circulation in contrast to intracellular compartments.<sup>[158]</sup> Further, core polarity and thus functionality of PSar-*b*-PCys(SO<sub>2</sub>Et)-based carriers can be conveniently adjusted by the choice of the dithiol cross-linker as demonstrated in Chapter 12. The core-compartment can hence be devised to suit various therapeutic cargoes. A broad range of core polarities is available from hydrophobic cross-linkers for accommodation of hydrophobic chemotherapeutic agents e.g. paclitaxel to polycationic moieties for complexation of negatively charged nucleic acids e.g. small interfering RNA (siRNA).<sup>[22]</sup> non-covalent In addition, PSar-*b*-PCys(SO<sub>2</sub>Et) block copolypept(o)ides mediate end-group functionality<sup>[327]</sup> for further modification of the resulting carrier systems as presented in Chapter 10. Since non-covalently loaded or labeled nanocarriers are prone to loss of (hydrophobic) cargo upon introduction into biological environments,<sup>[151]</sup> covalent modification is key to ensure carrier integrity *in vivo*. As demonstrated in Chapter 14, fluorescently labeled core cross-linked polymeric micelles in full human blood (30 h exposure) maintained their size and definition upon covalent attachment of the fluorescent probe in contrast to a non-covalently loaded micelle. Covalent modification is thus a crucial factor for carriers in systemic application, since co-localization of the monitored label with the carrier system has to be guaranteed for reliable tracking as well as successful delivery of therapeutic cargo.

*On the in vivo fate of nanocarriers in systemic application.*

Blood circulation and tissue distribution of a nanocarrier in systemic application depends on several factors such as morphology, overall hydrodynamic dimensions and surface properties. Particle size serves as a first parameter to estimate the biodistribution *in vivo*. Large particles of several microns are commonly retained in the lung capillaries upon first passage after intravenous administration and small-sized nanoparticles (<5 nm) are subject to rapid renal filtration.<sup>[110]</sup> Under pathophysiological conditions in cancerous or inflamed tissue, accumulation of particles sized roughly between several tens to 100 nm is observed.<sup>[122,123]</sup> Upon prolonged blood circulation, extravasation of nanoparticles through irregular fenestrated vasculature and retention due to defective lymphatic

drainage is exploited for passive tumor accumulation mediated by the enhanced permeability and retention (EPR) effect<sup>[122]</sup>. Accumulation and tumor penetration profits from a decrease in size, as demonstrated by Cabral *at al.* for of 30-100 nm sized systems.<sup>[124]</sup> Upon increasing size beyond 150 nm, however, particles accumulate progressively in the liver and spleen.<sup>[115]</sup> In context of prolonged blood circulation, shielding properties of the particle corona are crucial, since opsinization by plasma proteins accelerates blood clearance by the mononuclear phagocyte system (MPS) in the liver, the lymph nodes and the spleen.<sup>[109,112]</sup> High surface charge promotes blood clearance and especially positive surface charge is associated with poor systemic circulation and toxicity.<sup>[109,120]</sup> Neutral or slightly negatively charged nanoparticles, on the other hand, show reduced adsorption of serum proteins leading to longer circulation times as demonstrated by Kataoka and co-workers.<sup>[121]</sup> In addition, particle morphology can have an effect on the biodistribution, as differences in flow-characteristics affect blood circulation time, cell membrane interactions and macrophage uptake.<sup>[115]</sup> Effects of shape-anisotropy on systemic circulation are mediated by physical forces in flowing blood and may not applicable for particularly rigid or short elongated structures with approximate spherical hydrodynamic dimensions due to rotation. However, for strong shape anisotropic filament-like micelles on the size scale of micrometers, prolonged circulation in comparison to spherical counterparts was observed due to alignment in the blood flow, as shown by Discher and co-workers.<sup>[116]</sup> Further, rigidity of the carrier promotes retention in the lungs, the liver as well as in the spleen.<sup>[110]</sup>

In light of the manifold parameters affecting *in vivo* performance of nanocarriers, this work focuses on PSar-*b*-PCys(SO<sub>2</sub>Et)-based carrier systems in systemic application. Blood circulation as well as biodistribution is monitored and evaluated with respect to particle morphology, hydrodynamic dimensions and chemical properties. For this purpose, covalently labeled core cross-linked polymeric micelles with hydrophobic cores and cationic nanohydrogels with spherical and worm-like morphologies were investigated *in vivo*. Biological experiments in this chapter were conducted in cooperation with Prof. Horacio Cabral (University of Tokyo, Japan).

## 15.2 INTRAVITAL REAL-TIME CONFOCAL MICROSCOPY OF CORE CROSS-LINKED POLYMERIC MICELLES (CCPMs).

The technique of intravital real-time confocal laser scanning microscopy (IVRT-CLSM) allows for instantaneous observation of intravenously injected substances in the blood stream of a living organism by observation of multicolor fluorescence in the ear-lobe of mice.<sup>[530,531]</sup> Thus, fluorescently labeled hydrophobic core cross-linked micelles could be evaluated with regard to blood circulation continuously over an extended period of time (15 h). In analogy to near-infrared fluorescence correlation spectroscopy (NIR-FCS) studies of core cross-linked polymeric micelles in full blood in Chapter 14, samples were prepared from PSar<sub>203</sub>-*b*-

PCys(SO<sub>2</sub>Et)<sub>11</sub> (P1, see Table 15.3 for characterization). Self-assembly was performed under identical conditions with variation whether a chaotropic agent was present or not, yielding micelles differing in morphology as illustrated in Figure 15.1 A and Table 15.1.

Table 15.1: Characterization of covalently labeled core cross-linked polymeric micelles (CCPMs) employed in intravital microscopy.

No	$D_{h,DLS}^a$ / nm	polymer	$X_n/X_m^b$	thiourea	morphology <sup>c</sup>	dye
wCCPM	80	P1	203/11	-	worm-like	Cy5
sCCPM	90	P1	203/11	+	spherical	Cy3

<sup>a</sup> Particle sizes rounded for simplification, accurate values are given in Table 15.4.

<sup>b</sup>  $X_n$  PSar relative to PSar standards,<sup>[47]</sup>  $X_m$  from <sup>1</sup>H NMR relative to  $X_{n,GPC}$ .

<sup>c</sup> Morphology determined by AFM.

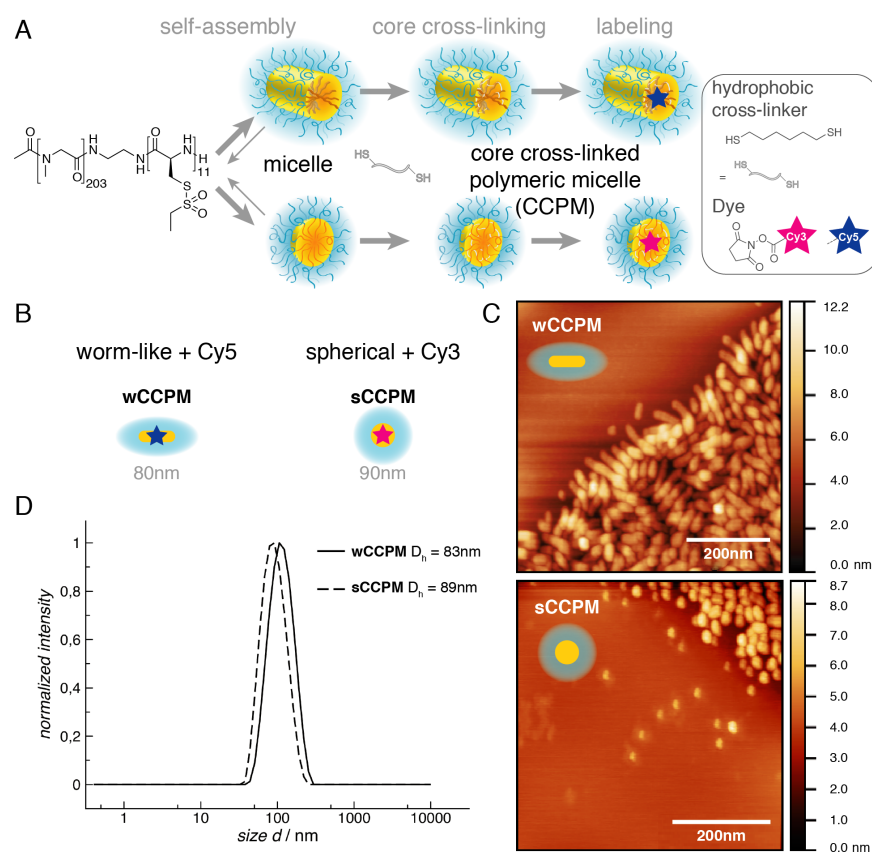


Figure 15.1: Particles evaluated by intravital real-time confocal laser scanning microscopy: A) Self-assembly of PSar-*b*-PCys(SO<sub>2</sub>Et) into micelles varying in morphology. Core cross-linking with hexanedithiol as hydrophobic disulfide cross-linker gives core cross-linked polymeric micelles with worm-like (wCCPM) and spherical morphology (sCCPM), which were labeling covalently in the core-compartment (Cy5 and Cy3, respectively). B) Summary of sizes and morphologies of CCPMs and characterization by C) AFM imaging (performed by Dr. Kristina Klinker) as well as D) dynamic light scattering.



Subsequent core cross-linking of the polymeric micelles by hexanedithiol yielded core cross-linked polymeric micelles designated as **wCCPM** with worm-like and **sCCPM** with spherical morphology (see Table 15.1 and Table 15.4 for characterization). NIR-FCS experiments in Chapter 14 emphasized the significance of covalent modification for *in vivo* applications of polymeric nanocarriers. Thus, labeling was performed in analogy by covalent modification at the amine end-group in the core with amine-reactive NHS-ester derivatives of fluorescent dyes.<sup>[327]</sup> One of the remarkable features of IVRT-CLSM, is the possibility to follow simultaneously two species with distinct spectral properties. Thus, to ensure sufficient spectral separation, Cy3 and Cy5 were chosen as fluorophores. Ultimately, the difference in morphology was confirmed by atomic force microscopy (AFM), while comparable hydrodynamic diameters of 83 nm for **wCCPM** and 89 nm for **sCCPM** were determined by dynamic light scattering (DLS) as shown in Figure 15.1 D.

Both fluorescently labeled CCPMs were co-administered by intravenous injection of a healthy BALB/c mouse and fluorescence intensity was observed in a confocal volume of a vein in the ear-lobe. Figure 15.2 shows exemplary frames of the consecutive recording at different time points of 3 min, 3 h and 15 h of consecutive recording. The rows represent the channels for separate observation of **wCCPM** (*top*) and **sCCPM** (*middle*) fluorescence as well as a merged display (*bottom*).

*Intravital  
microscopy of core  
cross-linked  
polymeric micelles.*

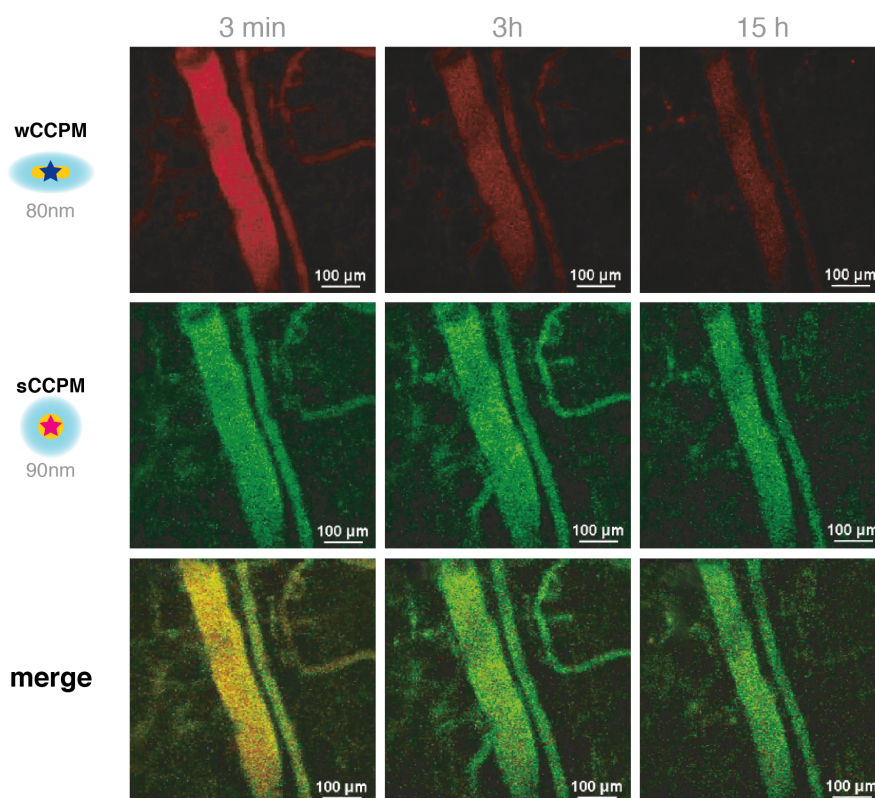


Figure 15.2: Co-injected **wCCPM** and **sCCPM** as observed by IVRT-CLSM in frames at different time points.

Throughout the measurement fluorescence was detected in the blood stream even in smaller blood vessels, indicating circulating particles. In consistency with findings from Chapter 14 by exposure of CCPMs to full blood, no aggregation with blood components is observed *in vivo*. In addition to the qualitative character of the recorded images, the confocal setup of the intravital real-time confocal laser scanning microscopy allows for quantification of fluorescence intensity. Covalent attachment of dye molecules ensures co-localization of observed fluorescence with the circulating particle, thus monitored fluorescence intensity is directly proportional to the particle fraction circulating in the blood stream. Quantification of blood circulation of worm-like **wCCPM** and spherical **sCCPM** given in Figure 15.3 as the normalized fluorescence intensity over time.

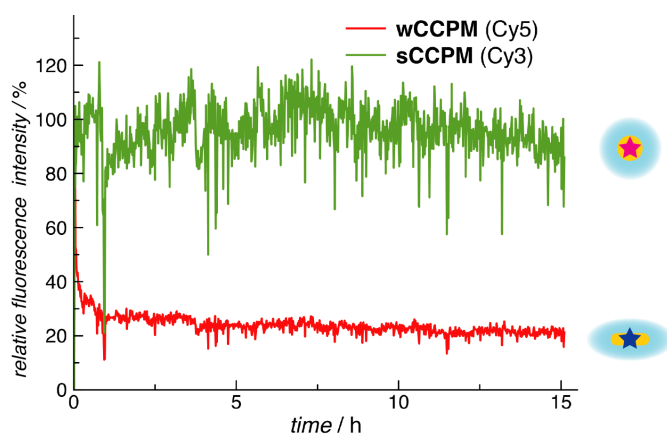


Figure 15.3: Quantification of Cy5 (**wCCPM**) and Cy3 (**sCCPM**) fluorescence in the blood vessel.

Both particles achieve stable systemic circulation over 15 h, indicating good shielding of the PSAr particle shell, which is a desirable property in terms of passive accumulation. Worm-like **wCCPM** shows an initial drop in fluorescence intensity followed by constant circulation around 20-25%, while spherical **sCCPM** maintains constant fluorescence intensity of 90-100%. The fraction of free dye was determined by fluorescence correlation spectroscopy (FCS) prior to *in vivo* tracking (< 10%), thus different content of free fluorescent molecules and consequently differences in clearance e.g. by renal filtration, can be ruled out. Further, **wCCPM** and **sCCPM** exhibit very similar hydrodynamic diameters (83 nm and 89 nm, respectively), thus sole morphology related effects on circulation seem unlikely. In addition, polypept(o)ide-based cylindrical brushes of varying aspect ratios employed in our group show contrasting *in vivo* circulation (close to 100%) without initial drop. Thus, the systemic circulation observed for **wCCPM** and **sCCPM** may be attributed to chemical properties, rather than variation in physical flow-dynamics of worm-like and spherical shapes. This interpretation will be discussed subsequently in the next section, upon *in vivo* evaluation of particles of inversed core-polarity.

### 15.3 BIODISTRIBUTION OF CORE CROSS-LINKED CATIONIC NANOHYDROGELS (NHGs).

Introduction of charge in nanoparticles for systemic administration is known to pose challenges in terms of blood circulation<sup>[109,115]</sup> and especially carrier systems featuring polycationic moieties for delivery of negatively charged nucleic acids suffer rapid blood clearance within few hours.<sup>[101,135]</sup> In this context, PSar-*b*-PCys(SO<sub>2</sub>Et)-based systems offer the possibility of variation in core polarity by dithiol cross-linkers without affecting particle size and morphology.<sup>[22]</sup> Hence, on account of the stable systemic circulation of hydrophobic core cross-linked polymeric micelles shown by intravital microscopy for over 15 h, other carrier types were investigated *in vivo*. Core cross-linking by a dithiol cross-linker with cationic moieties yielded nanohydrogels as suitable carriers for nucleic acid delivery of e. g. siRNA. And in order to evaluate biodistribution as well as potential accumulation sites for siRNA based therapeutics, tumor bearing mice were injected with core cross-linked cationic nanohydrogels varying in size and morphology and blood circulation was monitored as well as organ distribution.

Thus, block copolypept(o)ides **P1-4** (see Table 15.3 for characterization) were employed in self-assembly to give worm-like or spherical structures upon variation of secondary structure stabilization as illustrated in Figure 15.4 A. Core cross-linking was performed by a cationic triethylenetetramine  $\alpha,\omega$ -di(cysteine)diamide (TETA) cross-linker yielding cationic nanohydrogels (NHGs). The replacement of the hydrophobic *S*-ethylsulfonyl group with the poly(ethyleneimine)-based side chain modification resulted in inverted core-polarity (as illustrated by the transition of the core compartment from *yellow* to *dark blue*).

Ultimately, two cationic nanohydrogels with worm-like morphology (**wNHG1** and **2**) and three of spherical morphology (**sNHG1-3**) were obtained as illustrated in Figure 15.4 B. In addition, a non cross-linked, spherical polymeric micelle (**sPM**) was employed as a control to demonstrate the positive effect on circulation by core cross-linking stabilization *in vivo*. A near-infrared (NIR) dye was chosen as the reporting fluorescent agent due to the favorable *in vivo* signal to background ratio of dyes with excitation and emission maxima in the region between 650 and 900 nm.<sup>[350]</sup> In addition, covalent attachment of the dye is essential to ensure co-localization of the monitored fluorescence signal with the actual nanoparticle as discussed in Chapter 14. Thus, covalent labeling was performed in analogy to CCPMs in the core compartment using an amine reactive IRDye® 800CW succinimidyl ester.<sup>[327]</sup> The resulting particles employed in the evaluation of biodistribution are summarized in Table 15.2. Characterization of hydrodynamic dimensions was performed by DLS (see Figure 15.4 C and 15.5) and the morphology was deduced from imaging by cryogenic transmission electron microscopy (cryoTEM) and atomic force microscopy (AFM) as illustrated in Figure 15.5.

*Synthesis and characterization of nanohydrogels.*

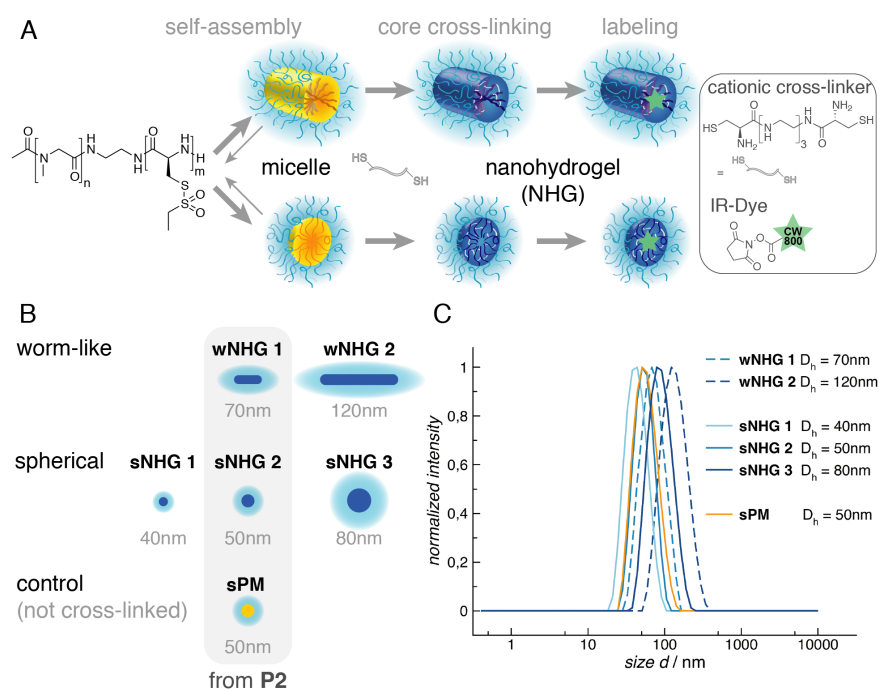


Figure 15.4: Particles evaluated *in vivo* in terms of biodistribution: A) Preparation of particles by self-assembly of PSar-*b*-PCys(SO<sub>2</sub>Et) into structures varying in morphology. Core cross-linking with TETA as a cationic disulfide cross-linker yields nanohydrogels (NHGs), followed by covalent labeling in the core-compartment (IRDye<sup>®</sup> 800CW). B) Summary of particle sizes and morphologies evaluated *in vivo*. C) Size of core cross-linked NHGs and control micelle (DLS).

Table 15.2: Characterization of core cross-linked nanohydrogels (NHGs) and control micelle evaluated in terms of biodistribution. Covalent labeling was performed with an IRDye<sup>®</sup> 800CW dye for all particles.

No	$D_{h, DLS}^a$ / nm	polymer	$X_n/X_m^b$	thiourea	morphology <sup>c</sup>
wNHG1	70	P2	186/17	-	worm-like
wNHG2	120	P3	203/20	-	worm-like
sNHG1	40	P4	94/15	+	spherical
sNHG2	50	P2	186/17	+	spherical
sNHG3	80	P1	203/11	+	spherical
sPM <sup>d</sup>	50	P2	186/17	+	spherical

<sup>a</sup> Sizes rounded for simplification, accurate values are given in Table 15.4.

<sup>b</sup>  $X_n$  PSar relative to PSar standards,<sup>[47]</sup>  $X_m$  from <sup>1</sup>H NMR relative to  $X_n$ , GPC.

<sup>c</sup> Morphology determined by cryoTEM.

<sup>d</sup> Non cross-linked polymeric micelle.

Visualization by means of cryoTEM is based on transmitted electrons from a vitrified sample, allowing particle imaging in aqueous solution. As staining or fixation are not necessary, contrast results solely from the electron density of the specimen. Visualization by means of AFM is based on the measurement of forces between a cantilever tip and the specimen



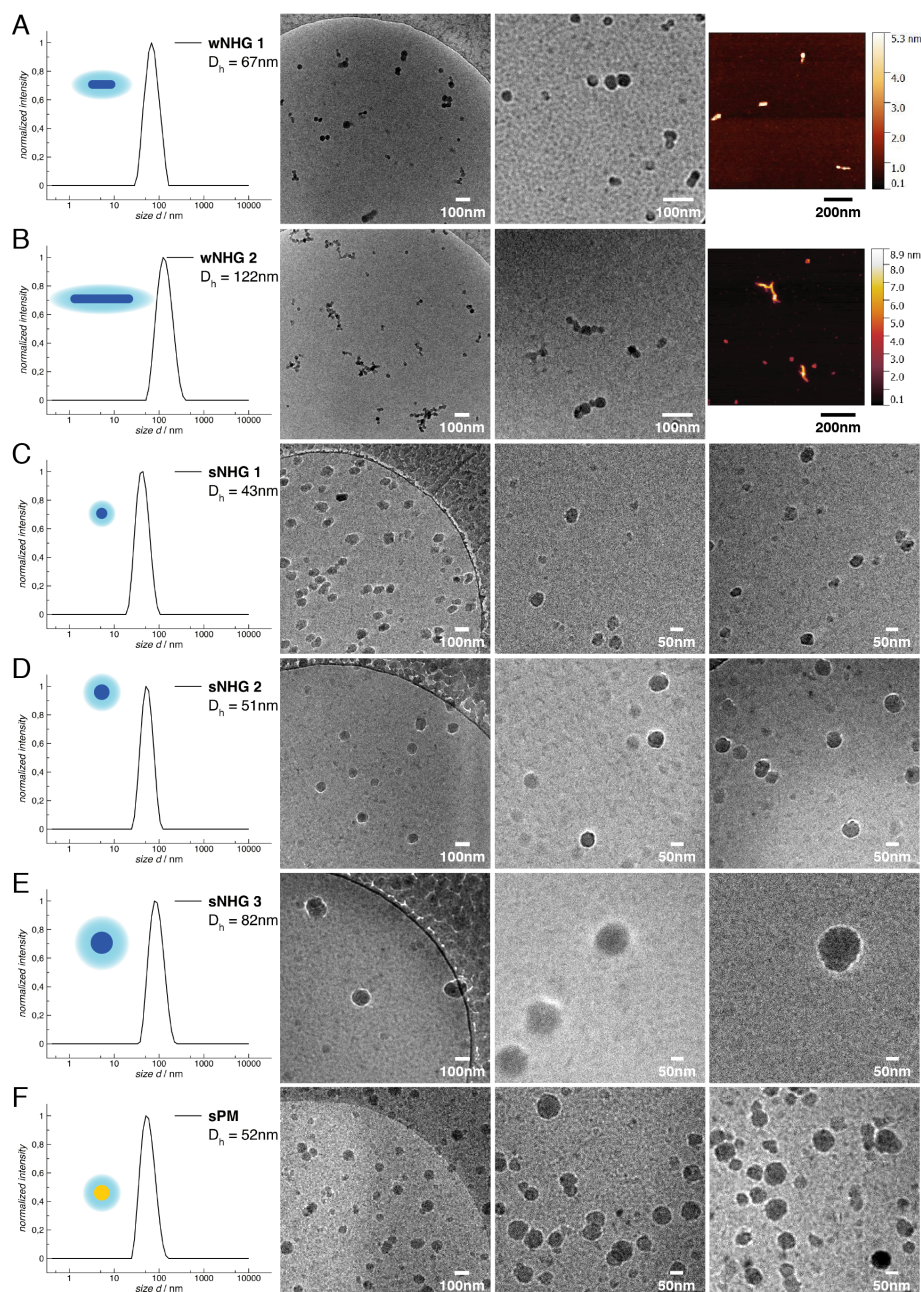


Figure 15.5: Size and shape of particles evaluated *in vivo* as characterized by DLS and visualized by cryoTEM (performed by Benjamin Weber), as well as AFM (performed by Tobias Bauer) for nanohydrogels with worm-like (A and B) and spherical morphology (C - E) as well as a spherical, non cross-linked micelle (F).

surface. Thus, in case of PSar-*b*-PCys(SO<sub>2</sub>Et) based systems, cryoTEM imaging shows predominantly electron density in the particle core due to the sulfur content of the core-forming PCys(SO<sub>2</sub>Et) block in contrast to the PSar corona, while AFM height micrographs depict the overall particle surface. wNHG1 and wNHG2 were found to exhibit elongated morphologies (as depicted in Figure 15.5 A and B) with hydrodynamic diameters around 70 nm and 120 nm, respectively as determined by DLS. In contrast, sNHG1-3 and sPM were prepared in presence of thiourea as a chao-

tropic agent and exhibit thus a spherical morphology (Figure 15.5 C - F, with equal results in AFM imaging). Hydrodynamic diameters of 40, 50 and 80 were determined by DLS for sNHG1, sNHG2 and sNHG3, respectively, as well as 50 nm for the non cross-linked micelle sPM.

Systemic circulation  
of cationic  
nanohydrogels.

Ultimately, the covalently labeled nanohydrogels were investigated in systemic application in a tumor bearing animal model towards blood circulation as well as biodistribution. Therefore, as illustrated in Figure 15.6 A, BALB/c mice bearing 4T1-luc mammary tumors (n = 3) were injected intravenously with the respective nanohydrogel or the non cross-linked control. Blood samples were collected from tail incision at time point of 1 h, 4 h and 24 h post injection. After 24 h, tumor accumulation was evaluated *in vivo* by fluorescence imaging by an *in vivo* imaging system (IVIS). As outlined in Section 5.3.3 on methodology of IVIS, imaging of deep tissues as well as the use of hairy mice is challenging in terms of accuracy and does not allow for quantification of the tissue distribution. Thus, *ex vivo* biodistribution was performed. Animals were sacrificed 24 h post injection and fluorescence imaging of the tumor tissue, spleen, kidney, liver and lung as well as the collected blood samples was performed. Figure 15.6 B summarizes findings on blood circulation of nanohydrogels and the non cross-linked control micelle (data is provided in Table 15.5 in the supporting information).

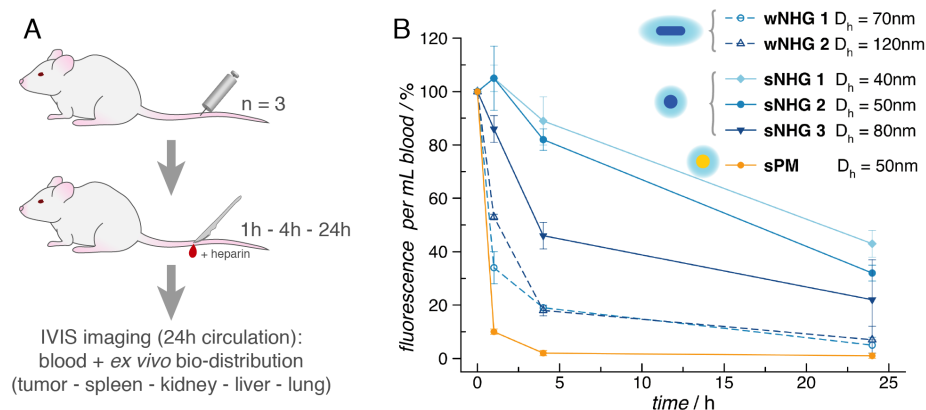


Figure 15.6: A) Experimental setup of *in vivo* evaluation of core cross-linked NHGs: BALB/c mice bearing 4T1-luc mammary tumors were injected with covalently fluorescent labeled particles *via* tail-vein injection (n=3); after 1h, 4h and 24h blood samples were collected and preserved with heparin; 24 h post injection imaging of blood samples as well as an *ex vivo* organ-distribution was performed by IVIS. B) Blood circulation profiles of IR-labeled particles expressed as percentage of initial fluorescence intensity over time. Data are expressed as mean; bars  $\pm$  SE.

The non cross-linked micelle sPM was cleared rapidly and already 4 h post injection fluorescence intensity in the blood is barely detectable. These findings are in line with rapid systemic clearance commonly observed for amphiphilic micelles without further stabilization,<sup>[115,153]</sup>

stressing the importance of covalent stabilization e.g. by core cross-linking. The circulation of nanohydrogels with worm-like morphology wNHG is similar to blood circulation observed by intravital microscopy for hydrophobic worm-like wCCPM (compare Figure 15.3). Both worm-like nanohydrogels show an initial decrease of blood fluorescence to 5% and 7% fluorescence intensity after 24 h in systemic circulation for wNHG1 and wNHG2, respectively. Spherical nanohydrogels sNHG, in contrast, exhibit a slow decrease in blood fluorescence over time with a residual fluorescence 24 h post injection of 43%, 32% and 22% for sNHG1, sNHG2 and sNHG3, respectively.

The observed prolonged systemic blood circulation of polymeric core-shell nanoparticles featuring cationic moieties, especially without any charge compensating nucleic acid cargo, is remarkable. Unmodified cationic particles (e.g. poly(L-lysine)-pDNA complexes) are fully degraded within 10 min in blood.<sup>[532]</sup> In contrast, systemic circulation of approximately 30-60 min is achieved for plasmid DNA carriers upon shielding with poly(ethylene glycol) (PEG) as demonstrated for poly(ethyleneimine) (PEI) based carriers<sup>[533,534]</sup> or poly(L-lysine) based systems.<sup>[521,535]</sup> In addition, stabilization by cross-linking has a positive effect on carrier circulation.<sup>[535,536]</sup> However, blood clearance below 10% of initial dose is commonly observed within 1-2 h for systemic administration.<sup>[537]</sup> Thus, extension of systemic circulation up to 24 h for nanoparticles with a cationic core compartment is a substantial progress in light of prolonged blood circulation necessary for passive tumor accumulation.

As mentioned in the previous section, differences in circulation observed for worm-like morphologies from spherical ones (CCPM and NHG alike) may originate from differences in chemical properties, rather than physical flow-dynamics based on aspect ratio. The obvious contrast between preparation of worm-like and spherical particles is the presence or absence of secondary structure of the PCys(SO<sub>2</sub>R) segment.<sup>[209]</sup> Since  $\beta$ -sheets tend to arrange in twisted structures,<sup>[519]</sup> (resulting in e.g.  $\beta$ -sheet barrels in natural peptides),<sup>[520]</sup> the polymer density in the core of worm-like and spherical micelles is expected to be unequal.

Twisted and rigid  $\beta$ -sheets are present in the absence of a chaotropic agent and result in elongated morphologies as exploited for formation of wCCPM and wNHG1-2.<sup>[22]</sup> Thus, disulfide stabilization is sterically more challenging and leads most likely to intra-molecular cross-linking and hence a loosely cross-linked core and impaired stabilization. In addition, differences in the effective shielding have to be considered. Cylindrical polysarcosine-*block*-poly(L-lysine) brushes employed in our group show stable systemic circulation on the time scale of days. In comparison, grafting density of shielding PSar chains in worm-like PSar-*b*-PCys(SO<sub>2</sub>Et) micelles is presumably lower, as it is dictated by arrangement of the PCys(SO<sub>2</sub>R) segments in the core. And in comparison to spherical micelles, the overall higher surface to volume ratio of elongated cores of worm-like micelles obstruct effective shielding. Another effect is the po-

sitioning of a *N*-terminally attached fluorescent probe. The placement onto the rigid  $\beta$ -sheet segment may be different in worm-like particles compared to the positioning on a flexible random-coil segment in spherical particles. Since most fluorescent dye molecules are of hydrophobic nature, their placement outside of the hydrophobic core, for instance, protruding in the hydrophilic sarcosine corona, may cause deviating overall chemical surface properties of the particle. Ultimately, sterically challenging secondary structures constitute the core of worm-like structures and can result in decreased disulfide cross-linking density and thus lesser stabilization along with diminished shielding by the PSar corona. Those chemical factors increase the possibility of interaction with proteins or other particles and thus accelerate clearance.

Systemic circulation of worm-like structures was thus found to be lower compared to spherical particles with 20-25 % for sCCPM after 15 h and below 10 % for wNHG1-2 after 24 h. In contrast, random coil conformation upon suppression of  $\beta$ -sheets for formation of spherical morphologies allows for densely packed PCys(SO<sub>2</sub>R) chains in the core during phase separation by self-assembly. Thus, a greater inter-molecular cross-linking density of polymer chains can be achieved upon introduction of dithiol cross-linkers. As a result, better stabilization of spherical CCPMs and NHGs is achieved resulting in stable systemic circulation of 90-100 % for sCCPM after 15 h and 20-40 % for sNHG1-3 after 24 h.

*Biodistribution  
of cationic  
nanohydrogels.*

The findings on pronounced blood circulation of cationic nanohydrogels after 24 h are highly encouraging, since systemic circulation of cationic nanoparticles beyond several hours is not reported so far. Further evaluation included *ex vivo* biodistribution 24 h post injection. Tumor tissue and relevant filter organs for intravenously administered nanoparticles (spleen, kidney, liver and lung)<sup>[110,115]</sup> were examined *ex vivo* by IVIS imaging. The relative fluorescence intensities were normalized on individual tissue weight and results are given in Table 15.5 and depicted in Figure 15.7.

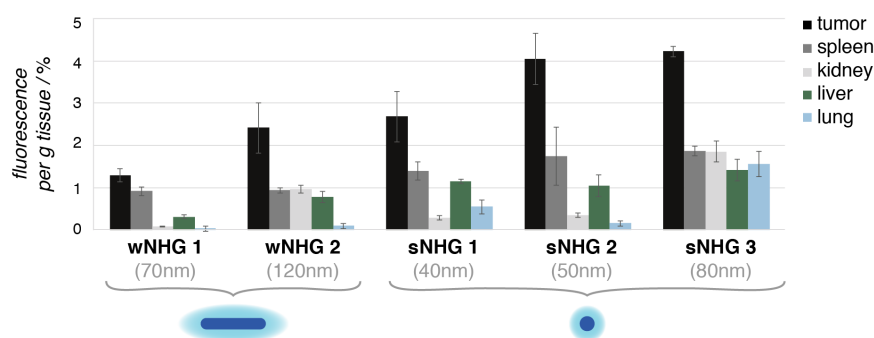


Figure 15.7: Tissue distribution of IR-labeled NHGs 24 h after systemic administration as percentage of initial fluorescence intensity normalized on individual tissue mass. Data are expressed as mean; bars  $\pm$  SE.

For non cross-linked micelle sPM, no fluorescence above background levels was detected in the examined tissues *ex vivo*. This observation is in



line with the rapid blood clearance of sPM and reinforces the importance of covalent carrier stabilization *in vivo*.

All nanohydrogels, however, show pronounced tumor associated fluorescence (up to 4% 24 h post injection) in comparison to signals from the spleen, kidneys, the liver as well as the lung. Passive tumor accumulation mediated by the EPR effect is thus likely for long circulating nanohydrogels. In general, organ accumulation is low with maximum 2%, which is desirable in order to achieve long systemic circulation for passive tumor accumulation and reduce off target effects of therapeutic cargoes. Aggregates of several microns would lead to sequestration in the lung. As only minor fluorescence below 1% was co-localized with the lung tissue for all nanohydrogels, particle aggregation or pronounced interaction with blood components can be ruled out.<sup>[109,110]</sup> Accumulation of fluorescence in the kidney due to renal filtration of <5 nm species<sup>[110]</sup> e. g. dissociated dye molecules or free polymer chains, was also not observed. Further, the spleen and the liver as the main phagocytotic active organs exhibit also very low fluorescence intensities of 1-1.5%. Thus, nanohydrogels successfully avoided opsonization by plasma proteins and blood clearance by the mononuclear phagocyte system (MPS) in the liver and the spleen<sup>[109,112]</sup> due to PSar mediated shielding. This observation is very promising in light of tumor targeting strategies, since passive targeting of cationic polyplexes or nanohydrogels is predominantly employed for applications based on their pronounced liver accumulation.<sup>[107,534,537]</sup> As discussed for systemic circulation, variances of worm-like and spherical particles may be attributed to differences in chemical properties. Due to presence of  $\beta$ -sheets in worm-like wNHG1-2, carrier stability by core cross-linking as well as shielding efficiency may be impaired, resulting in faster blood clearance and thus lower accumulation. Further, spherical nanohydrogels sNHG1-3 are still in systemic circulation after 24 h, thus progressing passive tumor accumulation can be anticipated. Due this prolonged circulation, later time points of 48 h and 72 h need to be evaluated in the future to complete the biodistribution profile.

Ultimately, the importance of covalent stabilization *in vivo* by core cross-linking was demonstrated, as the non cross-linked amphiphilic micelle was fully cleared from blood within hours and showed no tissue accumulation. Further, exceptional long blood circulation in combination with pronounced tumor accumulation and low systemic distribution, identified PSar-*b*-PCys(SO<sub>2</sub>Et)-based cationic nanohydrogels as attractive carriers for intravenous delivery of nucleic acids e. g. siRNA.

#### 15.4 CONCLUSION

In order to deduce generally valid information on *in vivo* performance of PSar-*b*-PCys(SO<sub>2</sub>Et)-based core-shell nanoparticles a range of factors require throughout evaluation. Future biodistribution studies need to investigate the influence of chemical core-variation by appropriate dithiol

cross-linkers (at least 4 core-types: hydrophilic, hydrophobic as well as positively and negatively charged). Further, both morphologies (2 variations: elongated and spherical) are required, as well as particle sizes between of 30 nm and 150 nm to cover the range relevant in passive tumor accumulation (5 sufficiently distinct sizes e. g. 30, 50, 70, 100, 150 nm). Thus, already 40 particles need to be synthesized and characterized. Additionally, in-depth *in vivo* studies should use larger cohort sizes to reduce intergroup variation ( $n > 5$ ), resulting in 200 laboratory animals (excluding potential control groups). And as demonstrated in this work, long systemic circulation needs to be considered in order to evaluate biodistribution based on passive accumulation (at least 5 time points: <5 min as value for 100 %, several hours as intermediate and 24, 48 and 72 h as long term range). Considering *ex vivo* tissue distribution for long circulating particles at more than the last time point, doubled or even tripled amounts of animals would be necessary. A study even closely resembling this extensive design was beyond the scope of this work, thus presented *in vivo* results are unpublished.

However, first advances were made in order to elucidate on blood circulation, biodistribution and tumor accumulation of PSar-*b*-PCys(SO<sub>2</sub>Et)-based core-shell nanoparticles *in vivo*. Worm-like and spherical particles of varying sizes were prepared by self-assembly and subsequent core cross-linking yielded hydrophobic core cross-linked polymeric micelles and allowed to introduce cationic moieties for formation of nanohydrogels. Covalent fluorescent labeling was performed in the core compartment for *in vivo* evaluation. Intravital microscopy revealed stable systemic circulation of hydrophobic core cross-linked polymeric micelles over 15 h with 20-25 % and 90-100 % for worm-like and spherical morphology, respectively. Spherical cationic nanohydrogels prepared under chaotropic conditions were found to circulate at 20-40 % after 24 h as determined by blood sampling and IVIS imaging. This stable systemic circulation of cationic systems is singular in the field of cationic gene delivery vectors has great potential with regard to passive tumor accumulation. Thus, the *ex vivo* biodistribution of cationic nanohydrogels was evaluated and revealed pronounced tumor accumulation combined with low systemic organ burden. In conclusion, prolonged systemic circulation of cationic nanocarriers in combination with tumor specificity characterizes PSar-*b*-PCys(SO<sub>2</sub>Et)-based core cross-linked cationic nanohydrogels as excellent carriers for systemic gene delivery e. g. siRNA.

## 15.5 ACKNOWLEDGMENTS

We thank Prof. Horacio Cabral for conduction of the IVRT-CLSM and *in vivo* experiments and for fruitful discussions on this topic. K.K. acknowledges financial support from the graduate school MAINZ and the Excellence Initiative (DFG/GSC 266). O.S. acknowledges support by the "Evangelisches Studienwerk e.V. Villigst" and M.B. acknowledges financial support by the SFB 1066-2.

## 15.6 SUPPORTING INFORMATION

*Preparation of Core Cross-Linked Polymeric Micelles and Nanohydrogels*

For preparation of polysarcosine-*block*-poly(*S*-ethylsulfonyl-L-cysteine) (PSar-*b*-PCys(SO<sub>2</sub>Et)) block copolypept(o)ides and the cationic cross-linker triethylenetetramine  $\alpha,\omega$ -di(cysteine)diamide (TETA), see Chapter 12.<sup>[22]</sup> Characterization of polymers employed in nanoparticle preparation for *in vivo* studies is summarized in Table 15.3.

Table 15.3: Characterization of PSar<sub>n</sub>-*b*-PCys(SO<sub>2</sub>Et)<sub>m</sub> diblock copoly-pept(o)ides.

No	$X_{n, GPC}^a$	$X_{m, NMR}^b$	$M_{n, GPC}^c / \text{g mol}^{-1}$	$D_{GPC}^c$
P1	203	11	28700	1.31
P2	186	17	27900	1.21
P3	203	20	29800	1.31
P4	94	15	22500	1.17

<sup>a</sup>  $X_n$  PSar relative to PSar standards.<sup>[47]</sup>

<sup>b</sup>  $X_m$  from <sup>1</sup>H NMR relative to  $X_{n, GPC}$  PSar.

<sup>c</sup> Relative to PMMA standards.

Self-assembly of amphiphilic block copolypept(o)ides and core cross-linking was performed using a protocol reported previously.<sup>[22]</sup> The resulting core cross-linked polymeric micelles (CCPMs) and nanohydrogels (NHGs) evaluated *in vivo* are summarized in Table 15.4. Briefly, the respective polymer was dissolved in *N,N*-dimethyl acetamide (DMAc) at a concentration of 7.5 g L<sup>-1</sup> for 2 h. 1 mM acetate buffer (pH = 4.7) was then added as the block-selective solvent. For self-assembly processes with suppression of the  $\beta$ -sheet formation of the polycysteine segment, DMAc contained 1 M and the 1 mM acetate buffer contained 10 mM thiourea as chaotropic agent. The solutions were left to equilibrate for 3 h, dialyzed against the respective buffer and filtered using a 200 nm filter (GHP). Micelles were stored in the respective buffer at 4°C.

Hydrophobic CCPMs were prepared as followed: The cross-linker hexanedithiol was added as a DMAc solution to the micelle solution in 1 mM acetate buffer with 10 mM thiourea with SH-groups equimolar to the number of cysteines. The reaction mixture was shaken and allowed to stand for 18 h and dialyzed against water. Core cross-linking for cationic NHGs was achieved by addition of the cross-linker TETA with SH-groups equimolar to the number of cysteines as a 100 g L<sup>-1</sup> stock solution in water. The reaction mixture was shaken and allowed to stand for 18 h. Purification for both systems was performed by repetitive spin filtration (MWCO 100 kDa) and dilution steps concluding in H<sub>2</sub>O followed by filtration *via* a 200 nm syringe filter (GHP).

Covalent labeling was performed for all particles with equimolar amount of fluorophore in DMF (5 mM).<sup>[327]</sup> The labeling reactions were carried out at room temperature overnight followed by purification. For

covalent labeling, 10-fold concentrated phosphate buffered saline (PBS) was added to adjust the pH to 8 and followed exemplarily by 14.1  $\mu$ L IRDye®800CW succinimidyl ester (NHS ester, LI-COR Biotechnology) solution. Purification was performed by repetitive spin filtration (MWCO 100 kDa) diluting at least 10 times with EtOH/H<sub>2</sub>O followed by 10 times with H<sub>2</sub>O.

Table 15.4: Characterization of PSar-*b*-PCys(SO<sub>2</sub>Et)-based particles *in vivo*.

No	thiourea	$D_{h,DLS}$ / nm	PDI <sub>DLS</sub>	polymer	$X_n/X_m$ <sup>a</sup>
wCCPM	-	83.1 ± 0.3	0.127 ± 0.012	P1	203/11
sCCPM	+	89.4 ± 0.7	0.161 ± 0.007	P1	203/11
wNHG1	-	66.9 ± 0.5	0.127 ± 0.015	P2	186/17
wNHG2	-	122.2 ± 2.4	0.161 ± 0.007	P3	203/20
sNHG1	+	42.6 ± 1.6	0.195 ± 0.029	P4	94/15
sNHG2	+	50.7 ± 1.7	0.109 ± 0.037	P2	186/17
sNHG3	+	81.7 ± 0.5	0.125 ± 0.014	P1	203/11
sPM <sup>a</sup>	+	52.1 ± 0.4	0.229 ± 0.019	P2	186/17

<sup>a</sup>  $X_n$  PSar relative to PSar standards,<sup>[47]</sup>  $X_m$  from <sup>1</sup>H NMR relative to  $X_n$ , GPC.

<sup>b</sup> Non cross-linked polymeric micelle.

#### *In vivo* Evaluation of PSar-*b*-PCys(SO<sub>2</sub>Et)-based Core-Shell Structures

Female BALB/c mice were purchased from Charles River Co. (Tokyo, Japan). All animal experiments were conducted in accordance with the Guidelines for the Care and Use of Laboratory Animals as stated by the University of Tokyo. For intravital microscopy<sup>[531]</sup> of core cross-linked polymeric micelles, a healthy BALB/c mouse was co-injected intravenously with samples labeled CCPM as listed in Table 15.4. The mouse was anesthetized by 1-3% isoflurane (Abbot Laboratories) and placed onto a temperature-controlled microscope stage. The ear lobe was attached beneath the cover slip with a single drop of immersion oil. Core cross-linked polymeric micelles in millipore water were filtered *via* GHP200 syringe filter and co-administered by tail vein injection. Consecutive video acquisition of the dermis tissue was performed for 15 h. All picture and movie acquisitions were performed using a Nikon A1R confocal laser scanning microscope system attached to an upright ECLIPSE FN1 machine equipped with a CFI Apo 40x WI  $\lambda$ S objective lens (Nikon, Tokyo, Japan). Acquired data was further processed using Nikon NIS Elements software for a region of interest (ROI), which was manually defined in the vein.

For biodistribution of core cross-linked nanohydrogels, BALB/c mice bearing orthotropic 4T1-luc mammary tumors (n = 3) were injected intravenously with samples labeled NHG for nanohydrogel and PM for the non cross-linked control as listed in Table 15.4. Female mice were inocu-

lated subcutaneously in the mammary gland with  $1 \times 10^6$  4T1-luc cells to prepare the orthotropic 4T1-luc mammary tumors model. After the primary tumors were sufficiently developed, fluorescently labeled nanohydrogels and the control micelle in  $H_2O$  were filtered *via* a GHP200 syringe filter and administered by tail vein injection. Blood samples (10  $\mu$ L) were collected from tail incision at time point of 1 h, 4 h and 24 h post injection upon heparin addition to prevent coagulation. *In vivo* and *ex vivo* fluorescent imaging was performed with an *in vivo* imaging system (IVIS) (Xenogen Corporation) comprised of a highly sensitive, S2 cooled CCD camera mounted in a light-tight specimen box. The animals were anesthetized using 1-3 % isoflurane (Abbot Laboratories). 24 h post injection, *in vivo* fluorescence imaging was performed using an IVIS spectrum to confirm tumor accumulation *in vivo*. Animals were subsequently sacrificed and tumors, spleen, kidney, liver and lung were harvested. Fluorescence imaging of tissue samples as well as blood samples was performed using the IVIS setup. The regions of interest (ROIs) were selected by an automated grid to measure the fluorescence intensity from individual tissues as well as the the background. Photons emitted from ROIs were quantified using Living Image software (ver. 4.5.5). Fluorescence was detected as radiant efficiency (photons/sec/cm<sup>2</sup>/sr per  $\mu$ W/cm<sup>2</sup>). Blood circulation over time was obtained from comparison of initial fluorescence from the nanoparticle sample with the residual fluorescence intensity of the blood samples. Fluorescence intensity of blank blood was subtracted as background from blood samples and normalized on the actual injected fluorescence intensity to give a relative percentage of the initial fluorescence intensity. For evaluation of *ex vivo* biodistribution, fluorescence intensity devoid of background was normalized on mass of the individual tissue and initial fluorescence intensity of the respective sample. Results from the biodistribution as well as blood circulation of nanohydrogels and the micelle control are summarized in Table 15.5.

Table 15.5: Blood circulation and *ex vivo* tumor accumulation of nanohydrogels 24 h post injection.

No	$D_{h, DLS}^a$ / nm	morphology <sup>b</sup>	fluorescence per g tumor tissue / %	fluorescence per mL blood / %
wNHG1	70	worm-like	$1.29 \pm 0.15$	$5.25 \pm 2.66$
wNHG2	120	worm-like	$2.41 \pm 0.59$	$7.15 \pm 4.68$
sNHG1	40	spherical	$2.68 \pm 0.60$	$43.32 \pm 5.43$
sNHG2	50	spherical	$4.04 \pm 0.61$	$31.69 \pm 3.08$
sNHG3	80	spherical	$4.22 \pm 0.12$	$22.23 \pm 4.92$
sPM <sup>c</sup>	50	spherical	- <sup>d</sup>	$1.26 \pm 0.54$

<sup>a</sup> Sizes rounded for simplification, accurate values are given in Table 15.4.

<sup>b</sup> Morphology determined by cryoTEM.

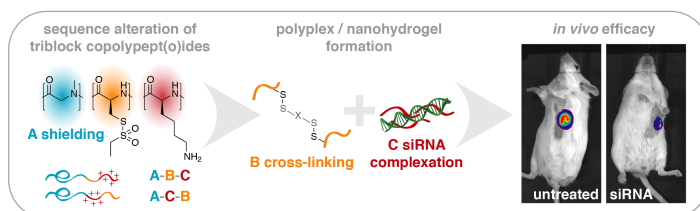
<sup>c</sup> Non cross-linked polymeric micelle.

<sup>d</sup> No fluorescence was detected.



BLOCK-SEQUENCE OF REACTIVE TRIBLOCK COPOLYPEPT(O)IDES DETERMINES SELF-ASSEMBLY AND RNAi EFFICACY *IN VIVO*

Olga Schäfer, Takuya Miyazaki, Leon Capelôa, Lydia Braun, Thahomina Khan, Jingyu Wan, Jennifer Schultze, Kaloian Koynov, Yu Nie, Kazunori Kataoka, Horacio Cabral, Matthias Barz, *to be submitted*.



**ABSTRACT:** The fundamental cellular mechanism of RNA interference enables the silencing of gene expression and thus, provides enormous therapeutic potential. A systemic application of therapeutic small interfering RNA (siRNA) requires a delivery system for transport to the site of action in the cytosol of targeted cells, e. g. in a solid tumor. To fulfill this task, a carrier need to combine bioreversible entrapment of siRNA to avoid degradation with stability in the blood stream for prolonged circulation. In this work, we report on the synthesis of triblock terpolymers, which combine a cationic polylysine block for efficient siRNA complexation, a PCys(SO<sub>2</sub>Et) segment for chemoselective disulfide formation and a stealth-like polysarcosine in a single polymer. The triblock copolymers can be realized by straightforward sequential ring-opening polymerization of the corresponding  $\alpha$ -amino acid *N*-carboxyanhydride, allowing control over polymer microstructure. Since the sequential polymerization allows permutation of block sequence, we report the influence of triblock copolymer microstructure and block sequence on nanoparticle carrier properties and RNA interference (RNAi) *in vivo*.



## 16.1 INTRODUCTION

The mechanism of RNA interference (RNAi) is one of the recent additions to the repertoire of nucleic acid-based therapies and shows great potential for treatment of multiple diseases including cancer.<sup>[79,86]</sup> By base-pairing of small interfering RNA (siRNA) with messenger RNA (mRNA) of complementary sequence, enzymatic degradation of mRNA is induced, resulting in silencing of gene expression relevant in the underlying pathologies.<sup>[77,89]</sup> However, several challenges prevail for systemic application of RNAi therapeutics e. g. enzymatic degradation by ribonucleases, short circulation times and entrapment in cellular compartments.<sup>[80,83,84]</sup> These delivery barriers can be addressed by nano dimensional delivery strategies based on lipid<sup>[538–541]</sup> or polymer-based formulation,<sup>[542–544]</sup> showing promising results in preclinical studies as well as in translation to the clinic.<sup>[72,76]</sup> While local application or delivery to the liver or lung can take profit on multiple delivery systems, current strategies in siRNA delivery to solid tumors are gravitating towards polymer based core-shell systems such as nanohydrogels<sup>[104–106]</sup> or polyplex systems.<sup>[101,122,135]</sup> On the structural level, these systems share a polycationic core for complexation of negatively charged siRNA and a shielding corona to ensure prolonged systemic circulation for passive tumor accumulation. Further, covalent cross-linking of carriers was shown to improve stability,<sup>[153,529,545]</sup> which is substantial for small siRNA molecules.<sup>[546]</sup>

As a consequence, ideal polymeric materials should combine a shielding segment with a cross-linkable one as well as a cationic block for efficient siRNA complexation. These demanding structural requirements are met by ABC-type amphiphilic cationic triblock terpolymers.<sup>[492]</sup> The outer A block is constituted by a hydrophilic polymer with shielding properties.<sup>[27,138–140,144,145]</sup> The B block can serve either as a protective layer, e. g. employing poly( $\epsilon$ -caprolactone)<sup>[139,547,548]</sup> or poly(propylene sulfide)<sup>[549]</sup> as well as a biodegradable<sup>[550,551]</sup>, pH or redox responsive one.<sup>[552,553]</sup> Although Kataoka and coworkers employed poly(L-lysine) as the B segment in combination with a hydrophobic core forming block C, ultimately creating a carrier with siRNA loading capacity in the intermediate layer,<sup>[554]</sup> most commonly segment C is of cationic nature to efficiently complex siRNA e. g. linear poly(ethyleneimine) (IPEI),<sup>[139]</sup> poly(2-(dimethylamino)ethyl methacrylate) (PDMA),<sup>[548]</sup> poly(2-aminoethylethylene phosphate) (PPEEA),<sup>[547]</sup> cationic peptides,<sup>[549]</sup> poly(L-arginine)<sup>[555]</sup> or poly(L-lysine).<sup>[550]</sup> Stimuli responsive moieties can also be incorporated in the C block of siRNA delivery vectors e. g. for hypoxia targeting<sup>[556]</sup> or mediating pH sensitivity.<sup>[557,558]</sup>

Interestingly, up to now the influence of block sequence on nanoparticle as well as delivery properties has not been investigated in such systems. In contrast, there is a broad consensus that the properties of nanoparticles formed by triblock copolymers are governed by the microstructure of the employed terpolymer<sup>[493–498]</sup> To derive first structure-



property relationships, we synthesized triblock copolymers, which all contain a polysarcosine (PSar), a poly(*S*-ethylsulfonyl-L-cysteine) (PCys(SO<sub>2</sub>Et)) and a polylysine (PLys) block by sequential ring-opening polymerization of the corresponding  $\alpha$ -amino acid *N*-carboxyanhydrides, but upon alteration of block sequence. In polymer P1 the sequence is PSar-*block*-PCys(SO<sub>2</sub>Et)-*block*-PLys (A-B-C) and in P2 PSar-*block*-PLys-*block*-PCys(SO<sub>2</sub>Et) (A-C-B) while the overall block length of PCys(SO<sub>2</sub>Et) and PLys are kept constant. The PCys(SO<sub>2</sub>Et) block was introduced for bioreversible cross-linking by chemoselective disulfide formation, which provides stability in circulation and degradability upon cellular uptake.<sup>[158]</sup> Our group recently demonstrated modification of PLys in triblock copolypept(o)ides (polypeptoid-*block*-peptide-*block*-peptide) with *N*-succinimidyl 3-(2-pyridyl-dithio)propionate (SPDP) and subsequent dithiol cross-linking, creating a library of polypept(o)ide-based pDNA polyplexes.<sup>[154]</sup> However, this strategy involved three post polymerization modification steps to achieve thiol-reactivity, while the presented *S*-alkylsulfonyl group introduces thiol-reactive moieties in polypept(o)ides, bypassing all post polymerization modification and activation steps.<sup>[173,327]</sup>

Thus, in the present study we report on the synthesis of triblock copolypept(o)ides differing in block sequence of cross-linkable and complexing segments to investigate the role of block sequence alteration on nanocarrier formation and efficacy as siRNA delivery vectors. The functional elements are a hydrophilic, non-ionic shielding block based on PSar,<sup>[27,143]</sup> combined with a polycationic PLys block for complexation of siRNA, as well as a hydrophobic PCys(SO<sub>2</sub>Et) segment mediating chemoselective disulfide stabilization without the need of post polymerization modification steps.<sup>[22,173]</sup>

## 16.2 RESULTS AND DISCUSSION

The synthesis of triblock copolypept(o)ides was performed by sequential ring-opening polymerization (ROP) of  $\alpha$ -amino acid *N*-carboxyanhydrides (NCAs), enabling precise control over block length and block sequence according to Birke *et al.*<sup>[26]</sup> Polysarcosine (PSar) was chosen as the starting block A with a degree of polymerization of 85 units to mediate sufficient shielding of the resulting carrier systems (see supporting information for polymerization procedures).<sup>[70]</sup> For the hydrophobic PCys(SO<sub>2</sub>R) B block, 25-30 repeating units were chosen, in order to provide sufficient carrier stability upon disulfide cross-linking.<sup>[154]</sup> The polycationic PLys block C was set to 12-13 repeating units to be able to form polyplexes by electrostatic interactions with negatively charged nucleic acids as shown by Heller *et al.*<sup>[70,367]</sup> For complexation of small siRNA molecules, a relatively short cationic segment is sufficient, particularly in combination with a cationic cross-linker.<sup>[22,154]</sup> For the synthesis of the A-B-C block copolymer the bifunctional initiator approach was chosen as reported by Schäfer *et al.*<sup>[327]</sup> while for the A-C-B block copoly-

*Synthesis of A-B-C and A-C-B triblock copolypept(o)ides.*

mer sequential polymerization provided best control over block length (see Figure 16.1 A and B).

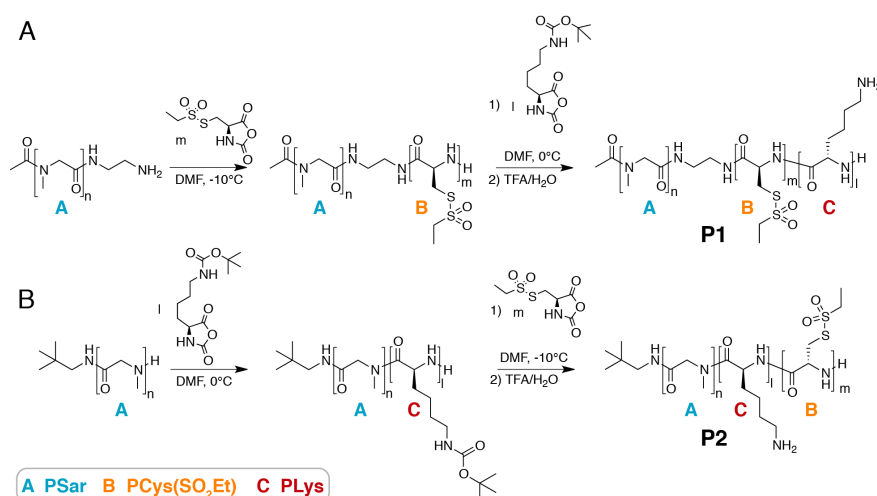


Figure 16.1: Polymerization scheme of triblock copolypept(o)ides by sequential ring-opening polymerization of NCAs: A) A-C-B triblock copolypept(o)ide (**P1**) with A: PSar<sub>n</sub>, B: PCys(SO<sub>2</sub>Et)<sub>m</sub> and C: PLys<sub>1</sub> as well as B) A-C-B triblock copolypept(o)ide (**P2**) upon inversed sequence of the cross-linking and polycationic block.

*Polymer  
characteritaion.*

Characterization of triblock copolypept(o)ides was performed by <sup>1</sup>H NMR as well as gel permeation chromatography (GPC) as summarized in Table 16.1, indicating well-defined block copolymers with narrow size distribution. Successful chain extension into triblock copolymers and the absence of homopolymers or diblock copolymer impurities was confirmed by GPC and diffusion ordered <sup>1</sup>H NMR spectroscopy (DOSY) as illustrated in Figure 16.2 A, 16.6 and 16.9. Block lengths of PSar macroinitiators were determined by GPC relative to PSar standards<sup>[47]</sup> and were in good agreement with <sup>1</sup>H NMR experiments. Repeating units of PCys(SO<sub>2</sub>Et) and PLys(Boc) were determined by <sup>1</sup>H NMR by evaluation of the α-proton signal at 4.70 ppm and ε-amide proton signal at 6.3–6.7 ppm, respectively (compare Figure 16.5 and 16.8 in the supporting information).

Table 16.1: Characterization of triblock copolypept(o)ides.

No	polypept(o)ide architecture <sup>a, b</sup>	$M_{n, GPC}^c$ /g mol <sup>-1</sup>	$M_{n, GPC}^d$ /g mol <sup>-1</sup>	$D_{GPC}^d$
<b>P1</b>	PSar <sub>71-b</sub> -PCys(SO <sub>2</sub> Et) <sub>29-b</sub> - PLys <sub>13</sub>	9050	26200	1.14
<b>P2</b>	PSar <sub>104-b</sub> -PLys <sub>12-b</sub> - PCys(SO <sub>2</sub> Et) <sub>26</sub>	9190	26500	1.27

<sup>a</sup> X<sub>n</sub> PSar relative to PSar standards.<sup>[47]</sup>

<sup>b</sup> X<sub>m</sub> and X<sub>l</sub> from <sup>1</sup>H NMR relative to X<sub>n, GPC</sub> PSar.

<sup>c</sup> Relative to PSar standards.

<sup>d</sup> Relative to PMMA standards.

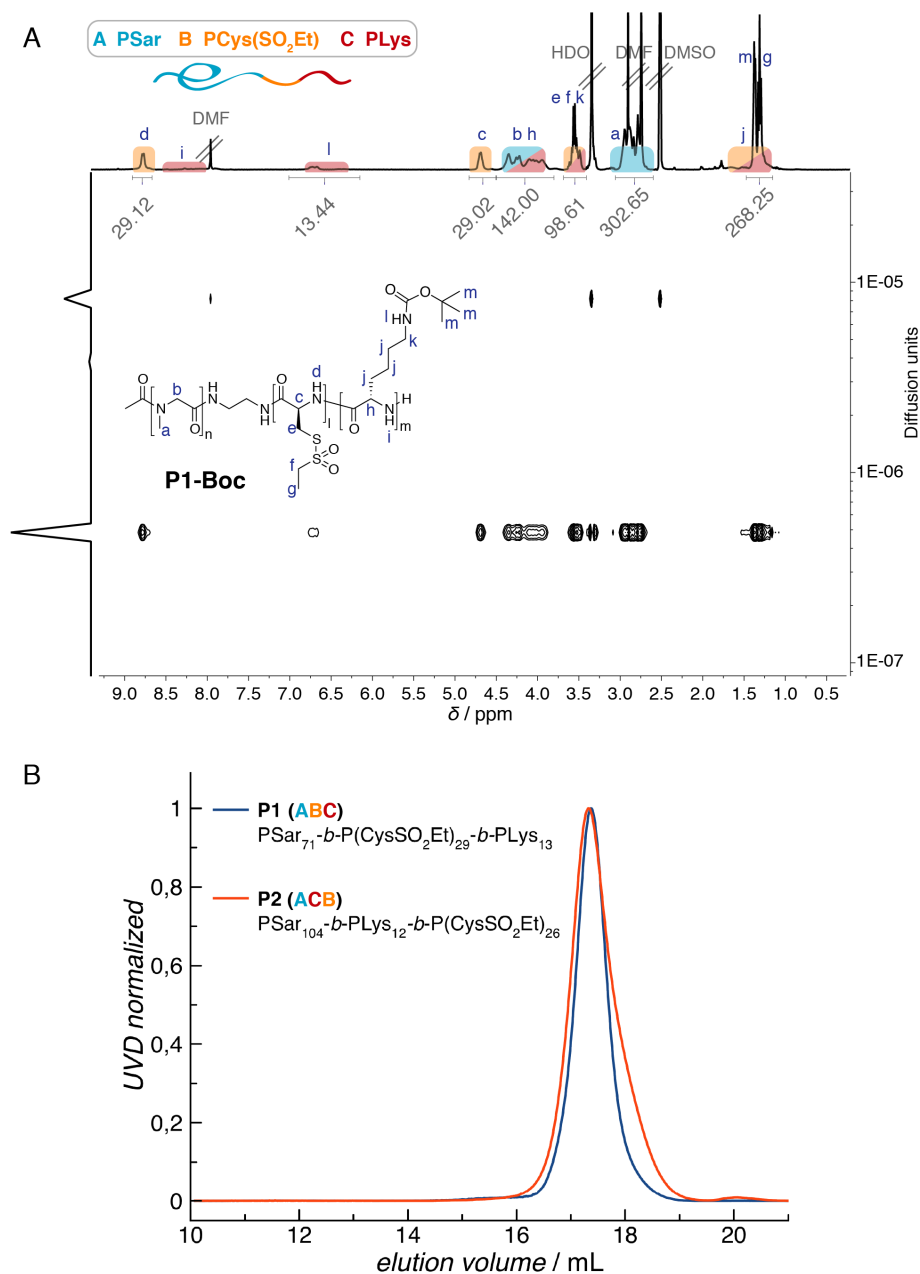


Figure 16.2: Characterization of triblock polypept(o)ides: A) <sup>1</sup>H NMR and <sup>1</sup>H DOSY NMR spectrum in DMSO-*d*<sub>6</sub> of A-B-C triblock **P1-Boc**, indicating only one diffusing species with a uniform diffusion coefficient and B) GPC elugrams in HFIP of **P1** and **P2** after deprotection of the PLys segment.

Quantitative removal of the Boc protective group was accomplished by cleavage with a 1:1 mixture of H<sub>2</sub>O / TFA as reported previously<sup>[367]</sup> and verified by disappearance of the characteristic Boc signal at 1.3–1.5 ppm (compare Figure 16.7 and 16.10 in the supporting information). As illustrated in Figure 16.2 B, both triblock copolypept(o)ides **P1** and **P2** exhibit monomodal molecular weight distributions in HFIP GPC. Moreover, virtually identical molecular weights and distributions are obtained for both polymers, independent from A-B-C or A-C-B block sequence al-

teration. The higher dispersity of 1.27 for A-C-B polymer **P2**, in contrast to a PDI of 1.14 for A-B-C polymer **P1**, may arise from the inverted block sequence, as **P2** features a terminal hydrophobic B segment in contrast to terminal hydrophilic A and C blocks in **P1**. Since  $^1\text{H}$  DOSY NMR confirms equivalent diffusion coefficients, the observed dispersity of **P2** may be attributed to secondary effects, e. g. interactions with the column material in GPC.

*Nanohydrogels and polyplexes based on triblock copolypept(o)ides.*

In order to investigate the influence of block-microstructure on resulting gene delivery vectors, both triblock copolypept(o)ides were utilized in two strategies to construct siRNA carrier systems, namely nanohydrogel (NH) or polyplex (PP) (Figure 16.3 A and B). While polyplexes are formed in the presence of siRNA followed by cross-linking resulting in entrapment of siRNA, nanohydrogels are initially formed in the absence of siRNA (see supporting information for details on particle preparation) and loaded afterwards with the oligonucleotide.

Thus, starting from 2 polymers, 2 polyplexes and 2 nanohydrogels are generated (see Figure 16.3). The 2 polyplexes **PP1** and **PP2** differ in the location of the siRNA. While the PSar-*block*-PCys(SO<sub>2</sub>Et)-*block*-PLys triblock copolymer **P1** can form core-shell polyplexes in which the siRNA is trapped in the core, polyplexes based on **P2** have a hydrophobic core due to the terminal PCys(SO<sub>2</sub>R) block. Although this block will be cationic by core cross-linking with the dithiol triethylenetetramine  $\alpha,\omega$ -di(cysteine)-diamide (TETA) (transition from *yellow* to *dark blue* compartments), siRNA may remain in the PLys segment and is thus less likely located in the inner core. The same differences in microstructure are valid for nanohydrogels. **NH1** features the PLys part in the inner core, while TETA shapes the outer part of the core and will thus mostly contribute to the complexation of siRNA. In the case of **NH2** the situation is inversed and the PLys side chains of the triblock copolymer complexate the oligonucleotide. Most importantly, in all 4 cases the microstructure of the triblock copolypept(o)ides dictates the inner structure of the carrier and compartmentalizes the nanoparticle<sup>[559]</sup> and the hydrophilic PSar segment forms in all cases a hydrophilic corona (*light blue*).

*Structure-property relationship based on triblock sequence.*

The loading capacities with siRNA of all four different structures was evaluated first by gel electrophoresis (see Figure 16.11 and 16.12) and later confirmed by fluorescence correlation spectroscopy (FCS) using a fluorescently labeled ATTO<sub>647</sub> siRNA<sup>[344,345]</sup> For correlation of freely diffusing siRNA a hydrodynamic diameter of 4-5 nm is derived, while complexation by a cationic nanocarrier shifts the autocorrelation function considerably to prolonged diffusion times (compare Figure 16.13). Further, the fraction of free siRNA can be determined by application of a bimodal fit of the autocorrelation function, thus quantifying complexation efficacy. Successful siRNA loading was confirmed for both nanohydrogels **NH1** and **NH2** as well as for polyplex **PP1** (compare Figure 16.13). In contrast, **PP2** based on A-C-B triblock copolypept(o)ide **P2** did not yield uniform fluorescent species and a large fraction of free siRNA was observed (46 %

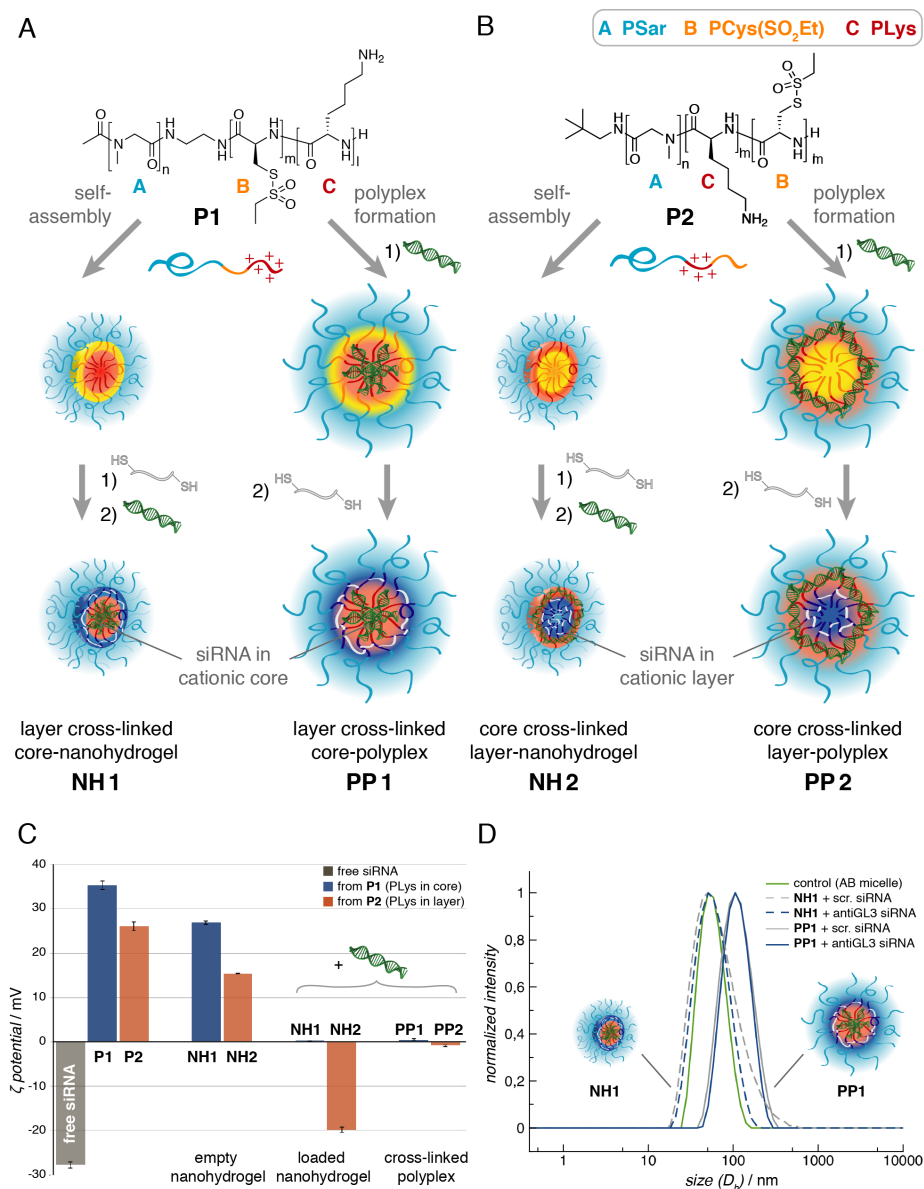


Figure 16.3: Particle platform derived from triblock polypept(o)ides by self-assembly into nanohydrogels (NH) or polyplex formation (PP). Block A constitutes the hydrophilic PSar corona (*light blue*). Subsequent cross-linking by a cationic cross-linker (triethylenetetramine  $\alpha,\omega$ -di(cysteine)diamide (TETA), *light gray*) inverts polarity of the hydrophobic S-ethylsulfonyl-cysteine segment (illustrated by transition from *yellow* to *dark blue*). A) A-B-C triblock polypept(o)ide P1 gives systems with a cationic lysine-core (*red*) and a cross-linked cysteine-layer (NH1 and PP1) and B) A-C-B triblock polypept(o)ide P2 yields systems with an inverted functionality upon a cationic lysine-layer (*red*) and a cross-linked cysteine-core (NH2 and PP2). C)  $\zeta$ -potential of triblock copolypept(o)ides, empty and loaded cross-linked nanohydrogels and cross-linked polyplexes. D) Size range of particles evaluated *in vivo* as determined by DLS: non cross-linked polymeric micelle as control, layer cross-linked nanohydrogel NH1 and polyplex PP1 derived from A-B-C triblock polypept(o)ide P1.

free siRNA). This drastic difference seem to originate solely from the variation in microstructure between A-B-C and A-C-B polymers, since all other parameters are identical, indicating that a terminal hydrophobic PCys(SO<sub>2</sub>R) block in **P2** hinders efficient complexation of siRNA. In contrast, the terminal cationic C block in **P1** is readily available for interaction with siRNA molecules compared to an intermediate cationic layer in **P2**. Preformed nanohydrogels, in contrast, compensate the poor template effect of small siRNA molecules, resulting in stable complexation by **NH1** and **NH2** independently from block sequence.

Table 16.2: Characterization of cross-linked nanohydrogels and polyplexes based on triblock copolypept(o)ides **P1** and **P2** as determined by DLS (in 10 mM HEPES buffer).

No	mircostructure	$D_h$ / nm	$\zeta$ -potential / mV	net charge
triblock copolypept(o)ides				
<b>P1</b>	A-B-C	–	35	positive
<b>P2</b>	A-C-B	–	26	positive
cross-linked nanohydrogels				
<b>NH1</b> (empty)	Lys - core	42	27	positive
<b>NH1</b> (siRNA)	Lys - core	52	0.2	neutral
<b>NH2</b> (empty)	Lys - layer	52	15	positive
<b>NH2</b> (siRNA)	Lys - layer	68	–20	negative
cross-linked polyplexes				
<b>PP1</b> (siRNA)	Lys - core	100	0.5	neutral
<b>PP2</b> (siRNA)	Lys - layer	109	–0.9	neutral

$\zeta$ -potential naked siRNA = –27.7 mV.

As expected from the proposed model, the triblock copolymer sequence governs particle properties, such as size and surface charge as determined by measurement of the  $\zeta$ -potential (Table 16.2 and Figure 16.3 C). Nanohydrogels increased slightly in size upon siRNA loading, while maintaining their size distribution (42 nm to 52 nm for **NH1** and 52 nm to 68 nm for **NH2**). Polyplexes were considerably larger upon hydrodynamic diameters around 100 nm due to reduced contribution of small siRNA molecules to a polyplex compaction process. As discussed for FCS experiments, only the terminal cationic P<sub>Lys</sub> segment in **P1** yields well defined polyplexes (**PP1**), while polyplexes **PP2** based on **P2** are polydisperse (PDI above 0.7). The  $\zeta$ -potential of **P1** and **P2** with 26.1 and 35.3 mV, respectively, is strongly cationic independent of block sequence and both nanohydrogel architectures remain positively charged when empty, although the P<sub>Sar</sub> block reduces the observed  $\zeta$ -potential. Upon introduction of negatively charged siRNA (–27.7 mV), however, **NH1** based on A-B-C triblock achieves full charge compensation (from 26.9 mV to 0.2 mV) in contrast to **NH2** based on A-C-B triblock



(from 15.4 mV to -19.8 mV) which indicates insufficient shielding. Both polyplexes mediate full charge compensation (0.5 mV and -0.9 mV for PP1 and PP2, respectively), however, PP2 proved insufficiently defined. On the way to *in vivo* studies, this choice was further reinforced by investigation of cellular toxicity of the carrier systems as intermediate step (see Figure 16.14 in the supporting information). No cytotoxic effect for siRNA loaded carriers derived from A-B-C-type polymer P1 was observed in agreement with their neutral surface potential, in contrast to charge-imbalanced structures based on P2, which showed concentration dependent toxicity. Based on these findings, the selection of siRNA carrier systems was reduced to NH1 and PP1.

Ultimately, NH1 and PP1, both derived from the A-B-C-type triblock P1, were investigated in terms of RNAi efficacy *in vivo*. Knockdown efficacy was evaluated upon systemic administration in an orthotropic mammary carcinoma model expressing luciferase (4T1-luc).<sup>[560]</sup> The target in the 4T1-luc cell line is the mRNA transcribed from genes encoding for the luciferase enzyme which catalyzes an oxidative decarboxylation and bioluminescence ( $\lambda = 480$  nm) upon administration of the substrate D-luciferin. Bioluminescence intensity is thus directly correlated to luciferase expression levels and the readout directly monitors enzymatic activity. Therefore, BALB/c mice bearing 4T1-luc mammary tumors were treated with 450  $\mu$ M antiGL3 siRNA as the therapeutic cargo in NH1 and PP1. As specificity control, a nonfunctional scramble siRNA was employed. Further, a polymeric micelle derived from AB diblock copolypept(o)ide was employed as additional control to exclude effects of PSar or PCys(SO<sub>2</sub>R) blocks. NH1 and PP1 were both loaded with functional or nonfunctional siRNA, without variation in size between control groups and upon neutral surface charge of -0.6 mV to 0.9 mV (see Table 16.4 and Figure 16.3 D for characterization). Administration was performed by tail vein injection and after 24 h, D-luciferin was administered intravenously as substrate for luciferase in bioluminescence imaging by an *in vivo* imaging system (IVIS) (see Figure 16.15).

Representative IVIS images (Figure 16.4 A) clearly visualize a reduced luciferase activity from the group treated with antiGL3 siRNA loaded in PP1 (*right* panel) in comparison to the empty AB micelle and nonfunctional scramble siRNA (*left* and *middle*, respectively) indicating intratumoral RNAi *in vivo*. This observation was confirmed by quantification of the bioluminescence data, where we observed a reduction of the luciferase signal of more than 60 % compared to control for antiGL3 siRNA loaded PP1, while scr. siRNA showed no effect on luciferase activity (see Figure 16.4 C). For NH1, however, an unspecific decrease in enzymatic activity was observed (42 % and 52 % reduction of the luciferase signal for antiGL3 and scr. siRNA, respectively). This lack of specificity is an indication for toxicity related effects and does not support successful intratumoral RNAi. In contrast, PP1 showed no concentration dependent toxicity with siRNA concentrations ranging as high as 800 nM (see Figure 16.4 B) and potent intratumoral RNAi.

*In vivo* evaluation of siRNA carriers derived from A-B-C triblock.

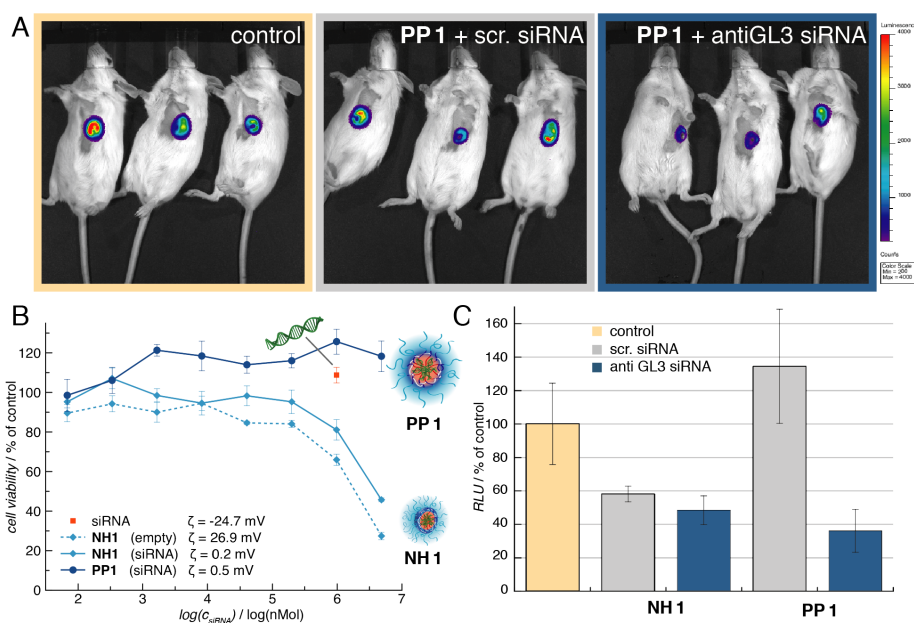


Figure 16.4: Effects of A-B-C triblock copolypept(o)ide based nanocarriers for systemic delivery of therapeutic siRNA in orthotropic 4T1-luc mammary tumor model (n = 3). NH1 and PP1 were each loaded with scr. siRNA as well as antiGL3 siRNA (450  $\mu$ Mol per mouse) and an unloaded AB polymeric micelle was used as the control. BALB/c mice were injected intravenously and knock-down efficacy was evaluated 24 h post injection *in vivo* by bioluminescence imaging. A) Representative bioluminescence images of control and PP1 with scr. siRNA and antiGL3 siRNA. B) Cytotoxicity of NH1 as well as PP1 loaded with gradually increasing siRNA concentrations (CCK8 cell viability assay, 6.25 to 800 nM siRNA). C) Relative luminescence intensity (RLU) by IVIS imaging after 10 min of luciferin injection (RLU determined by IVIS and normalized on individual weight of tumor tissue; data are expressed as mean; bars  $\pm$  SE.).

Since both carrier systems, PP1 and NH1, are derived from the same A-B-C triblock copolypept(o)ide P1, deviation of *in vivo* performance can be attributed solely to the process of carrier formation. While siRNA molecules are complexed in the core during polyplex formation of PP1, loading of a nanohydrogel requires diffusion into inner compartments. Thus, upon exposure to biological fluids, dissociation of siRNA and carrier is more likely for the performed particle in contrast to the polyplex. Loss of cargo, however, can lead to charge-mediated cytotoxicity as observed along with unspecific decrease of enzymatic activity *in vivo* for NH1. Ultimately, the polyplex PP1 derived from an A-B-C triblock copolypept(o)ide allowed for specific *in vivo* siRNA mediated silencing of luciferase expression in 4T1-luc tumors based on the favorable composition of the polymer microstructure of A: a shielding block, B: an intermediate hydrophobic segment combined with bioreversible disulfide stabilization and C: a terminal cationic block for polyplex formation.



### 16.3 CONCLUSION

In summary, we prepared A-B-C and A-C-B triblock copolypept(o)ides in order to evaluate the impact of block sequence alterations on formation and *in vivo* performance of siRNA delivery systems. As functional elements, a PSar-based shielding block, a hydrophobic PCys(SO<sub>2</sub>R) segment for bioreversible disulfide stabilization and a polycationic PLys block for complexation of siRNA were combined in triblock copolymers. Synthesis was performed by sequential ring-opening polymerization of  $\alpha$ -amino acid *N*-carboxyanhydride yielding well defined triblock copolypept(o)ides with permuted block sequence but identical individual block lengths and effective hydrodynamic volume. Both triblock copolypept(o)ide architectures were employed in the formation of nanohydrogels as well as polyplexes and characterized in light of their structure-property relationship based on sequence alteration. While A-C-B type triblock copolymers did only form polydisperse polyplexes and nanohydrogels with enhanced toxicity, polyplexes (PP1) and nanohydrogels (NH1) derived from an A-B-C polymer provide stable siRNA complexation, charge-shielding properties and low cytotoxicity. *In vivo*, however, only the polyplex PP1 achieved specific siRNA mediated knockdown of intratumoral luciferase expression. These findings underline the significance of block sequence in multifunctional triblock polymers employed in formation of gene delivery vectors for systemic applications.

### 16.4 ACKNOWLEDGMENTS

We thank Prof. Horacio Cabral for conduction of the *in vivo* experiments and fruitful discussions, Dr. Kaloian Koynov for providing FCS facilities and Prof. Kanjiro Miyata for providing siRNA sequences. O.S. acknowledges support by the "Evangelisches Studienwerk e.V. Villigst" and M.B. acknowledges financial support by the SFB 1066-2.

## 16.5 SUPPORTING INFORMATION

### 16.5.1 Materials and Instrumentation

DMF was purchased from Acros and dried over BaO and molecular sieve (3 Å), fractionally distilled *in vacuo* at 20 °C and stored at -80 °C under exclusion of light. Prior to use, *N,N*-dimethyl formamide (DMF) was degassed *in vacuo* to remove residing traces of dimethylamine. tetrahydrofuran (THF) and hexane were distilled from Na/K and ethyl acetate from CaH<sub>2</sub>. Neopentylamine was purchased from TCI Europe and was dried over NaOH followed by distillation. Cysteine and lysine were purchased from OPREGEN, sarcosine from Sigma-Aldrich and diphosgene from Alfa Aesar. Hexafluoro-2-propanol (HFIP) and *N*-Boc-1,2-diaminoethane were purchased from Fluorochem and deuterated solvents were obtained from Deutero GmbH. Millipore water was prepared by a MILLI-Q<sup>®</sup> Reference A+ System used at a resistivity of 18.2 MΩ cm<sup>-1</sup> and total organic carbon < 5 ppm.

<sup>1</sup>H NMR spectra were recorded on a Bruker Avance II HD 400 at a frequency of 400 MHz or a Bruker Avance III HD 300 at 300 MHz. Two-dimensional nuclear magnetic resonance (NMR) spectra (<sup>1</sup>H diffusion ordered spectroscopy (DOSY)) were recorded on a Bruker Avance III HD 400 at 400 MHz. All spectra were recorded at room temperature (25 °C) and calibrated using the solvent signals.<sup>[394]</sup> Melting points were measured using a Mettler FP62 melting point apparatus at a heating rate of 1 °C min<sup>-1</sup>.

Gel permeation chromatography (GPC) was performed with HFIP containing 3 g l<sup>-1</sup> potassium trifluoroacetate (KTFA) as eluent at 40 °C and a flow rate of 0.8 ml min<sup>-1</sup>. GPC columns were packed with modified silica (PFG columns particle size: 7 μm, porosity: 100 Å and 1000 Å). Polymethyl methacrylate PMMA standards (Polymer Standards Services GmbH) were used for calibration and toluene was used as internal standard. A refractive index detector (G1362A RID) and an UV/Vis detector (at 230 nm or as indicated; Jasco UV-2075 Plus) were used for polymer detection.

Single-angle dynamic light scattering (DLS) measurements and ζ-potential measurements were performed with a ZetaSizer Nano ZS instrument (Malvern Instruments Ltd., Worcestershire, UK) equipped with a He-Ne laser (λ = 633 nm) as the incident beam. All measurements were conducted at 25 °C and a detection angle of 173 °C. The particle mean diameter (z-ave.), size distribution (intensity-weighted) histograms, the width of the fitted Gaussian distribution, which is displayed as the polydispersity index (PDI), as well as the average ζ-potential values were calculated based on the autocorrelation function of samples, with automated attenuator adjustment and multiple scans (typically 10–15 scans) for optimal accuracy. Data are displayed as the mean value of at least three measurements ± standard deviation. Agarose gel electrophoresis was performed using a 0.5 w % agarose gel prepared with TBE buffer and GelRed for staining. Electrophoresis was carried out at 120 V for 30 min.

Visualization was performed in a dark hood under UV light (365 nm) and documented by a conventional digital camera. Fluorescence correlation spectroscopy (FCS) experiments were performed using a commercial setup (Zeiss, Germany), consisting of a ConfCor2 module and an inverted microscope (Axiovert200). For excitation of ATTO647-labeled siRNA, a helium-neon laser (633 nm) was used and focused through a Zeiss C-Apochromat 40x/1.2 W water immersion objective into the sample solutions. The emission of the ATTO647 fluorophore was detected in the spectral range 642–696 nm and the observations volumes were calibrated using AlexaFluor647 as reference dye with known diffusion coefficient. An eight-well polystyrene, chambered cover glass (Laboratory-Tek, Nalge Nunc International) was used as a sample cell. For each sample, a series of ten measurements with (10 seconds each) was performed.

siRNA sequences were purchased from Hokkaido System Science Co., Ltd. (Hokkaido, Japan) and used as follows: Firefly GL<sub>3</sub> luciferase siRNA (antiGL3 siRNA) sense strand with sequence 5'-CUUACGCUGAGUACUUC-GAdTdT-3' and antisense strand 3'-dTdTGA AUGCGACUCAUGAAGCU-5'. Scramble luciferase (scr. siRNA) sense strand 5'-UUCUCCGAACGUGUAC-CGUdTdT-3' and antisense strand 3'-dTdTAAAGAGGCUUGCACUGAGCA-5'. Murine breast adenocarcinoma 4T1 cells expressing luciferase (4T1-luc) were purchased from Japanese Collection of Research Bioresources Cell Bank (Osaka, Japan). The cells were cultured in Dulbecco's Modified Eagle Medium (DMEM) with 10% fetal bovine serum FBS and 1% streptomycin/penicillin and maintained at 37 °C and 5% CO<sub>2</sub>. The Cell Counting Kit-8 (CCK8) was purchased from Dojindo Laboratories, absorbance of the cell viability assay was measured by a microplate reader (Tecan Trading AG, Switzerland) and evaluated by a Spark Control Method editor (ver. 2.1) software.

Female BALB/c mice were purchased from Charles River Co. (Tokyo, Japan). All the experiments were conducted in accordance with the Guidelines for the Care and Use of Laboratory Animals as stated by the University of Tokyo. The mice were inoculated subcutaneously with  $1 \times 10^6$  4T1-luc cells to prepare the orthotropic 4T1-luc mammary tumors model. *In vivo* bioluminescent imaging was performed with an IVIS Imaging System (Xenogen Corporation) comprised of a highly sensitive, S2 cooled CCD camera mounted in a light-tight specimen box. Images and measurements of bioluminescent signals were acquired and analyzed using Living Image Software (Xenogen, ver. 4.5.5). The animals were anesthetized using 1-3% isoflurane (Abbot Laboratories). 10 minutes prior to *in vivo* imaging, animals received D-luciferin (Promega) as the luciferase substrate at 150 mg/kg in PBS by intravenous injection. Mice were placed on a warmed stage inside the camera box and received continuous exposure to 1-2% isoflurane to sustain sedation during imaging. Imaging times ranged from 10 to 60 s, depending on magnitude of the bioluminescence of the metastatic lesions.

## 16.5.2 Synthetic Procedures

## MONOMER SYNTHESIS

*Ethanesulfinic acid sodium salt*

A solution of sodium sulfite (391.98 g, 3.11 mol) in water (800 mL) was heated to 80 °C. Ethanesulfonyl chloride (147.40 mL, 199.30 g, 1.55 mol) and sodium carbonate (329.63 g, 3.11 mol) were added simultaneously while significant quantities of CO<sub>2</sub> evolved. The reaction mixture was stirred for one hour at 80 °C, afterwards water was removed *in vacuo* at 60 °C. The resulting solid was suspended in methanol and filtered. Evaporation of methanol gave ethanesulfinic acid sodium salt (153.54 g, 1.32 mol, 85 % yield) as a colorless solid.

<sup>1</sup>H NMR (400 MHz, DMSO-*d*<sub>6</sub>) δ [ppm] = 1.79 (q, <sup>3</sup>J<sub>H,H</sub> = 7.6 Hz, 2H, -CH<sub>2</sub>-), 0.90 (t, <sup>3</sup>J<sub>H,H</sub> = 7.6 Hz, 3H, -CH<sub>3</sub>).

*S-ethylsulfonyl-L-cysteine (Cys(SO<sub>2</sub>Et))*<sup>[173]</sup>

An ice-cold solution of sodium nitrite (5.94 g, 86 mmol) in degassed water (45 mL) was slowly added to a stirred solution of L-cysteine hydrochloride (13.57 g, 86 mmol) in previously degassed 2 N HCl (90 mL) at 0 °C. After 1 h, ethanesulfinic acid sodium salt (20.00 g, 172 mmol) was added to the deep red solution and was stirred for 2 h. Additional sodium ethanesulfinate (5.00 g, 43 mmol) was added and eventually a colorless solid precipitated. The reaction mixture was stirred at 0 °C overnight. The precipitate was filtered off and the pH of the colorless filtrate was adjusted with 2 N NaOH to pH 4-5, resulting in additional colorless solid precipitating. The filtrate was allowed to stand at 4 °C until precipitation was complete. The combined precipitates were washed with MeOH to remove residual sulfinate and dried *in vacuo* yielding Cys(SO<sub>2</sub>Et) (5.03 g, 24 mmol, 27 %) as a colorless, crystalline solid.

<sup>1</sup>H NMR (400 MHz, DMSO-*d*<sub>6</sub>/ TFA-*d*) δ [ppm] = 4.34 (t, <sup>3</sup>J<sub>H,H</sub> = 6.4 Hz, <sup>3</sup>J<sub>H,H</sub> = 6.0 Hz, 1H, α-H), 3.66 (dd, <sup>2</sup>J<sub>H,H</sub> = 14.4 Hz, <sup>3</sup>J<sub>H,H</sub> = 6.0 Hz, 1H, -CHH-S), 3.62 (q, J<sub>H,H</sub> = 7.2 Hz, 2H, -CH<sub>2</sub>-SO<sub>2</sub>), 3.53 (dd, <sup>3</sup>J<sub>H,H</sub> = 14.4 Hz, <sup>3</sup>J<sub>H,H</sub> = 6.4 Hz, 1H, -CHH-S), 1.30 (t, <sup>3</sup>J<sub>H,H</sub> = 7.2 Hz, 3H, -CH<sub>3</sub>).

*S-ethylsulfonyl-L-cysteine N-carboxyanhydride (Cys(SO<sub>2</sub>Et) NCA)*<sup>[173]</sup>

Dried Cys(SO<sub>2</sub>Et) (7.00 g, 32.82 mmol) was suspended in absolute THF (100 mL) and heated to 70 °C. Diphosgene (3.60 mL, 5.84 g, 29.52 mmol) was slowly added and the suspension was heated for an additional 4 h. Dry nitrogen was bubbled through the reaction mixture overnight into a gas washing bottle with an aqueous KOH solution to remove excess diphosgene, HCl and most of the solvent. The remaining solvent was removed *in vacuo* and the residue was dissolved in 100 mL absolute ethyl acetate. Any insoluble compounds were removed by filtration avoiding contact with air and the NCA was precipitated by adding 800 mL absolute hexane. After recrystallization a total of 6.43 g of purified product

(26.87 mmol, 82 % yield, colorless and crystalline powder, melting point: 113–115 °C) was obtained and stored in a Schlenk tube at -80 °C.

$^1\text{H}$  NMR (400 MHz,  $\text{DMSO-}d_6$ )  $\delta$  [ppm] = 9.32 (s, 1H, -NHCO), 4.86 (td,  $^3J_{\text{H,H}} = 6.0$  Hz,  $^3J_{\text{H,H}} = 4.8$  Hz,  $^3J_{\text{H,H}} = 1.6$  Hz, 1H,  $\alpha\text{-H}$ ), 3.64 (dd,  $^2J_{\text{H,H}} = 14.4$  Hz,  $^3J_{\text{H,H}} = 4.8$  Hz, 1H, -CHH-S), 3.62 (q,  $^3J_{\text{H,H}} = 7.2$  Hz, 2H, -CH<sub>2</sub>-SO<sub>2</sub>), 3.57 (dd,  $^2J_{\text{H,H}} = 14.4$  Hz,  $^3J_{\text{H,H}} = 6.4$  Hz, 1H, -CHH-S), 1.29 (t,  $^3J_{\text{H,H}} = 7.2$  Hz, 3H, -CH<sub>3</sub>).

*N-ε-tert-butyloxycarbonyl-L-lysine N-carboxyanhydride (Lys(Boc) NCA)*<sup>[59]</sup>

9.8 g (39.8 mmol) of *N-ε*-Boc-protected lysine was weighed into a three-necked flask and dried *in vacuo* for 1 h. The solid was suspended in 300 mL of absolute THF under a steady flow of dry nitrogen. Afterward, 9.9 mL (79.6 mmol) of absolute trimethyl-silylchloride and 11.0 mL (79.6 mmol) of absolute triethylamine TEA were added slowly *via* syringe. The suspension was stirred for 2 h followed by addition of 4.8 mL (39.8 mmol) of diphosgene, *via* syringe. The suspension was mildly refluxed for another 2 h. Overnight, a steady flow of dry nitrogen was lead through the solution into two gas washing bottles filled with aqueous NaOH solution removing excess phosgene and HCl. The suspension was filtered under dry nitrogen atmosphere to remove the salts of TEA and unconverted amino acid. The solid was washed with absolute THF and the filtrate was evaporated under reduced pressure. Subsequently, absolute THF was added to completely dissolve the crude reaction product. The solution was precipitated with absolute hexane and stored at 4 °C for 1 h. The solid was collected by filtration under dry nitrogen atmosphere and washed with absolute hexane. The crude reaction product was then recrystallized twice with absolute THF/hexane. A total of 6.52 g of purified product (23.9 mmol, 68 % yield, colorless needles, melting point: 138.3 °C) was obtained and stored in a Schlenk tube at -80 °C.  $^1\text{H}$  NMR (400 MHz,  $\text{DMSO-}d_6$ )  $\delta$  [ppm] = 9.07 (s, 1H, -NH-CO-O-CO), 6.95–6.34 (br, 1H, -NH-CO-O-C(CH<sub>3</sub>)<sub>3</sub>), 4.42 (t, 1H,  $^3J_{\text{H,H}} = 6.35$  Hz, -CO-CH-CH<sub>2</sub>-), 2.90 (q, 2H,  $^3J_{\text{H,H}} = 6.03$  Hz, -CH<sub>2</sub>-NH-CO-O-C(CH<sub>3</sub>)<sub>3</sub>), 1.79–1.56 (m, 2H, -CH-CH<sub>2</sub>-CH<sub>2</sub>-CH<sub>2</sub>-CH<sub>2</sub>-NH-), 1.45–1.12 (m, 13H, -CH-CH<sub>2</sub>-CH<sub>2</sub>-CH<sub>2</sub>-CH<sub>2</sub>-NH<sup>-</sup>, -NH-CO-O-C(CH<sub>3</sub>)<sub>3</sub>).

*Sarcosine N-carboxyanhydride (Sar NCA)*<sup>[26]</sup>

The synthesis of sarcosine NCA was adapted from literature and modified.<sup>[44]</sup> A total of 14.92 g (167.4 mmol) sarcosine, dried *in vacuo* for 1 h, was weighed into a pre-dried, three-neck, round-bottom flask. A total of 300 mL of absolute THF was added under a steady flow of nitrogen and 16.2 mL (134 mmol) of diphosgene were added slowly *via* syringe, and the nitrogen stream was reduced. The colorless suspension was mildly refluxed for 3 h, yielding a clear solution. Afterward, a steady flow of dry nitrogen was led throw the solution for another 3 h into two gas washing bottles filled with aqueous NaOH solution. The solvent was evaporated under reduced pressure, yielding a brown oil as crude reaction product. The oil was heated to 50 °C and dried under

reduced pressure (20 mbar, then  $< 10^{-2}$  mbar for 2 h) to obtain an amorphous solid, free of phosgene and HCl, confirmed by testing against silver nitrate solution. The crude product was dissolved in 40 mL absolute THF and precipitated with 300 mL absolute hexane. The solution was cooled to  $-18^{\circ}\text{C}$  overnight for complete precipitation. The solid was filtered under dry nitrogen atmosphere, dried in a stream of dry nitrogen for 60–90 min and afterwards under high vacuum for 2 h in a sublimation apparatus. The crude product was sublimated at  $80\text{--}85^{\circ}\text{C}$  and  $< 10^{-2}$  mbar. The product was collected from the sublimation apparatus in a glovebox on the same day. This procedure yielded 12.64 g of purified product (110 mmol, 65 % yield, colorless crystals, melting point:  $102\text{--}104^{\circ}\text{C}$ ) which was stored in a Schlenk tube at  $-80^{\circ}\text{C}$  and only handled under nitrogen atmosphere.

$^1\text{H}$  NMR (400 MHz,  $\text{CDCl}_3$ )  $\delta$  [ppm] = 4.22 (s, 2H,  $-\text{CH}_2-$ ), 2.86 (s, 3H,  $-\text{CH}_3$ ).

#### SYNTHESIS OF A-B-C TRIBLOCK COPOLYPEPT(O)IDE (P1)

##### *Polysarcosine initiated by N-Boc-1,2-diaminoethane*<sup>[327]</sup>

1.5 g (13.1 mmol) sarcosine NCA were dried *in vacuo* and dissolved in 9.5 mL dry DMF and 41.5  $\mu\text{L}$  (262  $\mu\text{mol}$ ) *N*-Boc-1,2-diaminoethane in 0.5 mL dry DMF were added. The clear, colorless solution was stirred at room temperature under a steady flow of dry nitrogen for 2 days (complete conversion was monitored by IR-spectroscopy). The sarcosine amino terminus was quenched by addition of 726  $\mu\text{L}$  (0.52 mmol) triethylamine and 248  $\mu\text{L}$  (0.26 mmol) acetic anhydride. The clear solution was allowed to stir for an additional day at room temperature. Precipitation in diethylether yielded 980 mg (95 %) of a colorless solid. The Boc protective group was removed in a mixture of  $\text{H}_2\text{O}/\text{TFA}$  1:1 for 2 h. The clear yellow solution was stirred under an argon atmosphere at room temperature for 1 hour under the exclusion of light. Precipitation in diethyl ether yielded a colorless solid, which was dialyzed against Millipore water (MWCO 3.5 kDa), saturated with  $\text{NaHCO}_3$  for 2 days followed by dialysis in pure Millipore water for additional 2 days. The polymer was lyophilized from water and 450 mg (46 %) of a colorless solid were obtained.

$^1\text{H}$  NMR (400 MHz,  $\text{DMSO}-d_6$ )  $\delta$  [ppm] = 4.35–3.94 (m, 2nH,  $-\text{CH}_2-$ ), 2.97–2.73 (m, 3nH,  $-\text{CH}_3$ ), 2.01–1.99 (m, 3H,  $-\text{OCCH}_3$ ). Additionally 1.37 (m, 9H,  $-\text{OC}(\text{CH}_3)_3$ ) for Boc-terminated.

##### *Polysarcosine-block-poly(S-ethylsulfonyl-L-cysteine) (PSar-b-PCys(SO<sub>2</sub>Et))*<sup>[327]</sup>

208 mg (40.5  $\mu\text{mol}$ ) amine terminated polysarcosine macroinitiator were dried *in vacuo* and dissolved in 5 mL dry DMF. The pale yellow monomer solution of 485 mg (2.0 mmol) *Cys*( $\text{SO}_2\text{Et}$ ) NCA in 4 mL dry DMF was added. The polymerization was carried out at  $-10^{\circ}\text{C}$  under a steady flow of dry nitrogen and monitored *via* IR spectroscopy. After 2 days (conversion rate of 51%), the reaction was stopped by precipitation in



THF/diethyl ether 1:5. The work-up by precipitation and centrifugation was repeated two times in THF/diethyl ether 1:5 and then once in pure diethyl ether. After extensive drying *in vacuo*, 252 mg (42%) of a colorless solid were obtained.

$^1\text{H}$  NMR (400 MHz,  $\text{DMSO-}d_6$ )  $\delta$  [ppm] = 8.76 (m, 1mH,  $-\text{NHCO}$ )<sub>Cys</sub>, 4.69 (m, 1mH,  $\alpha\text{-H}$ )<sub>Cys</sub>, 4.34–3.92 (m, 2nH,  $-\text{CH}_2\text{-}$ )<sub>Sar</sub>, 3.57–3.47 (m, 4mH,  $-\text{CH}_2\text{-SSO}_2\text{-CH}_2\text{-}$ )<sub>Cys</sub>, 2.93–2.72 (m, 3nH,  $-\text{CH}_3$ )<sub>Sar</sub>, 1.29 (t, 3mH,  $-\text{CH}_3$ )<sub>Cys</sub>.

*Polysarcosine-block-poly(S-ethylsulfonyl-L-cysteine)-block-poly-L-lysine*  
(PSar-*b*-PCys(SO<sub>2</sub>Et)-*b*-PLys P2)

252 mg (23.7  $\mu\text{mol}$ ) PSar-*b*-PCys(SO<sub>2</sub>Et) macroinitiator were dried *in vacuo* and dissolved in 2.5 mL dry DMF. 4.0  $\mu\text{L}$  (23.7  $\mu\text{mol}$ ) dry *N,N*-diisopropylethylamine (DIPEA) were added and the macroinitiator solution was stirred at 0 °C for 0.5 h. A monomer solution of 258 mg (0.95 mmol) Lys(Boc) NCA in 2.5 mL dry DMF was added. The polymerization was carried out at 0 °C under a steady flow of dry nitrogen and monitored *via* IR spectroscopy. After 2 days (conversion rate of 46%), the reaction was stopped by precipitation in THF/diethyl ether 1:5. The work-up by precipitation and centrifugation was repeated two times in THF/diethyl ether 1:5 and once in pure diethyl ether, yielding 375 mg (88 %) Boc-protected A-B-C triblock copolymer as a colorless solid. The Boc protective group of 158 mg Boc-protected triblock copolymer was removed in a mixture of H<sub>2</sub>O/TFA 1:1 for 2 h. The clear yellow solution was stirred under an argon atmosphere at room temperature for 1 hour under the exclusion of light. Precipitation in diethyl ether yielded a colorless solid, which was dialyzed against 2 vol% acetic acid in Millipore water (MWCO 3.5 kDa) for 3 days. Lyophilisation yielded 129 mg (82 %) PSar-*b*-PCys(SO<sub>2</sub>Et)-*b*-PLys as a colorless solid.

$^1\text{H}$  NMR (400 MHz,  $\text{DMSO-}d_6$ )  $\delta$  [ppm] = 8.78 (m, 11H,  $-\text{NHCO}$ )<sub>Cys</sub>, 8.12 (m, 1mH,  $-\text{NH-CO-O-CO}$ )<sub>Lys</sub>, 4.68 (m, 11H,  $\alpha\text{-H}$ )<sub>Cys</sub>, 4.35–3.94 (m, 2nH  $-\text{CH}_2\text{-Sar}$ , 1mH  $-\text{CO-CH-CH}_2\text{-Lys}$ ), 3.56 (m, 41H,  $-\text{CH}_2\text{-SSO}_2\text{-CH}_2\text{-}$ )<sub>Cys</sub>, 3.31 (m, 2mH,  $-\text{CH}_2\text{-NH-CO-O-C(CH}_3\text{)}_3$ )<sub>Lys</sub>, 2.94–2.73 (m, 3nH,  $-\text{CH}_3$ )<sub>Sar</sub>, 1.51 (m, 6mH,  $-\text{CH-CH}_2\text{-CH}_2\text{-CH}_2\text{-CH}_2\text{-NH-}$ )<sub>Lys</sub>, 1.30 (t, 31H,  $-\text{CH}_3$ )<sub>Cys</sub>.

SYNTHESIS OF A-C-B TRIBLOCK COPOLYPEPT(O)IDE (P2)

*Polysarcosine initiated by neopentylamine*<sup>[26]</sup>

1. g (8.9 mmol) sarcosine NCA were dried *in vacuo* and dissolved in 5 mL dry DMF. To the monomer solution 10.4  $\mu\text{L}$  absolute neopentylamine (7.7 mg, 89  $\mu\text{mol}$ ) were added. The clear, colorless solution was stirred at room temperature under a steady flow of dry nitrogen. The reaction was completed after 2 days (monitored by IR-spectroscopy). Precipitation in diethyl ether yielded 559 mg (55 %) of a colorless solid.

$^1\text{H}$  NMR (400 MHz,  $\text{DMSO-}d_6$ )  $\delta$  [ppm] = 4.34–3.92 (m, 2nH,  $-\text{CH}_2\text{-}$ ), 2.93–2.73 (m, 3nH,  $-\text{CH}_3$ ), 0.82 (s, 9H,  $-(\text{CH}_3)_3$ ).

*Polysarcosine-block-poly(N-ε-tert-butylloxycarbonyl-L-lysine)*  
(*PSar-b-PLys(Boc)*)

172 mg (23.1 μmol) polysarcosine macroinitiator were dried *in vacuo* and dissolved in 1.7 mL dry DMF. 3.9 μL (23.1 μmol) dry *N,N*-diisopropylethylamine (DIPEA) were added and the macroinitiator solution was stirred at 0 °C for 0.5 h. The monomer solution of 314 mg (1.15 mmol) Lys(Boc) NCA in 3 mL dry DMF was added. The polymerization was carried out at 0 °C under a steady flow of dry nitrogen and monitored *via* IR spectroscopy. After 24 h full conversion was reached and the reaction was terminated by precipitation in diethyl ether. The work-up by precipitation and centrifugation was repeated two times and 300 mg (69%) of a colorless solid were obtained.

<sup>1</sup>H NMR (400 MHz, DMSO-*d*<sub>6</sub>) δ [ppm] = 8.16 (m, 1mH, -NH-CO-O-CO)<sub>Lys</sub>, 6.67–6.63 (m, 1mH, -NH-CO-O-C(CH<sub>3</sub>)<sub>3</sub>)<sub>Lys</sub>, 4.35–3.94 (m, 2nH -CH<sub>2</sub>-Sar, 1mH -CO-CH-CH<sub>2</sub>-Lys), 3.32 (m, 2mH, -CH<sub>2</sub>-NH-CO-O-C(CH<sub>3</sub>)<sub>3</sub>)<sub>Lys</sub>, 2.96–2.73 (m, 3nH, -CH<sub>3</sub>)<sub>Sar</sub>, 1.52 (m, 6mH, -CH-CH<sub>2</sub>-CH<sub>2</sub>-CH<sub>2</sub>-CH<sub>2</sub>-NH-)<sub>Lys</sub>, 1.35 (m, 9mH, -NH-CO-O-C(CH<sub>3</sub>)<sub>3</sub>)<sub>Lys</sub>, 0.82 (m, 9H, -(CH<sub>3</sub>)<sub>3</sub>)<sub>Neo</sub>.

*Polysarcosine-block-poly-L-lysine-block-poly(S-ethylsulfonyl-L-cysteine)*  
(*PSar-b-PLys-b-PCys(SO<sub>2</sub>Et) P1*)

221 mg (21.1 μmol) PSar-*b*-PLys(Boc) macroinitiator were dried *in vacuo* and dissolved in 3 mL dry DMF. 3.6 μL (21.1 μmol) dry DIPEA were added the macroinitiator solution was stirred at -10 °C for 0.5 h. The pale yellow monomer solution of 253 mg (1.1 mmol) Cys(SO<sub>2</sub>Et) NCA in 3.5 mL dry DMF was added. The polymerization was carried out at -10 °C under a steady flow of dry nitrogen and monitored *via* IR spectroscopy. After 2 days (conversion rate of 43%), the reaction was stopped by precipitation in THF/diethyl ether 1:5. The work-up by precipitation and centrifugation was repeated two times in THF/diethyl ether 1:5 and then once in pure diethyl ether, yielding 328 mg (75 %) Boc-protected triblock copolymer as a colorless solid. The Boc protective group of 151 mg Boc-protected A-C-B triblock copolymer was removed in a mixture of H<sub>2</sub>O/TFA 1:1 for 2 h. The clear yellow solution was stirred under an argon atmosphere at room temperature for 1 hour under the exclusion of light. Precipitation in diethyl ether yielded a colorless solid, which was dialyzed against 2 vol% acetic acid in Millipore water (MWCO 3.5 kDa) for 3 days. Lyophilisation yielded 124 mg (82 %) PSar-*b*-PLys-*b*-PCys(SO<sub>2</sub>Et) as a colorless solid.

<sup>1</sup>H NMR (400 MHz, DMSO-*d*<sub>6</sub>) δ [ppm] = 8.79 (m, 1H, -NHCO)<sub>Cys</sub>, 8.16 (m, 1mH, -NH-CO-O-CO)<sub>Lys</sub>, 4.68 (m, 1H, α-H)<sub>Cys</sub>, 4.35–3.94 (m, 2nH -CH<sub>2</sub>-Sar, 1mH -CO-CH-CH<sub>2</sub>-Lys), 3.56 (m, 4H, -CH<sub>2</sub>-SSO<sub>2</sub>-CH<sub>2</sub>-)<sub>Cys</sub>, 3.32 (m, 2mH, -CH<sub>2</sub>-NH-CO-O-C(CH<sub>3</sub>)<sub>3</sub>)<sub>Lys</sub>, 2.96–2.73 (m, 3nH, -CH<sub>3</sub>)<sub>Sar</sub>, 1.52 (m, 6mH, -CH-CH<sub>2</sub>-CH<sub>2</sub>-CH<sub>2</sub>-CH<sub>2</sub>-NH-)<sub>Lys</sub>, 1.30 (t, 3H, -CH<sub>3</sub>)<sub>Cys</sub>, 0.82 (m, 9H, -(CH<sub>3</sub>)<sub>3</sub>)<sub>Neo</sub>.



## SYNTHESIS OF CATIONIC CROSS-LINKER TETA

*Triethylenetetramine  $\alpha,\omega$ -di((S-Trt-N-Boc)cysteine)diamide*

1.20 g (2.60 mmol) Cys(S-Trt)N-Boc and 472 mg (3.50 mmol) HOBt (12 % water) were dissolved in 10 mL DMF and 589 mg (3.12 mmol) EDC·HCl were added. The solution was stirred for 1 h at rt. 193  $\mu$ L triethylenetetramine were added and the solution was stirred for 30 more minutes. The solvent was removed *in vacuo* and the product purified by flash chromatography (AcOEt:MeOH (3:5) +2 % NEt<sub>3</sub>).

<sup>1</sup>H NMR (300 MHz, CDCl<sub>3</sub>)  $\delta$  [ppm] = 7.45–7.33 (m, 12H, *m*-H<sub>Ar</sub>), 7.29–7.21 (m, 12H, *o*-H<sub>Ar</sub>), 7.22–7.13 (m, 6H, *p*-H<sub>Ar</sub>), 6.62 (s, 2H, -CO-NH-), 5.05 (s, br, 2H,  $\alpha$ -H), 3.92 (s, 2H, -NH), 3.39–3.09 (m, 4H, -CH<sub>2</sub>-S-), 2.68 - 2.60 (m, 8H, --CO-NH-CH<sub>2</sub>-CH<sub>2</sub>-), 2.58 (s, 4H, -NH-CH<sub>2</sub>-CH<sub>2</sub>-NH-), 1.39 (s, 18H, -O-C(CH<sub>3</sub>)<sub>3</sub>).

ESI-MS:  $m/z$  = 1038.7 [M+H]<sup>+</sup>, (calc. 1037.5 g mol<sup>-1</sup>); 1059.6 [M+Na]<sup>+</sup>, (calc. 1059.5 g mol<sup>-1</sup>).

*Triethylenetetramine  $\alpha,\omega$ -di(cysteine)diamide*

442 mg (0.426 mmol) triethylenetetramine  $\alpha,\omega$ -di((S-Trt-N-Boc)cysteine)diamide and 263 mg (1.7 mmol) dithiothreitol (DTT) were dissolved in 18 mL DCM. 0.7 mL (3.4 mmol) triisopropylsilane followed by 2 mL TFA. The solution was stirred under argon for 3 h and precipitated in diethyl ether. The crude product was dissolved in 4 mL water/acetonitrile (97:3 + 0.1% TFA), 130 mg DTT were added and the mixture was purified by HPLC. Lyophilization yielded 287 mg triethylenetetramine  $\alpha,\omega$ -di(cysteine) diamide tetratrifluoroacetate.

<sup>1</sup>H NMR (400 MHz, D<sub>2</sub>O)  $\delta$  [ppm] = 4.24 (dd, <sup>3</sup>J<sub>H,H</sub> = 6.3, 5.2 Hz, 2H,  $\alpha$ -H), 3.79–3.66 (m, 2H, -CH<sub>2</sub>-S-), 3.65–3.54 (m, 2H, -CH<sub>2</sub>-S-), 3.52 (s, 4H, -NH-CH<sub>2</sub>-CH<sub>2</sub>-NH-), 3.33 (q, <sup>3</sup>J<sub>H,H</sub> = 5.8 Hz, 4H, -CO-NH-CH<sub>2</sub>), 3.17–3.02 (dq, <sup>3</sup>J<sub>H,H</sub> = 5.8, 14.1 Hz, 4H, -CH<sub>2</sub>-NH-).

ESI-MS:  $m/z$  = 353.2 [M+H]<sup>+</sup>, (calc. 353.2 g mol<sup>-1</sup>).

## 16.5.3 Particle Preparation

For preparation of cross-linked cationic nanohydrogels, **P1** or **P2** was dissolved in *N,N*-dimethyl acetamide (DMAc) at a concentration of 7.5 g L<sup>-1</sup> overnight. 25 vol. % of 1 mM acetate buffer (pH = 4.7) were then added as the block-selective solvent. The solutions were left to equilibrate for 4 h, dialyzed against 1 mM acetate buffer (MWCO = 3.5 kDa). Cross-linking was performed by addition of the cationic cross-linker TETA with SH-groups equimolar to the number of cysteines as a 50 g L<sup>-1</sup> stock solution in water. The reaction mixtures were vortexed and allowed to stand overnight. Subsequently, the solutions were diluted with 1 mM acetate buffer (pH 4.7), purified by repetitive spin filtration (MWCO 100 kDa) and dilution steps concluding in 10 mM HEPES buffer and filtered *via* a 200 nm syringe filter (GHP). Loading with siRNA was

performed as follows: The desired amount of siRNA in sterile water (70  $\mu\text{M}$  for antiGL3 siRNA and 76.9  $\mu\text{M}$  for scr. siRNA) was diluted with a solution of the respective nanohydrogel (3.5  $\text{g L}^{-1}$  in 10 mM HEPES) at a mass ratio of 20:1 and vortexed for 10 s. The solutions were incubated for 1 h at room temperature and the final concentration was adjusted with 10 mM HEPES buffer prior to use.

For the formation of cross-linked polyplexes, P1 or P2 was dissolved in 10 mM HEPES buffer at a concentration of 10  $\text{g L}^{-1}$ . The desired amount of siRNA in sterile water (70  $\mu\text{M}$  for antiGL3 siRNA and 76.9  $\mu\text{M}$  for scr. siRNA) was diluted with the respective polymer solution at a N:P ratio of 15:1 (corresponding mass ratio of 18:1) and vortexed for 10 s. The solutions were incubated for 30 min at room temperature. Cross-linking was performed with the cationic cross-linker TETA with SH-groups equimolar to the number of cysteines as a 50  $\text{g L}^{-1}$  stock solution in water. The cross-linker was added and the solution was vortexed immediately for 10 s. The solutions were incubated for 1-2 h at room temperature and the final concentration was adjusted with 10 mM HEPES buffer prior to use.

Table 16.3: Characterization of cross-linked nanohydrogels and polyplexes based on triblock copolypept(o)ides P1 and P2 as determined by DLS (in 10 mM HEPES buffer).

No	$D_h$ / nm	PDI	$\zeta$ -potential / mV
triblock copolypept(o)ides			
P1	–	–	35.3 $\pm$ 1.2
P2	–	–	26.1 $\pm$ 1.1
cross-linked nanohydrogels			
NH1 (empty)	41.7 $\pm$ 0.9	0.224 $\pm$ 0.024	26.9 $\pm$ 0.5
NH1 (siRNA)	52.4 $\pm$ 1.7	0.223 $\pm$ 0.015	0.2 $\pm$ 0.2
NH2 (empty)	52.2 $\pm$ 0.5	0.230 $\pm$ 0.024	15.4 $\pm$ 0.6
NH2 (siRNA)	68.1 $\pm$ 5.7	0.237 $\pm$ 0.019	–19.8 $\pm$ 1.3
cross-linked polyplexes			
PP1 (siRNA)	100.4 $\pm$ 0.2	0.237 $\pm$ 0.006	0.5 $\pm$ 0.2
PP2 (siRNA)	109.3 $\pm$ 12.6	0.759 $\pm$ 0.074	–0.9 $\pm$ 0.5

$\zeta$ -potential naked siRNA = –27.7 mV.

#### 16.5.4 Biological Evaluation

##### *In Vitro Cytotoxicity Assay*

The cytotoxicity of triblock copolypept(o)ides and the derived delivery systems were evaluated in 4T1-luc cells using the Cell Counting Kit-8. The cells (10000 cells/100  $\mu\text{L}$ ) were cultured for 24 h at 37  $^{\circ}\text{C}$  in DMEM containing 10 % FBS in a 96-well multiplate. The cells were then exposed to the respective samples for additional 24 h at 37  $^{\circ}\text{C}$ . The medium was discarded, replaced with 100  $\mu\text{L}$  fresh medium and followed by addition

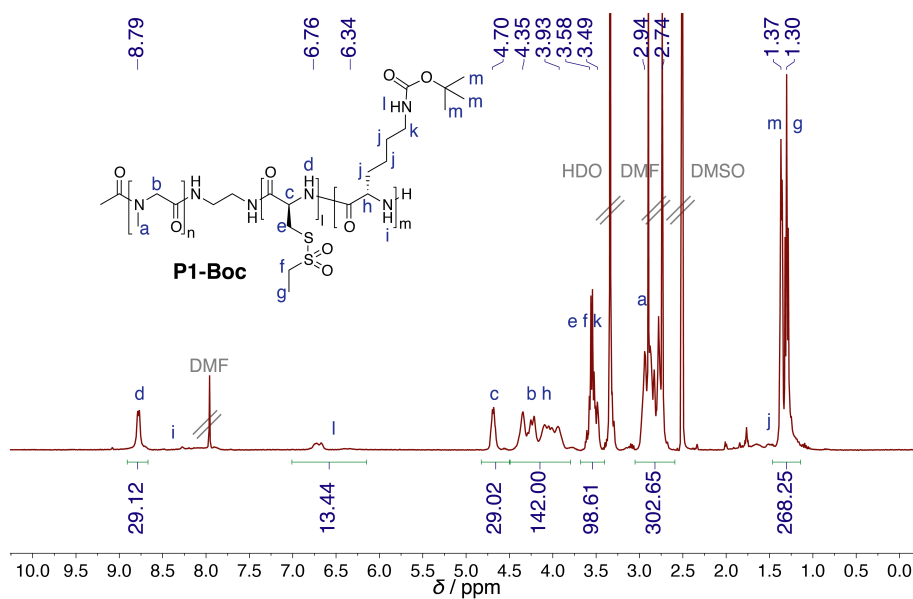
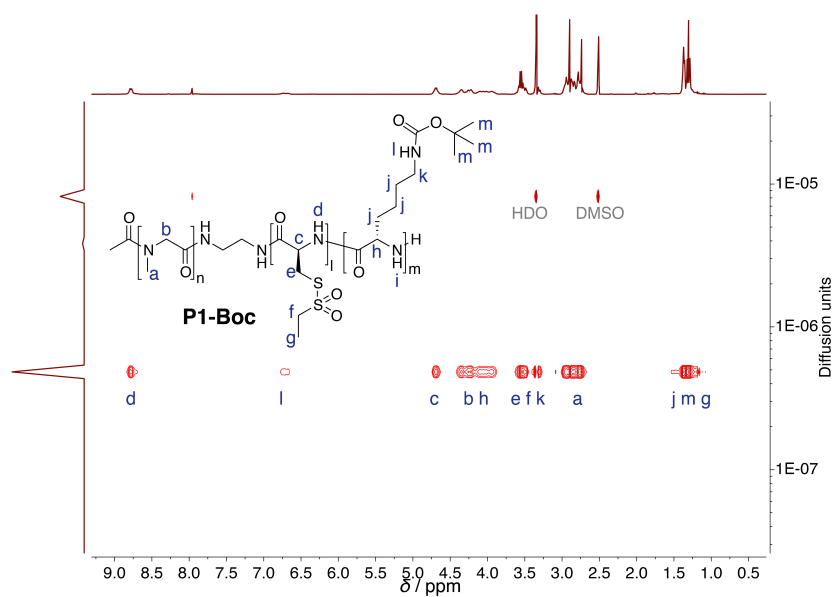
of the manufacturer's reagent (10  $\mu$ L). After 1 h incubation at 37  $^{\circ}$ C the absorbance was measured at 450 nm using a microplate reader. For data shown in Figure 16.14, siRNA concentrations were 100, 200 and 400 nM, respectively. For detailed evaluation of cytotoxicity prior to *in vivo* application (data shown in Figure 16.4 B), siRNA concentrations were 6.25, 12.5, 25, 50, 100, 200, 400 and 800 nM for loaded **NH1** and **PP1**, or an equivalent amount of 10 mM HEPES for empty **NH1** and free polymer **P2**.

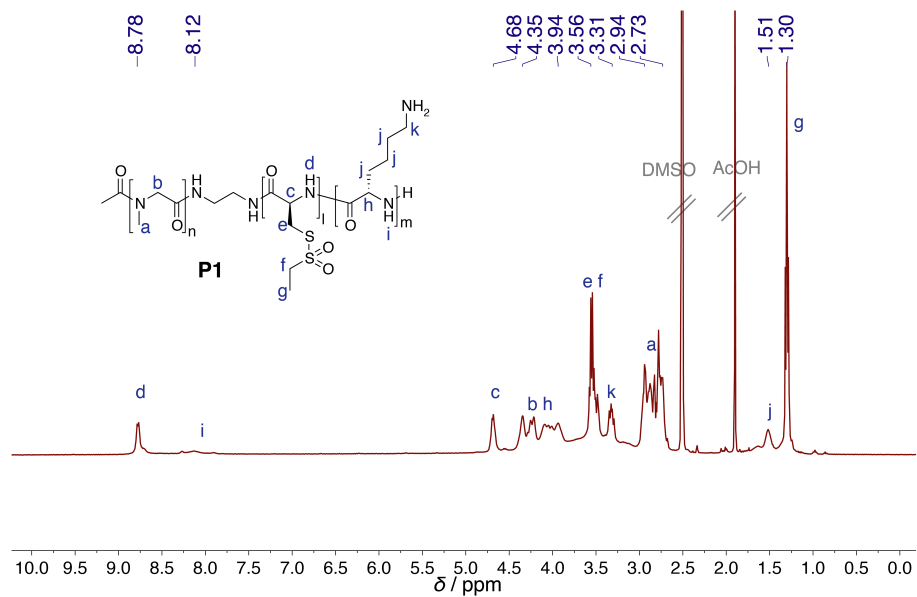
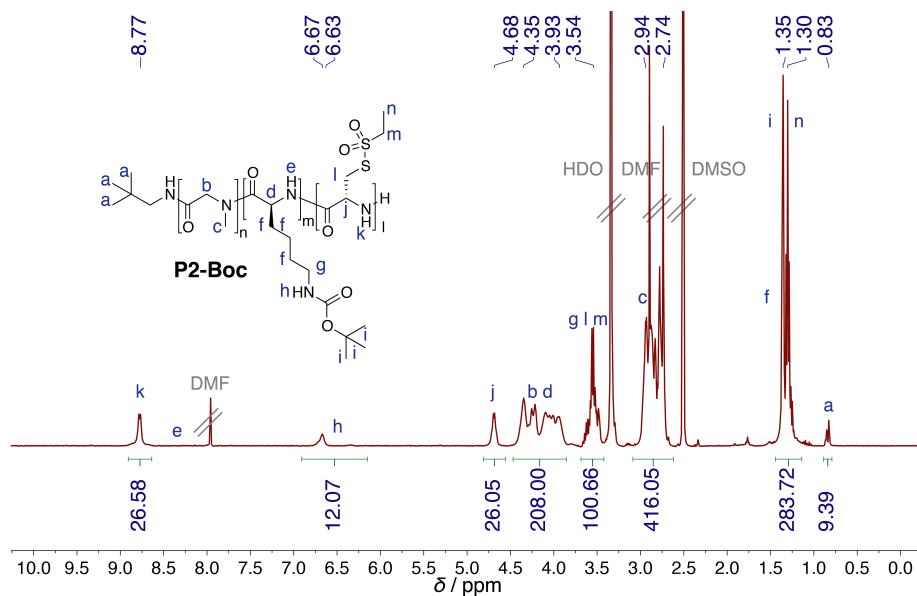
#### *In Vivo Bioluminescence Assay*

In order to evaluate the knock-down efficacy of siRNA delivery vectors based on triblock copolypept(o)ides, female BALB/c mice bearing orthotropic 4T1-luc mammary tumors (n = 3) were treated intravenously with 450  $\mu$ M antiGL3 siRNA or scr. siRNA as a control, encapsulated in **NH1** or **PP1**, respectively (200  $\mu$ L injected volume, siRNA concentration of 2.25  $\mu$ M prior to injection). The control group was treated with an unloaded, non stabilized polymeric micelle derived from PSar-*b*-PCys(SO<sub>2</sub>Et) diblock copolypept(o)ide (see Table 16.4 for characterization of individual samples). Female BALB/c mice were inoculated with  $1 \times 10^6$  cell subcutaneously in the mammary gland. After the primary tumors were sufficiently developed, samples were administered *via* tail vein injection and 24 h post injection, *in vivo* bioluminescence imaging was performed using an IVIS spectrum. The mice were anesthetized with isoflurane and injected intravenously with luciferin as a substrate for luciferase. At 10 min after luciferin injection, the mice were imaged for 10-60 s. The regions of interest (ROIs) were selected to measure the tumor volume and background. Photons emitted from ROIs were quantified using Living Image software (ver. 4.5.5). The *in vivo* luciferase activity was expressed as relative luminescence units and normalized on individual tumor weight as determined after excision.

Table 16.4: Characterization of nanocarriers evaluated *in vivo*.

No + siRNA	$D_h$ / nm	PDI	$\zeta$ -potential / mV
control (empty micelle)	$52.1 \pm 0.4$	$0.229 \pm 0.019$	$0.8 \pm 0.3$
<b>NH1</b> + scr. siRNA	$53.0 \pm 1.8$	$0.240 \pm 0.005$	$-0.6 \pm 0.2$
<b>NH1</b> + antiGL3 siRNA	$50.7 \pm 0.2$	$0.232 \pm 0.009$	$0.2 \pm 0.2$
<b>PP1</b> + scr. siRNA	$103.7 \pm 1.9$	$0.252 \pm 0.005$	$0.9 \pm 0.1$
<b>PP1</b> + antiGL3 siRNA	$101.8 \pm 0.8$	$0.261 \pm 0.028$	$0.5 \pm 0.2$

16.5.5  $^1\text{H}$  NMR Characterization of Triblock CopolymersFigure 16.5:  $^1\text{H}$  NMR spectrum (400 MHz) of **P1-Boc** in  $\text{DMSO}-d_6$ .Figure 16.6: DOSY  $^1\text{H}$  NMR spectrum (400 MHz) of **P1-Boc** in  $\text{DMSO}-d_6$ .

Figure 16.7:  $^1\text{H}$  NMR spectrum (400 MHz) of **P1** in  $\text{DMSO-}d_6$ .Figure 16.8:  $^1\text{H}$  NMR spectrum (400 MHz) of **P2-Boc** in  $\text{DMSO-}d_6$ .

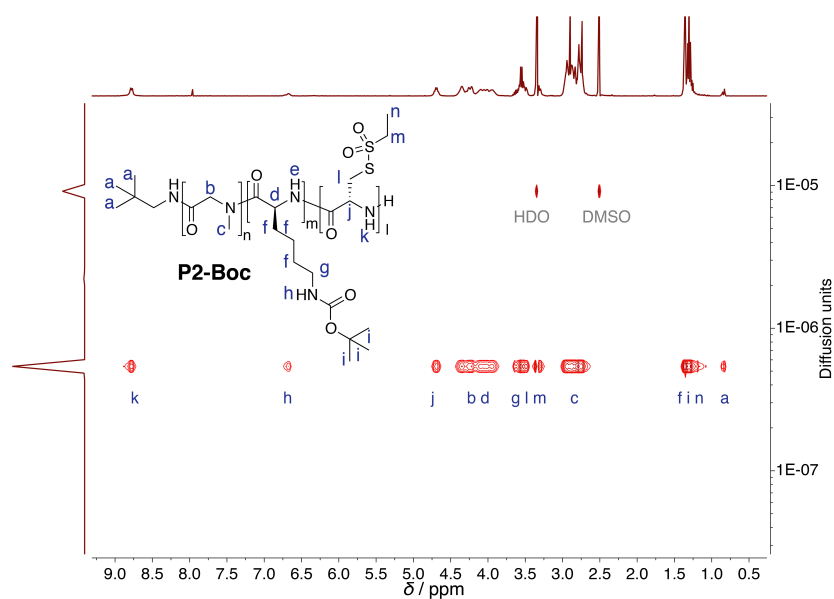


Figure 16.9: DOSY  $^1\text{H}$  NMR spectrum (400 MHz) of **P2-Boc** in  $\text{DMSO-}d_6$ .

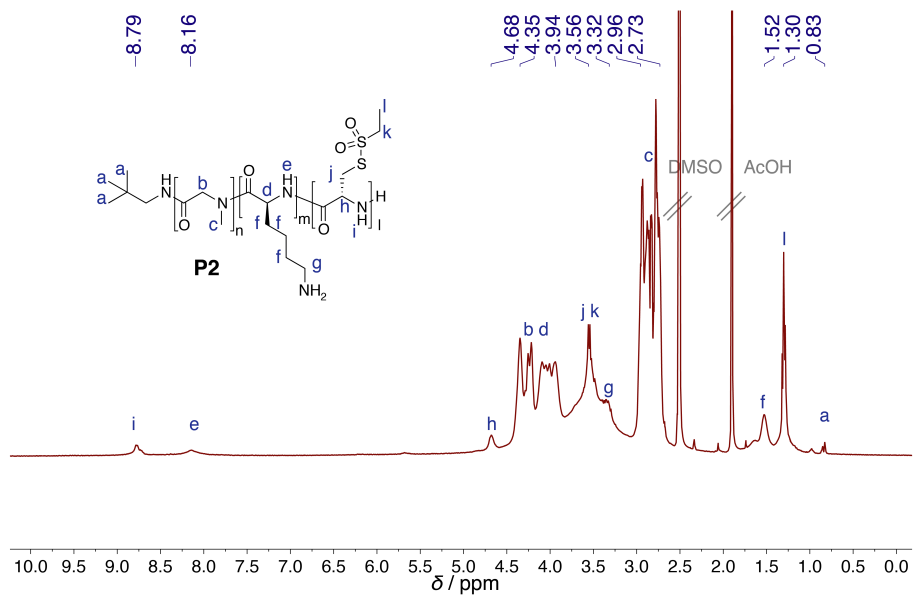


Figure 16.10:  $^1\text{H}$  NMR spectrum (400 MHz) of **P2** in  $\text{DMSO-}d_6$ .

## 16.5.6 Additional Results

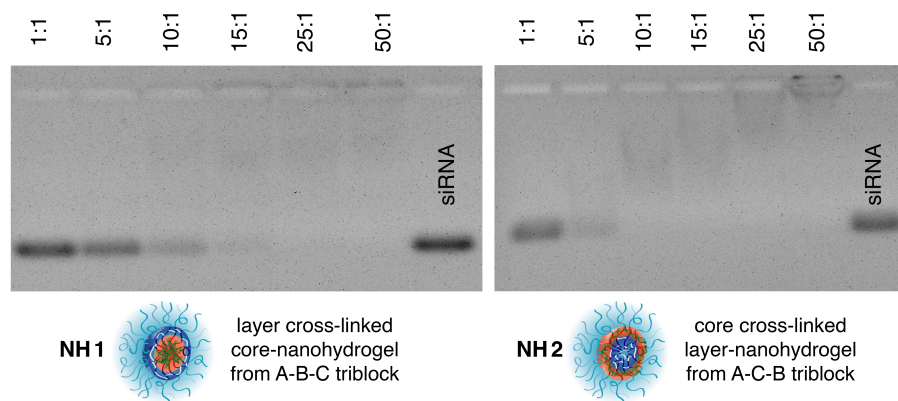


Figure 16.11: Agarose gel electrophoresis of siRNA loaded cross-linked nanohydrogels: **NH1** derived from A-B-C polymer **P1** and **NH2** derived from A-C-B polymer **P2**.

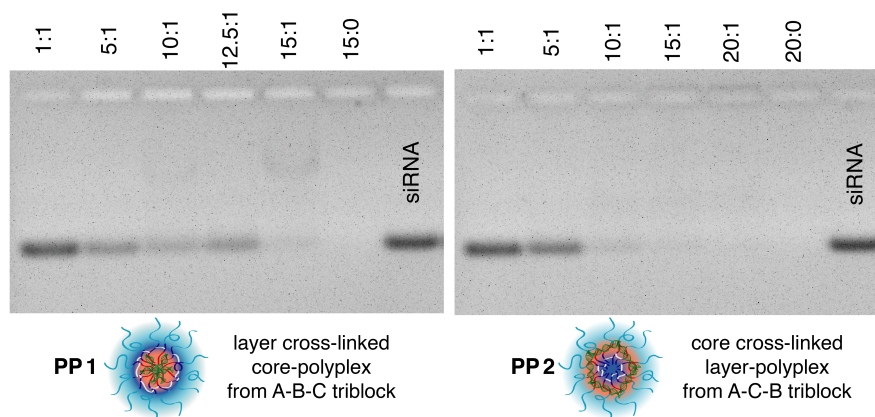


Figure 16.12: Agarose gel electrophoresis of siRNA loaded cross-linked polyplexes: **PP1** derived from A-B-C polymer **P1** and **PP2** derived from A-C-B polymer **P2**.

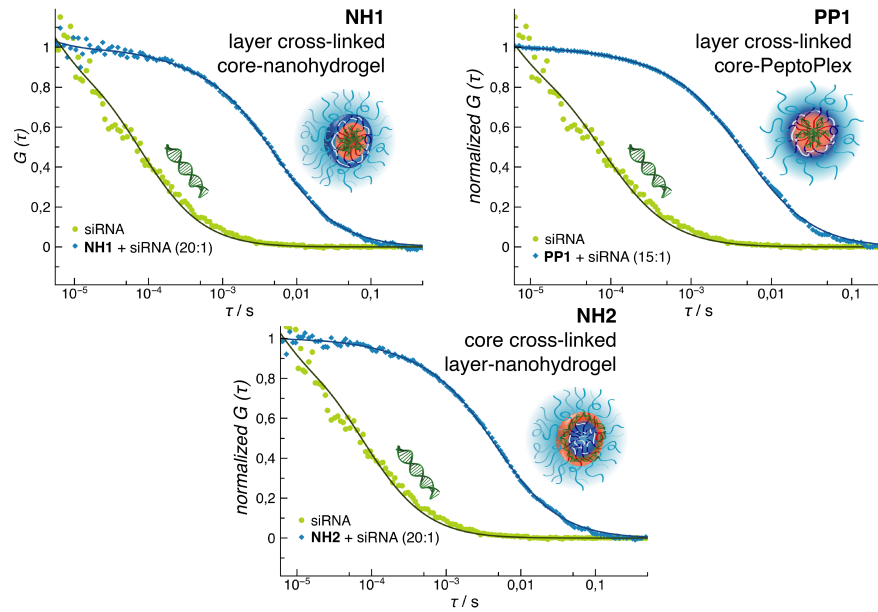


Figure 16.13: Auto-correlation curves measured for free ATTO647-siRNA, ATTO488-siRNA loaded cross-linked nanohydrogels NH1, NH2 and cross-linked polyplex PP1.

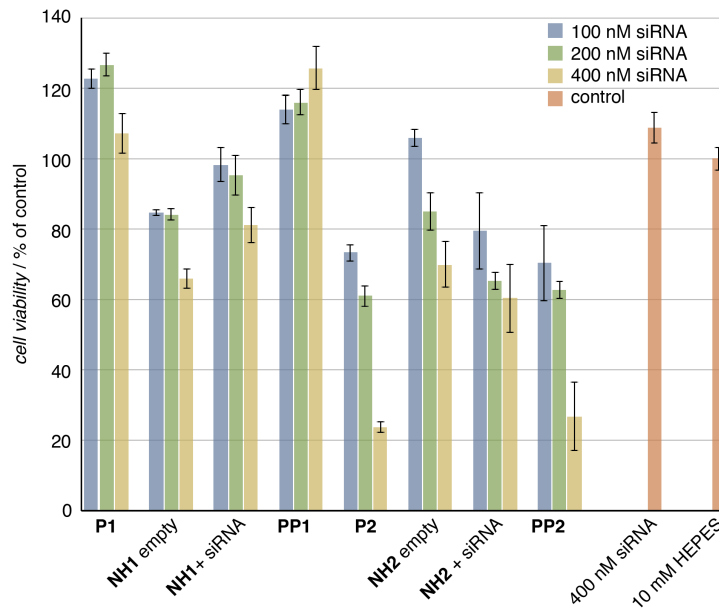


Figure 16.14: Cell viability assay (CCK8) of 4T1-luc cells exposed to triblock copolypept(o)ides (P1, P2) as well as derived cross-linked nanohydrogels (NH1, NH2) and cross-linked polyplexes (PP1, PP2) loaded with varying concentrations of scr. siRNA.



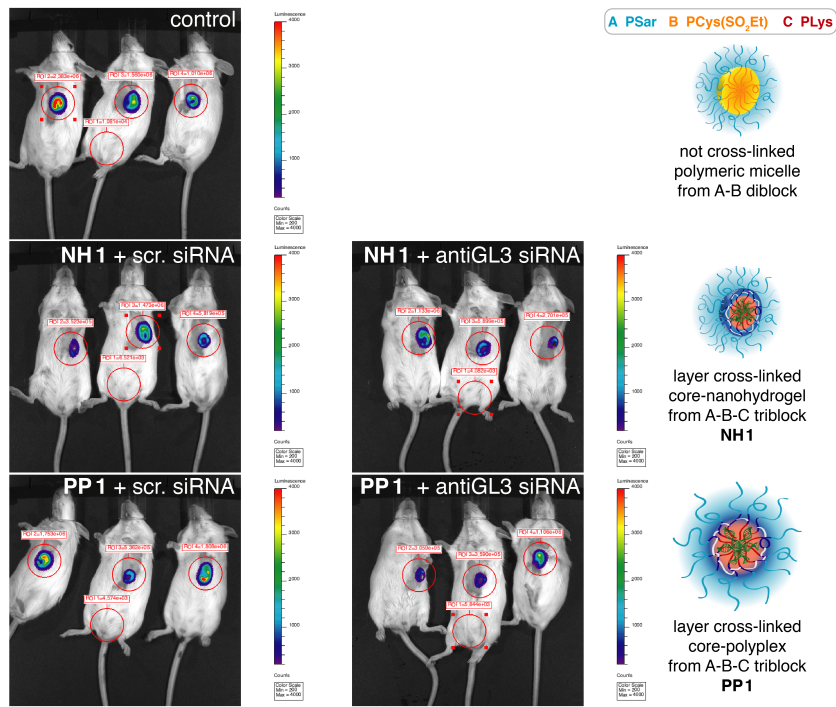


Figure 16.15: *In vivo* bioluminescence imaging 24 h post injection of female BALB/c mice bearing orthotropic 4T1-luc mammary tumors ( $n=3$ ). Groups were divided as follows: not cross-linked polymeric micelle as the control, cross-linked nanohydrogel **NH1** and cross-linked polyplex **PP1** derived from  $\text{PSar}_{71}\text{-}b\text{-PCys}(\text{SO}_2\text{Et})_{29}\text{-}b\text{-PLys}_{13}$  (**P1**) loaded with  $450\ \mu\text{M}$  scr. siRNA or antiGL3 siRNA per mouse.



Part VI  
SUMMARY AND OUTLOOK





## SUMMARY

The goal of this thesis was the development of stabilized polypept(o)ide-based core-shell carrier systems for systemic application as nanomedicines e. g. for gene delivery. Bioreversible chemoselective disulfide stabilization was mediated by *S*-alkylsulfonyl-L-cysteines, which were employed as building blocks in synthesis of (multi)block copolypept(o)ides by controlled ring-opening polymerization of  $\alpha$ -amino acid *N*-carboxyanhydrides (NCAs). Preparation of core-shell nanoparticles by secondary structure-modulated self-assembly of the resulting polypept(o)ides offered control over size, morphology and functionality in combination with disulfide stabilization by cross-linking. The resulting core-shell systems were evaluated *in vivo* and showed exceeding stable systemic circulation for hydrophobic core cross-linked polymeric micelles and, remarkably, for cationic nanohydrogels. Ultimately, RNA interference (RNAi) in solid tumors was demonstrated upon systemic delivery by cationic, cross-linked polypept(o)ide-based systems.

Polypept(o)ides were chosen as the platform for nanoparticle preparation and the impact of absolute monomer purity promoting on control over the polymerization was demonstrated by correlating crystal structure and melting point of NCAs to the quality of resulting polypeptides. Based on the importance of bioreversible nanoparticle stabilization in systemic applications, options for disulfide-mediated stabilization were evaluated with focus on the amino acid cysteine. Since moieties for directed disulfide formation that are compatible with polypept(o)ide synthesis by nucleophilic ring-opening polymerization of NCAs were completely lacking, protective and activating groups for thiols were synthesized and investigated towards stability against *N*-nucleophiles and reactivity towards *S*-nucleophiles.

*S*-alkylsulfonyl-L-cysteines met these demanding criteria by balancing the electrophilic character of the cysteine sulfur atom with steric hindrance of the protective group, which ultimately allowed for sequential polymerization by ring-opening polymerization of the respective NCAs. In addition, the resulting poly(*S*-alkylsulfonyl-L-cysteines) (PCys(SO<sub>2</sub>R)) segment showed pronounced tendency to form secondary structures, as antiparallel  $\beta$ -sheets conformation was confirmed in aqueous solution as well as in organic solvents. Thorough kinetic evaluation on PCys(SO<sub>2</sub>R) polymerization characteristics laid the groundwork for synthesis of di- and triblock polypept(o)ides by sequential polymerization. Trifunctional PSar-*b*-PCys(SO<sub>2</sub>R) diblock copolymers were obtained with independently addressable functional groups in spatial separation upon nanoparticle preparation. The *S*-alkylsulfonyl group remained intact during conver-

sion of azide and amine polymer chain ends and was readily addressable by thiols for bioreversible disulfide formation.

Amphiphilic PSar-*b*-PCys(SO<sub>2</sub>Et) block copolypept(o)ides were implemented in secondary structure-driven self-assembly to control the size and shape of polymeric core-shell nanostructures. In addition, core functionality was adjusted by bioreversible core cross-linking in an independent, single post-polymerization step. The self-assembly behavior of PSar-*b*-PCys(SO<sub>2</sub>Et) was systematically screened by varying the block-length ratio of the polymer, solvent composition during self-assembly and, most importantly, by modulating secondary structure formation in order to switch the conformation of the polycysteine segment from rod to coil. Ultimately a versatile platform of disulfide stabilized nanoparticles was available with adjustable hydrodynamic dimensions between approximately 30 nm and 150 nm. Variation was achieved between elongated or spherical morphology and functionalities can be included ranging from hydrophobic core cross-linked polymeric micelles for e. g. hydrophobic chemotherapeutic agents, to cationic nanohydrogels for complexation of negatively charged nucleic acids e. g. small interfering RNA (siRNA). Near-infrared fluorescence correlation spectroscopy performed in flowing human blood, demonstrated the importance of covalent modification of nanocarriers in biological relevant environment. Thus covalent labeling and cross-linking of PSar-*b*-PCys(SO<sub>2</sub>Et)-based core-shell nanoparticles was self-evident for *in vivo* applications.

Blood circulation, biodistribution and tumor accumulation of cross-linked polymeric micelles and cationic nanohydrogels was elucidated, revealing stable systemic circulation of hydrophobic core cross-linked polymeric micelles over 15 h and, astonishingly, of cationic nanohydrogels 24 h post injection as determined by blood sampling and *in vivo* imaging system (IVIS). This stable systemic circulation of cationic systems is singular for polycationic gene delivery vectors and has great potential regarding passive tumor accumulation. Thus, *ex vivo* biodistribution of cationic nanohydrogels was evaluated and revealed pronounced tumor accumulation in combination with low accumulation in the lungs, kidneys, the spleen and the liver. These promising result on circulation and biodistribution of cross-linked polypept(o)ide based nanoparticles prompted the investigation of polypept(o)ide-based carriers for systemic delivery of siRNA. As carrier systems, amphiphilic cationic triblock copolypept(o)ides were sequentially polymerized featuring PSar as a shielding block, a hydrophobic PCys(SO<sub>2</sub>Et) segment for bioreversible disulfide stabilization and a polycationic PLys block for complexation of siRNA, all in one polymer. The triblock copolypept(o)ides were employed in the formation of nanohydrogels and polyplexes as siRNA delivery systems and characterized in light of their structure-property relationship based on sequence alteration. Ultimately, lead candidates were identified and upon systemic delivery by a cross-linked PSar-*b*-PCys(SO<sub>2</sub>R)-*b*- PLys polyplex, a specific RNAi mediated knockdown in mammary tumors was demonstrated.

## OUTLOOK

This thesis provided a vital contribution towards polypept(o)ide-based core-shell carrier systems as gene delivery vectors in systemic application. A versatile nanoparticle platform was presented regarding secondary structure-directed self-assembly of nanocarriers, (multi)block copolypept(o)ide structure and bioreversible disulfide stabilization.

This modular approach enables stepwise adjustment of individual parameters to further optimize these polypept(o)ide-based carrier systems. The influence of other secondary structures can be evaluated, for example  $\alpha$ -helical arrangement of recently developed poly(L-homocysteine) derivatives. In conjunction with the S-alkylsulfonfyl group they present an appealing option for synthesis of larger segments for chemoselective disulfide stabilization, as nanoprecipitation does not occur in contrast to  $\beta$ -sheet forming polypeptides. In addition to disulfide stabilization, the S-alkylsulfonfyl group can be exploited for covalent attachment of therapeutic cargoes by pro-drug cross-linkers based on e. g. lipoic acid. Bioreversible covalent attachment is expected to increase stability during systemic circulation and improve the therapeutic effect in comparison to free drug and non-covalent loading.

Further *in vivo* studies in terms of blood circulation and biodistribution of cross-linked polypept(o)ide-based nanoparticles are necessary. Systematic variations in core polarity, size and morphology should be considered and, due to the long systemic circulation, evaluation over several days to ensure complete tumor accumulation. Additionally, site-specific modification of the PS<sub>ar</sub> corona e. g. by azide moieties is an attractive strategy for selective targeting achieved by appropriate ligands such as peptide sequences, sugars, antibodies or their fragments.

The location of siRNA in the presented multicompartiment gene delivery vectors based on triblock copolypept(o)ides, can be determined using fluorescently labeled siRNA molecules and evaluation by super resolution fluorescence microscopy. In addition, covalent fluorescent labeling of the polypept(o)ide carrier and siRNA with dyes of a spectroscopically independent range will allow to elaborate on co-localization of carrier and cargo in systemic delivery. The introduction of functional cross-linkers in gene delivery vectors can be readily realized by reaction of the S-alkylsulfonfyl group with thiol bearing molecules, preferably with endosomolytic properties such as pH buffering capacities or introduction of fusogenic peptides. As demonstrated recently in the preparation of functional polyplex libraries, this approach provides a screening strategy towards lead candidates in transfection efficacy. Ultimately, a therapeutic *in vivo* readout towards antitumor efficacy mediated by polypept(o)ide-based core-shell siRNA delivery systems is appealing and should be evaluated on the level of mRNA.





Part VII  
APPENDIX





## LIST OF FIGURES

---

Figure 2.1	Schematic of nanotherapeutic platforms. . . . .	5
Figure 2.2	Polymer-based nanomedicines. . . . .	7
Figure 2.3	External and internal stimuli. . . . .	7
Figure 2.4	NCA synthesis. . . . .	9
Figure 2.5	Ring-opening NCA polymerization. . . . .	9
Figure 2.6	Options in block copolypept(o)ides. . . . .	11
Figure 3.1	Mechanism of RNA interference. . . . .	13
Figure 3.2	Biological barriers in systemic RNAi delivery. . . .	17
Figure 3.3	Systemic circulation pathways. . . . .	18
Figure 3.4	Blood filtration in kidney, liver and spleen. . . . .	19
Figure 3.5	Influence of particle properties on biodistribution. . .	20
Figure 3.6	Illustration of <i>in vivo</i> targeting strategies. . . . .	21
Figure 3.7	Internalization pathways of nanocarriers. . . . .	23
Figure 3.8	Strategies for polymer-based vectors for gene de- livery. . . . .	24
Figure 3.9	Micelle formation by self-assembly. . . . .	25
Figure 3.10	Strategies for stabilization by core cross-linking. . .	26
Figure 4.1	Synthesis and reactivity profile of Cys(SO <sub>2</sub> R). . . . .	41
Figure 4.2	Polymerization of Cys(SO <sub>2</sub> R) NCA. . . . .	42
Figure 4.3	Thiol-reactivity of PCys(SO <sub>2</sub> Et) and PSar- <i>b</i> -PCys(SO <sub>2</sub> Et). .	43
Figure 4.4	Secondary-structure-driven self-assembly of PSar- <i>b</i> -PCys(SO <sub>2</sub> Et). . . . .	44
Figure 4.5	Cross-linking mediated by the thiol reactivity of the S-ethylsulfonyl group . . . . .	45
Figure 5.1	Schematic representation of X-ray diffraction. . . .	49
Figure 5.2	Elastic light scattering. . . . .	51
Figure 5.3	Influence of particle size on interference pattern. . .	51
Figure 5.4	Influence of Brownian motion on interference pat- tern and scattering intensity. . . . .	52
Figure 5.5	Schematic representation of a DLS setup. . . . .	52
Figure 5.6	Fluctuating scattering intensity at a fixed angle. . .	53
Figure 5.7	Illustration of $\zeta$ -potential of a charged particle. . .	54
Figure 5.8	Schematic representation of a SLS setup. . . . .	55
Figure 5.9	Zimm plot analysis. . . . .	55
Figure 5.10	Confocal fluorescence correlation spectroscopy. . .	56
Figure 5.11	Fluorescence cross-correlation spectroscopy. . . . .	57
Figure 5.12	Cell viability detection mechanism with CCK-8. . . .	58
Figure 5.13	Oxidative decarboxylation of D-luciferin. . . . .	59
Figure 5.14	The NIR window for <i>in vivo</i> imaging. . . . .	60
Figure 5.15	Autofluorescence of vital organs and bodily fluids. .	60
Figure 5.16	Bioluminescence and fluorescence mode. . . . .	61
Figure 5.17	Construction of a typical IVIS image. . . . .	62
Figure 6.1	Side reaction resulting in chain termination. . . . .	79

Figure 6.2	GPC plot of PCys(oNTP). . . . .	79
Figure 6.3	GPC plot of PCys(PFTP). . . . .	79
Figure 6.4	GPC plot of PCys(oFTP). . . . .	80
Figure 6.5	GPC plot of PCys(SO <sub>2</sub> Ph). . . . .	80
Figure 7.1	Cys(SO <sub>2</sub> Et) and Cys(SO <sub>2</sub> <sup>i</sup> Pr). . . . .	83
Figure 7.2	Reactivity of Cys(SO <sub>2</sub> R) towards nucleophiles. . . . .	84
Figure 7.3	<sup>1</sup> H NMR of Cys(SO <sub>2</sub> R) with thiols. . . . .	85
Figure 7.4	Reaction of Cys(SO <sub>2</sub> <sup>i</sup> Pr) nucleophiles and DFT calculations. . . . .	87
Figure 7.5	GPC of PCys(SO <sub>2</sub> Et) and PCys(SO <sub>2</sub> <sup>i</sup> Pr). . . . .	88
Figure 7.6	MALDI-TOF spectrum of PCys(SO <sub>2</sub> <sup>i</sup> Pr). . . . .	89
Figure 7.7	Reaction of PCys(SO <sub>2</sub> <sup>i</sup> Pr) with benzylmercaptan. . . . .	90
Figure 7.8	pH influence on Cys(SO <sub>2</sub> R). . . . .	100
Figure 7.9	Reaction of Cys(SO <sub>2</sub> Et) nucleophiles and DFT calculations. . . . .	102
Figure 7.10	Crystallographic data of L-Cys(SO <sub>2</sub> Et). . . . .	103
Figure 7.11	Crystallographic data of L-Cys(SO <sub>2</sub> <sup>i</sup> Pr). . . . .	103
Figure 7.12	<sup>1</sup> H NMR spectrum of <b>2 a</b> . . . . .	104
Figure 7.13	<sup>13</sup> C NMR spectrum of <b>2 a</b> . . . . .	104
Figure 7.14	COSY NMR spectrum of <b>2 a</b> . . . . .	105
Figure 7.15	HSQC NMR spectrum of <b>2 a</b> . . . . .	105
Figure 7.16	<sup>1</sup> H NMR spectrum of <b>2 b</b> . . . . .	106
Figure 7.17	<sup>13</sup> C NMR spectrum of <b>2 b</b> . . . . .	106
Figure 7.18	COSY NMR spectrum of <b>2 b</b> . . . . .	107
Figure 7.19	HSQC NMR spectrum of <b>2 b</b> . . . . .	107
Figure 7.20	<sup>1</sup> H NMR spectrum of <b>5 a</b> . . . . .	108
Figure 7.21	<sup>13</sup> C NMR spectrum of <b>5 a</b> . . . . .	108
Figure 7.22	<sup>1</sup> H NMR spectrum of <b>5 b</b> . . . . .	109
Figure 7.23	<sup>13</sup> C NMR spectrum of <b>5 b</b> . . . . .	109
Figure 7.24	<sup>1</sup> H NMR spectrum of <b>6 a</b> . . . . .	110
Figure 7.25	<sup>1</sup> H NMR spectrum of <b>6 b</b> . . . . .	110
Figure 7.26	<sup>1</sup> H NMR spectrum of <b>7 a</b> . . . . .	111
Figure 7.27	<sup>13</sup> C NMR spectrum of <b>7 a</b> . . . . .	111
Figure 7.28	COSY NMR spectrum of <b>7 a</b> . . . . .	112
Figure 7.29	HSQC NMR spectrum of <b>7 a</b> . . . . .	112
Figure 7.30	<sup>1</sup> H NMR spectrum of <b>7 b</b> . . . . .	113
Figure 7.31	<sup>13</sup> C NMR spectrum of <b>7 b</b> . . . . .	113
Figure 7.32	COSY NMR spectrum of <b>7 b</b> . . . . .	114
Figure 7.33	HSQC NMR spectrum of <b>7 b</b> . . . . .	114
Figure 7.34	<sup>1</sup> H NMR spectrum of <b>8</b> . . . . .	115
Figure 8.1	Crystal structure of NCA. . . . .	124
Figure 8.2	GPC traces of polymers synthesized by ROP of NCAs. . . . .	128
Figure 8.3	NCAs evaluated by X-ray powder diffraction. . . . .	139
Figure 9.1	Synthesis and characterization of Cys(SO <sub>2</sub> Et) NCA. . . . .	152
Figure 9.2	Polymerization of Cys(SO <sub>2</sub> Et) NCA. . . . .	152
Figure 9.3	β-sheet formation of PCys(SO <sub>2</sub> Et). . . . .	154
Figure 9.4	IR spectra of a PCys(SO <sub>2</sub> Et) polymerization. . . . .	154
Figure 9.5	MALDI-TOF spectrum of PCys(SO <sub>2</sub> Et). . . . .	156

Figure 9.6	Labeling reactions of PCys(SO <sub>2</sub> Et). . . . .	158
Figure 9.7	Reaction of PCys(SO <sub>2</sub> Et) with benzylmercaptan. . .	159
Figure 9.8	<sup>1</sup> H NMR coupling of Cys(SO <sub>2</sub> Et). . . . .	165
Figure 9.9	<sup>1</sup> H NMR of PCys(SO <sub>2</sub> Et). . . . .	166
Figure 9.10	hoch1H DOSY NMR of PCys(SO <sub>2</sub> Et). . . . .	166
Figure 9.11	HFIP GPC of PCys(SO <sub>2</sub> Et). . . . .	167
Figure 9.12	pH-Influence on PCys(SO <sub>2</sub> Et). . . . .	168
Figure 9.13	Kinetic plots and HFIP GPC traces of PCys(SO <sub>2</sub> Et). . .	169
Figure 9.14	<sup>1</sup> H NMR spectrum of Cys(SO <sub>2</sub> Et) NCA . . . . .	169
Figure 9.15	<sup>13</sup> C NMR spectrum of Cys(SO <sub>2</sub> Et) NCA . . . . .	170
Figure 9.16	COSY NMR spectrum of Cys(SO <sub>2</sub> Et) NCA . . . . .	170
Figure 9.17	HSQC NMR spectrum of Cys(SO <sub>2</sub> Et) NCA . . . . .	171
Figure 10.1	Characterization of P3. . . . .	177
Figure 10.2	PSar <sub>n</sub> - <i>b</i> -PCys(SO <sub>2</sub> R) <sub>m</sub> end group conversion. . . . .	178
Figure 10.3	Self-assembly of trifunctional block copolymers. . .	180
Figure 10.4	FT-IR spectrum of PSar-N <sub>3</sub> . . . . .	189
Figure 10.5	PSar macroinitiator before and after deprotection. .	189
Figure 10.6	<sup>1</sup> H NMR spectrum of P1. . . . .	190
Figure 10.7	<sup>1</sup> H NMR spectrum of P2. . . . .	190
Figure 10.8	<sup>1</sup> H NMR spectrum of P4. . . . .	191
Figure 10.9	<sup>1</sup> H NMR spectrum of P5. . . . .	191
Figure 10.10	<sup>1</sup> H NMR spectrum of P5 after DBCO conversion. . . .	192
Figure 10.11	<sup>1</sup> H NMR spectrum of P5 after NHS conversion. . . .	192
Figure 10.12	UV-Vis absorbance spectra of labeled P5. . . . .	193
Figure 10.13	Dual labeled particles in FCCS. . . . .	193
Figure 10.14	PSar- <i>b</i> -PCys(SO <sub>2</sub> Et) with benzylmercaptane. . . . .	194
Figure 10.15	PSar- <i>b</i> -PCys(SO <sub>2</sub> <sup>i</sup> Pr) with benzylmercaptane. . . . .	194
Figure 11.1	Triblock copolypept(o)ide synthesis. . . . .	196
Figure 11.2	<sup>1</sup> H DOSY NMR of triblock polymers. . . . .	197
Figure 11.3	GPC characterization of of triblock polymers. . . .	198
Figure 12.1	Schematic of the nanoparticle platform. . . . .	205
Figure 12.2	Control over size and shape. . . . .	208
Figure 12.3	Core cross-linking of nanostructures by dithiols. .	209
Figure 12.4	Core cross-linked nanostructures with hydrophobic and charged cargo. . . . .	211
Figure 12.5	HFIP GPC traces of P1-4. . . . .	224
Figure 12.6	Dynamic aggregation behavior of P2. . . . .	225
Figure 12.7	Statistical particle analysis by AFM and TEM. . . .	226
Figure 12.8	CD analysis of P2 and particles thereof. . . . .	227
Figure 12.9	AFM apparent height profiles. . . . .	228
Figure 12.10	Multi-angle DLS of swNHG3 + sNHG4. . . . .	228
Figure 12.11	Multi-angle DLS of wNHG5 + wNHG6. . . . .	229
Figure 12.12	Degradation of NHGs and CCPMs by glutathione. .	229
Figure 12.13	HFIP GPC elugram of NHGs and CCPMs. . . . .	230
Figure 12.14	Agarose gel electrophoresis of loaded wNHG1. . . .	231
Figure 12.15	DLS of chol-siRNA-loaded NHGs. . . . .	231
Figure 13.1	Self-assembly of amphiphilic block copolymers. .	237
Figure 13.2	Diblock copolypept(o)ides of varying composition.	238

Figure 13.3	Evaluation of self-assembly behavior . . . . .	240
Figure 13.4	Size range and PDI of micelles from <b>P1</b> . . . . .	243
Figure 13.5	Size range and PDI of micelles from <b>P2</b> . . . . .	244
Figure 13.6	Size range and PDI of micelles from <b>P3</b> . . . . .	244
Figure 13.7	Size range and PDI of micelles from <b>P4</b> . . . . .	245
Figure 13.8	Size range and PDI of micelles from <b>P5</b> . . . . .	245
Figure 14.1	Illustration of nanocarriers in the blood stream. . .	247
Figure 14.2	NIR-FCS of core cross-linked nanocarriers in blood. .	249
Figure 15.1	Particles evaluated by IVRT-CLSM. . . . .	258
Figure 15.2	IVRT-CLSM results on blood circulation of CCPMs. . .	259
Figure 15.3	Quantification of fluorescence in the blood vessel. .	260
Figure 15.4	Particles evaluated in terms of biodistribution. . .	262
Figure 15.5	Size and shape of particles evaluated <i>in vivo</i> . . . .	263
Figure 15.6	Experimental setup of <i>in vivo</i> evaluation. . . . .	264
Figure 15.7	Biodistribution 24 h after systemic administration. .	266
Figure 16.1	Triblock copolypept(o)ide synthesis. . . . .	276
Figure 16.2	Characterization of triblock polypept(o)ides. . . .	277
Figure 16.3	Particle platform from triblock polypept(o)ides. . .	279
Figure 16.4	Triblock siRNA nanocarriers <i>in vivo</i> . . . . .	282
Figure 16.5	<sup>1</sup> H NMR spectrum of <b>P1-Boc</b> . . . . .	294
Figure 16.6	DOSY <sup>1</sup> H NMR spectrum of <b>P1-Boc</b> . . . . .	294
Figure 16.7	<sup>1</sup> H NMR spectrum of <b>P1</b> . . . . .	295
Figure 16.8	<sup>1</sup> H NMR spectrum of <b>P2-Boc</b> . . . . .	295
Figure 16.9	DOSY <sup>1</sup> H NMR spectrum of <b>P2-Boc</b> . . . . .	296
Figure 16.10	<sup>1</sup> H NMR spectrum of <b>P2</b> . . . . .	296
Figure 16.11	Agarose gel electrophoresis of polyplexes. . . . .	297
Figure 16.12	Agarose gel electrophoresis of nanohydrogels. . .	297
Figure 16.13	FCS of nanohydrogels and cross-linked polyplex. .	298
Figure 16.14	Cell viability assay in 4T1-luc cells. . . . .	298
Figure 16.15	<i>In vivo</i> bioluminescence imaging. . . . .	299

## LIST OF SCHEMES

---

4.1	Synthesis strategy for the chemoselective formation of asymmetric disulfides. . . . .	31
4.2	Entries for directed disulfide formation in ATRP and RAFT. . . . .	33
4.3	Approaches for directed disulfide formation in SPPS. . . . .	37
4.4	Approaches for directed disulfide formation in NCA ring-opening polymerization. . . . .	40
6.1	Synthesis of disulfide-based NCAs. . . . .	69
6.2	Synthesis of a thiosulfonyl-based NCAs. . . . .	70
7.1	Synthesis of Cys(SO <sub>2</sub> R). . . . .	83
7.2	Reactions of Cys(SO <sub>2</sub> R) with thiols of varying pK <sub>a</sub> . . . . .	85
7.3	Synthesis of Cys(SO <sub>2</sub> R) NCA and polymerization as well as synthesis of Fmoc-Cys(SO <sub>2</sub> R) and the resulting dipeptide. . . . .	87
8.1	Scheme of NCA synthesis by the Fuchs-Farthing method. . . . .	123
8.2	Polymerization of NCA by an amine initiator. . . . .	126
10.1	Reaction scheme of block copolymer synthesis. . . . .	175
10.2	Scheme of functional group conversion. . . . .	192
12.1	Polymerization scheme of PSar <sub>n</sub> - <i>b</i> -PCys(SO <sub>2</sub> Et) <sub>m</sub> . . . . .	223
12.2	Synthetic scheme describing micelle cross-linking. . . . .	230

## LIST OF TABLES

---

Table 2.1	Approved nanotherapeutics. . . . .	6
Table 3.1	siRNA based therapeutics in the clinic. . . . .	15
Table 4.1	Activating groups for chemoselective disulfide formation. . . . .	32
Table 6.1	Analytical data of cysteine homopolymers. . . . .	78
Table 7.1	Characterisation of PCys(SO <sub>2</sub> Et) and PCys(SO <sub>2</sub> <sup>i</sup> Pr). . . . .	89
Table 7.2	Apparent rate constants for hydrolysis of Cys(SO <sub>2</sub> R). . . . .	100
Table 7.3	Rate constants for amine reactions of Cys(SO <sub>2</sub> R). . . . .	100
Table 7.4	HOMO/LUMO energy levels. . . . .	102
Table 8.1	Melting points of NCA. . . . .	125
Table 8.2	Characterization of polypeptides and polypeptoids. . . . .	127
Table 9.1	Characterization of PCys(SO <sub>2</sub> R). . . . .	153
Table 10.1	Characterization of block copolymers. . . . .	176
Table 11.1	Characterization data of triblock polymers. . . . .	197
Table 12.1	Characterization of cross-linked nanostructures. . . . .	207
Table 12.2	Characterization of CCPMs and NHGs. . . . .	222
Table 12.3	Characterization of PSar <sub>n</sub> -b-PCys(SO <sub>2</sub> Et) <sub>m</sub> . . . . .	224
Table 12.4	Log <i>P</i> values for cross-linkers. . . . .	230
Table 13.1	Characterization of diblock copolypept(o)ides. . . . .	243
Table 15.1	Characterization of CCPMs in intravital real-time confocal laser scanning microscopy. . . . .	258
Table 15.2	Characterization of core cross-linked particles <i>in vivo</i> . . . . .	262
Table 15.3	Characterization of diblock copolypept(o)ides. . . . .	269
Table 15.4	Characterization of nanoparticles <i>in vivo</i> . . . . .	270
Table 15.5	Quantification of biodistribution and circulation. . . . .	271
Table 16.1	Characterization of triblock copolypept(o)ides. . . . .	276
Table 16.2	Characterization of triblock particles. . . . .	280
Table 16.3	Characterization details of triblock particles. . . . .	292
Table 16.4	Characterization of nanocarriers <i>in vivo</i> . . . . .	293



## ACRONYMS

---

AFM	atomic force microscopy
AMM	activated monomer mechanism
ATRP	atom transfer radical polymerization
CCDC	Cambridge Crystallographic Data Centre
CCPM	core cross-linked polymeric micelle
CD	circular dichroism
Cys(SO <sub>2</sub> R)	<i>S</i> -alkylsulfonyl-L-cysteine
Cys(SO <sub>2</sub> Et)	<i>S</i> -ethylsulfonyl-L-cysteine
Cys(SO <sub>2</sub> <sup>i</sup> Pr)	<i>S</i> -isopropylsulfonyl-L-cysteine
COSY	correlation spectroscopy
CRP	controlled radical polymerization
cryoTEM	cryogenic transmission electron microscopy
CuAAC	copper-catalyzed alkyne azide cycloaddition
Cys	cysteine
DCM	dichloromethane
DFT	density functional theory
DIPEA	<i>N,N</i> -diisopropylethylamine
DLS	dynamic light scattering
DMAc	<i>N,N</i> -dimethyl acetamide
DMF	<i>N,N</i> -dimethyl formamide
DMSO	dimethylsulfoxide
DOSY	<sup>1</sup> H diffusion ordered spectroscopy
DTT	dithiothreitol
EPR	enhanced permeability and retention
ESI-MS	electrospray ionization mass spectrometry
EWG	electron-withdrawing group
FCCS	fluorescence cross-correlation spectroscopy

FCS	fluorescence correlation spectroscopy
FD-MS	field desorption mass spectrometry
Fmoc	<i>N</i> -(9-Fluorenylmethoxycarbonyl)
GPC	gel permeation chromatography
GSH	glutathione
HEPES	4-(2-hydroxyethyl)-1-piperazineethanesulfonic acid
HFIP	hexafluoro 2-propanol
HOMO	highest occupied molecular orbital
HSQC	heteronuclear single-quantum correlation spectroscopy
IR	infrared
IVIS	<i>in vivo</i> imaging system
IVRT-CLSM	intravital real-time confocal laser scanning microscopy
LUMO	lowest unoccupied molecular orbital
Lys	lysine
MALDI-TOF	matrix assisted laser desorption/ionization-time of flight
MPS	mononuclear phagocyte system
mRNA	messenger RNA
NAM	normal amine mechanism
NCA	$\alpha$ -amino acid <i>N</i> -carboxyanhydride
NHG	nanohydrogel
NHS	<i>N</i> -hydroxysuccinimide
NIR	near-infrared
NMP	nitroxide-mediated polymerization
NMR	nuclear magnetic resonance
Nps	2- or 4-nitrophenyl
Npys	3-nitro-2-pyridyl
PBS	phosphate buffered saline
PCys(SO <sub>2</sub> R)	poly( <i>S</i> -alkylsulfonyl-L-cysteine)
PCys(SO <sub>2</sub> Et)	poly( <i>S</i> -ethylsulfonyl-L-cysteine)
PCys(SO <sub>2</sub> <sup>i</sup> Pr)	poly( <i>S</i> -isopropylsulfonyl-L-cysteine)

Pyr	2- or 4-pyridyl
RAFT	reversible addition–fragmentation chain transfer
RNAi	RNA interference
ROP	ring-opening polymerization
Sar	sarcosine
siRNA	small interfering RNA
SLS	static light scattering
SPAAC	strain-promoted azide–alkyne cycloaddition
SPDP	<i>N</i> -succinimidyl 3-(2-pyridyldithio)-propionate
SPPS	solid phase peptide synthesis
TCEP	tris(2-carboxyethyl)phosphine
TEM	transmission electron microscopy
TETA	triethylenetetramine $\alpha,\omega$ -di(cysteine)diamide
UV	ultra violet
Vis	visible
XRD	X-ray diffraction



## BIBLIOGRAPHY

---

- [1] O. C. Farokhzad, R. Langer, *Adv. Drug Deliv. Rev.* **2006**, *58*, 1456–1459.
- [2] B. Y. Kim, J. T. Rutka, W. C. Chan, *N. Engl. J. Med.* **2010**, *363*, 2434–2443.
- [3] A. Wicki, D. Witzigmann, V. Balasubramanian, J. Huwyler, *J. Control. Release* **2015**, *200*, 138–157.
- [4] British Standards Institution, *Publicly Available Specif.* **2007**, 16.
- [5] M. L. Etheridge, S. A. Campbell, A. G. Erdman, C. L. Haynes, S. M. Wolf, J. McCullough, *Nanomedicine Nanotechnology Biol. Med.* **2013**, *9*, 1–14.
- [6] J. M. Caster, A. N. Patel, T. Zhang, A. Wang, *Wiley Interdiscip. Rev. Nanomedicine Nanobiotechnology* **2017**, *9*, e1416.
- [7] K. Cooper, A. Nathan, M. Vyakarnam, *Biodegradable Polymers in Clinical Use and Clinical Development*, (Eds.: A. J. Domb, N. Kumar, A. Ezra), John Wiley & Sons, Inc., Hoboken, NJ, USA, **2011**, pp. 401–415.
- [8] R. van der Meel, T. Lammers, W. E. Hennink, *Expert Opin. Drug Deliv.* **2017**, *14*, 1–5.
- [9] G. Southard, R. Dunn, S. Garrett, *Expert Opin. Investig. Drugs* **1998**, *7*, 1483–1491.
- [10] P. D. Darney, C. M. Klaisle, S. E. Monroe, C. Edgar Cook, N. R. Phillips, A. Schindler, *Fertil. Steril.* **1992**, *58*, 137–143.
- [11] K. S. Lee, H. C. Chung, S. A. Im, Y. H. Park, C. S. Kim, S.-B. Kim, S. Y. Rha, M. Y. Lee, J. Ro, *Breast Cancer Res. Treat.* **2008**, *108*, 241–250.
- [12] F. J. Attenello, D. Mukherjee, G. Dato, M. J. McGirt, E. Bohan, J. D. Weingart, A. Olivi, A. Quinones-Hinojosa, H. Brem, *Ann. Surg. Oncol.* **2008**, *15*, 2887–2893.
- [13] A. A. Ranade et al., *Ann. Oncol.* **2013**, *24*, v6–v12.
- [14] C Heijckmann, *Neth. J. Med.* **2001**, *59*, 286–291.
- [15] H. Mitchell, *Eur. J. Oncol. Nurs.* **2004**, *8*, S95–S103.
- [16] J. M. Hartley, J. Kopeček in *Smart Pharm. Nanocarriers*, Imperial College Press, **2016**, pp. 373–413.
- [17] S. Mura, J. Nicolas, P. Couvreur, *Nat. Mater.* **2013**, *12*, 991–1003.
- [18] R. Tong, L. Tang, L. Ma, C. Tu, R. Baumgartner, J. Cheng, *Chem. Soc. Rev.* **2014**, *43*, 6982–7012.

- [19] S. Matsumoto, R. J. Christie, N. Nishiyama, K. Miyata, A. Ishii, M. Oba, H. Koyama, Y. Yamasaki, K. Kataoka, *Biomacromolecules* **2009**, *10*, 119–127.
- [20] G. Kocak, C. Tuncer, V. Bütün, *Polym. Chem.* **2017**, *8*, 144–176.
- [21] T. J. Deming, *Chem. Rev.* **2016**, *116*, 786–808.
- [22] K. Klinker et al., *Angew. Chemie Int. Ed.* **2017**, *56*, 9608–9613.
- [23] E. T. Kaiser, F. J. Kezdy, *Proc. Natl. Acad. Sci.* **1983**, *80*, 1137–1143.
- [24] D. Huesmann, A. Birke, K. Klinker, S. Türk, H. J. Räder, M. Barz, *Macromolecules* **2014**, *47*, 928–936.
- [25] K. Klinker, M. Barz, *Macromol. Rapid Commun.* **2015**, *36*, 1943–1957.
- [26] A. Birke, D. Huesmann, A. Kelsch, M. Weilbacher, J. Xie, M. Bros, T. Bopp, C. Becker, K. Landfester, M. Barz, *Biomacromolecules* **2014**, *15*, 548–57.
- [27] A. Birke, J. Ling, M. Barz, *Prog. Polym. Sci.* **2018**, *81*, 163–208.
- [28] T. Kidchob, S. Kimura, Y. Imanishi, *J. Control. Release* **1998**, *51*, 241–248.
- [29] H. Tanisaka, S. Kizaka-Kondoh, A. Makino, S. Tanaka, M. Hiraoka, S. Kimura, *Bioconjug. Chem.* **2008**, *19*, 109–117.
- [30] M. Barz, R. Luxenhofer, R. Zentel, M. J. Vicent, *Polym. Chem.* **2011**, *2*, 1900.
- [31] F. Wessely, F. Sigmund, *Hoppe-Seyler's Zeitschrift für Physiol. Chemie* **1926**, *159*, 102–119.
- [32] M Szwarc in *Fortschritte der Hochpolym. Vol. 4*, Springer-Verlag, Berlin/Heidelberg, **1965**, pp. 1–65.
- [33] D. G. H. Ballard, C. H. Bamford, *Proc. R. Soc. A Math. Phys. Eng. Sci.* **1954**, *223*, 495–520.
- [34] D. G. H. Ballard, C. H. Bamford, *Proc. R. Soc. A Math. Phys. Eng. Sci.* **1956**, *236*, 384–396.
- [35] H. R. Kricheldorf, *Die Makromol. Chemie* **1971**, *149*, 127–133.
- [36] R. Katakai, M. Oya, K. Uno, Y. Iwakura, *Biopolymers* **1971**, *10*, 2199–2208.
- [37] H. R. Kricheldorf, *Angew. Chem. Int. Ed. Engl.* **2006**, *45*, 5752–84.
- [38] N. Hadjichristidis, H. Iatrou, M. Pitsikalis, G. Sakellariou, *Chem. Rev.* **2009**, *109*, 5528–5578.
- [39] H. Leuchs, *Berichte der Dtsch. Chem. Gesellschaft* **1906**, *39*, 857–861.
- [40] F. Fuchs, *Berichte der Dtsch. Chem. Gesellschaft (A B Ser.)* **1922**, *55*, 2943–2943.
- [41] C. J. Brown, D. Coleman, A. C. Farthing, *Nature* **1949**, *163*, 834–835.
- [42] A. C. Farthing, *J. Chem. Soc.* **1950**, 3213.

- [43] H. Leuchs, W. Geiger, *Berichte der Dtsch. Chem. Gesellschaft* **1908**, *41*, 1721–1726.
- [44] C. Fetsch, A. Grossmann, L. Holz, J. F. Nawroth, R. Luxenhofer, *Macromolecules* **2011**, *44*, 6746–6758.
- [45]  *$\alpha$ -Aminoacid-N-Carboxy-Anhydrides and Related Heterocycles*, (Ed.: H. R. Kricheldorf), Springer, Berlin, **1987**.
- [46] J. Huang, A. Heise, *Chem. Soc. Rev.* **2013**, *42*, 7373.
- [47] B. Weber, A. Birke, K. Fischer, M. Schmidt, M. Barz, *Macromolecules* **2018**, *51*, 2653–2661.
- [48] H. Peng, J. Ling, Z. Shen, *J. Polym. Sci. Part A Polym. Chem.* **2012**, *50*, 1076–1085.
- [49] I. Dimitrov, H. Schlaad, *Chem. Commun. (Camb)*. **2003**, 2944–2945.
- [50] T. J. Deming, *Nature* **1997**, *390*, 386–389.
- [51] I. Conejos-Sánchez, A. Duro-Castano, A. Birke, M. Barz, M. J. Vicent, *Polym. Chem.* **2013**, *4*, 3182.
- [52] H. Lu, J. Cheng, *J. Am. Chem. Soc.* **2007**, *129*, 14114–14115.
- [53] T. Aliferis, H. Iatrou, N. Hadjichristidis, *Biomacromolecules* **2004**, *5*, 1653–6.
- [54] W. Vayaboury, O. Giani, H. Cottet, A. Deratani, F. Schué, *Macromol. Rapid Commun.* **2004**, *25*, 1221–1224.
- [55] G. J. M. Habraken, M. Peeters, C. H.J. T. Dietz, C. E. Koning, A. Heise, *Polym. Chem.* **2010**, *1*, 514–524.
- [56] J. Zou, J. Fan, X. He, S. Zhang, H. Wang, K. L. Wooley, *Macromolecules* **2013**, *46*, 4223–4226.
- [57] G. J. M. Habraken, K. H.R. M. Wilsens, C. E. Koning, A. Heise, *Polym. Chem.* **2011**, *2*, 1322.
- [58] C. Deng, J. Wu, R. Cheng, F. Meng, H. A. Klok, Z. Zhong, *Prog. Polym. Sci.* **2014**, *39*, 330–364.
- [59] P. Heller, N. Mohr, A. Birke, B. Weber, A. Reske-Kunz, M. Bros, M. Barz, *Macromol. Biosci.* **2015**, *15*, 63–73.
- [60] K. Klinker, R. Holm, P. Heller, M. Barz, *Polym. Chem.* **2015**, *6*, 4612–4623.
- [61] R. Holm, K. Klinker, B. Weber, M. Barz, *Macromol. Rapid Commun.* **2015**, *36*, 2083–2091.
- [62] R. Holm, B. Weber, P. Heller, K. Klinker, D. Westmeier, D. Docter, R. H. Stauber, M. Barz, *Macromol. Biosci.* **2017**, *17*, 1600514.
- [63] C. Secker, S. M. Brosnan, R. Luxenhofer, H. Schlaad, *Macromol. Biosci.* **2015**, *15*, 881–891.
- [64] T. Kidchob, S. Kimura, Y. Imanishi, *J. Appl. Polym. Sci.* **1997**, *40*, 453–458.
- [65] T. Kidchob, S. Kimura, Y. Imanishi, *J. Control. Release* **1998**, *50*, 205–214.

- [66] S. Kimura, T. Kidchob, Y. Imanishi, *Polym. Adv. Technol.* **2001**, *12*, 85–95.
- [67] A. Makino, R. Yamahara, E. Ozeki, S. Kimura, *Chem. Lett.* **2007**, *36*, 1220–1221.
- [68] E. Hara, A. Makino, K. Kurihara, F. Yamamoto, E. Ozeki, S. Kimura, *Int. Immunopharmacol.* **2012**, *14*, 261–266.
- [69] C. Hörtz, A. Birke, L. Kaps, S. Decker, E. Wächtersbach, K. Fischer, D. Schuppan, M. Barz, M. Schmidt, *Macromolecules* **2015**, *48*, 2074–2086.
- [70] P. Heller, A. Birke, D. Huesmann, B. Weber, K. Fischer, A. Reske-Kunz, M. Bros, M. Barz, *Macromol. Biosci.* **2014**, *14*, 1380–1395.
- [71] P. Heller, J. Zhou, B. Weber, D. Hobernik, M. Bros, F. Schmid, M. Barz, *Small* **2017**, *13*, 1603694.
- [72] S. L. Ginn, A. K. Amaya, I. E. Alexander, M. Edelstein, M. R. Abedi, *J. Gene Med.* **2018**, e3015.
- [73] J. Tabernero et al., *Cancer Discov.* **2013**, *3*, 406–417.
- [74] L. Jiang, J. M. Frederick, W. Baehr, *Front. Mol. Neurosci.* **2014**, *7*, 4–11.
- [75] K. Lundstrom, *Viruses* **2015**, *7*, 4482–4487.
- [76] C. Chakraborty, A. R. Sharma, G. Sharma, C. G. P. Doss, S. S. Lee, *Mol. Ther. - Nucleic Acids* **2017**, *8*, 132–143.
- [77] A. Fire, S. Xu, M. K. Montgomery, S. A. Kostas, S. E. Driver, C. C. Mello, *Nature* **1998**, *391*, 806–11.
- [78] R. Robinson, *PLoS Biol.* **2004**, *2*, E28.
- [79] C. V. Pecot, G. A. Calin, R. L. Coleman, G. Lopez-Berestein, A. K. Sood, *Nat. Rev. Cancer* **2011**, *11*, 59–67.
- [80] K. a. Whitehead, R. Langer, D. G. Anderson, *Nat. Rev. Drug Discov.* **2009**, *8*, 129–38.
- [81] T. A. Rand, K. Ginalski, N. V. Grishin, X. Wang, *Proc. Natl. Acad. Sci.* **2004**, *101*, 14385–14389.
- [82] P. D. Zamore, *Cell* **2006**, *127*, 1083–1086.
- [83] D. Castanotto, J. J. Rossi, *Nature* **2009**, *457*, 426–433.
- [84] R. J. Christie, N. Nishiyama, K. Kataoka, *Endocrinology* **2010**, *151*, 466–473.
- [85] J.-M. Williford, J. Wu, Y. Ren, M. M. Archang, K. W. Leong, H.-Q. Mao, *Annu. Rev. Biomed. Eng.* **2014**, *16*, 347–370.
- [86] P. Barata, A. K. Sood, D. S. Hong, *Cancer Treat. Rev.* **2016**, *50*, 35–47.
- [87] C. A. Lipinski, F. Lombardo, B. W. Dominy, P. J. Feeney, *Adv. Drug Deliv. Rev.* **2001**, *46*, 3–26.
- [88] M. A. Behlke, *Oligonucleotides* **2008**, *18*, 305–320.



- [89] D. Bumcrot, M. Manoharan, V. Koteliansky, D. W. Y. Sah, *Nat. Chem. Biol.* **2006**, *2*, 711–719.
- [90] J. DeVincenzo et al., *Antiviral Res.* **2008**, *77*, 225–231.
- [91] F. Czauderna, M. Fechtner, S. Dames, H. Aygün, A. Klippel, G. J. Pronk, K. Giese, J. Kaufmann, *Nucleic Acids Res.* **2003**, *31*, 2705–2716.
- [92] D. V. Morrissey et al., *Nat. Biotechnol.* **2005**, *23*, 1002–1007.
- [93] B. R. Meade et al., *Nat. Biotechnol.* **2014**, *32*, 1256–1261.
- [94] J. E. Zuckerman, I. Gritli, A. Tolcher, J. D. Heidel, D. Lim, R. Morgan, B. Chmielowski, A. Ribas, M. E. Davis, Y. Yen, *Proc. Natl. Acad. Sci.* **2014**, *111*, 11449–11454.
- [95] M. E. Davis, *Mol. Pharm.* **2009**, *6*, 659–668.
- [96] B. Schultheis et al., *J. Clin. Oncol.* **2014**, *32*, 4141–4148.
- [97] T. S. Zimmermann et al., *Nature* **2006**, *441*, 111–114.
- [98] Y. Bao et al., *Pharm. Res.* **2013**, *30*, 342–351.
- [99] J. C. Burnett, J. J. Rossi, *Chem. Biol.* **2012**, *19*, 60–71.
- [100] R. Kanasty, J. R. Dorkin, A. Vegas, D. Anderson, *Nat. Mater.* **2013**, *12*, 967–77.
- [101] H. J. Kim, A. Kim, K. Miyata, K. Kataoka, *Adv. Drug Deliv. Rev.* **2016**, *104*, 61–77.
- [102] K. Miyata, N. Nishiyama, K. Kataoka, *Chem. Soc. Rev.* **2012**, *41*, 2562–2574.
- [103] U. Lächelt, E. Wagner, *Chem. Rev.* **2015**, *115*, 11043–11078.
- [104] A. V. Kabanov, S. V. Vinogradov, *Angew. Chemie* **2009**, *121*, 5524–5536.
- [105] D. J. Siegwart et al., *Proc. Natl. Acad. Sci.* **2011**, *108*, 12996–13001.
- [106] L. Nuhn, M. Hirsch, B. Krieg, K. Koynov, K. Fischer, M. Schmidt, M. Helm, R. Zentel, *ACS Nano* **2012**, *6*, 2198–2214.
- [107] N. Leber et al., *J. Control. Release* **2017**, *248*, 10–23.
- [108] O. M. Merkel, T. Kissel, *J. Control. Release* **2014**, *190*, 415–423.
- [109] K. Xiao, Y. Li, J. Luo, J. S. Lee, W. Xiao, A. M. Gonik, R. G. Agarwal, K. S. Lam, *Biomaterials* **2011**, *32*, 3435–3446.
- [110] N. Bertrand, J.-C. Leroux, *J. Control. Release* **2012**, *161*, 152–63.
- [111] B. Davies, T. Morris, *Pharm. Res.* **1993**, *10*, 1093–1095.
- [112] F. Alexis, E. Pridgen, L. K. Molnar, O. C. Farokhzad, *Mol. Pharm.* **2008**, *5*, 505–515.
- [113] J. B. Delehanty, H. Mattoussi, I. L. Medintz, *Anal. Bioanal. Chem.* **2009**, *393*, 1091–1105.
- [114] M. Longmire, P. L. Choyke, H. Kobayashi, *Nanomedicine (Lond)* **2008**, *3*, 703–717.

- [115] E. Blanco, H. Shen, M. Ferrari, *Nat. Biotechnol.* **2015**, *33*, 941–951.
- [116] Y. Geng, P. Dalhaimer, S. Cai, R. Tsai, M. Tewari, T. Minko, D. E. Discher, *Nat. Nanotechnol.* **2007**, *2*, 249–255.
- [117] J. A. Champion, S. Mitragotri, *Proc. Natl. Acad. Sci.* **2006**, *103*, 4930–4934.
- [118] D. A. Christian, S. Cai, O. B. Garbuzenko, T. Harada, A. L. Zajac, T. Minko, D. E. Discher, *Mol. Pharm.* **2009**, *6*, 1343–1352.
- [119] T. Yeung, G. E. Gilbert, J. Shi, J. Silvius, A. Kapus, S. Grinstein, *Science (80-. )*. **2008**, *319*, 210–213.
- [120] J. D. Clogston, A. K. Patri in, **2011**, pp. 63–70.
- [121] Y. Yamamoto, Y. Nagasaki, Y. Kato, Y. Sugiyama, K. Kataoka, *J. Control. Release* **2001**, *77*, 27–38.
- [122] H. Maeda, *J. Control. Release* **2012**, *164*, 138–44.
- [123] H. Maeda, H. Nakamura, J. Fang, *Adv. Drug Deliv. Rev.* **2013**, *65*, 71–9.
- [124] H. Cabral et al., *Nat. Nanotechnol.* **2011**, *6*, 815–823.
- [125] Q. Leng, M. C. Woodle, A. J. Mixson, *J. Drug Deliv.* **2017**, *2017*, 1–22.
- [126] Y. Yi et al., *J. Control. Release* **2016**, *244*, 247–256.
- [127] I. Tannock, D. Rotin, *Cancer Res.* **1989**, *49*, 4373–4384.
- [128] E. Fleige, M. A. Quadir, R. Haag, *Adv. Drug Deliv. Rev.* **2012**, *64*, 866–884.
- [129] L. Y. T. Chou, K. Ming, W. C. W. Chan, *Chem. Soc. Rev.* **2011**, *40*, 233–45.
- [130] C. Le Roy, J. L. Wrana, *Nat. Rev. Mol. Cell Biol.* **2005**, *6*, 112–126.
- [131] U. Lungwitz, M. Breunig, T. Blunk, A. Göpferich, *Eur. J. Pharm. Biopharm.* **2005**, *60*, 247–266.
- [132] M. Meyer, E. Wagner, *Expert Opin. Drug Deliv.* **2006**, *3*, 563–571.
- [133] Y. Lee, H. Mo, H. Koo, J. Y. Park, M. Y. Cho, G. W. Jin, J. S. Park, *Bioconjug. Chem.* **2007**, *18*, 13–18.
- [134] D. He, E. Wagner, *Macromol. Biosci.* **2015**, *15*, 600–612.
- [135] S. Reinhard, E. Wagner, *Macromol. Biosci.* **2017**, *17*, 1600152.
- [136] Q. Sun, T. Ojha, F. Kiessling, T. Lammers, Y. Shi, *Biomacromolecules* **2017**, *18*, 1449–1459.
- [137] R. Cheng, F. Meng, C. Deng, Z. Zhong, *Nano Today* **2015**, *10*, 656–670.
- [138] K. Osada, R. J. Christie, K. Kataoka, *J. R. Soc. Interface* **2009**, *6*, S325–S339.
- [139] T. K. Endres, M. Beck-Broichsitter, O. Samsonova, T. Renette, T. H. Kissel, *Biomaterials* **2011**, *32*, 7721–7731.

- [140] Y. Nie, M. Günther, Z. Gu, E. Wagner, *Biomaterials* **2011**, *32*, 858–869.
- [141] L. Nuhn, S. Tomcin, K. Miyata, V. Mailänder, K. Landfester, K. Kataoka, R. Zentel, *Biomacromolecules* **2014**, *15*, 4111–4121.
- [142] T. W. Chu, J. Feng, J. Yang, J. Kopeček, *J. Control. Release* **2015**, *220*, 608–616.
- [143] D. Huesmann, A. Sevenich, B. Weber, M. Barz, *Polymer (Guildf)*. **2015**, *67*, 240–248.
- [144] N. Gangloff, J. Ulbricht, T. Lorson, H. Schlaad, R. Luxenhofer, *Chem. Rev.* **2016**, *116*, 1753–1802.
- [145] R. Hoogenboom, *Angew. Chemie - Int. Ed.* **2009**, *48*, 7978–7994.
- [146] J. F. Lutz, A. Hoth, *Macromolecules* **2006**, *39*, 893–896.
- [147] T. Steinbach, F. R. Wurm, *Angew. Chemie - Int. Ed.* **2015**, *54*, 6098–6108.
- [148] T. F. Martens, K. Remaut, J. Demeester, S. C. De Smedt, K. Braeckmans, *Nano Today* **2014**, *9*, 344–364.
- [149] L. Wasungu, D. Hoekstra, *J. Control. Release* **2006**, *116*, 255–264.
- [150] W.-f. Dong, A. Kishimura, Y. Anraku, S. Chuanoi, K. Kataoka, *J. Am. Chem. Soc.* **2009**, *131*, 3804–3805.
- [151] C. J. Rijcken, M. Talelli, C. F. van Nostrum, G. Storm, W. E. Hennink, *Eur. J. Nanomedicine* **2010**, *3*, 19–24.
- [152] T. Miller, A. Hill, S. Uezguen, M. Weigandt, A. Goepferich, *Biomacromolecules* **2012**, *13*, 1707–18.
- [153] M. Talelli, M. Barz, C. J. Rijcken, F. Kiessling, W. E. Hennink, T. Lammers, *Nano Today* **2015**, *10*, 93–117.
- [154] P. Heller, D. Hobernik, U. Lächelt, M. Schinnerer, B. Weber, M. Schmidt, E. Wagner, M. Bros, M. Barz, *J. Control. Release* **2017**, *258*, 146–160.
- [155] E. S. Read, S. P. Armes, *Chem. Commun. (Camb)*. **2007**, 3021–35.
- [156] M. Iijima, Y. Nagasaki, T. Okada, M. Kato, K. Kataoka, *Macromolecules* **1999**, *32*, 1140–1146.
- [157] C. J. Rijcken, C. J. Snel, R. M. Schiffelers, C. F. van Nostrum, W. E. Hennink, *Biomaterials* **2007**, *28*, 5581–93.
- [158] F. Q. Schafer, G. R. Buettner, *Free Radic. Biol. Med.* **2001**, *30*, 1191–1212.
- [159] C. S. Sevier, C. A. Kaiser, *Nat. Rev. Mol. Cell Biol.* **2002**, *3*, 836–847.
- [160] I. Kranner, S. Birtić, K. M. Anderson, H. W. Pritchard, *Free Radic. Biol. Med.* **2006**, *40*, 2155–2165.
- [161] F. Meng, W. E. Hennink, Z. Zhong, *Biomaterials* **2009**, *30*, 2180–98.
- [162] A. N. Zelikin, J. F. Quinn, F. Caruso, *Biomacromolecules* **2006**, *7*, 27–30.

- [163] H. Liu, K. D. Moynihan, Y. Zheng, G. L. Szeto, A. V. Li, B. Huang, D. S. Van Egeren, C. Park, D. J. Irvine, *Nature* **2014**, *507*, 519–522.
- [164] Y. Kakizawa, A. Harada, K. Kataoka, *J. Am. Chem. Soc.* **1999**, *121*, 11247–11248.
- [165] T. Maeda, H. Otsuka, A. Takahara, *Prog. Polym. Sci.* **2009**, *34*, 581–604.
- [166] D.-J. Lee et al., *Bioconjug. Chem.* **2017**, acs.bioconjchem.7b00383.
- [167] L. Novo, E. V. Van Gaal, E. Mastrobattista, C. F. Van Nostrum, W. E. Hennink, *J. Control. Release* **2013**, *169*, 246–256.
- [168] J.-G. Piao, J.-J. Yan, M.-Z. Wang, D.-C. Wu, Y.-Z. You, *Biomater. Sci.* **2014**, *2*, 390.
- [169] K. Miyata, Y. Kakizawa, N. Nishiyama, A. Harada, Y. Yamasaki, H. Koyama, K. Kataoka, *J. Am. Chem. Soc.* **2004**, *126*, 2355–2361.
- [170] V. S. Trubetskoy, A. Loomis, P. M. Slattum, J. E. Hagstrom, V. G. Budker, J. A. Wolf, *Bioconjug. Chem.* **1999**, *10*, 624–628.
- [171] D. Oupickí, R. C. Carlisle, L. W. Seymour, *Gene Ther.* **2001**, *8*, 713–724.
- [172] M. Neu, J. Sitterberg, U. Bakowsky, T. Kissel, *Biomacromolecules* **2006**, *7*, 3428–3438.
- [173] O. Schäfer, D. Huesmann, C. Muhl, M. Barz, *Chem. - A Eur. J.* **2016**, *22*, 18085–18091.
- [174] G. T. Hermanson in *Bioconjugate Tech.* Elsevier, New York, **2008**, pp. 666–706.
- [175] T. Wang, A. Pfisterer, S. L. Kuan, Y. Wu, O. Dumele, M. Lamla, K. Müllen, T. Weil, *Chem. Sci.* **2013**, *4*, 1889–1894.
- [176] T. Wang et al., *Chem. - A Eur. J.* **2015**, *21*, 228–238.
- [177] E. Lallana, N. Tirelli, *Macromol. Chem. Phys.* **2013**, *214*, 143–158.
- [178] P. J. Kocięński, *Protecting Groups*, Vol. 128, 3. ed., Georg Thieme Verlag, Stuttgart, **2005**.
- [179] T. W. Greene, P. G. M. Wuts, *Greene's Protective Groups in Organic Synthesis*, 5. ed., (Ed.: P. G. M. Wuts), John Wiley & Sons, Inc., Hoboken, New Jersey, **2014**.
- [180] H. P. Latscha, U. Kazmaier, H. A. Klein in *Org. Chemie*, Springer Spektrum, Berlin, Heidelberg, **2016**, pp. 175–182.
- [181] E. M. Sletten, C. R. Bertozzi, *Angew. Chemie Int. Ed.* **2009**, *48*, 6974–6998.
- [182] H. E. Swaisgood, *Biotechnol. Adv.* **2005**, *23*, 71–73.
- [183] T. M. Postma, F. Albericio, *European J. Org. Chem.* **2014**, *2014*, 3519–3530.
- [184] D. He, K. Müller, A. Krhac Levacic, P. Kos, U. Lächelt, E. Wagner, *Bioconjug. Chem.* **2016**, *27*, 647–659.

- [185] R. Duncan, *Nat. Rev. Drug Discov.* **2003**, *2*, 347–60.
- [186] R. Langer, D. A. Tirrell, *Nature* **2004**, *428*, 487–492.
- [187] J.-F. Lutz, H. G. Börner, *Prog. Polym. Sci.* **2008**, *33*, 1–39.
- [188] C. P. R. Hackenberger, D. Schwarzer, *Angew. Chem. Int. Ed. Engl.* **2008**, *47*, 10030–10074.
- [189] M. Schnölzer, S. B. H. Kent, *Science (80-. )*. **1992**, *256*, 221–225.
- [190] P. Dawson, T. Muir, I Clark-Lewis, S. Kent, *Science (80-. )*. **1994**, *266*, 776–779.
- [191] A. B. Lowe, *Polym. Chem.* **2014**, *5*, 4820–4870.
- [192] P. M.S. D. Cal, G. J. L. Bernardes, P. M. P. Gois, *Angew. Chemie* **2014**, *126*, 10758–10760.
- [193] L. N. Tumey et al., *Bioconjug. Chem.* **2014**, *25*, 1871–1880.
- [194] S. D. Fontaine, R. Reid, L. Robinson, G. W. Ashley, D. V. Santi, *Bioconjug. Chem.* **2015**, *26*, 145–152.
- [195] A. Wilson, G. Gasparini, S. Matile, *Chem. Soc. Rev.* **2014**, *43*, 1948–62.
- [196] K.-D. Zhang, S. Matile, *Angew. Chemie* **2015**, *127*, 9108–9111.
- [197] G. Saito, J. a. Swanson, K.-D. Lee, *Adv. Drug Deliv. Rev.* **2003**, *55*, 199–215.
- [198] M. Le Neindre, R. Nicolaÿ, *Polym. Chem.* **2014**, *5*, 4601–4611.
- [199] Z. Q. Lei, H. P. Xiang, Y. J. Yuan, M. Z. Rong, M. Q. Zhang, *Chem. Mater.* **2014**, *26*, 2038–2046.
- [200] Y. Amamoto, H. Otsuka, A. Takahara, K. Matyjaszewski, *Adv. Mater.* **2012**, *24*, 3975–3980.
- [201] Y. Yang, X. Lu, W. Wang, *Mater. Des.* **2017**, *127*, 30–36.
- [202] J. Wu et al., *Angew. Chemie - Int. Ed.* **2015**, *54*, 9218–9223.
- [203] H. Otsuka, S. Nagano, Y. Kobashi, T. Maeda, A. Takahara, *Chem. Commun.* **2010**, *46*, 1150–1152.
- [204] B. Yameen, C. Vilos, W. I. Choi, A. Whyte, J. Huang, L. Pollit, O. C. Farokhzad, *Chem. - A Eur. J.* **2015**, *21*, 11325–11329.
- [205] T. Fuoco, D. Pappalardo, A. Finne-Wistrand, *Macromolecules* **2017**, *50*, 7052–7061.
- [206] J. L. Kice, *Acc. Chem. Res.* **1968**, *1*, 58–64.
- [207] C. Boyer, A. H. Soeriyadi, P. J. Roth, M. R. Whittaker, T. P. Davis, *Chem. Commun.* **2011**, *47*, 1318–1320.
- [208] P. J. Roth, D. Kessler, R. Zentel, P. Theato, *J. Polym. Sci. Part A Polym. Chem.* **2009**, *47*, 3118–3130.
- [209] O. Schäfer, D. Huesmann, M. Barz, *Macromolecules* **2016**, *49*, 8146–8153.
- [210] D. Bontempo, K. L. Heredia, B. A. Fish, H. D. Maynard, *J. Am. Chem. Soc.* **2004**, *126*, 15372–15373.

- [211] V. Bulmus, *Polym. Chem.* **2011**, *2*, 1463.
- [212] J Carlsson, H Drevin, R Axén, *Biochem. J.* **1978**, *173*, 723–37.
- [213] T. M. Kitson, K. M. Loomes, *Anal. Biochem.* **1985**, *146*, 429–430.
- [214] A. J. Van Der Vlies, C. P. Oneil, U. Hasegawa, N. Hammond, J. A. Hubbell, *Bioconjug. Chem.* **2010**, *21*, 653–662.
- [215] E. Boccu, F. M. Veronese, A. Fontana, C. A. Benassi, *Eur. J. Biochem.* **1970**, *13*, 188–192.
- [216] P. Laidler, L. Konieczny, K. Bobrzecka, *Mol. Immunol.* **1979**, *16*, 141–144.
- [217] J. J. Pastuszak, A. Chimiak, *J. Org. Chem.* **1981**, *46*, 1868–1873.
- [218] S. J. Brois, J. F. Pilot, H. W. Barnum, *J. Am. Chem. Soc.* **1970**, *92*, 7629–7631.
- [219] K. Nokihara, H. Berndt, *J. Org. Chem.* **1978**, *43*, 4893–4895.
- [220] A. L. Schroll, G. Barany, *J. Org. Chem.* **1989**, *54*, 244–247.
- [221] G. L. Ellman, *Arch. Biochem. Biophys.* **1959**, *82*, 70–77.
- [222] D. Crimmins, *Pept. Res.* **1989**, *2*, 395–401.
- [223] R. Matsueda, R. Walter, *Int. J. Pept. Protein Res.* **1980**, *16*, 392–401.
- [224] U. Weber, P. Hartter, *Hoppe-Seyler's Zeitschrift für Physiol. Chemie* **1970**, *351*, 1384–1388.
- [225] T. M. Postma, M. Giraud, F. Albericio, *Org. Lett.* **2012**, *14*, 5468–71.
- [226] K. Matyjaszewski, N. V. Tsarevsky, *Nat. Chem.* **2009**, *1*, 276–288.
- [227] C. J. Hawker, A. W. Bosman, E. Harth, *Chem. Rev.* **2001**, *101*, 3661–3688.
- [228] J. Chiefari et al., *Macromolecules* **1998**, *31*, 5559–5562.
- [229] M. A. Tasdelen, M. U. Kahveci, Y. Yagci, *Prog. Polym. Sci.* **2011**, *36*, 455–567.
- [230] P. J. Roth, C. Boyer, A. B. Lowe, T. P. Davis, *Macromol. Rapid Commun.* **2011**, *32*, 1123–1143.
- [231] L. Garamszegi, C. Donzel, G. Carrot, T. Q. Nguyen, J. Hilborn, *React. Funct. Polym.* **2003**, *55*, 179–183.
- [232] N. V. Tsarevsky, K. Matyjaszewski, *Macromolecules* **2002**, *35*, 9009–9014.
- [233] N. V. Tsarevsky, K. Matyjaszewski, *Macromolecules* **2005**, *38*, 3087–3092.
- [234] G. Carrot, J. Hilborn, J. L. Hedrick, M. Trollsås, *Macromolecules* **1999**, *32*, 5171–5173.
- [235] V. Vázquez-Dorbatt, Z. P. Tolstyka, C. W. Chang, H. D. Maynard, *Biomacromolecules* **2009**, *10*, 2207–2212.
- [236] G. Moad, *Polym. Chem.* **2017**, *8*, 177–219.



- [237] F. Goethals, D. Frank, F. Du Prez, *Prog. Polym. Sci.* **2017**, *64*, 76–113.
- [238] L. Tao, J. Liu, B. H. Tan, T. P. Davis, *Macromolecules* **2009**, *42*, 4960–4962.
- [239] X. Hu, G. Liu, Y. Li, X. Wang, S. Liu, *J. Am. Chem. Soc.* **2015**, *137*, 362–368.
- [240] Y. Zhuang, H. Deng, Y. Su, L. He, R. Wang, G. Tong, D. He, X. Zhu, *Biomacromolecules* **2016**, *17*, 2050–2062.
- [241] C. D. Vo, J. Rosselgong, S. P. Armes, N. C. Billingham, *Macromolecules* **2007**, *40*, 7119–7125.
- [242] L. Zhang, W. Liu, L. Lin, D. Chen, M. H. Stenzel, *Biomacromolecules* **2008**, *9*, 3321–3331.
- [243] S. R. Ting, E. H. Min, P. B. Zetterlund, M. H. Stenzel, *Macromolecules* **2010**, *43*, 5211–5221.
- [244] J. An, X. Dai, Y. Zhao, Q. Guo, Z. Wu, X. Zhang, C. Li, *Polym. Chem.* **2015**, *6*, 6529–6542.
- [245] S. Pal, M. R. Hill, B. S. Sumerlin, *Polym. Chem.* **2015**, *6*, 7871–7880.
- [246] Z. Cao, H. Wu, J. Dong, G. Wang, *Macromolecules* **2014**, *47*, 8777–8783.
- [247] K. Tappertzhofen, S. Beck, E. Montermann, D. Huesmann, M. Barz, K. Koynov, M. Bros, R. Zentel, *Macromol. Biosci.* **2016**, *16*, 106–120.
- [248] G. Moad, E. Rizzardo, S. H. Thang, *Polym. Int.* **2011**, *60*, 9–25.
- [249] C. W. Scales, A. J. Convertine, C. L. McCormick, *Biomacromolecules* **2006**, *7*, 1389–1392.
- [250] A. B. Lowe, *Polym. Chem.* **2014**, *5*, 4820–4870.
- [251] Q. Zhang, L. Voorhaar, B. G. De Geest, R. Hoogenboom, *Macromol. Rapid Commun.* **2015**, *36*, 1177–1183.
- [252] B. A. Abel, C. L. McCormick, *Macromolecules* **2016**, *49*, 6193–6202.
- [253] P. J. Roth, D. Kessler, R. Zentel, P. Theato, *Macromolecules* **2008**, *41*, 8316–8319.
- [254] C. Boyer, V. Bulmus, J. Liu, T. P. Davis, M. H. Stenzel, C. Barner-Kowollik, *J. Am. Chem. Soc.* **2007**, *129*, 7145–7154.
- [255] Y. Zhuang, Y. Su, Y. Peng, D. Wang, H. Deng, X. Xi, X. Zhu, Y. Lu, *Biomacromolecules* **2014**, *15*, 1408–1418.
- [256] C. K. Riener, G. Kada, H. J. Gruber, *Anal. Bioanal. Chem.* **2002**, *373*, 266–276.
- [257] A. N. Zelikin, G. K. Such, A. Postma, F. Caruso, *Biomacromolecules* **2007**, *8*, 2950–2953.
- [258] S. Matsumura, A. R. Hlil, C. Lepiller, J. Gaudet, D. Guay, Z. Shi, S. Holdcroft, A. S. Hay, *Am. Chem. Soc. Polym. Prepr. Div. Polym. Chem.* **2008**, *49*, 511–512.

- [259] J. Xu, L. Tao, J. Liu, V. Bulmus, T. P. Davis, *Macromolecules* **2009**, *42*, 6893–6901.
- [260] C. L. Duvall, A. J. Convertine, D. S. W. Benoit, A. S. Hoffman, P. S. Stayton, *Mol. Pharm.* **2010**, *7*, 468–476.
- [261] L. Wong, C. Boyer, Z. Jia, H. M. Zareie, T. P. Davis, V. Bulmus, **2008**, 1934–1944.
- [262] L. Wong, S. Sevimli, H. M. Zareie, T. P. Davis, V. Bulmus, *Macromolecules* **2010**, *43*, 5365–5375.
- [263] Y. Wang, C.-Y. Hong, C.-Y. Pan, *Biomacromolecules* **2013**, *14*, 1444–1451.
- [264] A. W. York, F. Huang, C. L. McCormick, *Biomacromolecules* **2010**, *11*, 505–514.
- [265] J. S. Carlson, M. R. Hill, T. Young, P. J. Costanzo, *Polym. Chem.* **2010**, *1*, 1423.
- [266] C. Boyer, J. Liu, L. Wong, M. Tippett, V. Bulmus, T. P. Davis, *J. Polym. Sci. Part A Polym. Chem.* **2008**, *46*, 7207–7224.
- [267] A. J. Van Hell, D. J. Crommelin, W. E. Hennink, E. Mastrobattista, *Pharm. Res.* **2009**, *26*, 2186–2193.
- [268] A. J. Van Hell, M. M. Fretz, D. J. Crommelin, W. E. Hennink, E. Mastrobattista, *J. Control. Release* **2010**, *141*, 347–353.
- [269] D. L. McKenzie, E. Smiley, K. Y. Kwok, K. G. Rice, *Bioconjug. Chem.* **2000**, *11*, 901–909.
- [270] K. Tanaka, T. Kanazawa, T. Ogawa, Y. Takashima, T. Fukuda, H. Okada, *Int. J. Pharm.* **2010**, *398*, 219–224.
- [271] F. Li, R. I. Mahato, *Mol. Pharm.* **2017**, *14*, 1321–1324.
- [272] A. Isidro-Llobet, M. Alvarez, F. Albericio, *Chem. Rev.* **2009**, *109*, 2455–504.
- [273] D. Andreu, F. Albericio, N. A. Solé, M. C. Munson, M. Ferrer, G. Barany in *Pept. Synth. Protoc. Vol. 35*, Humana Press, New Jersey, **1994**, pp. 91–170.
- [274] J. P. Tam, C. R. Wu, W. Liu, J. W. Zhang, *J. Am. Chem. Soc.* **1991**, *113*, 6657–6662.
- [275] P. Verdié, L. Ronga, M. Cristau, M. Amblard, S. Cantel, C. Enjalbal, K. Puget, J. Martinez, G. Subra, *Chem. - An Asian J.* **2011**, *6*, 2382–2389.
- [276] G. K. S. Prakash, T. Mathew, C. Panja, G. A. Olah, *J. Org. Chem.* **2007**, *72*, 5847–5850.
- [277] X. Hou, X. Zhao, Y. Zhang, A. Han, S. Huo, S. Shen, *Molecules* **2017**, *22*, 338.
- [278] M. Iwaoka, T. Takahashi, S. Tomoda, *Heteroat. Chem.* **2001**, *12*, 293–299.



- [279] K. Arai, W. Shibagaki, R. Shinozaki, M. Iwaoka, *Int. J. Mol. Sci.* **2013**, *14*, 13194–13212.
- [280] T. M. Postma, F. Albericio, *Org. Lett.* **2013**, *15*, 616–619.
- [281] B. Kamber, *Helv. Chim. Acta* **1971**, *54*, 927–930.
- [282] D. F. Veber, J. D. Milkowski, S. L. Varga, R. G. Denkewalter, R. Hirschmann, *J. Am. Chem. Soc.* **1972**, *94*, 5456–5461.
- [283] H. Qian, W. Chen, J. P. Zhou, W. L. Huang, H. B. Zhang, J. Jin, *Chinese Chem. Lett.* **2010**, *21*, 388–390.
- [284] M. Muttenthaler, Y. G. Ramos, D. Feytens, A. D. de Araujo, P. F. Alewood, *Biopolymers* **2010**, *94*, 423–432.
- [285] A. Verdini, S. Terenzi, V. Brossard, M. Roggero, G. Corradin, *J. Pept. Sci.* **2008**, *14*, 1271–1282.
- [286] M. Royo, J. Alsina, E. Giralt, U. Slomczynska, F. Albericio, *J. Chem. Soc. Perkin Trans. 1* **1995**, 1095.
- [287] G. Bulaj, *Biotechnol. Adv.* **2005**, *23*, 87–92.
- [288] B. Mandal, B. Basu, *RSC Adv.* **2014**, *4*, 13854.
- [289] P. Agarwal, C. R. Bertozzi, *Bioconjug. Chem.* **2015**, *26*, 176–192.
- [290] B. D. Reeves et al., *Org. Biomol. Chem.* **2014**, *12*, 7942–7956.
- [291] G. Casi, N. Huguenin-Dezot, K. Zuberbühler, J. Scheuermann, D. Neri, *J. Am. Chem. Soc.* **2012**, *134*, 5887–5892.
- [292] K. Akaji, T. Tatsumi, M. Yoshida, T. Kimura, Y. Fujiwara, Y. Kiso, *J. Am. Chem. Soc.* **1992**, *114*, 4137–4143.
- [293] D. Arnelle, J. Stamler, *Arch. Biochem. Biophys.* **1995**, *318*, 279–285.
- [294] J. Zhang, S. Li, D. Zhang, H. Wang, A. R. Whorton, M. Xian, *Org. Lett.* **2010**, *12*, 4208–4211.
- [295] E. Wünsch, *Synthesis of Peptides (including the Chemistry of Protection Groups) I (Houben-Weyl Methods of Organic Chemistry Vol. XV/1)*, 4th editio, Georg Thieme Verlag, Stuttgart, **2014**, p. 789.
- [296] M. Góngora-Benítez, J. Tulla-Puche, M. Paradís-Bas, O. Werbitzky, M. Giraud, F. Albericio, *Biopolymers* **2011**, *96*, 69–80.
- [297] M. R. Levengood, X. Zhang, J. H. Hunter, K. K. Emmerton, J. B. Miyamoto, T. S. Lewis, P. D. Senter, *Angew. Chemie - Int. Ed.* **2017**, *56*, 733–737.
- [298] B. Kamber, *Helv. Chim. Acta* **1973**, *56*, 1370–81.
- [299] R. G. Hiskey, N. Muthukumaraswamy, R. R. Vunnam, W. R. Kennan, *J. Org. Chem.* **1975**, *40*, 950–953.
- [300] D. G. Mullen, B. Weigel, G. Barany, M. D. Distefano, *J. Pept. Sci.* **2010**, *16*, 219–222.
- [301] J. V. Castell, A. Tun-Kyi, *Helv. Chim. Acta* **1979**, *62*, 2507–2510.
- [302] H. Huang, R. I. Carey, *J. Pept. Res.* **2009**, *51*, 290–296.

- [303] R. Matsueda, S. Higashida, R. J. Ridge, G. R. Matsueda, *Chem. Lett.* **1982**, 921–924.
- [304] R. Matsueda, T. Kimura, E. T. Kaiser, G. R. Matsueda, *Chem. Lett.* **1981**, 737–740.
- [305] A. L. Schroll, R. J. Hondal, S. Flemer, *J. Pept. Sci.* **2012**, *18*, 1–9.
- [306] A. S. Galanis, F. Albericio, M. Grøtli, *Biopolymers* **2009**, *92*, 23–34.
- [307] A. Taguchi, K. Kobayashi, A. Kotani, K. Muguruma, M. Kobayashi, K. Fukumoto, K. Takayama, H. Hakamata, Y. Hayashi, *Chem. - A Eur. J.* **2017**, *23*, 8262–8267.
- [308] F. Alberico, D. Andreu, E. Giralt, C. Navalpotro, E. Pedroso, B. Ponsati, M. Rue-Gayo, *Int. J. Pept. Protein Res.* **2009**, *34*, 124–128.
- [309] R. G. Simmonds, D. E. Tupper, J. R. Harris, *Int. J. Pept. Protein Res.* **1993**, *43*, 363–366.
- [310] M. Amblard, J.-a. Fehrentz, J. Martinez, G. Subra, *Mol. Biotechnol.* **2006**, *33*, 239–254.
- [311] G. J. M. Habraken, C. E. Koning, J. P. A. Heuts, A. Heise, *Chem. Commun.* **2009**, 3612.
- [312] J. R. Kramer, T. J. Deming, *J. Am. Chem. Soc.* **2012**, *134*, 4112–5.
- [313] K.-S. Krannig, H. Schlaad, *J. Am. Chem. Soc.* **2012**, *134*, 18542.
- [314] A. J. Rhodes, T. J. Deming, *ACS Macro Lett.* **2013**, *2*, 351–354.
- [315] H. Cabral, K. Kataoka, *J. Control. Release* **2014**, *190*, 465–476.
- [316] R. Duncan, *J. Control. Release* **2014**, *190*, 371–380.
- [317] J. Fan, R. Li, X. He, K. Seetho, F. Zhang, J. Zou, K. L. Wooley, *Polym. Chem.* **2014**, *5*, 3977–3981.
- [318] S. Takae, K. Miyata, M. Oba, T. Ishii, N. Nishiyama, K. Itaka, Y. Yamasaki, H. Koyama, K. Kataoka, *J. Am. Chem. Soc.* **2008**, *130*, 6001–6009.
- [319] W.-F. Dong, A. Kishimura, Y. Anraku, S. Chuanoi, K. Kataoka, *J. Am. Chem. Soc.* **2009**, *131*, 3804–3805.
- [320] D. Huesmann, K. Klinker, M. Barz, *Polym. Chem.* **2017**, *8*, 957–971.
- [321] D. Huesmann, O. Schäfer, L. Braun, K. Klinker, T. Reuter, M. Barz, *Tetrahedron Lett.* **2016**, *57*, 1138–1142.
- [322] J. P. Weidner, S. S. Block, *J. Med. Chem.* **1964**, *7*, 671–673.
- [323] B. D. Reeves, J. K. Hilmer, L. Mellmann, M. Hartzheim, K. Poffenberger, K. Johnson, N. Joshi, D. J. Singel, P. a. Grieco, *Tetrahedron Lett.* **2013**, *54*, 5707–5710.
- [324] J. L. Kice, L. F. Mullan, *J. Am. Chem. Soc.* **1976**, *98*, 4259–4268.
- [325] R. G. Pearson, *J. Am. Chem. Soc.* **1963**, *85*, 3533–3539.
- [326] R. G. Pearson, J. Songstad, *J. Am. Chem. Soc.* **1967**, *89*, 1827–1836.
- [327] O. Schäfer, K. Klinker, L. Braun, D. Huesmann, J. Schultze, K. Koynov, M. Barz, *ACS Macro Lett.* **2017**, *6*, 1140–1145.

- [328] M. A. Gauthier, M. I. Gibson, H.-A. Klok, *Angew. Chemie Int. Ed.* **2009**, *48*, 48–58.
- [329] P. Theato, H.-A. Klok, *Functional Polymers by Post-Polymerization Modification*, (Eds.: P. Theato, H.-A. Klok), Wiley-VCH, Weinheim, Germany, **2012**.
- [330] C. Lin, J. F. Engbersen, *Expert Opin. Drug Deliv.* **2009**, *6*, 421–439.
- [331] P. Akkapeddi, S.-A. Azizi, A. M. Freedy, P. M.S. D. Cal, P. M. P. Gois, G. J. L. Bernardes, *Chem. Sci.* **2016**, *7*, 2954–2963.
- [332] T. H. Pillow et al., *Chem. Sci.* **2017**, *8*, 366–370.
- [333] S. L. Perry et al., *Nat. Commun.* **2015**, *6*, 6052.
- [334] W. Friedrich, P. Knipping, M. Laue, *Ann. Phys.* **1912**, *346*, 303–322.
- [335] R. Das, M. Eaquab Ali, S. B. Abd Hamid, *Rev. Adv. Mater. Sci* **2014**, *38*, 95–109.
- [336] A. A. Bunaciu, E. gabriela Udriștioiu, H. Y. Aboul-Enein, *Crit. Rev. Anal. Chem.* **2015**, *45*, 289–299.
- [337] W. Schärtl, *Light Scattering from Polymer Solutions and Nanoparticle*, Springer Laboratory, Berlin, Heidelberg, **2007**, p. 199.
- [338] B. Berne, R. Pecora, *Dynamic Light Scattering: With Applications to Chemistry, Biology, and Physics*. Courier Dover Publications, Mineola, **2000**.
- [339] <https://www.lsinstruments.ch>.
- [340] G. V. Lowry, R. J. Hill, S. Harper, A. F. Rawle, C. O. Hendren, F. Klaessig, U. Nobbmann, P. Sayre, J. Rumble, *Environ. Sci. Nano* **2016**, *3*, 953–965.
- [341] <http://group.nanovietech.com/products/pa-field-esa.html>.
- [342] R. Tantra, P. Schulze, P. Quincey, *Particuology* **2010**, *8*, 279–285.
- [343] R. J. Hunter, *Foundations of colloid science*, 2nd, Oxford University Press, New York, **2001**.
- [344] Y. Tian, M. M. Martinez, D. Pappas, *Appl. Spectrosc.* **2011**, *65*, 115–124.
- [345] K. Koynov, H.-j. Butt, *Curr. Opin. Colloid Interface Sci.* **2012**, *17*, 377–387.
- [346] <http://www2.mpip-mainz.mpg.de>.
- [347] <http://www.dojindo.eu.com/store/p/456-Cell-Counting-Kit-8.aspx>.
- [348] S. J. Gould, S Subramani, *Anal Biochem* **1988**, *175*, 5–13.
- [349] E. M. C. Hillman, C. B. Amoozegar, T. Wang, A. F. H. McCaslin, M. B. Bouchard, J. Mansfield, R. M. Levenson, *Philos. Trans. R. Soc. A Math. Phys. Eng. Sci.* **2011**, *369*, 4620–4643.
- [350] R. Weissleder, *Nat. Biotechnol.* **2001**, *19*, 316–317.
- [351] J Frangioni, *Curr. Opin. Chem. Biol.* **2003**, *7*, 626–634.

- [352] J. C. Tseng, K. Vasquez, J. D. Peterson, *PerkinElmer - Tech. Note* **2015**, 1–18.
- [353] <http://www.perkinelmer.de/category/in-vivo-imaging-instruments>.
- [354] O. Iwakura, K. Uno, M. Oya, R. Katakai, *Biopolymers* **1970**, *9*, 1419–1427.
- [355] A. Duro-Castano, I. Conejos-Sánchez, M. Vicent, *Polymers (Basel)*. **2014**, *6*, 515–551.
- [356] F. Alberico, D. Andreu, E. Giralt, C. Navalpotoro, E. Perdosó, B. Ponsati, M. Rue-Gayo, *Int. J. Pept. Protein Res.* **1989**, *34*, 124–128.
- [357] M. I. Gibson, G. J. Hunt, N. R. Cameron, *Org. Biomol. Chem.* **2007**, *5*, 2756.
- [358] G. Liu, C.-m. Dong, *Biomacromolecules* **2012**, *13*, 1573–83.
- [359] B. J. Sparks, J. G. Ray, D. a. Savin, C. M. Stafford, D. L. Patton, *Chem. Commun.* **2011**, *47*, 6245.
- [360] J. Zhou, P. Chen, C. Deng, F. Meng, R. Cheng, Z. Zhong, *Macromolecules* **2013**, *46*, 6723–6730.
- [361] R. J. Christie et al., *Biomacromolecules* **2011**, *12*, 3174–3185.
- [362] Y. Oe et al., *Biomaterials* **2014**, *35*, 7887–7895.
- [363] T. Xing, B. Lai, X. Ye, L. Yan, *Macromol. Biosci.* **2011**, *11*, 962–969.
- [364] M. Barz, D. Huesmann, O. Schäfer, Thiol-protected amino acid derivatives and uses thereof, **2014**.
- [365] I Phocas, C Yovanidis, I. Photaki, L Zervas, *J. Chem. Soc. C Org.* **1967**, *3*, 1506.
- [366] J. Shang, W.-M. Wang, Y.-H. Li, H.-B. Song, Z.-M. Li, J.-G. Wang, *J. Agric. Food Chem.* **2012**, *60*, 8286–8293.
- [367] P. Heller, B. Weber, A. Birke, M. Barz, *Macromol. Rapid Commun.* **2015**, *36*, 38–44.
- [368] L. Field in *Org. Chem. Sulfur*, (Ed.: S. Oae), Springer US, **1977**, pp. 303–382.
- [369] A. Rajca, M. Wiessler, *Tetrahedron Lett.* **1990**, *31*, 6075–6076.
- [370] J. L. Kice, T. E. Rogers, *J. Am. Chem. Soc.* **1974**, *96*, 8015–8019.
- [371] T. W. Hart, M. B. Vine, N. R. Walden, *Tetrahedron Lett.* **1985**, *26*, 3879–3882.
- [372] T. W. Hart, *Tetrahedron Lett.* **1985**, *26*, 2013–2016.
- [373] J. P. Weidner, S. S. Block, *J. Med. Chem.* **1972**, *15*, 564–567.
- [374] T. J. Deming, *J. Polym. Sci. Part A Polym. Chem.* **2000**, *38*, 3011–3018.
- [375] H. Lu, J. Cheng, *J. Am. Chem. Soc.* **2008**, *130*, 12562–12563.

- [376] G. R. Fulmer, A. J. M. Miller, N. H. Sherden, H. E. Gottlieb, A. Nudelman, B. M. Stoltz, J. E. Bercaw, K. I. Goldberg, *Organometallics* **2010**, *29*, 2176–2179.
- [377] C. R. Bertozzi, *Acc. Chem. Res.* **2011**, *44*, 651–653.
- [378] K. Lang, J. W. Chin, *Chem. Rev.* **2014**, *114*, 4764–806.
- [379] C. C. Price, G. W. Stacy, *J. Am. Chem. Soc.* **1946**, *68*, 498–500.
- [380] J. Dunbar, J. Rogers, *J. Org. Chem.* **1966**, *31*, 2842–2846.
- [381] N. S. Zefirov, N. V. Zyk, E. K. Beloglazkina, A. G. Kutateladze, *Thiosulfonates: Synthesis, Reactions and Practical Applications*, **1993**.
- [382] L. H. Sommer, J. Rockett, *J. Am. Chem. Soc.* **1951**, *73*, 5130–5134.
- [383] M. Morgenthaler et al., *ChemMedChem* **2007**, *2*, 1100–15.
- [384] I. H. Pitman, K. Uekama, T Higuchi, W. E. Hall, *J. Am. Chem. Soc.* **1972**, *94*, 8147–8152.
- [385] A. Mirzahasseini, A. Szilvay, B. Noszál, *Chem. Phys. Lett.* **2014**, *610-611*, 62–69.
- [386] R. E. Benesch, R. Benesch, *J. Am. Chem. Soc.* **1955**, *77*, 5877–5881.
- [387] D. L. Rabenstein, *J. Am. Chem. Soc.* **1973**, *95*, 2797–2803.
- [388] W. Wojnowski, A Herman, *Zeitschrift für Anorg. und Allg. Chemie* **1976**, *425*, 91–96.
- [389] A. Kozak, M. Czaja, L. Chmurzyński, *J. Chem. Thermodyn.* **2006**, *38*, 599–605.
- [390] R. G. Pearson, H. R. Sobel, J. Songstad, *J. Am. Chem. Soc.* **1968**, *90*, 319–326.
- [391] S. Oae, R. Nomura, Y. Yoshikawa, W. Tagaki, *Bull. Chem. Soc. Jpn.* **1969**, *42*, 2903–2906.
- [392] R. E. Davis, L. A. Suba, P. Klimishin, J. Carter, *J. Am. Chem. Soc.* **1969**, *91*, 104–107.
- [393] R. B. Merrifield, *J. Am. Chem. Soc.* **1963**, *85*, 2149–2154.
- [394] H. E. Gottlieb, V. Kotlyar, A. Nudelman, *J. Org. Chem.* **1997**, *62*, 7512–7515.
- [395] M. C. Burla, R. Caliandro, M. Camalli, B. Carrozzini, G. L. Cascarano, L. De Caro, C. Giacovazzo, G. Polidori, R. Spagna, *J. Appl. Crystallogr.* **2005**, *38*, 381–388.
- [396] G. M. Sheldrick, *Acta Crystallogr. Sect. C Struct. Chem.* **2015**, *71*, 3–8.
- [397] S Trimpin, A Rouhanipour, R Az, H. J. Räder, K Müllen, *Rapid Commun. Mass Spectrom.* **2001**, *15*, 1364–73.
- [398] F. Neese, *Wiley Interdiscip. Rev. Comput. Mol. Sci.* **2012**, *2*, 73–78.
- [399] A. D. Becke, *J. Chem. Phys.* **1993**, *98*, 5648–5652.
- [400] F. Weigend, R. Ahlrichs, *Phys. Chem. Chem. Phys.* **2005**, *7*, 3297.

- [401] S. Sinnecker, A. Rajendran, A. Klamt, M. Diedenhofen, F. Neese, *J. Phys. Chem. A* **2006**, *110*, 2235–2245.
- [402] E. V. Lenthe, E. J. Baerends, J. G. Snijders, *J. Chem. Phys.* **1993**, *99*, 4597–4610.
- [403] C. van Wüllen, *J. Chem. Phys.* **1998**, *109*, 392–399.
- [404] R. Izsák, F. Neese, *J. Chem. Phys.* **2011**, *135*, 144105.
- [405] S. Kossmann, F. Neese, *Chem. Phys. Lett.* **2009**, *481*, 240–243.
- [406] F. Weigend, *Phys. Chem. Chem. Phys.* **2006**, *8*, 1057.
- [407] H. R. Kricheldorf, *Die Makromol. Chemie* **1977**, *178*, 905–939.
- [408] J. P. Magnusson, A. O. Saeed, F. Fernández-Trillo, C. Alexander, *Polym. Chem.* **2011**, *2*, 48–59.
- [409] F. Canal, J. Sanchis, M. J. Vicent, *Curr. Opin. Biotechnol.* **2011**, *22*, 894–900.
- [410] J. Cheng, T. J. Deming, *Top. Curr. Chem.* **2012**, *310*, 1–26.
- [411] C. A. Janeway, M. Sela, *Immunology* **1967**, *13*, 29–38.
- [412] N. Benkirane, M. Friedej, G. Guichard, J.-p. Briand, M. H.V. V. Regenmortel, S. Muller, *Biochemistry* **1993**, *268*, 26279–26285.
- [413] M Sela, E Zisman, *FASEB J.* **1997**, *11*, 449–456.
- [414] H. Kanazawa, Y. Matsuura, N. Tanaka, M. Kakudo, T. Komoto, T. Kawai, *Bull. Chem. Soc. Jpn.* **1976**, *49*, 954–956.
- [415] H. Kanazawa, Y. Matsuura, N. Tanaka, M. Kakudo, T. Komoto, T. Kawai, *Acta Crystallogr. Sect. B Struct. Crystallogr. Cryst. Chem.* **1976**, *32*, 3314–3315.
- [416] H. Kanazawa, T. Kawai, Y. Ohashi, Y. Sasada, *Bull. Chem. Soc. Jpn.* **1978**, *51*, 2205–2208.
- [417] H. Kanazawa, *Acta Crystallogr. Sect. E Struct. Reports Online* **2003**, *59*, o1309–o1311.
- [418] H. Kanazawa, T. Kawai, Y. Ohashi, Y. Sasada, *Bull. Chem. Soc. Jpn.* **1978**, *51*, 2200–2204.
- [419] H. Kanazawa, Y. Ohashi, Y. Sasada, *Acta Crystallogr. Sect. C Cryst. Struct. Commun.* **1984**, *40*, 1094–1096.
- [420] H. Kanazawa, H. Uekusa, Y. Ohashi, *Acta Crystallogr. Sect. C Cryst. Struct. Commun.* **1997**, *53*, 1154–1156.
- [421] H. Kanazawa, *Acta Crystallogr. Sect. C Cryst. Struct. Commun.* **2000**, *56*, 469–470.
- [422] H. Kanazawa, *Mol. Cryst. Liq. Cryst. Sci. Technol. Sect. A. Mol. Cryst. Liq. Cryst.* **1998**, *313*, 205–210.
- [423] H. Kanazawa, A. Inada, *Acta Crystallogr. Sect. E Crystallogr. Commun.* **2015**, *71*, 110–112.
- [424] M. Oya, R. Katakai, H. Nakai, Y. Iwakura, *Chem. Lett.* **1973**, *2*, 1143–1144.



- [425] W. D. Fuller, M. S. Verlander, M. Goodman, *Biopolymers* **1976**, *15*, 1869–1871.
- [426] W. H. Daly, D. Poche', *Tetrahedron Lett.* **1988**, *29*, 5859–5862.
- [427] R. Wilder, S. Mobashery, *J. Org. Chem.* **1992**, *57*, 2755–2756.
- [428] D. Mavrogiorgis, P. Bilalis, A. Karatzas, D. Skoulas, G. Fotinogiannopoulou, H. Iatrou, *Polym. Chem.* **2014**, *5*, 6256–6278.
- [429] M. Frankel, A. Berger, *Nature* **1949**, *163*, 213–214.
- [430] M. Frankel, A. Berger, *J. Org. Chem.* **1951**, *16*, 1513–1518.
- [431] P. Doty, A. M. Holtzer, J. H. Bradbury, E. R. Blout, *J. Am. Chem. Soc.* **1954**, *76*, 4493–4494.
- [432] E. R. Blout, R. H. Karlson, *J. Am. Chem. Soc.* **1956**, *78*, 941–946.
- [433] R. Roeske, *J. Org. Chem.* **1963**, *28*, 1251–1253.
- [434] E. Katchalski, I. Grossfeld, M. Frankel, *J. Am. Chem. Soc.* **1946**, *68*, 879–880.
- [435] G. D. Fasman, M. Idelson, E. R. Blout, *J. Am. Chem. Soc.* **1961**, *83*, 709–712.
- [436] M. K. Dygert, G. T. Taylor, F. Cardinaux, H. A. Scheraga, *Macromolecules* **1976**, *9*, 794–801.
- [437] L. T. Plante, E. J. Crawford, M. Friedkin, *J. Med. Chem.* **1976**, *19*, 1295–1299.
- [438] M. Sela, R. Arnon, I. Jacobson, *Biopolymers* **1963**, *1*, 517–525.
- [439] H. R. Kricheldorf, *Chem. Ber.* **1971**, *104*, 87–91.
- [440] P. I. Haris, D Chapman, *Biopolymers* **1995**, *37*, 251–63.
- [441] A. Carlsen, S. Lecommandoux, *Curr. Opin. Colloid Interface Sci.* **2009**, *14*, 329–339.
- [442] X. He, J. Fan, K. L. Wooley, *Chem. - An Asian J.* **2016**, *11*, 437–447.
- [443] N. M. B. Smeets, P. L. J. van der Weide, J. Meuldijk, J. A. J. M. Vekemans, L. A. Hulshof, *Org. Process Res. Dev.* **2005**, *9*, 757–763.
- [444] C. Bonduelle, S. Mazzaferro, J. Huang, O. Lambert, A. Heise, S. Lecommandoux, *Faraday Discuss.* **2013**, *166*, 137.
- [445] M. a. Quadir, M. Martin, P. T. Hammond, *Chem. Mater.* **2014**, *26*, 461–476.
- [446] F. Zhang et al., *J. Am. Chem. Soc.* **2015**, *137*, 2056–2066.
- [447] J. Huang, G. Habraken, F. Audouin, A. Heise, *Macromolecules* **2010**, *43*, 6050–6057.
- [448] D. S. Poche, S. J. Thibodeaux, V. C. Rucker, I. M. Warner, W. H. Daly, **1997**, *9297*, 8081–8084.
- [449] H. Lu, Y. Bai, J. Wang, N. P. Gabrielson, F. Wang, Y. Lin, J. Cheng, *Macromolecules* **2011**, *44*, 6237–6240.
- [450] J. R. Kramer, T. J. Deming, *Biomacromolecules* **2012**, *13*, 1719–1723.

- [451] H. Tang, D. Zhang, *Biomacromolecules* **2010**, *11*, 1585–1592.
- [452] J. Ding, C. Xiao, Z. Tang, X. Zhuang, X. Chen, *Macromol. Biosci.* **2011**, *11*, 192–198.
- [453] J. Hwang, T. J. Deming, *Biomacromolecules* **2001**, *2*, 17–21.
- [454] Y. Ma, B. Chen, N. He, G. Chen, L. Li, C. Wu, *Macromol. Biosci.* **2014**, n/a–n/a.
- [455] A. Berger, J. Noguchi, E. Katchalski, *J. Am. Chem. Soc.* **1956**, *78*, 4483–4488.
- [456] X. Fu, Y. Shen, W. Fu, Z. Li, *Macromolecules* **2013**, *46*, 3753–3760.
- [457] J. T. Pelton, L. R. McLean, *Anal. Biochem.* **2000**, *277*, 167–76.
- [458] T. Miyazawa, *J. Chem. Phys.* **1960**, *32*, 1647.
- [459] M. Iguchi, *J. Polym. Sci. Part A-1 Polym. Chem.* **1970**, *8*, 1013–1021.
- [460] T. Komoto, M. Oya, T. Kawai, *Die Makromol. Chemie* **1974**, *175*, 301–310.
- [461] T. Kawai, T. Komoto, *J. Cryst. Growth* **1980**, *48*, 259–282.
- [462] W. Vayaboury, O. Giani, H. Cottet, S. Bonaric, F. Schué, *Macromol. Chem. Phys.* **2008**, *209*, 1628–1637.
- [463] E. Riedel, *Allgemeine und Anorganische Chemie*, De Gruyter, Berlin, New York, **2010**.
- [464] T. Sekine, K. Ando, M. Machida, Y. Kanaoka, *Anal. Biochem.* **1972**, *48*, 557–568.
- [465] A. W. York, C. W. Scales, F. Huang, C. L. McCormick, *Biomacromolecules* **2007**, *8*, 2337–41.
- [466] R. K. Iha, K. L. Wooley, A. M. Nystrom, D. J. Burke, M. J. Kade, C. J. Hawker, *Chem. Rev.* **2009**, *109*, 5620–5686.
- [467] P. Theato, *J. Polym. Sci. Part A Polym. Chem.* **2008**, *46*, 6677–6687.
- [468] K. A. Günay, P. Theato, H. A. Klok, *J. Polym. Sci. Part A Polym. Chem.* **2013**, *51*, 1–28.
- [469] B. R. Maughon, T. Morita, C. W. Bielawski, R. H. Grubbs, *Macromolecules* **2000**, *33*, 1929–1935.
- [470] J. T. Kopping, Z. P. Tolstyka, H. D. Maynard, *Macromolecules* **2007**, *40*, 8593–8599.
- [471] L. M. Campos, K. L. Killops, R. Sakai, J. M. J. Paulusse, D. Dameron, E. Drockenmuller, B. W. Messmore, C. J. Hawker, C. B. Lyon, *Macromolecules* **2008**, *41*, 7063–7070.
- [472] H. R. Kricheldorf, C. v. Lossow, G. Schwarz, D. Fritsch, *Macromol. Chem. Phys.* **2005**, *206*, 1165–1170.
- [473] L. Mespouille, M. Vachaudéz, F. Suriano, P. Gerbaux, O. Coulem-bier, P. Degée, R. Flammang, P. Dubois, *Macromol. Rapid Commun.* **2007**, *28*, 2151–2158.



- [474] W. Agut, D. Taton, S. Lecommandoux, *Macromolecules* **2007**, *40*, 5653–5661.
- [475] K. Matyjaszewski, V. Coessens, Y. Nakagawa, J. Xia, J. Qiu, S. Gaynor, S. Coca, C. Jasieczek in, **1998**, pp. 16–27.
- [476] P. J. Roth, F. D. Jochum, R. Zentel, P. Theato, *Biomacromolecules* **2010**, *11*, 238–244.
- [477] K. L. Heredia, G. N. Grover, L. Tao, H. D. Maynard, *Macromolecules* **2009**, *42*, 2360–2367.
- [478] M. Nakanishi, K. Kataoka, *Macromol. Symp.* **2009**, *279*, 14–20.
- [479] J. A. Opsteen, J. C. M. van Hest, *Chem. Commun.* **2005**, 57.
- [480] J. Zheng, S. Jung, P. W. Schmidt, T. P. Lodge, T. M. Reineke, *ACS Macro Lett.* **2017**, *6*, 145–149.
- [481] H. Gao, K. Matyjaszewski, *J. Am. Chem. Soc.* **2007**, *129*, 6633–6639.
- [482] K. Khanna, S. Varshney, A. Kakkar, *Polym. Chem.* **2010**, *1*, 1171.
- [483] B. Le Droumaguet, J. Nicolas, *Polym. Chem.* **2010**, *1*, 563.
- [484] C. Boyer, J. Liu, V. Bulmus, T. P. Davis, C. Barner-Kowollik, M. H. Stenzel, *Macromolecules* **2008**, *41*, 5641–5650.
- [485] F. Lecolley, L. Tao, G. Mantovani, I. Durkin, S. Lautru, D. M. Hadleton, *Chem. Commun.* **2004**, *23*, 2026.
- [486] J. Kopeček, *Adv. Drug Deliv. Rev.* **2013**, *65*, 49–59.
- [487] E. Elacqua, D. S. Lye, M. Weck, *Acc. Chem. Res.* **2014**, *47*, 2405–2416.
- [488] K. Kataoka, A. Harada, Y. Nagasaki, *Adv. Drug Deliv. Rev.* **2001**, *47*, 113–131.
- [489] M. Barz, *Nanomedicine* **2015**, *10*, 3093–3097.
- [490] T. Lammers, *Int. J. Pharm.* **2013**, *454*, 527–9.
- [491] D. Schaeffel, A. Kreyes, Y. Zhao, K. Landfester, H. J. Butt, D. Crespy, K. Koynov, *ACS Macro Lett.* **2014**, *3*, 428–432.
- [492] N. H. Hoang, C. Lim, T. Sim, K. T. Oh, *J. Pharm. Investig.* **2017**, *47*, 27–35.
- [493] X. S. Wang, M. A. Winnik, I. Manners, *Angew. Chemie Int. Ed.* **2004**, *43*, 3703–3707.
- [494] W. B. Lee, R. Elliott, K. Katsov, G. H. Fredrickson, *Macromolecules* **2007**, *40*, 8445–8454.
- [495] Y. Mai, A. Eisenberg, *Chem. Soc. Rev.* **2012**, *41*, 5969–85.
- [496] J. E. Poelma, B. P. Fors, G. F. Meyers, J. W. Kramer, C. J. Hawker, *Angew. Chemie - Int. Ed.* **2013**, *52*, 6844–6848.
- [497] A. H. Gröschel, F. H. Schacher, H. Schmalz, O. V. Borisov, E. B. Zhulina, A. Walther, A. H. Müller, *Nat. Commun.* **2012**, *3*, 710.
- [498] A. H. Gröschel, A. Walther, T. I. Löblich, F. H. Schacher, H. Schmalz, A. H. E. Müller, *Nature* **2013**, *503*, 247–251.

- [499] A. Blanz, S. P. Armes, A. J. Ryan, *Macromol. Rapid Commun.* **2009**, *30*, 267–277.
- [500] H.-A. Klok, S. Lecommandoux, *Adv. Mater.* **2001**, *13*, 1217.
- [501] C. Cai, J. Lin, Y. Lu, Q. Zhang, L. Wang, *Chem. Soc. Rev.* **2016**, *45*, 5985–6012.
- [502] M. Lee, B.-K. Cho, W.-C. Zin, *Chem. Rev.* **2001**, *101*, 3869–3892.
- [503] H. M. König, A. F. M. Kilbinger, *Angew. Chemie Int. Ed.* **2007**, *46*, 8334–8340.
- [504] G. Fuks, R. Mayap Talom, F. Gauffre, *Chem. Soc. Rev.* **2011**, *40*, 2475–93.
- [505] J. T. Chen, E. L. Thomas, C. K. Ober, G.-p. Mao, *Science (80-. )*. **1996**, *273*, 343–346.
- [506] X. Wang, G. Guerin, H. Wang, Y. Wang, I. Manners, M. a. Winnik, *Science (80-. )*. **2007**, *317*, 644–647.
- [507] J. B. Gilroy, T. Gädt, G. R. Whittell, L. Chabanne, J. M. Mitchels, R. M. Richardson, M. a. Winnik, I. Manners, *Nat. Chem.* **2010**, *2*, 566–570.
- [508] L. Sun, A. Pitto-Barry, N. Kirby, T. L. Schiller, A. M. Sanchez, M. A. Dyson, J. Sloan, N. R. Wilson, R. K. O'Reilly, A. P. Dove, *Nat. Commun.* **2014**, *5*, 5746.
- [509] L. C. Palmer, S. I. Stupp, *Acc. Chem. Res.* **2008**, *41*, 1674–1684.
- [510] P. A. Korevaar, C. J. Newcomb, E. W. Meijer, S. I. Stupp, *J. Am. Chem. Soc.* **2014**, *136*, 8540–8543.
- [511] E. Krieg, M. M. C. Bastings, P. Besenius, B. Rybtchinski, *Chem. Rev.* **2016**, *116*, 2414–2477.
- [512] T. S. Burkoth, T. L. S. Benzinger, D. N. M. Jones, K. Hallenga, S. C. Meredith, D. G. Lynn, *J. Am. Chem. Soc.* **1998**, *120*, 7655–7656.
- [513] I. W. Hamley, I. a. Ansari, V Castelletto, H Nuhn, A. Rösler, H.-A. Klok, *Biomacromolecules* **2005**, *6*, 1310–1315.
- [514] T. Shimada, S. Lee, F. S. Bates, A. Hotta, M. Tirrell, *J. Phys. Chem. B* **2009**, *113*, 13711–13714.
- [515] D. Eckhardt, M. Groenewolt, E. Krause, H. G. Börner, *Chem. Commun.* **2005**, 2814.
- [516] Y. Mochida, H. Cabral, Y. Miura, F. Albertini, S. Fukushima, K. Osada, N. Nishiyama, K. Kataoka, *ACS Nano* **2014**, *8*, 6724–6738.
- [517] S. Lecommandoux, M.-F. Achard, J. F. Langenwalter, H.-A. Klok, *Macromolecules* **2001**, *34*, 9100–9111.
- [518] H.-A. Klok, J. F. Langenwalter, S. Lecommandoux, *Macromolecules* **2000**, *33*, 7819–7826.
- [519] T. S. Burkoth, T. L. S. Benzinger, V. Urban, D. G. Lynn, S. C. Meredith, P. Thiagarajan, *J. Am. Chem. Soc.* **1999**, *121*, 7429–7430.
- [520] C Chothia, *J. Mol. Biol.* **1973**, 295–302.

- [521] T. A. Tockary et al., *Macromolecules* **2013**, *46*, 6585–6592.
- [522] J. F. Quinn, M. R. Whittaker, T. P. Davis, *Polym. Chem.* **2017**, *8*, 97–126.
- [523] M. M. Pakulska, S. Miersch, M. S. Shoichet, *Science (80-. )*. **2016**, *351*, 4750.
- [524] C. Lawatscheck, M. Pickhardt, S. Wieczorek, A. Grafmüller, E. Mandelkow, H. G. Börner, *Angew. Chemie Int. Ed.* **2016**, *55*, 8752–8756.
- [525] A. Dirisala et al., *Biomaterials* **2014**, *35*, 5359–5368.
- [526] M. Muthukumar, C. K. Ober, E. L. Thomas, *Science (80-. )*. **1997**, *277*, 1225–1232.
- [527] C. Allen, D. Maysinger, A. Eisenberg, *Colloids Surfaces B Biointerfaces* **1999**, *16*, 3–27.
- [528] R. J. Williams, M. Lipowska, G. Patonay, L. Strekowski, *Anal. Chem.* **1993**, *65*, 601–605.
- [529] C. F. van Nostrum, *Soft Matter* **2011**, *7*, 3246.
- [530] Y. Matsumoto et al., *Biomed. Opt. Express* **2010**, *1*, 1209.
- [531] T. Nomoto, Y. Matsumoto, K. Miyata, M. Oba, S. Fukushima, N. Nishiyama, T. Yamasoba, K. Kataoka, *J. Control. Release* **2011**, *151*, 104–109.
- [532] P. M. Mullen et al., *Biochim. Biophys. Acta - Gen. Subj.* **2000**, *1523*, 103–110.
- [533] M. Ogris, S. Brunner, S. Schüller, R. Kircheis, E. Wagner, *Gene Ther.* **1999**, *6*, 595–605.
- [534] T. Merdan, K. Kunath, H. Petersen, U. Bakowsky, K. H. Voigt, J. Kopecek, T. Kissel, *Bioconjug. Chem.* **2005**, *16*, 785–792.
- [535] Y. Vachutinsky, M. Oba, K. Miyata, S. Hiki, M. R. Kano, N. Nishiyama, H. Koyama, K. Miyazono, K. Kataoka, *J. Control. Release* **2011**, *149*, 51–57.
- [536] M. Neu, O. Germershaus, M. Behe, T. Kissel, *J. Control. Release* **2007**, *124*, 69–80.
- [537] M. Oba, Y. Vachutinsky, K. Miyata, M. R. Kano, S. Ikeda, N. Nishiyama, K. Itaka, K. Miyazono, H. Koyama, K. Kataoka, *Mol. Pharm.* **2010**, *7*, 501–509.
- [538] A. D. Miller, *Angew. Chemie - Int. Ed.* **1998**, *37*, 1768–1785.
- [539] A. Akinc et al., *Nat. Biotechnol.* **2008**, *26*, 561–569.
- [540] M. Jayaraman et al., *Angew. Chemie - Int. Ed.* **2012**, *51*, 8529–8533.
- [541] C. Jiménez Calvente, A. Sehgal, Y. Popov, Y. O. Kim, V. Zevallos, U. Sahin, M. Diken, D. Schuppan, *Hepatology* **2015**, *62*, 1285–1297.
- [542] T. Yu, X. Liu, A.-L. Bolcato-Bellemin, Y. Wang, C. Liu, P. Erbacher, F. Qu, P. Rocchi, J.-P. Behr, L. Peng, *Angew. Chemie* **2012**, *124*, 8606–8612.

- [543] L. Nuhn, L. Braun, I. Overhoff, A. Kelsch, D. Schaeffel, K. Koynov, R. Zentel, *Macromol. Rapid Commun.* **2014**, *35*, 2057–2064.
- [544] H. S. Min et al., *Biomacromolecules* **2018**, *19*, 2320–2329.
- [545] T. Fröhlich et al., *J. Control. Release* **2012**, *160*, 532–541.
- [546] C. Scholz, E. Wagner, *J. Control. Release* **2012**, *161*, 554–565.
- [547] C. Q. Mao, J. Z. Du, T. M. Sun, Y. D. Yao, P. Z. Zhang, E. W. Song, J. Wang, *Biomaterials* **2011**, *32*, 3124–3133.
- [548] W. Zhang, J. He, Z. Liu, P. Ni, X. Zhu, *J. Polym. Sci. Part A Polym. Chem.* **2010**, *48*, 1079–1091.
- [549] T. Segura, J. A. Hubbell, *Bioconjug. Chem.* **2007**, *18*, 736–745.
- [550] J. Du, Y. Sun, Q. S. Shi, P. F. Liu, M. J. Zhu, C. H. Wang, L. F. Du, Y. R. Duan, *Int. J. Mol. Sci.* **2012**, *13*, 516–533.
- [551] T. Sim, G. Park, H. Min, S. Kang, C. Lim, S. Bae, E. S. Lee, Y. S. Youn, K. T. Oh, *J. Bioact. Compat. Polym.* **2017**, *32*, 280–292.
- [552] M. Guo, Y. Yan, X. Liu, H. Yan, K. Liu, H. Zhang, Y. Cao, *Nanoscale* **2010**, *2*, 434–441.
- [553] L. Du et al., *Theranostics* **2017**, *7*, 3432–3445.
- [554] H. J. Kim, K. Miyata, T. Nomoto, M. Zheng, A. Kim, X. Liu, H. Cabral, R. J. Christie, N. Nishiyama, K. Kataoka, *Biomaterials* **2014**, *35*, 4548–4556.
- [555] Z. X. Zhao et al., *Biomaterials* **2012**, *33*, 6793–6807.
- [556] F. Perche, S. Biswas, T. Wang, L. Zhu, V. P. Torchilin, *Angew. Chemie - Int. Ed.* **2014**, *53*, 3362–3366.
- [557] H. Takemoto, K. Miyata, S. Hattori, T. Ishii, T. Suma, S. Uchida, N. Nishiyama, K. Kataoka, *Angew. Chemie - Int. Ed.* **2013**, *52*, 6218–6221.
- [558] L. Du et al., *Biomaterials* **2018**, *176*, 84–93.
- [559] J. Xin, D. Liu, C. Zhong, *J. Phys. Chem. B* **2009**, *113*, 9364–9372.
- [560] B Pulaski, S Ostrand-Rosenberg, *Curr. Protoc. Immunol.* **2001**, *Chapter 20*, Unit 20.2.

*Ich habe mich mein Leben lang  
dagegen gewehrt, das zu werden, was man  
heutzutage einen richtigen Erwachsenen nennt:  
nämlich jenes entzauberte, banale, aufgeklärte Krüppelwesen,  
das in einer entzauberten, banalen, aufgeklärten Welt  
sogenannter Tatsachen existiert.*

**— Michael Ende**

Zettelkasten. Skizzen und Notizen (1994)

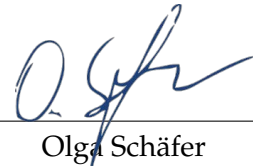


## DECLARATION

---

I hereby declare that I wrote the dissertation submitted without any unauthorized external assistance and used only sources acknowledged in the work. All textual passages which are appropriated verbatim or paraphrased from published and unpublished texts as well as all information obtained from oral sources are duly indicated and listed in accordance with bibliographical rules. In carrying out this research, I complied with the rules of standard scientific practice as formulated in the statutes of Johannes Gutenberg University Mainz to insure standard scientific practice.

*Mainz, June 2018*



---

Olga Schäfer





## COLOPHON

This document was typeset using the typographical look-and-feel `classicthesis` developed by André Miede. The style was inspired by Robert Bringhurst's seminal book on typography "*The Elements of Typographic Style*". `classicthesis` is available for both  $\text{\LaTeX}$  and  $\text{\LyX}$ :

<https://bitbucket.org/amiede/classicthesis/>